

DELHI COLLEGE OF ENGINEERING

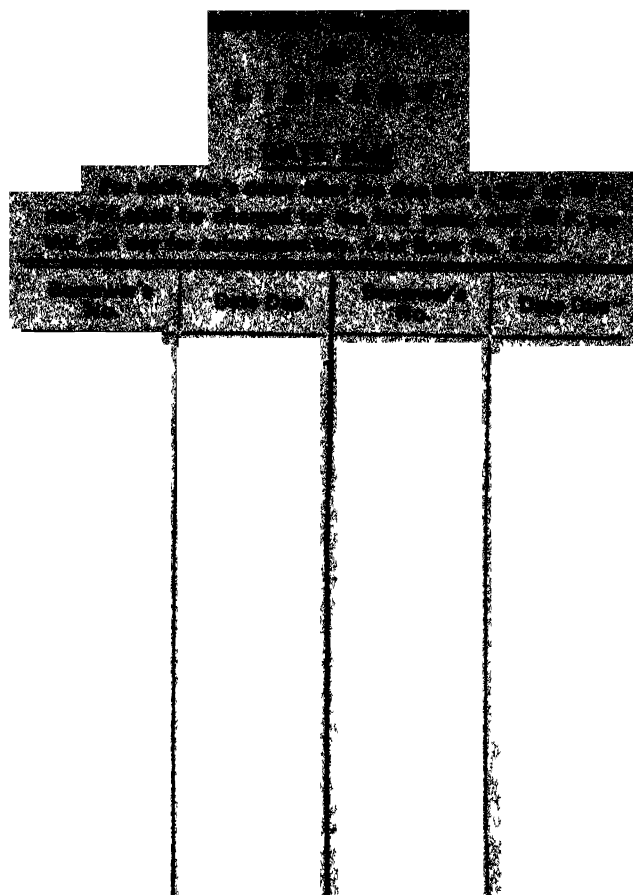


LIBRARY

Class No. _____

Book No. _____

Accession No. _____



Applied Scientific Research

**An International Journal on
the Applications of Fluid Dynamics**

VOLUME 50 / 1993

Kluwer Academic Publishers

P.O. Box 17, 3300 AA Dordrecht, The Netherlands
P.O. Box 17, 3300 AA Dordrecht, The Netherlands

Applied Scientific Research

An International Journal on
the Applications of Fluid Dynamics

Editor-in-Chief

F.T.M. Nieuwstadt, Laboratory for Aero- and Hydrodynamics, Technical University of Delft,
Rotterdamseweg 145, 2628 AL Delft, The Netherlands.

BITNET: WBAHNIE @ HDDETUD1.

Associate Editors

P.C.T. de Boer, Sibley School of Mechanical and
Aerospace Engineering, Cornell University,
Ithaca, NY 14853, U.S.A.

BITNET: W6YJ @ CORNELLA

A.M. Savill, Department of Engineering, T
pington Street, Cambridge CB2 1PZ, England

EARN/BITNET: AMS3 @ PHX.CAM.AC.UK

Editorial Board

R.B. Bird, University of Wisconsin-Madison, Wis.,
U.S.A.

H. Buggisch, University of Karlsruhe, Karlsruhe,
Germany

A.K. Chesters, Unilevers Research, Vlaardingen,
The Netherlands

J.F. Dijksman, Philips Lighting, Eindhoven, The
Netherlands

L. Hesselink, Stanford University, Stanford, Calif.,
U.S.A.

T. Kambe, University of Tokyo, Tokyo, Japan

G.D.C. Kuiken, Technical University of Delft, Delft,
The Netherlands

G.E.A. Meier, Max-Planck-Institut für Strömu
forschung, Göttingen, Germany

G. Ooms, Koninklijke-Shell Exploration
Production Laboratory, Rijswijk, The Netherlands

J.K. Platten, University of Mons, Mons, Belgium

A. Pollard, Queens University of Kingston, Onto
Canada

J.A. Steketee, Technical University of Delft, D
The Netherlands

L. van Wijngaarden, Technical University
Twente, Enschede, The Netherlands

J.S. Walker, University of Illinois, Urbana,

ISSN 0003-6994

All Rights Reserved

© 1993 Kluwer Academic Publishers

No part of the material protected by this copyright notice may be reproduced or
utilised in any form or by any means, electronic or mechanical,
including photocopying, recording or by any information storage and
retrieval system, without written permission from the copyright owner

Printed in the Netherlands

Contents of Volume 50 (1993)

Vol 50 No. 1 January 1993

<i>Publisher's announcement</i>	v
M. Bouthier: Vorticity in plane parallel, axially symmetrical or spherical flows of viscous fluid	1
A. Nakayama, F. Kuwahara and H. Koyama: Transient non-Darcy free convection between parallel vertical plates in a fluid saturated porous medium	29
M. Mani, S.N. Tiwari and J.P. Drummond: Investigation of chemically reacting and radiating supersonic flow in channels	43
G. Rehlinger: Damped pitching of a slender body partially immersed in a liquid	69
A. Nakayama and A.V. Shenoy: Combined forced and free convection heat transfer in power law fluid saturated porous media	83

Vol 50 No 2 March 1993

G. Petre, M.A. Azouni and K. Tshinyama: Marangoni convection at alcohol aqueous solutions-air interfaces	97
F.A. Mohamed: The energy integral method: application to linear hyperbolic heat conduction problems	107
N. Hatta, H. Fujimoto and H. Takuda: Numerical analysis of flow pattern of impinging liquid sprays in a cold model for cooling a hot flat plate	129
S.M. Sami and J. Schnotale: Prediction of forced convective condensation of non-azeotropic refrigerant mixtures inside enhanced surface tubing	149
J.B.W. Kok: Collision dynamics of bubble pairs moving through a perfect liquid	169

Preface

VII

S. Tardu, T.V. Truong and B. Tanguay: Bursting and structure of the turbulence in an internal flow manipulated by riblets	189
Y.P. Tang and D.G. Clark: On near-wall turbulence generating events in a turbulent boundary layer on a riblet surface	215
A.D. Schwarz-van Manen, A.F.M. van Geloven, J. Nieuwenhuizen, J.C. Stouthart, K. Krishna Prasad and F.T.M. Nieuwstadt: Friction velocity and virtual origin estimates for mean velocity profiles above smooth and triangular riblet surfaces	233
P. Luchini: Viscous sublayer analysis of riblets and wire arrays	255
L. Djenidi and R.A. Antonia: Riblet flow calculation with a low Reynolds number k - ϵ model	267
B.E. Launder and S.P. Li: On the prediction of riblet performance with engineering turbulence models	283
S. Tullis and A. Pollard: Modelling the time-dependent flow over riblets in the viscous wall region	299
K.S. Choi and N. Fujisawa: Possibility of drag reduction using d -type roughness	315
E. Savory, N. Toy, P.J. Disimile and R.G. DiMicco: The drag of three-dimensional rectangular cavities	325
H.-W. Bewersdorff and H. Thiel: Turbulence structure of dilute polymer and surfactant solutions in artificially roughened pipes	347
A. Hamdouni and J.P. Bonnet: Effect of external manipulators on the heat transfer on a flat plate turbulent boundary layer	369

Vorticity in plane parallel, axially symmetrical or spherical flows of viscous fluid

M. BOUTIER

Laboratoire de Modélisation en Mécanique, C.N.R.S., 166, Place Jussieu, F-75230 Paris Cedex 05, France

Received 25 June 1990; accepted in revised form 8 July 1991

Abstract. For viscous (barotropic or incompressible) fluids it is shown that, if the vorticity and the viscous force are orthogonal, vortex lines are convected by a vector field which fits with the velocity field when viscosity vanishes (extension of Helmholtz theorem); it is also found that energy remains constant along the field lines of this vector field (extension of Bernoulli theorem).

If moreover vorticity and velocity are orthogonal too, the magnitude of the vorticity then behaves as the density of a fluid which flows along streamlines according to this very same vector field. These properties are mainly encountered for plane parallel flows, axial-symmetrical flows, spherical flows, but also for some other miscellaneous flow geometries such as unidirectional or radial flows. The set of the former three flows can even be characterized by these properties: that enhances this set of important flow geometries, avails a general view on vorticity behavior, and explains the great simplicity of vorticity equations in these cases. Numerous examples and comments are given for illustrating.

1. Introduction

When dealing with perfect fluid flows, two celebrated theorems are valuable: Bernoulli's theorem and Helmholtz's theorem [1-4]. The former connects the pressure, the velocity and the body force potential; the latter asserts that perfect fluid flows are circulation preserving motion, and so vortex lines are convected by the fluid. In plane parallel flows of viscous incompressible fluids, some extensions of these theorems can be set up: both theorems remain true if one replaces velocity (resp. the streamlines) by a vector (resp. field lines) which fits with the fluid velocity (resp. the streamlines) when viscosity vanishes; moreover, it can be stated that the magnitude of the vorticity behaves as the density of a (compressible) fluid which flows according to the same so-defined vector field. For want of a precise term for this behavior, we shall use for the time being the term *vortex flow*, and abbreviate this difficulty of terminology.

In fact, the occurrence of these properties is not fortuitous: here, it is shown that the extensions of these theorems merely stem from the fact that *the viscous force is everywhere orthogonal to vorticity*: this provides a condition which turns out to be satisfied as well for (barotropic) compressible fluids as for several other flow geometries. The analysis can even be successfully applied to isoenergetic flows,

isothermal flows, etc. . . . In other respects, the vortex flow appears to result from the threefold connection of:

$$\boldsymbol{\omega} \cdot \mathbf{v} = \boldsymbol{\omega} \cdot \text{curl } \boldsymbol{\omega} = \boldsymbol{\omega} \cdot \nabla \text{ div } \mathbf{v}. \quad (7)$$

Referring to a time-honored use [8, 13, 14], we shall say that a vector field \mathbf{v} is a complex lamellar if $\mathbf{v} \cdot \text{curl } \mathbf{v}$ equals zero everywhere. Thus, the vanishing of the two first terms of (7) amounts to assuming the velocity field and the vorticity field being both complex lamellar. Because of (7), vortex is claimed flowing also in axially symmetrical flows, spherical flows, unidirectional flows, and radial flows from a point. That list is rather exhaustive: if, for instance, flow geometry is specified by prescribing a set of streamsheets, then the threefold condition is proved to define the set of three very usual motion geometries only: these are the plane parallel flows, axially symmetrical flows, and spherical flows.

After some remarks about ideal fluids flows (section 2), the case of viscous fluids is dealt with in section 3. Applications to usual flow geometries are given in section 4, while incompressible fluids are especially studied in section 5. Finally, the characterization of the set of the three most important flow geometries is reported in section 6.

2. Preliminary remarks concerning ideal fluids flows

In this preliminary section, we prove that Bernoulli and Helmholtz theorems can be formulated in a general way, so that they are relevant also for isoenergetic flows and isothermal flows. The method of proof will be useful for the sequel, and it shows that future extensions are available.

For ideal fluids, the velocity \mathbf{v} , the vorticity $\boldsymbol{\omega} = \text{curl } \mathbf{v}$, and the pressure p are connected via Euler's equation, i.e.:

$$\frac{\partial \mathbf{v}}{\partial t} + \boldsymbol{\omega} \wedge \mathbf{v} = -\frac{1}{\rho} \nabla p - \frac{1}{2} \nabla v^2 - \nabla e.$$

Here, the body forces are assumed deriving from a potential e ; mass density is denoted by ρ , and the symbol ∇ stands for del operator. Owing to thermodynamics, the pressure term can be expressed by:

$$\frac{1}{\rho} \nabla p = \nabla h - T \nabla S, \quad (1)$$

with T , h , S designating temperature, specific enthalpy, and specific entropy.

Related to ideal fluid hypothesis, entropy is usually supposed to be constant throughout the flow. One is thus led to consider barotropic fluids for which $p = p(\rho)$

and for which energy F is to be defined by

$$\int_V dp = \frac{1}{\gamma} + c \left(\int_V T dS \right)$$

Nevertheless, other assumption about constitutive equations may be done in order to account for diverse phenomena: for example, the hypothesis of isoeNERgetic flow can be more appropriate for certain problems of combustion (that is the so-called Crocco hypothesis [6]); then total enthalpy H is introduced as being

$$h = \dots \quad (7)$$

and it is specified to be constant throughout the flow (H and h are different whenever $dS \neq 0$).

* One may also consider isothermal flows without referring to any supplementary law (for instance this hypothesis has been handled for fluids of grad N by Casal and Gouin [15] section 3): the fluid is not prescribed as gas* or a perfect gas (that may account for thermocapillary fluids, suspensions, mixtures of fluids or crystal liquids).

In all these cases, the right hand side of Euler's equation turns to take the form ∇B with A and B standing for two scalar functions ($A = 1/B = 1/T$ for barotropic flow, $A = 1/B = S$ for isoeNERgetic flows, $A = 1/B = H = 1/T$ for isothermal flows). One may then restrict analysis to steady cases, and can infer

$$\mathbf{v} \cdot \nabla B = \boldsymbol{\omega} \cdot \nabla B = 0 \quad \text{curl} \left(\boldsymbol{\omega} - \frac{\mathbf{v}}{A} \right) = 0$$

The first two equations follow from multiplying Euler's equation by \mathbf{v} and $\boldsymbol{\omega}$ whereas the last one is obtained by dividing by A and taking curl. The first line means that the quantity B remains constant along the streamlines as well as along the vortex lines: this is the Bernoulli theorem for a more general class of flows than barotropic fluid flows. From the second line, it is deduced that velocity circulation is preserved by the motion $\mathbf{v} = A$ (see Germain [7] p. 38) and, owing to classical proofs, both vortex lines and vortex tubes are merely convected by the very same flow. In particular, we can state that: *for steady isoeNERgetic flows, entropy is constant along both the streamlines and the vortex lines, while the vortex lines move in accordance with the velocity $\mathbf{v} = T$.*

When can such new forms of Helmholtz and Bernoulli theorems be obtained in general? The answer stems from the fact that a vector field (say the right-hand side of Euler's equations) gets the general form $A \nabla B$ if and only if it is complex lamellar (see

*Here gas means that there are no more than two independent internal variable.

4 M. Bouthier

[5] section 33, p. 824); that leads to the condition:

$$(-\nabla H + T\nabla S) \cdot (\nabla T \wedge \nabla S) = 0.$$

which after expansion becomes:

$$\nabla H \cdot (\nabla T \wedge \nabla S) = 0.$$

Thus the Jacobian-determinant of H, T, S vanishes and the quantities H, T, S must be dependent according to:

$$F(H^*, T, S) = 0 \quad \text{throughout the flow.} \quad (3)$$

Here, F stands for any scalar function. For instance, the following particular cases are important:

Isentropic flows	$(S = \text{const})$	$B \equiv E$	$A = 1$
Isoenergetic flows	$(H = \text{const})$	$B \equiv S$	$A = T$
Isothermal flows	$(T = \text{const})$	$B = H - TS$	$A = 1$
Barotropic flows	$\left. \begin{array}{l} S \equiv S(T) \\ \text{similarly } \rho = \rho(p) \end{array} \right\}$	$B = E$	$A = 1.$
Incompressible flows			

For each of these flows, variants of Bernoulli and Helmholtz theorems can be stated. This list ought not to be closed, and in future other interesting cases can be considered.

3. Viscous fluids, vortex flow

Hereinafter, we are concerned with viscous fluid flows which are governed by the Navier-Stokes equation, i.e.:

$$\frac{\partial \mathbf{v}}{\partial t} + \boldsymbol{\omega} \wedge \mathbf{v} = -\frac{1}{\rho} \nabla p - \frac{1}{2} \nabla v^2 - \nabla e + \frac{\mu}{\rho} \Delta \mathbf{v} + \lambda \nabla(\text{div } \mathbf{v}),$$

where the symbol Δ stands for Laplace operator, and μ, λ stand for coefficients of viscosity (they are assumed to be constant); it can also be written as:

$$\frac{\partial \mathbf{v}}{\partial t} + \boldsymbol{\omega} \wedge \mathbf{v} = -\frac{1}{\rho} \nabla p - \frac{1}{2} \nabla v^2 - \nabla e - \frac{\mu}{\rho} \text{curl } \boldsymbol{\omega} + \frac{\lambda + \mu}{\rho} \nabla(\text{div } \mathbf{v}). \quad (4)$$

The viscous force is the sum of the two last terms, and it will be referred to as:

$$\mathbf{F}_{\text{viscous}} \equiv -\frac{\mu}{\rho} \mathbf{curl} \, \boldsymbol{\omega} + \frac{\lambda + \mu}{\rho} \nabla \operatorname{div} \mathbf{v}. \quad (5)$$

In this section, two general examples can be considered:

1. Barotropic or incompressible fluid flows (here are included isentropic flows); for this case, Navier-Stokes equation is reduced to:

$$\frac{\partial \mathbf{v}}{\partial t} + \boldsymbol{\omega} \wedge \mathbf{v} = -\nabla H - \frac{\mu}{\rho} \mathbf{curl} \, \boldsymbol{\omega} + \frac{\lambda + \mu}{\rho} \nabla \operatorname{div} \mathbf{v},$$

with H being defined above.

2. Isoenergetic flows: the related form of Navier-Stokes equation is:

$$\frac{\partial \mathbf{v}}{\partial t} + \boldsymbol{\omega} \wedge \mathbf{v} = T \nabla S - \frac{\mu}{\rho} \mathbf{curl} \, \boldsymbol{\omega} + \frac{\lambda + \mu}{\rho} \nabla \operatorname{div} \mathbf{v}.$$

We shall now prove the following result (where the magnitude of $\boldsymbol{\omega}$ is designated by ω):

Consider a flow of viscous barotropic or incompressible fluid; if everywhere in a domain vorticity stands orthogonal to the viscous force (5), then vorticity flux is convected by the vector field:

$$\mathbf{v}^* = \mathbf{v} + \frac{\boldsymbol{\omega}}{\omega^2} \wedge \mathbf{F}_{\text{viscous}} \quad (6)$$

(and so vortex lines move according to the velocity \mathbf{v}^) in that domain. Moreover, if the flow is steady, the energy H is constant along the vector lines of \mathbf{v}^* as well as along the fluid flow vortex lines (in the same domain).*

The assertion similarly holds true for steady flows which agree with (3) provided that one replaces " \mathbf{v}^* " and "the energy E " respectively by \mathbf{v}^*/A and the quantity B . For instance, vortex lines move according to the velocity \mathbf{v}^*/T in isoenergetic flows, and there entropy is constant along the vector lines of \mathbf{v}^*/T .

When viscosity vanishes, the vector \mathbf{v}^* tends toward the fluid velocity; thus, classical Helmholtz and Bernoulli theorems are retrieved as a particular case.

The assumption of orthogonality between viscous forces and vorticity may seem to be inconvenient or not realistic; in fact, this condition will turn out to be verified for most usual flow geometries such as plane parallel flows, axially symmetrical flows, spherical flows, unidirectional flows, and radial flows from a point.

The proof is readily obtained from section 2 by recalling that Euler's equation has been written as:

$$\boldsymbol{\omega} \wedge \mathbf{v} = -\nabla E \quad (\text{or } A\nabla B).$$

Within these considerations, we seek to transform the viscous terms of Navier–Stokes equation into a vector product $\boldsymbol{\omega} \wedge \mathbf{G}$; such a form is possible if (and only if) $\mathbf{F}_{\text{viscous}}$ stands orthogonal to $\boldsymbol{\omega}$. Now, the result is defined within undetermination for an additional vector colinear with $\boldsymbol{\omega}$. This undetermination can be dropped out without lack of generality (the surfaces spanned by $\boldsymbol{\omega}, \mathbf{v}^*$ remain the same) by choosing the vector \mathbf{G} as being:

$$\mathbf{G} = -\frac{\boldsymbol{\omega}}{\omega^2} \wedge \mathbf{F}_{\text{viscous}}.$$

Thereby Navier–Stokes equation is transformed into:

$$\frac{\partial \mathbf{v}}{\partial t} + \boldsymbol{\omega} \wedge \mathbf{v}^* = -\nabla E \quad (\text{or } A\nabla B).$$

So, we get the same form of equation as Euler's equation, and the assertion is inferred from it (for flows which agree with (3) the part of the theorem involving unsteadiness holds true only if A stands for a constant).

Let us now consider flows for which the velocity field is moreover complex-lamellar (Ionescu-Bujor [8] has studied the properties of such flows when dealing with ideal fluids). By taking into account this complementary hypothesis, the following result can be obtained:

In a steady barotropic (or incompressible) viscous fluid flow, if the three following conditions hold everywhere:*

$$\boldsymbol{\omega} \cdot \mathbf{v} = \boldsymbol{\omega} \cdot \text{curl } \boldsymbol{\omega} = \boldsymbol{\omega} \cdot \nabla \text{div } \mathbf{v} = 0, \quad (7)$$

then the vorticity can be considered as the surface density of a fictitious (compressible) fluid flowing along streamsheets (perpendicular to the vortex lines) according to the velocity \mathbf{v}^ . The streamlines of that vortex flow are but the energy lines $E = \text{Const}$ of the actual fluid flow.*

That is, indeed, a noticeable property for vorticity: in the most general case, when the kinematical condition (7) does not hold, vorticity is in fact partly diffused, partly convected. This enhances the class of flows which is associated to (7).

*The assertion is also true for unsteady flows provided that the vortex lines remain steady.

For proof, we remark that from (7) the field ω is complex lamellar and hence there exists a family of surfaces perpendicular to the vortex lines (see [5] section 33, p. 824). Since ω stands everywhere normal to \mathbf{v}^* as well as to \mathbf{v} , every surface of this family is a streamsheet with respect to the flows \mathbf{v} and \mathbf{v}^* . Let (Σ) designate anyone of these surfaces, the main part of the proof is obtained from getting the curl of the new form of Navier–Stokes equation, that is:

$$\text{curl}(\omega \wedge \mathbf{v}^*) = 0.$$

Due to this, the flux of ω is convected by the flow \mathbf{v}^* ; this holds true in particular for the flux of ω through any area Σ^* of (Σ) , that is:

$$\frac{d^*}{dt} \iint_{\Sigma^*} \omega \cdot \mathbf{n} \, d\sigma^* = 0.$$

Here, d^*/dt stands for the material derivative with respect to the flow \mathbf{v}^* ; $\mathbf{n} \, d\sigma$ denotes the vector normal to the surface Σ^* ; and $d\sigma^*$ is the elementary area of Σ^* . Because of the orthogonality of ω and (Σ) , we now have:

$$\iint_{\Sigma^*} \omega \cdot \mathbf{n} \, d\sigma^* = \iint_{\Sigma^*} \omega \, d\sigma^*.$$

Then, the material derivative of the right-hand side vanishes, and the amount of ω thus appears to be wholly convected by the flow \mathbf{v}^* : that is the known result.

At first sight, the constraints imposed by (7) may indeed seem very restrictive. However, when the author sought for geometries such as $\omega \cdot \mathbf{F}_{\text{viscous}} = 0$, he found only flows for which the three conditions were satisfied altogether. To conclude, let us remark that, whenever the fluid is incompressible, the last condition of (7) is automatically fulfilled, and thus a special study seems to be suitable; that will be performed in section 4.

4. Application to plane parallel flows, axially symmetrical flows, and spherical flows

Let us first consider the plane parallel flows: the vorticity is $\omega \mathbf{k}$ (\mathbf{k} being the unit vector perpendicular to the flow plane), and the curl of it is $-\mathbf{k} \wedge \nabla \omega$. This last vector lies in the flow plane as well as $\nabla \text{div } \mathbf{v}$, hence (7) is verified.

The family of the surface (Σ) is the set of planes parallel to the flow plane; the vector \mathbf{v}^* is expressed by:

$$\mathbf{v}^* = \mathbf{v} + \frac{\mathbf{k}}{\rho\omega} \wedge [\mu \mathbf{k} \wedge \nabla \omega + (\lambda + \mu) \nabla \text{div } \mathbf{v}],$$

and this can be reduced to:

$$\mathbf{v}^* = \mathbf{v} - \frac{\mu}{\rho} \nabla \log \omega + \frac{\lambda + \mu}{\rho \omega} \mathbf{k} \wedge \nabla(\operatorname{div} \mathbf{v}). \quad (8)$$

Vortex does flow along the plane (Σ), but it flows also in any three dimensional domain: as a matter of fact, let the amount of vorticity contained in the elementary volume $d\sigma^* dx$ be $\omega d\sigma^* dx$; then, while the elementary volume is moving in accordance with the velocity \mathbf{v}^* , this amount remains constant as well as $\omega d\sigma^*$ for plane parallelism. For that, continuity of vorticity motion implies the following equation to hold true:

$$\frac{\partial \omega}{\partial t} + \operatorname{div} \omega \mathbf{v}^* = 0. \quad (9)$$

Figure 1 depicts energy lines (i.e. streamlines of vortex flow) for the Poiseuille flow, the Blasius boundary layer, the flow past a wedge* and the two-dimensional stagnation flow. In all these cases, vorticity spouts out from the wall, whereas the axis of symmetry stands for singular sink lines. (The streamlines of the fluid flow are represented by the following values of Ψ/v : 0, 7, 21, 35, 49 for (d) the Blasius boundary layer; 0, 4, 12, 20, 28 for (e) the flow past a wedge; 0, 0.05, 0.2, 0.5, 1, 1.5, 2 for (f) the stagnation flow. Throughout these examples, the streamline of value 0 stands for the axis.)

For studying axially symmetrical flows, the cylindrical coordinates (r, θ, z) may be suitably introduced: the velocity is supposed to be lying in the meridional planes $\theta = \text{const}$, and not depending upon θ ; thus, the following relations holds true with $(\mathbf{e}_r, \mathbf{e}_\theta, \mathbf{k})$ being the triplet of canonical unit vectors related to cylindrical coordinates:

$$\begin{aligned} \omega &= \omega(r, z) \mathbf{e}_\theta, \\ \operatorname{curl} \omega &= -\frac{\partial \omega}{\partial z} \mathbf{e}_r + \frac{1}{r} \frac{\partial(r\omega)}{\partial r} \mathbf{k}, \\ \nabla \operatorname{div} \mathbf{v} &= \frac{\partial}{\partial r} (\operatorname{div} \mathbf{v}) \mathbf{e}_r + \frac{\partial}{\partial z} (\operatorname{div} \mathbf{v}) \mathbf{k}. \end{aligned}$$

The conditions (7) are thus obviously verified, and the vector \mathbf{v}^* turns out to be:

$$\mathbf{v}^* = \mathbf{v} - \frac{\mu}{\rho} \nabla \log r\omega + \frac{\lambda + \mu}{\rho} \mathbf{e}_\theta \wedge \frac{\nabla \operatorname{div} \mathbf{v}}{\omega}. \quad (10)$$

*It is the so-called Falkner-Skan flows (see [11] section 9a). Figures (d), (e) have been set up with the help of Kaplun's optimal coordinates [9, 10]).

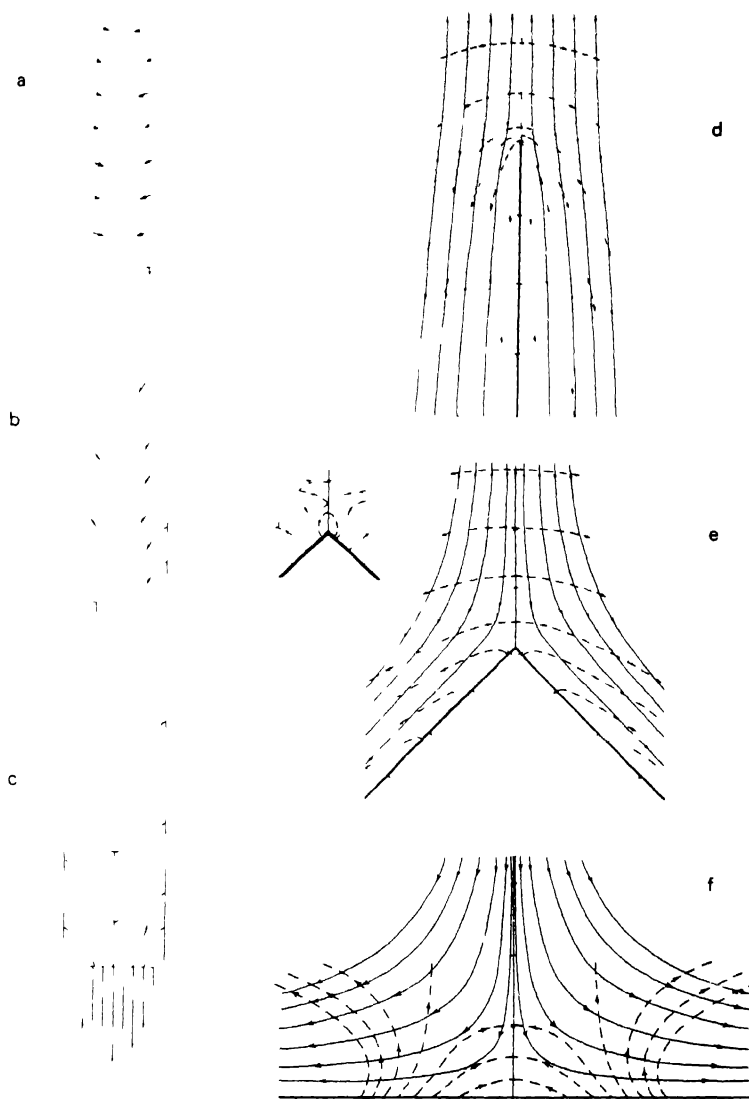


Fig 1 Plane parallel flows of incompressible viscous fluid The dashed curves are streamlines of the vortex flow (a), (b), (c) Poiseuille flow in a tube for different increasing Reynolds numbers, velocities are reminded in the bottom parts (d) Blasius boundary layer on a sem infinite plate, streamlines of the fluid flow are represented by solid curves, axis graduations are related to the distances from the leading edge $U_{\infty}x/\nu = 50, 100, 150$. (e) Boundary layer flow past a wedge (Falkner-Skan flows), the angle of the wedge is $\pi/2$, enlargement of the apex vicinity is shown on the left there is appearing backward vortex flow Marks are plotted for the distances $(3U_1/4\nu)^{1/3}x = 5, 10, 15$ from the wedge vertex (f) Stagnation in plane flow (Hiemenz flow), graduations are located at distance $(a/\nu)^{1/2}x = 0, 1, 2$ apart from the stagnation point The notations a and U_1 are copied out from [11] sections IX a and V 9

Each meridional plane is a surface (Σ), but now vortex is no longer flowing in space: the surface amount $\omega \, dr \, dz$ is indeed convected by the flow \mathbf{v}^* , but in cylindrical coordinates, the elementary volume is $d\tau = r \, dr \, dz \, d\theta$, thus, the volume amount which is preserved, by symmetry is

$$\omega \, dr \, dz \, d\theta = \frac{\omega}{r} \, d\tau.$$

Therefore, the vorticity amount $\omega \, d\tau$ is not flowing in space, but what is convected by three dimensional flows is the amount of ωr^{-1} . As above, there is inferred an equation of continuity, it is.

$$\frac{\partial}{\partial t} \left(\frac{\omega}{r} \right) + \text{div} \left(\frac{\omega}{r} \mathbf{v}^* \right) = 0 \quad (11)$$

The streamlines of \mathbf{v}^* (which are also the energy lines of the actual fluid flow) are

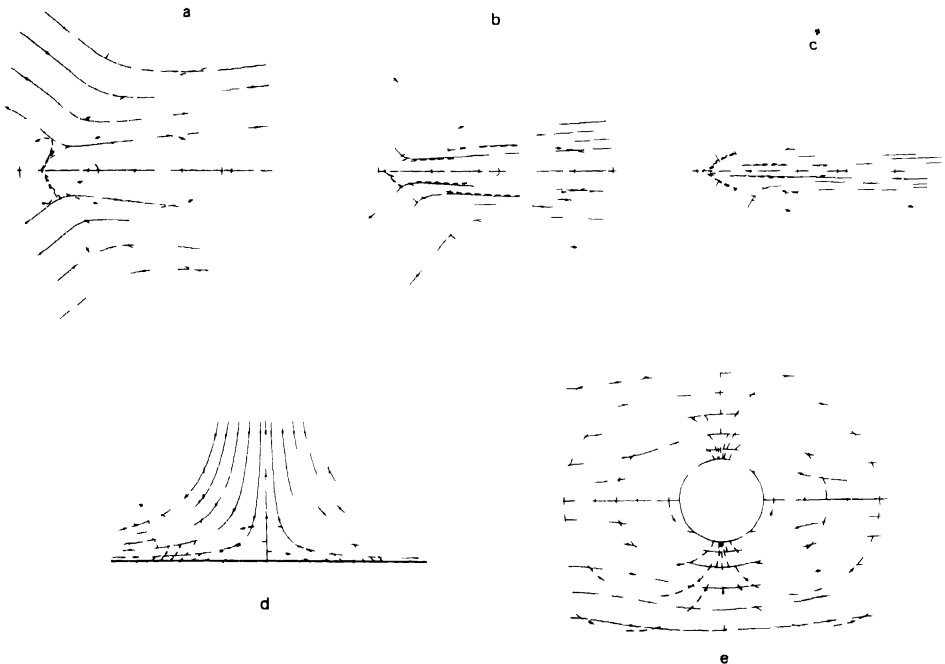


Fig 2 Axially symmetrical flows (a), (b), (c) There is represented the submerged jet of Landau-Squire for the half apex angle values $\varphi = \pi/3, \pi/4, \pi/6$ respectively (The axis graduation is related to the distances from the jet nozzle $x/L = 10, 20, 30, 40$) (d) Stagnation in three dimensional flow (the marks are located at distance $(a/v)^{1/2} x = 1, 2, 3$ from the stagnation point) (e) Stokes flow past a sphere, the sphere radius is 0.4, here the streamlines of the vortex flow fit with the pressure lines, they intersect the axis of symmetry at points $x = 0.5, 1.5$

drawn in Fig. 2 for the submerged jet of Squire–Landau, and for stagnation in three dimensional flows. A comment must be noted for the former case: the vector lines of \mathbf{v}^* are easily found, being defined by:

$$\frac{E}{2\nu(A^2-1)} R^2 = \frac{A^2-1}{(A-\cos \varphi)^4} - \frac{1}{(A-\cos \varphi)^2}, \quad (A > 1, R^2 = r^2 + z^2).$$

Here, A stands for a parameter depending on the strength of the momentum source (for definition and notations of that flow, one can refer to Landau and Lifschitz [12], p. 81), and φ stands for the polar angle measured from the z axis. When the energy E is varied, one curve is deduced from the other by a change of scale of R . Hence, vortex spouts out from the origin, and flows either forward or backward according to the angle φ whether smaller or greater than $\cos^{-1}(A - \sqrt{A^2-1})$. Because of that feature, and because the energy which goes backward is rather small, it may be convenient to define this half apex angle as the jet limit instead of Landau's constant $\cos^{-1}(A^{-1})$. (The streamlines of the fluid flow are represented for the following values: $\Psi/\nu L = 0, 14, 28, 42, 56$ for (a), (b), (c) the submerged jet*; $\Psi(a/\nu^3)^{1/2} = 0, 0.04, 0.36, 1, 1.96, 3.24$ for (d) the stagnation flow; 0 being the value associated to the axis of symmetry*.)

At last, spherical flows can be considered: for dealing with them, the spherical coordinates (R, θ, φ) are appropriately introduced (the radius R is equal to $(r^2 + z^2)^{1/2}$, the angles θ and φ are the same as above), and let $(\mathbf{e}_R, \mathbf{e}_\theta, \mathbf{e}_\varphi)$ be the triplet of unit vectors associated to R, θ, φ : fluid velocity and vorticity are specified by:

$$\mathbf{v} = \frac{1}{R} V_\theta(\theta, \varphi) \mathbf{e}_\theta + \frac{1}{R} V_\varphi(\theta, \varphi) \mathbf{e}_\varphi,$$

$$\boldsymbol{\omega} = \omega \mathbf{e}_R, \quad \text{with} \quad \omega = \frac{1}{R^2 \sin \varphi} \left[\frac{\partial}{\partial \varphi} V_\theta \sin \varphi - \frac{\partial}{\partial \theta} V_\varphi \right].$$

From these formulas, there are derived:

$$\text{curl } \boldsymbol{\omega} = -\frac{1}{R} \frac{\partial \omega}{\partial \varphi} \mathbf{e}_\theta + \frac{1}{R \sin \varphi} \frac{\partial \omega}{\partial \theta} \mathbf{e}_\varphi,$$

$$\nabla(\text{div } \mathbf{v}) = \frac{-2}{R} (\text{div } \mathbf{v}) \mathbf{e}_R + \frac{1}{R} \frac{\partial}{\partial \varphi} (\text{div } \mathbf{v}) \mathbf{e}_\varphi + \frac{1}{R \sin \varphi} \frac{\partial}{\partial \theta} (\text{div } \mathbf{v}) \mathbf{e}_\theta.$$

Thus, it appears that the requirements (7) are satisfied if (and only if) incompressibility

* L is an arbitrary reference length, a is a parameter which appears in the definition of the outer flow $U = ar$ (see [11] section V 10)

occurs. We shall henceforth restrict the study to that case. First, the vector \mathbf{v}^* is found to be:

$$\mathbf{v}^* = \mathbf{v} - v \nabla \log \omega R^2, \quad v = \frac{1}{\omega}. \quad (12)$$

So the flow \mathbf{v}^* turns to be spherical. Since the elementary volume is $d\tau = d\sigma dR$, we have both vortex surface and volume flows; that avails the very same equation of continuity as in plane parallel flows, namely:

$$\frac{\partial \omega}{\partial t} + \operatorname{div} \omega \mathbf{v}^* = 0. \quad (13)$$

It is remarkable to find that (13) expresses a vortex conservation law of viscous fluid flows as defined above. Is it not, therefore, natural to seek the relation between the basic equations of motion and the conservation law (13) (and also (9) or (11))? Indeed, these are but distinguished scalar forms of the so-called equation of vorticity transport. Within the context of the flow geometries considered here, the direction of the vorticity is automatically prescribed. Thus, the vectorial equation of vorticity can be reduced to its unique remaining component along the said direction and thereby one obtains one scalar equation identical to (9), (11) or (13). The calculations used to prove these results are tedious and in the next section we may consider it sufficient to check this assertion partly, and to carry out the calculations for incompressible fluids only.

Before proceeding on, let us take the curl of Navier–Stokes equation for barotropic or incompressible fluids:

$$\frac{\partial \boldsymbol{\omega}}{\partial t} + \operatorname{curl}(\boldsymbol{\omega} \wedge \mathbf{v}) = \frac{\mu}{\rho} \Delta \boldsymbol{\omega} - \left(\nabla \frac{\mu}{\rho} \right) \wedge \operatorname{curl} \boldsymbol{\omega} + \left(\nabla \frac{\lambda + \mu}{\rho} \right) \wedge \nabla \operatorname{div} \mathbf{v}.$$

It is known that the first part of this equation can be transformed according to:

$$\begin{aligned} \frac{\partial \boldsymbol{\omega}}{\partial t} + \operatorname{curl}(\boldsymbol{\omega} \wedge \mathbf{v}) &= \frac{\partial \boldsymbol{\omega}}{\partial t} + (\nabla \boldsymbol{\omega}) \mathbf{v} - (\nabla \mathbf{v}) \boldsymbol{\omega} + \boldsymbol{\omega} \operatorname{div} \mathbf{v} \\ &= \frac{d \boldsymbol{\omega}}{dt} - (\nabla \mathbf{v}) \cdot \boldsymbol{\omega} + \boldsymbol{\omega} \left(-\frac{1}{\rho} \frac{d \rho}{dt} \right) \\ &\quad \left[\frac{d}{dt} \left(\frac{\boldsymbol{\omega}}{\rho} \right) - (\nabla \mathbf{v}) \cdot \frac{\boldsymbol{\omega}}{\rho} \right], \end{aligned}$$

where the equation of continuity has been used at the second line; the term $\nabla \mathbf{v}$ may also be replaced by the rate of strain tensor $\frac{1}{2}(\nabla \mathbf{v} + \nabla^T \mathbf{v})$. Then, the expression of the first member avails an equation which is a generalized form of Helmholtz–Silberstein

equation for viscous barotropic fluids:

$$\begin{aligned} \frac{d}{dt} \left(\frac{\omega}{\rho} \right) - \frac{1}{2} (\nabla \mathbf{v} + \nabla' \mathbf{v}) \frac{\omega}{\rho} \\ = \frac{\mu}{\rho^2} \Delta \omega - \frac{1}{\rho} \nabla \left(\frac{\mu}{\rho} \right) \wedge \text{curl } \omega + \frac{1}{\rho} \left(\nabla \frac{\lambda + \mu}{\rho} \right) \wedge \text{div } \mathbf{v}. \end{aligned} \quad (14)$$

Three parts of this equation can be distinguished: (1) the material derivative, (2) the straining term which acts on ω/ρ as if it would be a material element, (3) the dissipative terms.

5. The special case of incompressible fluids

Let us now prove that the equations of continuity for the vorticity are but concise forms of the so-called vorticity equation: first, we bring the expression of \mathbf{v}^* (8), (10) and (12) into (9), (11) and (13) respectively, and we obtain:

$$\frac{\partial \omega}{\partial t} + \text{div} \left[\omega \mathbf{v} - \omega \frac{\mu}{\rho} \nabla \log \omega + \frac{\lambda + \mu}{\rho} \mathbf{k} \wedge \nabla \text{div } \mathbf{v} \right] = 0, \quad (15)$$

$$\frac{\partial}{\partial t} \left(\frac{\omega}{r} \right) + \text{div} \left[\frac{\omega}{r} \mathbf{v} - \frac{\omega}{r} \frac{\mu}{\rho} \nabla \log r \omega + \frac{1}{r} \frac{\lambda + \mu}{\rho} \mathbf{e}_\theta \wedge \nabla \text{div } \mathbf{v} \right] = 0, \quad (16)$$

$$\frac{\partial \omega}{\partial t} + \text{div} [\omega \mathbf{v} - \omega v \nabla \log \omega R^2] = 0. \quad (17)$$

The logarithmic terms must be derived according to:

$$\nabla \log \omega = \omega^{-1} \nabla \omega,$$

$$\nabla \log r \omega = \omega^{-1} \nabla \omega + r^{-1} \nabla r,$$

$$\nabla \log \omega R^2 = \omega^{-1} \nabla \omega + 2R^{-1} \nabla R.$$

In other respects, we can process the first two terms of equations (15) in order to exhibit the ratio ω/ρ as follows:

$$\begin{aligned} \frac{\partial \omega}{\partial t} + \text{div } \omega \mathbf{v} &= \frac{\partial}{\partial t} \rho \left(\frac{\omega}{\rho} \right) + \text{div} \left(\frac{\omega}{\rho} \right) \rho \mathbf{v} \\ &= \rho \left[\frac{\partial}{\partial t} \left(\frac{\omega}{\rho} \right) + \mathbf{v} \cdot \nabla \left(\frac{\omega}{\rho} \right) \right] + \frac{\omega}{\rho} \left[\frac{\partial \rho}{\partial t} + \text{div } \rho \mathbf{v} \right] \\ &= \rho \frac{d}{dt} \left(\frac{\omega}{\rho} \right). \end{aligned}$$

Here the equation of continuity has been used in the last line. Similarly we have:

$$\frac{\partial}{\partial t} \left(\frac{\omega}{r} \right) + \operatorname{div} \frac{\omega}{r} \mathbf{v} = \rho \frac{d}{dt} \left(\frac{\omega}{\rho r} \right).$$

Then, by using these results, the former equations become:

$$\begin{aligned} \rho \frac{d}{dt} \left(\frac{\omega}{\rho} \right) + \operatorname{div} \left[-\frac{\mu}{\rho} \nabla \omega + \frac{\lambda + \mu}{\rho} \mathbf{k} \wedge \nabla \operatorname{div} \mathbf{v} \right] &= 0, \\ \rho \frac{d}{dt} \left(\frac{\omega}{\rho r} \right) + \operatorname{div} \left[-\frac{\mu}{\rho} \left(\frac{\nabla \omega}{r} + \frac{\omega}{r^2} e_r \right) + \frac{\lambda + \mu}{\rho} \frac{\mathbf{e}_\theta}{r} \wedge \nabla \operatorname{div} \mathbf{v} \right] &= 0, \\ \frac{d\omega}{dt} + \operatorname{div} \left[-v \left(\nabla \omega + 2 \frac{\omega}{R} \nabla R \right) \right] &= 0. \end{aligned}$$

Next, we need values of the other terms, namely:

$$\begin{aligned} \begin{cases} \operatorname{div}(\mathbf{k} \wedge \nabla \operatorname{div} \mathbf{v}) = 0, \\ \nabla \left(\frac{\lambda + \mu}{\rho} \right) \cdot (\mathbf{k} \wedge \nabla \operatorname{div} \mathbf{v}) = J_{xy} \left(\operatorname{div} \mathbf{v}, \frac{\lambda + \mu}{\rho} \right), \end{cases} \\ \begin{cases} \operatorname{div}(r^{-1} \mathbf{e}_\theta \wedge \nabla \operatorname{div} \mathbf{v}) = -r^{-2} \operatorname{div} \frac{\partial v}{\partial z}, \\ \nabla \left(\frac{\lambda + \mu}{\rho} \right) \cdot \left(\frac{1}{r} \mathbf{e}_\theta \wedge \nabla \operatorname{div} \mathbf{v} \right) = r^{-1} J_{rz} \left(\frac{\lambda + \mu}{\rho}, \operatorname{div} \mathbf{v} \right), \end{cases} \\ \operatorname{div} 2 \frac{\omega}{R} \nabla R = -2 \frac{\omega}{R^2} \quad \left(\text{since } \frac{\partial \omega}{\partial R} = -\frac{2}{R} \omega \right), \end{aligned}$$

where $J_{xy}(\cdot, \cdot)$ stands for the determinant of Jacobian matrix with respect to the variables (x, y) .

By making use of these values, the equations (15)–(17) can finally be written as:

$$\begin{aligned} \rho \frac{d}{dt} \left(\frac{\omega}{\rho} \right) - \frac{\mu}{\rho} \Delta \omega - \nabla \frac{\mu}{\rho} \cdot \nabla \omega + J_{xy} \left(\operatorname{div} \mathbf{v}, \frac{\lambda + \mu}{\rho} \right) &= 0, \\ \rho \frac{d}{dt} \left(\frac{\omega}{\rho r} \right) - \frac{\mu}{\rho r} \Delta \omega - \frac{\nabla \mu}{\rho} \cdot \frac{\nabla \omega}{r} - \left(\frac{\partial}{\partial r} \frac{\mu}{\rho r} \right) \frac{\omega}{r} \\ + r^{-1} J_{rz} \left(\frac{\lambda + \mu}{\rho}, \operatorname{div} \mathbf{v} \right) &= 0, \end{aligned}$$

$$\frac{d\omega}{dt} - v \Delta \omega + 2v \frac{\omega}{R^2} = 0.$$

For incompressible fluids, these equations are especially simple, namely they are:

$$\frac{d\omega}{dt} = \nu \Delta \omega, \quad (18)$$

$$\frac{d}{dt} \left(\frac{\omega}{r} \right) = \frac{\nu}{r} \Delta \omega - \nu \frac{\omega}{r^3}, \quad (19)$$

$$\frac{d\omega}{dt} = \nu \Delta \omega - 2\nu \frac{\omega}{R^2}. \quad (20)$$

These equations can be found in (Schlichting [11], p. 73, formula (4.7)) as directly stemming from the vorticity transfer equation (14); then, the equations of continuity (9), (11) and (13) indeed turns out to be but equivalent to (14).

When dealing with incompressible ideal fluids, an interesting lemma can be inferred from this matter: the velocity \mathbf{v}^* then fits with the fluid velocity itself, and this avails a first integral for Euler's equation:

For plane parallel flows and spherical flows of ideal fluids, the magnitude of the vorticity is purely convected by the fluid. In particular, if the flow is steady, vorticity magnitude is constant along the streamlines. For axially symmetrical flows, the same statement holds true for ideal fluids, but with ωr^{-1} replacing ω .

The proof is readily obtained by vanishing ν in (18), (19) and (20).

Now, incompressibility owes to reduce the main formulas of section 4 to:

$$\left. \begin{aligned} \mathbf{v}^* &= \mathbf{v} - \nu \nabla \log \omega \\ \frac{\partial \omega}{\partial t} + \operatorname{div} \omega \mathbf{v}^* &= 0 \end{aligned} \right\} \text{ for plane parallel flows,}$$

$$\left. \begin{aligned} \mathbf{v}^* &= \mathbf{v} - \nu \nabla \log \omega r \\ \frac{\partial}{\partial t} \left(\frac{\omega}{r} \right) + \operatorname{div} \left(\frac{\omega}{r} \mathbf{v}^* \right) &= 0 \end{aligned} \right\} \text{ for axially symmetrical flows,}$$

$$\left. \begin{aligned} \mathbf{v}^* &= \mathbf{v} - \nu \nabla \log \omega R^2 \\ \frac{\partial \omega}{\partial t} + \operatorname{div} \omega \mathbf{v}^* &= 0 \end{aligned} \right\} \text{ for spherical flows.}$$

By inspection of these equations, it readily appears that $\operatorname{curl} \mathbf{v}^*$ is always equal to the fluid vorticity; due to this, one can at once inverse the relations defining \mathbf{v}^* as follows:

$$\begin{aligned} \mathbf{v} &= \mathbf{v}^* + \nu \nabla \log \omega^*, \\ \mathbf{v} &= \mathbf{v}^* + \nu \nabla \log \omega^* r, \\ \mathbf{v} &= \mathbf{v}^* + \nu \nabla \log \omega^* R^2, \quad \text{with} \quad \omega^* = \operatorname{curl} \mathbf{v}^*. \end{aligned}$$

Moreover, one can write Navier–Stokes equation as:

$$\frac{\partial \mathbf{v}^*}{\partial t} + \boldsymbol{\omega}^* \wedge \mathbf{v}^* = -\nabla E.$$

This shows that vortex is flowing as an ideal fluid, and that the specific energy related to this flow is but merely the energy of the actual fluid flow.

This can be summed up on asserting:

For plane parallel flows, axially symmetrical flows, and spherical flows, vortex flows as a perfect fluid does; the vorticity and the energy related to this fictitious flow equal the vorticity and the energy of the actual fluid flow respectively; there is a one to one mapping between these two flows.

Next the non-slip conditions at the walls may be stated as:

$$\begin{aligned} \omega^* \mathbf{v}^* + \mathbf{v} \nabla \omega^* &= 0, & \text{for plane parallel flows,} \\ r \omega^* \mathbf{v}^* + \mathbf{v} \nabla r \omega^* &= 0, & \text{for axially symmetrical flows,} \\ R^2 \omega^* \mathbf{v}^* + \mathbf{v} \nabla \omega^* R^2 &= 0, & \text{for spherical flows.} \end{aligned}$$

Because of the flow geometry, each of these conditions must be accounted for by two scalar classical conditions; with regard to the unique scalar slipping condition of ideal fluid, the present conditions are too restrictive; for this reason, some singularities must occur in the field of \mathbf{v}^* : these are sinks along the lines $\omega = 0$; it is however difficult to fit characteristics of these sinks so as to comply with remote boundary wall conditions.

In other respects because $\omega^* = \omega$, irrotational perfect fluid flows are mapped onto irrotational viscous fluid flows: since most of the usual viscous flows are rotational, no interesting method of viscous fluid flow calculation can be obtained from the powerful conformal mappings.

6. Flow geometries endowed with both a complex lamellar velocity field and a complex lamellar vorticity field

One may define flow geometries in various ways. Here we shall consider flow geometries that can be associated to a one-parameter family of surfaces, say (Σ) , which in their turn define a family of streamsheets. For (7) our attention has been focused on flows for which both velocity and vorticity vector fields are complex-lamellar, namely

$$\boldsymbol{\omega} \cdot \mathbf{v} = \boldsymbol{\omega} \cdot \text{curl } \boldsymbol{\omega} = 0.$$

The latter equality owes a whole of surfaces to exist standing orthogonal to vortex

lines; because of the former one, each of these surfaces appears as a streamsheet. Then, we are led to look for flow geometries and the related families (Σ) such that the vortex lines are perpendicular to (Σ) .

Some preliminaries are now necessary before stating the result associated with this section: let the parameter associated to (Σ) be denoted by ζ , and let curvilinear coordinates ξ, η be assigned to one of the surfaces of (Σ) . In prescribing ξ, η to remain constant along each vortex line, one makes the triad ξ, η, ζ to be curvilinear coordinates system for the whole space. In this system, elementary curve lengths will be expressed owing to:

$$d\mathbf{OM} = h_1 \mathbf{e}_\xi d\xi + h_2 \mathbf{e}_\eta d\eta + h_3 \mathbf{e}_\zeta d\zeta,$$

with $\mathbf{e}_\zeta = \mathbf{e}_\xi \wedge \mathbf{e}_\eta$ and $\cos \alpha \equiv \mathbf{e}_\zeta \cdot \mathbf{e}_\eta$. Here, $\mathbf{e}_\xi, \mathbf{e}_\eta, \mathbf{e}_\zeta$ are unit vectors, and h_1, h_2, h_3 designate positive scalar functions of (ξ, η, ζ) , and the angle α depends on (ξ, η, ζ) . The fluid velocity is:

$$\mathbf{v} = V_1 \mathbf{e}_\xi + V_2 \mathbf{e}_\eta.$$

With the help of Lichnerowicz ([12], p. 99), the elementary differential operators can be expressed for any function F and any vector $\mathbf{B} = B_1 \mathbf{e}_\xi + B_2 \mathbf{e}_\eta + B_3 \mathbf{e}_\zeta$ as follows:

$$\begin{aligned} \nabla F = & \left(\frac{1}{h_1 \sin^2 \alpha} \frac{\partial F}{\partial \xi} - \frac{\cotg \alpha}{h_2 \sin \alpha} \frac{\partial F}{\partial \eta} \right) \mathbf{e}_\xi \\ & + \left(\frac{1}{h_2 \sin^2 \alpha} \frac{\partial F}{\partial \eta} - \frac{\cotg \alpha}{h_2 \sin \alpha} \frac{\partial F}{\partial \xi} \right) \mathbf{e}_\eta + \frac{1}{h_3} \frac{\partial F}{\partial \zeta} \mathbf{e}_\zeta, \end{aligned} \quad (21)$$

$$\begin{aligned} \operatorname{div} \mathbf{B} = & \frac{1}{h_1 h_2 h_3 \sin \alpha} \left[\frac{\partial}{\partial \xi} (h_2 h_3 B_1 \sin \alpha) \right. \\ & \left. + \frac{\partial}{\partial \eta} (h_3 h_1 B_2 \sin \alpha) + \frac{\partial}{\partial \zeta} (h_1 h_2 B_3 \sin \alpha) \right], \end{aligned} \quad (22)$$

$$\begin{aligned} \operatorname{curl} \mathbf{B} = & \frac{1}{h_2 h_3 \sin \alpha} \left[\frac{\partial}{\partial \eta} (h_3 B_3) - \frac{\partial}{\partial \zeta} h_2 (B_2 + B_1 \cos \alpha) \right] \mathbf{e}_\xi \\ & + \frac{1}{h_3 h_1 \sin \alpha} \left[\frac{\partial}{\partial \zeta} h_1 (B_1 + B_2 \cos \alpha) - \frac{\partial}{\partial \xi} (h_3 B_3) \right] \mathbf{e}_\eta \\ & + \frac{1}{h_1 h_2 \sin \alpha} \left[\frac{\partial}{\partial \xi} h_2 (B_2 + B_1 \cos \alpha) - \frac{\partial}{\partial \eta} h_1 (B_1 + B_2 \cos \alpha) \right] \mathbf{e}_\zeta. \end{aligned} \quad (23)$$

From (23), the assumption $\omega \cdot \mathbf{v} = 0$ can be replaced by:

$$\frac{\partial}{\partial \xi} h_2 (V_2 + V_1 \cos \alpha) = 0, \quad \frac{\partial}{\partial \xi} h_1 (V_1 + V_2 \cos \alpha) = 0.$$

By solving this system, we obtain:

$$V_1 = \frac{1}{\sin^2 \alpha} \left(\frac{A_1}{h_1} - \frac{A_2}{h_2} \cos \alpha \right), \quad V_2 = \frac{1}{\sin^2 \alpha} \left(\frac{A_2}{h_2} - \frac{A_1}{h_1} \cos \alpha \right) \quad (24)$$

with A_1, A_2 denoting two undetermined functions depending only on (ξ, η) . In other respects, the condition $\omega \cdot \text{curl } \omega = 0$ is automatically verified since vortex lines stand orthogonal to the family (Σ) ; thus, it remains to investigate the last condition of (7), namely $\omega \cdot \nabla \text{div } \mathbf{v} = 0$. Since ω is taken as tangent to ζ -line, it follows that:

$$\frac{1}{h_3} \frac{\partial}{\partial \xi} (\text{div } \mathbf{v}) = 0,$$

where (21) has been used. Integrating this once and making use of (22)–(24) we get:

$$\begin{aligned} & \frac{\partial}{\partial \xi} \left(A_1 \frac{h_2 h_3}{h_1 \sin \alpha} - A_2 h_3 \cot \alpha \right) + \frac{\partial}{\partial \eta} \left(A_2 \frac{h_3 h_1}{h_2 \sin \alpha} - A_1 h_3 \cot \alpha \right) \\ &= A_3 h_1 h_2 h_3 \sin \alpha. \end{aligned} \quad (25)$$

Here, A_3 denotes another undetermined scalar function depending only on (ξ, η) .

Now, with our definition of flow geometries (associated to (Σ)) in mind, we look for availing a continuous set of functions A_i ($i = 1, 2, 3$) whereas h_i ($i = 1, 2, 3$) and α are prescribed. Since they are functions of (ξ, η, ζ) while A_i depends only on ξ, η , equation (25) cannot hold true identically unless h_i and α comply with suitable conditions. In the sequel, we shall set:

$$\begin{aligned} X &= \frac{h_2 h_3}{h_1 \sin \alpha}, & Y &= -h_3 \cot \alpha, \\ Z &= \frac{h_1 h_3}{h_2 \sin \alpha}, & W &= h_1 h_2 h_3 \sin \alpha. \end{aligned} \quad (26)$$

Equation (25) can now be expanded as:

$$X \frac{\partial A_1}{\partial \xi} + Y \frac{\partial A_1}{\partial \eta} + Y \frac{\partial A_2}{\partial \xi} + Z \frac{\partial A_2}{\partial \eta} + \left(\frac{\partial X}{\partial \xi} + \frac{\partial Y}{\partial \eta} \right) A_1 + \left(\frac{\partial Y}{\partial \xi} + \frac{\partial Z}{\partial \eta} \right) A_2 = W A_3. \quad (27)$$

Let us deal first with incompressible fluids which correspond to the subcase $A_3 \equiv 0$. In \mathbb{R}^5 , we may consider the hyperplane which has the equation:

$$Xx_1 + Yx_2 + Yx_3 + Zx_4 + \left(\frac{\partial X}{\partial \xi} + \frac{\partial Y}{\partial \eta}\right)x_5 + \left(\frac{\partial Y}{\partial \xi} + \frac{\partial Z}{\partial \eta}\right) = 0,$$

$$(x_1, x_2, x_3, x_4, x_5) \in \mathbb{R}^5;$$

Upon varying ζ alone and thus letting both A_1 and A_2 together with their derivatives remain constant, the hyperplane should be pivoted around the point

$$P = \frac{1}{A_2} \left(\frac{\partial A_1}{\partial \xi}, \frac{\partial A_1}{\partial \eta}, \frac{\partial A_2}{\partial \xi}, \frac{\partial A_2}{\partial \eta}, A_1 \right).$$

Further this plane must also contain every pivot point associated with any flow pertaining to the flow geometry (associated to Σ). Consequently, provided that the dimension of the affine space spanned by such points is greater than 3*, the hyperplane in question is fixed and uniquely related to the flow geometry. Because of this, the coefficients of the hyperplane equation are functions of (ξ, η) only, save for a multiplying common factor, namely:

$$\frac{X}{a} = \frac{Y}{b} = \frac{Z}{c} = \frac{\partial X/\partial \xi + \partial Y/\partial \eta}{d} = \frac{\partial Y/\partial \xi + \partial Z/\partial \eta}{e} = \lambda(\xi, \eta, \zeta), \quad (28)$$

with a, b, c, d, e being scalar functions of (ξ, η) , and λ being an unknown factor.

When eliminating X, Y, Z , we obtain

$$a \frac{\partial \lambda}{\partial \xi} + b \frac{\partial \lambda}{\partial \eta} = \left(d - \frac{\partial a}{\partial \xi} - \frac{\partial b}{\partial \eta} \right) \lambda, \quad b \frac{\partial \lambda}{\partial \xi} + c \frac{\partial \lambda}{\partial \eta} = \left(e - \frac{\partial b}{\partial \xi} - \frac{\partial c}{\partial \eta} \right) \lambda.$$

This linear system must be solved to specify the factor λ . First we write the derivatives of λ in the form:

$$\frac{\partial \lambda}{\partial \xi} = p\lambda, \quad \frac{\partial \lambda}{\partial \eta} = q\lambda,$$

*In the opposite case, let this affine subspace be determined by

$$\sum_1^5 \alpha_i x_i + \alpha_6 = 0, \quad \sum_1^5 \beta_i x_i + \beta_6 = 0,$$

where α, β , depend only on (ξ, η) . Since $1/A_1(\partial A_1/\partial \xi, \partial A_1/\partial \eta, \partial A_2/\partial \xi, \partial A_2/\partial \eta, A_2)$ must satisfy all of these equations and Navier-Stokes equation, this results in an overdetermined system for A_1, A_2 ; henceforth this case must be precluded.

with p, q being two coefficients depending on (ξ, η) only; these equations have the solution $\lambda = \chi(\zeta)g(\xi, \eta)$ on condition that we satisfy a compatibility condition (i.e. $\partial p/\partial \eta = \partial q/\partial \xi$). Here χ, g are two scalar functions. Upon changing the coordinate ζ into ζ' such that $d\zeta' = \chi(\zeta)d\zeta$ we can get rid of χ . Hence inserting the value of λ back into (26) and (28), we are led to the following set of conditions:

1. h_2/h_1 must depend on (ξ, η) only (owing to $\sqrt{X/Z}$),
 2. α must depend on (ξ, η) only (owing to $\cos^{-1}\sqrt{Y^2/XZ}$),
 3. h_3 must depend on (ξ, η) only.
- (29)

These requirements are also sufficient to ensure that equation (27) holds true whatever the value of ζ^{**} .

Now as far as the general case of compressible fluids is concerned, we may likewise consider a hyperplane in \mathbb{R}^6 and follow the same approach as above, to find the conditions corresponding to (29) are:

$$h_1, h_2, h_3, \alpha \text{ must be independent of } \zeta. \quad (30)$$

At present we plan to show that the preliminary conditions (29) and (30) enable us to prove the following proposition:

PROPOSITION: *All the flow geometries endowed with both a complex lamellar velocity field and a complex lamellar vorticity field are:*

Plane parallel flows

Axially symmetrical flows *for incompressible fluids,*

Spherical flows

Plane parallel flows

and *for compressible fluids.*

Axially symmetrical flows

We shall first demonstrate the assertion for incompressible fluids: to this end, we need to express the derivatives of e_ξ, e_η, e_ζ as follows:

$$\frac{\partial e_\xi}{\partial \eta} = \left(\frac{\partial \alpha}{\partial \eta} + h_2 \gamma_{\eta\zeta} \right) \left(e_\xi \cotg \alpha - \frac{1}{\sin \alpha} e_\eta \right) + h_2 (-\tau_{\eta\zeta} \sin \alpha + \gamma_{\eta\zeta} \cos \alpha) e_\zeta,$$

*For the sake of brevity in the sequel we omit the prime of ζ'

$$\frac{\partial \mathbf{e}_\zeta}{\partial \zeta} \sin \alpha = \left(h_3 \tau_{\zeta\eta} - \frac{\partial \alpha}{\partial \eta} \right) \mathbf{e}_\eta - h_3 [\tau_{\zeta\zeta} \cos \alpha \cdot \mathbf{e}_\zeta + (\gamma_{\zeta\zeta} \cos \alpha + \gamma_{\zeta\eta}^0) \mathbf{e}_\zeta], \quad (31,a)$$

$$\frac{\partial \mathbf{e}_\eta}{\partial \xi} = - \left(\frac{\partial \alpha}{\partial \xi} + h_1 \gamma_{\zeta\zeta} \right) \left(\frac{1}{\sin \alpha} \mathbf{e}_\zeta - \mathbf{e}_\eta \cotg \alpha \right) + h_1 (\tau_{\zeta\zeta} \sin \alpha - \gamma_{\zeta\zeta}^0 \cos \alpha) \mathbf{e}_\zeta, \quad (31,b)$$

$$\frac{\partial \mathbf{e}_\eta}{\partial \zeta} \sin \alpha = \left(-h_3 \tau_{\zeta\zeta} - \frac{\partial \alpha}{\partial \xi} \right) \mathbf{e}_\zeta + h_3 [\mathbf{e}_\eta \tau_{\zeta\eta} \cos \alpha - (\gamma_{\zeta\eta} \cos \alpha + \gamma_{\zeta\zeta}^0) \mathbf{e}_\zeta], \quad (31,c)$$

$$\frac{\partial \mathbf{e}_\zeta}{\partial \xi} = -h_1 \left[\gamma_{\zeta\eta} \mathbf{e}_\zeta + \tau_{\zeta\eta} \left(-\mathbf{e}_\zeta \cotg \alpha + \frac{1}{\sin \alpha} \mathbf{e}_\eta \right) \right], \quad (31d)$$

$$\frac{\partial \mathbf{e}_\zeta}{\partial \eta} = -h_2 \left[\gamma_{\eta\zeta} \mathbf{e}_\eta + \tau_{\eta\zeta} \left(-\frac{1}{\sin \alpha} \mathbf{e}_\zeta + \mathbf{e}_\eta \cotg \alpha \right) \right]. \quad (31,e)$$

Here, $\gamma_{\zeta\eta}$, $\tau_{\zeta\eta}$, $\gamma_{\zeta\eta}^0$ are the normal curvature, geodesic torsion, and geodesic curvature of ξ -lines with respect to $\xi\eta$ -surfaces (viz. the surfaces $\zeta = \text{const}$). The remaining coefficients γ , τ , γ^0 are defined in like manner by exchanging subscripts. These formulas result from Darboux–Ribaucour's formula, namely: for any surface, the derivative of the normal unit vector \mathbf{n} can be specified along any curve lying on the surface by:

$$\frac{d\mathbf{n}}{ds} = -\gamma \mathbf{t} - \tau \mathbf{g},$$

where s , γ , τ stand for curvilinear absciss, normal curvature, and geodesic torsion related to the curve; \mathbf{t} , \mathbf{g} are the tangential unit and the geodesic normal vectors. For example, we can check the expression of $d\mathbf{e}_\zeta/d\xi$, as follows:

$$\frac{d\mathbf{e}_\zeta}{d\xi} = \frac{d\mathbf{e}_\zeta}{ds} \cdot \frac{ds}{d\xi} = h_1 \left[-\gamma_{\zeta\eta} \mathbf{e}_\zeta - \tau_{\zeta\eta} \left(-\frac{1}{\tg \alpha} \mathbf{e}_\zeta + \frac{1}{\sin \alpha} \mathbf{e}_\eta \right) \right].$$

Now, we also note that:

$$\begin{aligned} \frac{\partial}{\partial \eta} (h_1 \mathbf{e}_\zeta) &= \frac{\partial}{\partial \xi} (h_2 \mathbf{e}_\eta), & \frac{\partial}{\partial \zeta} (h_2 \mathbf{e}_\eta) &= \frac{\partial}{\partial \eta} (h_3 \mathbf{e}_\zeta), \\ \frac{\partial}{\partial \xi} (h_3 \mathbf{e}_\zeta) &= \frac{\partial}{\partial \zeta} (h_1 \mathbf{e}_\zeta). \end{aligned}$$

After expanding this, with help of (31), we hence have nine relations between the

22 M. Bouthier

derivatives of h_1 , h_2 , h_3 and α , namely:

$$\frac{\partial h_1}{\partial \eta} \sin \alpha + h_1 \left(\frac{\partial \alpha}{\partial \eta} + h_2 \gamma_{\eta\zeta} \right) \cos \alpha + h_2 \left(\frac{\partial \alpha}{\partial \xi} + h_1 \gamma_{\xi\zeta} \right) = 0, \quad (32,a)$$

$$\frac{\partial h_2}{\partial \xi} \sin \alpha + h_2 \left(\frac{\partial \alpha}{\partial \xi} + h_1 \gamma_{\xi\zeta} \right) \cos \alpha + h_1 \left(\frac{\partial \alpha}{\partial \eta} + h_2 \gamma_{\eta\zeta} \right) = 0, \quad (32b)$$

$$\tau_{\xi\zeta} + \tau_{\eta\zeta} = (\gamma_{\xi\zeta}^0 + \gamma_{\eta\zeta}^0) \cot \alpha, \quad (32c)$$

$$\frac{\partial h_2}{\partial \zeta} + h_2 h_3 [\gamma_{\eta\zeta} + (\tau_{\zeta\eta} + \tau_{\eta\zeta}) \cot \alpha] = 0, \quad (33,a)$$

$$\frac{\partial h_3}{\partial \eta} \sin \alpha + h_2 h_3 (\gamma_{\xi\zeta} + \gamma_{\zeta\eta} \cos \alpha) = 0, \quad (33,b)$$

$$h_3 (\tau_{\eta\zeta} + \tau_{\zeta\eta}) + \frac{\partial \alpha}{\partial \zeta} = 0, \quad (33,c)$$

$$\frac{\partial h_3}{\partial \xi} \sin \alpha + h_1 h_3 (\gamma_{\zeta\eta} + \gamma_{\xi\zeta} \cos \alpha) = 0, \quad (34,a)$$

$$\frac{\partial h_1}{\partial \zeta} + h_1 h_3 [\gamma_{\xi\eta} - (\tau_{\zeta\eta} + \tau_{\eta\zeta}) \cot \alpha] = 0, \quad (34,b)$$

$$h_3 (\tau_{\zeta\eta} + \tau_{\eta\zeta}) - \frac{\partial \alpha}{\partial \zeta} = 0. \quad (34,c)$$

First we shall take into account the first two conditions of (29) (α and h_2/h_1 being independent of ζ) and we shall prove that any $\xi\eta$ -surface must be either a sphere or a plane.

The equations (33,c) and (34,c) become:

$$\tau_{\eta\zeta} + \tau_{\zeta\eta} = \tau_{\zeta\eta} + \tau_{\xi\eta} = 0.$$

One can then refer to the definition of geodesic torsion, namely $\tau = 1/T + d\theta/ds$ (where T is the torsion of any curve lying on the surface, and θ is the angle subtended by the principal normal to the curve and the normal to the surface). From this, one can state that $\tau_{\xi\zeta} = \tau_{\zeta\eta}$, because α does not depend on ζ . The relations between the torsions are thus reduced to:

$$\tau_{\xi\eta} = \tau_{\eta\xi} = -\tau_{\xi\zeta} = -\tau_{\zeta\eta}.$$

We should also make use of (33,a) and (34,b) in connection with the assumption that

$\partial/\partial\zeta(h_1/h_2)=0$; (33,a) and (34,b) are multiplied by h_1, h_2 , respectively, and they are subtracted from each other, yielding:

$$\left(h_1 \frac{\partial h_2}{\partial \zeta} - h_2 \frac{\partial h_1}{\partial \zeta}\right) \\ = h_1 h_2 h_3 [\gamma_{\xi\eta} - \gamma_{\eta\xi} - (\tau_{\xi\eta} + \tau_{\zeta\xi} + \tau_{\zeta\eta} + \tau_{\eta\xi}) \cotg \alpha] = 0.$$

Taking into account the values of the torsions, this simply leads to $\gamma_{\xi\eta} = \gamma_{\eta\xi}$. Now, we consider the so-called Euler's formula which is

$$\gamma = \frac{\cos^2 \omega}{R_1} + \frac{\sin^2 \omega}{R_2}.$$

Here, R_1, R_2 are the radii of principal curvature of the $\xi\eta$ -surface; γ stands for the normal curvature of any curve for which the angle subtended by its tangent and the principal direction of curvature 1 is ω .

In polar coordinates, the curve associated to this formula possesses two axis of symmetry: these are the principal directions of curvature. Since $\gamma_{\xi\eta} = \gamma_{\eta\xi}$, ξ -line and η -line must be symmetrical with respect to these principal directions. Therefore, $\tau_{\xi\eta} = -\tau_{\eta\xi}$ due to the so-called following Ossian-Bonnet formula:

$$\tau = \left(\frac{1}{R_2} - \frac{1}{R_1}\right) \sin \omega \cos \omega,$$

where ω is the same angle as above.

Then, since $\tau_{\xi\eta}$ and $\tau_{\eta\xi}$ are simultaneously equal and opposite, it can be concluded that these torsions are null. From the formula of Ossian Bonnet, this means that ξ -lines and η -lines are lines of principal curvature.

Finally, since $\gamma_{\xi\eta} = \gamma_{\eta\xi}$, every point of $\xi\eta$ -surface is an ombilic ($R_1 = R_2$ everywhere) and this implies that every $\xi\eta$ -surface must be either a sphere or a plane.

Now, it remains to take into consideration the dependence of h_3 on ζ alone. To this end, the cases of spherical $\xi\eta$ -surfaces and plane $\xi\eta$ -surfaces must be separately processed: this part of proof is rather elementary, and it is reported in the appendix. There it is shown that the former case leads to spherical flows whereas the latter yields both plane parallel and axially symmetrical flows. So the above assertion mentioned indeed holds true for incompressible fluids.

The case of compressible fluids can be readily dealt with by considering (30) as a special case of (29), and this needs only checking that the proposition does not hold true for spherical flows.

7. Conclusion

We have shown that vortex appears to flow along the energy lines of certain viscous fluid flows according to a velocity which coincides with the fluid velocity when the viscosity vanishes. That turns out to be especially true for the following three important flow geometries of incompressible fluids: plane parallel flows, axially symmetrical flows, and spherical flows. For viscous fluid flows this, unfortunately, yields no general procedure of flow calculation. Nevertheless the present work is of interest for any complete study of vorticity behavior; it enhances the importance of the energy lines and suggests to exhibit them in numerical results of viscous fluid flows.

Appendix

1. The case of spherical surfaces

The center P of each sphere and its radius are functions of ζ alone; therefore, every point of the space can be represented by means of:

$$\mathbf{OM} = \mathbf{OP}(\zeta) + a(\zeta)\mathbf{u}(\xi, \eta; \zeta), \quad |\mathbf{u}| = 1. \quad (35)$$

By differentiating this we have:

$$d\mathbf{OM} = a \frac{\partial \mathbf{u}}{\partial \xi} d\xi + a \frac{\partial \mathbf{u}}{\partial \eta} d\eta + \left(\tau + \frac{\partial a \mathbf{u}}{\partial \zeta} \right) d\zeta,$$

where $\tau = d\mathbf{OP}/d\zeta$ is tangent to the center line at point P ; it depends only on σ . From this equation the six quantities $h_1, h_2, h_3, \mathbf{e}_\xi, \mathbf{e}_\eta, \mathbf{e}_\zeta$ can be specified: it is found that $\mathbf{e}_\zeta \equiv \mathbf{u}$ (on account of: $\mathbf{e}_\zeta = \mathbf{e}_\xi \wedge \mathbf{e}_\eta$, $\mathbf{e}_\xi \approx \partial \mathbf{u} / \partial \xi$, $\mathbf{e}_\eta \approx \partial \mathbf{u} / \partial \eta$, $|\mathbf{u}| = 1$) and this leads to writing the following relation:

$$h_3 \mathbf{u} = \tau + \frac{\partial a \mathbf{u}}{\partial \zeta}. \quad (36)$$

Now our starting hypothesis is that h_3 depends on ξ, η only. From this it can be inferred that h_3 must be a constant: as a matter of fact we can multiply (36) by $a\mathbf{u}$ to yield:

$$a\mathbf{u} \cdot \tau = h_3 a - a \frac{\partial a}{\partial \zeta}.$$

We can moreover calculate the derivative $\partial(a\mathbf{u} \cdot \tau) / \partial a$ with help of both (36) and its first

derivative to yield the relation:

$$\frac{\partial}{\partial \sigma}(a\mathbf{u} \cdot \boldsymbol{\tau}) = -\frac{h_3}{a}(a\mathbf{u} \cdot \boldsymbol{\tau}) + h_3^2 - \frac{d}{d\zeta}\left(a \frac{da}{d\zeta}\right).$$

By eliminating the product $a\mathbf{u} \cdot \boldsymbol{\tau}$ between these two equations there is obtained an algebraic equation for h_3 ; the coefficients of this one are depending on ζ alone hence h_3 is really a constant.

According to the previous expression of $a\mathbf{u} \cdot \boldsymbol{\tau}$, the product $\mathbf{u} \cdot \boldsymbol{\tau}$ should also depend on ζ alone; this result is absurd, because M should describe only a circle as (ξ, η) is varied.

Since when using the representation (35), there is no appropriate solution, it remains to study the disregarded case $\mathbf{OP}(\zeta) = \mathbf{O}$. The formula (35) is then to be reduced to $\mathbf{OM} = a(\zeta)\mathbf{u}(\xi, \eta)$ and it is easy to see that this defines but spherical flows.

2. The case of plane surfaces $\zeta = \text{const}$

A family of planes depending on one parameter can be regarded as osculating planes associated with a cuspidal edge: let this cuspidal edge be designated by \mathcal{C} , and let it be defined by $\mathbf{OP} = \mathbf{OP}(\sigma)$ (here, σ stands for the curvilinear abscissa along the cuspidal edge). For every point, we shall use the following representation:

$$\mathbf{OM}(\xi, \eta, \zeta) = \mathbf{OP}(\sigma) + X(\xi, \eta; \sigma)\boldsymbol{\tau}(\sigma) + Y(\xi, \eta; \sigma)\mathbf{v}(\sigma),$$

where the unit vectors $\boldsymbol{\tau}$, \mathbf{v} lie respectively on the tangent and the principal normal to \mathcal{C} ; there is a bijective mapping between ζ and σ ; X and Y stands for cartesian coordinates of the point M in the plane $\zeta = \text{const}$.

Owing to the basic assumption $\mathbf{e}_\zeta = \mathbf{e}_\xi \wedge \mathbf{e}_\eta$, $\partial\mathbf{OM}/\partial\zeta$ must be orthogonal to $\boldsymbol{\tau}$ and \mathbf{v} , hence:

$$1 + \frac{\partial X}{\partial \sigma} - \frac{Y}{R(\sigma)} = 0, \quad (37,a)$$

$$\frac{\partial Y}{\partial \sigma} + \frac{X}{R(\sigma)} = 0, \quad (37,b)$$

where $R(\sigma)$ is the radius of curvature of \mathcal{C} . Consequently our hypothesis associated with h_3 can be stated as.

$$\left(\left| \frac{\partial \mathbf{OM}}{\partial \zeta} \right| \right) \equiv \frac{Y}{T(\sigma)} \frac{d\sigma}{d\zeta} = Z(\xi, \eta). \quad (38)$$

Here, the function Z is undeterminate, and T stands for torsion of \mathcal{C} . According to (38)–(37,b), the forms of X and Y must be the following:

$$Y = f(\sigma)Z(\xi, \eta), \quad X = -Rf'(\sigma)Z(\xi, \eta),$$

where f is an undeterminate function of σ . This can be brought into (37,a) then it is inferred that Z as well as X and Y must be constant. This yields a contradictory result and we must consider the special cases which have been hitherto precluded, they are:

1. the cuspidal edge is removed to infinity,
2. the cuspidal edge is reduced to a straight line,
3. the cuspidal edge is reduced to a single point.

The first case is concerned with planes $\zeta = \text{const}$ standing parallel: it can be readily verified that there is only the plane parallel flow geometry.

For treating the second case, we shall utilize the following cylindrical coordinates:

$$\mathbf{OM}(\xi, \eta, \zeta) = z(\xi, \eta; \theta)\mathbf{k} + r(\xi, \eta; \theta)\mathbf{e}_r(\theta),$$

where the axis $r=0$ stands for the cuspidal edge. Here, there is also a bijective mapping between θ and ζ . By referring to the relation $\mathbf{e}_\zeta = \mathbf{e}_\xi \wedge \mathbf{e}_\eta$ once more, we find that:

$$\left(\frac{\partial \mathbf{OM}}{\partial \zeta}\right) \equiv \left(\frac{\partial z}{\partial \theta}\mathbf{k} + \frac{\partial r}{\partial \theta}\mathbf{e}_r + r\mathbf{e}_\theta\right) \frac{d\theta}{d\zeta} \quad \text{must be colinear with } \mathbf{e}_\theta.$$

Hence z and r must depend only on (ξ, η) : this is simply the geometry of axially symmetrical flows owing to the bijective mapping between (r, z) and (ξ, η) .

The third case defines the planes $\zeta = \text{const}$ as being tangent to a cone. Let the origin be the vertex of that cone, and let the cone intersect the unit sphere according to the curve \mathcal{C}' : $\mathbf{OM} = \mathbf{v}(\sigma)$ (where σ is the curvilinear absciss along that curve). Then, any point M can be determined with the help of:

$$\mathbf{OM}(\xi, \eta, \zeta) = X(\xi, \eta; \sigma)\boldsymbol{\tau}(\sigma) + Y(\xi, \eta; \sigma)\mathbf{v}(\sigma);$$

here, $\boldsymbol{\tau}(\sigma)$ denotes unit vector tangent to \mathcal{C}' . Then, the formula appears to be formally the same as the one for the general case, but with $\mathbf{OP} = \mathbf{0}$ and $\boldsymbol{\tau} = d\mathbf{v}/d\sigma$. Following a similar reasoning to the one for the general case, we are led to the very same contradictory outcome.

References

1. Lamb, H., *Hydrodynamics*. Cambridge: University Press; New York: Dover (1945).
2. Prager, W., *Introduction to Mechanics of Continua*. Boston: Ginn and Company (1961).
3. Sedov, L., *Foundations of the Non-Linear Mechanics of Continua*. Oxford: Pergamon Press (1966).

- Appel, P., *Traité de Mécanique Rationnelle, Tome 3, Equilibre et Mouvement des Milieux Continus*. Paris: Gauthiers Villars (1903).
- Ericksen, J.L., Tensor fields. In: S. Flugge (ed.), *Principles of classical mechanics and field theory, Encyclopedia of Physics/Hanbuch der Physik*, Vol. 3.1. Berlin: Springer Verlag (1960) pp. 794–858.
- Crocco, L. and Pascucci, L., Diagrammi termodinamici dei gas di combustione; indicazioni per l'applicazione dei diagrammi al calcolo del ciclo del motore a scoppio (1947) *Monograf. Scient. di aeronautica*, 2, pl. 23 (Roma-Stabilimento Tipografico Fausto Failli). See also: Serrin, J., Mathematical principles of classical fluid mechanics. In: S. Flugge (ed.), *Fluid Dynamics I, Encyclopedia of Physics/Hanbuch der Physik*, Vol. 8.1 (1959) pp. 125–263 §38–39.
- Germain, P., *Mécanique des Milieux Continus*. Paris: Masson (1962).
- Ionescu-Bujor, Etude intrinsèque des écoulements permanents et rotationnels d'un fluide parfait (1961). Paris: Thèse Faculté des Sciences de Paris.
- Kaplun, S., The role of coordinate systems in boundary layer theory. *J. Applied Math. and Phys. (ZAMP)* 5 (1954) 111–135.
- Legner, H., On Kaplun's optimal coordinates. *J. Fluid Mech.* 115 (1982) 379–393.
- Schlichting, H., *Boundary Layer Theory*, 7th edn. New York: McGraw-Hill (1979).
- Landau, L. and Lifschitz, E., *Fluid Mechanics, Course of Theoretical Physics*, Vol. 6 2nd edn. Oxford: Pergamon Press (1987).
- Truesdell, C. and Toupin, R., *The classical field theories*. In: S. Flugge (ed.), *Encyclopedia of Physics/Hanbuch der Physik*, Vol. 3.1, *Principles of Classical Mechanics and Field Theory*. Berlin: Springer Verlag (1960) pp. 226–793.
- Oroveanu, T., On a class of viscous fluid motions. *Revue Roumaine des Sciences Techniques-Serie de Mécanique Appliquée*, Vol. 33. (1988) 135–144.
- Casal, P. and Gouin, H., Invariance properties of inviscid fluids of grade N . *Lecture Notes in Physics* Vol. 344. Springer-Verlag (1989) pp. 85–98.

Transient non-Darcy free convection between parallel vertical plates in a fluid saturated porous medium

A. NAKAYAMA, F. KUWAHARA & H. KOYAMA

*Dept. of Energy and Mechanical Engineering, Shizuoka Univ.,
 3-5-1 Johoku, Hamamatsu, 432 Japan*

Received 11 December 1990; accepted in revised form 23 August 1991

Key words: porous media, free convection, transient problem, non-Darcy flow, similarity solution

Abstract. Transient non-Darcy free convection between two parallel vertical plates in a fluid saturated porous medium is investigated using the generalized momentum equation proposed by Vafai and Tien. The effects of porous inertia and solid boundary are considered in addition to the Darcy flow resistance. Exact solutions are found for the asymptotic states at small and large times. The large time solutions reveal that the velocity profiles are rather sensitive to the Darcy number Da when $Da < 1$. It has also been found that boundary friction alters the velocity distribution near the wall, considerably. Finite difference calculations have also been carried out to investigate the transient behaviour at the intermediate times in which no similarity solutions are possible. This analytical and numerical study reveals that the transient free convection between the parallel plates may well be described by matching the two distinct asymptotic solutions obtained at small and large times.

Nomenclature

C = empirical constant for the Forchheimer term	T = temperature
f = velocity function for the small time solution	u, v = Darcian velocity components
F = velocity function for the large time solution	x, y = Cartesian coordinates
g = acceleration due to gravity	α = effective thermal diffusivity
Gr^* = micro-scale Grashof number	β = coefficient of thermal expansion
H = a half distance between two infinite plates	ε = porosity
K = permeability	ζ = dimensionless time
Nu = Nusselt number	η = similarity variable
Pr = Prandtl number	θ = dimensionless temperature
t = time	μ = viscosity
	ν = kinematic viscosity
	ρ = density
	σ = the ratio of heat capacities

Introduction

Extensive investigations have been reported on the problems of transient convection in Newtonian fluids, such as free convection problems by Siegel [1] and Goldstein and Brigg [2], forced convection problems by Nanbu [3] and Watkins [4], and film

condensation problems by Sparrow and Siegel [5] and Wilson [6]. The problems of transient convective heat transfer within a porous medium, however, have received very little attention, despite considerable practical and theoretical interest related to geophysical and engineering applications of geothermal energy.

Johnson and Cheng [7] obtained similarity solutions for a semi-infinite vertical flat plate in a porous medium, with specific variations of wall temperatures in both time and position. Asymptotic expansions were used by Ingham and his group to attack the problem of transient free convection on a vertical flat plate in a porous medium, for the suddenly cooled case (Ingham et al., [8]) and suddenly heated case (Ingham and Brown, [9]), while a finite difference solution was obtained by Jang and Ni [10] for transient free convection with mass transfer from an isothermal vertical flat plate. An elegant integral method was introduced by Cheng and Pop [11] to analyse the transient free convection boundary layer flow in a porous medium. Sparrow and Siegel's approximate analytical solution for laminar condensate flow was extended by Cheng and Chui [12] to attack the same problem for a porous medium. In all these previous studies on convective heat transfer in porous media, the Darcy model was assumed. The model, however, is valid only for slow flows through porous media with low permeability. In general, we must consider the effect of the porous inertia, as well as the viscous diffusion which may well become significant for materials with high porosities such as fibrous media and foam materials. Recently, Chen et al. [13] employed a finite difference method to investigate the non-Darcy effects on transient free convection over a vertical flat plate in a porous medium, while Nakayama et al. [14] attacked the boundary layer problem of non-Darcian forced convection from a flat plate. Numerical results are presented only for a limited number of sets of system parameters.

In this study, we shall consider one of the most fundamental transient convection problems, namely, the transient free convection between parallel vertical plates embedded in a fluid-saturated porous medium (see Fig. 1). This fundamental problem is of great interest in view of its applications to building insulations. In order to account for the non-Darcy effects, the generalised volume-averaged momentum equation derived by Vafai and Tien [15] will be solved along with the unsteady energy equation, assuming that one of the walls is suddenly heated and the other suddenly cooled. Thus, the velocity and thermal boundary layers grow upward at the hot plate and downward at the cold plate (provided that the thermal expansion coefficient is positive). At a short distance from the ends where the boundary layers meet, the velocity and temperature profiles are fully developed. We shall focus on the transient behavior of temperature and velocity fields in the fully developed region, assuming that both walls in the mathematical model are infinitely long. It will be shown that exact solutions exist under the two distinct asymptotic states, at small and large times, respectively. Finite difference calculations are also carried out for the intermediate times, in which no similarity solutions exist. Comparison of the asymptotic solutions and finite difference calculation results reveals that the transient behavior of free

convection between parallel plates may well be described by matching the two distinct asymptotic solutions obtained at small and large times, respectively.

Governing equations, initial and boundary conditions

Let us consider infinitely long vertical parallel plates embedded in a fluid saturated porous medium, as shown in Fig. 1. Both the plates and porous medium are initially at the same temperature, T_0 . Suppose that the fluid in a porous medium is at rest at $t = 0$, at which time, one of the plates is suddenly heated up to temperature, $T_0 + \Delta T$, while the other is suddenly cooled down to temperature, $T_0 - \Delta T$. Thus, a fluid motion is induced as the result of the buoyancy force. (The present solution procedure can be extended to the case where only one of the wall temperatures is subjected to a sudden change. In fact, the small time solution to be discussed later, is directly applicable for an initial period of such a case also, as we assume that there is an imaginary wall at the channel center plane. It should also be pointed out that some circulatory flow motions exist in an actual free convective space of finite extent. The present model should be regarded as the limiting case of closely spaced parallel plates.)

Upon treating a fluid-saturated porous medium as a continuum, Vafai and Tien [15] integrated the Navier-Stokes equation for a fluid over a local control volume, and derived a volume averaged momentum equation. This generalised momentum

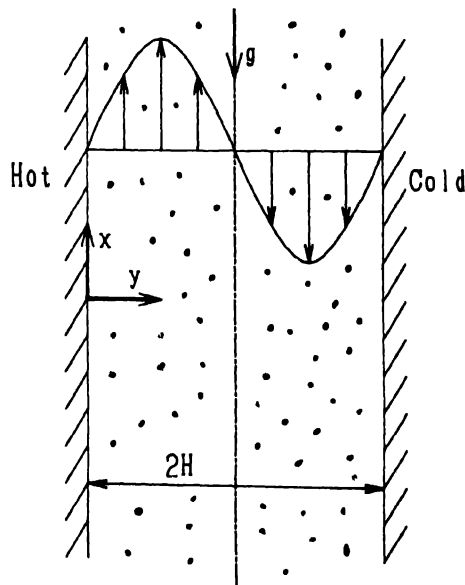


Fig. 1. Physical model and its coordinates.

equation for non-Darcy flows reveals the importance of the viscous diffusion term known as the Brinkman term for comparatively high porous materials. Details of the derivation of the generalised momentum equation can be found in [15].

We assume that the properties of the fluid and porous medium are constant, and that the Boussinesq approximation is valid. (In reality, thermophysical properties may depend on the local temperature. Such temperature influences are assumed to be negligible in the analysis, for the first approximation.) Since the plates are infinitely long, both the temperature and velocity are independent of the coordinate x . Thus, the governing equations, namely, the unsteady energy equation and the generalised momentum equation (Vafai and Tien, [15]), reduce to

$$\sigma \frac{\partial T}{\partial t} = \alpha \frac{\partial^2 T}{\partial y^2}, \quad (1)$$

$$\frac{\rho}{\varepsilon} \frac{\partial u}{\partial t} = \frac{\mu}{\varepsilon} \frac{\partial^2 u}{\partial y^2} - \frac{\mu}{K} u - \frac{\rho C}{\sqrt{K}} |u|u + \rho g \beta (T - T_0). \quad (2)$$

The Darcian (apparent) velocity component in the x direction is denoted by u , while T is the local temperature of the fluid which is assumed to be in local thermal equilibrium. K is the permeability of the porous medium; ε , its porosity; μ , the fluid viscosity; ρ , its density; α , the effective thermal diffusivity of the saturated porous medium; σ , the ratio of heat capacity of the saturated porous medium to that of fluid; C , the empirical constant associated with the porous inertia term; g , the acceleration of gravity; β , the coefficient of thermal expansion. The continuity equation and impermeability at the wall have been already utilized to find the velocity component $v = 0$ everywhere. The associated initial and boundary conditions are as follows:

Initial conditions ($t = 0$):

$$u = 0 \quad \text{and} \quad T = T_0 \quad (3a, b)$$

Boundary conditions ($t > 0$):

$$y = 0: \quad u = 0 \quad \text{and} \quad T = T_0 + \Delta T \quad (4a, b)$$

$$y = 2H: \quad u = 0 \quad \text{and} \quad T = T_0 - \Delta T \quad (5a, b)$$

or we may replace Eqs. (5a, b) by

$$y = H: \quad u = 0 \quad \text{and} \quad T = T_0 \quad (6a, b)$$

due to the symmetric nature of the boundary conditions, with respect to the channel center line at $y = H$.

Solution to the energy equation

The energy equation (1) (subject to Eqs. (3b), (4b) and (6b)), which is independent of the velocity u , may be solved by means of the standard trigonometric Fourier series, as

$$\theta = 1 - \frac{y}{H} - \frac{2}{\pi} \sum_{n=1}^{\infty} \frac{1}{n} \exp(-n^2 \pi^2 \zeta) \sin\left(n\pi \frac{y}{H}\right) \quad (7)$$

where

$$\theta = (T - T_0)/\Delta T \quad (8)$$

and

$$\zeta = \alpha t / \sigma H^2 \quad (9)$$

Eq. (7) reduces to

$$\theta = 1 - \operatorname{erf}(\eta/2) \quad \text{for small } \zeta \quad (10a)$$

and

$$\theta = 1 - (y/H) \quad \text{for large } \zeta \quad (10b)$$

where

$$\eta = y/(\alpha t / \sigma)^{1/2} \quad (11)$$

Small time solution

Within a sufficiently small time period after the sudden change on the wall temperature, neither Darcy nor Forchheimer resistance is significant, since the induced velocity level may not be appreciable yet. Upon substituting Eq. (10a) into the fourth term on the right-hand-side of Eq. (2), and neglecting the second and third terms,

$$\frac{\rho}{\varepsilon} \frac{\partial u}{\partial t} = \frac{\mu}{\varepsilon} \frac{\partial^2 u}{\partial y^2} + \rho g \beta \Delta T \left\{ 1 - \operatorname{erf}\left(\frac{\eta}{2}\right) \right\} \quad (12)$$

Let us assume a functional form for the velocity u as

$$u = u_{\text{ref}} \zeta f(\eta) \quad (13)$$

where

$$u_{\text{ref}} = \frac{\varepsilon g \beta \Delta T H^2}{\nu} \quad (14)$$

After some manipulation, Eq. (12) may be transformed into an ordinary differential equation in terms of $f(\eta)$:

$$f'' + \frac{1}{\text{Pr} \sigma} (\frac{1}{2} \eta f' - f) + \left\{ 1 - \text{erf} \left(\frac{\eta}{2} \right) \right\} = 0 \quad (15)$$

where $\text{Pr} = \nu/\alpha$ is the Prandtl number. The boundary conditions given by Eqs. (4a) and (6a) may be rewritten in terms of $f(\eta)$ as

$$f(0) = 0 \quad \text{and} \quad f(\infty) = 0 \quad (16a, b)$$

where ζ is sufficiently small to replace $\eta = \zeta^{-1/2}$ by $\eta \rightarrow \infty$. For a given value of the product $\text{Pr} \sigma$, Eq. (15) subject to the boundary conditions (16), may be solved by any standard integration scheme such as the Runge-Kutta-Gill method. Thus, similarity solutions exist for this small time case.

Large time solution (steady state solution)

As the time elapses, the temperature profile becomes linear (see Eq. (10b)). Then, the unsteady term on the left-hand-side of Eq. (2) vanishes, and the equation reduces to

$$\frac{\mu}{\varepsilon} \frac{d^2 u}{dy^2} - \frac{\mu}{K} u - \frac{\rho C}{\sqrt{K}} |u| + \rho g \beta \Delta T \left(1 - \frac{y}{H} \right) = 0 \quad (17)$$

Upon introducing another function $F(y/H)$ such that

$$u = u_{\text{ref}} F \left(\frac{y}{H} \right) \quad (18)$$

Eq. (17) may be rewritten as

$$\frac{d^2 F}{d(y/H)^2} - \frac{1}{\text{Da}} F \left(1 + \frac{\text{Gr}^*}{\text{Da}} |F| \right) + \left(1 - \frac{y}{H} \right) = 0 \quad (19)$$

where

$$Da = K/\epsilon H^2 \quad (20a)$$

is the Darcy number, and

$$Gr^* = CK^{3/2}g\beta\Delta T/\nu^2 \quad (20b)$$

is the "micro-scale" Grashof number, in which the reference length scale is chosen to be the length scale of the micro-structure, namely, the square root of the permeability of the porous medium. The boundary conditions for the function $F(y/H)$ are

$$F(0) = 0 \quad \text{and} \quad F(1) = 0 \quad (21a, b)$$

For a given set of the parameters, Da and Gr^* , the ordinary differential equation (19) for $F(y/H)$ must be integrated, numerically to find u . However, for slow flows in which the Forchheimer term is negligible (i.e. $Gr^* = 0$), the following analytical solution exists:

$$F(y/H) = Da \left[1 - (y/H) - \frac{\sinh\{[1 - (y/H)]/Da^{1/2}\}}{\sinh(1/Da^{1/2})} \right] \quad (22)$$

which, under the limiting condition $Da \rightarrow \infty$, leads to the well-known solution for Newtonian fluids:

$$F(y/H) = \frac{1}{6} \left\{ \left(1 - \frac{y}{H} \right) - \left(1 - \frac{y}{H} \right)^3 \right\} \quad (23)$$

Under the other physical limiting condition, namely, $Da \rightarrow 0$, the viscous (Brinkman) term can be dropped. Then, Eq. (19) reduces to a quadratic equation in terms of F , which may be solved to give

$$F(y/H) = Da \frac{[1 + 4Gr^*\{1 - (y/H)\}]^{1/2} - 1}{2Gr^*} \quad \text{for } 0 \leq y/H \leq 1 \quad (24a)$$

and

$$F(y/H) = -Da \frac{[1 + 4Gr^*\{(y/H) - 1\}]^{1/2} - 1}{2Gr^*} \quad \text{for } 1 \leq y/H \leq 2 \quad (24b)$$

Finite difference solution at intermediate times

For the intermediate times in which ζ is the order of unity, no similarity solutions exist. We may appeal to a finite difference method to integrate the original partial differential equations (1) and (2) with the initial and boundary conditions given by (4) and (6). The personal computer finite volume method program "SUNSET" developed by Katsuki and Nakayama [15] for flow and heat transfer analysis of unsteady incompressible flows, was used after minor modifications, to solve only the unsteady energy and u momentum equations in one dimension. Calculations were performed using 41 grids across the channel, with a dimensionless time increment of 5×10^{-4} . (Preliminary sample calculations using 41 and 81 grids, revealed that the coarser grid already gives sufficient accuracy.)

Results and discussion

In Fig. 2, transient temperature profiles generated from the analytic expression (7) are compared against numerical results obtained directly from Eq. (1) by the finite difference scheme. The two sets of profiles are almost identical, as they should. Thus, we may calculate the transient Nusselt number Nu from Eq. (7) as

$$Nu = -H \left. \frac{\partial \theta}{\partial y} \right|_{y=0} = 1 + 2 \sum_{n=1}^{\infty} \exp(-n^2 \pi^2 \zeta) \quad (25)$$

The finite difference solution agrees well with the analytic solution as can be seen from Fig. 3.

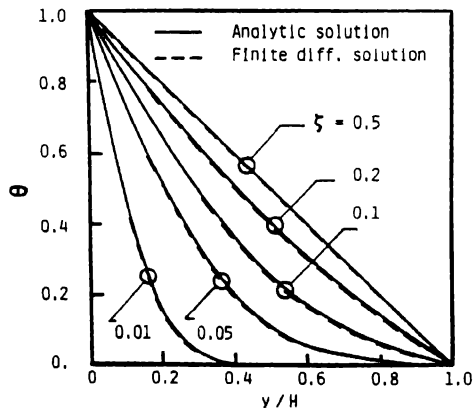


Fig. 2 Temporal development of temperature profiles

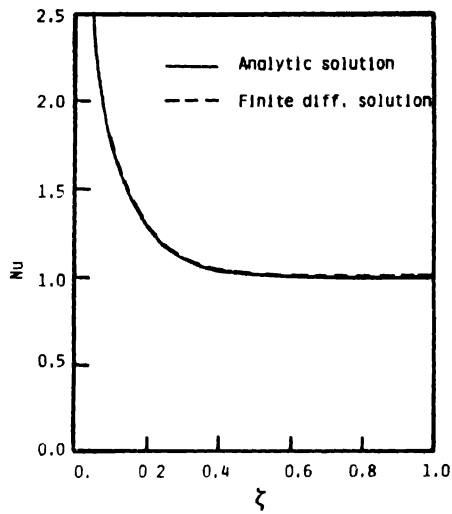


Fig 3 Temporal development of Nusselt number

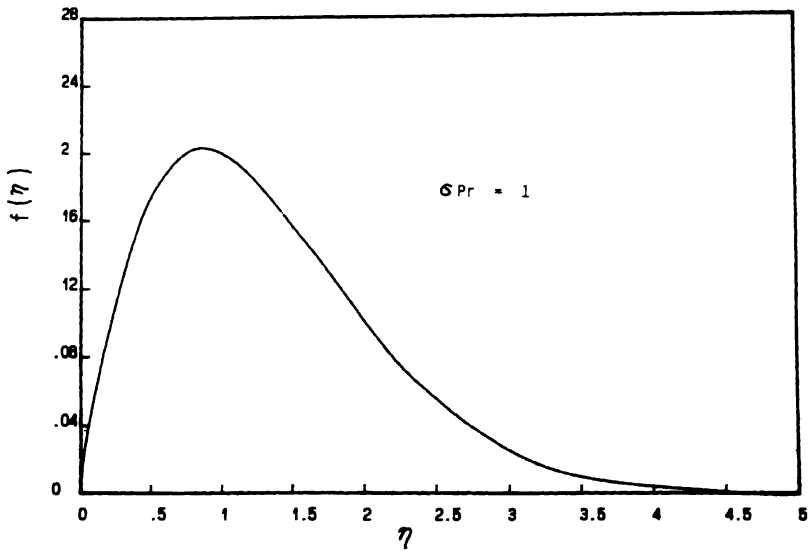


Fig 4 Velocity profile based on the small time solution.

For $Pr\sigma = 1$, numerical integrations of Eq. (15) have been carried out with an increment of $\Delta\eta = 0.05$, to find $f(\eta)$. The upper bound of integration, $\eta \rightarrow \infty$, was replaced by $\eta = 10$, which was confirmed to be sufficiently far from the wall. The integration results are presented in Fig. 4 in terms of the function $f = u/u_{ref}\zeta = u/\epsilon g\beta\Delta T t$ and the similarity variable $\eta = y/(\alpha t/\sigma)^{1/2} = (y/H)/\zeta^{1/2}$. It should be noted that the resulting $f(\eta)$ profile shown in Fig. 4 represents all possible transient velocity profiles we get under $Pr\sigma = 1$ within an initial time period, since the small time solution is independent of Da and Gr^* . The results from the small time solution are replotted in Fig. 5, changing the ordinate and abscissa variables to $u/u_{ref} = \zeta f$ and y/H , respectively, such that we may directly compare the small time solution against the finite difference calculation results (obtained with $Da = \infty$). Excellent agreement can be seen between the two solutions for $\zeta \leq 0.1$. For large ζ , the small time solution tends to overestimate the velocity level. Yet, even for large ζ , the velocity near the wall closely follows the profile of the small time similarity solution.

Finite difference calculation results obtained at $\zeta = 0.4, 0.5, 0.6$ and 1.0 are compared with the large time solution (the steady state solution), in Fig. 6, for the case

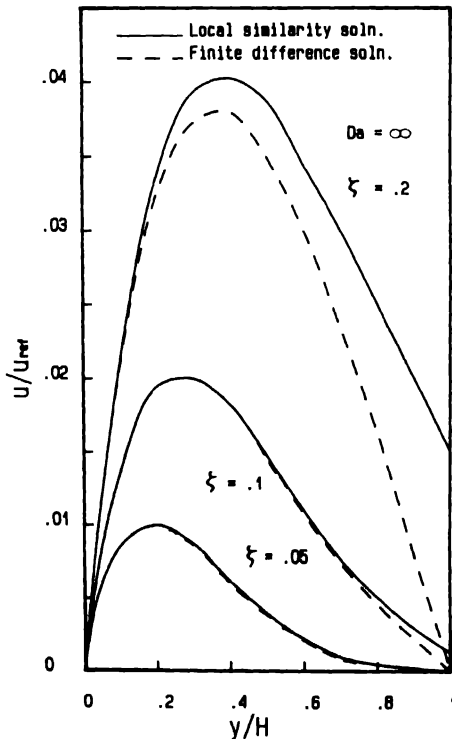


Fig. 5 Comparison of the small time solution and finite difference solution

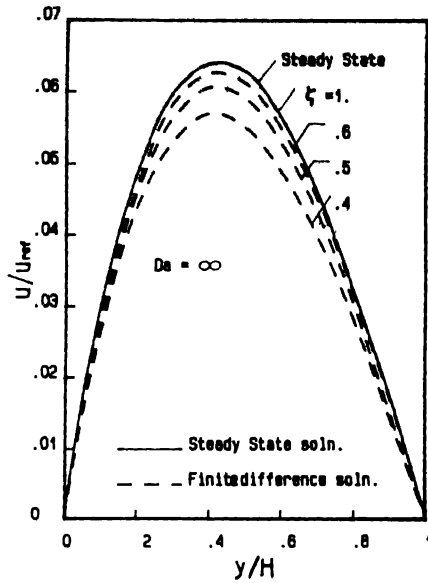


Fig. 6 Comparison of the large time solution and finite difference solution

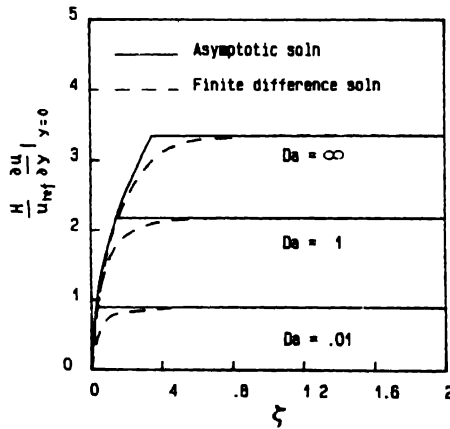


Fig. 7 Matching of the small and large time solutions

of $Da = \infty$ (i.e. Eq. (23)). The profile obtained at $\zeta = 0.5$ from the finite difference calculations is already close to the steady state solution, and the profile at $\zeta = 1.0$ appears to be almost identical to the steady state profile.

The preceding observation on the present small and large time solutions suggests that these two asymptotic solutions cover a considerably wide range of ζ . Subsequent-

ly, the range where the finite difference solution departs significantly from both of the asymptotic solutions can be restricted to a rather narrow range of ζ , say $0.2 < \zeta < 0.5$ for the case of $Da = \infty$. For a further examination in this respect, the temporal development of the dimensionless vorticity at the wall $(H/u_{ref})(\partial u/\partial y)_{y=0}$ is illustrated in Fig. 7, for the case of $Gr^* = 0$, with Da from 10^{-2} , 10^{-1} and ∞ . The results from the small time solution, the large time solution and the finite difference solution are plotted in the figure. The figure suggests that the solid lines generated by connecting the small time solution, namely,

$$\frac{H}{u_{ref}} \frac{\partial u}{\partial y} \bigg|_{y=0} = \left(\frac{\zeta}{\pi} \right)^{1/2} \quad (26a)$$

with the large time solution, namely,

$$\frac{H}{u_{ref}} \frac{\partial u}{\partial y} \bigg|_{y=0} = Da \left(\frac{1}{Da^{1/2} \tanh(1/Da^{1/2})} - 1 \right) \quad (26b)$$

may be used to describe the transient behavior of the velocity field with a reasonable accuracy.

The steady state velocity profiles for $Gr^* = 0$ generated from Eq. (22) with $Da = 10^{-2}$, 10^{-1} and ∞ , are plotted in Fig. 8 to illustrate the effects of Da on the

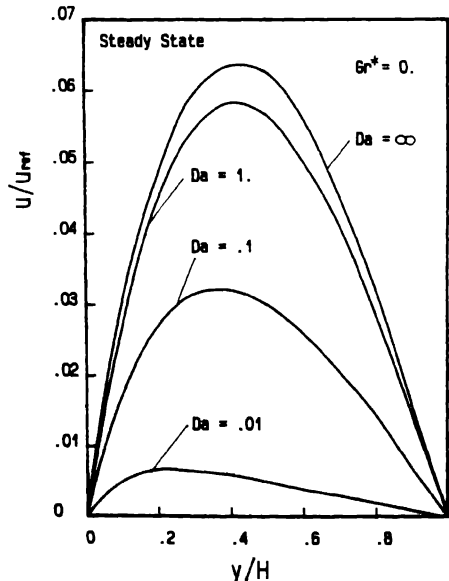


Fig. 8. Effects on Da on the velocity profile.

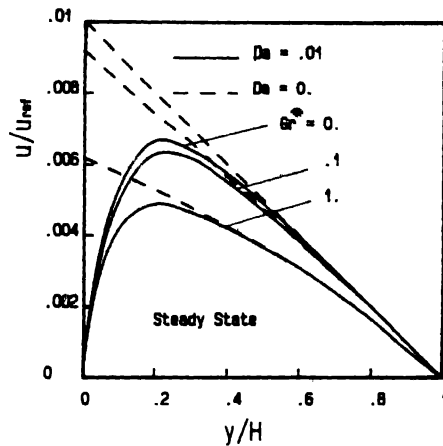


Fig. 9 Effects on Gr^* on the velocity profile

velocity profiles. The velocity becomes quite sensitive to Da , especially when $Da < 1$. Finally, the effects of the Forchheimer term are examined in Fig. 9. The steady state velocity profiles obtained for $Gr^* = 0, 0.1$ and 1.0 by integrating Eq. (19) with $Da = 10^{-2}$ are shown in the figure. As the Forchheimer resistance (Gr^*) becomes large, the velocity naturally decreases, and its profile tends to be somewhat flatter, as the result of the velocity square term. In the figure, the slip velocity profiles based on Eq. (24a) are also indicated by dashed lines, so as to isolate the effect of the viscous diffusion term (i.e. the Brinkman term). It is clearly seen that the boundary friction due to the presence of the impermeable wall significantly alters the velocity distribution near the wall.

Conclusions

The problem of transient non-Darcy free convection between two parallel vertical plates embedded in a fluid saturated porous medium was treated. One of the infinitely long walls is suddenly heated, while the other suddenly cooled. The generalized momentum equation proposed by Vafai and Tien, which considers the effects of porous inertia and solid boundary in addition the Darcy flow resistance, was solved along with the unsteady energy equation. Exact solutions are found for the asymptotic states at small and large times. Finite difference calculations were also carried out to find numerical solutions for the intermediate times in which no similarity solutions are possible. It has been found that the transient free convection between the parallel plates may well be described by matching the two distinct asymptotic solutions at small and large times.

References

1. Siegel, R., Transient free convection from a vertical flat plate. *Trans. ASME* 80 (1958) 347–359.
2. Goldstein, R. J. and Briggs, D. G., Transient free convection about vertical plates and cylinders. *J. Heat Transfer* 86C (1984) 490–500.
3. Nanbu, B. K., Unsteady Falkner-Skan flow. *Z. Angew. Math. Phys.* 22 (1971) 1167–1172.
4. Watkins, C. B., Heat transfer in the boundary layer over an impulsively started flat plate. *J. Heat Transfer* 97 (1975) 482–484.
5. Sparrow, E. M. and Siegel, R., Transient film condensation. *J. Applied Mechanics* 81(1) (1959) 120–121.
6. Wilson, S. D. R., Unsteady and two-dimensional flow of condensate film. *J. Heat Transfer* 98 (1976) 313–315.
7. Johnson, C. H. and Cheng, P., Possible similarity solution for free convection boundary layers adjacent to flat plates in porous media. *Int. J. Heat Mass Transfer* 21 (1978) 709–718.
8. Ingham, D. B., Merkin, J. H. and Pop, I., Flow past a suddenly cooled vertical flat surface in a saturated porous medium. *Int. J. Heat Mass Transfer* 25 (1982) 1916–1919.
9. Ingham, D. B. and Brown, S. N., Flow past a suddenly heated vertical plate in a porous medium. *Proc. R. Soc. Lond.* A403 (1986) 51–80.
10. Jang, J.-Y. and Ni, J.-R., Transient free convection with mass transfer from an isothermal vertical flat plate embedded in a porous medium. *Int. J. Heat Fluid Flow* 10 (1989) 59–65.
11. Cheng, P. and Pop, I., Transient free convection about a vertical flat plate embedded in a porous medium. *Int. J. Engng Sci.* 22 (1984) 253–264.
12. Cheng, P. and Chui, D. K., Transient film condensation on a vertical surface in a porous medium. *Int. J. Heat Mass Transfer* 27 (1984) 795–798.
13. Chen, C.-K., Hung, C.-I. and Horng, H.-C., Transient natural convection on a vertical flat plate embedded in a high-porosity medium. *J. Heat Transfer* 109 (1989) 112–118.
14. Nakayama, A., Kokudai, T. and Koyama, H., Non-Darcy boundary layer flow and forced convective heat transfer over a flat plate in a fluid-saturated porous medium. *J. Heat Transfer* 112 (1990) 157–162.
15. Vafai, K. and Tien, C. L., Boundary and inertia effects on flow and heat transfer in porous media. *Int. J. Heat Mass Transfer* 30 (1981) 1391–1405.
16. Katsuki, M. and Nakayama, A., *Numerical Simulation of Heat and Fluid Flow*. Tokyo: Monkita Shuppan (1990) pp. 35–117 (in Japanese).

Investigation of chemically reacting and radiating supersonic flow in channels

M MANI¹, S.N TIWARI^{2,*} & J.P DRUMMOND³

¹Department of Propulsion and Thermodynamics McDonnell Aircraft Company, St. Louis, MO 63166, USA

²Department of Mechanical Engineering and Mechanics Old Dominion University Norfolk, VA 23529–0247 USA (*author for correspondence)

³Computational Methods Branch High Speed Aerodynamics Division NASA Langley Research Center, Hampton VA 23665 USA

Received 7 November 1990; accepted in revised form 7 October 1991

Abstract The two-dimensional time dependent Navier–Stokes equations are used to investigate supersonic flows undergoing finite rate chemical reaction and radiation interaction for a hydrogen–air system. The explicit multi-stage finite volume technique of Jameson is used to advance the governing equations in time until convergence is achieved. The chemistry source term in the species equation is treated implicitly to alleviate the stiffness associated with fast reactions. The multidimensional radiative transfer equations for a nongray model are provided for general configuration, and then reduced for a planar geometry. Both pseudo-gray and nongray models are used to represent the absorption–emission characteristics of the participating species.

The supersonic inviscid and viscous nonreacting flows are solved by employing the finite volume technique of Jameson and the unsplit finite difference scheme of MacCormack to determine a convenient numerical procedure for the present study. The specific problem considered is of the flow in a channel with a 10° compression–expansion ramp. The calculated results are compared with the results of an upwind scheme and no significant differences are noted. The problem of chemically reacting and radiating flows are solved for the flow of premixed hydrogen–air through a channel with parallel boundaries, and a channel with a compression corner. Results obtained for specific conditions indicate that the radiative interaction can have a significant influence on the entire flowfield.

Nomenclature

A = band absorptance (m^{-1})
 A_0 = band width parameter (m^{-1})
 C_j = concentration of the j th species (kg mol/m^3)
 C_0 = correlation parameter ($(\text{N/m}^2)^{-1} \text{m}^{-1}$)
 C_p = constant pressure specific heat (J/kg K)
 e_ω = Planck's function ($\text{J/m}^2 \text{s}$)
 E = total internal energy (J/kg)
 f_j = mass fraction of the j th species
 h = static enthalpy of mixture (J/kg)
 H = total enthalpy (J/kg)
 I = identity matrix
 I_ν = spectral intensity (J/m s)

$I_{b\nu}$ = spectral Planck function
 k = thermal conductivity (J/m sK)
 K_b = backward rate constant
 K_f = forward rate constant
 \mathbf{l} = unit vector in the direction of $\overline{PP_w}$
 M_j = molecular weight of the j th species (kg/kg mol)
 P = pressure (N/m^2)
 P_j = partial pressure of the j th species (N/m^2)
 P_e = equivalent broadening pressure ratio
 Pr = Prandtl number
 P_w = a point on the wall
 q_R = total radiative heat flux ($\text{J/m}^2 \text{s}$)

$q_{R_{\text{so}}}$ = spectral radiative heat flux ($\text{J/m}^2 \text{s}$)
 R = gas constant (J/Kg K)
 r_w = distance between the points P and P_w (m)
 S = integrated band intensity ($(\text{N/m}^2)^{-1} \text{m}^{-2}$)
 S = integrated band intensity ($(\text{N/m}^2)^{-1} \text{m}^{-2}$)
 T = temperature (K)
 u, v = velocity in x and y direction (m/s)
 \dot{w}_j = production rate of the j th species ($\text{kg/m}^3 \text{s}$)
 x, y = physical coordinate
 z = dummy variable in the y direction

Greek symbols

γ = ratio of specific heats

Δt_{ch} = chemistry time step (s)
 Δt_f = fluid-dynamic time step (s)
 κ = absorption coefficient (m^{-1})
 $\kappa_\lambda, \kappa_\nu$ = spectral absorption coefficient (m^{-1})
 κ_p = Planck mean absorption coefficient
 λ = second coefficient of viscosity, wavelength (m)
 μ = dynamic viscosity (laminar flow) (kg/m s)
 ξ, η = computational coordinates
 ρ = density (kg/m^3)
 σ = Stefan-Boltzmann constant ($\text{erg/s cm}^2 \text{K}^3$)
 τ = shear stress (W/m^2)
 ϕ = equivalence ratio
 ω = wave number (m^{-1})
 ν_c = frequency at the band center

Introduction

In the last several years, there has been a great deal of research towards the development of a hypersonic transatmospheric vehicle. At the NASA Langley Research Center, the hydrogen-fueled supersonic combustion ramjet (scramjet) engine has been a strong candidate for propelling such a vehicle. Both experimental and numerical techniques are being employed to develop a better understanding of the complex flow field in different regions of the engine. Numerical modeling of the flow in various sections has proven to be a valuable tool for gaining more insight into the complex nature of these flows [1–4].

The combustion of hydrogen and air in the scramjet combustor results in absorbing-emitting gases such as water vapor and hydroxyl radical. The presence of such gases makes the study of radiation heat transfer an important issue. There are several models available in the literature to represent the absorption-emission characteristics of molecular gases [5–11]. One- and two-dimensional radiative heat transfer equations for various flow and combustion related problems are available in [12–18]. In an earlier study [18], both pseudo-gray and nongray gas models were employed to evaluate radiative heat transfer for chemically reacting supersonic flow. The radiative heat transfer was evaluated only in the normal direction to the flow. The results of both models were compared, and the pseudo-gray model was found to be fairly accurate and computationally more efficient.

The objectives of the present study are to extend the radiative heat transfer formulation to the multi-dimensional case, and to investigate the effect of radiative heat transfer in both the transverse and streamwise directions. The finite volume scheme using the four-stage Runge-Kutta technique developed by Jameson, Schmidt and Turkel [19] is used to solve the governing equations. The results are compared

with the unsplit MacCormack predictor-corrector scheme [20]. The modified Runge-Kutta scheme originally was developed for the solution of the Euler equations and has proven to be an efficient and effective scheme. This scheme was extended by Swanson and Turkel to solve the thin layer Navier-Stokes equations for transonic flows over airfoils [21]. Here, the scheme is used to solve supersonic chemically reacting and radiating viscous channel flows.

The flow field in the combustor is represented by the Navier-Stokes equations and the appropriate number of species continuity equations [2, 3]. Incorporation of the finite rate chemistry model into the fluid dynamic equations can create a set of stiff differential equations. Recently, Drummond used a more complete chemistry model in the simulation of a supersonic chemically reacting mixing layer [2]. It was pointed out that the use of a more complete chemistry model rather than the global model in the fluid dynamics equations did not result in a set of temporally stiff equations as in the global chemistry case. The global chemistry model is a two-step model for hydrogen-air combustion which involves the species O_2 , N_2 , OH , H_2 , and H_2O . Information on a more complete model is available in the cited reference. Stiffness is due to a large disparity in the characteristic time scales of the governing equations. In the time accurate solution, after the fast transients have decayed and the solutions are changing slowly, taking a larger time step is more efficient. But explicit methods still require small time steps to maintain stability. An eigenvalue problem associated with a stiff ODE has been solved to express this point clearly in [2]. One way around this problem is to use a fully implicit method. This method, however, requires the inversion of a block multi-diagonal system of algebraic equations. This is difficult to implement to take full advantage of vector processing computers such as VPS-32. The use of a semi-implicit technique, suggested by several investigators [22-24], provides an alternative to the above problems. This technique treats the chemical source term (which is the cause of the stiffness) implicitly, and solves the remaining terms in the equations explicitly. Since the source term is treated implicitly, it is possible to advance the equations in time using the fluid-dynamical time scale. Further discussions on this procedure are provided in [2, 3, 18, 25].

In this study, a modified form of the explicit multi-stage finite volume technique of references [19, 21] is employed to investigate the extent of radiative interactions in a chemically reacting hydrogen-air system. The validity of the basic method, however, is established first by comparing selected results with available results of well established codes [3, 15, 25]. After this validation, the radiative flux terms are included in the basic code for further investigation.

Basic formulation

The physical models for analyzing the flow field in a scramjet engine are described in

[1-4]. For two-dimensional flows, the Navier-Stokes and species continuity equations are represented in physical coordinates as

$$\frac{\partial U}{\partial t} + \frac{\partial F}{\partial x} + \frac{\partial G}{\partial y} + H = 0, \quad (1)$$

where vectors, U , F , G and H are expressed as

$$U = \begin{bmatrix} \rho \\ \rho u \\ \rho v \\ \rho E \\ \rho f_j \end{bmatrix},$$

$$F = \begin{bmatrix} \rho u \\ \rho u^2 + P + \tau_{xx} \\ \rho uv + \tau_{xy} \\ (\rho E + P)u + \tau_{xx}u + \tau_{xy}v + q_{cx} + q_{Ry} \\ \rho u f_j - \rho D \frac{\partial f_j}{\partial x} \end{bmatrix},$$

$$G = \begin{bmatrix} \rho v \\ \rho uv + \tau_{yx} \\ \rho v^2 + P + \tau_{yy} \\ (\rho E + P)v + \tau_{yy}v + \tau_{xy}u + q_{cy} + q_{Rx} \\ \rho v f_j - \rho D \frac{\partial f_j}{\partial y} \end{bmatrix},$$

$$H = \begin{bmatrix} 0 \\ 0 \\ 0 \\ 0 \\ -\dot{W}_j \end{bmatrix}.$$

The viscous tensors in the F and G terms of equation (1) are given as

$$\tau_{xx} = -\lambda \left(\frac{\partial u}{\partial x} + \frac{\partial v}{\partial y} \right) - 2\mu \frac{\partial u}{\partial x}, \quad (2a)$$

$$\tau_{xy} = -\mu \left(\frac{\partial u}{\partial y} + \frac{\partial v}{\partial x} \right), \quad (2b)$$

$$\tau_{yy} = -\lambda \left(\frac{\partial u}{\partial x} + \frac{\partial v}{\partial y} \right) - 2\mu \frac{\partial v}{\partial y} \quad (2c)$$

The quantities q_{cx} and q_{cy} in the F and G terms involve combined energy contributions from molecular conduction and mass diffusion and are expressed as

$$q_{cx} = -k \frac{\partial T}{\partial x} - \rho D \sum_{j=1}^m h_j \frac{\partial f_j}{\partial x}, \quad (3a)$$

$$q_{cy} = -k \frac{\partial T}{\partial y} - \rho D \sum_{j=1}^m h_j \frac{\partial f_j}{\partial y} \quad (3b)$$

For the Lewis number of unity, equations (3) reduce to [25]

$$q_{cx} = -\frac{\gamma\mu}{Pr} \frac{\partial e}{\partial x}, \quad (4a)$$

$$q_{cy} = -\frac{\gamma\mu}{Pr} \frac{\partial e}{\partial y}, \quad (4b)$$

where $e = h - P/\rho$. The molecular viscosity μ is evaluated from the Sutherland's formula. The total internal energy E in equation (1) is given by

$$E = -P/\rho + \frac{u^2 + v^2}{2} + \sum_{j=1}^m h_j f_j \quad (5)$$

The justifications for considering the Lewis number of unity and using the Sutherland's relation for the viscosity variation are given in [25].

For the physical model considered in this study, the boundary conditions employed are as follows. Since the flow is supersonic, the inflow properties are assumed to be chemically frozen. The outflow conditions are calculated from adjacent nodes using a first order extrapolation. The pressure at walls are calculated by a second order one-sided differencing procedure. Depending on the specific case investigated either constant wall temperature or adiabatic wall conditions are employed. The free stream

conditions considered for each case are indicated in discussing the results. Specific relations are needed for the chemistry source and radiative flux terms. These are discussed briefly in the following sections.

Chemistry and thermodynamic model

For the numerical solution of reacting flows, a chemistry model is needed to represent the combustion process. The chemistry model used in this study is the two-step global finite rate hydrogen-air combustion model developed by Rogers and Chinitz [26]. This chemistry model was deduced from a 28 reaction model, and it is adequate for initial (ignition) temperatures between 1,000 K and 2,000 K and for equivalence ratios between 0.2 and 2.0. In the first step, hydrogen and air react and produce hydroxyl radical and in the second step, hydroxyl radical and hydrogen react to produce water vapor. The reactions are expressed as



where K_{f1} and K_{b1} represent the forward and reverse reaction rate constants respectively. The relations for K_{f1} , K_{b1} , and the details of the chemistry models can be found in [26].

The chemistry source terms, on a mass basis, are found by multiplying the molar changes and corresponding molecular weight

$$\dot{w}_j = \dot{C}_j M_j. \quad (8)$$

By applying the law of mass action to the global model, the chemistry source terms of the four species are obtained as

$$\dot{C}_{\text{O}_2} = -K_{f1} C_{\text{H}_2} C_{\text{O}_2} + K_{b1} C_{\text{OH}}^2, \quad (9)$$

$$\dot{C}_{\text{H}_2\text{O}} = 2(K_{f2} C_{\text{OH}}^2 C_{\text{H}_2} - K_{b2} C_{\text{H}_2\text{O}}^2), \quad (10)$$

$$\dot{C}_{\text{H}_2} = \dot{C}_{\text{O}_2} - 1/2 \dot{C}_{\text{H}_2\text{O}}, \quad (11)$$

$$\dot{C}_{\text{OH}} = -(2\dot{C}_{\text{O}_2} + \dot{C}_{\text{H}_2\text{O}}). \quad (12)$$

The value of specific heat at constant pressure, C_p , is assumed to be a linear function of the temperature, i.e.,

$$C_{p,j} = a_j T + b_j, \quad (13)$$

where a_j and b_j are constants. For species considered in this study, the numerical values of these constants are given in [4]. The gas constant for the mixture can be evaluated by a mass weighted summation over all species as

$$\bar{R} = \sum_{j=1}^5 f_j R_j. \quad (14)$$

The equation of state for the mixture can be written as

$$P = \rho \bar{R} T. \quad (15)$$

Radiation transfer model

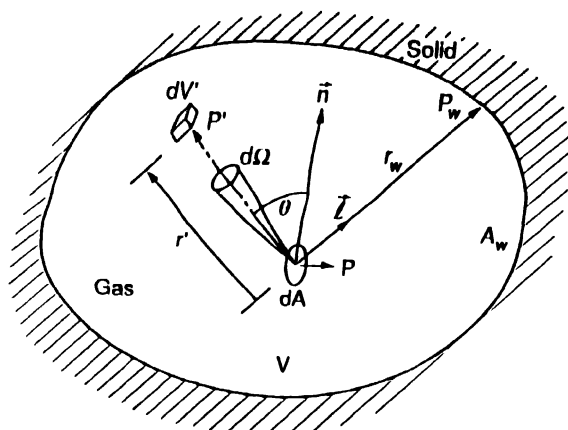
Evaluation of the energy equation presented in equation (1) requires an appropriate expression for the net radiative flux terms, q_{Rx} and q_{Ry} . Therefore, a suitable radiative transport model is needed. Various models are available in the literature to represent the absorption-emission characteristics of molecular species; a review of the important models is available in [11].

The equations of radiative transport are expressed generally in integro-differential forms; integration involves both the frequency spectrum and physical coordinates. In many realistic three-dimensional physical problems, the complexity of the radiative transport equations can be reduced by introducing the tangent-slab approximation. This approximation treats the gas layer as a one-dimensional slab in evaluation of the radiative flux [18]. The multi-dimensional equations of radiative heat transfer are provided for an arbitrary geometry, and then an approximate method is used to present the formulation for nongray and gray gases. Finally, these equations are reduced for channel flows.

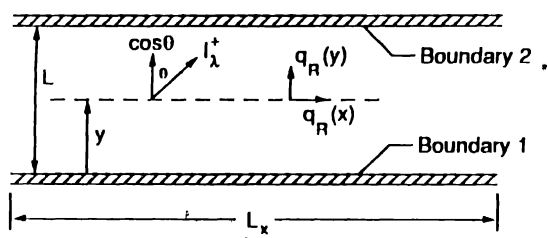
The radiative transport equations in the present study are obtained for a nonscattering medium contained within solid walls of an arbitrary configuration as shown in Fig. 1. The general formulation of radiative transfer for the gas under the condition of local thermodynamic equilibrium is given as [13, 25]

$$\begin{aligned} q_R = & \int_{4\pi} I(P_w) l \, d\Omega - \int_{4\pi} I_{vc}(P_w) A(r_w) l \, d\Omega \\ & + \int_{4\pi} \int_0^{r_w} I_{bvc}(P') A'(r') l \, dr' \, d\Omega. \end{aligned} \quad (16)$$

The first term on the right-hand side of equation (16) represents the radiative flux in the absence of participating medium; the second term gives the portion of the wall radiation which is absorbed by the gas, and the last term indicates the emission from the gas which arrives at point P .



(a) Arbitrary configuration



(b) Plane radiating layer between parallel boundaries

Fig 1 Physical model for absorbing-emitting medium

For a nongray planar system with two parallel walls at different temperatures (Fig 1), equation (16) reduces to [13, 17, 18]

$$\begin{aligned}
q_R = & e_1 - e_2 - \int_{-\alpha}^{\infty} \int_{-\infty}^{\infty} \int_0^y e_{vc_1}(x', z') A(r_1) \frac{dx' dy' dz'}{\pi r_1^3} \\
& + \int_{-\infty}^{\infty} \int_{-\alpha}^{\alpha} \int_y^L e_{vc_2}(x', z') A(r_2) \frac{dx' dy' dz'}{\pi r_2^3} \\
& + \int_{-\alpha}^{\alpha} \int_{-\infty}^{\infty} \int_y^L e_{vc}(x', y', z) \frac{A'(r')}{\pi r_1^3} dx' dy' dz', \quad (17)
\end{aligned}$$

where

$$r_1 = [(x-x')^2 + y^2 + (z-z')^2]^{1/2},$$

$$r_2 = [(x-x')^2 + (y-L)^2 + (z-z')^2]^{1/2},$$

$$r' = [(x-x')^2 + (y-y')^2 + (z-z')^2]^{1/2}$$

Equation (17), e_{vc_1} and e_{vc_2} represent the Planck function values at the band center and wall temperatures T_1 and T_2 , respectively. The term e_w represents the value of the Planck function at the band center and local gas temperature. It should also be pointed out that the last term in equation (17) is expressed in the absolute form [5, 17, 18]. With proper modifications, equation (17) can be applied to both x - and y -directions.

For a one-dimensional multi-band gaseous system equation (17) reduces to,

$$q_R(y) = e_1 - e_2 + \sum_{i=1}^N \left\{ \int_0^y F_{1vc_i}(y') A'_i(y-y) dy' - \int_y^L F_{2vc_i}(y') A'_i(y'-y) dy' \right\}, \quad (18)$$

where

$$F_{1vc}(y) = e_{vc}(y) - e_{vc_1}, \quad F_{2vc}(y) = e_{vc}(y) - e_{vc_2}$$

The equation resulting from employing the tangent slab approximation and exponential kernel approximation for evaluating the exponential function is of the same general form as equation (18). The detailed derivation of the radiative flux and its divergence is given in [17, 18]. The relation for the radiative flux is given by

$$q_R(y) = e_1 - e_2 + \frac{3}{2} \sum_{i=1}^N \left\{ \int_0^y F_{1vc_i}(y') A'_i \left[\frac{3}{2}(y-y') \right] dy' - \int_y^L F_{2vc_i}(y') A'_i \left[\frac{3}{2}(y'-y) \right] dy' \right\} \quad (19)$$

Equations (18) and (19) are in proper form for obtaining nongray solutions for radiatively participating molecular species. However, in order to be able to use the band model correlations, these equations must be transformed in terms of the correlation quantities. It should be noted here that for nongray gases, the divergence of radiative flux is used as a source term in the energy equation. This is more convenient and also avoids scheme dependencies in the computation. The correlation quantities and details of transformations are given in [17]. After the transformation, the divergence of equation (19) is expressed in terms of the wavenumber as

$$\frac{dq_R}{dy} = \frac{3}{2} \sum_{i=1}^n \frac{A_{0i} U_{0i}}{L} \left\{ \int_0^y \frac{de_{\omega_i}(y)}{dy} \bar{A}_i \left[\frac{3}{2} \frac{U_{0i}}{L} (y-y') \right] dy' - \int_y^L \frac{de_{\omega_i}(y)}{dy'} \bar{A}_i \left[\frac{3}{2} \frac{U_{0i}}{L} (y-y) \right] dy' \right\} \quad (20)$$

Equations (18)–(20) reduce to simplified forms in the optically thin and large path length limits, these relations are available in [8, 17, 18]. Expressions similar to equations (18)–(20) can be obtained for radiative transfer in the x -direction. The

derivative \bar{A}_i appearing in equations (18)–(20) is obtained by employing a convenient correlation for the total band absorptance. In this study, the continuous correlation proposed by Tien and Lowder is employed. This correlation is relatively simple and provides accurate results for pressure higher than 0.5 atm [6, 11].

For a gray medium, κ , is independent of the frequency, and therefore it is possible to write the radiative flux equation in terms of an ordinary differential equation as [5, 18]

$$\frac{d^2 q_R(r)}{dr^2} - \frac{9}{4} \kappa^2 q_R(r) = 3\kappa de_b(r)/dr. \quad (21)$$

The solution of equation (21) requires two boundary conditions, which for nonblack diffuse surfaces are given as

$$(1/\varepsilon_1 - 0.5)[\kappa q_R(r)]_{r=0} - (1/3)[dq_R(r)/dr]_{r=0} = 0, \quad (22a)$$

$$(1/\varepsilon_2 - 0.5)[\kappa q_R(r)]_{r=L} + (1/3)[dq_R(r)/dr]_{r=L} = 0. \quad (22b)$$

In this study, both gray and nongray results are obtained by assuming black bounding surfaces.

In the absence of a convenient relation for the average gray gas absorption coefficient, it is customary to replace κ in equations (21) and (22) by the Planck mean absorption coefficient κ_p . For a multi-band gaseous system, κ_p is defined by [5]

$$\kappa = \kappa_p = \frac{P_j}{\sigma T^4(r)} \sum_{i=1}^N e_{\omega_i}(T) S_i(T). \quad (23)$$

It should be noted that κ_p is function of the temperature and the species partial pressure. Since the gray gas formulation is based on the Planck mean absorption coefficient, which accounts for the detailed information on different molecular bands, this approach of radiative formulation is referred to as the “pseudo-gray formulation.” Other models for the mean absorption coefficient are available in the literature but they impose certain spectral restrictions [5, 27].

Method of solution

Modified Runge-Kutta (R-K) finite-volume technique

The governing equation, equation (1), for a region Ω with boundary $\partial\Omega$ can be written as

$$\frac{\partial}{\partial t} \iint_{\Omega} U dx dy + \oint_{\partial\Omega} (F dy - G dx) + \iint_{\Omega} H dx dy = 0. \quad (24)$$

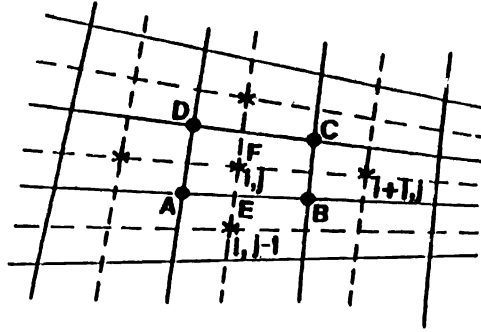


Fig. 2 Finite volume discretization

The discretization procedure follows the method of lines in decoupling the approximation of the spatial and temporal terms. The computational domain is divided into quadrilateral cells (Fig. 2), and equation (24) is applied to each cell separately to obtain the following system of ordinary differential equations:

$$\frac{d}{dt} (A_{ij} U_{ij}) + L U_{ij} + A_{ij} H_{ij} = 0, \quad (25)$$

where L is the spatial discretization operator, and

$$L U_{ij} = FLX_{AB} + FLX_{BC} + FLX_{CD} + FLX_{DA}.$$

The components of U_{ij} are cell averaged quantities, and A_{ij} is the cell area of $ABCD$. The vectors FLX represent the fluxes through the cell sides. For example, FLX_{AB} is written as follows

$$FLX_{AB} = F_{AB} \Delta Y_{AB} - G_{AB} \Delta X_{AB},$$

where F_{AB} and G_{AB} are the viscous and inviscid fluxes in x - and y -directions respectively on the side AB . The inviscid fluxes are evaluated using the average of U of two adjacent cells and the viscous fluxes are evaluated from Green's theorem.

To remove the unwanted oscillations and prevent odd-even decoupling, one must add artificial viscosity. The artificial viscosity employed in this study is the blend of second and fourth order dissipation. The fourth order dissipation is required for the convergence to steady state and the second-order dissipation is necessary to prevent excessive oscillations in the vicinity of shocks. Equation (25) with the inclusion of artificial viscosity is written as

$$\frac{d}{dt} (A_{ij} U_{ij}) + L U_{ij} - D U_{ij} + A_{ij} H_{ij} = 0, \quad (26)$$

where

$$DU_{ij} = D_x^2 U_{ij} + D_y^2 U_{ij} - D_x^4 U_{ij} - D_y^4 U_{ij}.$$

The second and fourth order dissipation terms are evaluated as

$$D_x^2 U_{ij} = \Delta_x \left\{ \frac{A_{i-1/2,j}}{\Delta t} [\varepsilon_{i-1/2,j}^{(2)} (\nabla_x U_{ij})] \right\}, \quad (27)$$

$$D_x^4 U_{ij} = \Delta_x \left\{ \frac{A_{i-1/2,j}}{\Delta t} [\varepsilon_{i-1/2,j}^{(4)} \Delta_x \nabla_x^2 U_{ij}] \right\}, \quad (28)$$

$$\varepsilon_{i-1/2,j}^{(2)} = K^{(2)} \max(v_{i-1,j}, v_{ij}), \quad (29)$$

$$\varepsilon_{i-1/2,j}^{(4)} = \max(0, (K^{(4)} - \varepsilon_{i-1/2,j}^2)), \quad (30)$$

$$v_{ij} = \frac{|P_{i+1,j} - 2P_{i,j} + P_{i-1,j}|}{P_{i+1,j} + 2P_{i,j} + P_{i-1,j}},$$

where $K^{(2)}$ and $K^{(4)}$ are $1/4$ and $1/256$, while Δ_x and ∇_x are forward and backward differences, respectively.

It should be noted that the above damping originally was used to solve the Euler equations on a grid with an aspect ratio close to one. But to solve the Navier–Stokes equations a fine mesh is required near the solid boundary in the normal direction to the flow in order to capture the boundary layer. For computational efficiency, the grid spacing in the flow direction is generally chosen to solve the inviscid terms. Therefore, the aspect ratio is very large (two orders of magnitude). These large distortions create difficulties both for convergence and for the accuracy or steady state results [21].

The damping can be modified to make the scheme behave locally like a TVD scheme [25]. This modification limits the dissipation flux in the high gradient region and removes the oscillations in the vicinity of shocks. To have an effective sensor for the presence of shock waves,

$$\bar{v}_{i-1/2,j} = \max(v_{i+1,j}, v_{i,j}, v_{i-1,j}, v_{i-2,j}).$$

Equations (29) and (30) are then modified as

$$\varepsilon_{i-1/2,j}^{(2)} = \min(1/2, K^{(2)} \bar{v}_{i-1/2,j}) \quad (31)$$

and

$$\varepsilon_{i-1/2,j}^{(4)} = \max(0, K^{(4)} - \alpha \bar{v}_{i-1/2,j}), \quad (32)$$

where

$$K^{(2)} = 1, \quad K^{(4)} = 1/64, \quad \alpha = 2.$$

Equation (26) is discretized temporally and written as

$$A_{ij} \left(\frac{U_{ij}^{n+1} - U_{ij}^n}{\Delta t} \right) + LU_{ij}^n - DU_{ij}^n + A_{ij} H_{ij}^{n+1} = 0. \quad (33)$$

The source term H is then linearized to give

$$H^{n+1} = H^n + \Delta t \frac{\partial H}{\partial U} \left(\frac{U^{n+1} - U^n}{\Delta t} \right). \quad (34)$$

A substitution of equation (34) into equation (33) gives the temporally discrete equations in delta form as

$$\left[I + \Delta t \left(\frac{\partial H}{\partial U} \right) \right] \Delta U^{n+1} = - \frac{\Delta t}{A_{ij}} [LU_{ij} - DU_{ij} + A_{ij} H_{ij}]^n, \quad (35)$$

where $\partial H / \partial U$ is the Jacobian matrix of H and I is the identity matrix.

To advance equation (35) in time, the Householder technique [28, 29] in combination with the modified 4-stage R-K scheme is employed. At time level n , the scheme is written as

$$U^{(0)} = U^{(n)}, \quad (36a)$$

$$\left[I + \Delta t \left(\frac{\partial H}{\partial U} \right) \right] \Delta U^{(k)} = - \frac{\alpha_k \Delta t}{A_{ij}} (LU^{(k-1)} - DU^{(0)} + A_{ij} H_{ij}^n), \quad (36b)$$

$$U^{(k)} = U^{(0)} + \Delta U^{(k)}; \quad U^{(n+1)} = U^{(4)}, \quad (36c)$$

where

$$k = 1, 4; \quad \alpha_1 = 1/4, \quad \alpha_2 = 1/3, \quad \alpha_3 = 1/2, \quad \alpha_4 = 1.$$

For efficiency purposes, the natural and artificial viscosities, chemistry and radiation are evaluated at the first stage and frozen for the remaining stages.

A further discussion on the dissipation techniques of the finite volume schemes, as applied to the present study, is provided here. For simplicity, the original damping technique proposed by Jameson et al. in [19] is referred here as Damp1 and the modified version presented in this study is referred to as Damp2. In the numerical

experiment with Damp1, it is found that the tangential component of the second order dissipation ($\epsilon^{(2)}$) becomes large at the inlet region and this causes the flow to separate near the boundary. The excessive damping is because of the pressure jump, which is caused by the shock emanating from the leading edge. This behavior was also observed by Turkel [31] at the leading and trailing edges of an airfoil. He suggested multiplying the artificial viscosity by M^4 . Chen et al. [32] suggested multiplying $\epsilon^{(2)}$ by a linear factor which is zero near the boundary and one in the farfield. Also the coefficients $K^{(2)}$ and $K^{(4)}$ must be readjusted each time by changing the freestream conditions or the grid size. The above problems makes Damp1 less desirable. On the other hand, Damp2 leads to a scheme which will behave locally like a total variational diminishing (TVD) scheme as long as $\epsilon^{(2)}$ in equation (31a) is equal to 1/2 in the neighborhood of a shock wave [25]. This technique is used in the present study. It should be noted that only the fourth order dissipation is turned off in the high gradient regions. The second order dissipation is smaller than viscous dissipations by one to two orders of magnitude and does not alter the results.

Modified MacCormack's finite-difference scheme

To apply the MacCormack technique, the governing equations are transformed from the physical domain (x, y) to a computational domain (ξ, η) using an algebraic grid generation technique similar to the one used by Smith and Weigel [30]. The governing equations, equation (1), are expressed in the computational domain as

$$\frac{\partial \hat{U}}{\partial t} + \frac{\partial \hat{F}}{\partial \xi} + \frac{\partial \hat{G}}{\partial \eta} + \hat{H} = 0, \quad (37)$$

where

$$\begin{aligned} \hat{U} &= UJ, & \hat{F} &= Fy_\eta - Gx_\eta, & \hat{G} &= Gx_\xi - Fy_\xi, \\ \hat{H} &= HJ, & J &= x_\xi y_\eta - y_\xi x_\eta. \end{aligned}$$

Once the temporal discretization has been performed, the resulting system is spatially differenced using the unsplit MacCormack predictor-corrector scheme [20]. This results in a spatially and temporally discrete, simultaneous system of equations at each grid point [23, 24]. Each simultaneous system is solved using the Householder technique [28, 29], and is marched in time until convergence is achieved. The details of the numerical procedure are available in [25].

Results and discussion

Based on the theory and the computational procedures described previously, two algorithms were developed to solve the two-dimensional Navier–Stokes equations for chemically reacting and radiating supersonic flows. The Navier–Stokes equations without radiative fluxes and chemical reaction are first solved by a finite difference and a finite volume scheme, and the results are compared with an upwind scheme (the Roe scheme). The extent of radiative heat transfer in supersonic chemically reacting flow of hydrogen and air is investigated next. For the temperature range considered in this study, the important radiating species are OH and H₂O. Extensive results for nonreacting and for reacting and radiating flows have been obtained, and these are provided in [25]. Selected results are presented here to demonstrate the essential features of the flow field and the nature of radiative interactions.

The flow properties of a non-reacting and non-radiating flow are calculated by finite difference and finite volume schemes for the physical geometry shown in Fig. 3. The results were obtained by using a 31×31 grid; this was found to be an appropriate grid for the model. The grid distribution was based on the procedure given in [30]. It was noted through various numerical experimentations that the finite volume scheme requires more grid points in the boundary layer and at the shocks than the finite difference scheme. The results are compared with the calculations performed by Chakravarthy using the Roe scheme [33]. The pressure profiles are illustrated in Figs 4 and 5 for the lower and upper boundaries, respectively. The free stream properties considered are $M_\infty = 5$, $T_\infty = 293$ K, and $P_\infty = 0.1$ atm. The calculated results indicate a pressure jump at the inlet, which is caused by the presence of a shock from the leading edge of the channel. Downstream of the compression on the lower wall there is an increase in the pressure, and the pressure decreases beyond the expansion corner.

The shock interaction with the upper boundary creates a small separation bubble. The flow is fully separated at $x/L_x = 0.7$. The pressure profiles at the upper boundary of the channel illustrated in Fig. 5 show that the Jameson scheme predicts an increase in pressure before the shock. This is due to the excessive amount of artificial viscosity inherent in the Jameson damping scheme. The MacCormack scheme shows an oscillation of the pressure in that region. In the region of shock interaction and

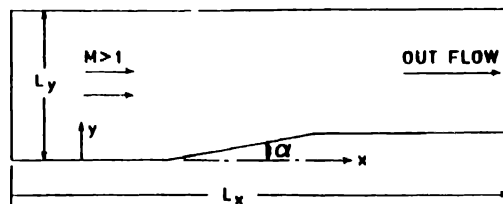


Fig. 3. Flow in a channel with compression–expansion corners.

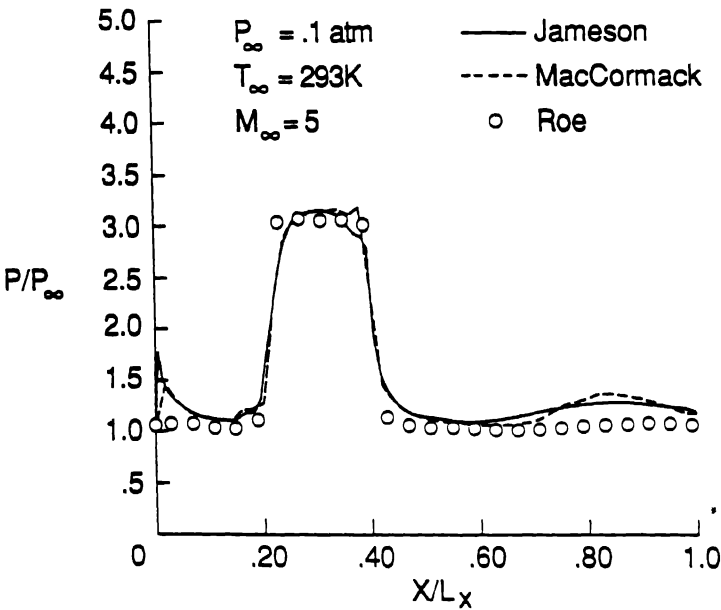


Fig 4 Pressure variation with x for viscous flow ($J=2$)

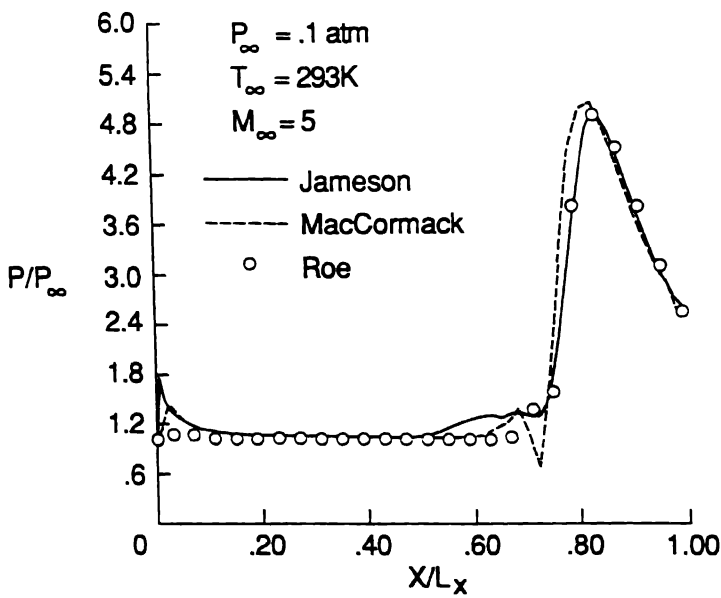


Fig 5 Pressure variation with x for viscous flow ($J=50$)

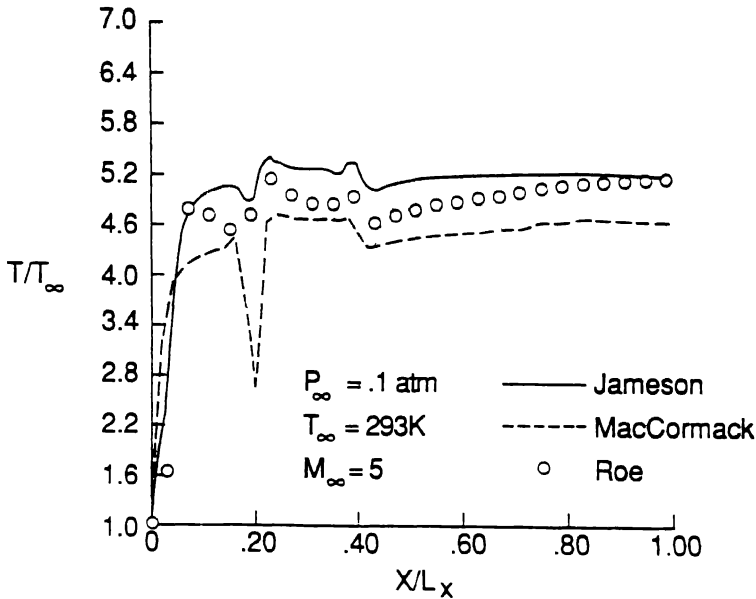


Fig 6 Temperature variation with x for viscous flow ($T_w = T_1$, $J = 2$).

reflection from the upper boundary, the pressure calculated by the finite volume scheme is precisely the same as the results predicted by the Roe scheme.

The temperature profiles at the lower boundary are illustrated in Fig. 6 and results for other locations are provided in [25]. In the finite difference calculations, temperature is strongly dependent on the implementation of the boundary conditions. In obtaining results presented in Figs 4–6, it is assumed that the walls are adiabatic. This could be enforced by either $\partial T/\partial y|_{y=0} = 0$ or $\partial H/\partial y|_{y=0} = 0$. The results shown here were obtained by enforcing the zero temperature gradient. The same trend is predicted, in general, by all three schemes. However, the MacCormack's scheme predicts a flow separation at about $x/L_x = 0.2$ and consequently a drop in temperature is predicted at this location [25]. The temperature recovery for a compressible laminar flow with $M_{\infty} = 5$ and $Pr = 0.72$ is approximately 5.25 (see [34]). This value is predicted by the Jameson and Roe schemes toward the channel outlet. The above recovery factor can be predicted with the finite difference scheme by enforcing the zero enthalpy gradient at the boundary. The results presented in Fig. 6 were obtained by enforcing the zero enthalpy gradient condition for the finite difference scheme. It is seen that the temperature increases very rapidly at the leading edge due to the flow stagnating from the free stream within one grid spacing.

All results involving radiative interactions are obtained by assuming constant wall temperature boundary conditions. Spectral information and correlation quantities

needed for the participating species are obtained from references [6–10]. Before proceeding with the discussion of the radiative heat transfer, divergence of the radiative flux is compared for several models to determine the optical range of radiative interactions and savings in computational resources. A comparison of the one-dimensional divergence of radiative flux for nongray, pseudo-gray, and their optically thin limit models is illustrated in Fig. 7 for the parallel plate geometry ($3\text{ cm} \times 10\text{ cm}$, see [18, 25]) for two different y -locations ($y=0.2$ and 1.5 cm). The free stream conditions considered are $P_\infty = 1\text{ atm}$, $T_\infty = 1700\text{ K}$, and $M_\infty = 4.3$. The magnitude of optical thickness calculated for this case ($0.003 < \tau < 0.4$) shows that the radiation regime is in the optically thin limit. The gray, nongray and optically thin formulations are employed, and their results confirm that the radiation regime is in the optically thin limit. For the physical conditions of the problem, no significant difference in the results is observed for the two y -locations. The solution of the gray formulation in the ordinary differential equation (ODE) form proves to be about ten times more efficient than the solution of the nongray formulation on a vector processing computer. This is because nongray analyses require solutions of an integral formulation. The radiative fluxes have been obtained by using the pseudo-gray gas formulation. Other results for this geometry are provided in [18, 25].

The effects of two-dimensional radiative heat transfer in chemically reacting flows are investigated for a channel with a compression corner on the lower boundary starting at $x=1\text{ cm}$ and ending at $x=3\text{ cm}$ (Fig. 3, $L_y=2\text{ cm}$, $\alpha=10^\circ$). Premixed

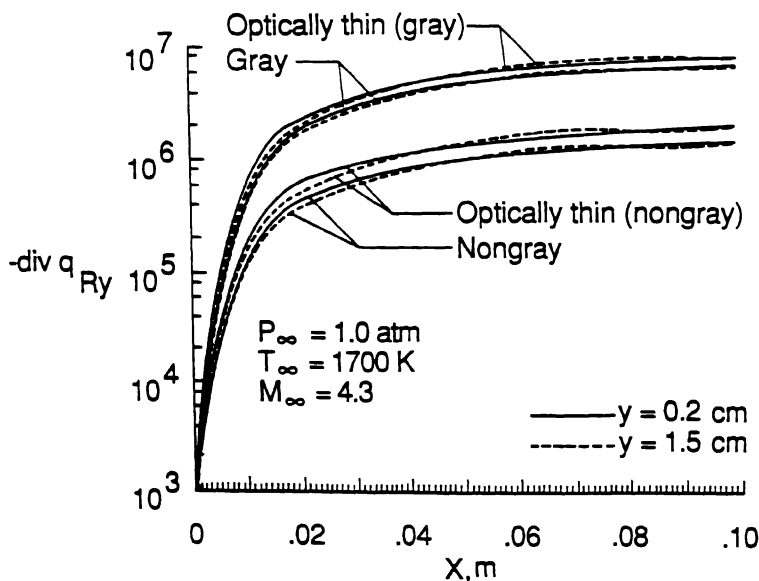


Fig. 7. Divergence of radiative flux along the channel for gray and nongray models.

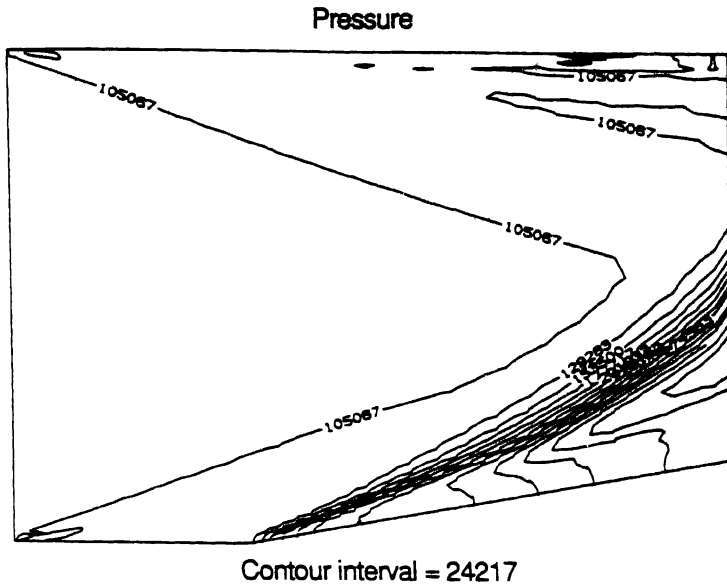


Fig. 8 Pressure contours for reacting and radiating flow in a channel with a compression corner.

hydrogen and air with an equivalence ratio of unity is ignited by the shock from the compression corner. The inlet conditions are $P_\infty = 1$ atm, $T_\infty = 900$ K, and $M_\infty = 4$. Figure 8 shows contour plots of the pressure with chemical reactions. The results for the nonreacting flow are available in [25]. It should be observed that the compression shock is curved when chemical reaction takes place. A series of shock waves is created due to the pressure increase caused by a sudden heat release from chemical reaction. Interaction of these shock waves with compression shocks increases the shock strength, and this causes the shock to curve.

Figure 9 illustrates the variation of nondimensional y -radiation flux for several locations across the channel. The radiative flux in the y -direction is negligible before the shock; this is due to the almost symmetrical condition and lower pressure and temperature. The radiative flux substantially increases after the shock due to the increase in radiative participating species, pressure and temperature. The radiative flux decreases away from the lower boundary due to the reduction in temperature. Radiative flux in the streamwise direction is illustrated in Fig. 10; it peaks at a short distance from the boundary, and then gradually decreases toward the center of the channel. The peak is due to the pressure gradient caused by the leading edge bow shock. The radiative flux (q_{R_x}) remains constant in the region with no chemical reaction, and gradually decreases in the region with chemical reaction. The reduction in q_{R_x} is caused by cancellation of fluxes in positive and negative directions. It should

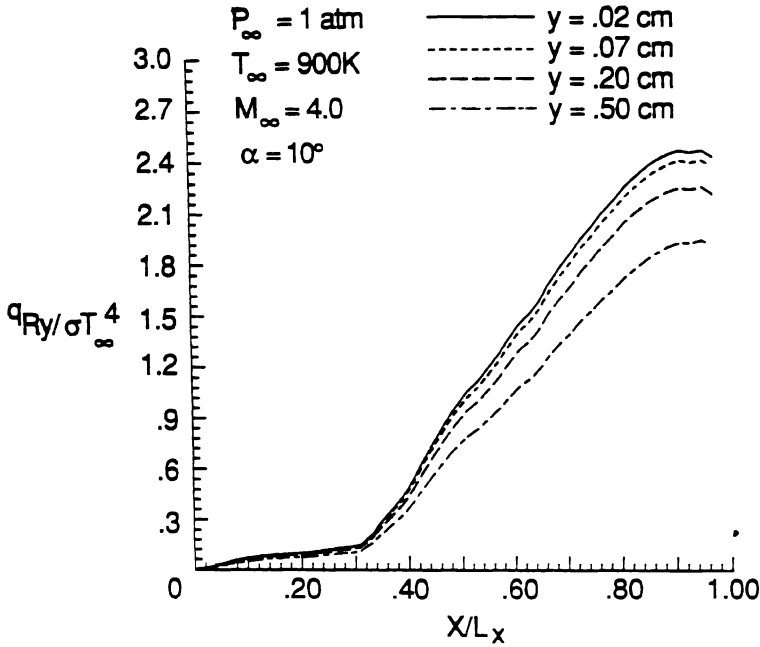


Fig 9 Variation of normal radiative flux with x for a channel with 10° compression corner ($M = 4$)

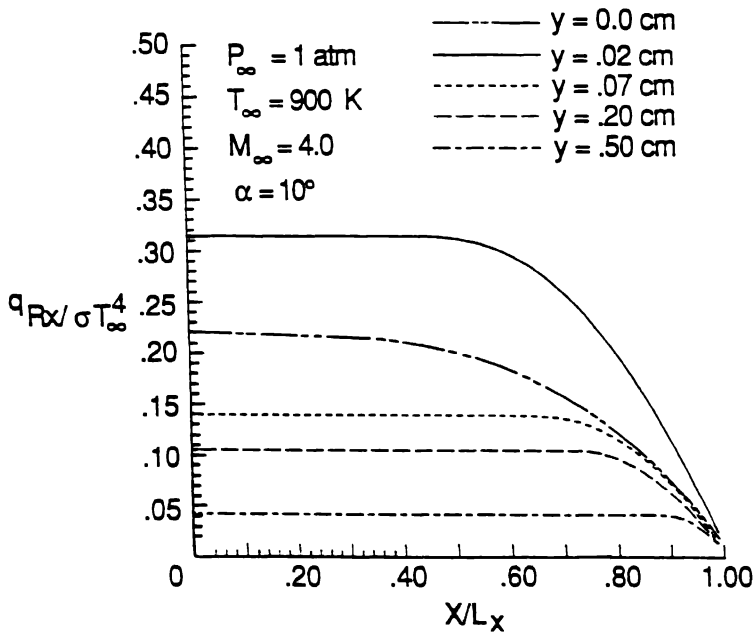


Fig 10 Variation of streamwise radiative flux with x for a channel with 10° compression corner ($M = 4$)

be noted that in this figure (as well as in Figs 12 and 14) the net radiative flux (q_{R_x}) is in the negative x -direction.

Figures 11 and 12 illustrate the radiative flux for the same inlet conditions but for a 15° compression corner. Comparing the results of Figs 9 and 11, it is noted that, due to the increase in the shock strength, the radiative flux in y -direction has a steep gradient through the shock. After the shock, it gradually decreases as some of the radiative flux from the lower boundary gets cancelled by the radiative flux from the upper boundary. The streamwise flux along the channel is illustrated in Fig. 12 for several locations across the channel. Comparing the results with the results of Fig. 10, it is noted that the radiative flux increases considerably with increasing the shock angle.

Figures 13 and 14 illustrate similar results as presented in Figs 9 and 10, for the same freestream conditions, but for $M_\infty = 6$. By increasing the Mach number, the shock angle decreases. As a result, there is no chemical reaction at $y = 0.5$ cm. Therefore, the streamwise radiative flux at this location reduces to zero. It is noted that the radiative flux increases substantially by increasing the Mach number.

The temperature profiles are illustrated in Fig. 15 for chemically reacting, and reacting and radiating flows along the channel with a compression corner for two locations ($y = 0.02$ and 0.2 cm). At location $y = 0.02$, where the value of q_{R_x} is greatest in comparison to the other locations, the temperature has been reduced. At $y = 0.2$, there is no change in the temperature before the shock because there are no participating species. After the shock, temperature has slightly increased over the

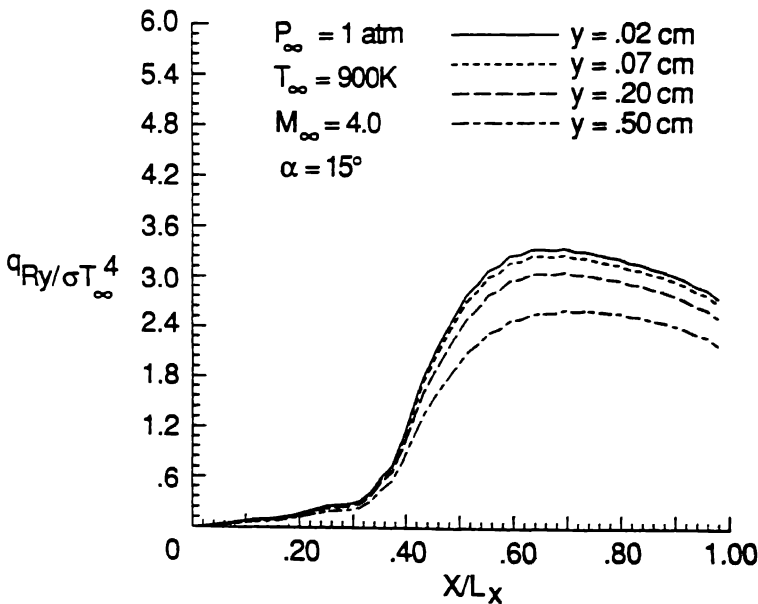


Fig. 11 Variation of normal radiative flux with x in a channel with 15° compression corner ($M = 4$).

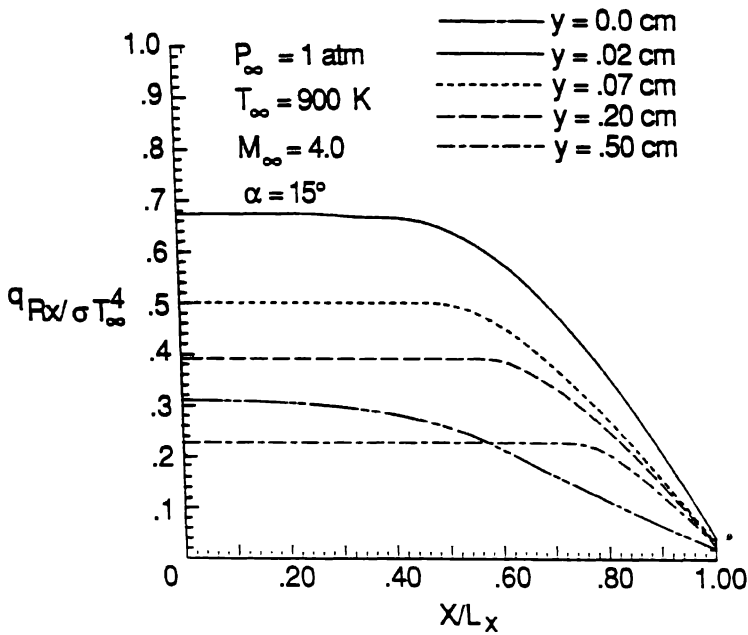


Fig. 12. Variation of streamwise radiative flux with x in a channel with 15° compression corner ($M = 4$).

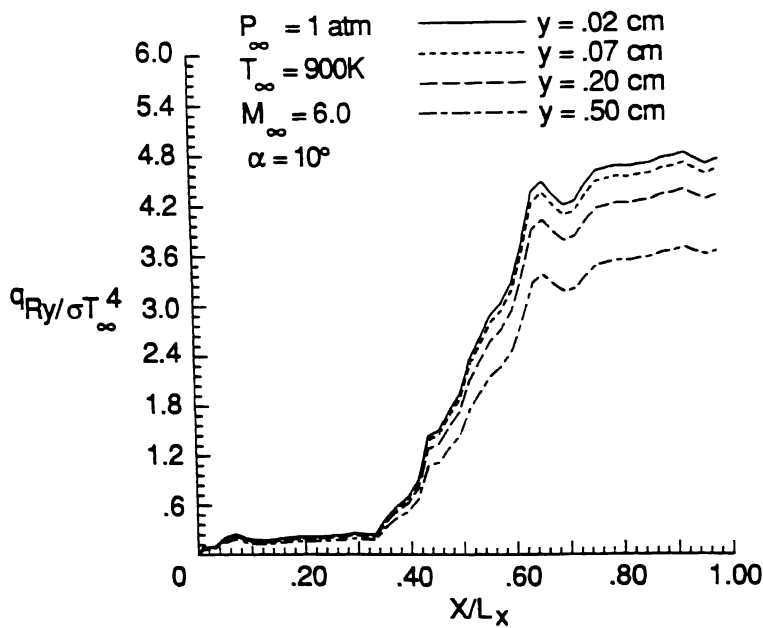


Fig. 13. Variation of normal radiative flux with x in a channel with 10° compression corner ($M = 6$).

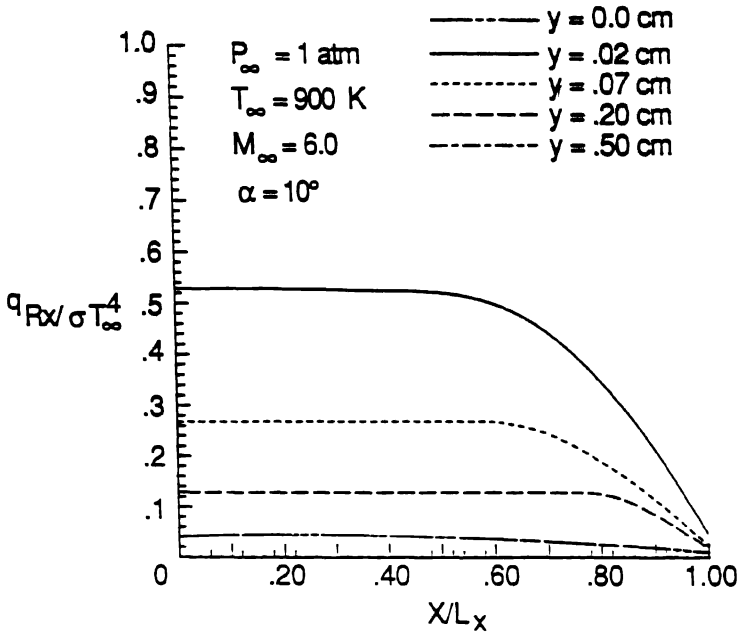


Fig. 14 Variation of streamwise radiative flux with x in a channel with 10° compression corner ($M=6$).

nonradiating case; this is due to the species distribution and contribution from q_R , [25]. The results presented in Fig. 15 are relatively lower than corresponding results for one-dimensional case presented in [18, 25]. This, however, would be expected because of two-dimensional consideration.

Concluding remarks

Based on the theory and computational procedure presented in this study, two algorithms were developed to solve the continuity, momentum, energy and species continuity equations for nonreacting, reacting, radiating and reacting supersonic channel flows. The finite volume algorithm with the appropriate damping scheme proved to be accurate, non-oscillatory and robust for reacting and nonreacting flows. The supersonic viscous flow in a channel with 10° compression and expansion ramps at the lower wall was solved by both the finite-volume and finite-difference schemes. The results of viscous flow were compared with the results of the upwind, flux-split scheme of Roe and no significant differences were noted.

Two-dimensional radiative interaction was investigated for supersonic chemically reacting flow in a channel with a compression corner. Some specific results were

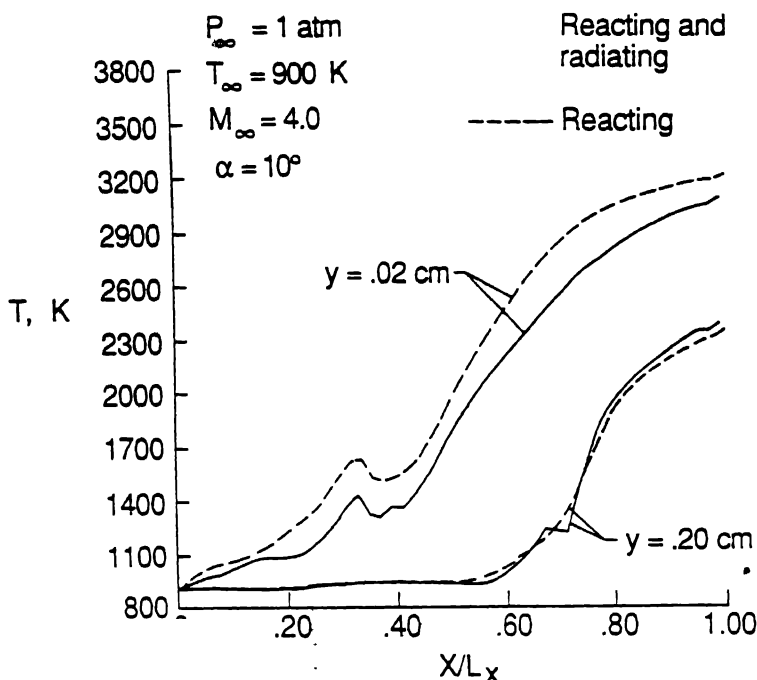


Fig. 15. Temperature variation with x for reacting, and radiating and reacting flows.

obtained by considering the radiative flux in both directions. The results revealed that radiation can have a significant influence on the entire flow field; however, the influence is stronger in the boundary layers. It was noted that the numerical scheme based on the pseudo-gray gas formulation for the radiative flux is highly efficient as compared to the scheme based on the nongray formulation. It is concluded that for the supersonic chemically reacting flows the radiation is in the optically thin range for the physical conditions considered in this study.

Acknowledgement

This work was supported, in part, by the NASA Langley Research Center through the ICAM Project Grant NAG-1-363.

References

1. Kumar, A., "Numerical Simulation of Scramjet Inlet Flow Field," NASA TP-2517, May 1986.
2. Drummond, J.P., Hussaini, M.Y. and Zang, T.A., Spectral methods for modeling supersonic chemically reacting flowfields. *AIAA Journal* 24 (1986) 1461-1467.

3. Drummond, J.P., Rogers, R.C. and Hussaini, M.Y., A numerical model for supersonic reacting flows. *Computer Methods in Applied Mechanics and Engineering* 64 (1987) 39–60.
4. Chitsomboon, T., Kumar, A., Drummond, J.P. and Tiwari, S.N., "Numerical Study of Supersonic Combustion Using a Finite-Rate Chemistry Model," AIAA Paper No. 86-0309, January 1986; also, Chitsomboon, T. and Tiwari, S.N., "Numerical Study of Hydrogen-Air Supersonic Combustion By Using Elliptic and Parabolized Equations," NASA-CR-179800 NAS 1.26:179800, August 1986.
5. Sparrow, E.M. and Cess, R.D., *Radiation Heat Transfer*, Brooks/Cole, Belmont, CA, 1966 and 1970; New Augmented Edition, Hemisphere Publishing Corp., Washington, D.C., 1978.
6. Tien, C.L. and Lowder, J.G., A correlation for total band absorptance of radiating gases. *International Journal of Heat and Mass Transfer* 9 (1966) 698–701.
7. Tien, C.L., *Thermal Radiation Properties of Gases*. Advances in Heat Transfer, Vol. 5. New York: Academic Press (1968).
8. Cess, R.D. and Tiwari, S.N., *Infrared Radiative Energy Transfer Gases*. Advances in Heat Transfer, Vol. 8. New York: Academic Press (1972).
9. Edwards, D.K., *Molecular Gas Band Radiation*. Advances in Heat Transfer, Vol. 12. New York: Academic Press (1976).
10. Tiwari, S.N., *Band Models and Correlations for Infrared Radiation*. Radiative Transfer and Thermal Control (Progress in Astronautics and Aeronautics), Vol. 49. New York: American Institute of Aeronautics and Astronautics (1979).
11. Tiwari, S.N., *Models for Infrared Atmospheric Radiation*. Advances in Geophysics, Vol. 20. New York: Academic Press (1978) pp. 1–85.
12. Tiwari, S.N. and Singh, D.J., "Interaction of Transient Radiation in Fully Developed Laminar Flow," AIAA Paper No. 87–1521, June 1987.
13. Tsai, S.S. and Chan, S.H., Multi-dimensional radiative transfer in nongray gases – general formulation and the bulk radiative exchange approximation. *Journal of Heat Transfer* 100 (1978) 486–491.
14. Chung, T.J. and Kim, J.Y., Two-dimensional combined mode heat transfer by conduction, convection and radiation in emitting, absorbing and scattering media solution by finite elements. *Journal of Heat Transfer* 106 (1984) 448–452.
15. Im, K.H. and Ahluwalia, R.K., Combined convection and radiation in rectangular duct. *International Journal of Heat Mass Transfer* 27 (1984) 221–231.
16. Soufiani, A. and Taine, J., Application of statistical narrow-band model to coupled radiation and convection at high temperature. *International Journal of Heat Mass Transfer* 30 (1987) 437–447.
17. Tiwari, S.N., "Radiative Interaction in Transient Energy Transfer in Gaseous System," NASA-CR-176644 NAS 1.26:176644, December 1985.
18. Mani, M., Tiwari, S.N. and Drummond, J.P., "Numerical Solution of Chemically Reacting and Radiating Flows," AIAA Paper No. 87–0324, January 1987; also, Mani, M. and Tiwari, S.N., "Investigation of Chemically Reacting and Radiating Supersonic Internal Flows," NASA-CR-180540 NAS 1.26:180540, December 1986.
19. Jameson, A., Schmidt, W. and Turkel, E., "Numerical Solution of the Euler Equations by Finite Volume Methods Using Runge-Kutta Time-Stepping Scheme," AIAA Paper No. 81–1259, June 1981.
20. MacCormack, R.W., "The Effect of Viscosity in Hypersonic Impact Cratering," AIAA Paper No. 69–354, May 1969.
21. Swanson, R.C. and Turkel, E., "Artificial Dissipation and Central Difference Schemes for the Euler and Navier–Stokes Equations," AIAA Paper No. 87-1107-CP, June 1987.
22. Smoot, L.D., Hecker, W.C. and Williams, G.A., Prediction of propagating methane-air flames. *Combustion and Flame* 26 (1976) 323–342.
23. Stalnaker, J.F., Robinson, M.A., Spradley, L.W., Kurzius, S.C. and Theoeres, D., "Development of the General Interpolants Methods for the Cyber 200 Series of Computers," Report TR 0867354, Lockheed-Huntsville Research and Engineering Center, Huntsville, AL, October 1983.
24. Bussing, T.R.A. and Murman, E.M., "A Finite Volume Method for the Calculation of Compressible Chemically Reacting Flows," AIAA Paper No. 85-0331, January 1985.
25. Mani, M., Tiwari, S.N. and Drummond, J.P., "Investigation of Two-Dimensional Chemically Reacting and Radiating Supersonic Channel Flows," AIAA Paper No. 88-0462, January 1988; also, Mani, M., "Investigation of Supersonic Chemically Reacting and Radiating Channel Flow," Ph.D. Dissertation, Old Dominion University, Norfolk, Virginia, May 1988.

26. Rogers, R.C. and Chinitz, W., Using a global hydrogen-air combustion model in turbulent reacting flow calculation. *AIAA Journal* 21 (1983) 586–592.
27. Patch, R.W., Effective absorption coefficients for radiant energy transport in nongray nonscattering gases. *Journal of Quantitative Spectroscopy and Radiative Transfer* 7 (1967) 611–637.
28. Wilkin, J.H., *The Algebraic Eigenvalue Problem*. Oxford: Oxford University Press (1965) pp. 233–236.
29. Householder, A.S., *The Theory of Matrices in Numerical Solution Analysis*. New York: Dover Publications (1964) pp. 122–140.
30. Smith, R.E. and Weigel, B.L., “Analysis and Approximate Boundary Fitted Coordinate System for Fluid Flow Simulation,” AIAA Paper No. 80-0192, January 1980.
31. Turkel, E., “Acceleration to a Steady State for the Euler Equations,” ICASE/NASA Langley Research Center, Hampton, Virginia, ICASE Report No. 84-32, July 1984.
32. Chen, H.C., Yu, N.J., Rubbert, P.E. and Jameson, A., “Flow Simulations for General Narelle Configurations Using Euler Equations, AIAA Paper No. 83-0539, 1983.
33. Chakravarthy, S.N., “Development of Upwind Schemes for the Euler Equations,” NASA Contractor Report 4043, January 1987.
34. White, F.M., *Viscous Fluid Flow*. New York: McGraw-Hill Inc. (1974).

Damped pitching of a slender body partially immersed in a liquid

GÖRAN REHBINDER

Department of Hydraulics, The Royal Institute of Technology, S-100 44 Stockholm, Sweden

Received 22 November 1990; accepted in revised form 7 October 1991

Abstract. A slender cylindrical body with a high metacentre was allowed to float in a large liquid container. The body was then displaced vertically and released so that it performed damped pitching oscillations. The motion of the body can be described by a coupled system of a second order ordinary differential equation and the cylindrical heat conduction equation. If the damping is weak, a simple solution exists and the damping coefficient and the natural frequency agree well with experimental results. The damping is proportional to the square root of the kinematic viscosity of the liquid and inversely proportional to the diameter of the body

Nomenclature

A = area of the wetted surface of the body
 F = total force
 F_v = viscous force
 g = gravitational acceleration
 l = length of the body
 m = mass of the body
 n = integer
 r = radial coordinate
 r_0 = radius of the body
 s = Laplace variable
 t = time
 T_e = oscillation period

$x(t)$ = displacement of the body
 x_m = displacement at the turning points
 V_b = volume of the displaced liquid
 $v(r, t)$ = velocity of the liquid
 δ = logarithmic decrement
 κ = auxiliary parameter
 μ = dynamic viscosity of the liquid
 ν = kinematic viscosity of the liquid
 ρ = density of the liquid
 $\xi(t)$ = amplitude function
 ω = natural frequency for undamped motion
 ω_e = natural frequency for damped motion

Introduction

Surge shafts or surge chambers in hydroelectric power plants must be designed in such a way that the oscillations of the water level are stable and adequately damped. These problems are traditional and a comprehensive presentation is given in [1]. The natural frequency and oscillation changes if a floating body is immersed in one or more shafts. The oscillating system becomes coupled and has several degrees of freedom. The simplest system of this kind is a *U*-tube in which a slender body is immersed. This arrangement which is easily analysed, is shown in [2]. The experimental results in [2] show that the motion of the body is more strongly damped than the liquid motion in the tube. It is therefore of interest to study how a slender body,

like a rod with a big metacentre, oscillates in the pitching motion with influence of viscous damping. In technical applications the damping is usually weak or at most moderate. From a physical viewpoint, strong damping appears more interesting since it seems intuitively clear that if the viscosity increases the damping will become supercritical.

This paper is a study of the simple case of damped oscillations, in the pitching mode, of a slender body with a high metacentre in a liquid container of great extent.

Formulation of the problem

A cylindrical body the length, radius and mass of which are l , r_0 and m , respectively, is immersed in a liquid the viscosity and density of which are μ and ρ respectively. The body is slender, i.e. $l/r_0 \gg 1$, and its centre of gravity is located at its bottom which makes its metacentric height so great that it can only perform pitching oscillations (Fig. 1). If the body is displaced from equilibrium and then released it performs damped oscillations. Moreover the dimensions of the vessel containing the liquid is much larger than the length of the body. Finally the flow is assumed axial and the deviation from axial flow at the bottom of the body is assumed negligible.

The above motion can be described by a coupled system of one ordinary differential equation with initial conditions and a heat conduction equation with initial and the appropriate boundary conditions. Newton's law for the body yields

$$m\ddot{x} = F, \quad (1)$$

where $x(t)$ is the vertical displacement of the body. The force F has three components. The first is floatation by Archimedes' principle, the second is viscous friction and the third is the weight of the body. Thus

$$F = V_b \rho g + F_v + mg. \quad (2)$$

The damping force F_v is caused by the shear stress $\tau(r=r_0, t)$ between the liquid and the body. The volume of the displaced liquid V_b is

$$V_b = \pi r_0^2(l + x). \quad (3)$$

The axial velocity of the liquid $v(r, t)$ satisfies the Navier–Stokes equation. In cylindrical coordinates it is

$$\rho \frac{\partial v}{\partial t} = \mu \left(\frac{\partial^2 v}{\partial r^2} + \frac{1}{r} \frac{\partial v}{\partial r} \right), \quad r \geq r_0. \quad (4)$$

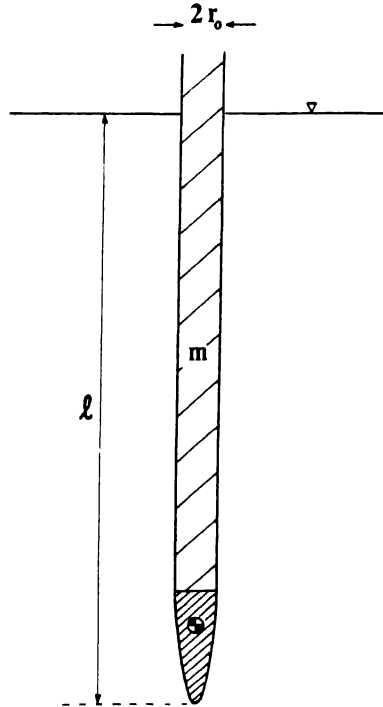


Fig. 1. A slender body with a big metacentre floating in a liquid. \circ indicates the centre of gravity.

The corresponding plane case is for the classical Stokesian boundary layer [3], which is given in many textbooks, e.g. [4]–[7].

The four equations above are coupled in two ways. The boundary condition of (4) at $r = r_0$ is given by the unknown velocity of the body, i.e.,

$$v(r = r_0, t) = \dot{x}(t) \quad (5)$$

and the damping force F_v is the shear stress acting on the body, integrated over the wetted surface $A = 2\pi r_0(l + x)$. If the amplitude is small, i.e., if $x \ll l$, the damping force is

$$F_v = \iint_A \tau(r_0, t) dA = 2\pi r_0 l \mu \left(\frac{\partial v}{\partial r} \right)_{r=r_0}; \quad x \ll l. \quad (6)$$

Then the total coupled system is as follows:

$$\begin{aligned}
 \ddot{x}(t) + \omega^2 x(t) - \frac{2\nu}{r_0} \frac{\partial v(r_0, t)}{\partial r} &= 0, \\
 x(0) &= x_0, \\
 \dot{x}(0) &= 0, \\
 \frac{\partial v(r, t)}{\partial t} &= \nu \left(\frac{\partial^2 v(r, t)}{\partial r^2} + \frac{1}{r} \frac{\partial v(r, t)}{\partial r} \right), \\
 v(r_0, t) &= \dot{x}(t), \\
 v(r \rightarrow \infty) &= 0, \\
 v(r, t < 0) &= 0,
 \end{aligned} \tag{7}$$

where $\nu = \mu/\rho$ is the kinematic viscosity and $\omega = \sqrt{g/l}$ is the natural frequency for undamped oscillations in the pitching mode.

The foregoing analysis is based on a number of important simplifications. The slenderness of the body implies that the main contribution to F_v consists of a frictional force on the wetted surface of the body and that no waves are generated at the free surface of the liquid. The slenderness of the body in combination with the large

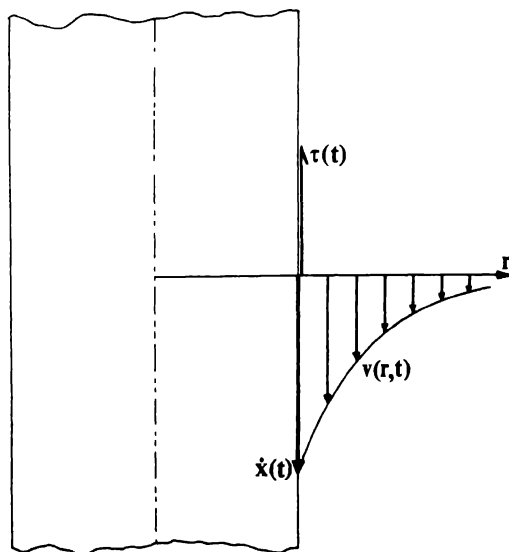


Fig. 2 Definition of variables

dimensions of the liquid container imply that the virtual mass due to acceleration of the liquid can be neglected.

Solution

The system of equations (7) is linear and is therefore in principle solvable but a closed solution is difficult to derive. However if one performs a Laplace transformation, one can discern some properties of the solution. Denote

$$\begin{aligned}\tilde{v}(r, s) &= \int_0^{\infty} v(r, t) e^{-st} dt, \\ \tilde{x}(s) &= \int_0^{\infty} x(t) e^{-st} dt.\end{aligned}\tag{8}$$

Then the transformation of (7) yields

$$\begin{cases} s^2 \tilde{x} - s x_0 + \omega^2 \tilde{x} - \frac{2v}{r_0} \frac{\partial \tilde{v}(r_0, s)}{\partial r} = 0, \\ s \tilde{v} = v \left(\frac{\partial^2 \tilde{v}}{\partial r^2} + \frac{1}{r} \frac{\partial \tilde{v}}{\partial r} \right), \\ \tilde{v}(r_0) = s \tilde{x} - x_0, \\ v(r \rightarrow \infty) = 0. \end{cases}\tag{9}$$

With the introduction of $\kappa^2 = sr_0^2/v$ and $v_0 = s\tilde{x} - x_0$ the transformed velocity is given by

$$\begin{cases} \frac{\partial^2 \tilde{v}}{\partial^2(r/r_0)} + \frac{1}{r/r_0} \frac{\partial \tilde{v}}{\partial(r/r_0)} = 0, \\ \tilde{v}(r/r_0 = 1) = \tilde{v}_0, \\ \tilde{v}(r/r_0 \rightarrow \infty) = 0, \end{cases}\tag{10}$$

which has the solution

$$\tilde{v} = \tilde{v}_0 \frac{K_0(\kappa r/r_0)}{K_0(\kappa)}.\tag{11}$$

Thus

$$\left(\frac{\partial \tilde{v}}{\partial r}\right)_{r=r_0} = -\frac{\kappa \tilde{v}_0}{r_0} \frac{K_1(\kappa)}{K_0(\kappa)}, \quad (12)$$

where $K_n(z)$ are modified Bessel functions of a complex argument z . (9) and (10) yield the solution

$$\frac{\tilde{x}}{x_0} = \frac{s + \frac{2\nu\kappa}{r_0^2} \frac{K_1(\kappa)}{K_0(\kappa)}}{s^2 + \frac{2\kappa\nu s}{r_0^2} \frac{K_1(\kappa)}{K_0(\kappa)} + \omega^2}. \quad (13)$$

If $\kappa \gg 1$, which means that the Stokesian boundary layer thickness is much smaller than r_0 , (13) becomes "quasi one dimensional". Since $K_1(\infty)/K_0(\infty) = 1$ [8], (13) becomes

$$\frac{\tilde{x}}{x_0} = \frac{s + 2(\sqrt{\nu/r_0})\sqrt{s}}{s^2 + 2(\sqrt{\nu/r_0})s\sqrt{s} + \omega^2}; \quad \kappa \gg 1. \quad (14)$$

If $\nu \equiv 0$, (13) becomes

$$\frac{\tilde{x}}{x_0} = \frac{s}{s^2 + \omega^2}; \quad \nu \equiv 0, \quad (15)$$

the inversion integral of which is $x = x_0 \cos \omega t$. A question is whether increasing viscosity would imply critical damping. The character of the poles of (13) reveal this. The complex conjugate poles are shown in Fig. 3. This diagram is very interesting since the poles have an imaginary part throughout the whole range of the damping coefficient $\sqrt{\nu/\omega/r_0}$ which would indicate that the motion is always periodic no matter how big the viscosity may be. Figure 3 has a remarkable feature, however. For small but increasing $\sqrt{\nu/\omega/r_0}$ the amplitude and the natural frequency decrease, as one would expect, but if $\sqrt{\nu/\omega/r_0} > 1$, the amplitude increases with increasing damping coefficient. Although this indication seems unphysical the explanation is simple. If $\sqrt{\nu/\omega/r_0} > 1$, the diffusion of vorticity extends so far from the rod that the thickness of the Stokesian boundary layer is not small compared to r_0 . Then (4) is no longer valid since the flow is not independent of the axial coordinate. Thus the question of critical damping can only be answered if the full boundary layer equations are solved. The inversion of (13) is quite complicated and has therefore been omitted. If the damping is weak, i.e. if $\sqrt{\nu/\omega/r_0} \ll 1$, an approximate solution can readily be derived. This case is the one for the experiments described later. In the case of weak damping an

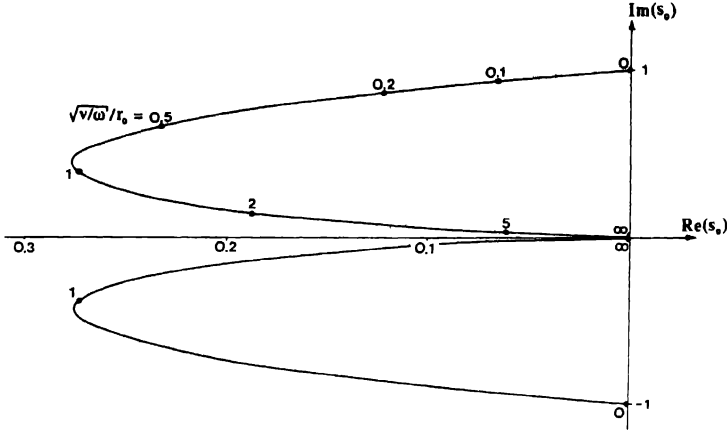


Fig. 3. The poles s_0 of equation (13) indicating the damping and natural frequency.

“amplitude function” $\xi(t)$, which is complex, is introduced such that

$$x(t) = \text{Re}\{\xi(t) e^{i\omega t}\}. \quad (16)$$

Since weak damping implies that $|\xi\omega^2| \gg |\ddot{\xi}|$, it follows that

$$x = \text{Re}\{\xi e^{i\omega t}\}, \quad (17)$$

$$\dot{x} = \text{Re}\{(\dot{\xi} + i\omega\xi) e^{i\omega t}\}, \quad (18)$$

$$\ddot{x} = \text{Re}\{(2i\omega\dot{\xi} - \omega^2\xi) e^{i\omega t}\}. \quad (19)$$

If

$$\dot{\xi} + i\omega\xi = v_0(t) \quad (20)$$

and $w(r, t)$ is defined in such a way that

$$v(r, t) = w(r, t) e^{i\omega t}, \quad (21)$$

$$\frac{\partial v}{\partial t} = \left(i\omega w + \frac{\partial w}{\partial t} \right) e^{i\omega t}. \quad (22)$$

However, since $|\xi\omega^2| \gg |\ddot{\xi}|$, it follows that

$$\frac{\partial v}{\partial t} = i\omega w e^{i\omega t}. \quad (23)$$

Then w is given by

$$\begin{cases} \frac{\partial^2 w}{\partial^2(r/r_0)} + \frac{1}{r/r_0} \frac{\partial w}{\partial(r/r_0)} - k^2 w = 0, \\ w(r/r_0 = 1) = v_0, \\ w(r/r_0 \rightarrow \infty) = 0, \end{cases} \quad (24)$$

where $k^2 = i\omega r_0^2/v$. (24) is identical with (10) and hence

$$\left(\frac{\partial w}{\partial r} \right)_{r=r_0} = \frac{v_0 k}{r_0} \frac{K_1(k)}{K_0(k)}. \quad (25)$$

If (17)–(19) and (25) are introduced in (7), the “amplitude function” $\xi(t)$ satisfies

$$\ddot{\xi} + \frac{vk}{i\omega r_0^2} \frac{K_1(k)}{K_0(k)} (\dot{\xi} + i\omega \xi) = 0. \quad (26)$$

Rearrangement shows that (26) is separable

$$\begin{cases} \frac{d\xi}{dt} = \frac{\sqrt{\frac{iv\omega}{r_0^2} \frac{K_1(k)}{K_0(k)}}}{1 + \sqrt{\frac{v}{i\omega r_0^2} \frac{K_1(k)}{K_0(k)}}} \xi, \\ \xi(0) = \xi_0. \end{cases} \quad (27)$$

The weak damping implies that $k \rightarrow \infty$ and since $K_1(\infty)/K_0(\infty) = 1$ follows that the solution to (27) is

$$\xi = \xi_0 \exp(-\sqrt{iv\omega/r_0^2} t), \quad (28)$$

x is given by (17) and (28)

$$x(t) = \xi_0 \operatorname{Re}\{\exp(-t\sqrt{\omega v/2r_0^2} + i\omega t(1 - \sqrt{v/2\omega r_0^2}))\}, \quad (29)$$

but since $\sqrt{v/2\omega r_0^2} \ll 1$ (29) represents a simple linearly damped oscillator

$$x(t) = \xi_0 \exp(-\sqrt{\omega v/2r_0^2} t) \cos \omega t. \quad (30)$$

Experiments

Two different bodies were used in experiments planned to test the theory. Both bodies were plastic tubes provided with a piece of shaped brass at one end. The degree of immersion was controlled by the amount of lead shot that was poured into the tube. The body was immersed in the large towing tank of the institute. With the aid of a thin string, the body was lifted from its equilibrium position. Once all motions has ceased, the string was burned with a match. The oscillations of the body were then recorded with a video camera. The arrangement is shown in Fig. 4. Thus the position of the body, i.e. the position of the identification mark, was recorded on a tape. The tape could be played and the motion can be "frozen" frame by frame. This method of recording the motion is acceptable if the frequency of the motion is much less than the frequency of the camera. In the present case the natural frequency of the body is ≈ 0.5 Hz, whereas the frequency of the camera is 50 Hz. The evaluation also requires that the amplitude $x(t)$, albeit small compared with the length of the body l , to be great enough to observe efficiently. In the experiments the maximum amplitude was about 50 mm. As the oscillation proceeds the amplitude becomes smaller and the evaluation of its magnitude becomes relatively less accurate. Fourteen oscillations were easily measured in test no. 1 and nine in test no. 2.

A third source of inaccuracy is the resolution and the distortion of the camera. The line density affects the resolution. If the width of the screen is D and the number of lines is N , the resolution is (D/N) . In the present case, the maximum amplitude was

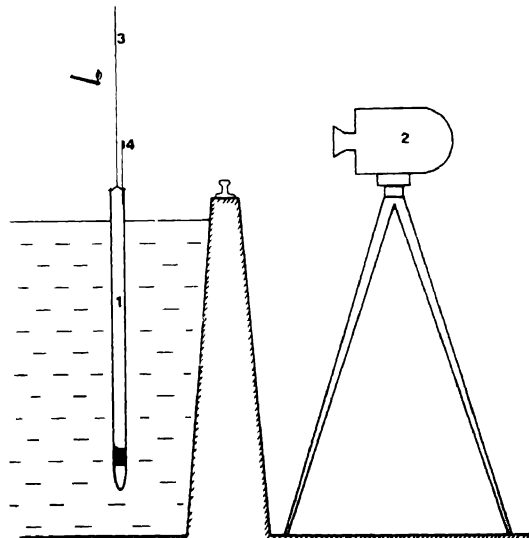


Fig. 4. Experimental arrangement. 1: Body. 2: Video camera. 3: String. 4: Identification mark.

about 30% of D . Hence the accuracy could not exceed $(D/N)/0.3D$. Since $N = 628$, the accuracy was not better than 0.5%. As a consequence the evaluation stopped when the amplitude became small. The distortion was negligible since the camera frequency was much higher than the natural frequency of the body and since the amplitude covered a limited part of the screen.

The evaluation comprised not only the maximum displacements of the body, $x_m(t_n)$, $n = 1, 2, 3, \dots$, but also the oscillation time T_e . From these quantities the frequency ω_e and the logarithmic decrement δ can be calculated. The relative errors of the measured $x_m(t_n)$ for $n \approx 10$ is estimated to be less than 5%.

If the damping is weak, as equation (30) presupposes, ω_e is related to the undamped natural frequency $\omega = \sqrt{l/g}$ as

$$\omega_e = \omega \sqrt{1 - \nu/2r_0^2\omega} \quad (31)$$

and consequently

$$\omega_e = \omega; \quad \nu/2r_0^2\omega \ll 1, \quad (32)$$

where

$$\omega_e = \frac{2\pi}{T_e}. \quad (33)$$

If the values of $x_m(t_n)$ $n = 1, 2, 3, \dots$ decrease as the terms in a geometric series the damping is linear and the logarithmic decrement δ is

$$\delta = \frac{x_m(t_n)}{x_m(t_{n+1})}, \quad n = 1, 2, 3, \dots \quad (34)$$

As mentioned in the foregoing two test bodies were used

$$\text{Test 1} \quad l = 2.180 \text{ m}, \quad r_0 = 2.7 \cdot 10^{-2} \text{ m}.$$

$$\text{Test 2} \quad l = 1.180 \text{ m}, \quad r_0 = 10^{-2} \text{ m}.$$

In both cases the damping was weak. The results are shown in Table 1 and in Fig. 5. The agreement between theory and experiment is good. An interesting discrepancy is revealed in Fig. 5. During the first few oscillations the ratio between consecutive maxima are not constant. The most probable explanation is that the velocity of the body was great enough to cause separation to occur at the end of the body, and this process added appreciably to the drag. Another possibility is that the experimental values agree with the exact transient solution (13), i.e. for small values of $\nu t/r_0^2$. This

explanation seems less likely since the approximate solution (30) is valid even for small vt/r_0^2 if the damping is weak. Therefore δ has been identified for $n > 6$ in test no. 1 and for $n > 2$ in test no. 2.

Table 1

Test 1		Test 2	
$l = 2.180 \text{ m}$		$l = 1.180 \text{ m}$	
$r_0 = 27 \text{ mm}$		$r_0 = 10 \text{ mm}$	
$v/2r_0^2\omega_e = 3.234 \cdot 10^{-4}$		$v/2r_0^2\omega_e = 1.734 \cdot 10^{-3}$	
Theory	Experiment	Theory	Experiment
$\omega_e = 2.121$	$\omega_e = 2.12$	$\omega_e = 2.883$	$\omega_e = 2.88$
$\delta = 0.1130$	$\delta = 0.113$	$\delta = 0.2617$	$\delta = 0.261$

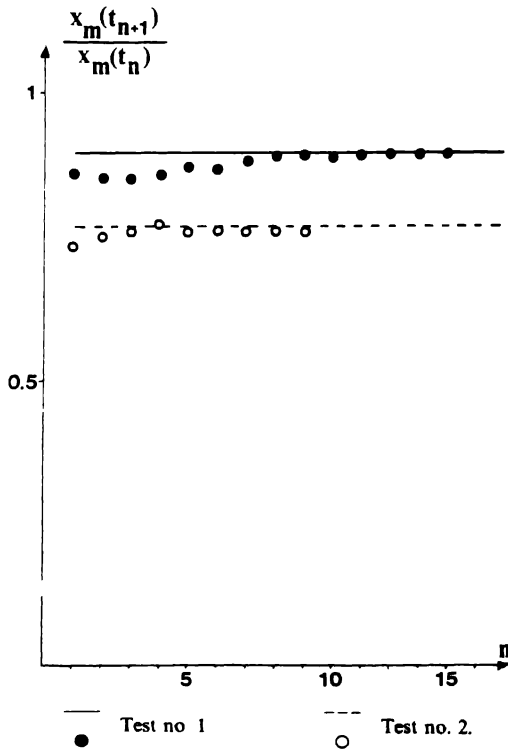


Fig. 5 The logarithmic decrement δ as a function of number of oscillations n .

Discussion

The comparison between theory and experiment has shown that the agreement is satisfactory if the displacement of the body is small and the damping is weak.

However, the analysis and experiments do not answer the interesting question namely in which circumstances critical damping occurs or whether it occurs at all. A similar phenomenon occurs in geohydraulics. The water level of a well, that is drilled in an aquifer, can oscillate if it is disturbed. If the skeleton of the aquifer is elastic it serves as a spring, the mass of the water in the well is the oscillating mass and the resistance to Darcyan flow in the aquifer is the damper [9].

In this case damping is always subcritical. However, if two wells are drilled in the same aquifer that is effectively rigid, the two levels oscillate exactly as a one-dimensional linear oscillator, i.e. the damping can be both subcritical or supercritical [10]. A natural extension of the above experiment is the study of a sufficiently thin rod oscillating in a sufficiently viscous liquid. For a suitable choice of r_0 , l and ν it would be possible to find the right combinations of these variables giving aperiodic motion. Another extension of the study would be to allow finite value of x , i.e. not to require $x \ll l$. Such experiments would not cause any problem but equation (6) and consequently (7) would become non linear. The reason that a finite value of $x(t)$ is significant is that the oscillations in surge shafts in hydroelectric power plants are great and the stability analysis has to include possible bifurcation points and limit cycles.

Appendix*Estimation of the aperiodic part of the solution for weak damping*

The Laplace transform, equation (14) has one branch point $s = 0$, and two complex conjugate simple poles, $s = s_p$ and $s = \bar{s}_p$. The pole is denoted $s_p = a + i\ell$. Thus (14) can be written

$$\frac{\tilde{x}(s)}{x_0} = \frac{f(s)}{(s - s_p)(s - \bar{s}_p)}.$$

The values of $f(s)$ at the poles are in turn complex conjugates. Let $f(s_p) = f' + i g$. The inversion of $\tilde{x}(s)$ is given by an integral along a Bromwich contour, which involves a branch cut along the negative real s -axis. Thus

$$\begin{aligned} \frac{x(t)}{x_0} &= \int_{s_0 - i\infty}^{s_0 + i\infty} e^{st} \frac{f(s)}{(s - s_p)(s - \bar{s}_p)} ds \\ &= a_{-1} + \bar{a}_{-1} - \frac{2\omega^2 \sqrt{\nu}}{\pi r_0} \int_0^\infty \frac{\sqrt{r} e^{-rt} dr}{(r^2 + \omega^2)^2 + 4\nu r^3 / r_0^2}, \end{aligned}$$

where a_{-1} and \bar{a}_{-1} are the complex conjugate residues of $e^{\pi f}(s)$ at the poles. Then the periodic part of the solution can be written

$$a_{-1} + \bar{a}_{-1} = \frac{e^{\alpha t}}{\ell} (\mathcal{G} \cos \ell t + \mathcal{J} \sin \ell t).$$

The values α , ℓ , \mathcal{J} and \mathcal{G} must be calculated numerically and so must the integral. However, the magnitude of the integral can be estimated, say after one period.

Therefore let $t = 2\pi/\omega$. Then the above integral can be written in the form

$$\begin{aligned} \frac{2\sqrt{v\omega}}{\pi r_0 \omega} \int_0^\infty \frac{\sqrt{\xi} e^{-2\pi\xi} d\xi}{(\xi^2 + 1)^2 + 4v\xi^3/\omega r_0^2} &< \frac{2\sqrt{v\omega}}{\pi r_0 \omega} \int_0^\infty \frac{e^{-2\pi\xi}}{(\xi^2 + 1)^2} d\xi \\ &= -\frac{\sqrt{v\omega}}{\pi r_0 \omega} (\text{si}(2\pi) + 2\pi \text{ci}(2\pi)) \approx \frac{\sqrt{v\omega}}{\pi r_0 \omega} 0.28. \end{aligned}$$

This estimate can be used to justify the approximation (30). In the experiments $\omega \approx 2 \text{ s}^{-1}$, $v = 10^{-6} \text{ m}^2/\text{s}^{-1}$ and $r_0 > 10^{-2} \text{ m}$, implying that the value of the above expression is 0.02. Thus it is obvious that the aperiodic part of the solution, which stems from the branch cut, is negligible after one period.

Acknowledgement

The author wants to thank Dr N. Apazidis for his kind interest in the problem and his assistance in finding the poles shown in Fig. 3.

References

- 1 Jaeger, Ch., Fluid transients in hydroelectric engineering practice. Glasgow & London (1977).
- 2 Reh binder, G., Oscillations of a body floating in a U-tube filled with a liquid. *Journ. Hydr. Res.* (to appear)
- 3 Stokes, G G, On the theories of the internal friction of fluids in motion and of the equilibrium and motion of elastic solids. *Trans. Camb. Soc.* 8 (1845) 287–305
- 4 Lamb, H., *Hydrodynamics* Cambridge (1932).
- 5 Schlichting, H., *Boundary layer theory*. New York (1979).
- 6 Batchelor, G K., *An Introduction to Fluid Dynamics*. Cambridge (1967).
- 7 Ryhming, I.L., *Dynamique des Fluides*. Lausanne (1985).
- 8 Jahnke-Emde-Losch *Tafeln Hoherer Funktionen* Stuttgart (1960).
- 9 van der Kamp, G, Determining aquifer transmissivity by means of well response tests. *Water Resource Res.* 12 (1976) 71–77
- 10 Reh binder, G., Oscillations in two wells drilled in a confined aquifer. *Transp. in Por. Media.* 4 (1989) 307–311.

Combined forced and free convection heat transfer in power-law fluid-saturated porous media

A. NAKAYAMA & A. V. SHENOY

Department of Energy and Mechanical Engineering, Shizuoka University, 3-5-1 Johoku, Hamamatsu, 432 Japan

Received 1 May 1991; accepted in revised form 11 November 1991

Abstract. The problem of combined forced and free convection heat transfer in power-law fluid-saturated porous media has been solved using the boundary layer approximations. A modified Peclet number based on the slip velocity at the wall has been introduced in order to uniquely transform the governing equations for all convection regimes, namely the pure forced convection regime, mixed convection regime and pure free convection regime. Possible similarity solutions are presented for vertical flat plates, cones, horizontal cylinders and spheres. It is found that the velocity close to the wall is comparatively higher for pseudoplastic fluids than for the Newtonian and dilatant fluids at the same external velocity, thus leading to a substantial heat transfer enhancement in the mixed convection regime.

Nomenclature

f = dimensionless stream function
 g_x = acceleration due to gravity
 l = function adjusting the boundary layer length scale
 k = effective thermal conductivity of a fluid-saturated porous medium
 K^* = modified permeability for power-law fluids
 m = exponent associated with the external velocity
 m_1 = exponent associated with the wall temperature distribution
 n = power-law index
 Nu_x = local Nusselt number
 p = pressure
 Pe_x = local Peclet number
 Pe_x^* = modified Peclet number
 q_w = local wall heat flux
 r = function representing a body shape
 r^* = 1 for plane flow and r for axisymmetric flow

Ra_x = local Rayleigh number
 $T, \Delta T_x$ = temperature, and wall-ambient temperature difference
 u, v = Darcian velocity components
 x, y = boundary layer coordinates

Greek letters

α = effective thermal diffusivity of a porous medium
 β = coefficient of thermal expansion
 ϵ = porosity
 η = similarity variable
 θ = dimensionless temperature
 μ^* = consistency index for power-law fluids
 ρ = density
 ψ = stream function

Subscripts

e = external
 w = wall

Introduction

The interest in convective heat transfer in porous media stems from several practical applications in areas such as geothermal engineering, thermal insulation systems,

ceramic processing, enhanced oil recovery, filtration processes, chromatography, etc. Review of the extensive work that has gone into this field of research is available in Combarous and Bories (1975), Cheng (1978), Bejan (1990), Kafoussias (1990), Tien and Vafai (1990), and Trevisan and Bejan (1990). It can be seen that the focus has been on studying the various heat transfer aspects with respect to Newtonian fluid-saturated porous media.

There is no denying that a number of fluids which could come in contact with porous media would show non-Newtonian flow behavior, especially in ceramic processing, enhanced oil recovery and filtration. Yet the number of studies dealing with heat transfer in non-Newtonian fluid-saturated porous media are limited.

Chen and Chen (1988a) were the first to consider the simplest free convection flow of non-Newtonian fluids past an isothermal vertical flat plate embedded in a porous medium. The analysis was later extended by Chen and Chen (1988b) to include other body shapes such as the horizontal cylinder and sphere. Boundary layer flow and heat transfer of non-Newtonian fluids in porous media was explored by Wang and Tu (1989). They obtained expressions for the local Nusselt numbers for the forced and free convection of a Herschel-Bulkley (1926) type non-Newtonian fluid past an isothermal semi-infinite plate in porous media. Pascal and Pascal (1989) considered non-linear effects of non-Newtonian fluids on natural convection in a porous medium. They analyzed the two cases of constant temperature boundary and constant flux boundary of Herschel-Bulkley fluid along a heated vertical cylinder. The rheological effects of some non-isothermal flows through a porous medium were studied by Pascal (1990a). Unsteady state solution for the case of a shear thinning fluid in the absence of a yield stress was obtained. The case of two-phase flows of non-Newtonian fluids through a porous medium was also analyzed by Pascal (1990b). Buoyancy-induced flow of non-Newtonian fluids over a non-isothermal body of arbitrary shape in a fluid-saturated porous medium was treated by Nakayama and Koyama (1991).

It is common knowledge that in any heat transfer circumstance, density differences are bound to arise and, in the presence of force field, free convection effects result. If the forces and momentum transport rates in forced convection are very large then the effects of free convection can be neglected. Similarly, if the buoyancy forces are of greater relative magnitude, forced convection effects may be ignored. In many practical circumstances, it is not unusual to expect that the two effects are of comparable order and that the heat transfer is determined by the combined effect. This aspect with respect to non-Newtonian fluids has not received any attention but for the published work of Wang et al. (1990) dealing with simplest case of the vertical flat plate embedded in a porous medium. In the case of Newtonian fluids Cheng (1977) studied the combined convection problem about inclined surfaces in porous media and Nakayama and Koyama (1987) used the integral method to solve the combined convection flow from a curved surface of arbitrary shape embedded in a fluid-saturated porous medium.

In the present paper, the procedures used earlier by the authors are utilized to study the mixed convection past non-isothermal bodies of arbitrary shape embedded in

non-Newtonian power-law fluid – saturated porous medium. Appropriate transformation of variables are attempted in order to seek exact solutions from the governing equations. These are done along the lines of Nakayama and Koyama (1991).

Analysis

It is assumed that the geometrical configuration has a smooth shape which could be planar or axisymmetric and the co-ordinate system is as shown in Fig. 1 with a wall geometry defined by the function $r(x)$. The wall surface temperature $T_w(x)$ is considered to be higher than the ambient temperature T_e which is assumed to be constant. The flow is considered to be occurring under mixed convection conditions.

The equation of continuity in terms of the Darcian (apparent) velocities can be written under the usual boundary layer co-ordinates (x, y) as

$$\frac{\partial}{\partial x} r^* u + \frac{\partial}{\partial y} r^* v = 0, \quad (1)$$

where

$$r^* = \begin{cases} 1: & \text{plane flow} \\ r(x): & \text{axisymmetric flow.} \end{cases} \quad (2)$$

The Darcy's law when combined with the Boussinesq approximation, for the present

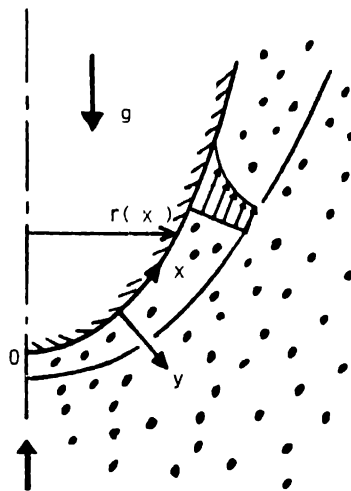


Fig. 1 Physical model and its coordinates.

case of mixed convection in power-law fluid-saturated porous medium can be written as

$$\frac{\mu^*}{K^*} u^n = - \left(\frac{dp}{dx} + \rho g_x \right) + \rho g_x \beta (T - T_e), \quad (3)$$

where

$$g_x = g \left[1 - \left(\frac{dr}{dx} \right)^2 \right]^{1/2}. \quad (4)$$

μ^* is the consistency index for the power-law fluid and K^* is the modified permeability for power-law fluids as defined below:

$$\frac{6}{25} \left(\frac{n\varepsilon}{3n+1} \right)^n \left(\frac{d\varepsilon}{3(1-\varepsilon)} \right)^{n+1} \quad [\text{Christopher and Middleman, 1965}] \quad (5a)$$

$K^* =$

$$C \left(\frac{n\varepsilon}{3n+1} \right)^n \left(\frac{d\varepsilon}{3(1-\varepsilon)} \right)^{n+1} \quad [\text{Dharmadhikari and Kale, 1985}] \quad (5b)$$

where

$$C = \frac{3}{4} \left(\frac{9n+3}{8n} \right)^n \left(\frac{6n+1}{10n-3} \right) \left(\frac{16}{75} \right)^{3(10n-3)/(0n+11)} \quad (6)$$

Note that for $n = 1$, $C = 6/25$ and the two expressions for K^* are then identical. In the above equations d is the particle diameter and ε is the porosity. The energy equation is given by the following:

$$u \frac{\partial T}{\partial x} + v \frac{\partial T}{\partial y} = \alpha \frac{\partial^2 T}{\partial y^2} \quad (7)$$

where α is the effective thermal diffusivity of the fluid-solid system. The boundary conditions are

$$y = 0: v = 0, T = T_w(x) \quad (8a, b)$$

$$y \rightarrow \infty: u = u_e, T = T_e \quad (8c, d)$$

The boundary conditions at the edge of the boundary layer, namely, equations (8c, d), provide the relation between the pressure gradient and the external velocity:

$$\frac{\mu^*}{K^*} u_e^n = - \left(\frac{dp}{dx} + \rho g_x \right). \quad (9)$$

Subtracting equation (9) from equation (3) gives

$$u^n = \frac{K^*}{\mu^*} \rho g_x \beta (T - T_c) + u_e^n. \quad (10)$$

Thus, the slip velocity at the wall u_w is given by

$$u_w = u_e \left\{ 1 + \frac{K^* \rho g_x \beta (T - T_c)}{\mu^* u_e^n} \right\}^{1/n}. \quad (11)$$

Transformations

Most previous studies on mixed convection correlate the local Nusselt number in terms of either the local Peclet number

$$Pe_x = u_e x / \alpha, \quad (12)$$

or the local Rayleigh number Ra_x which, according to Nakayama and Koyama (1991), is defined for the power-law fluids as

$$Ra_x = \frac{x}{\alpha} \left(\frac{\rho K^* g_x \beta \Delta T_w}{\mu^*} \right)^{1/n}. \quad (13)$$

However, any mixed convection analysis which uses either Pe_x or Ra_x inevitably suffers from a singularity under a certain physical limiting condition. (For example, if Pe_x is used for scaling, a singularity will appear as $Ra_x/Pe_x \rightarrow \infty$). In the study of Newtonian mixed convection in a porous medium, Nakayama and Pop (1991) argued that the velocity should be scaled using the slip velocity at the wall resulting from both the externally forced flow and the buoyancy force. Thus, along the lines of Nakayama and Pop (1991), we form the modified Peclet number as

$$Pe_x^* = \frac{u_w x}{\alpha} = Pe_x \left\{ 1 + \left(\frac{Ra_x}{Pe_x} \right)^n \right\}^{1/n}, \quad (14)$$

such that Pe_x^* transforms itself into relevant dimensionless numbers, namely, Pe_x for the forced flow dominated case (i.e. $Ra_x/Pe_x \ll 1$), and Ra_x for the buoyancy force dominated case (i.e. $Ra_x/Pe_x \gg 1$). Having established the modified Peclet number Pe_x^* , we propose the following transformations:

$$\psi = \alpha r^* (Pe_x^* I)^{1/2} f(x, \eta) \quad (15)$$

$$T - T_e = \Delta T_w \theta(x, \eta), \quad (16)$$

and

$$\eta = \frac{y}{x} (Pe_x^*/I)^{1/2}, \quad (17)$$

where

$$I = \frac{\int_0^x \Delta T_w^2 u_w r^{*2} dx}{\Delta T_w^2 u_w r^{*2} x}, \quad (18)$$

adjusts the scale in the normal direction in accordance with the body geometry, and the wall temperature distribution. Obviously, the function I reduces to unity for a vertical isothermal flat plate. ψ is the stream function such that

$$u = \frac{1}{r^*} \frac{\partial \psi}{\partial y} \quad \text{and} \quad v = -\frac{1}{r^*} \frac{\partial \psi}{\partial x}. \quad (19a, b)$$

Substitution of equations (15)–(17) into (7), (8) and (10) yields

$$f' = \left\{ \frac{1 + (Ra_x/Pe_x)^n \theta}{1 + (Ra_x/Pe_x)^n} \right\}^{1/n}, \quad (20)$$

and

$$\theta'' + \left(\frac{1}{2} - Im_t \right) f \theta' - Im_t f' \theta = x I \left(f' \frac{\partial \theta}{\partial x} - \theta' \frac{\partial f}{\partial x} \right). \quad (21)$$

The primes in the foregoing equations denote differentiation with respect to η . The transformed boundary conditions are

$$\eta = 0: f = 0, \theta = 1, \quad (22a, b)$$

$$\eta \rightarrow \infty: \theta = 0. \quad (22c)$$

The Darcian velocities are given by

$$u = u_w f' \quad (23a)$$

and

$$v = \frac{\alpha}{x} (\text{Pe}_x^*/I)^{1/2} \left[\left(Im_t - \frac{1}{2} \right) f + \left(\frac{1}{2} - Im_t - I \frac{d \ln u_w r^*}{d \ln x} \right) \eta f' - I x \frac{\partial f}{\partial x} \right], \quad (23b)$$

where

$$m_t = \frac{d \ln \Delta T_w}{d \ln x}. \quad (24)$$

Equation (23a) may be integrated using the boundary condition (22a) as

$$f = \frac{\int_0^\eta \{1 + (\text{Ra}_x/\text{Pe}_x)^n \theta\}^{1/n} d\eta}{\{1 + (\text{Ra}_x/\text{Pe}_x)^n\}^{1/n}}. \quad (25)$$

We now seek possible similarity solutions, assuming the following power functions for the streamwise variations of the wall temperature and external velocity as

$$\Delta T_w \propto x^{m_t}, \quad (26a)$$

and

$$u_e \propto x^m, \quad (26b)$$

where m is readily given according to a wedge angle or apex angle, such as $m = \phi/(\pi - \phi)$ where ϕ is the wedge half angle.

Since the ratio $(\text{Ra}_x/\text{Pe}_x) \propto (g_x \Delta T_w)^{1/n}/u_e$ in equation (25) must remain constant for the solution to be self-similar, the exponent m_t should follow

$$m_t = \begin{cases} nm: & \text{flow over a wedge or cone pointing downward} \\ n-1: & \text{stagnation flow over a horizontal cylinder or sphere.} \end{cases} \quad (27a, b)$$

Under these conditions, the transformed energy equation (21) reduces to the ordinary differential equation, namely,

$$\theta'' + \left(\frac{1}{2} - Im_t \right) f \theta' - Im_t f' \theta = 0, \quad (28)$$

where the product Im_t may be evaluated following equations (18) and (27) as

$$Im_t = \begin{cases} \frac{nm}{1 + (1 + 2n)m} : \text{flow over a vertical wedge,} & (29a) \\ \frac{nm}{3 + (1 + 2n)m} : \text{flow over a vertical cone,} & (29b) \\ \frac{n-1}{2n} : \text{stagnation flow over a horizontal cylinder,} & (29c) \\ \frac{n-1}{2(1+n)} : \text{stagnation flow over a sphere.} & (29d) \end{cases}$$

For a given value of the product Im_t , equation (28) along with (25) may be integrated using the boundary conditions (22b) and (22c), once for different flow situations. The numerical results thus furnished for various values of Im_t can readily be translated for the flow situation of concern via equations (29a)–(29d), as illustrated in Fig. 2, which shows the variation of Im_t with respect to the power-law index n . The product Im_t assumes a non-negative value for all possible similar mixed convective flows over wedges or cones, while its sign changes into negative for pseudoplastic stagnation flows over a horizontal cylinder or sphere, since $m_t = n - 1 < 0$ in such cases. We shall focus on the range, $-0.5 \leq Im_t \leq 0.5$, which includes most cases that allow similarity solutions.

Once $\theta(\eta)$ is known, the local Nusselt number $Nu_x = q_w x / \Delta T_w k$ of our primary

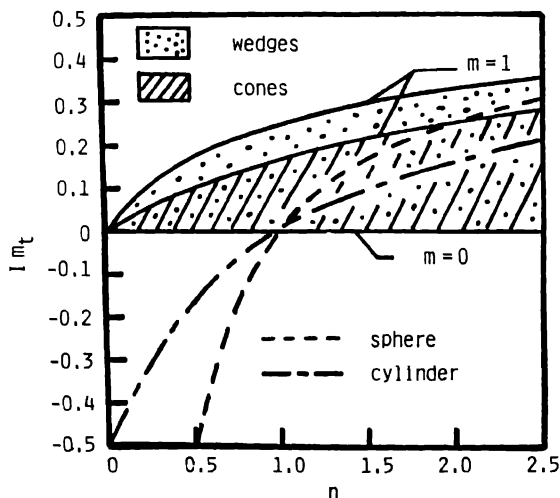


Fig. 2. Range of variation of parameter Im_t with respect to power law index n

concern may be evaluated from

$$\text{Nu}_x / (\text{Pe}_x^* / I)^{1/2} = -\theta'(0), \quad (30a)$$

or, in terms of the conventional Peclet number,

$$\text{Nu}_x / (\text{Pe}_x / I)^{1/2} = -\theta'(0) \{1 + (\text{Ra}_x / \text{Pe}_x)^n\}^{1/2n}, \quad (30b)$$

where

$$1/I = \begin{cases} 1 + (1 + 2n)m: & \text{flow over a vertical wedge,} & (31a) \\ 3 + (1 + 2n)m: & \text{flow over a vertical cone,} & (31b) \\ 2n: & \text{stagnation flow over a horizontal cylinder,} & (31c) \\ 2(n + 1): & \text{stagnation flow over a sphere.} & (31d) \end{cases}$$

Results and discussion

Numerical integrations were carried out changing the values of the power-law index n and the lumped parameter Im_t , using the standard Runge-Kutta-Gill integration scheme. In Fig. 3, the heat transfer results are presented for all similar mixed

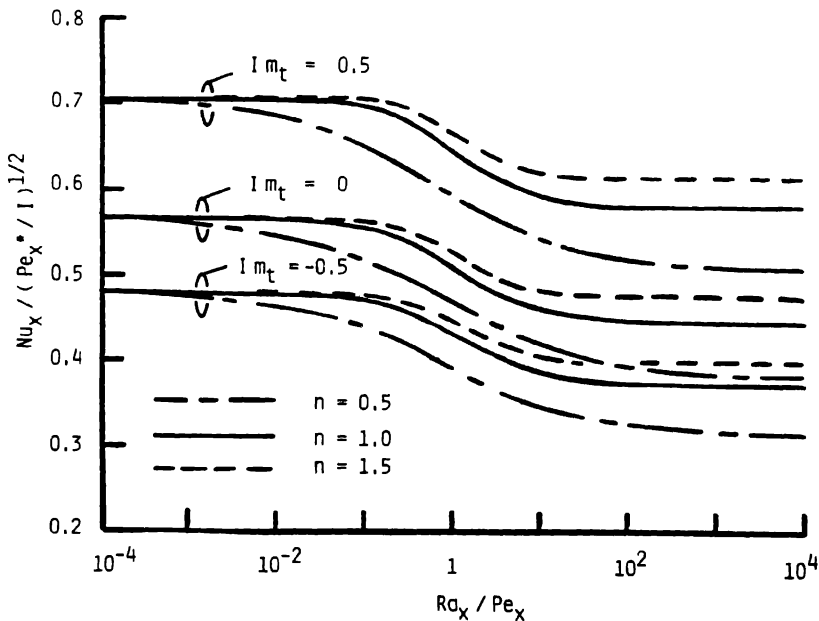


Fig. 3 Heat transfer function $\text{Nu}_x / (\text{Pe}_x^* / I)^{1/2}$.

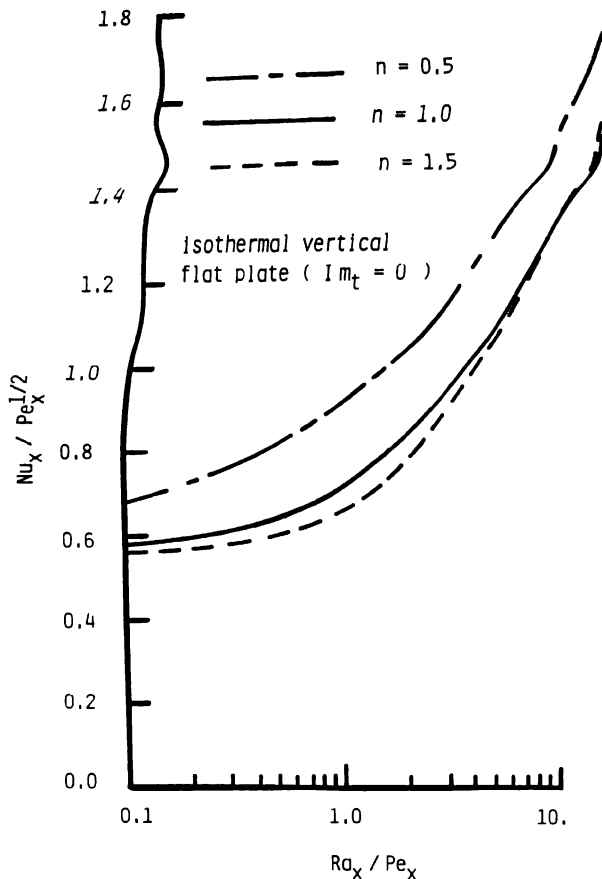


Fig. 4 Heat transfer results for an isothermal vertical flat plate

convective flows under consideration in terms of the heat transfer function $-\theta'(0) = Nu_x / (Pe_x^* / I)^{1/2}$ in Fig. 3 in which the ratio Ra_x / Pe_x is chosen for the abscissa variable. For small Ra_x / Pe_x , the three curves obtained for $n = 0.5, 1$ and 1.5 merge together at the level of forced convection asymptote. As Ra_x / Pe_x increases towards $Ra_x / Pe_x = 1$, the three curves diverge, and each value of $Nu_x / (Pe_x^* / I)^{1/2}$ starts to drop, and then gradually approaches the level of pure free convection asymptote. The figure clearly indicates that an increase in either n or Im_t results in an increase in $Nu_x / (Pe_x^* / I)^{1/2}$. The heat transfer results have been transformed into $Nu_x / (Pe_x / I)^{1/2} (= -\theta'(0) \{1 + (Ra_x / Pe_x)^n\}^{1/2n})$ in terms of the conventional local Peclet number, and replotted for $0.1 \leq Ra_x / Pe_x \leq 10$ in Fig. 4 for the case of an isothermal vertical flat plate, namely, $Im_t = 0$. It is clear from this conventional plot that, for fixed external velocity (i.e. for fixed Pe_x), the Nusselt number goes through a substantial enhancement as the buoyancy force becomes significant at higher Ra_x . At small Ra_x / Pe_x , the Nusselt number is higher for small n (However, the Nusselt number for

large n eventually exceeds that for small n , at the pure free convection limit, as can be seen from the figure which shows that the curve of $n = 1.5$ crosses over that of $n = 1$ at high Ra_x/Pe_x . The heat transfer function $Nu_x/(Pe_x/I)^{1/2}$ for the dilatant fluid ($n = 1.5$) varies closely following that of the Newtonian fluid, while a substantial difference in the heat transfer rates exists between the Newtonian and pseudoplastic fluids.

The corresponding temperature profiles θ for the isothermal vertical flat plate are plotted for $n = 0.5$ in Fig. 5(a) and for $n = 1$ and 1.5 in Fig. 5(b). The abscissa variable

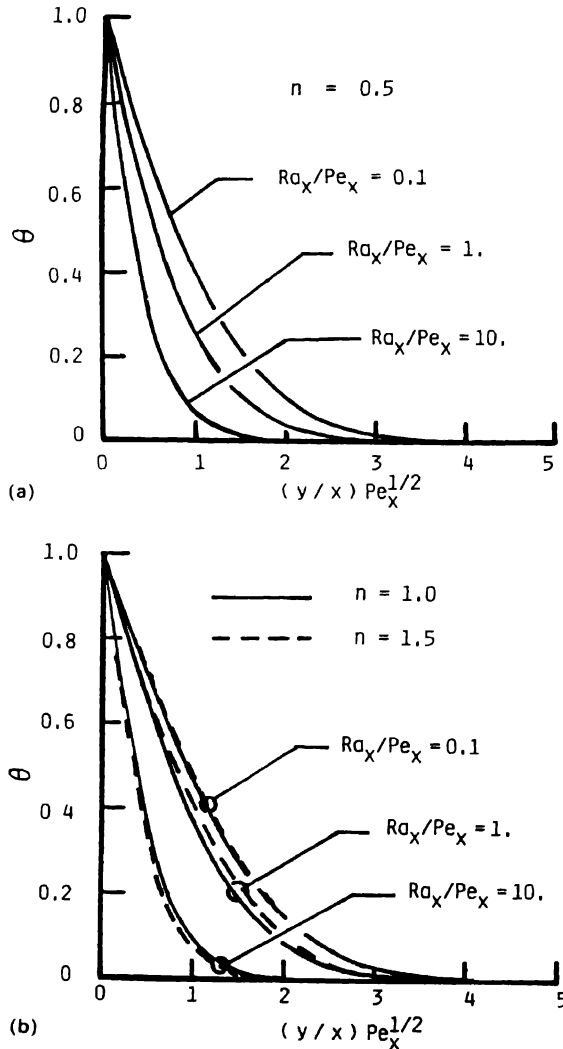


Fig. 5 Temperature profiles for an isothermal vertical flat plate, (a) $n = 0.5$, (b) $n = 1$ and $n = 1.5$.

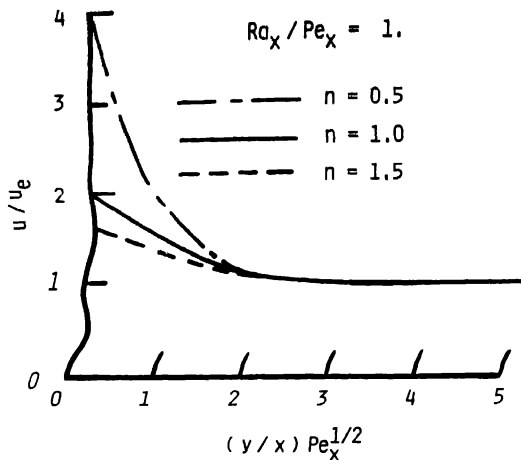


Fig. 6 Velocity profiles of mixed convective flow over an isothermal vertical flat plate

is chosen to be the conventional similarity variable, $(y/x)Pe_x^{1/2}$, such that the profiles obtained for different n can be compared directly under the same external velocity level. Naturally, the effect of the buoyancy is to make the thermal boundary layer thinner and thinner, as we increase the ratio Ra_x/Pe_x . Comparison of Fig. 5(a) and 5(b) reveals that the boundary layer of the pseudoplastic fluid ($n = 0.5$) is thinner than the others, when the external velocity is kept constant. As may be expected from the heat transfer results in Fig. 4, the temperature profiles obtained for the dilatant fluid ($n = 1.5$) differ only slightly from the Newtonian profiles. Figure 6 shows three distinct velocity profiles obtained for $n = 0.5, 1$ and 1.5 , under a typical mixed convection situation at $Ra_x/Pe_x = 1$. A substantially high velocity field is maintained near the wall in the pseudoplastic fluid, resulting in a significant heat transfer enhancement.

Conclusions

In this study of forced and free combined convection in power-law fluid-saturated porous media, we proposed a modified Peclet number based on the slip velocity at the wall, which is the total velocity resulting from both the external velocity and buoyancy force. The governing equations were transformed using this modified Peclet number such that all possible cases of mixed convection, including the two distinct asymptotic cases, namely, pure free and forced convection cases, can be treated without suffering from mathematical singularities.

Similarity solutions are found for vertical flat plates, cones, horizontal cylinders and spheres. Numerical integrations were carried out for a wide range of wall temperature distributions, and the heat transfer results are plotted in such a general manner (in terms of $Nu_x/(Pe_x^*/I)^{1/2}$) that we may readily translate them for a particular flow

situation of interest. It is found that the effect of pseudoplasticity is to make the thermal boundary layer thinner and thinner, leading to a substantial heat transfer enhancement in the mixed convection regime

Unfortunately, comparison of the present analytical solutions with experimental data is not possible at this moment since there are no such experimental data available on combined convection in power-law fluid-saturated porous media.

References

- Bejan A Convective heat transfer in porous media In S Kakac R K Shah and W Aung (eds), *Handbook of Single-Phase Convective Heat Transfer* Chapter 16 New York Wiley (1987)
- Chen H-T and Chen, C-K, Free convection flow of non-Newtonian fluids along a vertical plate embedded in a porous medium *Trans ASME J Heat Transfer* 110 (1988a) 257–260
- Chen H-T and Chen C-K Natural convection of a non-Newtonian fluid about a horizontal cylinder and a sphere in a porous medium *Int Comm Heat Mass Transfer* 15 (1988b) 605–614
- Cheng P Combined Free and Forced Convection Flow about Inclined Surfaces in Porous Media *Int J Heat Mass Transfer* 20 (1977) 807–814
- Cheng P Heat transfer in geothermal systems *Advances in Heat Transfer* 14 (1978) 1–105
- Christopher R H and Middleman S Power-law flow through a packed tube *I & EC Fundamentals* 4 (1965) 422–426
- Combarrous M A and Bones S A Hydrothermal convection in saturated porous media, *Advances in Hydroscience* 10 (1975) 231–307
- Dharmadhikari R V and Kale D D Flow of non-Newtonian fluids through porous media *Chem Engg Sci* 40 (1985) 527–529
- Herschel W H and Bulkley R Konsistenzmessungen von gummi-benzollösungen *Koll Z* 39 (1926) 291–300
- Kafousias N G Principles of flow through porous media with heat transfer in *Encyclopedia of Fluid Mechanics* Vol 10 Ch 20 (1990) 663–686
- Nakayama A and Koyama H An integral method for combined free and forced convection within a fluid saturated porous medium *Appl Sci Res* 44 (1987) 333–340
- Nakayama A and Koyama H Buoyancy-induced flow of non-Newtonian fluids over a non-isothermal body of arbitrary shape in a fluid-saturated porous medium *Appl Sci Res* 48 (1991) 55–70
- Nakayama A and Pop I A unified similarity transformation for free, forced and mixed convection in Darcy and non-Darcy porous media *Int J Heat Mass Transfer* 34 (1991) 357–367
- Pascal H and Pascal J P Nonlinear effects of non-Newtonian fluids on natural convection in a porous medium *Phys D* 40 (1989) 393–402
- Pascal H Non-isothermal flow of non-Newtonian fluids through a porous medium *Int J Heat Mass Transfer* 33 (1990) 1937–1944
- Pascal H Some self-similar two-phase flows of non-Newtonian fluids through a porous medium *Studies in Applied Math* 82 (1990) 305–318
- Tien, C L and Vafai K Convective and radiative heat transfer in porous media *Adv Appl Mech* 27 (1990) 225–281
- Trevisan O V and Bejan A Combined heat and mass transfer by natural convection in a porous medium *Adv Heat Transfer* 20 (1990) 315–352
- Wang C and Tu C Boundary-layer flow and heat transfer of non-Newtonian fluids in porous media *Int J Heat Fluid Flow* 10 (1989) 160–165
- Wang, C Tu C and Zhang X, Mixed convection of non-Newtonian fluids from a vertical plate embedded in a porous medium *Acta Mechanica Sinica* 6 (1990) 214–220

Marangoni convection at alcohol aqueous solutions–air interfaces

G. PÉTRÉ¹, M. A. AZOUNI² & K. TSHINYAMA¹

¹*ULB, Chimie Physique E. P.C.P. 165, 50 Avenue F.D. Roosevelt, B-1050 Brussels, Belgium*

²*Lab. d'Aérothermique, 4ter Route des Gardes, F-92190 Meudon, France*

Received 14 March 1991, accepted in revised form 29 September 1991

Key words: convection, Marangoni, surface tension minimum

Abstract. For aqueous *n*-heptanol solutions and in a nearly two-dimensional flow, two striking features have been detected

- a shift of the minimum of the surface tension
- a discrepancy between the observed Marangoni flow velocities and the expected ones from static surface tension values.

A qualitative explanation is given.

1. Introduction

Aqueous solutions of fatty alcohols present a minimum in surface tension versus temperature [10]. It was previously established experimentally in an axisymmetric device that for *n*-hexanol and *n*-heptanol it is possible to induce surface movements from the hot part of the surface to the cold one, or from the cold to the hot one by choosing the appropriate temperatures [7]. Other studies on thermal Marangoni flows in aqueous heptanol solutions were also performed in a smaller device on earth [4, 6, 8] and under microgravity conditions [4, 6].

The aim of this work is to compare the observed surface velocities with those predicted from static surface tension values of the investigated systems.

A new device where the thermal Marangoni flow is approximately two dimensional is built; it provides a configuration more suitable for quantitative evaluation.

2. Experimental set-up

A sketch of the device is given in Fig. 1. In the bottom of a Pyrex Petri-box (inner diameter 0.182 m) two parallel channels are grooved. The channels, nearly 0.12 m long and $4.8 \cdot 10^{-3}$ m wide are distant from $L = 12.2 \cdot 10^{-3}$ m. Each channel is closed by a glass plate glued to the box, and connected to a thermoregulated bath as indicated in Fig. 2. The Petri-box is thermostated in a larger glass vessel containing water at an adjustable temperature T_3 . The system is lit from below, and the telecentric objective

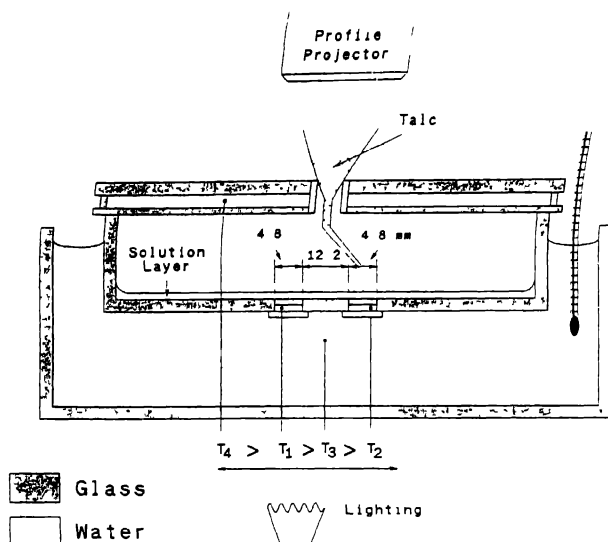


Fig. 1 Sketch of the device for measuring surface fluid velocities

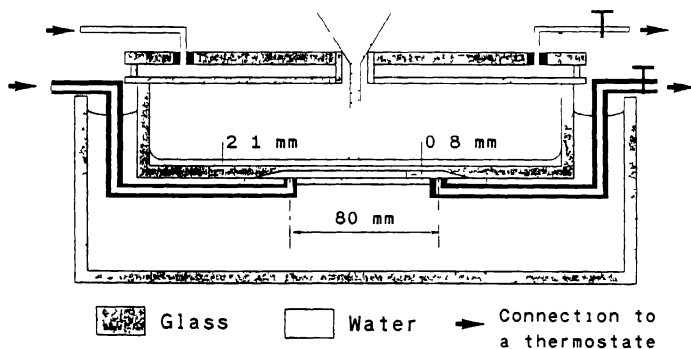


Fig. 2 Sketch of a channel of the used device

(small field depth) of a profile projector is focused on the liquid surface; a magnification of 10 is used. A Petri-box for which no distortion appears in the images reflected by the upper surface of the bottom was selected. Water flows at temperature T_4 higher than T_1 , T_2 and T_3 in a double-wall glass-lid. This appeared to be necessary to avoid a blurred image due to the condensation of the vapour emitted by the solution. A small aperture in the lid makes it possible to spread talc powder on the liquid surface to visualize the motions.

3. Experimental procedure

The Pyrex-box is cleaned with sulfochromic acid, rinsed with tridistilled water and dried under vacuum. The box is then placed in the device, the horizontality of the

upper face of the bottom being ensured. With a clean pipette, a known volume (V) of liquid is put in the box. The temperature of the introduced liquid has to reach the temperature T_3 of the surrounding water (Fig. 1). By opening the appropriate valves (Fig. 2), the circulation of water at the temperature T_1 higher than T_3 is established in channel 1 and the circulation of water at T_2 lower than T_3 in channel 2.

After a few minutes, a steady state is reached in the solution layer. Then some talc powder is spread on the free liquid surface. The movements of the talc particles indicate the channel over which the surface tension is the lowest (talc spreading is then focused on this channel). These movements are observed on the screen of the profile projector. If they are perpendicular to the two channels, the motion is considered as two-dimensional, and surface velocity measurements can start. Figure 3 gives a picture of the screen: A represents a talc particle on the surface (or a small aggregate of such particles). Lines L_1 , L_2 and L_3 drawn on the screen correspond to distances on the liquid surface of $3.6 \cdot 10^{-3}$, $6.6 \cdot 10^{-3}$ and $8.6 \cdot 10^{-3}$ m apart from the channel over which the surface tension is the lowest (Fig. 3).

The times necessary for a talc particle to travel from L_1 to L_3 and to L_2 are measured with a chronometer, and one can deduce the mean velocities over $3 \cdot 10^{-3}$ m and over $5 \cdot 10^{-3}$ m (denoted by v_3 and v_5). Measurements are repeated n times (n varies from 2 to 20) for given liquid composition, layer thickness, and temperatures T_1 , T_2 , T_3 and T_4 . The temperatures T_1 , T_2 and T_4 are read on the corresponding thermoregulated baths thermometers, T_3 is read on the thermometer shown in Fig. 1 (precision is 0.1°C).

The narrow field depth of the objective allows to observe tracers (wetted talc

IMAGE ON THE SCREEN

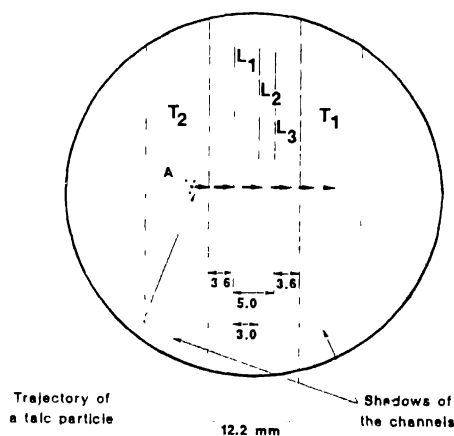


Fig. 3. Sketch of what is seen on the screen of the profile projector.

particles) inside the solution layer at different depths. It is observed that the liquid transported by the liquid surface in one direction returns in the opposite direction in the lower part of the liquid layer, forming apparently a stationary roll between the two channels.

Taking into account that the liquid wets perfectly the vertical wall of the Petri-box, the thickness h of the flat part of the liquid layer is calculated by the relation

$$h = \frac{1}{\pi R^2} \left(V - \frac{2\pi\sigma R}{\rho g} \right), \quad (1)$$

where V is the liquid volume, R is the radius of the Petri-box, σ is the surface tension of the liquid, g is the acceleration of gravity (9.81 m/s^2), and ρ is the density of the fluid.

The second term in the parenthesis of (1) gives the volume of the liquid raised in the meniscus.

4. Experimental results

The studied liquid was a $6.24 \cdot 10^{-3}$ molal aqueous solution of *n*-heptanol. The velocities of talc particles were measured at different temperatures T_3 as a function of the imposed temperature gradient. The values of T_3 were: 8.5, 20, 31, 40 and 51°C. The layer depth h obtained from (1) was $1.82 \cdot 10^{-3} \text{ m}$.

It was noticed that the reproducibility of the results is better when the temperature of the water in the channel towards which the surface moves (T_1 in Fig. 3) does not differ too much from T_3 .

Figure 4 summarizes the results. For each temperature T_3 , the surface velocities v_3 and v_s as defined in the preceding section are plotted against the value of $(T_1 - T_2)/L$, where $L = 12.2 \cdot 10^{-3} \text{ m}$.

In most cases, the difference between a mean value over v_3 and the corresponding mean value over v_s is less than the results scatter. The velocity is thus considered constant over the surface region where the velocity is measured. For each T_3 the surface velocities v_3 and v_s versus the imposed $T_1 - T_2$ are represented by the same straight line passing through the origin (at least for the lower temperature gradients). The slopes α of such experimental lines are given in Table 1, column 2.

For comparison, column 3 of Table 1 refers to the slopes calculated under the following assumptions:

- the surface velocity v_s is given by: (see e.g. [5] p. 383)

$$v_s = \frac{h}{4\mu} \frac{\partial \sigma}{\partial T} \frac{\partial T}{\partial x}; \quad (2)$$

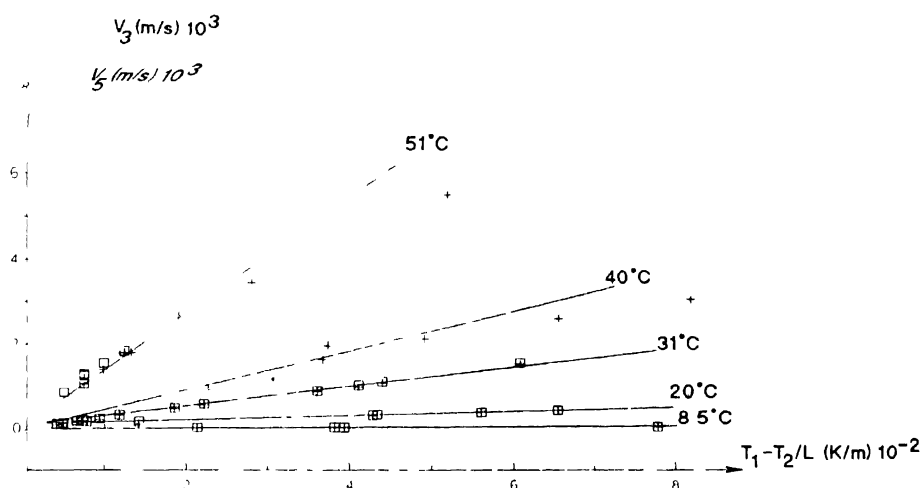


Fig. 4 The measured velocities of tracers on the liquid surface as function of the imposed temperature gradient around 51, 40, 31, 20 and 8.5°C

Table 1

T_1 , °C	$\alpha = \frac{12.2 \cdot 10^{-3}}{T_1 - T_2} \text{ m}^2 \text{ sec}^{-1} \text{ K}^{-1}$	$v_s \frac{12.2 \cdot 10^{-3}}{T_1 - T_2} \text{ m}^2 \text{ sec}^{-1} \text{ K}^{-1}$
8.5	$0.09 \cdot 10^{-6}$	$-0.89 \cdot 10^{-4}$
20	$0.5 \cdot 10^{-6}$	$-0.77 \cdot 10^{-4}$
31	$2.4 \cdot 10^{-6}$	$-0.40 \cdot 10^{-4}$
40	$4.6 \cdot 10^{-6}$	~ 0
51	$13 \cdot 10^{-6}$	$+0.65 \cdot 10^{-4}$

– the surface temperature gradient $\partial T / \partial x$ is equal to $(T_1 - T_2) / 12.2 \cdot 10^{-3} \text{ (}^\circ\text{K m}^{-1}\text{)}$;
– the value of $(\partial \sigma / \partial T)_T$ is equal to $(\partial \sigma_e / \partial T)_T$, where σ_e is the equilibrium surface tension measured in an isothermal system. The values of $\partial \sigma_e / \partial T$ (given in Table 2) for $6.24 \cdot 10^{-3}$ molal *n*-heptanol are obtained by interpolation between curves 8 and 9 in Fig. 3 of reference [10].

– the viscosity (μ) of the diluted *n*-heptanol solution is considered to be equal to that of pure water. This last point seems to be satisfied: for a $3 \cdot 10^{-3}$ molal solution of *n*-octanol, the viscosity measured at 20°C does not differ appreciably from that of water [3].

Comparison between the observed and the “expected” values (Table 1) for the surface velocities show striking discrepancies.

Table 2

$T_3/^{\circ}\text{C}$	$\left(\frac{\partial\sigma_e}{\partial T}\right) \text{ N m}^{-1} \text{ K}^{-1}$
8.5	$-2.64 \cdot 10^{-4}$
20	$-1.68 \cdot 10^{-4}$
31	$-0.69 \cdot 10^{-4}$
40	~ 0
51	$+0.76 \cdot 10^{-4}$

First of all the observed velocities are positive, this means that the flow at the surface is in the direction of increasing temperature (positive Marangoni number). For a solution of $6.24 \cdot 10^{-3}$ molal heptanol, in the dynamical conditions of our experiments, the minimum in surface tension versus T is thus shifted from 40°C in the σ_e/T curve (Fig. 5 obtained by measurements made by R. Vochten) to a temperature lower than 8.5°C .

Second, the observed velocities are (in absolute value) considerably lower than the "expected" ones.

5. Discussion

5.1. Shift of the surface tension minimum

Let us consider the system for which $T_3 \simeq 8.5^{\circ}\text{C}$.

We can see on Fig. 5 that a temperature difference of 8°C around 8.5°C corresponds to an equilibrium surface tension difference of approximately $2.4 \cdot 10^{-3} \text{ N/m}$. However, the evaporation of the n -heptanol over the area of higher temperature can raise the surface tension and, at the same time, condensation on the area of lower temperature can lower the surface tension.

An order of magnitude of the surface tension increase originated by the surfactant evaporation was determined experimentally by J. Hommelen [2] and studied theoretically by R. Hansen [1]. Hommelen measured the surface tension of a solution $3.5 \cdot 10^{-3}$ molal in n -heptanol by the ring method in a vessel closed by glass plates (with a very small hole for the suspension wire). After removing the glass plates acting as a lid for the vessel, the alcohol diffuses in the atmosphere and the surface tension increases by $1.2 \cdot 10^{-3} \text{ N/m}$, reaching a nearly stationary value. If we suppose the same order of magnitude for the decrease of the surface tension by condensation of alcohol from the vapour phase, then evaporation and condensation can produce a surface tension difference of $2 \times 1.2 \cdot 10^{-3} \text{ N/m}$ able to cancel $(\partial\sigma_e/\partial T)$. This could explain the

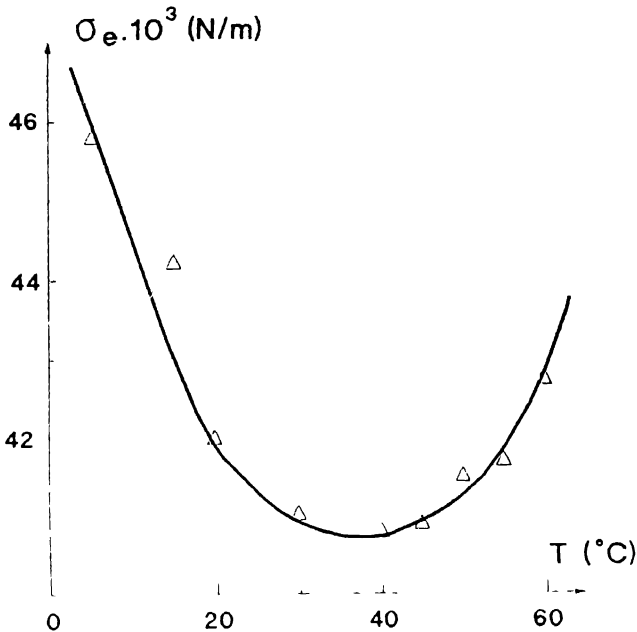


Fig 5 The equilibrium surface tension σ_e of a $6.24 \cdot 10^{-3}$ molal aqueous solution of *n*-heptanol as a function of the temperature. The curve is obtained from measurements [10] by Prof. R. Vochten (R.U.C. Antwerpen).

very low (and yet positive) values of the surface velocities around 8.5°C , as well as the shift of the temperature at which the actual $(\partial\sigma/\partial T)$ becomes negative to lower values.

It is worth emphasizing that the above explanation of the shift observed on the minimum in aqueous surface tension below 10°C is only qualitative. In our closed device, evaporation is obviously different from that originated by diffusion in an infinite space.

5.2. The observed velocities are lower than those expected

This unambiguously results from the measurements made around 50°C . Indeed, around 50°C σ_e increases with T , and hence the surface tension gradient would be increased by the evaporation-condensation process and v is expected to be higher than v_s . The actual ratio v/v_s is equal to 0.2 (see Table 1).

Two reasons can contribute to explain that the surface velocities are lower than those predicted by (2).

(i) We have used relation (2) assuming that $\partial T/\partial x = (T_1 - T_2)/L$. But, experiments carried out with water in the same set-up as the one used for the *n*-heptanol solution

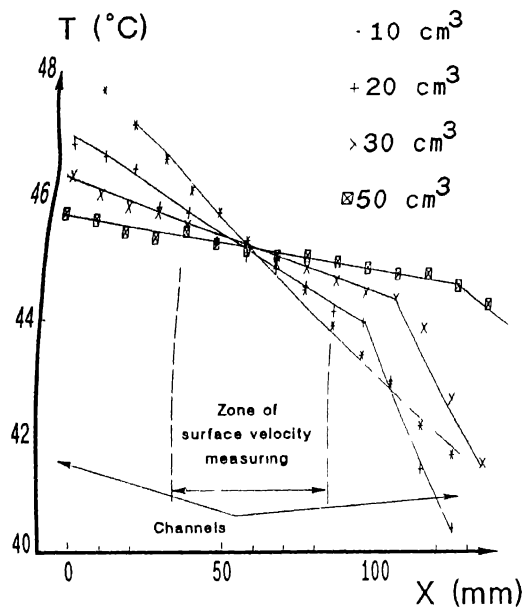


Fig. 6 Surface temperatures of water layers of increasing thicknesses as a function of the distance to the "hot channel" of the device (The imposed temperatures are 44.9 and 34.6°C) The surface temperature is measured by a bolometer from Heimann, Type Infrarot Strahlungsthermometer KT4

proved that the above equality is not fulfilled and that $\partial T / \partial x < (T_1 - T_2) / L$. In the used box, the introduced volumes of water of 10, 20, 30, 40, 50, 60 and 100 10^{-6} m^3 correspond to layer thicknesses ranging from $0.22 \cdot 10^{-3} \text{ m}$ to $3.8 \cdot 10^{-3} \text{ m}$. A temperature difference of 10.3°C is imposed (44.9°C – 34.6°C) between the channels. The decrease of the water surface temperature, from one channel to the other was measured with a bolometer (Heimann Infrarot-Strahlungsthermometer KT4).

For given T_1 , T_2 , T_3 , the gradient $\partial T / \partial x$ decreases when the layer thickness increases as shown on Fig. 6. For $h = 1.76 \cdot 10^{-3} \text{ m}$, the gradient is

$$\frac{\partial T}{\partial x} \cong 0.1 \frac{T_1 - T_2}{12.2}. \quad (3)$$

If we assume that (3) applies roughly to the used heptanol solution at 50°C , and put it in (2) we obtain

$$\frac{v}{v_s} = 2 \quad (4)$$

and

$$\frac{\partial \sigma}{\partial T} \cong 2 \frac{\partial \sigma_e}{\partial T}.$$

This can be attributed to an increase of the actual $\partial \sigma_e / \partial T$ by the evaporation-condensation process. Also, we suspect that the decrease of $\partial T / \partial x$ with increasing layer thickness is associated with the increase in surface velocity.

(ii) The relation (2) is established for a thin horizontal liquid layer limited by two parallel vertical rigid walls maintained at two different temperatures. This relation gives the stationary surface velocity of the surface tension driven convection roll supposed to extend from one wall to the other.

However, D. Villers ([9] Fig. II-46 and Fig. II-47) pointed out by numerical simulations that the Marangoni flow in a thin layer ($h = 3.3 \cdot 10^{-3}$ m) of a solution of *n*-heptanol becomes multicellular when the imposed temperature gradient is increased. He also showed, that in this case, velocities were lower than those predicted by (2).

We still believe that our results (Fig. 5) for 8.5, 20 and 31°C and those for 40 and 51°C at the lowest temperature gradients correspond to a unique convective roll: the mean velocities over $3 \cdot 10^{-3}$ m and $5 \cdot 10^{-3}$ m coincide and the extrapolation of the straight lines to the zero constraint indicates zero velocities. The experimental points at 40 and 51°C for the highest temperature gradients lie clearly under the straight lines crossing the origin. This might correspond to the transition from unicellular to multicellular Marangoni convection.

6. Conclusion

For the studied solution of *n*-heptanol, the velocities of Marangoni convection observed in a nearly two-dimensional flow differ appreciably from the predicted values based on the variation of the equilibrium surface tension with temperature.

The considerable shift to lower temperatures of the surface tension minimum finds a possible qualitative explanation in the evaporation-condensation phenomenon which is not taken into account by the equilibrium surface tension. The discrepancy between the observed velocities and the predicted ones, when we suppose that the surface temperature gradient is equal to $(T_1 - T_2)/L$, is partly due to the fact that the actual surface temperature gradient is much smaller. This has been established for water by bolometer measurements.

An additional cause would be the occurrence of a multicellular Marangoni flow. The latter point needs to be thoroughly investigated.

Acknowledgements

We thank Prof. Schawbe from University of Giessen who very kindly lent us his bolometer and B. Stockman who performed an important part of the measurements. We thank also Prof. J.C. Legros and Prof. G. Thomaes (ULB) for their aid. The work received financial support from the Belgian S.P.P.S. (P.A.I.)

References

1. Hansen, R., *J. Phys. Chem.* 64 (1960) 637.
2. Hommelen, J., *J. Coll. Interf. Sci.* 14 (1959) 385.
3. Kusman, L., Travail de fin d'études, Université Libre de Bruxelles (1960).
4. Legros, J.C., *Acta Astronautica* 13 (1986) 697.
5. Levich, L. G., *Physicochemical Hydrodynamics*. Englewood Cliffs: Prentice Hall (1962).
6. Limbourg, M. C., Legros, J. C. and Pétré, G., *Adv. Space Res.* 6 (1986) 35.
7. Pétré, G. and Azouni, M. A., *J. Coll. Interf. Sci.* 98 (1984) 261.
8. Villers, D. and Platten, J.K., *PCH* 8 (1987) 173.
9. Villers, D., Thesis, Université de Mons, Belgium (1989).
10. Vochten, R. and Pétré, G., *J. Coll. Interf. Sci.* 42 (1973) 320.

The energy-integral method: application to linear hyperbolic heat-conduction problems

FOUAD A. MOHAMED

Department of Mathematics, Texas Tech University, Lubbock, TX 79409, USA

Received 21 September 1990; accepted in revised form 15 October 1991

Abstract. This paper utilizes the energy-integral method to obtain approximate analytic solutions to a linear hyperbolic heat-conduction problem for a semi-infinite one-dimensional medium. As for the mathematical formulation of the problem, a time-dependent relaxation model for the energy flux is assumed, leading to a hyperbolic differential equation which is solved under suitable initial and boundary conditions. In fact, analytical expressions are derived for uniform as well as varying initial conditions along with (a) prescribed surface temperature, or (b) prescribed heat flux at the surface boundary. The case when a heat source (or sink) of certain type takes place has also been discussed. Comparison of the approximate analytic solutions obtained by the energy-integral method with the corresponding available or obtainable exact analytic solutions are made; and the accuracy of the approximate solutions is generally acceptable.

Nomenclature

A, C = constants
 $a_0(t), a_1(t), \dots, a_n(t)$ = arbitrary time-dependent coefficients, equation (3.2)
 b = thermal propagation speed
 C_p = specific heat of solid at constant pressure
 $g(x)$ = given function, equation (5.1)
 $h(t)$ = specified function of time
 I_n = modified Bessel function of the first kind
 K = thermal conductivity
 j, n = positive constants
 $P_n(x, t)$ = polynomial of degree n
 $q(x, t)$ = heat flux
 $Q(t), R(t), H(t), E(t)$ = see equations (3.9), (II.d), (4.10), (4.12), respectively
 $\delta(t)$ = thermal penetration depth
 $\tilde{\delta}(t, \tau)$ = approximate thermal penetration depth
 $T(x, t)$ = temperature distribution
 t = time
 y = dimensionless time, equation (3.17)
 $V(y)$ = dimensionless surface heat flux

$W(y)$ = dimensionless surface temperature
 $U_+(t)$ = unit-step function
 $G(x; t, \xi)$ = Green's function
 x = spatial variable
 $()_0$ = surface value (at $x = 0$)

Greek symbols

α = thermal diffusivity
 ρ = density of solid
 γ = parameter, see equations (3.11) and (3.13)
 λ = parameter depending on n and α
 μ = specified parameter, equations (4.5a) and (5.12b)
 $\eta(t), \nu(t)$ = given functions of time, equations (4.6) and (5.5b)
 β, ξ = dummy variables
 τ = relaxation time
 Θ = energy integral
 $\Phi(y), \Psi(y)$ = specified functions of y ; equations (3.22) and (4.19)

1. Introduction

There are various analytical methods available for solving heat transfer, and more especially diffusion and heat conduction, problems defined over simple geometries where the governing differential equation and the boundary conditions are linear (see, e.g. [3]). On the other hand, when the geometries are complicated, the exact analysis becomes not applicable. That is, approximate analytic solutions are useful when exact analytic solutions are too difficult or impossible to obtain or when the numerical solution of the problem cannot be justified. In fact, an analytic solution provides a better insight to the physical significance of various parameters affecting a given problem than a purely numerical solution.

As an elegant approximate analytic method for solving transient heat transfer problems is the so-called *energy-integral* (or sometimes, the *heat-balance integral*) method (EIM). Its main merits are that: (a) it frequently provides reasonable results quickly, and (b) it applies equally well to nonlinear transient heat transfer problems; such problems need not be linearized beforehand. It is noteworthy that when a heat conduction problem defined in a given region is solved exactly, the resulting solution is satisfied pointwise throughout the considered region but with the EIM the solution is satisfied only on the average over that region.

The use of EIM for the solution of parabolic partial differential equations dates back to von Karman and Pohlhausen, who applied the method for the approximate analysis of boundary-layer momentum and energy equations of fluid mechanics [13]. Landahl [8] used it in the field of biophysics to solve the diffusion equation in connection with the spread of a concentrate. Goodman [6, 7] utilized the method for solving a one-dimensional melting problem. Since then, the EIM has been applied in the solution of various types of one-dimensional heat-conduction problems and heat and momentum transfer problems involving a change of phase (see, e.g. [1, 4, 12, 14, 17]). See also [5, 9, 11, 19, 20] and the references cited there. In [11], however, Mohamed applied the method to obtain approximate analytic solution for hyperbolic one-phase Stefan problems.

The purpose of this paper is to utilize the EIM to obtain approximate analytic solutions to linear hyperbolic heat-conduction problems for a semi-infinite one-dimensional medium. In particular, the cases of constant and varying initial conditions together with time-dependent surface temperature or heat flux boundary conditions are treated. The solutions of the above problem in the case where there is a heat source (or sink) in the medium depending on the time and spatial variables as well as the relaxation parameter (which will be introduced in the next section) have also been discussed. Comparison of the approximate analytic solutions obtained by the EIM with the corresponding available or obtainable exact analytic solutions are made; and the accuracy of the approximate solutions is generally acceptable.

2. The energy-integral equation and penetration depth conditions

Consider a transient heat-conduction problem in a semi-infinite one-dimensional medium $x > 0$, which is initially at a uniform temperature A and for times $t > 0$ the boundary surface is maintained at temperature $T_0(t)$. In mathematical terms, this problem is described by the system

$$\alpha T_{xx} = \tau T_{tt} + T_t, \quad x > 0, t > 0, \quad (2.1)$$

$$T(x, 0) = A, \quad x > 0, \quad (2.2)$$

$$T_t(x, 0) = 0, \quad x > 0, \quad (2.3)$$

$$T(0, t) = T_0(t), \quad t > 0. \quad (2.4)$$

Here α is the thermal diffusivity of the heat conductor and the constant τ is the relaxation time of the model. For many solids, τ is of order 10^{-12} to 10^{-14} sec [18].

To solve this problem using the EIM, one firstly introduces the notion of a *thermal penetration depth* $\delta(t)$ such that effectively, for practical purposes, heat conduction only occurs for $0 \leq x \leq \delta(t)$ while in the region $x > \delta(t)$ there is no heat flow at all. With this in mind, one may write

$$T(x, t) = A, \quad T_x(x, t) = 0, \quad x > \delta(t). \quad (2.5)$$

In fact, this is not an unreasonable assumption, since according to the above discussion (see also [11]), heat physically cannot be transmitted at an infinite speed, and moreover it can be reconciled with the exact analytic solution (see section 3) by imagining $x = \delta(t)$ to be the point beyond which the temperature distribution $T(x, t)$ remains unaffected and the heat flux $q(x, t)$ is negligible. Furthermore, at $x = \delta(t)$ one has

$$T(\delta(t), t) = A, \quad t > 0, \quad (2.6)$$

$$q(\delta(t), t) = 0, \quad t > 0 \quad (2.7)$$

since on the most basic of the thermodynamic grounds both the temperature and heat flux must be continuous (the Zeroth Law of Thermodynamics and the Conservation of Energy). Problems (2.1)–(2.4), (2.6) and (2.7) will hereafter be referred to as problem I.

It is convenient for subsequent discussion to write (2.7) in terms only of the temperature gradient $T_x(\delta(t), t)$. Differentiating (2.7) along the curve $x = \delta(t)$ yields

$$q_x(\delta(t), t)\delta'(t) + q_t(\delta(t), t) = 0, \quad (2.8)$$

where the prime denotes the differential operator d/dt . Combining (2.6) with the First Law of Thermodynamics,

$$\rho C_p T_t(x, t) = -q_x(x, t), \quad (2.9)$$

and (2.7) with the relaxation model for the energy flux [2],

$$q(x, t + \tau) = -K T_x(x, t)$$

or, rather its approximation,

$$q(x, t) + \tau q_t(x, t) = -K T_x(x, t), \quad (2.10)$$

one obtains

$$q_x(\delta(t), t) = \rho C_p T_x(\delta(t), t) \delta'(t); \quad q_t(\delta(t), t) = -\tau^{-1} K T_x(\delta(t), t). \quad (2.11)$$

Here the thermal conductivity K , the density ρ and the specific heat at constant pressure C_p are assumed constant. Substituting (2.11) in (2.8) to get

$$\rho C_p T_x(\delta(t), t) [\delta'^2(t) - b^2] = 0 \quad (2.12)$$

with $b = (\alpha/\tau)^{1/2}$ being the finite speed of propagation. If the square bracket were zero, i.e. $\delta(t) = bt$, $t \geq 0$, then (2.6) implies that

$$b T_x(\delta(t), t) + T_t(\delta(t), t) = 0. \quad (2.13)$$

It follows from (2.9), (2.10) and (2.13) that

$$\tau^{-1} q(\delta(t), t) + q_t(\delta(t), t) + b q_x(\delta(t), t) = 0 \quad (2.14)$$

whose solution is

$$q(\delta(t), t) = C e^{-t/\tau}, \quad (2.15)$$

where C is an arbitrary constant. Expression (2.15) is, however, in violation of the thermal penetration depth condition (2.7), leading to the expected conclusion that the basic conditions constitute an overdetermined set of constraints if the thermal penetration depth is a characteristic line of (2.1).

On the other hand, it is easily verified that the function

$$T(x, t) = A + U_+(at - x) \left\{ \exp \left[\frac{a(x - at)}{\tau(a^2 - b^2)} \right] - 1 \right\}, \quad t > 0 \quad (2.16)$$

satisfies the conditions (2.1)–(2.3) and (2.6). Here $U_+(z)$ is the heaviside step function which is defined as unity for $t > 0$ and zero for $t \leq 0$. The boundary value of T is

$$T(0, t) = -1 + A + \exp \left[\frac{-a^2 t}{\tau(a^2 - b^2)} \right]. \quad (2.17)$$

Looking at this backwards, one can view (2.16) and

$$\delta(t) = at, \quad t > 0; \quad 0 < a, \quad a \neq b \quad (2.18)$$

as an explicit solution of (2.1)–(2.3) and (2.6) with the boundary condition (2.17) derived by means of the imposed temperature at the surface boundary $x=0$ of the medium, with $a \neq b$ as an input parameter.

At this stage, we distinguish between two cases according to the value of the input parameter $a \neq b$; namely: (i) if $a < b$, the thermal layer front propagates slower than the characteristic of the governing hyperbolic equation (2.1). To the left of this front, i.e., $x < \delta(t)$, it follows that $T(x, t) > A$ and hence we have a heated medium there. This is in great contrast with the case (ii) $a > b$, i.e. the speed of the thermal layer front exceeds the characteristic signal speed of (2.1). To the left of the front, $x < at$, one deduces from (2.16) that $T(x, t) < A$ so that we have a “supercooled” medium there. This “temperature” decreases exponentially fast, with $T_x(x, t) > 0$. Substituting T_x from (2.16) into (2.1), multiplying by the integrating factor $e^{t/\tau}$, integrating in t , and using (2.7) to determine the integration constant, we arrive at

$$q(x, t) = \frac{aK}{\tau b^2} \exp \left[\frac{a(x - at)}{\tau(a^2 - b^2)} \right], \quad 0 \leq x < at. \quad (2.19)$$

Thus, even though $T_x > 0$, the heat flux q is still positive and the heat is flowing to the thermal layer front within the “supercooled” medium phase. This unphysical situation is apparently an acceptable mathematical solution to problem I.

In consequence of the above arguments, (2.12) implies that

$$T_x(\delta(t), t) = 0. \quad (2.20)$$

An extra equation is obtained by differentiating (2.6) along $x = \delta(t)$ and employing (2.20). It follows that

$$T_t(\delta(t), t) = 0. \quad (2.21)$$

Then differentiating (2.20) and (2.21) with respect to time and combining the results with the governing equation (2.1) to deduce that

$$T_{xx}(\delta(t), t) = 0. \quad (2.22)$$

Analogously, we can derive the smoothing conditions

$$\frac{\partial^j T(\delta(t), t)}{\partial x^j} = 0; \quad j = 3, 4, \dots, n-1. \quad (2.23)$$

Finally, on integrating (2.1) over the domain $0 < x < \delta(t)$, one obtains the energy-integral equation in the form

$$\tau \left(\frac{d^2}{dt^2} + \frac{d}{dt} \right) [\Theta(t) - A\delta(t)] = -\alpha T_x(0, t) \quad (2.24)$$

which is to be solved subject to the initial conditions

$$\delta(0) = 0, \quad \delta'(0) = a. \quad (2.25)$$

Here (2.12) has been used and

$$\Theta(t) = \int_0^{\delta(t)} T(x, t) dx \quad (2.26)$$

is the total energy content of the region over the thermal penetration depth.

3. Solution of problem I using the energy-integral method

In the spirit of the EIM, the solution $T(x, t)$, of problem I may be approximated by a polynomial expression $P_n(x, t)$, of degree $n \geq 2$ (for some finite integer n), in the spatial variable with time-dependent coefficients, essentially any simple function may be used. In symbols, one may write

$$T(x, t) = \begin{cases} P_n(x, t), & 0 \leq x \leq \delta(t), \quad n \geq 2 \\ A & x > \delta(t). \end{cases} \quad (3.1)$$

In particular, $P_n(x, t)$ may be expressed in the form

$$P_n(x, t) = a_0(t) + a_1(t)x + a_2(t)x^2 + \dots + a_n(t)x^n \quad (3.2)$$

where the coefficients $a_0(t)$, $a_1(t)$, $a_2(t)$, \dots , $a_n(t)$ require n constraints on $P_n(x, t)$ for determination. For example, in the interest of obtaining the smoothest possible temperature profile, one may utilize the conditions

$$P_n(0, t) = T_0(t), \quad P_n(\delta(t), t) = A, \quad \frac{\partial^j P_n(\delta(t), t)}{\partial x^j} = 0, \quad j = 1, 2, \dots, n-1. \quad (3.3)$$

Then the utility of mathematical induction results in the approximation

$$\frac{P_n(x, t) - A}{T_0(t) - A} = \left(1 - \frac{x}{\delta(t)}\right)^n. \quad (3.4)$$

Substituting (3.4) in the energy-integral equation (2.24) gives

$$\left(\tau \frac{d^2}{dt^2} + \frac{d}{dt}\right)[\delta(t)(T_0(t) - A)] = \frac{\lambda(T_0(t) - A)}{\delta(t)}; \quad \lambda = n(n+1)\alpha. \quad (3.5)$$

For practical purposes, one may assume that $0 < \tau \ll 1$ (see section 2). Then according to the method of matched asymptotic expansions in singular perturbation theory [15] a formal uniform approximation, $\tilde{\delta}(t; \tau)$, for the solution $\delta(t)$ of the initial-value problem (3.5) subject to (2.25) is obtained in the form

$$\tilde{\delta}(t, \tau)h(t) \approx \left[2\lambda \int_0^t h^2(t_1) dt_1\right]^{1/2} + a\tau h(0)(1 - e^{-t/\tau}) \quad (3.6)$$

where $h(t) = T_0(t) - A$.

Equations (3.4) and (3.6) form a complete approximate analytic solution of problem I. Note that when $T_0(t)$ is independent of time, so is $h(t)$. In this case, (3.6) simplifies to

$$\tilde{\delta}(t, \tau) \approx \sqrt{2\lambda t} + a\tau(1 - e^{-t/\tau}) \quad (3.7)$$

so that $\lim_{\tau \rightarrow 0} \tilde{\delta}(t, \tau) = \sqrt{2\lambda t}$ which is, as expected, the same exact result obtained in the classical theory of transient heat conduction.

As an alternative approach to obtaining the smoothest temperature approximation, one may select the constraint involving the lower order derivatives. This rule arises because in approximating the temperature profile the priorities at the end points of the thermal penetration depth are first to obtain agreement with the temperature values themselves, then the first derivatives, then the second derivatives and so on. For purposes of illustration, it suffices to outline the cubic and quartic approximations for the solution of problem I over the thermal penetration depth.

In fact, the polynomial approximation

$$\frac{P_n(x, t) - A}{T_0(t) - A} = \left(1 + \frac{b(t)x}{\delta(t)}\right) \left(1 - \frac{x}{\delta(t)}\right)^{n-1} \quad (3.8)$$

for $n = 3$ satisfies the first three conditions of (3.3) and the coefficient $b(t)$ is determined from the surface boundary condition

$$T_{xx}(0, t) = \frac{\tau T_0''(t) + T_0'(t)}{\alpha} \equiv Q(t), \quad t > 0. \quad (3.9)$$

In this case, the cubic temperature profile has the form

$$\frac{P_3(x, t) - A}{T_0(t) - A} = \left(1 + \frac{x}{2\delta(t)} - \frac{\delta(t)Q(t)x}{4(T_0(t) - A)}\right) \left(1 - \frac{x}{\delta(t)}\right)^2 \quad (3.10)$$

and the energy-integral equation becomes

$$\left(\tau \frac{d^2}{dt^2} + \frac{d}{dt}\right) [\delta(t)(T_0(t) - A - \gamma\delta^2(t)Q(t))] = \frac{\lambda}{\delta(t)} [T_0(t) - A + 3\gamma\delta^2(t)Q(t)] \quad (3.11)$$

where $\lambda = 4\alpha$, $\gamma = 1/18$.

When $T_0(t)$ is a fixed surface temperature, (3.11) reduces to

$$\left(\tau \frac{d^2}{dt^2} + \frac{d}{dt}\right) \delta(t) = \frac{\lambda}{\delta(t)} \quad (3.12)$$

whose solution subject to (2.25) is approximated by (3.7).

Likewise, the quartic polynomial expression (3.8), $n = 4$, satisfies the first four conditions of (3.3). Again, the coefficient $b(t)$ is determined from (3.9) leading to the results

$$\frac{P_4(x, t) - A}{T_0(t) - A} = \left(1 + \frac{x}{\delta(t)} - \frac{\delta(t)Q(t)x}{6(T_0(t) - A)}\right) \left(1 - \frac{x}{\delta(t)}\right)^3 \quad (3.13)$$

and (3.11) with $\lambda = 20\alpha/3$, $\gamma = 1/36$. Hence the thermal penetration depth is approximated by (3.7) when $T_0(t)$ is independent of time.

It is worth pointing out that the above approximate analytic solutions of problem I reduce to the corresponding ones in the classical theory of heat conduction provided that the surface temperature remains unaffected with time. The same statement is also true for the exact analytic solution of problem I. Indeed, the exact solution of problem I for a constant surface temperature is formally given [10] by

$$\frac{T(x, t) - A}{T_0 - A} = U_+(bt - x) \left(e^{-x/2b\tau} + \frac{x}{2b\tau} \int_{x/b}^t \frac{I_1[(1/2\tau)\sqrt{\xi^2 - (x/b)^2}]}{\sqrt{\xi^2 - (x/b)^2}} e^{-\xi/2\tau} d\xi \right) \quad (3.14)$$

where b is defined as above and $I_n(z)$ is the modified Bessel function of the first kind and $U_+(z)$ is the causal unit-step function defined by

$$U_+(z) = \begin{cases} 1, & z > 0 \\ 0, & z \leq 0. \end{cases}$$

An interesting feature of the solution (3.14) is the inherent wave nature of the heat transfer process. In fact, the wave aspect is produced by the unit step function, $U_+(bt-x)$, and at any moment of time a thermal wake and an undisturbed region exists in the first quadrant (see Fig. 1). Essentially, the points of space lying at a distance farther than bt from the boundary surface have not felt the effect of the temperature change at the surface $x=0$. At the front of the progressing wave $x=bt$, however, the temperature suffers a discontinuity of magnitude

$$\frac{T(bt, t) - A}{T_0 - A} = e^{-t/2\tau},$$

which decays exponentially with time.

In general, the heat flux is a quantity of practical interest. For the purpose of this analysis, however, the interest centers on computing the heat flux at the boundary surface $x=0$ using the above temperature profiles.

The assumption (2.5) leads to the initial condition

$$q(x, 0) = 0, \quad x > 0. \quad (3.15)$$

Then the solution of the initial-value problem (2.10) and (3.15) is

$$q(x, t) = -\frac{K}{\tau} \int_0^t \exp(-(t-\xi)/\tau) T_x(x, \xi) d\xi. \quad (3.16)$$

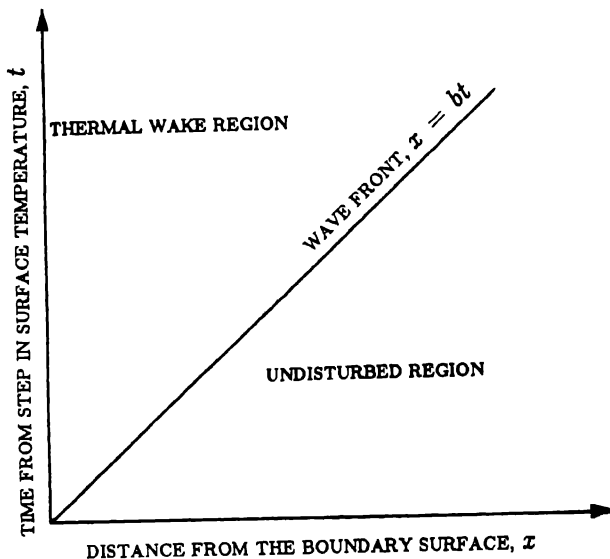


Fig. 1. Sketch of thermal wake and undisturbed regions.

From (3.14), it is easily verified that

$$\frac{T_x(0, t)}{T_0 - A} = -\frac{1}{2\sqrt{\alpha\tau}} e^{-y} [I_0(y) + I_1(y)]; \quad y = \frac{t}{2\tau} \quad (3.17)$$

so that (3.16) leads to

$$V(y) \equiv \frac{q(0, t)}{K(T_0 - A)/\sqrt{\alpha\tau}} = e^{-2y} [e^y I_0(y) - 1], \quad (3.18)$$

where $V(y)$ signifies the exact expression for the dimensionless surface heat flux as a function of the dimensionless time y .

For small values of τ the Bessel function $I_0(y)$ assumes its asymptotic behavior and (3.18) blends into the result predicted in the classical theory of the transient heat conduction by the error function

$$V(y) = \frac{1}{\sqrt{\pi}}. \quad (3.19)$$

As for the approximate solutions $P_j(x, t)$ of problem I, one may, without loss of generality, take a as $(\alpha/2\tau)^{1/2} = b/\sqrt{2}$ so that (3.7) reads

$$\tilde{\delta}_j(t, \tau) \approx \sqrt{\frac{\alpha\tau}{2}} [1 + \sqrt{8y\sigma_j} - e^{-2y}], \quad (3.20)$$

where $\sigma_j = j(j+1)$, $j = 2, 3, 4, \dots, n$. From (3.4), (3.16) and (3.20), it follows that

$$V_j(y) = j\Phi(y, \sigma_j); \quad (3.21)$$

$$\Phi(y, \sigma_j) \approx \sqrt{2} e^{-2y} \int_0^{2y} \frac{e^\beta}{1 + \sqrt{4\beta\sigma_j} - e^{-\beta}} d\beta. \quad (3.22)$$

Here $V_j(y)$ maintains the above definition of $V(y)$ but with $q(0, t)$ replaced by $q_j(0, t)$ for $j = 1, 2, \dots, n$. If (3.10) and (3.13) are utilized instead of (3.4), one respectively obtains

$$V_3(y) = \frac{3\sqrt{2}}{2} \Phi(y, 4), \quad (3.23)$$

$$V_4(y) = 2\Phi\left(y, \frac{20}{3}\right). \quad (3.24)$$

For purposes of graphical comparison, let the symbols QD , CB , QR , $CB1$, $QR1$ and the term *true* signify the dimensionless surface heat flux given respectively by (3.21) (for $j = 2, 3, 4$), (3.23), (3.24) and (3.18). An elementary calculus supported by our computational efforts shows that the dimensionless surface heat flux approximation generally increases with increasing the degree of the polynomial approximation. (See (3.21), (3.23) and (3.24)). The function $\Phi(y, \sigma)$ is integrated numerically using the Sinc method [16] (due to its superior accuracy over the traditional integration techniques), essentially, however, any numerical integration formula can be used, and hence the right sides of (3.21), (3.23) and (3.24) are readily evaluated. (See also Appendix A). A numerical comparison of these results with the exact expression (3.18) for the dimensionless surface heat flux indicates that the agreement is better for large values of the parameter $y = t/2\tau$. Figure 2 shows that the quadratic polynomial approximation (3.21) (with $j = 2$) leads to the best result.

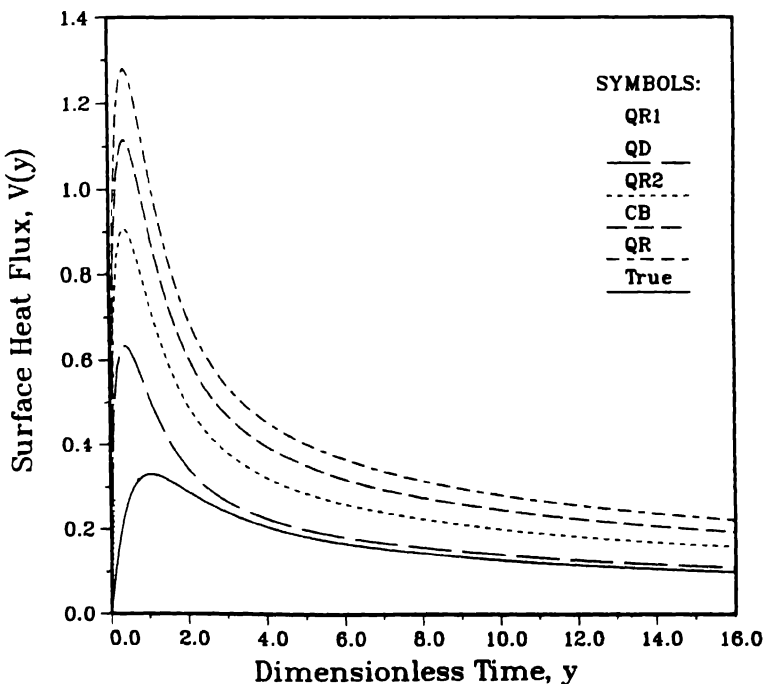


Fig. 2 Comparisons of the exact expression with energy-integral approximations for the surface heat flux as a function of time

4. Solution of problem II using the energy-integral method

This section is concerned with the treatment of problem II, which is identical to problem I except that the temperature boundary condition (2.4) is now replaced by

$$q(0, t) = q_0(t), \quad t > 0.$$

In other words, problem II consists of (2.1)–(2.3), (2.6), (2.7) (or its equivalence (2.12)) and

$$-KT_x(0, t) = \tau q'_0(t) + q_0(t) \equiv R(t), \quad t > 0. \quad (4.1)$$

In the present case, the energy-integral equation (3.4) takes the form

$$\left(\tau \frac{d^2}{dt^2} + \frac{d}{dt} \right) [\Theta(t) - A\delta(t)] = \frac{\alpha R(t)}{K}, \quad t > 0 \quad (4.2)$$

with $\Theta(t)$ defined by (2.26).

Equation (4.2) admits the integral representation

$$\int_0^{\delta(t)} T(x, t) dx - A\delta(t) = \frac{\alpha}{K} \int_0^t [1 - \exp(-(t-\xi)/\tau)] R(\xi) d\xi. \quad (4.3)$$

As mentioned in section 1, the solution of problem II utilizing the EIM is approximated over the region $[0, \delta(t)]$ by a suitable polynomial function, $P_n(x, t)$, of degree $n \geq 2$, while the temperature for $x > \delta(t)$ remains unaffected. Thus the solution of problem II may be represented by

$$T(x, t) = \begin{cases} P_n(x, t), & 0 \leq x \leq \delta(t), \quad t > 0; \\ A, & x > \delta(t), \quad t > 0. \end{cases} \quad (4.4)$$

Now we derive a number of polynomial expressions approximating the solution $T(x, t)$ over $[0, \delta(t)]$.

Assuming that $T(x, t)$ may be approximated by (3.2) and using (4.1) along with (3.3) for $j = 1, 2, \dots, n-1$ to determine the polynomial coefficients, one easily obtains

$$P_n(x, t) = A + \frac{\delta(t)R(t)}{nK} \left(1 - \frac{x}{\delta(t)} \right)^n. \quad (4.5)$$

In this case, (4.3) yields the following expression for the thermal penetration depth

$$\delta(t) = \sqrt{\lambda} \eta(t); \quad (4.6)$$

$$\eta(t) = \left(\frac{1}{R(t)} \int_0^t [1 - \exp(-(t-\xi)/\tau)] R(\xi) d\xi \right)^{1/2}, \quad \lambda = n(n+1)\alpha \quad (4.7)$$

which, for a constant value R of $R(t)$, reduces to

$$\delta(t) = \sqrt{\lambda} v(t); \quad v(t) = [t - \tau(1 - e^{-t/\tau})]^{1/2}. \quad (4.8)$$

The smoothest temperature profile (4.5) predicts the surface temperature approximation

$$P_n(0, t) - A = \frac{\delta(t)R(t)}{nK} \quad (4.9)$$

and moreover, $R(t) = R$ implies that

$$P_n(0, t) - A = \frac{R}{K} \sqrt{\frac{(n+1)\alpha}{n}} v(t) \quad (4.10)$$

with $v(t)$ defined as above.

In pursuance of the remark after (3.7) one may use instead of the smoothing condition

$$T_{xxx}(\delta(t), t) = 0 \quad (4.11)$$

the following surface boundary constraint

$$T_{xxx}(0, t) = \frac{-1}{\alpha K} [\tau R''(t) + R'(t)] \equiv H(t), \quad (4.12)$$

which results from combining (2.1) and (4.1), to determine the coefficients of the third-degree polynomial (3.2) for $n = 3$. However, (4.11) is advantageous since it involves a lower order derivative and overall results in a smoother approximating temperature profile.

Alternatively, using (4.1), the conditions corresponding to $j = 1, 2, 3$ of (3.3), and 4.12) to find the coefficients of the polynomial function

$$P_4(x, t) = A + \left[\frac{\delta(t)R(t)}{8K} \left(3 + \frac{x}{\delta(t)} \right) + \frac{H(t)\delta^3(t)}{16} \left(\frac{1}{3} + \frac{x}{\delta(t)} \right) \right] \left(1 - \frac{x}{\delta(t)} \right)^3. \quad (4.13)$$

The corresponding thermal penetration depth resulting from (4.3) and (4.13) satisfies the quartic equation

$$E(t)\delta^4(t) + \delta^2(t) = 10\alpha\eta(t); \quad E(t) = \frac{KH(t)}{12R(t)} \quad (4.14)$$

so that

$$\delta(t) = \left(\frac{-1 + \sqrt{1 + 40\alpha E(t)\eta(t)}}{2E(t)} \right)^{1/2}. \quad (4.15)$$

In the event that $R(t)$ is independent of time, (4.15) simplifies to

$$\delta(t) = \sqrt{10\alpha} v(t) \quad (4.16)$$

and $v(t)$ is defined as before.

The quartic temperature profile (4.13) predicts the surface temperature approximation

$$P_4(0, t) - A = \frac{3\delta(t)R(t)}{8K} + \frac{\delta^3(t)H(t)}{48} \quad (4.17)$$

which reduces to

$$P_4(0, t) - A = \frac{3R\sqrt{10\alpha}}{8K} v(t) \quad (4.18)$$

for a fixed value of $R(t)$.

On the other hand, the solution of (2.1)–(2.3) and (4.1) is known exactly [10] and the result for a constant value of R is

$$T(x, t) = A + U_+ (bt - x) \left(\frac{bR}{K} \int_{x/b}^t I_0[(1/2\tau)\sqrt{\xi^2 - (x/b)^2}] e^{-\xi/2\tau} d\xi \right) \quad (4.19)$$

where b and U_+ maintain the same definitions of section 3. Consequently, the surface temperature for problem II under the above assumption is given by

$$\begin{aligned} W(y) &\equiv \frac{T(0, t) - A}{R\sqrt{\alpha\tau}/K} = \frac{1}{\tau} \int_0^t I_0\left(\frac{\xi}{2\tau}\right) e^{-\xi/2\tau} d\xi \\ &= 2y e^{-y} [I_0(y) + I_1(y)]; \quad y = \frac{t}{2\tau}. \end{aligned} \quad (4.20)$$

Here $W(y)$ denotes the exact expression for the dimensionless surface temperature as a function of the dimensionless time y .

In terms of the dimensionless time y , the approximating polynomial prediction of the surface temperature in dimensionless form takes either the form

$$W_j(y) = \sqrt{\frac{j+1}{j}} \Psi(y), \quad j = 2, 3, 4, \dots, n \quad (4.21)$$

or

$$W_4(y) = \frac{3\sqrt{10}}{8} \Psi(y); \quad (4.22)$$

with

$$\Psi(y) = (2y - 1 + e^{-2y})^{1/2},$$

depending on whether the generating formula (4.10) or (4.18) is used. In this case $W_j(y)$ denotes the energy-integral approximations for the dimensionless surface temperature; which has the same definition as $W(y)$ but with $T(0, t)$ replaced by $P_j(0, t)$. Additionally, the symbols QD , CB , QR , $QR1$ and the term *true* will be used to signify the dimensionless surface temperature given respectively by (4.21), (4.22) and (4.20). The dimensionless surface temperature approximations in general decrease with increasing the degree of the polynomial approximations (see (4.21)). Note that the coefficients of Ψ in (4.21) decreases from 1.2247 to the limiting value 1. A numerical comparison of the energy-integral approximations (4.22) and (4.21) for $j = 2, 3, 4$ with the exact expression (4.20) for the dimensionless surface temperature indicates that increasing the degree of the polynomial does not necessarily increase the accuracy of the approximation. In fact, in terms of the four approximations considered, the cubic expression (4.21) for $j = 3$ yields the best result (see Fig. 3).

We again emphasize the fact that when τ is allowed to approach zero the results of this section reduce to the corresponding results in the classical theory of transient heat conduction. For instance, letting τ approach zero the Bessel function in (4.20) assumes its asymptotic behavior which results in

$$\frac{T(0, t) - A}{R\sqrt{\alpha t/K}} = \frac{2}{\sqrt{\pi}} \quad (4.23)$$

which is the known exact result [3].

Correspondingly, (4.21) and (4.22) reduce respectively to

$$\frac{P_j(0, t) - A}{R\sqrt{\alpha t/K}} = \sqrt{\frac{j+1}{j}} \quad (4.24)$$

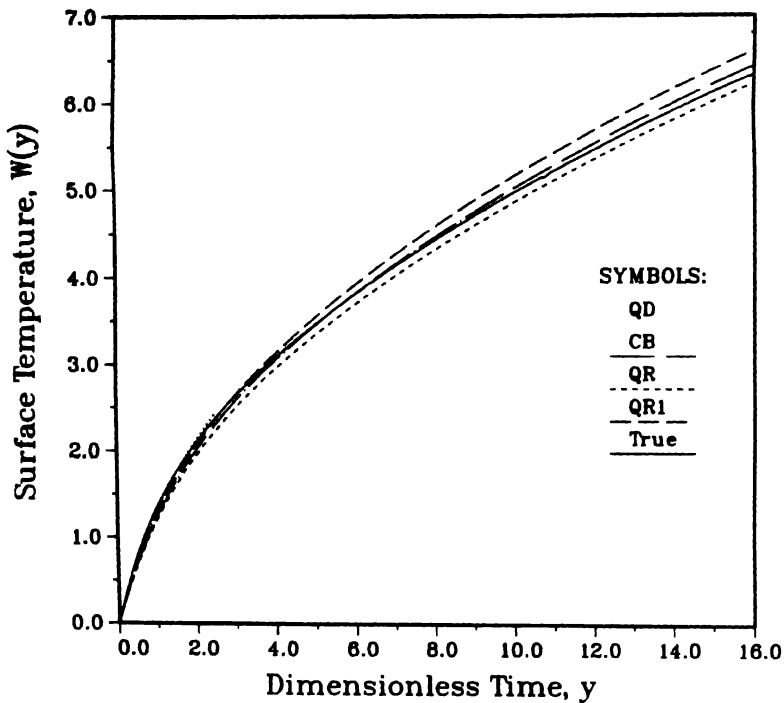


Fig. 3. Comparison of the exact expression with energy-integral approximations for the surface temperature as a function of time

and

$$\frac{P_4(0, t) - A}{R\sqrt{\alpha t/K}} = \frac{3\sqrt{10}}{8} \quad (4.25)$$

which agree with the classical heat conduction results utilizing the EIM.

5. Concluding remarks

REMARK 1. The EIM can be applied to derive the polynomial expressions for the temperature profiles approximating the solutions of problems I and II when the uniform initial condition (2.2) (or (4.1)) is replaced by

$$T(x, 0) = g(x), \quad x > 0. \quad (5.1)$$

For ease of reference, the new problems will be referred to as problem III or problem IV, respectively.

As for the definition of the thermal penetration depth, $x = \delta(t)$, one assumes that

$$\frac{\partial^j T(\delta(t), t)}{\partial x^j} = g^{(j)}(\delta(t)), \quad j = 0, 1, \dots, n-1 \quad (5.2)$$

and the solutions of either problem III or problem IV symbolically reads

$$T(x, t) = \begin{cases} P_n(x, t), & 0 \leq x \leq \delta(t) \\ g(x), & x > \delta(t) \end{cases} \quad (5.3)$$

where the n th degree approximating polynomial is conveniently represented by

$$P_n(x, t) = \sum_{j=0}^n a_j(t)(x - \delta(t)), \quad (n \geq 2). \quad (5.4)$$

Regarding the solution $T(x, t)$ of problem III over $[0, \delta(t)]$, the polynomial approximation $P_n(x, t)$ satisfying

$$P_n(0, t) = T_0(t), \quad \frac{\partial^j P(\delta(t), t)}{\partial x^j} = 0, \quad j = 0(1)n-1 \quad (5.5)$$

is given by

$$P_n(x, t) = \sum_{j=0}^{n-1} \frac{g^{(j)}(\delta)}{j!} (x - \delta)^j + \left[T_0(t) - \sum_{j=0}^{n-1} \frac{(-1)^{(j)} g^{(j)}(\delta)}{j!} \right] \left(1 - \frac{x}{\delta} \right)^n \quad (5.6)$$

where $\delta \equiv \delta(t)$.

By contrast, the cubic polynomial approximation $P_3(x, t)$ satisfying (3.9) and the first four conditions of (5.5) is

$$P_3(x, t) = g(\delta) + g'(\delta)(x - \delta) + \left([T_0(t) + \delta g'(\delta) - g(\delta)] \left(1 + \frac{x}{2\delta} \right) - \frac{\delta Q(t)x}{4} \right) \left(1 - \frac{x}{\delta} \right)^2 \quad (5.7)$$

while the quartic polynomial approximation satisfying (3.9) and the first four conditions of (5.5) is given by

$$P_4(x, t) = g(\delta) + g'(\delta)(x - \delta) + \left([T_0(t) + \delta g'(\delta) - g(\delta) - \frac{\delta^2 g''(\delta)}{2}] \left(1 + \frac{x}{\delta} \right) - \frac{x \delta (Q(t) - g''(\delta))}{6} \right) \left(1 - \frac{x}{\delta} \right)^3. \quad (5.8)$$

The n th degree polynomial $P_n(x, t)$ approximating the solution $T(x, t)$ of problem IV over $[0, \delta(t)]$ has the form

$$P_n(x, t) = \sum_{j=0}^{n-1} \frac{g^{(j)}(\delta)}{j!} (x-\delta)^j + \frac{\delta}{n} \left(\frac{R}{K} + \sum_{j=1}^{n-2} \frac{g^{(j)}(\delta)}{(j-1)!} \right) \left(1 - \frac{x}{\delta} \right)^n \quad (5.9)$$

which satisfies the conditions (4.1) and (5.5).

Finally, the quartic temperature profile $P_4(x, t)$ satisfying (4.1), (4.12), (5.5) for $j = 0, 1, 2$ is

$$P_4(x, t) = g(\delta) + g'(\delta)(x-\delta) + \frac{g''(\delta)}{2}(x-\delta)^2 + \left(\frac{\delta}{8} \left[\frac{R}{K} + g'(\delta) - \delta g''(\delta) \right] \right) \left(3 + \frac{x}{\delta} \right) + \frac{H\delta^3}{16} \left(\frac{1}{3} + \frac{x}{\delta} \right) \left(1 - \frac{x}{\delta} \right)^3. \quad (5.10)$$

Evidently, the restriction $g(x) \equiv \text{constant}$ reduces the above results to the corresponding results of sections 3 and 4.

The same statement holds true for the exact analytic solutions to problems III and IV. In fact, the solution of problem III is given [10] by

$$T(x, t) - g(x) = b^2 \int_0^t \int_0^\alpha G(x, z; \xi) g''(z) e^{-\xi/2\tau} dz d\xi + U_+(bt-x) \left\{ e^{-x/2b\tau} u_0 \left(t - \frac{x}{b} \right) + \frac{x}{2b\tau} \int_{x/b}^t \frac{I_1[(1/2\tau)\sqrt{\xi^2 - (x/b)^2}]}{\sqrt{\xi^2 - (x/b)^2}} e^{-\xi/2\tau} u_0(t-\xi) d\xi \right\} \quad (5.11)$$

where $u_0(t) = T_0(t) - g(0)$. In particular, if $g(x)$ is a fixed initial temperature and $T_0(t)$ is independent of time, (5.11) becomes identical with (3.14).

Similarly, the exact solution of problem IV [10] reads

$$T(x, t) - g(x) = b^2 \int_0^t \int_0^\alpha N(x, z; \xi) g''(z) e^{-\xi/2\tau} dz d\xi + U_+(bt-x) \left\{ \frac{b}{K} \int_{x/b}^t I_0[(1/2\tau)\sqrt{\xi^2 - (x/b)^2}] e^{-\xi/2\tau} (R(t-\xi) + Kg'(0)) d\xi \right\}. \quad (5.12)$$

Again, (5.12) specializes to (4.19) when $g(x)$ and $T_0(t)$ are uniformly fixed quantities.

REMARK 2. The EIM is also applicable to the solutions of the above problems when a heat source or sink, $f(x, t; \tau)$, exists within the medium. Our attention will focus on the event that $f(x, t; \tau)$ is expressible in the form $k_1 f_1(x; \tau) + k_2 f_2(t; \tau)$. For purposes of illustration, consider the following problem

$$\tau T_{tt} + T_t = \alpha T_{xx} + k_1 f_1(x; \tau) + k_2 f_2(t; \tau), \quad x > 0, t > 0, \quad (5.13)$$

$$T(x, 0) = A, \quad x > 0, \quad (5.14)$$

$$T_t(x, 0) = 0, \quad x > 0, \quad (5.15)$$

$$T(0, t) = T_0(t), \quad t > 0. \quad (5.16)$$

Introduce a new dependent variable $u(x, t)$ by

$$u(x, t) = T(x, t) + \frac{k_1}{\alpha} \int_0^x (x - \xi) f_1(\xi; \tau) d\xi - k_2 \int_0^t [1 - e^{-(t-\eta)/\tau}] f_2(\eta; \tau) d\eta. \quad (5.17)$$

Then problem (5.13)–(5.16) becomes

$$tu_{tt} + u_t = \alpha u_{xx}, \quad x > 0, t > 0, \quad (5.18)$$

$$u(x, 0) = A + \frac{k_1}{\alpha} \int_0^x (x - \xi) f_1(\xi; \tau) d\xi, \quad x > 0, \quad (5.19)$$

$$u_t(x, 0) = 0, \quad x > 0, \quad (5.20)$$

$$u(0, t) = T_0(t) - k_2 \int_0^t [1 - e^{-(t-\eta)/\tau}] f_2(\eta) d\eta \equiv u_0(t), \quad t > 0 \quad (5.21)$$

which has the same form as problem III. Hence the analysis of problem III is applied to (5.18)–(5.21) whose solution enables one to recover the solutions of (5.13)–(5.16) according to (5.17).

On the other hand, upon replacing (5.16) by (4.1) and utilizing (5.17), one obtains a problem of the same form as problem IV. Again the argument pertinent to problem IV can be duplicated here to deduce the solution of the latter problem. Such a solution yields at once the solution of the corresponding problem (5.13)–(5.15) and (4.1) under the transformation (5.17). Now, since the treatments of problems I, II, III, and IV are sufficiently familiar from sections 3, 4, and 5, it will not be repeated here.

In closing, one notices that the results pertinent to problem (5.13)–(5.16) reduce to problem I when the source (or sink) term vanishes identically. Also, when τ is allowed to approach zero, the results of problem I reduce to the corresponding results in the classical theory of parabolic heat conduction. Similar statements can be made about the other problems mentioned above.

6. Conclusions

The problem of finding analytic solutions to several linear hyperbolic problems for a semi-infinite medium using the EIM has been addressed. The solutions are approximated by polynomial expressions in the spatial variables with time-dependent coefficients, essentially any simple function may be used. The data specifications of the considered problems range over a variety of initial and boundary conditions. Also discussed is the case when the medium contains a source (or sink) that may be uniform or depend on the spatial and temporal variables as well as the relaxation parameter. Comparison of the approximate analytic solutions obtained by the EIM with the corresponding available or obtainable exact analytic solutions are made; and the accuracy is generally acceptable. It is the knowledge of the author that the applicability of the EIM to hyperbolic problems is not well known in the literature and hence the method will be of interest to engineering and applied science readers.

Appendix A

Consider the integral

$$\begin{aligned} I(a, b) &= \int_a^b f(t) dt \\ &= (b-a) \int_0^1 f[(1-\lambda)a + \lambda b] d\lambda. \end{aligned}$$

According to the sinc method [15], $I(a, b)$ may be approximated as

$$I(a, b) \approx (b-a)h \sum_{k=-N}^N z_k(1-z_k)f[(1-z_k)a + z_kb] \quad (*)$$

where N and k are integers, and

$$z_k = \frac{e^{kh}}{1 + e^{kh}}, \quad h = \left(\frac{2\pi d}{\alpha N} \right)^{1/2}.$$

For problem I, $d = \pi/2$, $\alpha = 1/2$ so that $h = \pi\sqrt{2/N}$. Substituting $a=0$ and $b=2y$ in (*) implies that

$$I(0, 2y) = 2\pi y \sqrt{\frac{2}{N}} \sum_{k=-N}^N C_k f(2yz_k)$$

and hence

$$\Phi(y, \sigma_j) = A(y) \sum_{k=-N}^N C_k f(2yz_k)$$

with

$$A(y) = \frac{4\pi}{\sqrt{N}} y e^{-2y} \quad \text{and} \quad C_k = z_k(1 - z_k).$$

It is noteworthy that the error of quadrature (*) for bounded f is $K e^{N-1/2}$ where K is a constant depending only on f, α, d .

References

1. Bengtson, H.H. and Kreith, F., Approximate solution of heat problems in systems with nonuniform initial temperature distribution. *J. Heat Transfer* 92 (1970) 182–184.
2. Beckurtz, K. and Wirtz, K., *Neutron Physics*. New York: Springer-Verlag (1964).
3. Carslaw, H.S. and Jaeger, J.C., *Conduction of Heat in Solids*, 2nd edn. London: Oxford University Press (1959).
4. Castello, F.A., An evaluation of several methods of approximating solutions to the heat conduction equation. *ASME* paper No. 63-HT-44 (1963).
5. Frankel, J.I., Vick, B. and Özisik, M.N., General formulation and analysis of hyperbolic heat conduction in composite media. *Int. J. Heat Mass Transfer* 30 (1987) 1293–1305.
6. Goodman, T.R., The heat-balance integral and its application to problems involving a change of phase. *ASME* 80 (1958) 335–342.
7. Goodman, T.R., The heat-balance integral: further considerations and refinement. *J. Heat Transfer* 83c (1961) 83–86.
8. Landahl, H.D., An approximation method for the solution of diffusion and related problems. *Bull. Math. Biophys.* 15 (1953) 49–61.
9. Lardner, T.J. and Pohle, F.B., Application of the heat balance integral to problems of cylindrical geometry. *J. Appl. Mech.* 83 (1961) 310–312.
10. Mohamed, F.A., Identification of certain physical parameters in hyperbolic boundary value problems from overspecified boundary data. *Int. J. Engng. Sci.* 26 (1988) 851–864.
11. Mohamed, F.A., The energy-integral method: application to hyperbolic one-phase Stefan problems. *Int. J. Heat Mass Transfer* 33 (1990) 409–416.
12. Reynolds, W.C. and Dolton, T.A., The use of integral methods in transient heat transfer analysis. *Department of Mechanical Engineering Report No. 36*, Stanford University, Stanford, California, Sept. 1 (1958).
13. Schlichting, H., *Boundary Layer Theory*, 6th edn. New York: McGraw-Hill Book Co., Inc. (1968) Chapter 13.
14. Schneider, P.J., Radiation cooling of finite heat-conducting solids. *J. Aerospace Sci.* 27 (1960) 546–549.
15. Smith, D.R., *Singular Perturbation Theory: An Introduction with Applications*. New York: Cambridge University Press (1985).
16. Stinger, F., Numerical methods based on Whittaker cardinal, or sinc functions. *SIAM Rev.* 23 (1981) 165–224.
17. Thorson, R. and Landis, F., Integral methods in transient heat conduction problems with non-uniform initial conditions. *Int. J. Heat Mass Transfer* 8 (1965) 189–192.

18. Weymann, H.D., Finite speed of propagation in heat conduction, diffusion, and viscous shear motion *Amer. J. Phys* 36 (1967) 488–496.
19. Yang, K.T., Transient heat conduction in a semi-infinite solid with variable thermal conductivity. *Trans. ASME* 80 (1958) 146–147.
20. Yang, K.T., Calculation of unsteady heat conduction in single layer and composite finite slab and without property variations by an improved integral procedure. *International Development in Heat Transfer ASME*, New York (1963) 18–27.

Numerical analysis of flow pattern of impinging liquid sprays in a cold model for cooling a hot flat plate

N. HATTA, H. FUJIMOTO & H. TAKUDA

Department of Mineral Science and Technology, Faculty of Engineering, Kyoto University, Kyoto 606, Japan

Received 7 November 1990; accepted in revised form 20 November 1991

Abstract. This paper treats the numerical analysis of two-phase mist jet flow, which is commonly adopted to cool the solidified shell in the secondary cooling zone of the continuous casting process. Flow structures of the two-phase subsonic jet impinging on a flat plate normal to flow, corresponding to the present cooling situation, are solved on the assumption that particles are perfectly elastically reflected from a surface. Again, the numerical experiments concerning mist flows composed of air and water-droplets are made in a cold model. The flow fields for both gas and particle phases strongly depend upon the particle size. When water-droplets mixing in the mist are very small, the impinging particles travel very closely to the surface. With increasing particle size, particles are reflected from the surface in a far distance. Therefore, also, the case is analysed where a low velocity annular gas-only flow surrounding a round nozzle co-axially is present so that such idle particles may be pushed back to the surface again. This is considered to result in an improvement of the mist cooling efficiency.

1. Introduction

There are many industrial situations in which a fine liquid spray contacts and cools a surface which is at a temperature in excess of the liquid saturation temperature. This process is commonly called the spray or mist cooling. In iron- and steel-making industries, the mist cooling method is an established technique and applied to the secondary cooling in the continuous casting system so that a comparatively precise cooling may be achieved to optimize the withdrawal velocity of cast slabs and the position of the crater end.

The purpose of the research reported herein is not to identify the fundamental heat transfer processes involved in spray cooling, but to analyze flow structures of the two-phase air-water droplet mixture jet impinging on a flat plate normal to flow.

The equations governing the steady quasi-one-dimensional nozzle flow of a gas containing suspended condensed phase, derived by Zucrow and Hoffman [1], have been extended to the case where a continuous distribution of particle size is present [2]. Then, the system of equations has been applied to the expanding flow of gas-particle mixtures not only in a subsonic nozzle but also in a De Laval nozzle [3–5].

Thereafter, the numerical analysis of gas-particle mixture flows in a free jet region has been made in such a situation that a two-phase mixture are exhausted from a subsonic nozzle into a quiescent gas [6]. The numerical result exhibits that smaller particles tend to follow the gas flow pattern, while the fluctuation of the particle motion becomes smaller for larger particles. The final purpose for a set of such

investigations is to find the theoretical heat transfer mechanism of the so-called mist cooling. Hence, the problems of impinging jet on a solid wall must be settled first. A theoretical analysis or experimental measurement approach to explaining this phenomenon may be difficult. The following are the probable reasons for not suggesting either of the two approaches mentioned above. First, the gas-phase and the particle-phase must be treated as different media. That is, the former is regarded as a continuum medium, and the latter is regarded partly as a discrete one. Second, the numerical procedure of impinging particles on the surface is very difficult. For the secondary cooling of cast slabs, the impinging droplets are deflected from the surface by a thin vapor film which is formed on impact. This is commonly referred to as the Leidenfrost state. In short, the non-wetting phenomenon occurs and the direct contact between droplet and hot wall is not observed. In fact, it is possible that in a hot model large droplets with a high velocity break up into small ones on impact and are deflected from the surface. On the other hand, it is anticipated that small particles can evaporate before reaching the hot surface.

Therefore, for simplicity, the numerical calculations of mist flows consisting of air and water-droplets are made on the assumption that particle reflection from the surface is perfectly elastic. Again, the present numerical model is a cold one. The numerical results so obtained exhibit that for larger particles they are dispersed in the flow field owing to the elastic reflection from the surface. The greater part of such particles becomes slow in motion, or simply stays because there is negligible gas velocity in the almost stagnant ambient region outside the mixing core flow. Contributions of these water-droplets to the intensity of the mist cooling may be reduced to a certain degree.

Subsequently, the usage of a low-velocity annular gas-only flow which surrounds a round nozzle co-axially is considered. By so doing, it may be possible to push back particles dispersed spatially from the core flow by the impingement on the surface, to the surface again. We wish to check the effect of the coaxial annular gas flow on the flow field of the particle phase. The present calculations are performed with a single particle size. The two-phase mixture is assumed to be composed of air and water-droplets.

The calculations have been performed on Fujitsu VP-2600 super computer at the Data Processing Center of Kyoto University. We note that the VP-rate of our computer program is approximately unity on the basis of the VP-analyzer.

2. Governing equations

The flow model for air-droplet mixture is constructed under the following assumptions. (i) No phase change takes place, because the calculation is made in a cold model. (ii) The volume occupied by the particles is negligible. (iii) The particle-particle collision is neglected, that is, the particles do not interact with each other. (iv) Particles are spherical in shape with a uniform diameter and a constant material density.

(v) The gas, as well as the particles, has a constant specific heat. (vi) As mentioned in the previous section, the particle reflection is elastic. (vii) Gravitational effects are not considered.

Here we consider the validity of the items (ii) and (iii). It is commonly accepted that the material density ρ_{mp} of liquid particle is larger by a magnitude of order of 10^3 than that of a gas ρ . We define the ratio, v , of the mass of the particle phase to that of the gas phase as $v = \varepsilon_p \rho_{mp} / (1 - \varepsilon_p) \rho \approx \varepsilon_p \rho_{mp} / \rho$, where ε_p denotes the volume fraction occupied by the particle phase per unit volume. Thus, we have $\varepsilon_p = v \rho / \rho_{mp}$. When a particle is injected into a uniform space involving the particle cloud of the mean particle spacing s_p , the particle mean free path λ_p is expressed by the order of $s_p / \varepsilon_p^{2/3}$. Thus, $\lambda_p / L \approx (s_p / L) / \varepsilon_p^{2/3}$, where L denotes a characteristic length of the flow field. Therefore, if $s_p / L = O(\varepsilon_p^{2/3})$, then $\lambda_p / L = O(1)$. In this case, the gas-particle mixture may be regarded as dilute, and the direct collisions between particles can be neglected. In the present simulation, the order of v is unity and therefore $\varepsilon_p \approx O(10^{-3})$. That is to say, if $v \approx O(1)$, $s_p / L \approx O(10^{-2})$ may be considered to be a sufficient condition for particles not to collide each other.

In our calculation, the dimensionless variables and parameters are introduced, and the governing equations to be solved will be expressed by dimensionless quantities. It is physically important to rewrite the dimensional equations into dimensionless ones and to solve them in such a way as to realize the similarity of the flow pattern as well as the general validity. The main dimensionless variables introduced into the system of governing equations are defined as

$$\left. \begin{aligned} t^* &= \frac{t}{L/c_r}, \quad x^* = \frac{x}{L}, \quad y^* = \frac{y}{L}, \quad u^* = \frac{u}{c_r}, \quad v^* = \frac{v}{c_r}, \\ p^* &= \frac{p}{p_r}, \quad \rho^* = \frac{\rho}{\rho_r}, \quad T^* = \frac{T}{T_r}, \quad c^* = \frac{c}{c_r}, \\ x_p^* &= \frac{x_p}{L}, \quad y_p^* = \frac{y_p}{L}, \quad u_p^* = \frac{u_p}{c_r}, \quad v_p^* = \frac{v_p}{c_r}, \quad T_p^* = \frac{T_p}{T_r} \end{aligned} \right\} \quad (1)$$

where t , x and y are the time, axial distance and radial distance, respectively. u , v , p , ρ , T and c are the axial velocity, radial velocity, pressure, density, temperature and speed of sound of the gas, respectively. The subscripts p and r denote particles and reference conditions, and the superscript $*$ denote the dimensionless quantities. L is the characteristic length of the flow system.

In addition to Eq. (1), for later convenience, we define the following non-dimensional parameters:

$$f_p = \frac{C_D}{C_{D, \text{Stokes}}}, \quad g_p = \frac{\text{Nu}}{\text{Nu}_{\text{Stokes}}}, \quad (2)$$

$$\Gamma_\tau = \frac{\tau_A}{\tau_F}, \quad \theta = \frac{C_{pp}}{C_{pg}}, \quad \gamma = \frac{C_{pg}}{C_{vg}}, \quad (3)$$

in which C_D and Nu represent the drag coefficient and the Nusselt number, respectively. The subscript, Stokes, denotes the Stokes flow regime (i.e., $Re < 1$, Re : the particle Reynolds number). C_{pg} and C_{vg} are the specific heat of the gas phase at a constant pressure and volume, respectively. C_{pp} denotes the specific heat of the particle material. τ_A is called the aerodynamic response time of a particle, assuming the Stokes drag law, and τ_F the characteristic time of the flow system. These are defined by

$$\tau_A = \frac{\rho_{mp}(2r_p)^2}{18\mu}, \quad \tau_F = \frac{L}{c_r}, \quad (4)$$

in which r_p is the particle radius. The gas viscosity μ is given by

$$\mu = \mu_r \left(\frac{T}{T_r} \right)^\delta = \mu_r T^{*\delta}, \quad (5)$$

where δ is an appropriate constant. Again, we introduce the following non-dimensional properties;

$$\mu^* = \frac{\mu}{\mu_r}, \quad \lambda^* = \frac{\lambda}{\lambda_r}, \quad (6)$$

in which λ is the thermal conductivity of the gas.

Here, it is noted that the particle drag coefficient C_D and the Nusselt number Nu used in the present study are those given by Henderson [7] and Carlson & Hoglund [8], respectively.

2.1. Particle phase

In the present model, the whole particle cloud is divided into a large number of small subclouds. It is assumed that all the particles belonging to each subcloud have the same velocity and temperature. The particle flow field is solved by selecting an appropriate and representative particle in each subcloud and by following the properties of the particle along the particle trajectory.

By labelling the particle subclouds by subscripts k ($k = 1, 2, 3, \dots$) and denoting the velocity components and temperature of a particle located at $(x_{pk}^*(t^*), y_{pk}^*(t^*))$ by $(u_{pk}^*(t^*), v_{pk}^*(t^*))$ and $T_{pk}^*(t^*)$, respectively, the momentum and energy equations of the k -th particle subcloud are expressed by

$$\frac{dE_{pk}^*}{dt} - I_{pk}^* = 0, \quad (7)$$

in which

$$E_p^* = \begin{bmatrix} x_p^* \\ y_p^* \\ u_p^* \\ v_p^* \\ T_p^* \end{bmatrix} \quad \text{and} \quad I_p^* = \begin{bmatrix} u_p^* \\ v_p^* \\ A_p^*(u^* - u_p^*) \\ A_p^*(v^* - v_p^*) \\ B_p^*(T^* - T_p^*) \end{bmatrix} \quad (8)$$

The parameters A_p^* and B_p^* appearing in the system of the foregoing particle equations are defined by

$$A_p^* = \frac{f_p}{\Gamma_r}, \quad B_p^* = \frac{2g_p}{3\Gamma_r \text{Pr} \theta}. \quad (9)$$

Here, one of the most important tasks is how to evaluate the particle number contained in the k -th subcloud. Since the flow is considered in the axisymmetric coordinate system, the particle cloud in the physical space forms a ring cloud. Denoting the number of particles contained in the k -th cloud per unit depth by N_{pk}^* ($= N_{pk}/n_{pr}/L^2$), where n_p is the number density of particles, the number of particles contained in the k -th subcloud may be given by $2\pi y_{pk} N_{pk}^*$ ($= 2\pi(L)y_{pk}^*(n_{pr}L^2N_{pk}^*)$). Thus, we have

$$2\pi y_{pk}^* N_{pk}^* = 2\pi y_{pk}^{*\dagger} N_{pk}^{*\dagger} \quad \text{or} \quad N_{pk}^* = (y_{pk}^{*\dagger}/y_{pk}^*) N_{pk}^{*\dagger}, \quad (10)$$

where the cross denotes the conditions of particles in the k -th subcloud at the nozzle exit.

2.2. Gas phase

The Stokes hypothesis is introduced into the equations governing the gas-phase flow in order to reduce the number of properties which characterize the field of stresses in a flowing compressible fluid from two to one. On this premise the system of the axisymmetric Navier-Stokes equations for the gas-phase interacting with the particle-phase can be written in conservation form as

$$\frac{\partial Q^*}{\partial t^*} + \frac{\partial F_1^*}{\partial x^*} + \frac{\partial F_2^*}{\partial y^*} + \frac{\partial G_1^*}{\partial x^*} + \frac{\partial G_2^*}{\partial y^*} + \frac{1}{y^*} H^* + H_p^* = 0, \quad (11)$$

where

$$\begin{aligned}
 Q^* &= \begin{bmatrix} e^* \\ \rho^* \\ \rho^* u^* \\ \rho^* v^* \end{bmatrix}, \quad F_1^* = \begin{bmatrix} u^*(e^* + p^*/\gamma) \\ \rho^* u^* \\ \rho^* u^{*2} + p^*/\gamma \\ \rho^* u^* v^* \end{bmatrix}, \quad F_2^* = \begin{bmatrix} v^*(e^* + p^*/\gamma) \\ \rho^* v^* \\ \rho^* u^* v^* \\ \rho^* v^{*2} + p^*/\gamma \end{bmatrix}, \\
 G_1^* &= \frac{1}{\text{Re}_r} \begin{bmatrix} u^* f_x^* - v^* \tau^* - \{1/(\gamma - 1)/\text{Pr}\} \lambda^* \partial T^*/\partial x^* \\ 0 \\ f_x^* \\ -\tau^* \end{bmatrix}, \\
 G_2^* &= \frac{1}{\text{Re}_r} \begin{bmatrix} v^* f_y^* - u^* \tau^* - \{1/(\gamma - 1)/\text{Pr}\} \lambda^* \partial T^*/\partial y^* \\ 0 \\ -\tau^* \\ f_y^* \end{bmatrix}, \\
 H^* &= \begin{bmatrix} v^*(e^* + p^*/\gamma) + [v^* f_y^* - u^* \tau^* - \{1/(\gamma - 1)/\text{Pr}\} \lambda^* \partial T^*/\partial y^*]/\text{Re}_r \\ \rho^* v^* \\ \rho^* u^* v^* - \tau^*/\text{Re}_r \\ \rho^* v^{*2} - \alpha^*/\text{Re}_r \end{bmatrix}, \\
 H_p^* &= \begin{bmatrix} 0 \\ F_{px}^* \\ F_{py}^* \\ \dot{Q}_p^* + \dot{W}_p^* \end{bmatrix}, \tag{12}
 \end{aligned}$$

with

$$\left. \begin{aligned}
 f_x^* &= \frac{2}{3} \mu^* \left(\frac{\partial v^*}{\partial y^*} + \frac{v^*}{y^*} - 2 \frac{\partial u^*}{\partial x^*} \right), \\
 f_y^* &= \frac{2}{3} \mu^* \left(\frac{\partial u^*}{\partial x^*} + \frac{v^*}{y^*} - 2 \frac{\partial v^*}{\partial y^*} \right), \\
 \tau^* &= \mu^* \left(\frac{\partial v^*}{\partial x^*} + \frac{\partial u^*}{\partial y^*} \right), \\
 \alpha^* &= 2 \mu^* \left(\frac{\partial v^*}{\partial y^*} - \frac{v^*}{y^*} \right), \\
 \text{Pr} &= \frac{c_p \mu_r}{\lambda_r}, \\
 \text{Re}_r &= \frac{L c_r \rho_r}{\mu_r}.
 \end{aligned} \right\} \tag{13}$$

Furthermore, F_{px}^* , F_{py}^* , \dot{Q}_p^* and \dot{W}_p^* are expressed by

$$\left. \begin{aligned} F_{px}^* &= \frac{v_E^*}{S_p^*} \sum N_{pk}^* A_{pk}^* (u^* - u_{pk}^*), \\ F_{py}^* &= \frac{v_E^*}{S_p^*} \sum N_{pk}^* A_{pk}^* (v^* - v_{pk}^*), \\ \dot{Q}_p^* &= \frac{v_E^*}{S_p^*} \sum N_{pk}^* B_{pk}^* (T^* - T_{pk}^*), \\ \dot{W}_p^* &= F_{px}^* u^* + F_{py}^* v^* - \frac{v_E^*}{S_p^*} \sum N_{pk}^* A_{pk}^* \{ (u^* - u_{pk}^*)^2 + (v^* - v_{pk}^*)^2 \}, \end{aligned} \right\} \quad (14)$$

in which

$$S_p^* = \frac{S_p}{L^2}, \quad N_p^* = \frac{N_p}{n_{pE} L^2}, \quad v_E^* = \frac{n_{pE} m_p}{\rho_E}. \quad (15)$$

Here the subscript E denotes the nozzle exit condition. m_p is the particle mass of r_p in radius $(= (4\pi/3)\rho_{mp}r_p^3)$. Again, the summation including in Eq. (14) is taken over the clouds whose centroids (x_{pk}^*, y_{pk}^*) are in the computational cell with the sectional area $S_p^* (= \Delta x^* \Delta y^*)$.

The system of the gas-phase equations is supplemented by

$$\left. \begin{aligned} e^* &= \frac{p^*}{\gamma(\gamma - 1)} + \frac{1}{2} \rho^* (u^{*2} + v^{*2}) \\ p^* &= \rho^* T^* \\ c^* &= \sqrt{T^*} \end{aligned} \right\} \quad (16)$$

3. Computational conditions

The nozzle exit condition can be numerically determined by solving the system of equations governing two-phase mixture nozzle flows which is described in Ref. [2]. The sectional area A^* of the nozzle is assumed to consist of the two regions from the reservoir to the nozzle exit as

$$\text{in the first region of } x^* < -5, \quad A^* = (x^* + 5)^2 + 1$$

$$\text{in the second region of } -5 \leq x^* \leq 0, \quad A^* = 1.$$

It should be kept in mind that the nozzle exit ($x^* = 0$) corresponds to the origin of the

jet axis. Again, the nozzle radius is taken to be $D/2 = 5 \times 10^{-3} [\text{m}]$ in the second region, and the area is made dimensionless by dividing A by the sectional area in the second region. The reservoir and ambient gas conditions are assumed to be as follows:

the reservoir conditions: $p_0 = 1.8 \times 10^5 [\text{Pa}]$

$$T_0 = 323 [\text{K}]$$

$$v_0 = 0.3$$

the ambient gas conditions: $P_\infty = 1.0 \times 10^5 [\text{Pa}]$

$$T_\infty = 300 [\text{K}],$$

where the subscripts 0 and ∞ denote the reservoir and the ambient gas conditions, respectively. It is noted that the reservoir condition is adopted as the reference condition by which the physical variables are non-dimensionalized. Also, in the present numerical experiment, it is assumed that water-particles contained in the mist have a single size. Three cases are treated where $r_p = 1.0 [\mu\text{m}]$, $5.0 [\mu\text{m}]$ and $10 [\mu\text{m}]$, respectively. Eventually, we have obtained the numerical flow properties at the nozzle exit as follows: $V_E^* = 0.779$, $V_{pE}^* = 0.764$, $T_E^* = 0.924$, $T_{pE}^* = 0.936$ and $p_E^* = 0.556$ for the mixture of $r_p = 1.0 [\mu\text{m}]$, $V_E^* = 0.779$, $V_{pE}^* = 0.627$, $T_E^* = 0.888$, $T_{pE}^* = 0.973$ and $p_E^* = 0.556$ for $r_p = 5.0 [\mu\text{m}]$, and $V_E^* = 0.790$, $V_{pE}^* = 0.519$, $T_E^* = 0.879$, $T_{pE}^* = 0.984$ and $p_E^* = 0.556$ for $r_p = 10 [\mu\text{m}]$, respectively. These numerical results provide the jet boundary condition at the origin of the two-phase jet impinging on a surface.

The gas-phase equations are solved by using the TVD (Total Variation Diminishing) scheme developed by Chakravarthy and Osher [9], and the particle-phase is solved by applying a discrete particle-cloud model. In the scheme, the computational domain is divided into a number of small cells and the physical variables are defined at the cell center. That is, the computational domain is divided into 120×200 cells (or meshes) in the x - and y -directions, respectively. Here, we wish to add that the physical variables at interface between two neighbouring cells is calculated by the Roe approach [10].

Figure 1 indicates the geometry of computational domain of the case where the coaxial annular gas-only flow is present. The annular pipe is assumed to consist of coaxial inner and outer circular tubes. The thickness of the inner tube is neglected and therefore $\pi(D_A^2 - D^2)/4$ corresponds to the annular gas-only flow region, where D_A is the inner diameter of the outer pipe. Again, the gas-phase is assumed to be discharged from the annular region at $x = 0$ ($x^* = 0$) with a uniform velocity u_A ($v_A = 0$). The pressure and temperature of the gas-phase discharged from the annular region are equal to p_∞ and T_∞ of the ambient gas, respectively. The computation of $D = D_A$, of course, corresponds to the case where the coaxial annular gas flow is absent.

The characteristic length of the flow field is taken to be equal to $D/2$ ($\equiv L$).

We wish to mention the effect of selecting the cell size Δx^* , Δy^* as well as the computational time interval Δt^* on the numerical accuracy. First, we consider the

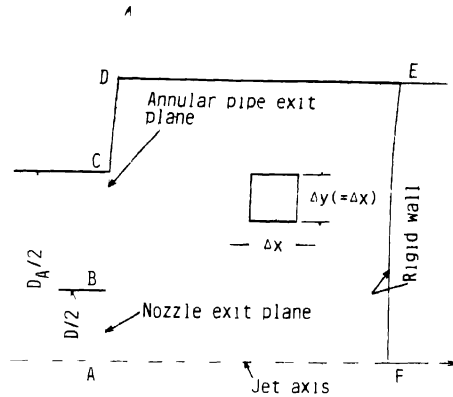


Fig 1 Geometry of computational domain

problem of the cell size. Δx^* has been determined (Δy^* is taken to be equal to Δx^*) by dividing the nozzle radius in n equal parts. For $n = 5, 10, 15, 20$ and 30 the numerical results, for example, the values of the pressure distribution along the x -axis have been compared with each other at a certain same time. It has been confirmed that the numerical results for the case where n is selected at 20 and 30 are almost unvaried, although the accuracy is improved, as n is increased. Then, $\Delta x^* (= \Delta y^*) = 0.05$, corresponding to $n = 20$, is selected in the present numerical simulation.

Next, the time interval Δt^* is determined by the CFL (Courant-Friedriches-Lewy) condition for the gas-phase flow [11]. The numerical results obtained by using various CFL numbers have been compared with each other at a certain same time, and then it has been confirmed that almost the same numerical results are obtained on the condition that the CFL number, $f \leq 0.25$. Throughout the present numerical experiments, the CFL number is selected at $f = 0.25$. Also, we wish to stress that the time interval, Δt^* , determined by this CFL number is always much smaller than the particle relaxation times $\tau_{pv}^* (= 1/A_p^*)$ and $\tau_{pT}^* (= 1/B_p^*)$ for the present flow conditions. Therefore, this Δt^* is also used in the particle-phase solution.

The numerical boundary conditions of the computational domain are employed in the following mode. The jet condition is applied on the line AB (see Fig. 1). The gas inflow condition is imposed to the line BC corresponding to $(D_A - D)/2$ of the annulation. The ambient gas condition is imposed to the upstream boundary CD and the side boundary DE . It is self-evident that for the case where the coaxial annular gas flow is absent, the boundary condition imposed to the line BC is the same as that of CD . The no-slip condition is applicable to the downstream boundary EF corresponding to the flat plate surface where $u = v = 0$. The symmetry condition is applied to the jet axis, AF . For detailed physical interpretation of each condition, refer to Matsuda et al. [12].

In addition, the initial ambient gas condition is that $p = 0.556$, $T = 0.929$ and $u = v = 0$ over the whole computational domain. The two-phase jet and the cocurrent

annular gas-only flow begin to blow at $t = 0$ from the round nozzle and the annular pipe, respectively.

The present calculations are performed by an explicit time-dependent difference scheme. Therefore, in order to obtain the time-converged two-phase flow structure we must require the numerical results at a sufficiently large number of time steps. In the present calculation, the gas-only flow field is solved for the first 20000 time steps, and then the flow field of the two-phase mixture is computed for the next 15000 time steps (from the 20001 to the 35000 time step) so that the time-converged solutions may be obtained as in short computational time as possible.

Physical constants of the gas and particles adopted here are listed in Table 1. Again, the thermal conductivity, λ , is formulated as

$$\lambda = \lambda_r + 7.5 \times 10^{-5} (T - T_r). \quad (17)$$

4. Numerical results

In various industrial fields, it is often crucially important to know the particle trajectories in a carrier gas. In this section, the behaviour of particles in the gas flow is investigated in detail. In the jet flows impinging on a flat plate, the particles are injected with an initial velocity determined by the particle size at fixed points on the nozzle exit plane at each time step after the final step in the one-phase solutions.

Figure 2 shows the one-phase solution at $N = 20000$ ($t^* \sim 135$, N ; time step) for the case where $D_A = 2D$ and $u_A = 0.5 u_E$, where u_E denotes the gas velocity at the exit of the inner nozzle. The viscous forces in the equations of gas motion are taken into consideration according to one of the reviewers of this paper. He has pointed out that the friction forces in free jets lead to the turbulent exchange with stagnant gas of the ambient region and herewith to the gas entrainment.

Now we consider the impinging two-phase mixture jet flow for the case where the coaxial annular gas-only flow is absent.

Figure 3 gives the velocity vector fields for the gas-phase and the particle-phase of $r_p = 1.0 [\mu\text{m}]$ at $t^* \sim 100$. The particles are exhausted from the nozzle exit plane at $y_{pk}^* = (k - 0.5)/20$ ($k = 1 \sim 20$) at every time interval Δt^* . Also, it is noted that only

Table 1 Physical constants of gas and particles.

Gas (Air)	Particle (Water droplet)
$\gamma = 1.4$	$C_{pp} = 4187 [\text{J/kg} \cdot \text{K}]$
$C_{pg} = 1009 [\text{J/kg} \cdot \text{K}]$	$\rho_{mp} = 1000 [\text{kg/m}^3]$
$\mu_r = 2.0 \times 10^{-5} [\text{Pa} \cdot \text{s}]$	
$\delta = 0.76$	
$\lambda_r = 0.028 [\text{W/m} \cdot \text{K}]$	
$\text{Pr} = 0.71$	

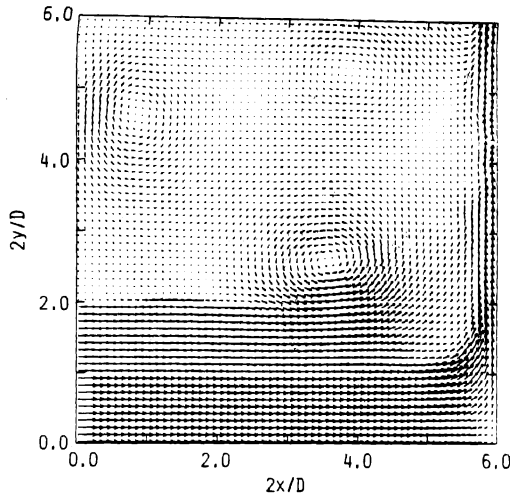


Fig. 2. Velocity vector field for interaction of impinging central single phase (gas-only) jet with low velocity annular one on a surface at $t^* \sim 135$.

the particles ejected from the nozzle at every 20 time steps are chosen in the present vector fields of the particle phase. It can be seen that the main jet flow of gas-phase interacts with the ambient gas at the jet boundary. Also, the magnitude of particle velocity becomes much smaller near the surface and the distance of the reflection from it is very small and hence the velocity of rebounding particles is negligibly small in magnitude. That is, the impinging particles can not be reflected from the surface at all, but can be transported only in the radial direction except for a small part of particles which is influenced by the motion of vortical structures of the gas-phase. An appreciable concentration of particles can be seen to occur on the surface.

Figure 4 indicates the corresponding velocity vector fields for $r_p = 5.0 [\mu\text{m}]$ at $t^* \sim 100$. At a glance, these flow fields are entirely different from the previous case of

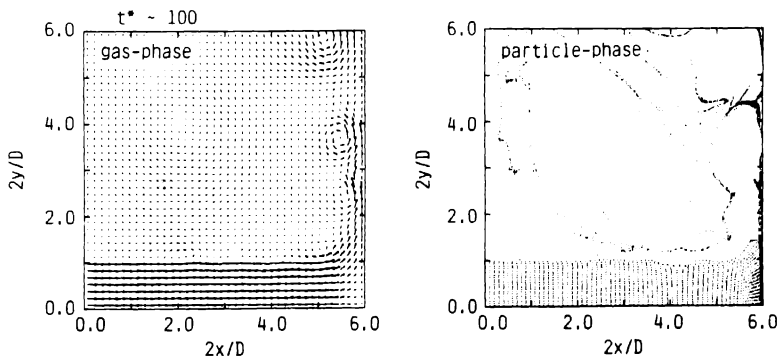


Fig. 3. Velocity vector fields for both gas and particle phases for mixture of $r_p = 1.0 [\mu\text{m}]$ at $t^* \sim 100$ without annular gas flow.

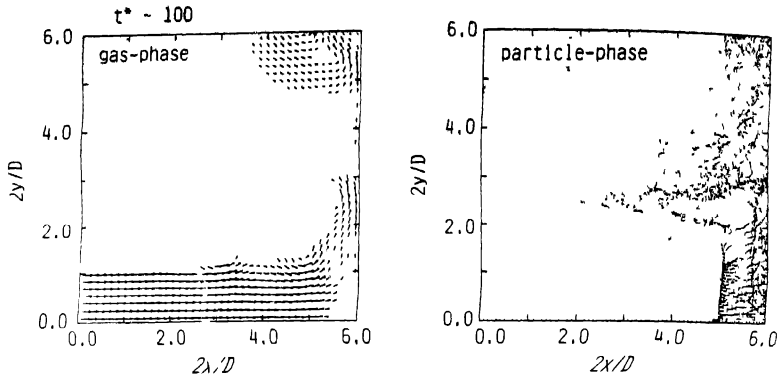


Fig 4 Velocity vector fields for $r_p = 50 [\mu\text{m}]$ corresponding to Fig 2 at $t^* \sim 100$

$1.0 [\mu\text{m}]$. With increasing particle size, the particles impinge on the plate surface with larger normal velocity components. It is empirically and theoretically reasonable to consider that larger particles are not decelerated due to the mass effect or inertia effect regardless of the decrease in the normal velocity components of gas-phase near the plate surface. As a result, the reflected particles travel upstream larger distances until these are decelerated by the gas flow and are again pushed back in the main flow direction. It is understood that an appreciable part of particles does not directly contact the plate surface.

Figure 5 indicates the corresponding results for $r_p = 10 [\mu\text{m}]$ at $t^* \sim 100$. It can be seen that a great part of droplets are reflected far from the surface after the impingement process. The dispersion state of particles are found to be widely different from that of smaller ones in comparison with the case where droplets of $r_p = 1.0 [\mu\text{m}]$ contact the surface or are very close to it, although the assumption of perfectly elastic reflection is introduced to the numerical model.

Next, we consider the flow fields of the gas and particle phases for the case where the

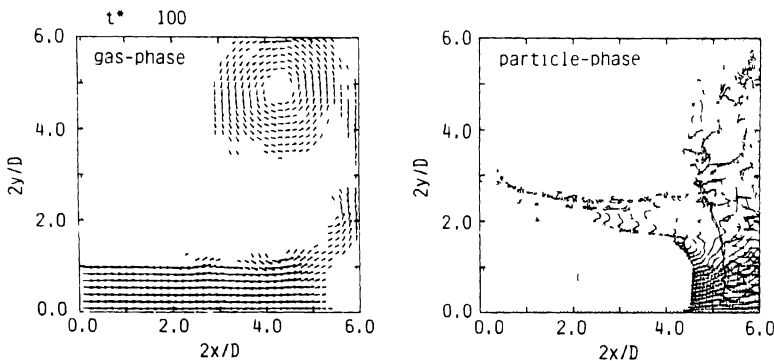


Fig 5 Corresponding velocity vector fields for $r_p = 10 [\mu\text{m}]$ at $t^* \sim 100$

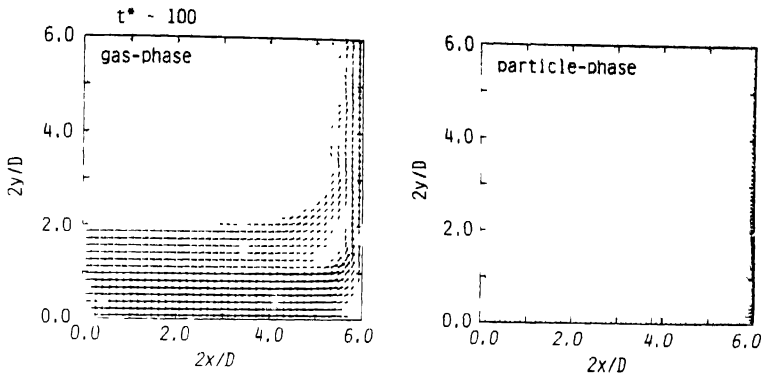


Fig. 6 Velocity vector fields of gas and particles of $r_p = 1.0 [\mu\text{m}]$ for the case where $D_A = 2D$ and $u_A = 0.5 u_E$ at $t^* \sim 100$

coaxial annular gas flow is present. The numerical calculations are performed on the condition that $D_A = 2D$ and $u_A = 0.5 u_E$.

Figure 6 gives the numerical results for $r_p = 1.0 [\mu\text{m}]$ at $t^* \sim 100$. It can be seen that the particles cover the surface in an almost sticking state. It is very interesting that there are almost no distinct vortical structures in the flow field of the gas phase and there are no distortions in the gas velocity vectors nearest to the surface. Therefore, the particles are transported by the gas flow in a regular manner on the surface, compared with the case where the coaxial gas flow is absent.

Figure 7 shows the calculated flow fields of $r_p = 5.0 [\mu\text{m}]$ at $t^* \sim 100$. The particles can be divided into two groups. One is the particles impinging on the surface near the jet axis which experience a few collisions with the surface, before they flow out of the free jet region. The other is the particles impinging on the surface near the jet boundary which experience only one collision. The latter particles are pushed back toward the surface by the coaxial flow. At any rate, it may be confirmed from this

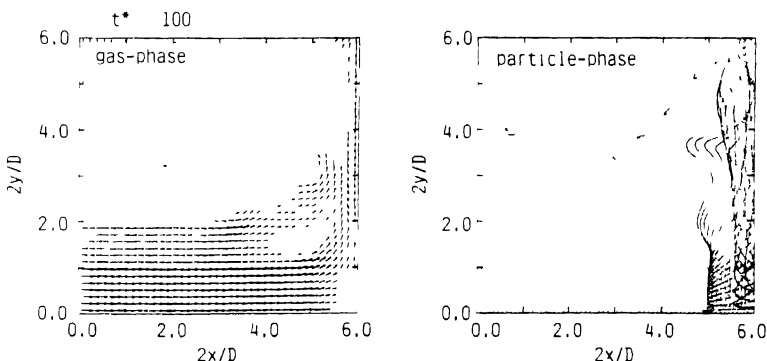


Fig. 7. Velocity vector fields for $r_p = 5.0 [\mu\text{m}]$ corresponding to Fig. 6.

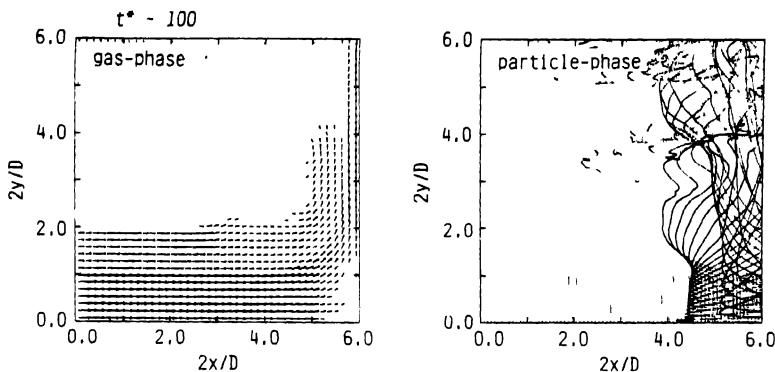


Fig. 8 Corresponding velocity vector fields for $r_p = 10[\mu\text{m}]$

numerical results that all of the particles are transported in the radial direction on the surface, although they are not so close to the surface.

Figure 8 indicates the numerical results of $r_p = 10[\mu\text{m}]$ at $t^* \sim 100$. This case is similar to the previous case of $r_p = 5.0[\mu\text{m}]$ except that the effect of the particle reflection from the surface is considerably large in comparison the previous case. The particles which experience a few collisions with the surface are pushed back to the surface by the coaxial gas flow. A part of particles is observed to be slow in motion, or simply stays because there is very small gas velocity in the downstream region of the wall jet. In truth, one of the reviewers of this paper has pointed out that the numerical results that single particles simply stay in a negligible gas velocity region are based on neglecting the body force in the derivation of the equations of particle motion. This approach, however, is not only very costly but also almost impossible in terms of computer time and storage requirements due to the fact that the introduction of the body force (the gravitational force) results in the three-dimensional problem, because the horizontal flows are considered here.

We note that for every gas-phase flow vortical structures occurring at the jet boundary near the nozzle exist are transported to the downstream and the same process is almost steadily repeated. It is a characteristic feature that the motion of smaller particles is strongly influenced by such vortical structures, especially on the wall jet boundary.

5. Discussion

It is important to characterize how the particles disperse in a gas flow according to the difference in the particle size, especially when the gas-particle two-phase flow is applied to the secondary cooling in the continuous casting system. This is because the flow fields for the gas and particle phases give a strong influence to the cooling intensity. Chung and Troutt [13] have numerically analyzed the particle dispersion in

an axisymmetric jet by following particle trajectories in a jet flow simulated by discrete vortex rings. According to their analysis, the effectiveness of the large turbulent structures for moving particles in the mixing region can be characterized by the Stokes number, that is, the ratio of the aerodynamic response time τ_A defined by Eq. (4) to the characteristic time scale D/u_E of the flow field. For the ratio $\gamma_t (= \rho_{mp}(2r_p)^2 u_E / 18\mu D) \gg 1$, the particles have not enough time to respond to the gas flow and move in approximately rectilinear path. For $\gamma_t \ll 1$ the particles have sufficient time to respond to the spreading velocity field of the gas jet and disperse laterally with the spreading rate of the gas jet. In addition, for $\gamma_t \sim 1$ the gas jet can capture the particles and fling them beyond the fluid momentum mixing region.

We consider the application of the above regime of the particle motion to the present numerical results by taking for example the case where the coaxial gas-only flow is absent, because the velocity difference at the jet boundary between the free jet and the ambient gas regions is larger than in another case.

Figure 9 shows the streaklines of particles exhausted from each starting radial point on the nozzle exit plane with the identical condition to that in Fig. 3 $\gamma_t = 0.34$ in this case. The particles form an almost straight trajectory except for those whose discharging points are closer to the nozzle wall, until they reach the surface. Also, the

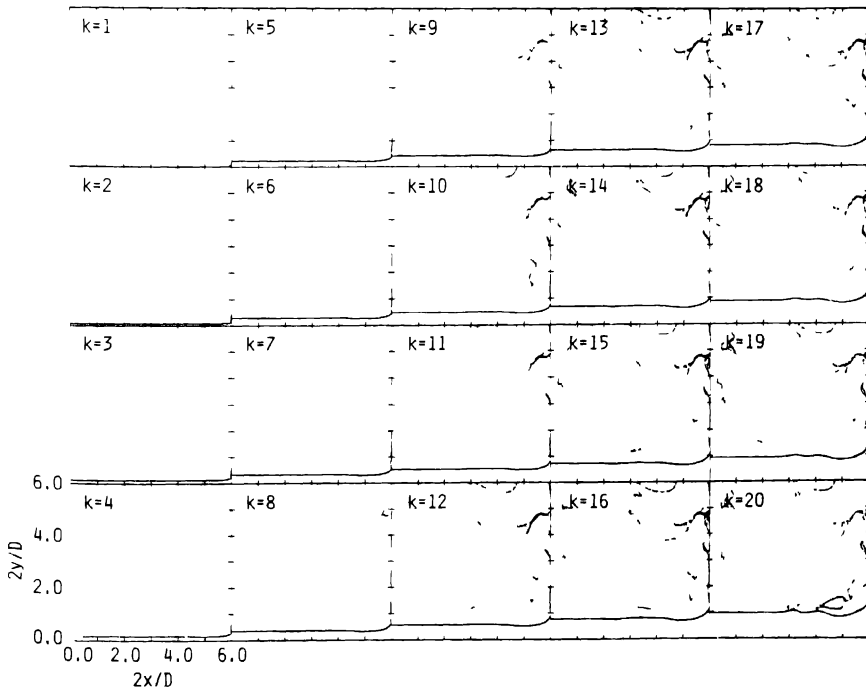


Fig. 9 Particle distribution pattern at $t^* \sim 100$ for particles of $r_p = 10 [\mu\text{m}]$ exhausted at each starting point on nozzle exit plane without annular gas flow.

particles closer to the jet boundary travel radially on the surface with a very small velocity and then are separated from it by a vortical structure of the flowing gas. At any rate, the particles follow the fluctuation of the gas phase. This is quite consistent with the above regime of the smaller Stokes number.

Figure 10 shows the corresponding result for $r_p = 5.0 [\mu\text{m}]$, $\gamma_r = 8.7$ in this case. For starting radial locations which are closer to the centerline, the particles interact with the core flow of the jet which carries more momentum in the axial direction. This means that particles exhausted at locations closer to the jet axis have higher axial momentum and then experience a few collisions and less reflection distance. After that, they are transported radially on the surface. But, the particles exhausted at locations near the nozzle wall experience only one collision. These particles reflected from the surface move away from the core flow of the jet and get flung out to the almost stagnant ambient region. They are not transported to the radial direction on the surface, but reveal somewhat complicated behaviour outside the free jet and the wall jet regions.

Figure 11 shows the corresponding result for $r_p = 10 [\mu\text{m}]$. The present case where $\gamma_r = 35.6$ demonstrates that the distance which the particles exhausted at locations near the nozzle wall travel by the reflection from the surface is notably large. As seen in Fig. 10, the particles exhausted at locations near the centerline tend to move

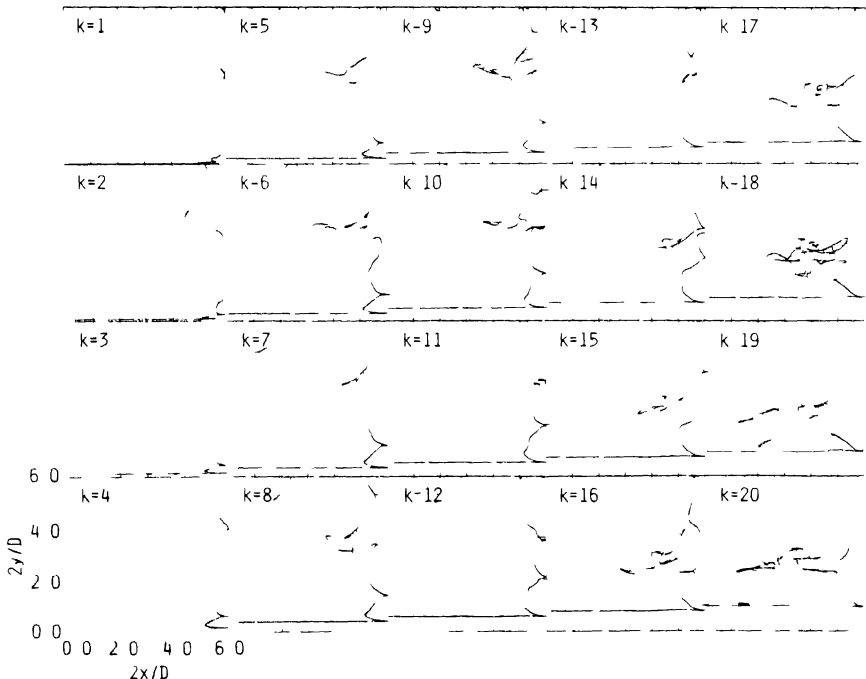


Fig. 10 Particle distribution pattern at $r^* \sim 100$ for $r_p = 5.0 [\mu\text{m}]$ corresponding to Fig. 9

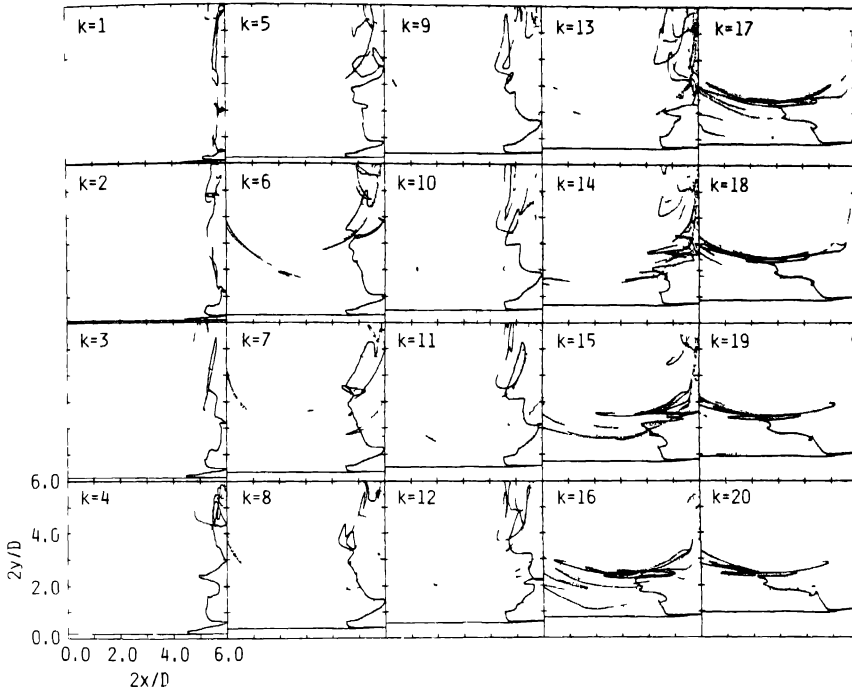


Fig 11 Corresponding numerical result for $r_p = 10[\mu\text{m}]$

radially on the surface after a few collisions, while the particles exhausted at locations near the nozzle wall do not always approach the surface after only one collision and move very unsteadily outside the core flow of the jet and the wall jet. This is due to the presence of a large scale leading vortex remaining downstream of the wall jet in an almost stationary state (see Fig. 5).

In general, relatively larger particles with smaller drag/inertia ratios move away from the core of relatively large vortical structures and penetrate the outer region. For even higher γ_r , particles become less influenced by the flow structures as shown in Figs 10 and 11 where the radial dispersion of $r_p = 10[\mu\text{m}]$ is much reduced as compared with that of $5[\mu\text{m}]$, and the latter is much smaller than that of $1[\mu\text{m}]$. It has been demonstrated from the previous numerical experiments that the annular gas flow can push back these dispersed particles to the surface. However, at the present stage, it is very difficult to evaluate the effect of including annular gas on the mist cooling intensity from a quantitative point of view. This problem remains for future study.

To predict the particle motion in the impinging jet flow a Lagrangian approach is followed. The trajectory of each particle in the flow is numerically solved directly from the equation of motion. Some assumptions in the particle motion analysis are introduced. First, virtual mass force, pressure gradient force and Basset force are all

neglected. An order of magnitude study based on the equation given in Maxey and Riley [14] reveals that virtual mass and pressure gradient are of the order of the density ratio, ρ/ρ_{mp} , and Basset force is of the order of $(\rho/\rho_{mp})^{1/2}$. Since ρ/ρ_{mp} is assumed to be 10^{-3} for a gas-water droplet flow system, the neglect of those forces may be justified. In addition, Chung and Troutt state that Basset force may become relatively important for $\gamma_\tau > O(10^2)$ as compared to the drag force which is the dominant force in the particle motion analysis. Other force fields including gravity are neglected in this analysis. The axisymmetric flow is considered to be horizontal, as mentioned already. The inclusion of the gravitational force is inhibitive costly in terms of computer time and memory. Also, the effect of fluid turbulence is neglected due to the same reason as the above.

It is assumed that no particle coalescence or particle breakup occurs. This implies that the particles are sufficiently dispersed that particle collisions are infrequent. In fact, $v = O(1)$ and $s_p/L = O(10^{-2})$ give a sufficient condition for the particle phase to be dilute, as described in the previous section. Therefore, we believe that the neglect of particle-particle collision is approximately justified.

The assumption that the particle reflection from the surface is elastic is not commonly justified regardless of whether the numerical model is in a hot or cold one. The mechanism of the reflection of water-droplets from the hot surface beyond the Leidenfrost point is considered to be entirely different from that of the solid particles. The reflection or deflection of droplets may occur owing to the fact that the thermal energy transferred from the hot surface to them changes into the kinetic energy. At the present stage, it is very tedious to follow the thermal process exactly. This problem also remains for future study.

6. Conclusion

The numerical analysis of flow pattern of two-phase mixture impinging on a flat plate has been performed by a time-dependent technique. The mixtures composed of air and water-droplets are treated. In order to put together droplets dispersed radially to the surface, the introduction of an annular gas-only flow has been proposed and the interaction of the central impinging two-phase jet on the surface with the low velocity annular jet has been simulated from a point of view of numerical experiments. The flow structures for air and droplets strongly depend upon the particle size. It is clearly demonstrated that for smaller particles the particle distribution pattern gives a good visualization of the jet vortex structures in the jet flow and particle dispersion is approximately equal to that of the fluid. For larger particles the particles do not have sufficient time to respond to the large vortex structures and move in somewhat rectilinear path.

The numerical results reveal that it is roughly possible to put together the dispersed particles to the surface by the annular gas-only flow, although the effect of including

the annular gas flow on the cooling intensity has not been examined from a quantitative point of view.

Acknowledgment

The authors would like to note that this study has been supported through the Grant-in-Aid for Scientific Research (01550532) of the Ministry of Education, Science and Culture in Japan.

References

1. Zucrow, M.J. and Hoffman, J.D., *Gas Dynamics*, Vol. II, John Wiley and Sons, New York (1977) 53.
2. Hatta, N., Ishii, R., Takuda, H., Ueda, K. and Kokado, J., Analytical study on subsonic nozzle flows of gas-particle mixture. *Trans. Iron Steel Inst. Jpn.* (1988) 930–938.
3. Hatta, N., Takuda, H., Ishii, R. and Fujimoto, H., A theoretical study on nozzle design for gas-particle mixture flow. *ISIJ International* 29 (1989) 605–613.
4. Hatta, N. and Nakamura, M., A note to the single-size approximation of mist flow in a nozzle. *ISIJ International* 29 (1989) 796–798.
5. Hatta, N., Fujimoto, H., Ishii, R., Umeda, Y. and Kokado, J., Numerical study on supersonic flows of gas-liquid particle mixture in a De Laval nozzle. *ISIJ International* 29 (1989) 911–918.
6. Hatta, N., Fujimoto, H., Ishii, R. and Kokado, J., Analytical study of gas-particle two-phase jet exhausted from a subsonic nozzle. *ISIJ International* 31 (1991) 53–61.
7. Henderson, C.B., Drag coefficients of spheres in continuum and rarefied flows. *AIAA Journal* 14 (1976) 707–708.
8. Carlson, D.J. and Hoglund, R.F., Particle drag and heat transfer in rocket nozzles. *AIAA Journal* 2 (1964) 1980–1984.
9. Chakravarthy, S.R. and Osher, S., A new class of high accuracy TVD schemes for hyperbolic conservation laws, AIAA 85-0363, AIAA 23rd Aerospace Sciences Meeting, Reno, Nevada (1985).
10. Roe, P.L., Approximate Riemann solvers, parameter vectors, and difference schemes. *Journal of Computational Physics* 43 (1981) 357–372.
11. Godunov, S.K., A finite difference method for the numerical solutions of the equations of fluid dynamics. *Matemat. Sbornik* 47 (1959) 271–290; also Cornell Aero-nautical Laboratory translation.
12. Matsuda, T., Umeda, Y., Ishii, R., Yasuda, A. and Sawada, K., Numerical and experimental studies on choked under-expanded jets. *Memoirs of the Faculty of Engg. Kyoto University*, Vol. 49, Part 1 (1987) 84–110.
13. Chung, J.N. and Troutt, T.R., Simulation of particle dispersion in an axisymmetric jet. *J. Fluid Mech.* 186 (1988) 199–222.
14. Maxey, M. R. and Riley, J. J., Equation of motion for a small rigid sphere in a nonuniform flow. *Phys. Fluids*. (1983) 883–889.

Prediction of forced convective condensation of non-azeotropic refrigerant mixtures inside enhanced surface tubing

S.M. SAMI & J. SCHNOTALE

Mechanical Engineering, School of Engineering, University of Moncton, Moncton, N.B., E1A 3E9, Canada

Received 15 March 1991; accepted in revised form 20 November 1991

Abstract. In this paper, an experimental study on the heat transfer characteristics of two phase flow condensation of pure refrigerants such as R-12 and R-22 as well as non-azeotropic refrigerant mixtures R-22/R-114 and R-22/R-152a on horizontal enhanced surface tubing is presented.

The enhanced surface tubing data showed a significant enhancement of the heat transfer compared to an equivalent smooth tube depending on the mixture components and their concentrations.

Correlations were proposed to predict the heat transfer characteristics such as average heat transfer coefficients as well as pressure drops of non-azeotropic refrigerant mixture flow condensation inside enhanced surface tubing. In addition, it was found that the refrigerant mixture's pressure drop is a weak function of the mixture composition.

Nomenclature

A = heat transfer area (m^2)
 C = Composition (mass fraction) (–)
 C_p = Specific heat ($\text{kJ kg}^{-1} \text{K}^{-1}$)
 D = Diameter of tube (m)
 D_e = Equivalent diameter of the annulus based on the bore diameter ($D_e = D_{oi} - D_{in}$) (m)
 Den = Equivalent diameter of the annulus based on the envelope diameter ($Den = Doi - Denv$) (m)
 f = Friction factor (–)
 G = Mass flux ($\text{kg m}^{-2} \text{s}^{-1}$)
 g = Gravitational acceleration (m s^{-2})
 h = Heat transfer coefficient ($\text{kW m}^{-2} \text{K}^{-1}$)
 h_{fg} = Latent heat of vaporization (kJ kg^{-1})
 K = Thermal conductivity of liquid ($\text{kW m}^{-1} \text{K}^{-1}$)
 L = Length (m)
 m = Mass flow rate (kg s^{-1})
 P = Pressure (kPa)
 Q = Heat input (kW)
 R_w = Wall thermal resistance (K kW^{-1})
 T = Temperature ($^{\circ}\text{C}$ or K)
 t = Thickness
 U = Overall heat transfer coefficient ($\text{kW m}^{-2} \text{K}^{-1}$)
 x = Quality based on mass (–)
 X_u = Martinelli parameter (–)
 Z = Characteristic length (m)

Greek symbols

μ = Viscosity of liquid (Pa s)
 α = Void fraction (–)
 Φ = Frictional multiplier (–)
 ρ = Density (kg m^{-3})

Dimensionless numbers

Ga = Galileo number ($\rho_l(\rho_l - \rho_v)De^3/\mu^2$)
 Ph = Phase change number ($h_{fg}/C_p(T_v - T_{wa})$)
 Pr = Prandtl number of liquid ($C_p\mu/K$)
 Re = Reynolds number ($G D_e/\mu$)
 Nu = Nusselt number ($h D_e/K$)

Subscripts

a = Acceleration
 b = Bore
 e = Equivalent
 f = Friction
 g = Gravitational
 i = Inside
 in = Inlet
 L = Liquid
 m = Measured
 O = Outside
 out = Outlet
 r = Refrigerant
 S = Shell side
 t = Tube side
 tp = Two-phase
 v = Vapour
 w = Water
 wa = Wall

1. Introduction

Although the Montreal Protocol bans CFCs by the year 2000, some nations are in favour of full phase-out by the year 1997. This definitely calls for accelerated development of new alternative refrigerants. In the past few years, a number of fluids that may serve as substitutes, either as pure fluids or as constituents of mixtures have been developed or identified [1–3].

A search for potential replacements for CFCs has been made with initial screening criteria of commercially available component, ozone-depletion potential, toxicity, flammability, stability, thermodynamics, properties and compatibility with system materials. This led to the introduction of binary or ternary non-azeotropic refrigerant mixtures. A mixture of two or more different fluids is classified as an azeotrope when such a mixture possesses its own thermodynamic properties and has identical liquid and vapour composites like a single fluid.

Non-azeotropic mixtures may produce environmentally sound superior working fluids depending on their components and their concentrations. At a given composition or concentration, the non-azeotropic mixture condenses and boils over a temperature range by an isobaric thermal process. Therefore, a non-azeotropic mixture has a temperature distribution parallel to that of the surrounding fluid with which heat transfer takes place during evaporation and condensation processes. This leads to an improved thermodynamic performance.

Research on the thermodynamic and heat transfer characteristics of non-azeotropic fluids is still in its infancy [1–3]. Studies on condensation of refrigerant mixtures inside horizontal smooth tubes [4–7] reported no remarkable effect of the mixture's composition on the flow pattern of condensation. However, a very limited number of studies have been reported in the literature on the condensation of mixed refrigerants on enhanced surface tubing.

Honda et al. [6] performed experiments to study condensation of refrigerants R-11 and R-113 in the annuli of horizontal double-tube condensers with an enhanced inner tube (corrugated inner tube with wire fins). Their finding showed that the local heat transfer coefficient was 2 to 13 times as large as those for horizontal annuli with smooth and corrugated inner tubes.

Another experimental study has been reported by Koyama et al. [7] on the condensation heat transfer of binary refrigerant mixtures of R-22 and R-114 inside a horizontal tube with internal spiral grooves. It appeared from their results that the local Nusselt number depends on the molar fraction, whereas the average Nusselt number can be correlated by an equation which is modified from a previously established equation for pure refrigerants inside a horizontal smooth tube.

To the authors' knowledge, the studies reported by Honda et al. and Koyama et al. are the only existing ones on the condensation inside enhanced surface tubing. However, none of these studies dealt with the condensation of non-azeotropic refrigerant mixtures in condensers with internally and externally enhanced surfaces such as doubly fluted tubes. Therefore, the current research work being undertaken

will enhance our understanding of the fluid flow condensation and heat transfer characteristics of non-azeotropic refrigerant mixtures on enhanced surface tubing (doubly fluted tubes).

2. Experimental apparatus and measurements

Figure 1 shows a schematic diagram of the experimental setup, which is a water/water vapour compression heat pump composed mainly of an 8 KW compressor, oil separator, condenser, pre-condenser, pre-evaporator, adjustable expansion device, and a test condenser. The oil content in the refrigerant loop was estimated to be about 1%. Schematic views of the evaporator and the test section are shown in Fig. 2. The horizontal 2.85 m condenser test section was constructed to eliminate entry length effects. The test section was composed of a double fluted tube condenser, where the refrigerant flows in the outer annulus of the double fluted tube with 0.0324 m envelope diameter and water flows counter-currently inside the inner tube. The inner tube was made of copper with dimension as follows; bore inside diameter 0.0212 m, bore outside diameter 0.0226 m, number of flutes 4 and total effective heat transfer area 0.431 m². The outer tube was smooth and made of copper with an inner diameter 0.0375 m. The outer annulus was subdivided into 20 sections to measure the temperatures. This was necessary to measure the local heat transfer characteristics. Pressure, temperature and flow rate measuring stations are shown in Fig. 1. All pressures were measured using calibrated pressure transducers (0–800 kPa). The accuracy of pressure transducers was 2.5%. Differential pressure transducers were

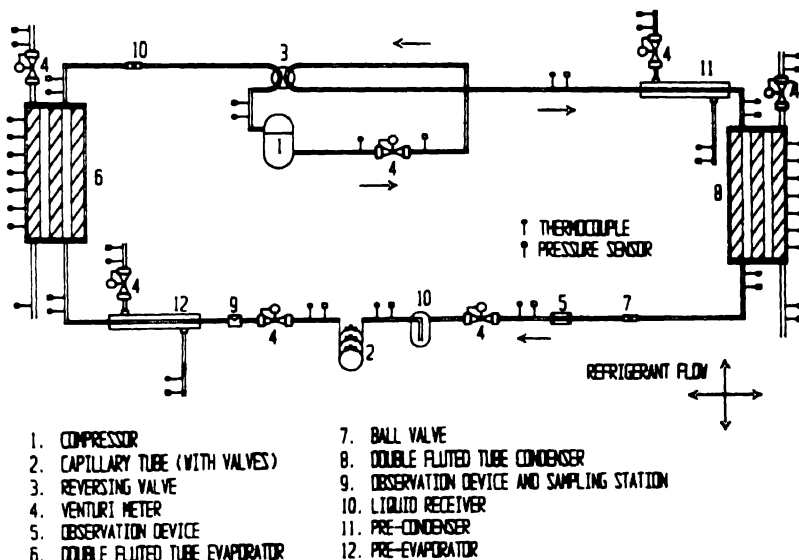


Fig. 1. Schematic view of the experimental setup.

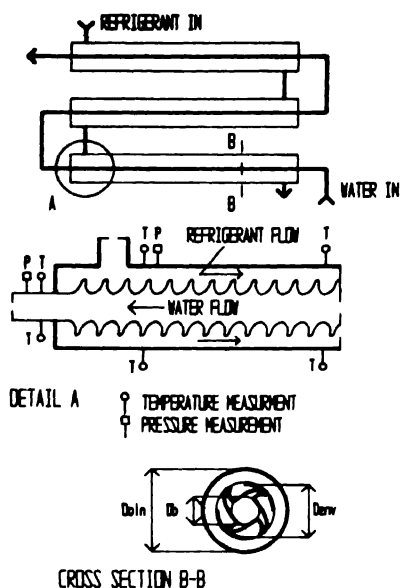


Fig. 2. Schematic view of the test condenser

employed to measure the refrigerant pressure drop. Temperatures were measured by thermocouples type J and K. Temperature measurements accuracy was within ± 1 K.

All recorded measurements were obtained at a sink water entering temperature of 16°C . On the other hand, the water cooled pre-condenser was employed to control the quality of the saturated vapour entering the condenser. The quality of the refrigerant entering the test condenser was kept at 0.90. The temperature difference across the condenser was controlled to achieve saturated liquid at the outlet of the condenser.

A calibrated orifice installed in the liquid line after a liquid receiver was used to measure the refrigerant mass flow rate. Both orifices' pressure taps were connected to a differential pressure transducer (0–250 kPa). Water mass flow rate was also measured by a calibrated orifice. The accuracy of the mass flow measurements was $\pm 3\%$ of the nominal flow.

Power supplied to the compressor and fans was measured because it is needed for the heat balance. An AC/DC clamp-on device was calibrated for power measurements with accuracy of $\pm 3\%$.

Refrigerant composition for each particular mixture has been determined with the aid of an electronic scale. In addition, a liquid sample of each mixture was expanded to superheated vapour and analyzed by gas chromatography to accurately determine the overall composition of the mixture prior to the testing.

Data collection was carried out using an AT/PC 286 equipped with a data acquisition system having a capacity of 112 channels. This enables us to record with a single scan, local properties such as pressure drops, pressures, temperatures, flow rates, heat flux and power.

All tests were performed under steady state conditions. The channels were scanned every second and stored every 10 seconds. The measured values were averaged over a period of 10 seconds.

The primary parameters observed during the course of this study were mixture overall composition, mass flux, heat flux, and quality for pure refrigerants; R-12 and R-22 as well as non-azeotropic refrigerant mixtures R-22/R-114 and R-22/R-152a at various concentrations. Mass flow rates ranged from 50 to 90 g/s. Input quality was kept constant at 0.9 and condensation took place so as to reach saturation condition at the exit of the condenser.

In order to develop the proposed correlations describing the flow condensation heat transfer characteristics, the thermodynamic properties as well as transport properties of pure and non-azeotropic refrigerant mixtures should be known. The Carnahan-Starling-DeSantes (CTD) equation of state [8] was used to evaluate the mixture characteristics during evaporation. On the other hand, the mixing rules suggested by Reid et al. [9] were employed with caution to determine the transport properties of the mixed refrigerants.

3. Results and discussion

In the following sections, the results of the heat transfer characteristics such as pressure drops, heat transfer coefficients at different conditions will be presented and discussed. Summary of the test conditions is presented in Table 1.

3.1. Heat transfer

The following equations have been employed to calculate the heat transfer coefficients from the data stored during each particular test.

The heat transfer rate in the pre-condenser or condenser test section can be determined from the heat balance or the water flow in the annulus

$$Q_w = \dot{m}_w C_{p_w} (T_{wout} - T_{win}). \quad (1)$$

The vapour quality at the entrance to the test section was calculated from an energy balance of the system

$$x_{out} = x_{in} + \frac{Q_w}{\dot{m}_r h_{fg}}. \quad (2)$$

Table 1 Test conditions

1	Condenser pressure	800 to 1500 kPa
2	Temperature of refrigerant	32 to 37 °C
3	Re number	2.3×10^3 to 8.9×10^3

The refrigerant properties were determined at saturation conditions in the test section.

The total heat transferred to the refrigerant is;

$$Q_n = \dot{m}_r h_{fg} \Delta x, \quad (3)$$

where x is the quality change in the test section.

The overall heat transfer coefficient based on the outside surface area of the test section is

$$U = \frac{Q_n}{A_o LMTD}, \quad (4)$$

where $LMTD$ is the mean logarithmic temperature difference based on the inlet/outlet temperatures of water/refrigerant flow.

Assuming no fouling and R_w is the thermal resistance in the copper wall of the tube, the refrigerant heat transfer coefficient h_r can be calculated as follows:

$$\frac{1}{h_r A_i} = \frac{1}{U A_o} - \left(\frac{1}{h_w A_o} + R_w \right), \quad (5)$$

where h_w is the water heat transfer coefficient and is calculated using the Wilson plot technique as described in Khartabil et al. [10]. R_w is the wall resistance evaluated using the actual thickness and the outside diameter of the tube.

During the course of this study for data resolution purposes, the enhanced surface tube (doubly fluted tube) annulus has been treated as a plain tube annulus with an equivalent diameter. Using the equivalent diameter is consistent with the approach suggested by references [6, 11] for the annuli of a horizontal double-tube condenser with an enhanced inner tube.

In order to check the reliability of the test facility, the thermal resistance of both tube-side and shell-side of single phase turbulent water flow have been measured and calculated using the modified Wilson plot technique and compared to well-known correlations [12]. The following correlations have been developed using the water data for single phase flow with the characteristic diameter as the bore diameter for the tube side:

Tube-side

$$Nu_t = 0.03 Re_t^{0.8} Pr_t^{0.4} \quad (6)$$

for $3 \times 10^3 < Re < 1.2 \times 10^4$

Shell-side

$$Nu = 0.116 Re^{0.75} Pr^{0.4}, \quad (7)$$

for $3.5 \times 10^3 < Re < 2.5 \times 10^4$

Wall resistance

$$R_w = 2.6 \times 10^{-2} \quad (K K_w^{-1}). \quad (8)$$

All recorded data were found to be in agreement with existing correlations [12] for turbulent single phase flow with an average of 4%.

In an attempt to correlate our two phase flow condensation experimental results performed with pure refrigerants R-12 and R-22 as well as non-azeotropic refrigerant mixtures R-22/R-114 and R-22/R-152a the Nusselt solution [13] has been considered. In the solution proposed by Nusselt, interior convection effects in the condensate film were negligible. In addition, the vapour liquid interface shear forces were not considered in that model. However, in this study, only the modified Nusselt solution proposed by Collier [13] has been adopted because most of the problems associated with the original Nusselt solution have been alleviated. It has been also assumed in the modified Nusselt correlation that the vapour shear forces are significant. The following correlation was presented by Collier [13] for calculating the condensation heat transfer coefficient on plain tube;

$$h = F \left(\frac{g \rho_1 (\rho_1 - \rho_v) h_{fg} K^3}{\mu Z (T_v - T_{wa})} \right)^{0.25}, \quad (9)$$

where F is the shear factor and is a vapour Reynolds number dependent;

$$F = n Re_v^d, \quad (10)$$

where

$$Re_v = G_v D / \mu_v.$$

It has been found by Rosson and Mayer [14] that n and d are 0.31 and 0.12 respectively.

On the other hand, in the particular case of doubly fluted tube condensation, additional shear forces are involved which are not accounted in the factor F . Therefore, the following modified dimensionless form of the Nusselt solution is proposed;

$$Nu = F_1 Ga^{0.25} Ph^{0.25} Pr^{0.25}, \quad (11)$$

where the F_1 is the liquid shear factor and is defined in terms of the liquid Reynolds number as follows;

$$F_1 = n Re_l^d, \quad (12)$$

where

$$Re = GD_e/\mu, \quad (12a)$$

and G is the total mass flux and is the equivalent diameter of the annuli;

$$D_e = D_{oi} - D_{bo}, \quad (12b)$$

where D_{oi} is the inner diameter of the outside tube and D_{bo} is defined as;

$$D_{bo} = D_b + 2t, \quad (12c)$$

where D_b and t are the bore diameter and the thickness of the doubly fluted tube respectively.

It was found from the experimental data of the pure refrigerants during forced convection condensation that the liquid shear factor can be expressed in the following form;

$$F_1 = 0.043 Re^{0.4}. \quad (13)$$

Figure 3 shows the comparison of the experimental data of pure refrigerants R-12 and R-22 with those predicted by the proposed modified Nusselt solution (equation

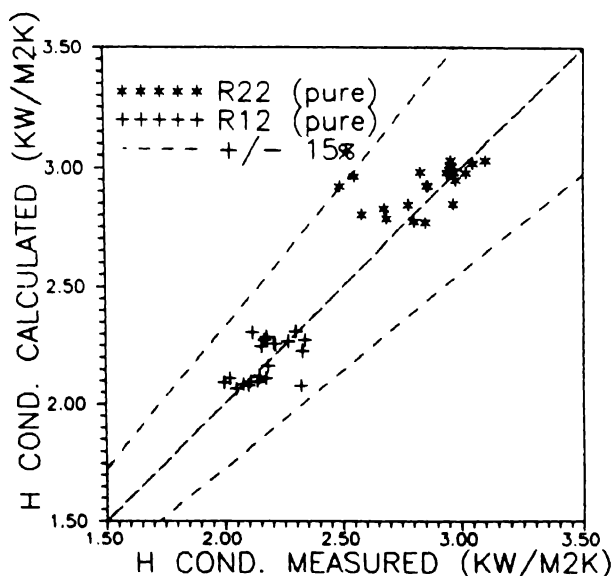


Fig. 3. Calculated vs. measured condensing heat transfer coefficient.

11) with F_1 given by equation (13). The agreement with the experimental data was very good. Also the figure illustrates that the mean deviation between the measured heat transfer coefficient values and the predicted ones is within 15%.

At this point, the heat transfer enhancement factor is introduced. At a constant mass flux, the heat transfer enhancement is defined as the ratio of the condensation heat transfer coefficient of mixed refrigerants on the enhanced surface to that of a pure refrigerant on a smooth tube.

The heat transfer coefficient of pure refrigerants for a smooth tube has been calculated with the well established correlation proposed by Traviss et al. [15]:

$$Nu = Re_1^{0.9} Pr F_1^\beta / F_2. \quad (14)$$

Where $Nu = (hD_e/K)$, and $\beta = 1.0$ for $F_1 \leq 1.0$

$$\beta = 1.15 \text{ for } F_1 > 1.0.$$

The parameters F_1 and F_2 are defined as follows;

$$F_1 = 0.15(X_{ii}^{-1} + 2.85X_{ii}^{0.574}), \quad (15)$$

and,

$$F_2 = 0.707 Pr Re_1^{0.5}, \quad (15a)$$

for $Re_1 < 50$

$$F_2 = 5 Pr + 5 \ln[1 + Pr(0.09636 Re_1^{0.585} - 1)] \quad (15b)$$

for $50 < Re_1 < 1125$

$$F_2 = 5 Pr + 5 \ln(1 + Pr) + [2.5 \ln(0.00313 Re_1^{0.812})] \quad (15c)$$

for $Re_1 > 1125$, and X_{ii} is the Lockhart Martinelli parameter [13];

$$X_{ii} = \left(\frac{1-x}{x} \right)^{0.9} \left(\frac{\rho_v}{\rho_l} \right)^{0.5} \left(\frac{\mu_l}{\mu_v} \right)^{0.1}. \quad (15d)$$

Results shown in Figs 4a illustrate that the measured condensation heat transfer coefficient of pure refrigerants such as R-22 has been enhanced on the average by 3.29 times that of the smooth tube having the same equivalent annulus diameter. It is worthwhile mentioning that the heat transfer enhancement factor was not a strong function of the mass flux.

Another series of tests were run with non-azeotropic refrigerant mixture R-22/R-

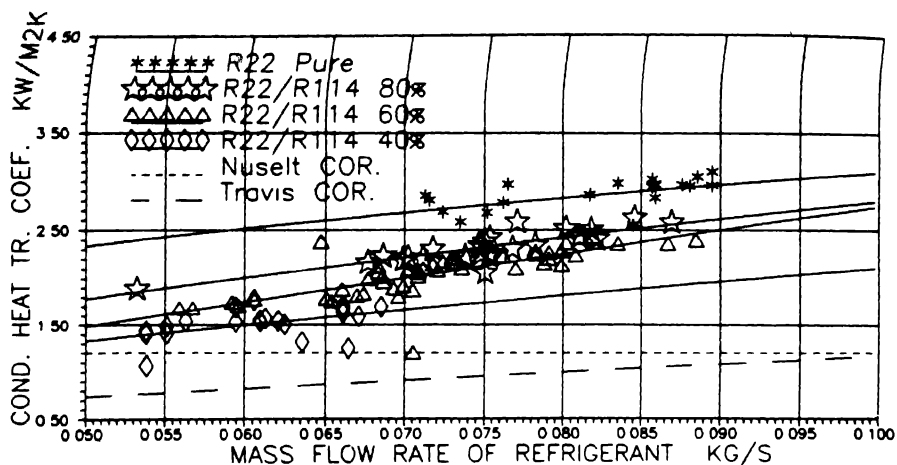


Fig 4a Condensing heat transfer coefficient vs. mass flow rate

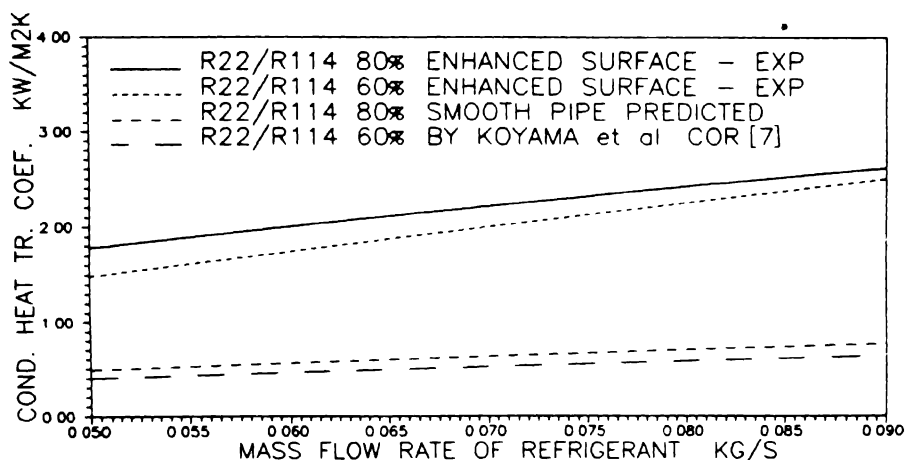


Fig 4b Condensing heat transfer coefficient vs. mass flow rate for enhanced surface and smooth pipe

114 at several overall compositions. Figures 4a and 4b illustrate the measured flow condensation heat transfer coefficients for R-22/R-114 plotted as a function of the mass flux and concentrations. As expected, the heat transfer coefficient increases at higher mass flux. On the other hand, samples of the condensation data of the mixture R-22/R-114 in enhanced surface tubing, were plotted as a function of the mass flux and compared to those of a smooth tube in Fig. 4b. The condensation heat transfer coefficient values for smooth tube shown in this figure were predicted using Koyama et al. correlation [7]. It is evident from the data presented in these figures that the doubly fluted tubes displays a significant increase in the heat transfer coefficient compared to a smooth tube with the same annulus equivalent diameter. In addition,

the data depicted in Fig. 4a shows that the heat transfer enhancement factor for refrigerant mixture R-22/R-114 is a strong function of the mixture composition.

To further examine the dependence of the mixed refrigerants' convective condensation on the composition and the mass flux, Fig. 5 has been constructed. The results depicted in this figure show that the increase of concentration of R-114 in the mixture decelerates the rate of condensation and consequently the heat transfer rate. In addition, this figure shows that at constant mass flux the heat transfer coefficient varies near linearly with the mixture composition.

The third series of tests were conducted with two phase flow condensation involving refrigerant mixtures of R-22/R-152a in various concentrations. The maximum permissible concentration of R-152a was limited to 30% because of flammability reasons. Samples of the heat transfer coefficients obtained through these runs were plotted and compared to smooth tube values calculated by the Fujii and Nagata correlation [16] in Fig. 6a. The data clearly indicates that the enhanced surface tubing leads to a substantial increase in the condensation heat transfer rate compared to that of a smooth tube. The figure also illustrates that the heat transfer coefficient depends upon the mass flux. Moreover, the effect of the mixture composition on the condensing heat transfer coefficient is shown in Fig. 6b. The figure is indicative of the qualitative behaviour of the heat transfer coefficient for different mixture compositions compared with pure refrigerants. As observed with R-22/R-114, the heat

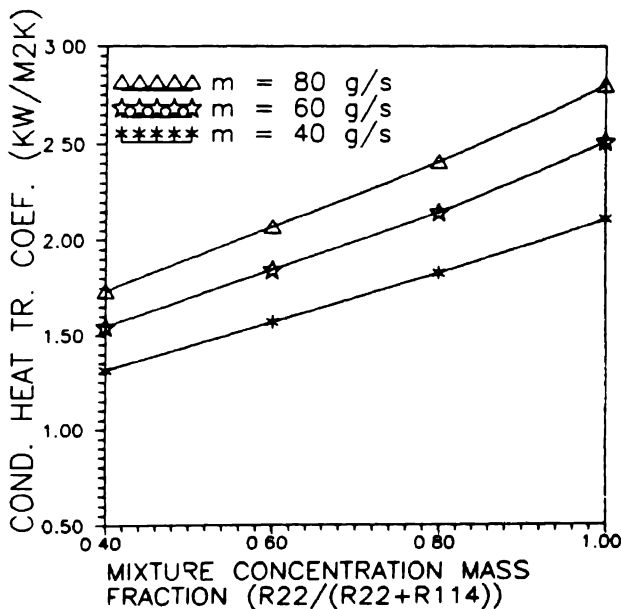


Fig. 5 Condensing heat transfer coefficient vs. mixture mass concentration for R22/R114 mixture at different mass flow rates, m .

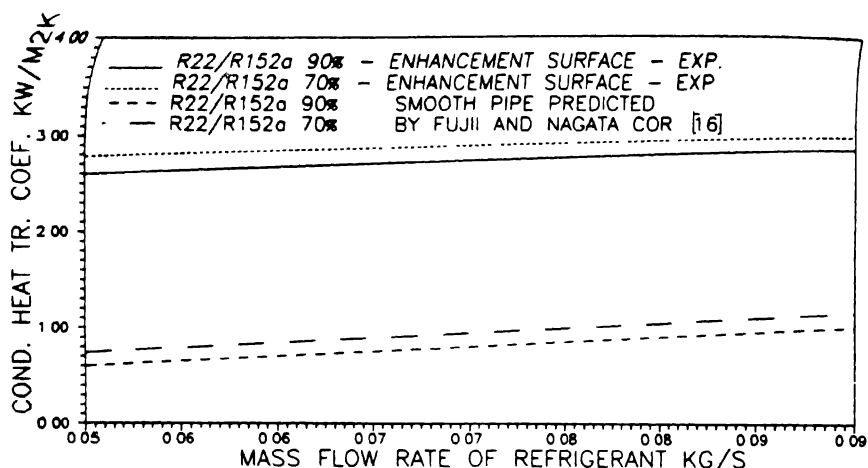


Fig 6a. Condensing heat transfer coefficient vs mass flow rate for enhanced surface and smooth pipe

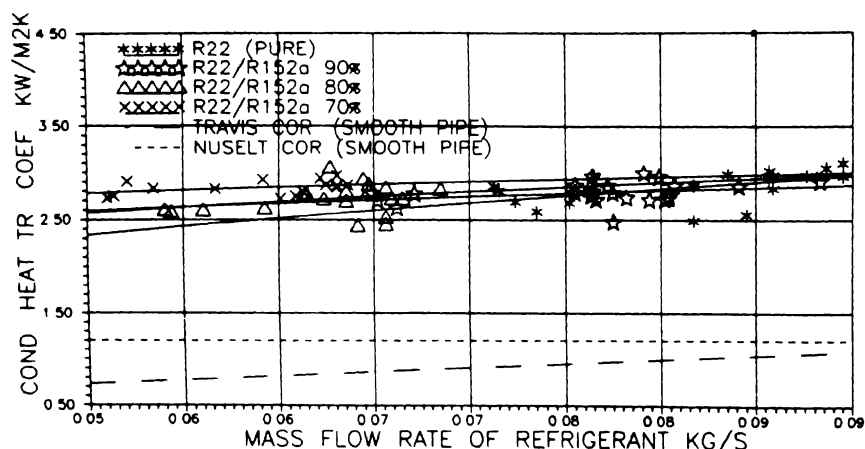


Fig 6b Condensing heat transfer coefficient vs mass flow rate

transfer coefficient increases when the mass flux increases. The data suggest that higher concentrations of R-152a in the mixture lead to a slight increase in the heat transfer coefficient. On the other hand, it appears that the mixture produces a heat transfer enhancement factor slightly higher than that of R-22. Also, this figure shows that the enhancement factor seems to have weak dependence on the mass flux.

Figure 7 displays the typical heat transfer characteristics for the mixture R-22/R-152a in the convective condensation region at different concentrations. As noticed, a slight increase in the heat transfer coefficient is associated with higher concentration of R-152a in the mixture. This result is contrary to what has been observed with the mixture R-22/R-114.

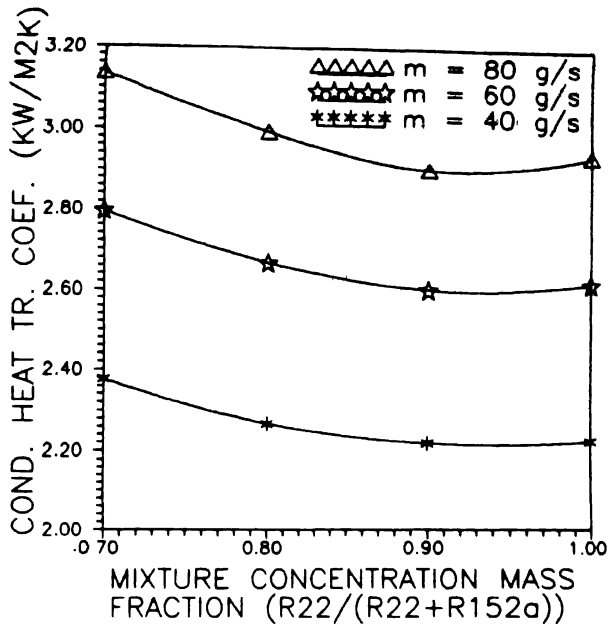


Fig. 7 Condensing heat transfer coefficient vs mixture mass concentration for R22/R152a mixture at different mass flow rates, m

A potential explanation for the observed phenomena is offered in the following. As individual components of a mixture evaporate at different boiling point temperatures, the component with the higher boiling point transfers preferentially into condensate at the vapour-liquid interface. Thus, more of the lower boiling volatile component is present in the vapour mixture at a greater distance from the interface [17]. An increase in the concentration of the lower boiling more volatile component, results toward the interface and consequently is transported by back diffusion into the vapour phase. Thus less condensation occurs at the vapour-liquid interface. Therefore, it is believed that greater volatility difference between the mixture components results in lowering the condensation rate.

The above preceding hypotheses explains the observed condensation behaviour of the non-azeotropic refrigerant mixtures R-22/R-114 and R-22/R-152a. It also highlights the role the mixture composition has in determining the resultant heat transfer coefficient.

After a detailed analysis of the forced convection condensation results of the mixtures under investigation, the following modified form of the Nusselt solution has been employed to correlate the present data;

$$Nu = n Re^d Ga^{0.25} Pr^{0.25}, \quad (16)$$

where n and d are constants determined experimentally.

All data showed that the Reynolds number exponent d has a constant value of 0.40 and the Reynolds number exponent n has a strong function of the mixture concentration.

The following expressions for n are proposed:

Non-azeotropic Mixture R-22/R-152a

$$n = 0.037 + 0.006C. \quad (16a)$$

Non-azeotropic Mixture R-22/R-114

$$n = 0.017 + 0.025C, \quad (16b)$$

where C is the mixture composition.

Figures 8 and 9 show the comparison between the measured condensation heat transfer coefficient and the one predicted by the proposed correlation. It is evident from these figures that the proposed correlation was applicable to the entire heat and mass flux ranges employed in the current study. In general, the deviation between the experimental and predicted values was less than 15%.

No attempt has been made to compare the proposed correlation to existing ones, because to the authors' knowledge none were available.

Finally, based on the experimental evidence and our observations of the condensing characteristics of pure and non-azeotropic refrigerant mixtures, a generalized corre-

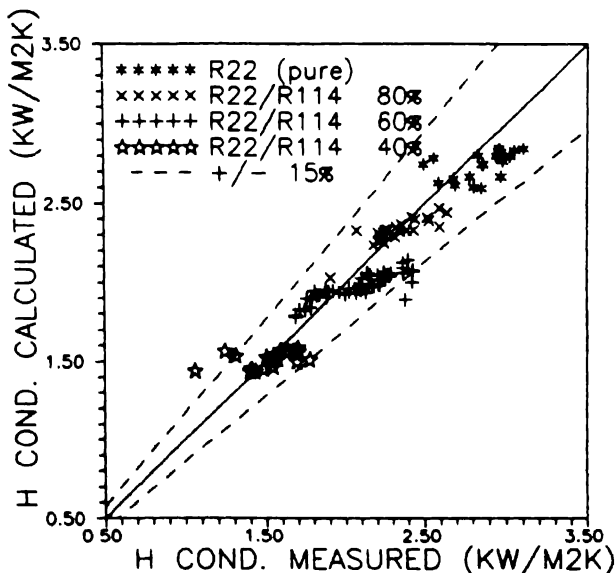


Fig. 8. Calculated vs. measured condensing heat transfer.

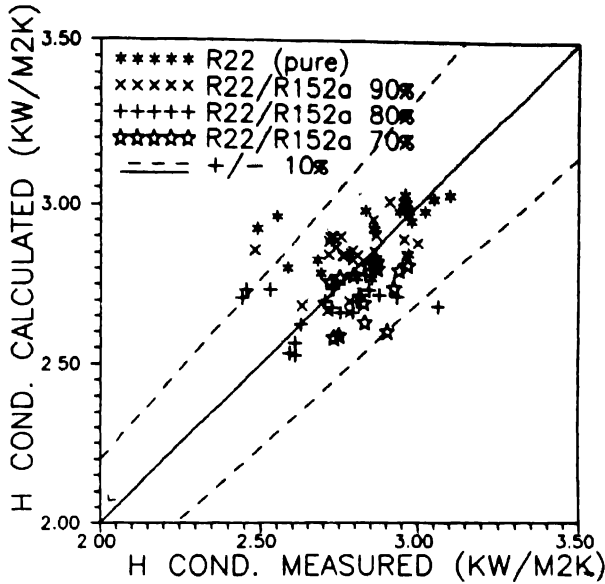


Fig. 9 Calculated vs. measured condensing heat transfer.

lation determined by a regression analysis of the data of heat transfer coefficients in the condensing region is proposed;

$$Nu = 0.04C^{0.48} Re^{0.4} Ph^{0.25} Ga^{0.75} Pr^{0.25}, \quad (17)$$

where C is the mixture composition.

Figure 10 shows that the proposed generalized correlation predicts the heat transfer coefficient for pure and mixed fluids in the convective condensation region with a mean deviation of 20%.

3.2. Pressure drop

In the flow conditions under investigation, the total two phase pressure drop during flow condensation of pure or non-azeotropic refrigerant mixtures is given by;

$$\Delta P_{\text{total}} = \Delta P_f + \Delta P_a + \Delta P_g, \quad (18)$$

where ΔP_{total} is the total two phase pressure drop, ΔP_f is the frictional pressure, P_a represents the acceleration pressure drop and ΔP_g is the gravitational pressure drop.

In a horizontal geometry, the gravitational pressure drop can be neglected,

$$\frac{dP}{dz} = \left. \frac{dP}{dZ} \right|_f + \left. \frac{dP}{dZ} \right|_M. \quad (19)$$

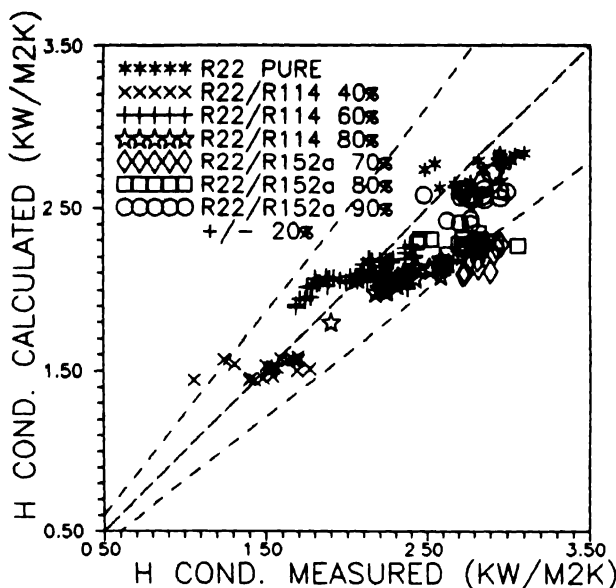


Fig 10 Calculated vs measured condensing heat transfer coefficient

The momentum pressure drop for a working fluid undergoing an condensation process over a length Z [13] can be written as follows;

$$\left. \frac{dP}{dZ} \right|_M = G^2 \frac{d}{dZ} \left[\frac{x^2}{\rho_v \alpha} + \frac{(1-x)^2}{\rho_1 (1-\alpha)} \right], \quad (20)$$

where α is the void fraction, x is the flow quality.

The void fraction was estimated using the Butterworth equation [18];

$$\alpha = 1 / \left[1 + 0.28 \left(\frac{1-x}{x} \right)^{0.64} \left(\frac{\rho_v}{\rho_1} \right)^{0.36} \left(\frac{\mu_1}{\mu_v} \right)^{0.07} \right]. \quad (21)$$

The frictional pressure gradient has been calculated with the aid of the Lockhart-Martinelli parameters [4];

$$\Phi_v = \left(\left. \frac{dP}{dZ} \right|_{tp} / \left. \frac{dP}{dZ} \right|_v \right)^{1/2}, \quad (22)$$

and;

$$X_{tt} = \left(\left. \frac{dP}{dZ} \right|_l / \left. \frac{dP}{dZ} \right|_v \right)^{1/2}. \quad (23)$$

The single phase pressure gradient can be obtained as follows;

$$\left. \frac{dP}{dZ} \right|_{1,v} = \frac{(f\rho u^2)_{1,v}}{2D_e} \quad (24)$$

The validity of the pressure drop data has been checked by comparing the measured single phase friction factor with those published by Blasius [18];

$$f = 0.34 \text{Re}_{en}^{-0.25} \quad (25)$$

Where Reynolds number was based on the equivalent diameter of the annulus, D_{en} .

Our single phase data yielded a 10% mean deviation with the existing ones [6, 19].

The series of friction factor tests performed with pure refrigerants R-12, R-22 as well as non-azeotropic refrigerant mixtures R-22/R-114 and R-22/R-152a at various compositions have been correlated using the form proposed by Blasius [17] as follows;

$$f = 0.6 \text{Re}_{en}^{-0.21} \quad (26)$$

and

$$\text{Re}_{en} = \frac{GD_{en}}{\mu}$$

Figure 11 shows the measured friction factor of the doubly fluted tube plotted as a function of the Reynolds number and compared to those of smooth annuli calculated

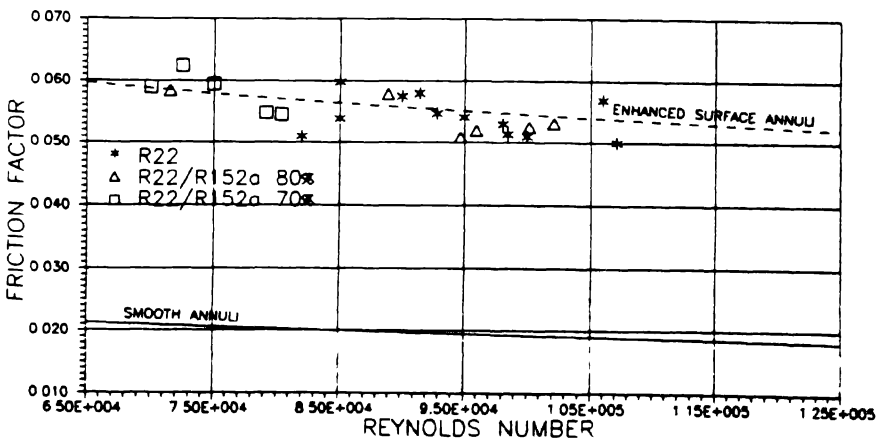


Fig. 11 Friction factor vs. Reynolds number for enhanced surface and smooth tube annulus.

by the Blassius equation. The present data were about three times as large as the smooth annuli values.

It has been reported by Honda et al. [6] that during forced convection condensation, the two phase flow multiplier can be calculated using the following expression established from experimental data with a mean absolute deviation of 7.3%;

$$\Phi_v = 1 + 1.8X_{II}^{0.9}. \quad (27)$$

The measured pressure drop data showed that the acceleration pressure drop gradient calculated by equations (20) and (21), is insignificant and accounted for less than 2% of the total pressure drop. Therefore, only the friction pressure drop is taken into consideration in this study. It was found that the experimental data of the two phase pressure drop of pure and non-azeotropic refrigerant mixtures can be correlated by the Lockhart-Martinelli parameters.

Figures 12 and 13 illustrate the comparison between the measured pressure drops and those calculated by the proposed correlation. It is quite clear from these figures that the proposed model was found to correlate the pressure drop data for pure and non-azeotropic refrigerant mixtures with a mean deviation of 30%.

It is worthwhile mentioning that the non-azeotropic refrigerant mixtures' pressure drop data showed that the ratio of the measured total two phase pressure drop to that calculated by the Lockhart-Martinelli model tended to be constant for a given

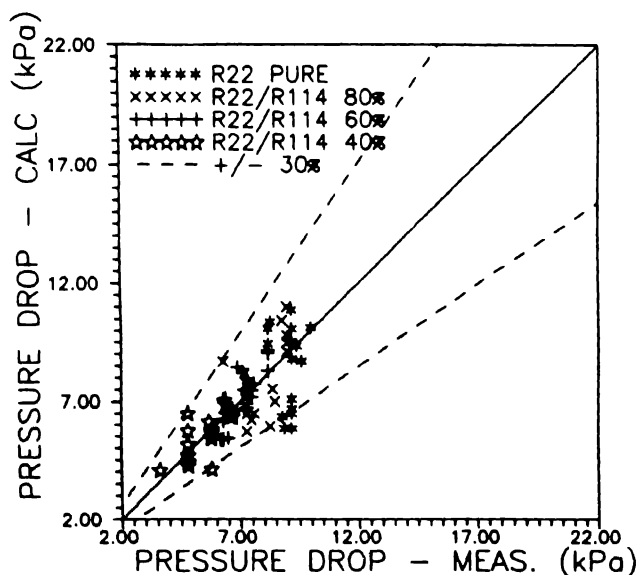


Fig. 12. Calculated vs. measured pressure drop for condenser

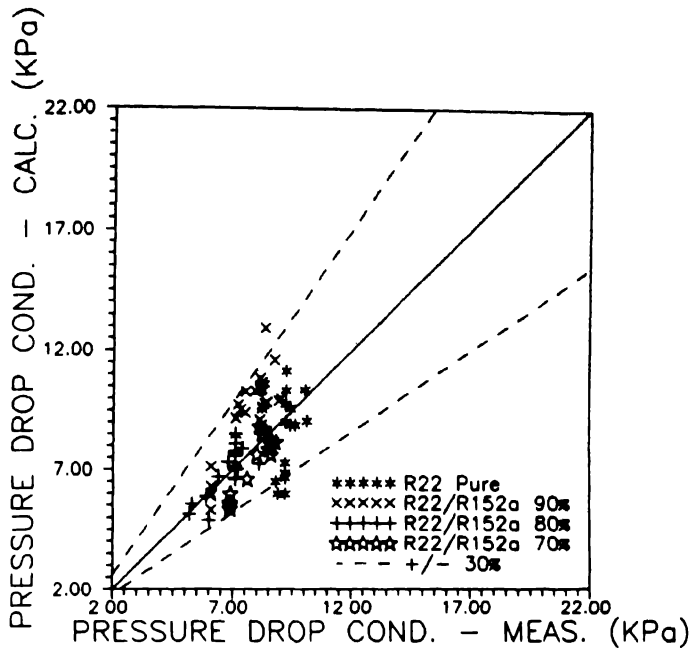


Fig 13 Calculated vs measured pressure drop for condenser

concentration, and has a weak function of the mixture compositions over the range investigated.

This finding is in agreement with the results published by Honda et al. [6] and Murphy et al. [20].

The authors are persuaded that the findings presented in this paper represent a significant contribution to our knowledge of the phenomena taking place during forced convective condensation of mixed refrigerants inside enhanced surface tubing.

It is believed that the proposed correlations for predicting the forced convective condensation characteristics are only applicable to fluted tube geometries presented hereby.

4. Conclusions

During the course of this experimental study, the behaviour of forced convective condensation of non-azeotropic refrigerant mixtures inside enhanced surface tubing has been investigated. Correlations have been proposed to predict the average heat transfer coefficient as well as pressure drop inside enhanced surface tubing. It has been found that the pressure drop of non-azeotropic refrigerant mixtures is a weak function of the mixture compositions.

5. Acknowledgment

The research work presented in this paper was possible through grants from N.B. Power and NSERC. The authors wish to acknowledge the continuous support of the Universities of Moncton and Cracow.

6. References

1. Gallagher, J.S., McLinden, M.O. and Morrison, G. Thermodynamic diagram for refrigerant mixtures. *ASHRAE Trans.*, Part 2 (1988) 2119.
2. Didion, D. and Bivens, D.B., The role of refrigerant mixtures as alternatives to CFCs. *Int. J. Refrigeration* 13 (1990) 163.
3. Sami, S.M., Non-azeotropic refrigerant mixtures potential substitutes for heat pumps, *Proceedings of the Int. Conf. on Heat Pumps in Cold Climates*, Moncton, Aug., (1990).
4. Stoeckor, W.F. and Kornota, E., Condensing coefficients when using refrigerant mixtures. *ASHRAE Trans.*, Part 2b, (1985).
5. Tandon, T.N., Varma, H.K. and Gupta, C.P., Generalized correlation for condensing of binary mixtures inside a horizontal tube. *Int. J. Refrigeration* 9 (1986).
6. Honda, H., Nozu, S., Matsuoka, Y. and Nakata, H. Condensation of R-11 and R-113 in the annuli of horizontal double-tube condensers with an enhanced inner tube. *Experimental Thermal and Fluid Science* 2 (1989) 173.
7. Koyama, S., Miyara, A., Takamatsu, H. and Fujii, T., Condensation heat transfer of binary refrigerant mixtures of R-22 and R-114 inside a horizontal tube with internal spiral grooves. *Int. J. Refrigeration* 13 (1990).
8. Morrison, G. and McLinden, M. Application of a hard sphere equation of state to refrigerants and refrigerant mixtures. *NBS Technical Note 1226*, NBS, Gaithersburg, Maryland (1986).
9. Reid, R.C., Prausnitz, J.M. and Poling, B.E. *The Properties of Gases and Liquids*, 4th edn. McGraw Hill, New York, (1987).
10. Khartabil, H.F., Christensen, R.W. and Richards, D.E. *A Modified Wilson Plot Technique for Determining Heat Transfer Correlations*, 2nd UK National Conference on Heat Transfer, 14–16 Sept. 1988, University of Strathclyde, Glasgow, Scotland, (1988).
11. Webb, R.L., Eckert, E.R.G. and Goldstein, R.J. Heat transfer and friction in tubes with repeated-ribs. *Int. J. Heat Mass Transfer*, 14 (1971) 601.
12. Richards, D.E., Grant, M.M. and Christensen, R.W. Turbulent flow and heat transfer inside doubly fluted tubes. *ASHRAE Trans.*, NT 87-21-4 (1987).
13. Collier, J.G. *Convective Boiling and Condensation*, 2nd edn. McGraw-Hill Book Co., New York, (1981).
14. Rosson, H.F. and Mayer, J.A., Point values of condensing film coefficient inside a horizontal tube, Heat transfer-Cleveland. *Chem. Engng. Prog. Symp. Series*, No. 59, 61 (1965) 190–199.
15. Traversi, D.P., Baron, A.B. and Rohsenow, W.M. *Forced Condensation inside Tubes*, Tech. Rept. No. 72591-74, MIT, Mass., Cambridge, (1971).
16. Fujii, T. and Nagata, T., *Condensation of Vapour in a Horizontal Tube*. Report of Research Institute of Industrial Science Kyushu University, 52 (1983) 35.
17. Kakac, S., Bergles, A.E. and Mayinger, F. *Heat Exchangers, Thermak-Hydraulic Fundamentals and Design*, Hemisphere Publishing Corp., McGraw-Hill (1981).
18. Butterworth, D. A comparison of some void fraction relations for co-current gas-liquid flow. *Int. J. Multiphase Flow* 1 (1975).
19. Kays, W.M., Perkins, H.C., Forced convection, internal flows in ducts, in *Handbook of Heat Transfer Fundamentals*, McGraw Hill, New York, (1985).
20. Murphy, R.W. et al., Condensing heat transfer of R-114 R-12 mixtures on horizontal finned tubes, *Int. J. Refrigeration* 11 (1988).

Collision dynamics of bubble pairs moving through a perfect liquid

J.B.W. KOK

Department of Thermal Engineering, University of Twente, P.O. Box 217, 7500 AE Enschede, The Netherlands

Received 7 November 1990; accepted in revised form 22 November 1991

Abstract. Equations are derived describing the inertial motion of a bubble pair through a perfect liquid. The relative bubble motion is driven by an interactional force induced by the centre of mass motion. This force can be derived from a potential that is proportional to s^n ($n \geq 3$) and that depends on the bubble pair orientation. The path of two bubbles passing each other is investigated. The angle of deflection of the relative velocity in a two-bubble encounter is calculated numerically as a function of the impact parameter, the relative velocity g and the ratio of the centre of mass velocity components c_2/c_1 . The specific conditions necessary for two bubbles to collide are determined. If $c_2/c_1 > 1$ there is a region with irregular behaviour of the deflection angle. The collision cross-section is calculated and depends smoothly on g , approximately proportional to g^{-1} , and has a weak dependence on c_2/c_1 .

Keywords: bubbles, interaction, scattering, deflection, collision, bouncing

1. Introduction

In mixtures of liquid and gas bubbles, interaction between the motions of the bubbles can be noticed at gas concentrations larger than 1%. Like the molecules in a gas the interaction is caused by scattering of the bubbles. Here binary scattering between bubbles will be discussed. Understanding of the collision dynamics of bubble pairs can lead to a better description of the behaviour of mixtures of gas bubbles and liquid. We think here of dilute mixtures with concentrations by volume of gas of about 1% to 10%. Using a statistical treatment as for example in kinetic gas theory [4], in plasma physics [19] or sedimentation [2], an equation for the distribution of the bubble positions and velocities can be derived from the microscale bubble dynamics. Solving this equation, effective properties of the bubbles, for example the effective added mass (as discussed in [13]), can be calculated. Here we will confine ourselves to the collision dynamics.

At the gas concentrations considered here, the interaction between the bubbles takes place for a major part via the hydrodynamic forces they exert on each other. Therefore this paper focusses on the deflection of the bubble paths due to hydrodynamic forces in a two-bubble encounter. Of course it is possible that in a number of encounters the bubbles actually collide. In order to calculate the deflection of the bubble paths in such an encounter with collision, the bouncing process has to be taken into account.

Until now, it is unknown what conditions are necessary in general for two bubbles to collide in an encounter. But there has been some research on what will happen if

two bubbles are certain to collide. For example for some specific situations, when the bubbles were on a central collision course, the flow in the gap between two bubbles very close to each other was investigated in [5].

One of the results aimed at by investigating the bubble path deflection due to hydrodynamic forces, is to determine the conditions necessary for collision. In combination with detailed analyses of the bouncing process this information will increase our knowledge of the behaviour of two interacting bubbles.

The hydrodynamic forces and the added mass of a pair of bubbles when they are in interaction are described in section 2. As a first approximation it will be assumed that the bubble motion is inertial. An analysis is made of the equations of motion for a scattering pair of bubbles. A comparison is made with the equations of motion of particles and vortex pairs.

In section 2 it will be shown that the hydrodynamic forces on the bubbles can be derived from a hydrodynamic potential field, in the inertial approximation. This potential field varies with the bubble separation s as s^{-p} with $p \geq 3$. It is interesting to make a comparison with the potential fields as encountered in classical kinetic gas theory and plasma physics:

potential field $\approx s^{-p}$: $p \geq 1$

Coulomb potential field: $p = 1$

hydrodynamic (bubbles) potential field: $p \geq 3$

Maxwell intermolecular potential field: $p = 4$

Lennard-Jones intermolecular potential field: $p \geq 6$

hard spheres intermolecular potential field: $p \rightarrow \infty$

This comparison shows that the range of the hydrodynamic forces in a bubbly mixture is intermediate between Coulomb forces in a plasma and intermolecular forces in a gas. This is of importance in the statistical treatment.

In section 3 it is described how the equations derived in section 2, determining the dynamics of a bubble pair, can be used to analyze the scattering process. When two bubbles touch in an encounter they will coalesce or bounce. The bouncing process is discussed in section 4. It is shown how the bouncing can be taken into account in the calculation of the deflection of the bubble paths in a binary collision.

The deflection of the relative bubble velocity in a binary collision was calculated and the results are described in section 5. These results are used to analyse the dynamics of the collision. The range of interaction as well as some irregularities related to the nonlinearity of the dynamics are discussed.

In section 6 the calculation of the collision cross-section, as defined by [4], from the angle of deflection is described. Unlike with Coulomb forces in plasma physics the integral, expressing the collision cross-section, is convergent in the case of interacting bubbles. This is thanks to the relatively short range character of the hydrodynamic forces. For that reason it is expected that a Fokker-Planck equation can be formulated to describe the evolution of the bubble distribution.

2. Equations of motion for a pair of bubbles moving through a perfect liquid

The motion of a pair of gas bubbles through a perfect and unbounded liquid is considered. The bubbles are assumed to be of equal volume and spherical. The viscosity of the gas is neglected. The bubbles have interaction through the hydrodynamic forces which they exert on each other. The dynamics of these bubbles is more complicated than the dynamics of a pair of molecules in a gas or an electron pair in a plasma. This is due to the coupling of the centre of mass motion to the relative motion of a bubble pair. A brief description of the equations of motion for a bubble pair will be given. A detailed discussion of the full equations of motion, taking into account viscous forces, can be found in [14, 15]. It is difficult to apply these complicated equations to a statistical analysis of the bubble motion. In [14, 15] it is shown that the viscous forces are of order Re^{-1} . As in most bubbly flows the Reynolds number (Re) is larger than 100, we can neglect these viscous forces in a first (inertial) approximation. Here we will study the much simpler (but not simple) inertial equations of motion. The inertial motion of the bubbles can serve as a start for the analysis of the scattering of gas bubbles moving through liquid.

The equations of motion are derived with the formalism of Lagrange:

$$\frac{d}{dt} \left(\frac{\partial T}{\partial \dot{q}^i} \right) - \frac{\partial T}{\partial q^i} = 0, \quad i = 1 \text{ to } 4 \quad (1)$$

with kinetic energy of the liquid T and bubble positions given by generalized coordinates q^i . Encounters between two bubbles will be considered in which the motion of the two bubbles is planar. In that case the bubble pair position is determined by four co-ordinates q^i .

The kinetic energy induced by the motion of the bubbles in the liquid is given by

$$T = \frac{1}{2} M a_{ij} \dot{q}^i \dot{q}^j, \quad i = 1 \text{ to } 4, j = 1 \text{ to } 4 \quad (2)$$

with mass M of the liquid displaced by a bubble and covariant components a_{ij} of the inertia tensor. In this paper the Einstein convention of summation is adopted. The position of the centre of mass of the bubble pair will be described by a cartesian co-ordinate system x, y and the relative position by polar co-ordinates s, θ (see Fig. 1). We take $q^1 = x, q^2 = y, q^3 = s, q^4 = \theta$. The co-ordinates x, y are at rest with respect to the liquid at infinity. In these co-ordinates the components a_{ij} of the inertia tensor can be calculated as polynomials in the ratio of (bubble radius)/(bubble separation): R/s . As we are interested here primarily in the dynamics of the bubble collision, I would like to refer to [15] for the calculation of the inertia tensor components a_{ij} . In the appendix the full results of these calculations are given for a_{ij} in the x, y, s, θ co-ordinate system. But for a qualitative understanding of the dynamics it is sufficient to consider terms of

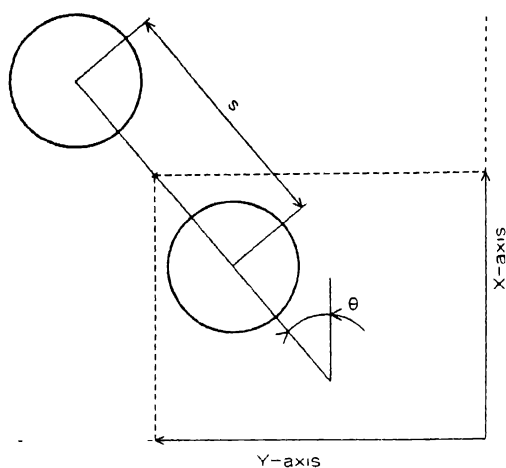


Fig 1 Co-ordinate systems for the two dimensional motion of two spherical bubbles

$O(1)$ and $O(R/s)^3$. These first two terms of the components a_{ij} of the inertia tensor are in the x, y, s, θ co-ordinate system:

$$\begin{aligned}
 a_{11} &= 1 + \frac{3}{2}(1 - 3 \cos^2 \theta) \left(\frac{R}{s} \right)^3 + \dots, \\
 a_{22} &= 1 + \frac{3}{2}(1 - 3 \sin^2 \theta) \left(\frac{R}{s} \right)^3 + \dots, \\
 a_{12} &= a_{21} = -\frac{9}{4} \sin 2\theta \left(\frac{R}{s} \right)^3 + \dots, \\
 a_{33} &= \frac{1}{4} \left(1 + 3 \left(\frac{R}{s} \right)^3 \right) + \dots, \\
 a_{44} &= \frac{1}{4} \left(1 - \frac{3}{2} \left(\frac{R}{s} \right)^3 \right) s^2 + \dots.
 \end{aligned} \tag{3}$$

The third term of the components a_{ij} , not written down in Eq. 3, is of order $(R/s)^6$. In the numerical calculations in section 5, where the components a_{ij} were calculated with accuracy $O(R/s)^{50}$, it was found that the higher order terms $O(R/s)^6$ to $O(R/s)^{50}$, resulted in only small corrections to the bubble paths. In Eq. 3 we see that the components a_{ij} depend on s, θ . With Eq. 1 we will show that for this reason centre of mass motion and relative motion are coupled. With Eqs 1 and 2 the following conservation laws for the centre of mass motion are found:

$$\begin{aligned}
 M(a_{11}(s, \theta)\dot{x} + a_{12}(s, \theta)\dot{y}) &= Mc_1, \\
 M(a_{12}(s, \theta)\dot{x} + a_{22}(s, \theta)\dot{y}) &= Mc_2
 \end{aligned} \tag{4}$$

with constants c_1, c_2 . We see in Eq. 4 that there is interaction of the centre of mass motion with the relative motion because $a_{ij} = a_{ij}(s, \theta)$. If s, θ change, there is also a change in $a_{ij}(s, \theta)$ that will have to be compensated by changes in \dot{x}, \dot{y} . In fact in Eqs 4 it is stated that the impulse of the liquid (as introduced by Lamb [16]) is conserved (see [14, 15]). Taking $s \rightarrow \infty$ we find with Eq. 3 that c_1, c_2 represent the velocities \dot{x}, \dot{y} when the bubbles are far apart. Using Eq. 4 the centre of mass velocities \dot{x}, \dot{y} can be eliminated from the expression for the kinetic energy (2). For the kinetic energy of the liquid is then obtained:

$$T = \frac{1}{2} M \{ \dot{s}^2 a_{33}(s) + \dot{\theta}^2 a_{44}(s) + \phi(s, \theta) \}. \quad (5)$$

Here $\phi(s, \theta)$ is a complicated expression depending on s, θ and quadratic in c_1, c_2 . To give an idea, in Eq. 6 the first two terms of $\phi(s, \theta)$, $O(1)$ and $O(R/s)^3$ respectively, are written down. In the numerical calculations in section 5 also the higher order terms of $\phi(s, \theta)$, $O(R/s)^6$ to $O(R/s)^{50}$, were taken into account.

$$\begin{aligned} \phi(s, \theta) = & c_1^2 + c_2^2 \\ & + \frac{3}{2} \left(\frac{R}{s} \right)^3 [(3 \cos^2 \theta - 1) c_1^2 + (3 \sin^2 \theta - 1) c_2^2 + 3 \sin 2\theta c_1 c_2] + \dots \end{aligned} \quad (6)$$

Similar to the case of two vortex pairs the phase space of two bubbles in a perfect liquid is reduced to four dimensions, but free parameters c_1, c_2 are introduced that determine the overall liquid impulse (see [1, 7]).

Combining Eqs 1 and 5 the following equations of motion for a pair of bubbles in hydrodynamic interaction in a perfect liquid are found:

$$\frac{d}{dt} (\dot{s} a_{33}(s)) = \frac{1}{2} \dot{s}^2 \frac{d}{ds} a_{33}(s) + \frac{1}{2} \dot{\theta}^2 \frac{d}{ds} a_{44}(s) + \frac{1}{2} \frac{\partial}{\partial s} \phi(s, \theta), \quad (7)$$

$$\frac{d}{dt} (\dot{\theta} a_{44}(s)) = \frac{1}{2} \frac{\partial}{\partial \theta} \phi(s, \theta). \quad (8)$$

From Eqs 7, 8 we can conclude that $\phi(s, \theta)$ in Eq. 5 can be interpreted as a potential term. This because the associated forces in Eqs 7, 8 are a gradient of $\phi(s, \theta)$. In Eq. 8 we see that due to the angular dependence of the potential field ϕ the forces on the bubbles are not central and the angular momentum $a_{44}(s)d\theta/dt$ is not conserved. For this reason an analytic solution of the full Eqs. 7, 8 is hard to find. In [22] a simplified version of Eq. 7 was solved analytically. Eq. 8 was eliminated by taking θ constant and equal to $\pi/2$ in all instances. This was used in a statistical calculation of the bubble concentration diffusion coefficient. In the analysis presented here the full Eqs 7 and 8 will be solved numerically.

3. Deflection of the bubble paths in an encounter of two bubbles

The relative motion of a bubble (2) with respect to a bubble (1), as depicted in Fig. 2, is investigated. Initially the bubbles are far apart (for example several bubble diameters) and do not have interaction. Bubble (2) approaches bubble (1) along a straight line with velocity \mathbf{g} . The spacing between this line and the line belonging to a head-on collision is b , the impact parameter. The x -axis is chosen such that it is aligned with the initial relative velocity \mathbf{g} . After the two-bubble encounter b and \mathbf{g} have changed to b' , \mathbf{g}' respectively, due to interaction. With Eqs 5 and 7 we see that the magnitude of \mathbf{g} is conserved: $g = g'$. But \mathbf{g} is deflected by an angle denoted with χ . The angular momentum is not conserved in an encounter: $bg \neq b'g'$. Therefore we have a change in the impact parameter in an encounter: $b \neq b'$. The dependence of χ on the initial conditions is investigated by calculation of the bubble paths for various values of g , b and c_1, c_2 .

The bubble paths are determined by four first-order nonlinear ordinary differential equations formulated in Eqs 7, 8. In these equations s, b were made dimensionless with R , velocities \dot{s}, g, c_1, c_2 with c_1 and time with R/c_1 . In the hydrodynamic potential ϕ the ratio of the centre of mass velocities c_2/c_1 occurs as a free parameter. We take $\tan(\gamma) = c_2/c_1$. The angle of deflection χ is calculated as a function of g, b, γ by numerical integration of the set of four first order differential equations. The relative velocity g and the impact parameter b were varied from 0.004 to 12 and from 0.05 to 30 respectively in 20 steps. The parameter γ was varied from 0° to 85° in steps of 5° .

4. Bouncing bubbles

There is a chance that the bubbles will actually collide in an encounter. In such a collision the bubbles will coalesce or bounce, depending on the circumstances. It is not the aim of the present analysis to describe this bouncing process in great detail. But when in a simulation of the bubble paths the bubbles actually collide, it is necessary to

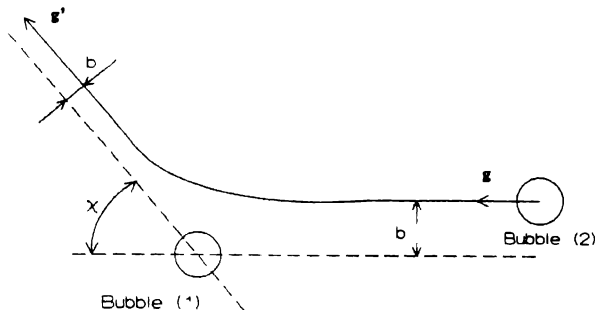


Fig. 2 Path of bubble (2) relative to bubble (1).

know what the direction and magnitude is of their relative velocity immediately after the collision.

For simplicity it will be assumed in all simulations that the bubbles bounce if they touch. It will now be investigated under what conditions the bubbles will bounce and how this bouncing can be described by a bouncing model that is simple and still fairly accurate.

There is some literature available describing the bouncing/coalescence of two bubbles. Well known is [18], presenting a theory of coalescence based on the change in thermodynamic surface potential due to solutes. This theory was however found to be in conflict with experimental results on the rate of coalescence in aqueous solutions of electrolytes in a bubble column ([17]).

In [5] bubble coalescence in pure liquids was studied. A set of partial differential equations describing the flow in the film separating the bubbles and the bubble deformation, was formulated. Subsequently these equations were solved numerically for several cases. In [5] it is suggested that during coalescence there are two processes in competition:

- (a) The liquid between the bubbles is squeezed out, accompanied by a flattening and even dimpling of the bubble surfaces. When the residual film reaches thicknesses of order 100Å, Van der Waals pressures become dominant. The film is rapidly ruptured and the bubbles coalesce.
- (b) The deformation of the bubbles increases their surface area and hence the free energy of the system at the expense of the kinetic energy associated with the relative motion. The bubbles therefore decelerate and bounce apart if (a) is not yet completed.

Assuming that in the bouncing/coalescence process energy is conserved, it can be stated that coalescence only occurs when the increase in potential energy of the two-bubble system is smaller than the relative kinetic energy. In a pure liquid the increase in potential energy is due to the increase in bubble surface area. In [5] it was shown that this potential energy at the instant of coalescence approximately is, given by:

$$\begin{aligned}
 R &= \text{bubble radius,} \\
 \sigma \Delta S &= \sigma 4\pi R^2 We^2 / 16 \quad \text{with } We = \rho \dot{S}^2 R / \sigma, \\
 \rho &= \text{liquid density,} \\
 \sigma &= \text{surface tension.}
 \end{aligned} \tag{9}$$

The kinetic energy associated with the relative motion is given by the term associated with co-ordinate $q^3 = s$ in Eq. 2:

$$T_{kin} = \frac{1}{2} Ma_{33} \dot{s}^2, \tag{10}$$

Coalescence occurs when the potential energy in Eq. 9 is smaller than the kinetic

energy in Eq. 10. In other words, it can be calculated from Eqs 9, 10, that bouncing occurs when $We > 4a_{33}/3$ (approximately $We > 0.33$). In this paper the bubbles are assumed to be spherical. In that case $We \ll 1$ and the bubbles will always coalesce. This was confirmed by experiments conducted by the author ([15]). Two bubbles of well known and exactly the same size (diameter 1.0 mm) were released in highly purified water. Their path was observed with multiple exposure photographic techniques. In pure water the bubbles always coalesced in a collision.

From the above it can be concluded that spherical bubbles will only bounce in water contaminated with surfactant.

In the literature several mechanisms are proposed that inhibit bubble coalescence in water contaminated with surface-active solutes. One of the mechanisms that is proposed is that coalescence is inhibited because short range repulsive forces are introduced. This leads to new terms in expression (9). In [12] the mechanism of coalescence inhibition by organic solutes is described as follows. Organic solute molecules consist of a hydrophilic group (for example $-\text{OH}$, $-\text{COOH}$) and a hydrophobic part (hydrocarbon structural group). Molecules of this type are surface-active which means that they will be enriched in the gas-liquid interface. On the liquid side of the interface the surface-active molecules will tend to form a monolayer whose stability depends on type, concentration, and size of the surface-active molecules. These molecules are pointing with their hydrophilic group into the water and with their hydrophobic group into the gas phase. On account of this orientation the liquid surface around gas bubbles will be electrically charged. This surface polarization will produce repulsive forces when two bubbles are coming very close to each other. These repulsive forces will add extra potential energy terms to Eq. 9.

Other coalescence inhibiting mechanisms that are forwarded are for example the effect of a gradient of the surface tension at the bubble surface due to convection [6]. It is however beyond the scope of the paper to discuss this.

In the experiments with a bubble column described in [12] it was found that at concentrations of $3 \times 10^{-3} \text{ mol/m}^3$ of *n*-octanol coalescence restraining becomes significant. This is in line with the experiments in [15] where it was found that the transition from coalescence to bouncing of two bubbles rising in contaminated water takes place between a concentration of 10^{-4} and 10^{-2} mol/m^3 of $\text{C}_{12}\text{H}_{25}(\text{OCH}_2\text{CH}_2)_4\text{OH}$.

It can be concluded that low levels of contamination are sufficient to have bubbles that will bounce. In a range of these low levels of contamination the boundary conditions at the bubble surface will still correspond with good approximation to those in a perfect liquid. Hence the theory derived in the preceding sections is still applicable.

In general, bouncing of two bubbles is a complicated process. The actual bouncing process however takes place at a very small timescale ([5, 6]) compared to the time the bubbles need to approach each other. The time scale of the actual bouncing process will be of the order of magnitude of the time scale of single-bubble volume oscillations: $(\rho R^3/\sigma)^{1/2}$, while the time scale of approach is given by R/g . The ratio of bouncing time

scale to approaching time scale is thus given by $(\rho R g^2 / \sigma)^{1/2} = (We)^{1/2}$. As remarked in the case of spherical bubbles $We \ll 1$ and hence the bouncing/approaching time ratio is small. Due to this relatively small time scale of the bouncing process and the assumption of energy conservation, the bouncing process can be taken as an elastic hard sphere collision in a first approximation. This is incorporated in the numerical integration routine by a change in sign of \dot{s} from negative to positive when the bubbles almost touch. After the bouncing the bubbles will escape from each other and go off to infinity.

It is possible that on some occasions the bubbles bounce several times before escaping from each other. Therefore the number of collisions (0, 1, 2, ...) in each encounter is recorded. The range of initial conditions where multiple collisions occur is probably small. It deserves however deeper investigation in future for in this region bubbles are for longer periods close together and then viscous forces may influence the collision process.

5. Calculated deflection of the bubble paths in an encounter

The angle of deflection χ and the number of collisions (encounters with bouncing) in an encounter of two bubbles were calculated as a function of g , b and γ . For each set of initial conditions g , b , γ the bubble paths were obtained by numerical integration of the Eqs 7 and 8. In case the bubbles touched the calculation process was continued as if a hard sphere collision had taken place (as described in section 4).

The recorded number of collisions (bouncings) as a function of b and g is depicted in Figs 3a to 3c for $\gamma = 0^\circ$, $\gamma = 40^\circ$ and $\gamma = 45^\circ$ respectively. At small values of γ , for example $\gamma = 0^\circ$ (Fig. 3a), the bubbles bounce only in a small region with $b < 2$ and $g > 0.6$. They bounce one time only. Apparently for small values of γ the bubbles tend to avoid a collision, even if the impact parameter is very small ($b \ll 2$).

At a value of $\gamma \approx 40^\circ$ a new (second) bouncing region is introduced for $b < 1$ and $g < 0.1$, with a different bouncing behaviour (see Fig. 3b with $\gamma = 40^\circ$). In this region the number of collisions is high, with a sensitive dependence on b, g . Apparently the bubbles bounce several times before they can escape from each other. At values of γ larger than 40° , see for example Fig. 3c with $\gamma = 45^\circ$, the bubbles bounce in a large region at $b < 3$, irrespective of g . There are sharp peaks in the number of collisions near the transition region, from bouncing to not bouncing, at small values of g : $g < 0.1$. We conclude: if γ is larger than 40° the bubbles have an interactional force driving them to collide.

Now the results concerning the deflection angle χ will be discussed. In Figs 4a to 4d the calculated value of $\cos(\chi)$ as a function of b and g is presented for $\gamma = 0^\circ$, $\gamma = 15^\circ$, $\gamma = 40^\circ$ and $\gamma = 45^\circ$ respectively. We see that in all cases $\cos(\chi) \cong 1$ at impact parameters larger than about 6 to 8. At these impact parameters the relative velocity g has to be decreased to a value less than 0.02 in order to observe deflection. Therefore the important conclusion can be drawn that (at not too low relative velocities) only

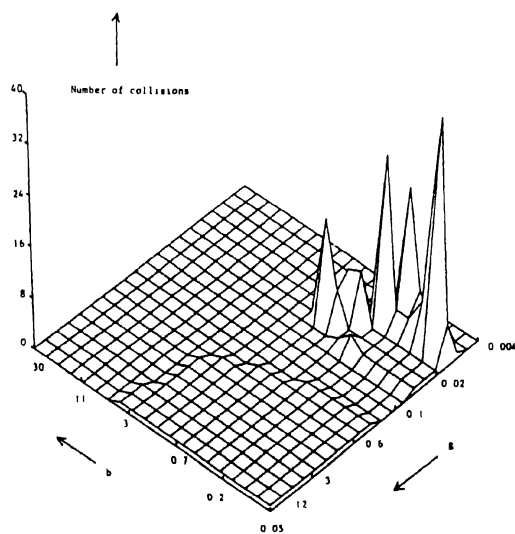
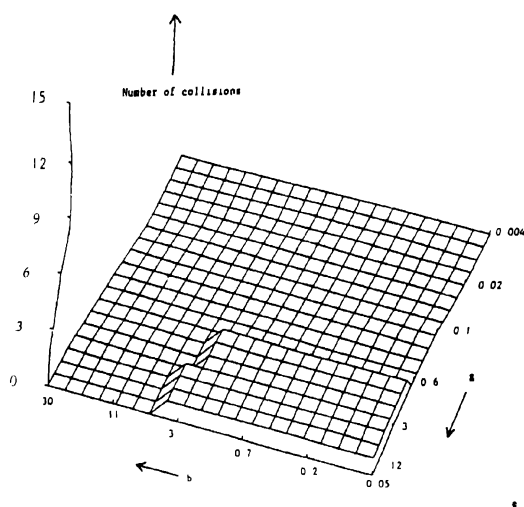
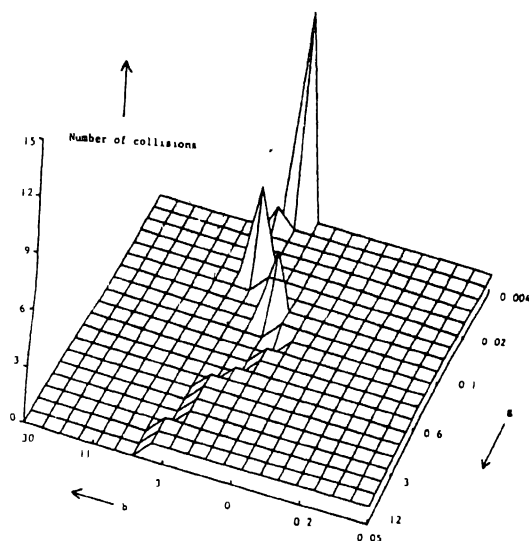


Fig 3 Recorded number of collisions with bouncing as a function of h and g (a) $\gamma = 0^\circ$, (b) $\gamma = 40^\circ$, (c) $\gamma = 45^\circ$



bubble pairs with impact parameter smaller than 6 to 8 are interesting, because only they have hydrodynamic interaction. We can translate this criterion for hydrodynamic interaction to an estimate of the local gas concentration by volume α with $\alpha \approx 4\pi/(3b^3)$. This results in the conclusion that hydrodynamic interaction becomes important if $\alpha > 0.8\%$ to 1.9% ($b = 6$ to 8). This is in line with the remark in section 1 that hydrodynamic interaction can be noticed at gas concentrations larger than 1% .

It can also be observed that if $b < 8$ the variation of $\cos(\chi)$ with the impact parameter b depends on γ . At $\gamma = 0^\circ$ and $\gamma = 15^\circ$ (Figs 4a, 4b) we see a very smooth dependence of $\cos(\chi)$ on b, g , even in the region $b < 2, g > 0.6$ where bouncing occurs. This situation changes at $\gamma = 40^\circ$. From Fig. 3b it was concluded that at $\gamma = 40^\circ$ a new region of bouncing is introduced for $b < 1$ and $g < 0.1$, different in character. Fig. 4c with $\gamma = 40^\circ$ shows that in this bouncing region there is a very sensitive dependence of $\cos(\chi)$ on b, g . When γ is increased further (see Fig. 4d, $\gamma = 45^\circ$) this "irregular scattering region" ([7]) shifts to larger values of b and g .

This sensitive dependence on initial conditions might be an indication for chaotic behaviour of the nonlinear differential Eqs 7, 8 in a limited range of initial conditions. It is possible to investigate this by the calculation of a so-called "scattering map" ([11]). The scattering map could show us in more detail in what range of b, g the bouncing of bubbles becomes a very complicated (chaotic) process. From a point of view of nonlinear dynamics this is interesting, but for a derivation of a Fokker-Planck equation the irregular scattering is not relevant for the statistical treatment ([8]). We will see in the next section that the irregular behaviour of the deflection angle does not result in irregular behaviour of the collision integral.

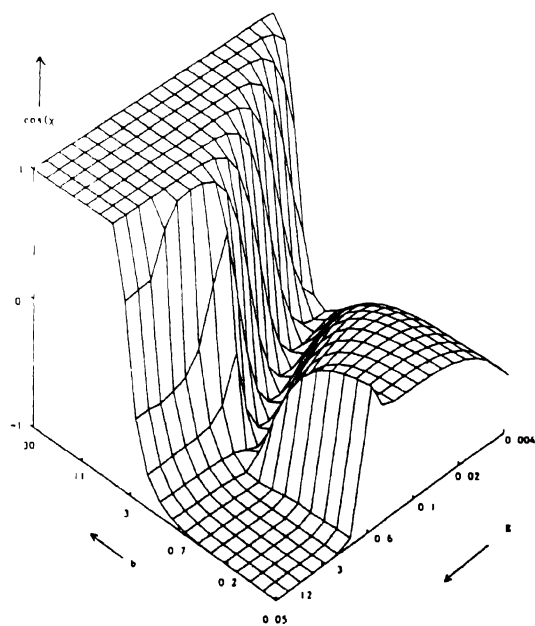
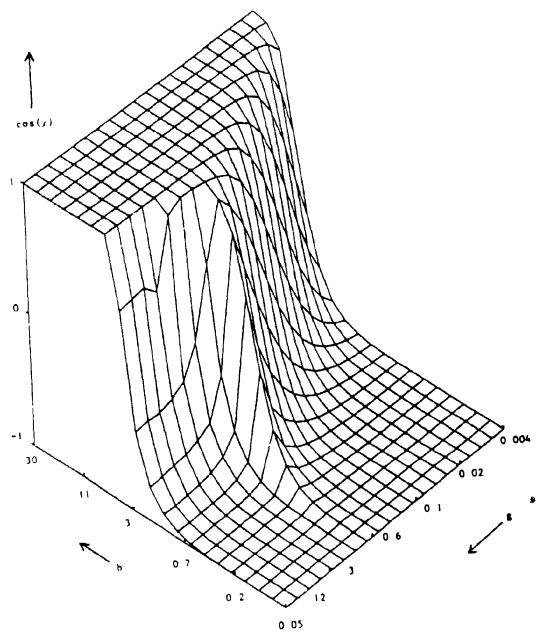
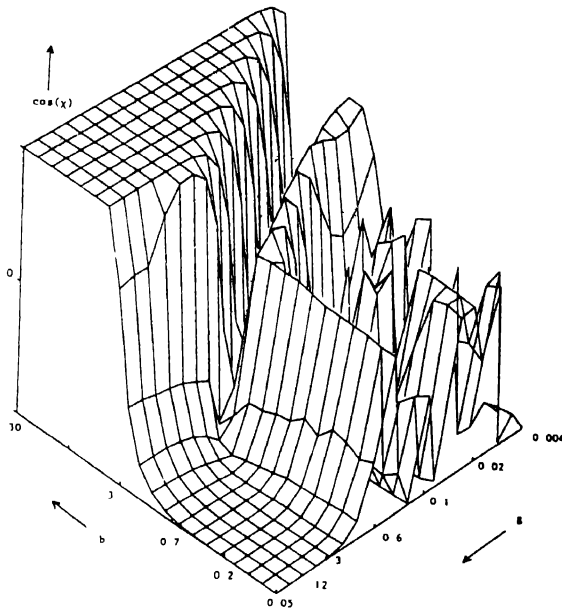


Fig 4 Deflection angle χ as a function of h and q (a) ; $= 0^\circ$ (b) ; $= 15^\circ$, (c) ; $= 40^\circ$, (d) , $= 45^\circ$



f

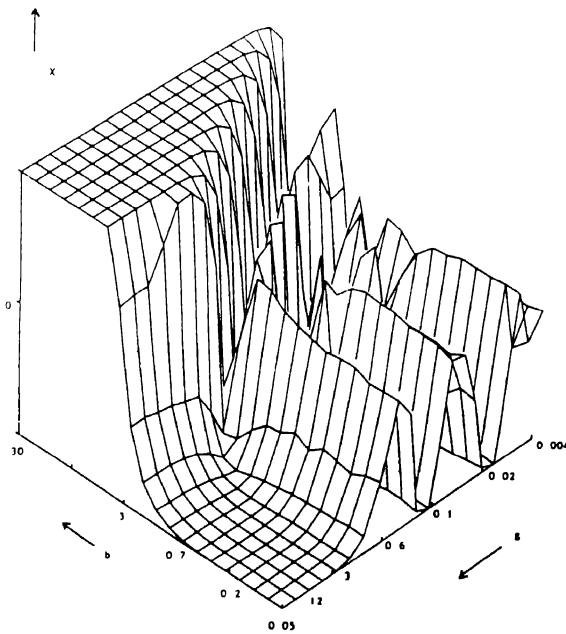


Fig 4 (cont)

6. Collision cross-section of two colliding bubbles

In the previous section the angle of deflection χ as a function of the relative velocity g , the impact parameter b and the ratio of the centre of mass velocities $\tan(\gamma)$ of a colliding bubble pair was calculated. Knowledge of the dependence of χ on b, g, γ can be used to calculate the collision cross-section of the two bubbles. In the classical kinetic gas theory from this collision cross-section the coefficients of viscosity and heat conductivity are obtained (see [3, 4, 10]). In plasma physics the collision cross-section occurs in the integral expressions for the coefficients of the Fokker-Planck equation (see [19, 20, 21]). In the introductory section it was suggested that a Fokker-Planck type of equation might apply as well for dilute mixtures of bubbles and liquid. Another interesting point is that in classical molecular dynamics, in plasma particle dynamics and in bubble dynamics the potential field varies as s^{-p} . But in bubble dynamics there is also an angular dependence. In view of these two points a calculation of the collision cross-section of two bubbles seems to be very interesting. The collision cross-section is defined by

$$S^1 = 2\pi \int_0^{\infty} (1 - \cos^1 \chi) b db, \quad 1 = 1, 2 \quad (11)$$

In the case of molecules in a gas colliding as hard spheres S^1 is simply the cross-section of the molecules:

$$\begin{aligned} S^1 &= \pi R^2, \\ S^2 &= \frac{4}{3} \pi R^2. \end{aligned} \quad (12)$$

If the interparticle potential field varies as

$$\phi = K s^{-p}, \quad (13)$$

with constant K and $p \geq 1$, the collision cross-section can be shown to vary as ([4, 21]):

$$S^1 = c(K, p) g^{-n}, \quad \text{with } n = \frac{p-1}{p} \quad (14)$$

In Eq. 14 $c(K, p)$ is a dimensionless integral of order unity if $p > 1$. At $p = 1$ (Coulomb potential field) the integral for $c(K, p)$ diverges however. For this reason in the case of Coulomb interaction the range of the potential field has to be cut off by introducing a Debye length of interaction ([9, 20]). In the case of bubbles in a hydrodynamic

potential field $p \geq 3$ and the range of interaction is short compared to Coulomb forces. Therefore in the case of bubbles the integrals in Eq. 11 are convergent without introducing an artificial cut-off.

Using the results for $\chi(b, g, \gamma)$ in section 5 the integral in Eq. 11 giving S^1 was evaluated numerically. The results are shown in Figs 5a, 5b and 5c. Here S^1 is shown as a function of g and γ : $S^1(g, \gamma)$. In Fig. 5a an overall view is given. We see clearly a dependence on the relative velocity g approximately as g^{-1} . This is in line with Eq. 14 for a simple not angular dependent potential field. There is only a weak dependence on γ . In Fig. 5b the region of large g is considered. In the region $\gamma < 40^\circ$ there is a minimum of the cross-section for $g \cong 1$. At larger values of γ this minimum has disappeared. The behaviour at moderate relative velocities g is shown in Fig. 5c. We see a very smooth dependence of S^1 on g and γ , qualitatively very well in line with Eq. 14. There is only a minor dependence on γ . This is a very interesting observation because the dynamics of the bubbles, and hence χ , does depend very much on γ . Another interesting point is that S^1 is smooth in spite of the regions of irregular scattering and in spite of the very simple description of the bouncing of the bubbles. Apparently this does not lead to irregularities in the collision cross-section.

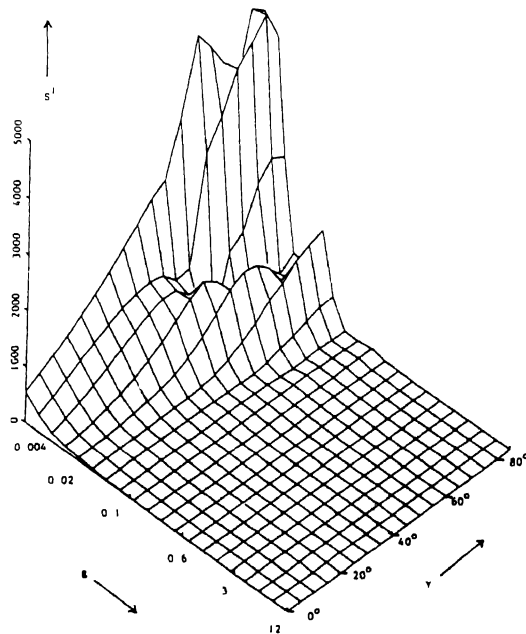


Fig. 5. Collision cross-section S^1 as a function of g and γ . (a) overall view; (b) region of moderate g ; (c) region of large g

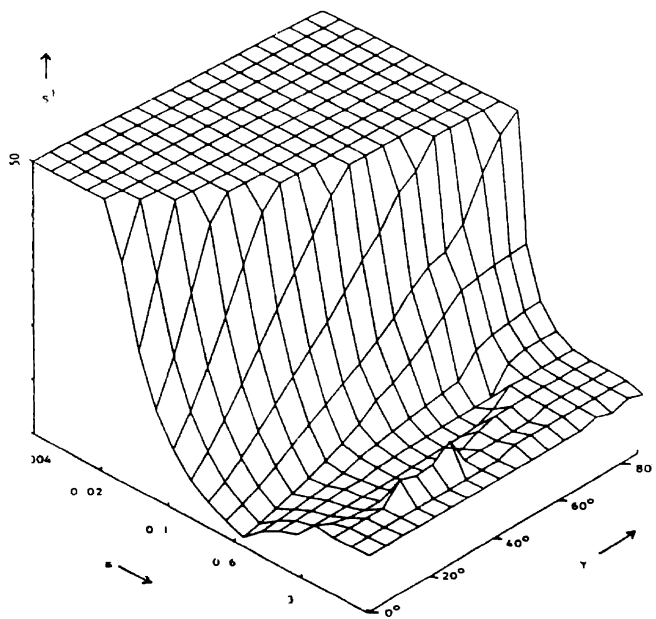
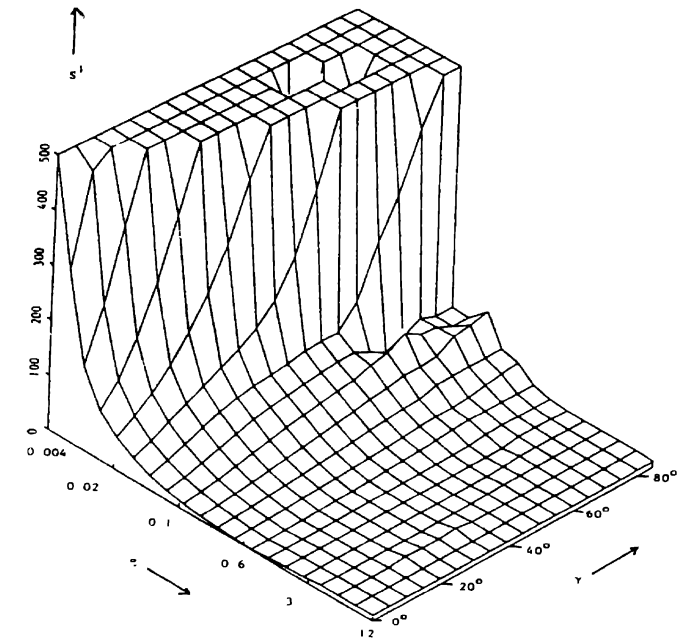


Fig 5 (Cont)

7. Conclusion

The inertial motion of pairs of gas bubbles in a dilute mixture of gas bubbles and liquid is investigated. New elements are that the components of the inertia tensor depend on the bubble separation (s) and that the centre of mass motion induces an interactional force between the bubbles. This force can be derived from a potential that depends on the bubble pair orientation and that is proportional to s^{-p} ($p \geq 3$). The angle of deflection of the relative velocity in a two-bubble encounter is calculated as a function of the impact parameter b , the relative velocity g and the ratio of the centre of mass velocities c_2/c_1 .

At impact parameters smaller than 6 to 8 the bubbles can be noticed to have interaction. If the centre of mass velocity is aligned with the relative velocity ($c_2/c_1 \ll 1$) the interaction is such that the bubbles avoid a collision in most cases. Increasing the ratio of the centre of mass velocities to $c_2/c_1 > 1$ two phenomena appear. The bubble interaction will now cause the bubbles to collide when they are close to each other. There occurs irregular behaviour of the deflection angle for $b < 1$ and $g < 1$. This irregular behaviour of the deflection angle is accompanied by the phenomenon that the bubbles bounce several times in an encounter. This leads to the conclusion that the irregular behaviour of the deflection angle is related to the transition from attraction to repulsion of the interactional force.

In order to investigate the possibility to use a statistical treatment such as the Fokker-Planck equation, the collision cross-section is calculated. The collision integral is found to be convergent and depends smoothly on the relative collision velocity g , approximately proportional to g^{-1} . There is only a weak dependence of the collision integral on c_2/c_1 . Hence the irregular behaviour of the deflection angle does not result in irregular behaviour of the collision integral. Also the efficient, but simple, hard sphere treatment of bouncing bubbles does not lead to peculiar behaviour in the collision integral. The above suggests that it is possible to derive a Fokker-Planck equation for the distribution of gas bubbles in a bubbly flow.

Appendix

Equations of motion were derived in section 2 from the kinetic energy by means of the formalism of Lagrange. Here the calculation of the kinetic energy will be sketched and the main results will be given.

The kinetic energy induced by the bubbles in the liquid is given by the expression (see [13, 15]):

$$T = \frac{1}{2} M a_{ij} \dot{q}^i \dot{q}^j = -\frac{1}{2} \sum_{i=1}^2 \mathbf{v}_i \cdot \int_{A_i} \rho_1 \Phi \, d\mathbf{A}, \quad (\text{A1})$$

where the integration is over the surface A_i of bubble i and $d\mathbf{A}$ is a surface element

directed normal to the bubble surface. The velocity of the i th bubble is v_i and ρ_l is the liquid density. The velocity potential Φ describes the velocity field around the bubble pair and can be found in [13, 15]. The mass of liquid displaced by a bubble is M , a_{ij} are components of the inertia tensor and q^i is the generalized velocity of the bubble pair in the i th direction. Substitution of the velocity potential and evaluation of the surface integrals in (A1) gives after some calculation an expression quadratic in the bubble velocities for a bubble pair in three dimensional motion. Here we are interested in the inertia tensor components a_{ij} of a bubble pair in two dimensional motion in the x, y, z, θ co-ordinate system. In that case the components a_{ij} are

$$a_{11} = -2 + 3(g_{01} - g_{11}) + 3(q_{01} + q_{11})\cos(2\theta), \quad (\text{A2})$$

$$a_{22} = -2 + 3(g_{01} - g_{11}) - 3(q_{01} + q_{11})\cos(2\theta), \quad (\text{A3})$$

$$a_{21} = a_{12} = 3(g_{01} + g_{11})\sin(2\theta), \quad (\text{A4})$$

$$a_{33} = \frac{1}{2}(-1 + 3f_{01}), \quad (\text{A5})$$

$$a_{44} = \frac{1}{2}(-1 - 3f_{11})s^2 \quad (\text{A6})$$

In Eqs A2 to A6 f_{mn} and g_{mn} are series in R/s given by

$$f_{mn} = \frac{1}{2} \sum_{p=0}^{\infty} L_{mnp} \left(\frac{R}{s}\right)^p, \quad m = 0, 1, n = 0, 1 \quad (\text{A7})$$

$$g_{mn} = \frac{1}{2} \sum_{p=0}^{\infty} K_{mnp} \left(\frac{R}{s}\right)^p, \quad m = 0, 1, n = 0, 1 \quad (\text{A8})$$

with

$$K_{mn0} = (-1)^m \delta_{1n} \quad (\text{A9})$$

$$K_{mnp} = (-1)^{m-1} \frac{n}{n+1} \sum_{q=1}^{2(p-n-3)} \binom{n+q}{n+m} K_{mq(p-q-m-1)}, \quad p \geq 1 \quad (\text{A10})$$

and

$$L_{mn0} = (-1)^m \delta_{1n} \quad (\text{A11})$$

$$L_{mnp} = (-1)^m \frac{n}{n+1} \sum_{q=1}^{2(p-n-3)} \binom{n+q}{n+m} L_{mq(p-q-m-1)}, \quad p \geq 1 \quad (\text{A12})$$

The coefficients K_{m1p} and L_{m1p} occurring in f_{m1} and g_{m1} can be calculated from Eqs A9 to A12. In the numerical calculations described in section 5 coefficients were taken

to account up to $p = 50$. It appeared however that the coefficients with $p \geq 6$ contributed little to the results in most cases. In the table below the coefficients K_{m1p} , L_{m1p} are shown up to $p = 10$.

p	0	1	2	3	4	5	6	7	8	9	10
K_{01p}	1	0	0	-1	0	0	1	0	3	-1	6
L_{01p}	1	0	0	1	0	0	1	0	3	1	6
K_{11p}	-1	0	0	-0.5	0	0	-0.25	0	-1	-0.125	-2.25
L_{11p}	-1	0	0	0.5	0	0	-0.25	0	-1	0.125	-2.25

Acknowledgements

The author would like to thank Prof. L. van Wijngaarden, Prof. F.W. Wiegel and Dr R. Pasmanter (K.N.M.I.) for their stimulating interest in bubble dynamics.

References

1. Aref, H., Integrable, chaotic and turbulent vortex motion in two-dimensional flows. *Ann. Rev. Fluid Mech.* 15 (1983) 345-389.
2. Batchelor, G.K. and Green, J.T., The determination of the bulk stress in a suspension of spherical particles to order c^2 . *J. Fluid Mech.* 56 (1972) 401-427.
3. De Boer, J. and Van Kranendonk, J., The viscosity and heat conductivity of gases with central intermolecular forces. *Physica* 14 (1948) 442-452.
4. Chapman, S. and Cowling, T.G., *The Mathematical Theory of Non-Uniform Gases*. Cambridge University Press, Cambridge, (1970).
5. Chesters, A.K. and Hofman, G., Bubble coalescence in pure liquids. *Appl. Sci. Res.* 38 (1982) 353-361.
6. Chesters, A.K., Eindhoven Univ. Techn. NL, private communication.
7. Eckhardt, B., Irregular scattering of vortex pairs. *Europhys. Lett.* (1988).
8. Eckhardt, B., Institut für Festkörperforschung der Kernforschungsanlage Jülich FRG, private communication.
9. Gasiorowicz, S., Neuman, M. and Riddell Jr., R.J., Dynamics of ionized media. *Phys. Rev.* 101 (1956) 922-934.
10. Hirschfelder, J.O., Curtiss, Ch.F. and Bird, R.B., *Molecular Theory of Gases and Liquids*. Wiley, New York (1964).
11. Jung, C., Poincaré map for scattering states. *J. Phys. A: Math. Gen.* 19 (1986) 1345-1353.
12. Keitel, G., Oaken, U., Inhibition of bubble coalescence by solutes in air/water dispersions. *Chem. Eng. Sc.* 37 (1982) 1635-1638.
13. Kok, J.B.W., Kinetic energy and added mass of hydrodynamically interacting gas bubbles in liquid. *Physica* 148 A (1988) 240-252.
14. Kok, J.B.W., Hydrodynamic equations and effective properties of bubbly flows. In: Afgan, N., *Proc. Int. Congr. on Transient Phenomena in Multiphase Flow*, Hemisphere, Washington (1988) 127-136.
15. Kok, J.B.W., Dynamics of gas bubbles moving through liquid, Ph.D.-thesis, University of Twente, Enschede (1989).
16. Lamb, H., *Hydrodynamics*. 6th edn., Cambridge University Press, Cambridge (1957).
17. Lessard, R. R., Zieminsky, S.A., Bubble coalescence and gas transfer in aqueous electrolytic solutions. *Ind. Eng. Chem. Fundls* 10 (1971) 260-269.

18. Marrucci, G., A theory of coalescence *Chem. Eng. Sc.* 24 (1969) 975-985
19. Montgomery, D.C. and Tidman, D.A., *Plasma Kinetic Theory*. McGraw-Hill, New York (1964).
20. Rosenbluth, M.N., MacDonald, W.M. and Judd, D.L. *Fokker-Planck equation for an inverse-square force*
Phys. Rev 107 (1957) 1-6
21. Tanenbaum, B.S. *Plasma Physics* McGraw-Hill, New York (1967)
22. Van Wijngaarden, L., Submitted to *J Fluid Mech*

Bursting and structure of the turbulence in an internal flow manipulated by riblets

S. TARDU¹, T.V. TRUONG & B. TANGUAY*

Swiss Federal Institute of Technology-Lausanne; 1015-Lausanne, Switzerland (*author for correspondence)

¹Institut de Mécanique de Grenoble-Laboratoire des Écoulements Géophysiques et Industriels; B.P. 53-X, F-38041 Grenoble-Cédex, France

Abstract. The buffer layer of an internal flow manipulated by riblets is investigated. The distributions of the ejection and bursting frequency from the beginning to the middle part of the buffer layer, together with high moments of the fluctuating streamwise velocity, u' , and its time derivative are reported. The profiles of the ejection and bursting frequency are determined and compared using three single point detection schemes. The effect of the riblets on the bursting mechanism is found confined in a localized region in the buffer layer. The multiple ejection bursts are more affected than the single ejection bursts. The skewness and flatness factors of the u' signal are larger in the manipulated layer than in the standard boundary layer. That, also, holds true for the flatness factor of the time derivative, but the Taylor and Liepmann scales are not affected. The spectrum of the u' signal is altered at the beginning part of the viscous sublayer.

Nomenclature

u_τ = Friction velocity
 ν = Viscosity
 l_τ ; f_τ = wall scales ν/u_τ ; u_τ^2/ν
 y = Vertical distance to the wall
 Δz = Spanwise extent
 $(^*)$ = Variable normalized with wall scales
 u = Velocity; u' = Turbulence intensity
 h, s = Height and width of the riblets
 f_e = Ejection frequency
 f_b = Bursting frequency
 f_{BME} = Frequency of the Bursts with Multiple Ejection
 f_{BSE} = Frequency of Single Ejection Bursts

$S_{u'}$ and $S_{du'/dt}$ = Skewness factor of u' and its time derivative
 F_u and $F_{du'/dt}$ = Flatness factor of u' and its time derivative

Abbreviations:

SBL = Standard (non-manipulated) Boundary Layer
 MBL = Manipulated Boundary Layer
 BME = Bursts with Multiple Ejections
 BSE = Bursts with Single Ejections
 VITA = Variable Interval Time Averaging technique
 $u'-l$ = u' -level technique
 mu = Modified u' -level technique

1. Introduction

There is a general consensus between several research groups on the efficiency of the riblets in reducing drag reduction in internal or external flows with or without adverse pressure gradients (Choi, 1989, 1990; Truong and Pulvin, 1989; Rohr et al., 1989) at high subsonic and transonic (Walsh and Anders, 1989; Coustols 1989) and supersonic (Gaudet, 1989) speeds (see Savill, 1990 for a recent review). However, it is quite interesting to note that there is a considerable discrepancy between the results aimed at determining the possible effects of riblets on the structure of the near wall

turbulence (Wallace and Balint, 1988). This is particularly true when the previously published results on the eventual reaction of the bursting process in the internally manipulated boundary layer are compared: although a number of very detailed investigations have been conducted, including single and multipoint turbulence quantities, it is striking to observe that the existing data ranges from an increase of the bursting frequency by a factor of 8 (Choi, 1989) to a decrease by about 30% (Gallagher and Thomas, 1984). The first explanation of this considerable disparity is of course due to the differences in the detection techniques and detection parameters applied, as well as the size and location of the probes used. Another point seems also to be important to point out: the maximum drag reduction obtained by the riblets is about 8% (Savill, 1990); this implies that the corresponding increase of the internal time scale (i.e. ν/u_τ^2) is also only 8%. If we assume that the unique effect of the riblets is probably the decrease of the bursting frequency – i.e. not the modification of the 3D coherent structures or the shear stress distribution within the burst (as suggested by Pulles et al., 1990) or other possible effects, and if the bursting frequency still scales with inner variables (ν and u_τ^2) the detected decrease should not be larger than 8% which is within the scatter of the previously published results concerning the bursting frequency in the standard boundary layer (SBL hereafter). Consequently more objective detection techniques, if possible, are needed to identify the modification of the bursting mechanism. Another difficulty which arises comes from the fact that the effect of the riblets on the flow structure is confined in the buffer and viscous sublayer (as clearly shown by Choi, 1989), and this implies careful and detailed measurements near the wall.

VITA is the most commonly used detection technique, certainly because it is a well known and documented scheme in the SBL and requires only a single signal. Walsh (1982) found no significant alteration of the bursting frequency nor of the contribution to the overall turbulent intensity during and between bursts. They conclude that the main effect of the riblets is to modify the wall streaks distribution in space and reduce the burst intensity. Hooshmand et al. (1983) reported conflicting results when the integration time T_i in the VITA scheme is chosen relative to the local u_τ computed from the sublayer profile or their modified Clauser method. Their data in the SBL case however, is well below the data of Blackwelder and Haritonidis (1983) indicating that the spanwise extend of their probe is too large. Gallagher and Thomas (1984) used a sufficiently small probe ($\Delta z^+ = 9$) and reported that the number of bursts on the riblet surface at $y^+ = 15$ was 30% lower than that detected on the flat surface. The same amount of decrease is also reported by Savill (1987) based on flow visualizations. The most interesting result reported by Gallagher and Thomas (1984), is the increase in size of the spanwise structures by about 15–30% obtained by long time spanwise correlation distributions at zero time delay. This is contrary to the smoke-wire visualisations of Hooshmand et al. (1983) which reported no apparent difference in the average spacing between structures. Their dye visualizations indicated also that the spanwise spread of the dye is constrained within the rib walls and the interaction of the flow between adjacent grooves is weak.

The increase of the spanwise streak spacing was also clearly shown by Bacher and Smith (1985). They identified the streak spacing by visual counting and they reported a 40% increase. They did not observe a modification of the bursting frequency, but they noted a wiggle preceding and following the sharp acceleration of the conditional patterns. They attributed these oscillations to the stabilization of the streak behaviour below $y^+ = 15$.

Choi (1986, 1987, 1989, 1990) reported very detailed measurements concerning the structure of the turbulence in the internally manipulated layer both with and without adverse pressure gradients. He detected the bursts using the instantaneous wall shear stress signal by using VITA with a threshold equal to one. The spanwise extend of the probe was about 10 wall units which is comparable with Gallagher and Thomas, 1984. He reported an increase of the bursting frequency by a factor of eight, but a decrease of the r.m.s. intensity of the turbulent wall shear stress by the same amount. The time scale of the conditional VITA averages at the wall was found to decrease by a factor of two so that the intermittency increased by a factor of four. The hot film was flush mounted within the spanwise distance of the riblets, and how the heat transfer to the substrate affected the measurements and the detection of the structures remains an open question. An increase in size of the near wall coherent structures was once more observed. A systematic increase of the skewness and flatness factors of the streamwise fluctuating velocity was also reported.

Another conflicting result came from the research group of the Tech. Un. of Eindhoven (Pulles et al. 1989). When VITA was applied to the streamwise $u'(t)$ signal at $y^+ = 14$, the frequency of the detected events was found to increase in the MBL (the increase is about 20% for a threshold $k = 0.4$). But when applied to $v'(t)$ signal, VITA gave a decrease of about the same amount. The physical meaning of these results is open to discussion. Their conclusion was that the single point measurements are inadequate to detect changes of the bursting process in the internally manipulated boundary layer. This conducted the same research group to investigate the bursting using quadrant techniques by uv measurements (Schwarz-van Manen et al. 1990). They identified individual ejections and grouped them into bursts. Their closest measurements point to the wall is $y^+ = 10$. They report that the bursting frequency in the SBL decreases with y^+ which is in contradiction with Tiederman (1988) and Bogard (1982) who reported constant bursting frequency for $y^+ > 15$. Although the scatter of their data is important they reported a 30% decrease of bursting frequency.

An important question concerns the effect of the riblets geometry on the coherent structures. To the authors knowledge, the only study which dealt with different groove types is the one conducted by Pulles et al. (1989) who used 8 different geometries. They did not report a spectacular effect of the groove geometry on the ejection frequency. On the other hand, some of the riblets which were used so far have particular geometries (for example Choi, 1988) and it is difficult to conclude from the published data a common trend because of the differences in the detection techniques and locations, the sizes of the probes, etc.

The main conclusion of this short review is that not only are the measurements on

the behaviour of the fine structure of the turbulence in MBL contradictory, but they are also generally limited to the outer part of the buffer layer and detailed analysis in the inner part of the buffer layer ($y^+ < 15$) are needed in order to elucidate the effect of the riblets, since there is a general concensus that (contrarily to LEBUs) the main effect of the riblets is confined near the wall. On the other hand it is known that in canonical turbulent boundary layer, the bursts originate from the low-speed streaks at $y^+ < 12$ (this is called the development stage of the bursting process in this study) and it is asked here if the process that generates the break-up of the low-speed streaks in the buffer layer is influenced by the presence of the riblets or not.

The first aim of this study is to use several detection and grouping schemes to identify bursting structure in the wall layer part of an internally manipulated layer. Several other characteristics such as the power spectra, high moments of the streamwise fluctuating signal together with statistics concerning the time derivatives, small and intermediate scales (Taylor and Lieppman scales) are also investigated.

2. Experimental set-up

The experiments were conducted in the closed loop wind tunnel with low turbulence level (0.5%) described in details by Pulvin (1989). The working section is a two dimensional channel, 2 m. long with two fixed transparent side walls and 2 aluminium flat plates with hydrodynamically smooth (or riblets) surface and adjustable in angle. The whole set of data was taken here in a zero pressure gradient. The measurements were taken at $x = \delta$ upstream of the end of the riblet plate.

Symmetrical V type Hoecht riblets were used in this study (Fig. 1). The height and width of the riblets were $h = s = 0.01'' = 0.25$ mm.

Most of the part of this study was investigated with a mean centerline velocity of $U_c = 15$ m/s, corresponding to a Reynolds number of $Re_\delta = 27500$. The drag reduction was evaluated using the momentum balance in the same way as Pulvin (1989) and found in the present working conditions ($h^+ = s^+ = 9$) to be $\Delta C_f = 0.94$. This value corresponds quite well to the previous measurements of Pulvin (1989). The

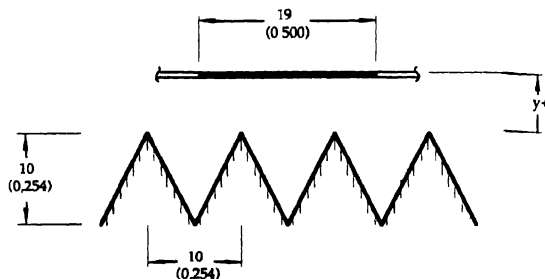


Fig. 1 Cross section of the riblets together with the hot film probe. The dimensions are in wall units. The values in brackets are in mm.

top of the grooved plate is used as the origin. The u_r measured here would correspond to the average value from the peak and valley values. Therefore the shift above of the velocity profiles (which is slight here) is less pronounced than that of Hooshmand et al. (1983). This means that, if we use the notion of the protrusion height, i.e. the virtual origin that the outer flow sees, as defined by Bechert et al. (1986), the y^+ computed should be shifted towards the centerline by an amount of $0.1-0.2 h^+ = 0.9-1.8$ (this value depends on the geometry of the riblets and no verification was made in this work; see the viscous analysis due to Bechert et al., 1986). This would of course accentuate the effects presented in this study. On the other hand, since the spanwise extent of the probe is 2 times the riblets spacing, the spanwise location of the probe should not change the detected characteristics, i.e. the probe is large enough to have average characteristics corresponding to the buffer layer, and can not detect the more detailed configuration of the flow within the ribs. (The case studied here is similar in this aspect to the previous measurements of Fulachier et al., 1987). The use of a smaller probe would clarify the dynamical process as a function of its lateral position with respect to the groove pattern. There is a real gap concerning this last point in the literature that future research should carry on.

A subminiature TSI 1260-10 hot-film probe is used. The spanwise length of the probe is $\Delta z^+ = 19$ in wall units; although it is somewhat large, it may be assumed that it is in the acceptable limit to avoid the spanwise averaging of the detected structures (Blackwelder and Haritonidis, 1983).

The sampling frequency is set equal to $f_v = u_\tau^2/\nu$ (20 kHz for $U_c = 15$ m/s). The signal was low pass filtered by a Krohn Hite filter at $f_v/2$. The data was transferred to the host computer and analyzed in several ways.

The total duration of each record was $T_r = 4600 \delta/U_\infty$ and this is enough to ensure the convergence of statistics up to 4-th order moments (Klewicky and Falco, 1990) and of the ejection and bursting frequency for the non-manipulated boundary layer. This, of course does not imply a priori that the statistical convergence is ensured in the manipulated boundary layer, since the development in high order moments for different surfaces can be quite different. To this end, the convergence of the results was checked especially for the flatness factor of the time derivatives which is the most likely affected by convergence problems. Such a test is shown in Fig. 2 for the Standard Boundary Layer (SBL) and the Manipulated Boundary Layer (MBL) at $y^+ = 7.3$. Only the results concerning the 4-th order moments are shown, since the lower moments converge more rapidly. Fig. 2a and 2b show respectively the flatness factor of the fluctuating streamwise velocity, and of its time derivative versus T_{data}/T_r , where T_{data} is the duration of the truncated record. It is seen that the results change by less than 1% once $T_{\text{data}}/T_r > 0.6$. The results concerning the flatness factor $F_{du'/dt}$ of the time derivative du'/dt converge at $T_{\text{data}}/T_r > 0.8$, therefore, less rapidly as it would be expected (Fig. 2b). Similar results are obtained for other sets of data investigated in this study. Note finally that the record length is almost 5 times longer than the value $T_r = 1000 \delta/U_\infty$ recommended for the convergence of bursting frequency (Blackwelder and Haritonidis, 1983).

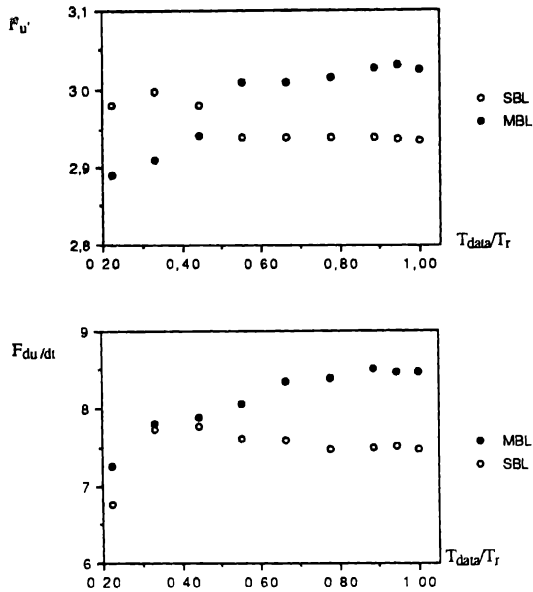


Fig. 2 Test of convergence of high order moments, (a) Flatness of the fluctuating streamwise velocity u' , (b) Flatness of the time derivative of u' $T_r = 4600 \delta/U_\alpha$

3. Detection and identification of the ejections and bursts

3.1. Detection of the ejections

Three independent detection techniques have been used to detect ejections, namely u' -level (u' -l), modified u' -level (mu), and the well established VITA (Variable Interval Time Averaging) technique. All of these detection schemes require a single signal, they essentially detect ejections but they may be slightly modified to identify sweeps as well (Bogard, 1982). Roughly speaking, the level crossing methods detect the leading edge, while VITA identifies the trailing edge of an ejection (Bogard and Tiederman, 1987). However it has to be pointed out that VITA is much more associated with near wall shear layers rather than ejections.

The rather new definition of the bursting mechanism is adopted here. Several authors indicated that the break-up of the low speed streaks may contain one or several individual lift up of the low momentum fluid from near the wall (Offen and Kline, 1975; Willmarth and Sharma, 1984; Bogard and Tiederman, 1986). They identified the break-up of a single streak as being the bursting phenomena, implying that a burst may contain one or several ejections. Recent direct simulation data also provides evidence of the existence of ejections coming close to each other (Kim and Spallart, 1987; Kline and Robinson, 1990; Robinson et al., 1988). Each one-point

scheme identifies the ejections. Specific methods are therefore needed in order to group ejections into the bursts.

The detector function $D(t)$ of the $m-u'$ and $u'-l$ schemes is defined as follows:

$$m-u': D(t) = 1 \quad \text{if} \quad -L_1 \sqrt{u' u'} > u'(t) > -L_2 \sqrt{u' u'},$$

$$u'-l: D(t) = 1 \quad \text{same as } m-u' \text{ but } L_1 = L_2.$$

The detector function for VITA is (Blackwelder & Kaplan, 1976):

$$D(t) = 1 \quad \text{if} \quad \sigma_v > k \overline{u' u'} \quad \text{and} \quad du'/dt > 0$$

$$D(t) = 0 \quad \text{otherwise} \quad (\)_v = 1/T_v \int_{t-T_v/2}^{t+T_v/2} (\) dt',$$

where $\sigma_v = (\overline{u'^2})_v - (\overline{u'})^2$.

During the whole study, the same detection parameters have been used and compared in situ with the standard boundary layer. According to Bogard and Tiederman (1986), Luchik and Tiederman (1987) and to Tardu and Binder (1989, 1991a; see also Tardu, 1988) these were later set as follows:

$$u'\text{-level: } L_1 = -1.2, L_2 = -0.9$$

$$mu'\text{-level: } L_1 = -1, L_2 = -0.25$$

$$\text{VITA: } k = 0.35, T_v^+ = 14.$$

3.2. Grouping of the ejections

Once the ejections are detected, they have to be grouped together, in order to identify the bursting frequency corresponding to the break-up of a single low-speed streak. Several independent grouping techniques are used in this study. Although it is a 'technical' problem, it is a crucial one, since a comparative study of the behaviour of the bursting process can clarify the effect of the riblets by those results common to several methods. Once the grouping is done, we can identify and study separately the bursts with multiple (BME), and single ejections (BSE). One of the reasons for this distinction is motivated by some recent findings that these two categories of bursts may result from different mechanisms (Tardu, 1988; Tardu and Binder, 1989, 1991a; Antonia et al., 1990).

Two different grouping methods are used here. The first one is based on the cumulative probability distribution of time between ejections (Barlow and Johnston, 1985; Bogard and Coughran, 1987). In the case of $u'-l$ ejections the probability distribution is based on the center to center time, and in the case of $m-u$ events, on the time between the trailing edge of one ejection and the leading edge of the next ejection

(Tiederman, 1988). These distributions have a break which marks the separation between the BME's and BSE's. A second method, originally developed by Tardu (1988) is also used and compared with the first one. It is based essentially on a specific pattern recognition technique. In an extensive study of simultaneous flow visualizations and probe measurements, Bogard and Tiederman (1986, 1987) showed that the conditional pattern of the trailing edge of the first ejection of a BME, is significantly different to that of the last ejection. In particular the maxima of the previous ejections of a BME are smaller by several orders of magnitude than the maximum of the last ejection. A typical time series of such events which would be detected by VITA is shown in Fig. 3. The method is based on a doubly iterative procedure which detects such typical events and will not be discussed here. The details may be found in Tardu (1988, 1991) and Tardu and Binder (1991a, 1992). Let us only point out that, this pattern recognition technique can be applied both to VITA, u -level and μ -level methods without modification as well as to the sweeps. It gives results comparable to the first method, and is judged to be more objective, because of the possible subjectivity made in determining the break point by use of the cumulative probability distribution.

4. Results

4.1. Profiles of the mean streamwise velocity

The streamwise velocity is scaled with the corresponding friction velocity versus the vertical distance from the wall, and the vertical distance from the top of the riblets surface in Fig. 4. It is seen that the data corresponding to the smooth plate is well represented by $u^+ = 14.5 \tanh(y^+/14.5)$ near the wall. The velocity profiles corresponding to the manipulated boundary layer is shifted slightly up in agreement with Choi (1988, 1990). An estimate of the virtual origin is done by making a least square

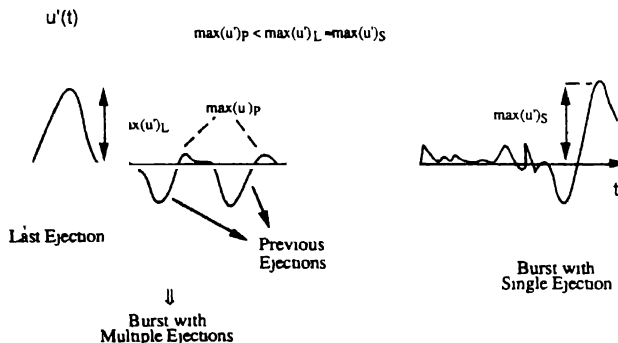


Fig. 3. Sketch of a typical burst with multiple ejections and burst with single ejection detected by the grouping method.

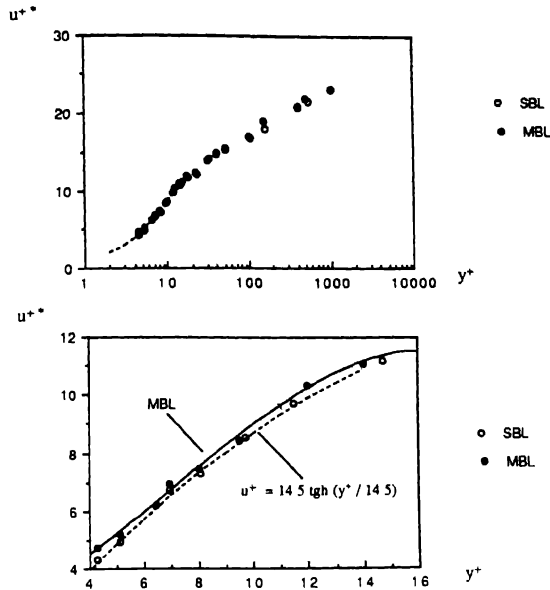


Fig. 4 Profiles of the mean streamwise velocity scaled with the corresponding friction velocity

analysis for the first four points corresponding to the locations nearest to the riblet surface and was found $y_v^+ = 0.8$ i.e. $y_v/h = 0.1$ a value which is smaller than the one given by Bechert et al. (1986). The first reason to explain this discrepancy is that some differences may result from the spanwise distribution of the velocity profiles. The second reason comes from the small number of points taken near the wall, although the thickness of the viscous sublayer seems to increase in agreement with Choi (1988, 1990).

4.2. Profiles of the turbulence intensity

Figure 5 shows the distribution of the rms of the streamwise velocity fluctuations related to the friction velocity of the standard boundary layer. It is seen that the riblets decrease the streamwise turbulent fluctuations by an amount of 5–8% in the beginning part of the buffer layer, i.e. at $y^+ < 15$. This is a general consensus on the effect of the riblets and is in agreement with most of the previous riblets studies. Even when the rms velocity is related to the friction velocity of each case (i.e. $u_{\tau(\text{SBL})}$, or $u_{\tau(\text{MBL})}$) this decrease is found persistent at $4 < y^+ < 7$, a region where the bursting mechanism is found to be mostly affected.

4.3. Profiles of the ejection and bursting frequency

4.3.1. Distribution of the u -level ejection frequency

Figure 6 shows the profiles of the u -level ejection frequency $f_{e(u)}^+$ as a function of y^+ .

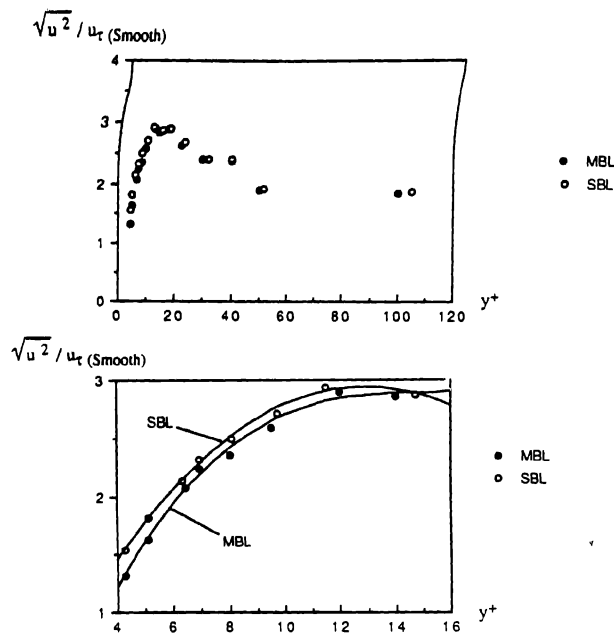


Fig 5 Profiles of the streamwise rms fluctuations related to the friction velocity of the smooth plate

Both f_e and the bursting frequency are non-dimensionalized with respect to the friction velocity corresponding to the SBL. It is seen, that the results for the smooth plate presented here agree in an excellent manner with the measurements of Bogard and Coughran (1987) which have used the same detection technique. This good correspondence seems to increase the degree of confidence that we may have in the results presented in this paper. Indeed, the probe used by Bogard and Coughran (1987) has a spanwise length of 10 wall units, therefore two times smaller than the one used in this study. Since the same distribution of the time-mean ejection frequency is found in both studies, it may be suggested that the spanwise extent of the most energetic eddies must be greater than $20 \nu / u_{\tau}$, otherwise large discrepancies should be

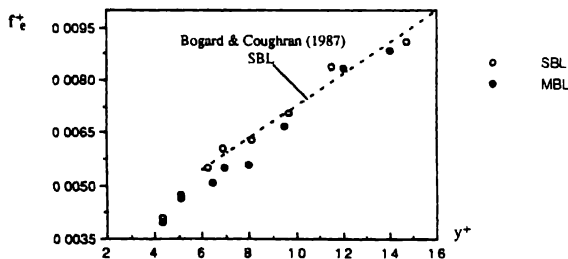


Fig 6 Distributions of the ejection frequency versus y^+ , u -level ejections

observed because of the consequence of averaging the turbulence structures. This last point is also in agreement with Blackwelder and Haritonidis (1983), who used VITA scheme with $k = 1$ and $T_v^+ = 10$ at $y^+ = 15$. They have obtained a plateau region for the bursting frequency for $\Delta z^+ < 20$. They have related these results to the fact that the bursting mechanism is related to the break-up of the low-speed streaks which have a spanwise extent which continuously varies between $20\nu/u_\tau$ and $200\nu/u_\tau$. Thus, although the length scales of the coherent quasi-streamwise vortices which are believed to be closely related to the ejections, decrease with decreasing y^+ (the diameter of these vortices varies between 2 and $0.41y^+$; Robinson, 1990), they are found quite intermittent in the streamwise direction, and always in the immediate vicinity of the low speed streaks and the "spanwise extent of the ejection regions is (only) roughly dependent on distance from the wall" (Robinson, 1991; p. 257). Based on these arguments and comparing the results with previously published data, it may be concluded that the length of the sensor is just small enough to avoid the averaging problem in the non-manipulated boundary layer, because the length of the probe is within the distribution of the spanwise extent of wall streaks at the wall. It is however not a priori true in the manipulated boundary layer, since the effect on the spatial extent of the streaks is not clearly established up to now. However, the common belief is that the riblets increase the streak spacing. The averaging problem seems, therefore, to be less critical in the manipulated boundary layer.

To check this point, a few measurements have been carried out by using both a DISA-R11 and TSI 1260-10 probe, at $y^+ = 7$ in the SBL and MBL with different Reynolds numbers. The riblet height and spacing were between $h^+ = s^+ = 6 - 9$. The Reynolds number could not be changed beyond a certain limit in order to keep the riblets geometry sufficiently effective for drag reduction. Fig. 7 shows the ejection frequency obtained by $u'-l$ in the MBL versus the dimensionless sensor length. The ejection frequency decreases by 27% at $\Delta z^+ = 35$, and varies by less than 7% for $15 < \Delta z^+ < 22$.

Figure 6 shows that the ejection frequency increases with y^+ because of the multiple break-up of a given streak as discussed in detail by Bogard (1982). The ejection frequency detected over the riblet surface is systematically smaller in the beginning part of the buffer layer with a maximum decrease of about 12% at $y^+ = 8$ (Fig. 8). The

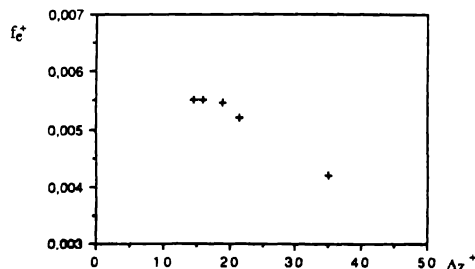


Fig. 7. Influence of the spanwise length of the probe on the ejection frequency.

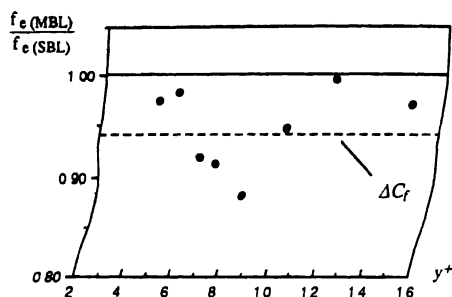


Fig. 8. Ratio of the time mean ejection frequency in MBL and SBL (u -level ejections).

difference between the ejection frequency in SBL and MBL decreases towards the outer layer. This behaviour is in some way contrary to what was observed in LEBUs, for which the principal effect was the decrease of the ejection frequency for $y^+ > 15$ (Tardu and Binder, 1991). The confined effect on the ejection frequency noted here is in agreement with the general consensus that the riblets essentially affect the inner layer with a pronounced effect in the buffer layer. The maximum decrease which takes place at $y^+ = 8$ is a rather new observation and is difficult to explain. While the ratio $f_{e(\text{MBL})}/f_{e(\text{SBL})}$ is systematically smaller than the drag reduction ΔC_d at $y^+ < 6$, closer to the wall the detected difference becomes negligible. This seems to be in contradiction with Choi (1988) who identified the bursts at the wall and found an increase of the bursting frequency. It is of course not a priori legitimate to extend the measurements here, to $y^+ = 0$. Another open question of course, is the validity of the detection techniques near the wall.

More physical insight on the ejection mechanism may be obtained by investigating the probability distribution of the ejection interarrival times. Fig. 9 shows such a distribution obtained at $y^+ = 8$ where the most pronounced effect on $f_{e(u-1)}$ is observed. The normalized ejection interarrival time t_e^* is $t_e^* = (t_e - \bar{t}_e)/\sigma_{te}$ where σ_{te} is the rms value. The rms values of the inter-arrival times are respectively $0.9\bar{t}_e$ and $1.\bar{t}_e$ for the manipulated and standard boundarylayer. The skewness and flatness of t_e are modified in the MBL, although slightly because the distributions are quite similar

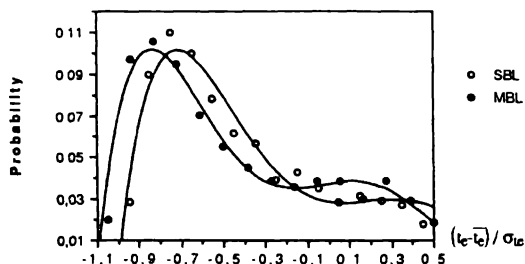


Fig. 9 Probability distribution of the ejection interarrival times; $y^+ = 8$

(Fig. 9). Skewness and flatness of t_e over the riblets and at $y^+ = 8$ are 1.2 and 1.9 respectively compared with 0.8 and 1.1 over the smooth surface. Although there is a trend indicating that the riblets produce a more pronounced "periodic" ejection frequency, because the inter-arrival times are more intermittent (the flatness factor is two times higher in MBL), it is difficult to conclude solely from the t_e distribution whether the riblets produce a more intermittent flow or not, since this distribution does not give information on the signal between the events which may behave differently in MBL. For instance, quiescent periods of the wall shear stress signal were observed by Choi (1989) due to the partial laminarization of the viscous sublayer near the bottom of the riblets.

The distribution of the time durations of the u-level ejections was also investigated, but the results are not reported here, since no significant differences were noted. Slightly longer ejections persist in the beginning part of the buffer layer in MBL, and they are slightly shorter in the viscous sublayer (Tardu 1991).

4.3.2. Distribution of the (u'-level) bursting frequency

The grouping of the ejections is done using the second method based on the individual patterns of the detected ejections. The analysis based on the break point of the cumulative probability distribution revealed very comparable results and will not be discussed here. Let us just point out that the statistics concerning the interarrival times of the ejections up to second moments were found very similar in MBL and SBL and slight differences in higher moments were observed as it has been discussed in the previous section.

The effect of the size of the probe on the number of detected events was found less critical once the grouping is done. For instance, in a case where a larger probe ($\Delta z^+ = 37$) was used and where a decrease of 20% of the ejection frequency was observed, the bursting frequency differed only by 10%.

Figure 10 elucidates the grouping technique. The maximas of the previous ejections of a multiple ejection burst are first of all systematically negative, and are significantly different than the maxima of the last ejection or the maxima of the single ejections. There is no apparent modification of this behaviour in the MBL.

The reaction of the bursts with multiple ejections (BME), and single ejection (BSE),

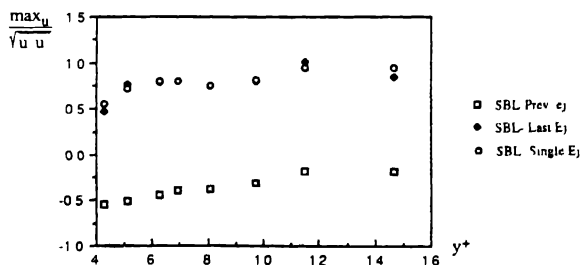


Fig 10. Maximas of the ejections belonging to different parts of the bursts (u-level technique).

are studied separately in this investigation. Previous investigations (although in a different context) have suggested that these two groups of bursts may result from different mechanisms (Tardu and Binder; 1989, 1991a). In their study of unsteady wall flows, these authors have shown that, the BME's and the BSE's respond quite differently to imposed oscillations. Recently, Antonia et al. (1990) have shown that reasonable correspondence exists between the end of a burst (defined as the last ejection of a BME, or a BSE) and δ scale u -discontinuities, making a possible link between the inner and outer layer. The aim, here was to determine if these two categories of bursts behaved differently or not in MBL.

Figures 11a and 11b shows the distributions of the time mean frequencies of the BME's and BSE's in manipulated and standard boundary layer respectively. The first impression is that there are no spectacular differences when the MBL is compared with SBL. However slight but systematical alterations exist. In order to elucidate this point the ratios of the f_{BME} and f_{BSE} are plotted in Fig. 11c. First of all $f_{\text{BME(MBL)}}/f_{\text{BME(SBL)}}$ is smaller than one in a large part of the buffer layer including $5 < y^+ < 11$. Furthermore, this ratio is smaller than ΔC_d in most of the part of the beginning part of the buffer layer. The frequency of the single ejection bursts is found to be smaller than its homologue in the SBL, only at the closest detection station. The recovery with the corresponding SBL value is surprisingly rapid to within $\Delta y^+ = 10$. The reduction of the frequency of BME (although small, with a maximum of 15%) is larger than the reduction of the frequency of BSE.

The distribution of the bursting frequency $f_b^+ = f_{\text{BME}}^+ + f_{\text{BSE}}^+$ is shown in Fig. 11d. Contrary to the behaviour of the BME's and BSE's for which some stronger influence of the riblets is noted, the decrease of the bursting frequency is only of the same amount as the drag reduction. That would imply that the bursting scales with inner variables in the buffer layer. Note once more that the decrease of the bursting frequency is limited to the beginning part of the buffer layer.

The analysis of the conditional patterns dealt with several parts of the burst structure, namely the previous ejections of a multiple ejection burst, the last ejection of a BME, and the single ejection bursts. This allowed a more efficient study locked at a particular phase of the process. No significant differences were observed except at $y^+ = 7 - 8$ where a slight phase shift, and a different pattern are noted before and after the arrival of the previous ejections, and at $y^+ = 5$ where larger maxima of the last ejections are noted (Tardu 1991). This might indicate, although with some caution, that the bursts in the manipulated boundary layer are more coherent in their early stage.

4.3.3. *Shear-layer (VITA and μ) events*

VITA detects the near wall shear layers rather than the ejections and there is no simple relationship between these structures and the ejection mechanism. The results and comparisons presented in this section should therefore be taken into consideration with some caution.

Figure 12a shows that the shear layer events detected by VITA are less modified by

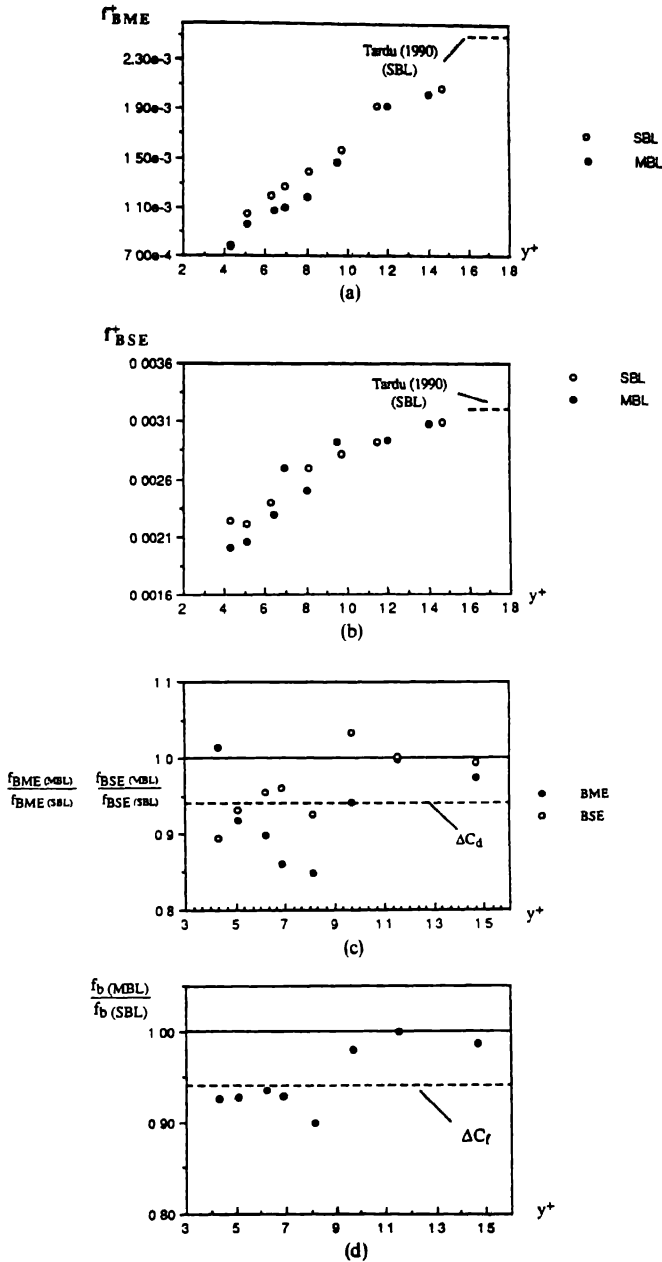


Fig 11 (a) Distribution of the frequency of multiple ejection bursts in manipulated and standard boundary layer (u-level scheme); (b) Distribution of the frequency of single ejection bursts in manipulated and standard boundary layer (u-level scheme); (c) Distribution of the ratio of the frequency of multiple and single ejection bursts in manipulated to the frequency in standard boundary layer (u-level scheme); (d) Distribution of the ratio of the bursting frequency (u-level scheme)

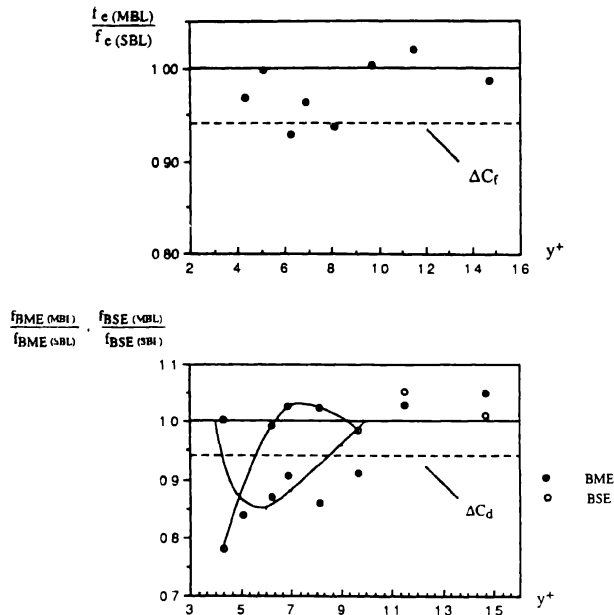


Fig. 12 (a) Ratio of the time mean frequency of the shear layer events (VITA) in MBL and SBL, (b) Ratio of the frequency of single and multiple shear layer events detected by VITA

the presence of the riblets than the u -level ejections. In the manipulated boundary layer the frequency of the shear layer events is almost the same as in SBL. The difference lies within the experimental error. That is in some way similar to the LEBU's where smaller effects were observed compared to the u -level events (Bogard and Coughran, 1987). It is also not surprising that the modified u -level technique gives comparable results, since it is a level-crossing version of VITA (Luchik and Tiederman, 1987).

The maxima corresponding to the conditional patterns obtained once the grouping of the VITA and m - u events is done are found to be fairly similar in MBL and SBL (Tardu, 1991). Despite the fact that, the frequency of the individual VITA shear layer events, is less affected than the frequency of u -level ejections, the grouped shear layer events show a close similarity with the u -level bursts (Fig. 12b). Therefore, the same discussion done in the previous paragraph is valid here, namely that the multiple shear layer events are more sensitive to the internal manipulation than the single shear layer events. Since the multiple events correspond to the successive break-up of a single streak, that behaviour may be explained by a relative stability of the streaks so that, fewer multiple break-ups occur in the manipulated boundary layer.

Similar results are obtained by mu -level, as it would be expected (Tardu, 1991). As a conclusion, and despite the fact that, the three detection schemes investigated here are

independent and identify different parts of the bursting mechanism, some common behaviors are noted, namely:

- (i) Riblets affect the bursting mechanism at an early stage. Since here, the effect is confined to the beginning part of the buffer layer, it implies that the riblets affect the bursting mechanism in its development stage. It would therefore be interesting to apply a spatio-temporal detection technique to investigate the bursting mechanism in the internally manipulated boundary layer.
- (ii) The effect is slight (10–15%), localized, and confined in the beginning part of the buffer layer. The reaction of the multiple events are different compared with the reaction of the single events.
- (iii) By altering the frequency of Multiple Ejection Bursts, the riblets probably affect also the stability of the low-speed streaks.

The sweeps could not be identified directly in this study, since this would require the $u'v'$ time series. A similar analysis was however conducted for shear layer events associated with sweeps supposing that they can be identified as decelerating VITA' events. The distribution of the frequency of decelerating VITA events is very similar to the distribution of $f_{e(u'-1)}$ (Fig. 13). The effect on the multiple sweeps is clear from Fig. 14 and is similar in several aspects to the results discussed previously. A reduction of

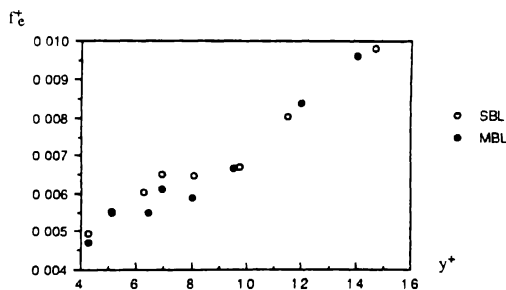


Fig. 13 Frequency of shear layer events associated with sweeps (VITA with deceleration)

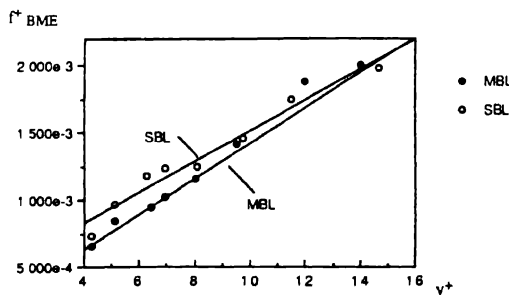


Fig. 14. Frequency of multiple sweep events in MBL and SBL.

10–20% of the frequency of the multiple sweep events is obtained between $5 < y^+ < 10$. This effect is not surprising since the sweeps are related to the ejections.

5. Characteristics of higher moments of streamwise fluctuating velocity

5.1. Distributions of the skewness factor of u'

Figure 15a shows the distributions of the skewness factor $S_u = \overline{u'^3}/\overline{u'^2}^{3/2}$ of the streamwise fluctuating signal in the MBL and SBL versus the vertical distance from the wall, together with results reported by Ueda and Hinze (1975) concerning the SBL. It is seen that the measurements presented here in SBL correspond quite well to Ueda & Hinze (1975) showing the good quality of the measurements near the wall together with some data of in SBL and MBL. The skewness factor S_u , presented on Fig. 15a is found to be systematically larger in the MBL than in the standard boundary layer. This observation agrees with Choi's (1988, 1990) and strengthens the idea that the riblets affect especially the higher moments. The increase of S_u , in Fig. 15a is about 20% in the MBL, indicating that the degree of asymmetry of the probability density of u' increases by the presence of riblets.

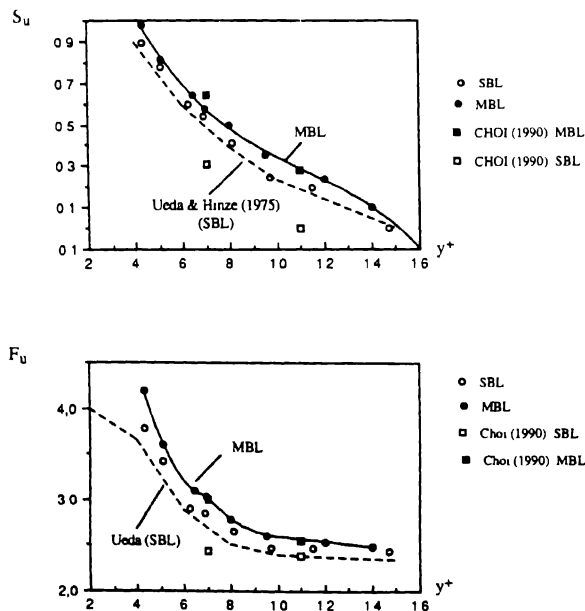


Fig 15 (a) Distributions of the skewness factor of the streamwise fluctuating signal, (b) Distributions of the flatness factor of u' in MBL and SBL versus y^+

5.2. Distributions of the flatness factor of the streamwise fluctuating velocity

The effect on the flatness factor $F_u = \overline{u'^4} / \overline{u'^2}^2$ becomes progressively important near the wall (Fig. 15b), where a 12% increase is noted. $F_{u'(\text{MBL})}$ is systematically larger than $F_{u'(\text{SBL})}$ when $y^+ < 15$. Although the flatness factor is not directly related to the intermittency γ , there is a close relationship between F_u and γ and it may be argued that the structure of the internally manipulated layer has a more intermittent character. This again in agreement with Choi (1988, 1990).

6. Statistics of the time derivative of the fluctuating streamwise velocity

6.1. The Taylor and Liepman scales

A 32 point Finite Impulse Response Digital Filter is used to compute the velocity time derivative. It is known that the signal to noise ratio has an important effect on the computation of the velocity derivatives (Kuo and Corrsin, 1971; Ueda and Hinze, 1975). Since the sampling frequency is high compared to the Kolmogoroff frequency here, the cut-off frequency of the digital differentiator was set equal to the Kolmogoroff frequency computed from the data given by Ueda and Hinze (1975), namely to $f_k^+ = U^+ / 2\pi\eta^+$ ($\eta^+ \approx 3$ at $y^+ < 10$). The same configuration of the digital differentiator is used when the computation of the velocity time derivative is computed in SBL and MBL.

The Taylor time scale is defined as:

$$\lambda = \sqrt{\overline{u'^2} / (\overline{du'/dt^2})}$$

and it is related to the viscous dissipation by:

$$\bar{\epsilon} = 15\nu \left(1 + \frac{u'^2}{\bar{u}^2} \right),$$

a result which is obtained by using Taylor's hypothesis and assuming approximate homogeneity and local isotropy (Ueda and Hinze, 1975). On the other hand, in the case of a gaussian signal, λ is related to the zero-crossing frequency f_0 by:

$$\lambda = \Lambda = (2\pi f_0)^{-1} \quad (\text{Rice, 1945})$$

where Λ is the Liepman scale. The near wall turbulence has an interesting characteristic because, despite its strongly non-gaussian character, the Taylor and Liepman scales are found almost equal (Sreenivasan et al., 1983).

Figure 16a compares the distribution of the Taylor time scale in manipulated and

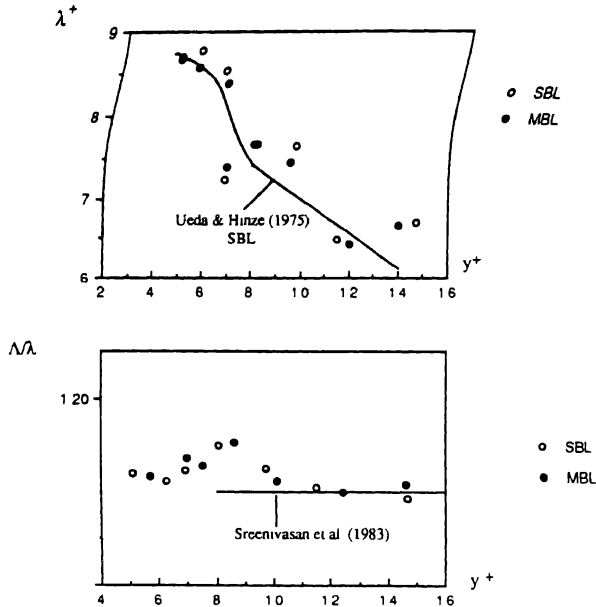


Fig. 16. (a) Distributions of the Taylor time scale in MBL and SBL versus y^+ ; (b) Ratio of the Liepman time scale to the Taylor time scale in MBL and SBL versus y^+

standard boundary layer. The agreement with the data of Ueda and Hinze is quite good. There is no effect of the riblets on the Taylor scale nor on the Liepman scale through the whole part of the middle part of the buffer layer. The ratio of the Liepman to the Taylor time scale does not show either any significant modification in the manipulated boundary layer (Fig. 16b). Λ/λ is about 1.1 as is the case in the boundary layer data given by Sreenivasan et al. (1983; Fig. 8a), and this ratio increases slightly near the wall. It may be concluded from the results presented in this paragraph that the Taylor and Liepman time scales are not affected in the MBL, and if the dissipation is altered, it may take place mainly through the differences in the distribution of $\overline{u'^2}/\bar{u}^2$.

6.2. High statistics of the time derivative

The skewness factor of the time derivative $S_{dw'/dt}$ is related to the production of vorticity by stretching. Any effect concerning this quantity may imply an alteration of the vorticity production mechanism in the manipulated boundary layer. Fig. 17a compares the $S_{dw'/dt}$ distribution in SBL with the $S_{dw'/dt}$ distribution in MBL. It is seen that the data presented here agrees well with Ueda and Hinze (1975). $S_{dw'/dt}$ is systematically larger in the MBL than in the SBL, at $y^+ < 10$, but this is no longer valid in the beginning part of the buffer layer. Since the variations are small and the trend is not systematic, it is judged that the skewness factor of the velocity derivative is not altered by the presence of the riblets.

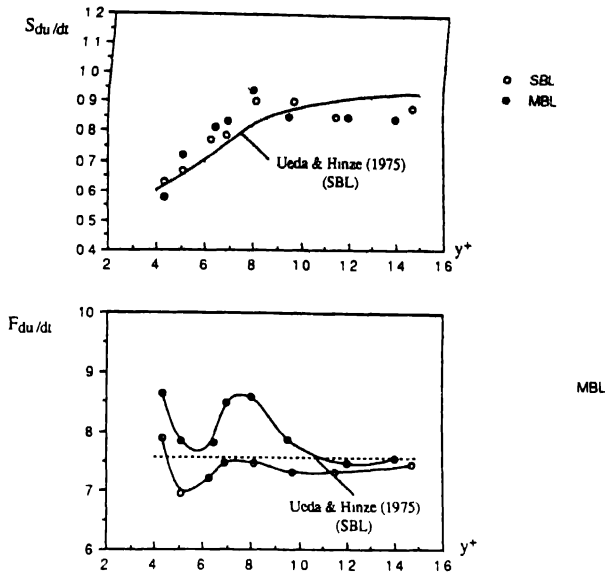


Fig. 17 (a) Distributions of the skewness factor of du'/dt in MBL and SBL versus y^+ , (b) Distributions of the flatness factor of du'/dt in MBL and SBL versus y^+

The flatness factor $F_{du'/dt}$ is slightly Reynolds number dependent, and the data of Ueda and Hinze shown on Fig. 17b was approximately interpolated to $Re_\delta = 27000$ corresponding to the case investigated here. One of the most pronounced effects of the riblets is found in that which concerned with the flatness factor of du'/dt . The increase of $F_{du'/dt}$ is clear and already becomes significant at $y^+ = 12$. One measurement at $y^+ = 14$ and $h^+ = 13.5$ (for which maximum drag reduction is obtained), showed an increase of 15% in the flatness factor of du'/dt , even in the middle part of the buffer layer (Tardu, 1991). These results combined with those concerning F_u show that the riblets have a significant effect on the intermittent structure of the near wall turbulence.

7. Spectra of the streamwise velocity fluctuations

An 8192 point standard FFT procedure was used to compute the spectra of the streamwise velocity fluctuations.

The spectra of the streamwise velocity fluctuations are presented in the same way as Maruyama and Tanaka (1987), in Fig. 18 and the frequency f is non-dimensionalized by the viscous time scale corresponding to the SBL.

The effect on the spectra is confined within $y^+ < 8$. At $y^+ = 4.2$ a decrease in the small frequency range is noted, indicating that the riblets induce a decrease of the large scale structures in connection with the decrease of the ejection and bursting frequency

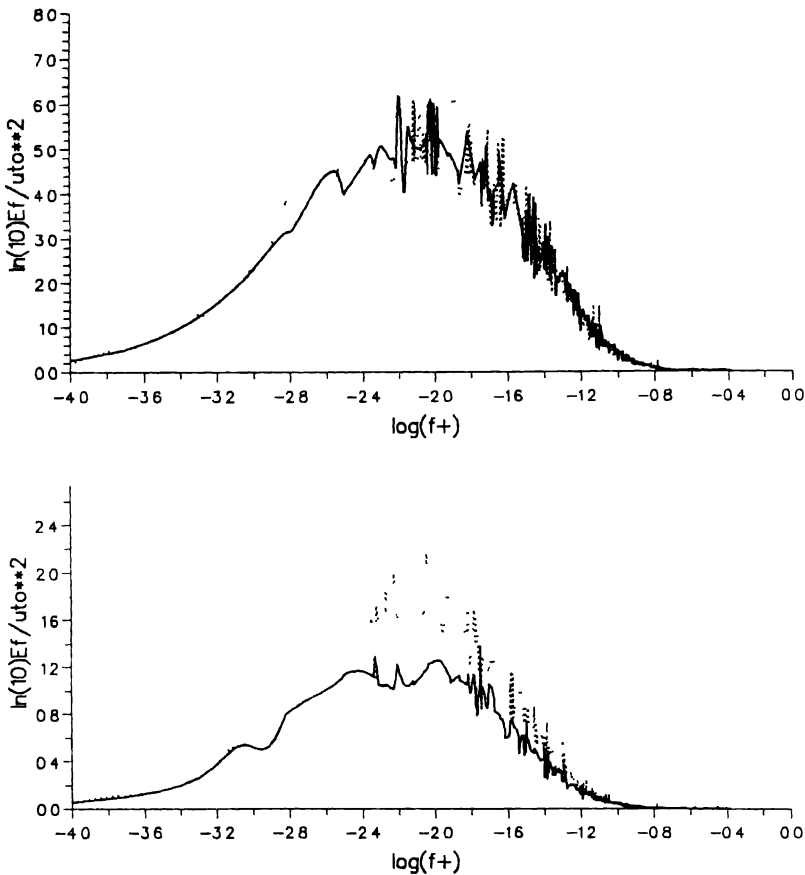


Fig. 18 Spectra of streamwise velocity fluctuations in MBL and SBL —, MBL, ---, SBL, (a) $y^+ = 14$, (b) $y^+ = 4.2$

(Fig. 18b). The range of the decrease is for $f^+ < 0.01$, at $y^+ = 5$, and coincides well with the ejection frequency f_e^+ at $y^+ = 15$ (Tardu 1991). These results show that in the viscous sublayer, a deficit of large scales is induced by the riblets, and this is in agreement with Coustols and Cousteix (1990). In the buffer layer, however, no significant alteration of the small or large scales can be noted from Fig. 18a. Coustols and Cousteix (1990), have reported an excess in the high frequency range, in the region of intense turbulence production, ($y^+ = 10 - 15$), showing that the ribs induce smaller structures there. This point was however not confirmed by the measurements of Choi (1990). Neither do our measurements show an excess in the high frequency range in the part of the buffer layer investigated in this study. The main conclusion of this paragraph is that the effect on the spectra of the fluctuating signal only becomes important in or immediately after the viscous sublayer.

8. Conclusion

A comparative study of the effect of the riblets on the near wall turbulence structure has been carried out. The main conclusions are the following:

- (i) The ejection frequency decreases in the middle part of the buffer layer by an amount 3 times larger than the decrease of the inner time scale.
- (ii) Both the single and the multiple ejections are affected. The effect on the Multiple Ejection Bursts is more pronounced than on the Single Ejection Bursts. The frequency of the bursts with multiple ejections decreases by 10–20% at the beginning part of the buffer layer. The same behaviour is also observed for the grouped sweeps.
- (iii) The skewness factor of the fluctuating streamwise signal increases in the presence of the riblets. The most pronounced effect is found on the flatness factor of both u' and du'/dt indicating an effect of the riblets on the intermittent structure of the near wall turbulence. This is in connection with the decrease of the bursting frequency, which implies a decrease of the intermittency, and consequently an increase of the flatness factor.
- (iv) The Taylor and Liepmann scales are not affected by the riblets. The spectra of the streamwise fluctuating velocity is modified at the beginning of the viscous sublayer.

It is difficult to explain why the effect on the bursting frequency (by accepting that it is significant) is found only in a limited range of y^+ . A possible different redistribution of the $u'v'$ into the bursts may be suspected in the presence of the riblets. More detailed measurements in the buffer layer would therefore be useful. On the other hand, the effect on the spatial extent of the coherent structures has to be investigated. This would clarify how the riblets affect the streak spacing, and how they modify the spatio-temporal distributions of the coherent structures near the wall.

Acknowledgments

This study was carried out while the first author was an invited scientist at the Ecole Polytechnique Fédérale de Lausanne for a period of nine months. He would like to extend his sincere thanks to Prof. I.L. Rhyming for this very kind invitation.

References

- Antonia, R.A., Bisset D.K. and Browne L.W.B., Effect of Reynolds number on the topology of organized motion in a Turbulent Boundary Layer. *J. Fluid Mech.* 213 (1990) 267.
- Bacher E.V., Smith, C.R., A combined visualization-anemometry study of the turbulent drag reducing mechanism of triangular micro-groove surface modifications. *AIAA paper AIAA-85-0548* (1985).
- Bechert, D.W., Bartenwerfer, M. and Hoppe, G., In: *Proc. 15th ICAS*, London (1986).
- Blackwelder, R.F. and Kaplan, R.E., *J. Fluid Mech.* 76 (1976) 89.

- Blackwelder, R.F. and Haritonidis, J.H., Scaling of the bursting frequency in turbulent boundary layers. *F. Fluid Mech.* 132 (1983) 87.
- Bogard, D.G., Ph.D. Thesis, Purdue University (1982).
- Bogard, D.G. and Tiederman, W.G., Burst detection with single point measurements. *J. Fluid Mech.* 162 (1986) 389.
- Bogard, D.G. and Tiederman, W.G., Characteristics of ejections in turbulent channel flow. *J. Fluid Mech.* 179 (1987) 179.
- Bogard, D.G. and Coughran, M.T., Bursts and ejections in a LEBU-modified boundary layer. In: *Seventh Symposium on Turbulent Shear Flows*, [Toulouse, France, 1987.]
- Choi, K.S., A new look at the near-wall structure. In: Matthieu, J. and Compte-Bellot, G. (eds), Berlin: Springer-Verlag (1986).
- Choi, K.S., The wall pressure fluctuations of modified turbulent boundary layer with riblets. In: Liepmann H.W. and Narasimha, R. (eds), *Turbulence Management and Relaminarization*, Berlin. Springer-Verlag (1988).
- Choi, K.-S., Near-wall structure of a turbulent boundary layer with riblets. *J. Fluid Mech.* 298 (1989) 417.
- Choi, K.-S., Effects of longitudinal pressure gradients on turbulent drag reduction with riblets. In: Coustols, E. (ed.), *Turbulence Control by Passive Means*. Dordrecht. Kluwer Academic Publishers (1990).
- Coustols, E., Behaviour of internal manipulators: riblet models in subsonic and transonic flows. *AIAA Paper* 89-0963 (1989).
- Coustols, E. and Cousteix, J., Experimental investigation of turbulent boundary layers manipulated with internal devices: riblets. In: Gyr, A. (ed.), *Structure of Turbulence and Drag Reduction*. Berlin Springer-Verlag (1990).
- Fulachier, L., Djenidi, L. and Anselmet, F., Couches Limites sur Parois Rainurées Longitudinalement, riblets. 24^{ème} Colloque d'Aérodynamique Appliquée, Poitiers (1987).
- Gallagher, J.A. and Thomas, S.W., Turbulent boundary layer characteristics over streamwise grooves. *AIAA Paper* 84-2185 (1984).
- Gaudet, L., Properties of riblets at supersonic speed. *Appl. Sci. Res.* (1989) 245-254.
- Kim, H.T., Kline, S.J. and Reynolds, W.C., The production of turbulence near a smooth wall in a turbulent boundary layer. *J. Fluid Mech.* 50 (1971) 139.
- Klewicki, J.C. and Falco, R.E., On accurately measuring statistics associated with small-scale structure in turbulent boundary layers using hot-wire probes. *J. Fluid Mech.* 219 (1990) 119.
- Kline, S.J. and Robinson, S.K., Turbulent boundary layer structure progress, status, and challenges. In: Gyr, A. (ed.), *Structure of Turbulence and Drag Reduction*. Berlin Springer-Verlag (1990).
- Kuo, A.Y.S. and Corrsin, S., *J. Fluid Mech.* 50 (1971) 285.
- Luchik, T.S. and Tiederman, W.G., Timescale and structure of ejections and bursts in turbulent channel flows. *J. Fluid Mech.* 174 (1987) 529.
- Hooshmand, D., Youngs, R. and Wallace, J.M., An experimental study of changes in the structure of a turbulent boundary layer due to surface geometry changes. *AIAA paper* AIAA-83-0230 (1983).
- Maruyama, S. and Tanaka, H., The effect of spatial restriction on the inner-layer structure of wall turbulence. *J. Fluid Mech.* 177 (1987) 485.
- Offen, G.R. and Kline, S.J., A proposed model of the bursting process in turbulent boundary layers. *J. Fluid Mech.* 62 (1975) 2.
- Rohr, J.J., Reidy, L.W. and Anderson, G.W. In: *Drag Reduction 89* Davos. Ellis Harwood Ltd. (1989).
- Pulles, C.J.A., Krishna Prasad, K. and Nieuwstadt, F.T.M., Turbulence measurements over longitudinal micro-grooved surfaces. *Appl. Sc. Res.* 46 (1989) 197-208.
- Pulles, C.J.A., Krishna Prasad K. and Nieuwstadt, F.T.M., Simultaneous flow visualization and LDA studies over longitudinal micro-grooved surfaces. In: Coustols, E. (ed.), *Turbulence Control by Passive Means*. Dordrecht: Kluwer Academic Publishers (1990).
- Pulvin, Ph., Contribution à l'étude des parois rainurées pour les écoulements internes avec gradient de pression positif. Thèse de Doctorat; EPFL, Lausanne, No. 809 (1989).
- Rice, S.O., Mathematical analysis of random noise. *Bell Syst. Tech. J.*, 24 (1945) 46.
- Robinson, S.K., Kline, S.J. and Spalart, P.R., Quasi-coherent structures in the turbulent boundary layer. Part II. Verification and new information from a numerically simulated flat plate layer. In: *Near Wall Turbulence*: [1988 Zang Memorial Conference]. Hemisphere (1988).
- Robinson, S.K., The kinematics of turbulent boundary layer structure. NASA Technical Memo. 103859 (1991).

- Savill, A.M., Effect on turbulent boundary layer structure of longitudinal riblets alone and in combination with outer devices. In: Charnay, L. (ed.), *Flow Visualizations IV*. Hemisphere (1987).
- Savill, A.M., Drag reduction by passive devices, a review of some recent developments. In: Gyr, A. (ed.), *Structure of Turbulence and Drag Reduction*. Berlin: Springer-Verlag (1990).
- Schwarz-van Manen, A.D., Thijssen, J.H.H., Nieuwvelt, C., Krishna Prasad, K. and Nieuwstad, F.T.M., The bursting process over drag reduction grooved surfaces. In: Gyr, A. (ed.), *Structure of Turbulence and Drag Reduction*. Berlin: Springer-Verlag (1990).
- Sreenivasan, K.R., Prabhu, A. and Narasimha, R., Zero-crossings in turbulent signals. *J. Fluid Mech.* 137 (1983) 137.
- Tardu, S., Ecoulements Instationnaires en Canal; Réponse des Structures Cohérentes. Ph.D. Thesis; Université J. Fourier-Grenoble-I (1988).
- Tardu, S. and Binder, G., In: *Proceedings of 7th Turbulent Shear Flows*. [1989, Stanford.] (1989).
- Tardu, S. and Binder, G., Response of bursting to imposed velocity oscillations. Submitted to *J. Fluid Mech.*
- Tardu, S. and Binder, G., Review: effect of the OLDs on near wall coherent structures; discussion and need for future work. In: Choi, K.-S. (ed.), *Recent Developments in Turbulence Management*. Dordrecht: Kluwer Academic Publishers (1991).
- Tardu, S., Investigation of the Structure of the Turbulence in an Internal Flow Manipulated by Riblets. Report IMHEF T-91-19; Swiss Federal Institute of Technology, Lausanne; 1015, Lausanne, Switzerland (1991).
- Tardu, S., Binder, G., A new method to identify bursting events with single point measurements. In: *Eddy Structure Identification in Free Turbulent Shear Flows* [UTAM Symposium, 12-14 October 1992, Poitiers, France], (1992).
- Tiederman, W.G., Eulerian detection of turbulent bursts. In: *Proceedings of Zaric International Seminar on Near Wall Turbulence* [16-20 May 1988], (1988).
- Truong, T.V. and Pulvin, Ph., Influence of wall riblets on diffuser flow. *Appl. Sci. Res.* 46 (1989) 217-227
- Ueda, H. and Hinze, J.O., Fine-structure turbulence in the wall region of a turbulent boundary layer. *J. Fluid Mech.* 67 (1975) 67.
- Wallace, J.M. and Balint, J.L., Viscous drag reduction using streamwise aligned riblets: survey and new results. In: Liepmann, H.W. and Narasimha, R. (eds), *Turbulence Management and Relaminarization*. Berlin: Springer-Verlag (1988).
- Walsh, M.J., Turbulent boundary layer drag reduction using riblets. *AIAA Paper AIAA-82-0169* (1982).
- Walsh, M.J. and Anders, J.B., Jr., Riblet/LEBU research at NASA Langley. *Appl. Sci. Res.* 46 (1989) 255-262.
- Wilmarth, W.W. and Sharma, L.K., Study of turbulent structure with hot wires smaller than viscous length. *J. Fluid Mech.* 142 (1984) 142.

On near-wall turbulence-generating events in a turbulent boundary layer on a riblet surface

Y P TANG¹ & D G CLARK*

*Department of Aeronautical Engineering, Queen Mary & Westfield College (University of London), Mile End Road, London E1 4NS, U.K. (*author for correspondence)*

Abstract. The boundary layer over a drag reducing riblet surface is investigated using hot-wire anemometry and flow visualisation. The concept of a 'riblet sublayer' is introduced, and a definition is proposed in terms of a region of reduced turbulence energy production formed near the wall by the addition of riblets. The hot wire records are examined using a modified form of quadrant analysis, and results obtained over plain and riblet surfaces are compared. Close to the wall, the addition of riblets produces a marked reduction in the occurrence of 'ejection' (2nd quadrant) events. A corresponding increase in the incidence of 'sweep' (4th quadrant) events is accompanied by the development of a strong tendency toward a preferred event duration, and a preferred interval between events. These changes diminish rapidly with distance from the surface, becoming almost undetectable beyond $y^+ = 40$. They are discussed in the light of flow visualisation results, and interpreted in terms of mechanisms associated with the interaction between the riblets and the inner boundary layer flow structures. A conceptual model of the flow mechanisms in the riblet sublayer is proposed.

Key words: Turbulent boundary layer, drag reduction, riblets

1. Introduction

Since the discovery of 'riblets' as one of the successful passive drag reduction devices investigated at the NASA Langley Research Centre towards the end of the 1970's, extensive investigations have been carried out on both their practical application and the mechanism by which they produce their effect. The latter studies provide information on the manner in which the turbulent boundary layer responds to the disturbance introduced by riblets, and thereby reveal further details about its structure and potential for control. They have therefore been of considerable academic as well as technological interest during the past decade.

Among the investigations which concentrate on the mechanisms of riblet action, that of Gallagher and Thomas (1984) suggested that riblets appear to work by effectively increasing the thickness of the viscous sublayer. Bacher and Smith (1985) considered the interaction of the counter-rotating longitudinal vortices with the small secondary eddies formed at the peaks of the riblets, arguing that the secondary eddies would act to weaken the longitudinal vortices associated with low-speed streaks, as well as to retain low-speed fluid in the grooves. Choi (1989) argued that there is more than one mechanism involved, but that the prime one is the restriction of spanwise movement of the longitudinal vortices, causing a premature and consequently weaker

¹Present address: Dept. of Jet Propulsion, Beijing University of Aeronautics and Astronautics, P.R.C.

near-wall burst. The turbulent wall skin friction is reduced when this happens since, in Choi's view, the near-wall burst is one of the main sources for its production. Walsh (1990) reviewed the various mechanisms which had been proposed to explain drag reduction by riblets. He wrote 'The valleys of narrow v-groove riblets contain low-speed quiescent fluid associated with low skin friction, which lowers the overall drag penalty of the riblets. As the height and spacing of the riblets increases, in terms of wall units, drag reduction is lost. The data indicate that the riblets are still providing lateral resistance to the vortical structures but that more surface area is exposed to high skin friction and the drag penalty has exceeded the benefit.'

A common feature of previous work is that the direct effects of riblets appear to be confined to a viscous flow layer built up in the wall region by the riblet's action, and extending from the surface to $y^+ \approx 18$. It seems reasonable to call this layer the 'riblet viscous sublayer', or just the 'riblet sublayer', although its structure may be very different from that of the sublayer on a plain surface. It is the flow in this riblet sublayer and its interaction with outer flow structures which is likely to be the key to the detailed mechanisms of drag reduction. Unfortunately, for reasons of scale, the flow structure of the riblet sublayer has not been studied in detail.

The present paper is concerned with the statistics of occurrence, and the nature of 'active' flow patterns in the riblet sublayer, and with the interaction between the riblet sublayer and outer flow structure. In this context, an 'active' flow pattern is one associated with a marked excursion of the velocity perturbation into the second or fourth quadrant of the $u' - v'$ plane. Such patterns account for the majority of turbulence energy generation in the layer, and their passage is detected by the perturbation 'event' they produce in the output from a stationary hot wire probe. Such events are referred to below as 'active events', but it must be emphasised that the occurrence of the 'event' does not necessarily imply any particularly rapid evolution of the associated flow pattern, but simply its passage downstream past the probe at the local convection velocity.

In the present investigation, a modified quadrant analysis (MQA) scheme was used for detection and data analysis. With this technique, some distinctive characteristics of active events have been found in the riblet sublayer, and some aspects of the associated flow structure have been examined with the help of the flow visualisation. A conceptual model of the riblet viscous sublayer has been proposed from the experimental findings.

2. Experimental arrangement and procedure

The experiments were conducted in the fully developed turbulent boundary layer on the floor of a low-speed wind tunnel, with the adjustable working section roof set to give zero longitudinal pressure gradient. The tunnel free stream turbulence level was

approximately 0.5% under these conditions. Further details of the facility and methods used, have been given by Clark (1990), and Tang and Clark (1991).

Two L-shape riblet surfaces were used. The first has dimensions $h = 3$ mm, $s = 4$ mm and $l = 1$ m, corresponding to $h^+ = 15$, $s^+ = 20$ and $l^+ = 5000$ at $R_\theta = 1400$. The second has the dimensions $h = 5$ mm, $s = 10$ mm and $l = 1$ m, corresponding to $h^+ = 12.5$, $s^+ = 25$ and $l^+ = 2500$ at $R_\theta = 650$. The two cross-sections are shown in Fig. 1. The riblets consist of strips of black polystyrene, glued to the surface with polystyrene adhesive, and subsequently shaped by scraping with a form cutter. In both cases, the underlying surface consists of a sheet of 6 mm plate glass, with a layer of matte-black paint on its upper face. The light planes for flow visualisation are formed by placing a line of 12 volt, cine-projector lamps beneath 1.5 mm slits cut in the paint layer.

Velocity measurement in the wind tunnel was made using a DISA 55P61 x-array hot wire probe. This probe has two wires $5\text{ }\mu\text{m}$ in diameter and 1.25 mm in length, with a spacing of 0.5 mm between the wires. When normalised with inner variables at the highest Reynolds number of the present experiments, this gives a length of 6 wall units and a spacing of 2.5 wall units. Two DISA 55M10 units were used to operate the probes. A square-wave test gave a frequency response of 30 kHz for the system with an over-heat ratio of 1.35.

The probe was directly calibrated at the centreline of the tunnel, over the range -18° to $+18^\circ$, at five different velocities. A DANTEC Precision Anemometer 54N60 was used to establish the tunnel centreline velocity. Effects due to spanwise velocity perturbations were neglected, the estimated maximum error due to this cause being less than 3.5% for streamwise velocity and negligible for normal-velocity measurements.

A High Performance Data Acquisition Card was installed in a PC-AT-286 personal computer to digitise the two channels of hot wire signals with 12 bit accuracy.

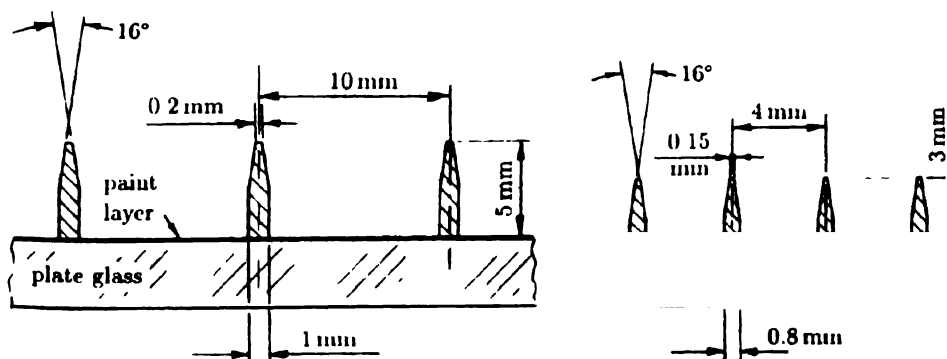


Fig. 1. Riblet dimensions.

For flow visualisation, smoke was introduced using a smoke wire $12\mu\text{m}$ in diameter. The estimated maximum Reynolds number of the wire was 1, consequently, no significant disturbance was anticipated from the wire itself. Single or multiple transverse light planes, sloping upstream from the surface, were used for illumination, the resulting sections being viewed from downstream in a direction approximately normal to the light planes (Clark 1990). Using multiple light planes, this technique provides a useful level of three dimensional information.

The visualisation studies were viewed, recorded and evaluated using a standard video system comprising a video camera (Panasonic WV-F15), a 14 in. colour monitor, and a high quality video recorder (Sony VO-9600P). A video sync separator chip, supplied with the video camera signal, was used to output synchronisation pulses to the computer data acquisition system in order to establish the precise relationship between the hot wire signal and the flow visualisation images. With the PAL interleaved line video system, the standard television framing rate of 25 full picture frames per second gives 50 field scans per second at half the full number of 625 lines per frame. The field scans can be viewed separately by the slow moving and freeze frame facility on a video recorder giving an effective framing rate of 50 fps. In the present work, this gave four or five frames during the average duration of the most active events at $R_\theta = 750$.

The basic scheme of the present experiment follows the observation of Bogard and Tiederman (1986), that hot wire measurement is effective in detecting 'events', whereas flow visualisation is effective in viewing the associated flow structure. The experiments were conducted in two phases. In the first phase, hot wire records were obtained on the riblet surfaces at $R_\theta = 1400$ without flow visualisation. The aims of this phase were as follows; (i) to compare the mean flow characteristics (mean velocity, turbulence intensity, turbulence shear stress and spectrum) between the plain and riblet surfaces, (ii) to compare the statistics of the active events on the plain and riblet surfaces detected by the MQA technique.

In the second phase, hot wire records were obtained at $R_\theta = 650$ with simultaneous flow visualisation, in order to identify flow structures associated with important active events in the hot wire record. Some calibration runs were also carried out without the flow visualisation, to check for changes in the perturbation statistics which could be attributed to effects of heat from the smoke wire or the lighting on the hot wire. No significant changes were found.

A basic data group was collected from phase one consisting of the statistics of occurrence of active events at four distances from the surface; $y^+ = 18, 30, 40$ and 60 , over both plain and riblet surfaces. A recording time of 240 s was used at each position, with a sampling rate of 500/s per channel. This corresponds to an interval between data points of $t^+ = 0.74$ and gives at least five data points in the duration of an interesting event. Several runs were made at each probe position, and no significant difference in the statistics was found between different runs. The statistics quoted below are all obtained from these data groups.

3. Data reduction

In the modified quadrant analysis (MQA) technique used in the data reduction, an active event is defined as one in which the perturbation product $u'v'$ is negative and has an absolute value above a certain threshold level. The individual events are then placed in categories depending on the maximum value of $|u'v'|$ reached, and whether the excursion is into the second or fourth quadrant of the $u' - v'$ plane. Further categories, depending on the nature of the trajectory in the $u' - v'$ plane, have also been examined (Tang and Clark (1991)), but are not used here.

Formally then:

(i) An active event is one associated with a velocity perturbation which makes a positive contribution to turbulence production, that is, the perturbation lies in the second or fourth quadrant of the $u' - v'$ plane. In addition, the absolute value of the perturbation product $u'v'$ must rise above a certain threshold value.

(ii) Threshold levels Th_n , are defined as follows;

$$\text{putting } Th = u'_{rms} v'_{rms},$$

$$Th_n = n \times Th \quad \text{for } n = 1, 2, 3, \text{ and } 4.$$

(iii) An event starts when $|u'v'|$ rises above the threshold Th_1 and ends when $|u'v'|$ falls below it.

(iv) Events are classified according to the highest threshold crossed by the value of $|u'v'|$. A Th_1 event is one in which the maximum value lies between Th_1 and Th_2 ; a Th_2 event, one in which the maximum reached lies between Th_2 and Th_3 , and so on, to Th_4 . Events which would fall into categories beyond Th_4 are not sufficiently numerous for their further classification to be statistically significant, hence effectively, $Th_5 = \infty$.

(v) Events for which v' is negative are characterised as 'sweeps', and events for which v' is positive are characterised as 'ejections'.

The time interval t_i between the peak values of two consecutive events and the duration t_d of individual active events are defined as shown in Fig. 2. Representative ejection and sweep events are shown in Fig. 3 as trajectories in the $u' - v'$ plane.

Results

The mean-velocity profiles measured at $Re = 1400$ on the plain and riblet surfaces are presented in Fig. 4. A single hot-wire probe was used, and a correction for wall proximity was applied to those points obtained at less than 500 wire diameters from the wall.

For the plain surface, the logarithmic region is well described using a von Karman

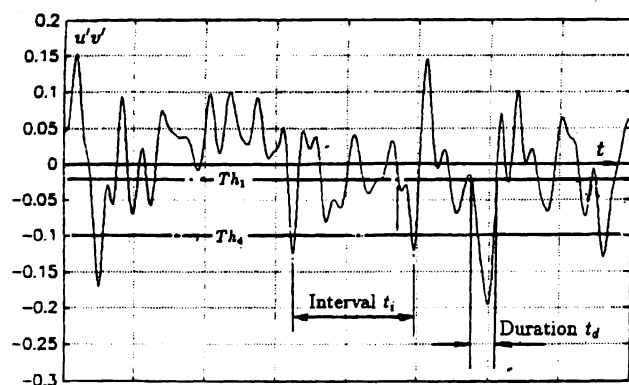


Fig. 2. Definition of interval and duration.

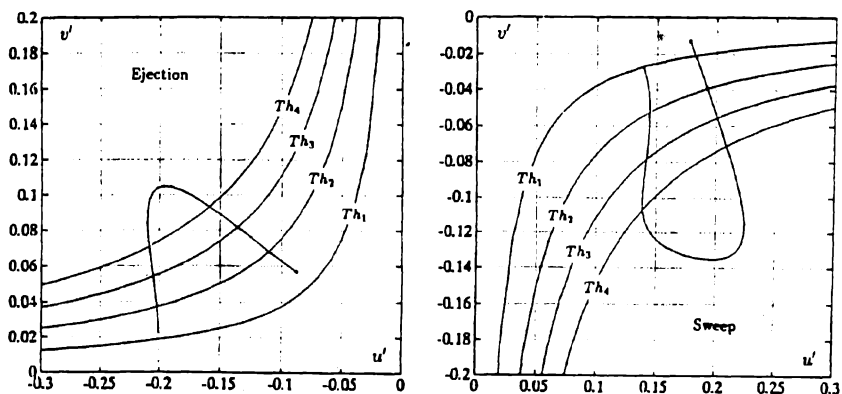


Fig. 3. Representative examples of event trajectories in the $u' - v'$ plane.

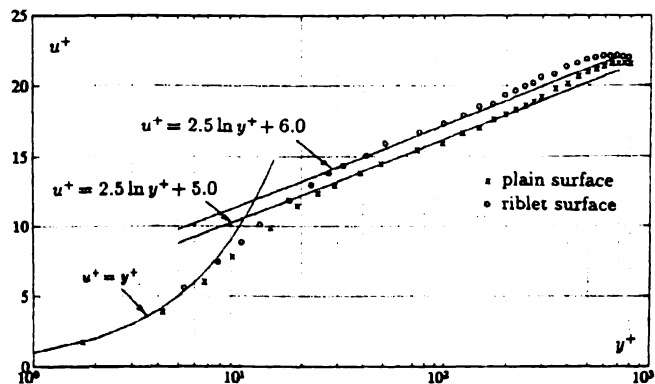


Fig. 4. Mean velocity over plain and riblet surfaces.

constant of 0.4 and a logarithmic intercept of 5.0. Estimates of the friction velocity u_τ , were made using both a Clauser plot and an estimate of the velocity gradient at the wall. The estimates agreed within 2%, and the mean of the two values was used in subsequent data reduction. The value of u_τ , the wall shear stress coefficient c_f , and shape factor H are shown in Table 1. The size of the corresponding wall units for length and time, y_τ and t_τ , are also given. For the riblet surface, the friction velocity u_τ and the virtual origin y_v were determined by Choi's method (Choi 1989), and the resulting values were used to obtain the points plotted in Fig. 4. These points indicate a logarithmic region extending from $y^+ = 35$ to about $y^+ = 200$, with a slope, $1/k$, unchanged from that on the plain surface, but with an intercept at $y = 0$ increased from 5.0 to 6.0; a shift away from the surface which is consistent with the results of other studies (e.g. Choi (1989)). The friction velocity u_τ is 2.5% lower than that on the plain surface, corresponding to a 5% reduction of shear stress at the wall, with $y_v = 2.4$ mm, that is $y_v^+ = 12$. The turbulence intensity of the u velocity component and the distribution of turbulence shear stress $u'v'$ are shown in Fig. 5, (a) and (b). Both figures cover the range $y^+ \leq 200$, to include the full logarithmic region. The origin in both these plots is the surface of the basic plate, and the variables are all reduced to non-dimensional form using the friction velocity u_τ on the plain surface. In Fig. 5(a) the peak in the u' profile shifts from $y^+ = 15$ on the plain surface to $y^+ = 25$ over the riblet surface, and the maximum value is reduced by 7%. However, beyond

Table 1 Boundary layer parameters for the plain surface

R_θ	u_τ m/s ²	c_f	H	y_τ mm	t_τ s
1400	0.0742	0.00417	1.41	0.196	0.0028

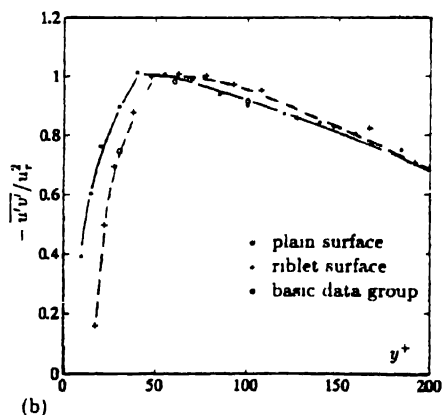
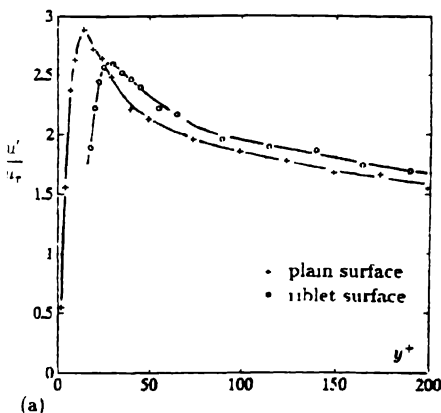


Fig. 5 (a) Turbulence intensity. (b) Turbulence shear stress

about $y^+ = 30$ the value of u' on the riblet surface is the higher of the two. Introducing a virtual origin for the riblet surface results would bring the two curves into close agreement except in the region of the peak between $y^+ \approx 10$ and $y^+ \approx 35$. In Fig. 5(b) the $\overline{u'v'}$ profile on the riblet surface shows features similar to those of the u' profile. No obvious decrease of shear stress is apparent.

The turbulence spectra for the riblet surface at $y^+ = 18$ and the plain surface at $y^+ = 6$ are shown in Fig. 6(a). Two lines with slopes of -1 and $-5/3$ are also shown for comparison. The spectrum over the plain surface does have identifiable linear regions parallel to these lines, but in the case of the riblet surface, the region with a slope of -1 is absent. The results suggest that the addition of riblets produces a significant decrease of energy-containing turbulence for wave numbers less than 0.02, and some increase for wave numbers between 0.02 and 0.2. The absence of the region with a slope of -1 is associated with this change.

Perry et al. (1986) pointed out the relationship between the turbulence spectrum and the presence of coherent flow structures, and reconstructed a spectrum with a slope of -1 by generating artificially the type of signal to be expected from the passage of a probe through vortex-like structures. This suggests that the change in the turbulence spectrum may result from a significant change in the flow structure when riblets are added to the surface.

The distribution of turbulence production from Figs 4 and 5(b) is shown in Fig. 6(b). For the purposes of discussion below, the boundary layer is divided into three regions based on these results. In region I ($y^+ < \approx 19$) the turbulence production over the riblet surface decreases rapidly and is apparently lower than that over the plain surface. In region II ($19 < y^+ < 60$), the turbulence production over the riblet surface is higher than that over the plain surface, mainly due to the fact that the local mean flow shear rate is higher. In region III ($y^+ > 60$), there are no significant differences between the plain and riblet surfaces.

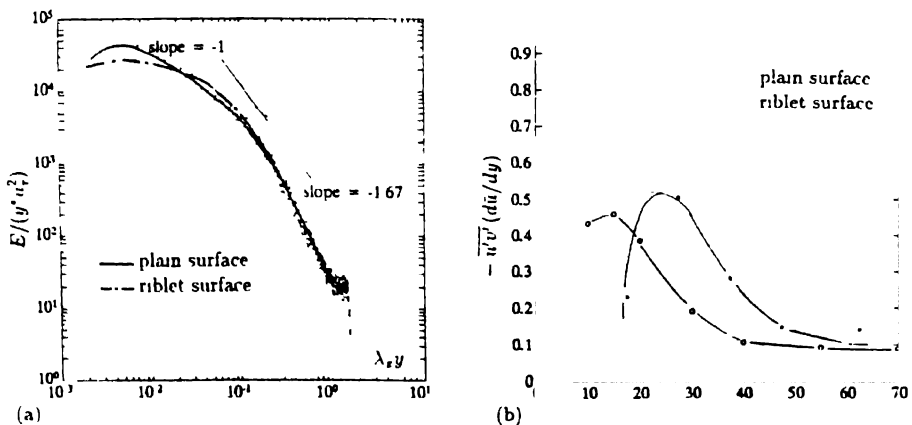


Fig. 6 (a) Turbulence spectra (b) Turbulence production

4.1. Examination of active events in region I

Histograms of the occurrence of active events over the plain and riblet surfaces at $y^+ = 18$ are shown in Fig. 7.

The probability is calculated by:

$$P_{nj} = N_{nj}/N, \quad \text{where } n = 1, 2, 3, 4 \quad \text{and } j = 1, 2.$$

Here N is the total number of active events. N_n is the number of events of rank n , and j denotes the type of event; $j = 1$ indicates an ejection ($v' > 0$), and $j = 2$ indicates a sweep ($v' < 0$). The most noticeable change associated with the addition of riblets is a dramatic increase in the number of sweep events. As the rank of the events increases, sweeps become the dominant event and ejection events become very rare.

A study which only included ejections in an assessment a 'bursting' rate, would conclude that riblets cause a marked reduction in bursting rate at this position. If both sweeps and ejections were included, the bursting rate over the riblet surface, (using Th_2 as a threshold) would be about 10% higher than that over the plain surface, but the burst duration would be about 10% lower. In other words, riblets appear to cause a shift toward more sweeps of short duration near the wall.

More details of this distinctive feature of the riblet surface data can be seen in Fig. 8. The threshold (or hole size) used here is Th_2 . Figure 8a shows the probability distribution versus time interval for individual sweep events and Fig. 8b shows the probability versus duration. From Fig. 8 the main difference between riblet and plain surfaces occurs when the interval, t_i^+ , is less than 200. In this low interval range the riblets create a peak of sweep probability at $t_i^+ = 18$, though the mean interval (averaged between $t_i^+ = 15$ and $t_i^+ = 200$) is about 36.

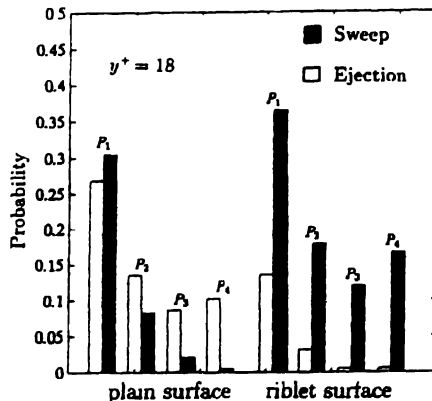


Fig. 7. Event histograms: region I

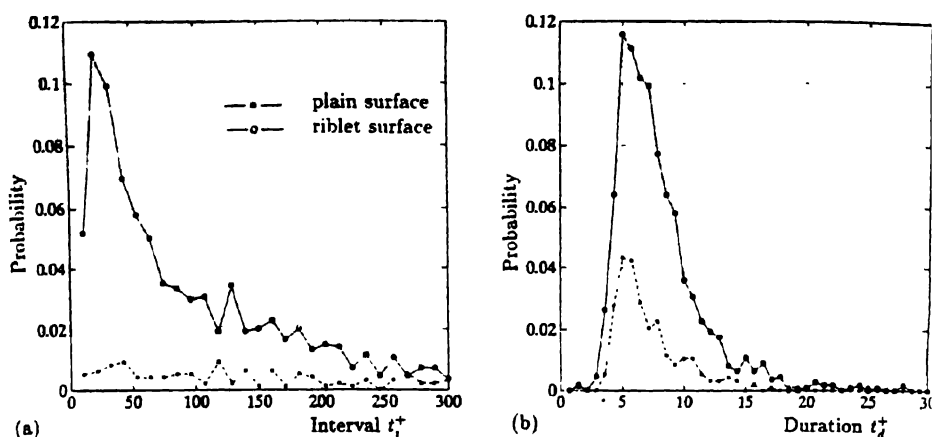


Fig. 8. Probability of a sweep event; region I.

Figure 8b shows that the increase of the probability of sweep events occurs for even durations, t_d^+ , of between 3.6 and 14. This is the range of duration for which the probability of a sweep event over the plain surface is also high. The position of the peaks is almost the same over the two types of surface and the form of the curves is similar.

Figure 9 shows the probability of ejection events versus interval and duration. Unlike the probability of sweep events, the probability of ejection events in this near wall region is reduced by the addition of riblets; a point which is also revealed by the histogram of Fig. 7.

The main changes shown in Fig. 7 and Fig. 12, were found to be independent of both the spanwise position of the probe and the threshold (or hole size) used.

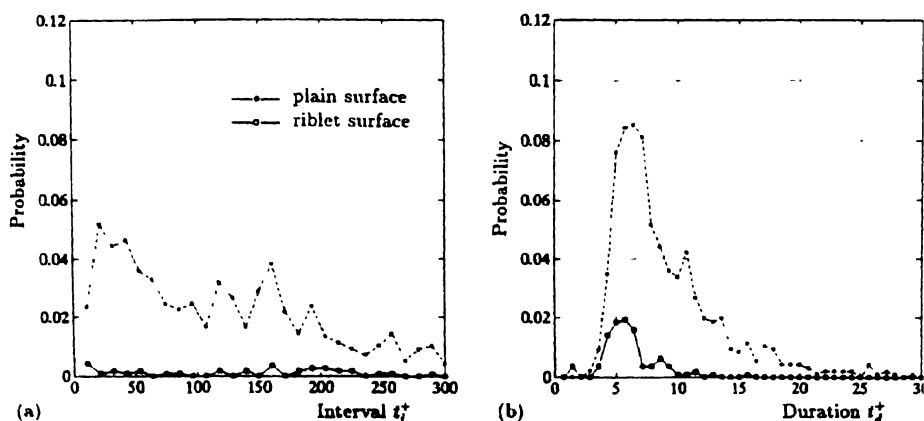


Fig. 9. Probability of an ejection event; region I.

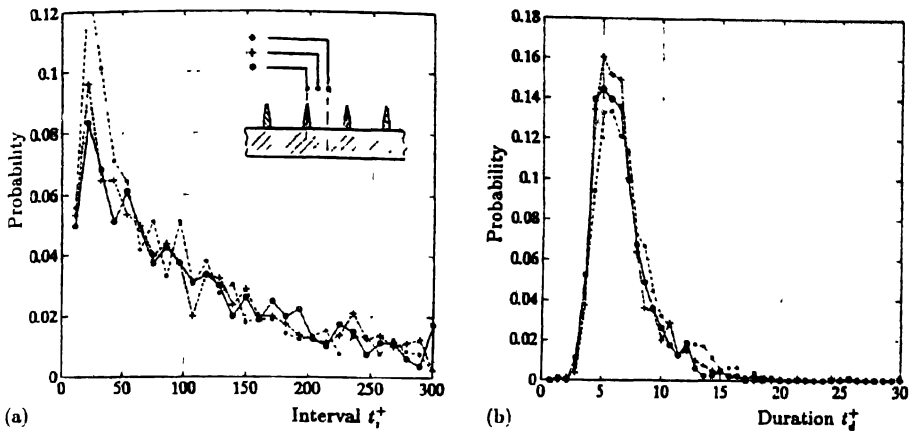


Fig. 10. Probability of a sweep event at three spanwise positions ($y^+ = 18$).

Figure 10 shows the probability of the sweep events versus (a) the interval, and (b) the duration, at $y^+ = 18$, measured at three different spanwise positions above one riblet groove. The basic characteristics, such as the interval corresponding to the peak of probability, are similar at all spanwise positions.

Differences in the amplitude of the probability are within the range of scatter of the results, except for considerable differences in the regions of peak probability.

Figure 11 shows the probability of sweep events versus the interval of individual sweep events at a threshold Th_4 . Compared with Fig. 8a the distribution is similar, though the preferred interval has increased to about $t_i^+ = 100$, and naturally, the peak probability is lower.

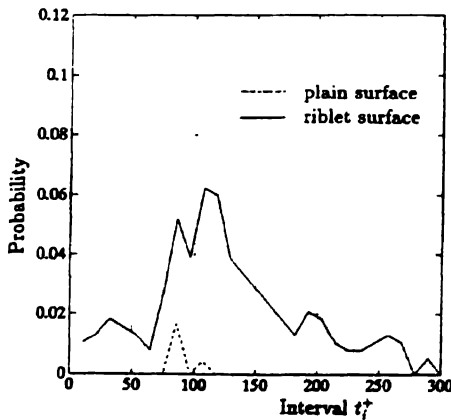


Fig. 11. Probability of Th_4 sweep events; region I.

4.2. Examination of active events in region II

A histogram of active events in region II is shown in Fig. 12. The probability of ejection events recovers rapidly with increasing distance from the surface, though at $y^+ = 30$ it is still lower than that over the plain surface, whilst for higher rank events, the probability of a sweep is still higher. The differences are further reduced at $y^+ = 40$.

Figure 13 shows the probability of sweep or ejection versus interval and duration of events using a Th_2 threshold. The scale of Fig. 13 is the same as that of Fig. 8 for comparison. The distinctive feature in Fig. 13a is that the occurrence of a sweep loses its dominant central interval and spreads over a wide range of intervals. The further from the wall, the flatter the distribution, until at $y^+ = 40$ it becomes similar to that over the plain surface. That the probability of occurrence of an ejection event increases, as the probe is moved away from the wall, can be seen in Fig. 13b, but the distribution is not substantially different from that over the plain surface.

Comparing the statistics of active events over the plain and riblet surfaces in Fig. 13 and Fig. 8; the probability versus the interval of sweep events over the plain surface retains similar characteristics at all probe positions; the amplitude of the probability is similar and sweeps occur at a wide range of intervals. The probability over the riblet surface has very different characteristics. In region I, there is a sudden increase of the probability of a sweep event occurring with a marked preferred interval. The characteristics return to those of the plain surface as the probe is moved out through region II.

Analysis of the statistical characteristics of ejection events leads to a similar picture. It is reasonable to ascribe these characteristics to the presence of local flow structures with a scale of region I.

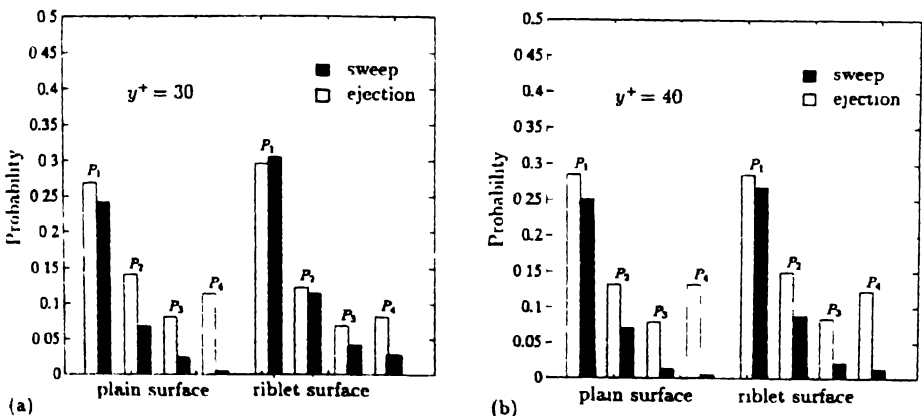


Fig. 12 Event histograms: region II

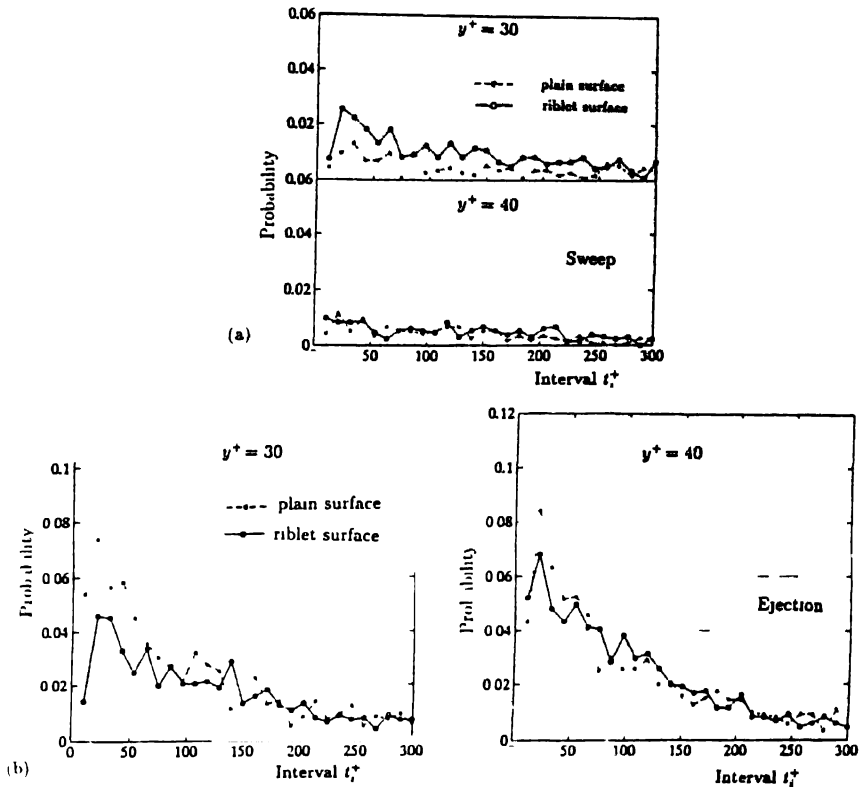


Fig. 13 Probability of sweep and ejection events, region II

4.3 Flow patterns associated with active events

Flow visualisation on the riblet surface, using both single and multiple light planes reveals very complex flow patterns with different time and space scales. Those associated with MQA events, can be identified with the aid of a simultaneous hot wire record from a probe situated in the field of view, and in spite of the apparent complexity, some characteristic features are apparent.

Two patterns originating in motions outside the riblet sublayer were identified as being associated with strong (Th4) sweep events at $y^+ = 18$. A representative example of the first type is shown in Fig. 14. Two frames of a video sequence are shown. These were obtained using single light plane, and with smoke originating from a wire at the level of the riblet tops. The time interval between the frames is 0.1 s ($t^+ \approx 36$). The second frame shows a local clearance of smoke-contaminated flow from the riblet grooves with no obvious flow structure visible within the cleared region. The clearance of smoke can only be due to a sweep originating from large scale motion in the outer layers, and the patterns are consistent with the occurrence of motion of the



Fig. 14. Flow visualisation during a strong sweep event in region I.

type which is responsible for the formation of a 'Falco pocket' in a near-wall smoke layer on a plain surface. Only by its absence can smoke originating from the inner layers reveal a sweep of this type.

The second example of a flow pattern associated with a strong (Th4) event is that of the interaction of a pair of longitudinal vortices causing a sweep at the position of the probe. In Fig. 15(a) an example of this feature is shown using a single light plane, and in Fig. 15(b) using multiple light planes with simultaneous hot wire measurement. The longitudinal vortices have a scale of $l^+ \approx 30$. As with the previous example, this feature is also found over a plain surface.

Figure 16(a) shows an example of the secondary eddy at the top of a riblet, mentioned by Bacher and Smith (1985). In the case shown, smoke was generated from a streamwise wire positioned along the top of the riblet. On the video record it is clear that the eddy results from crossflow at the riblet top, due to spanwise meandering of

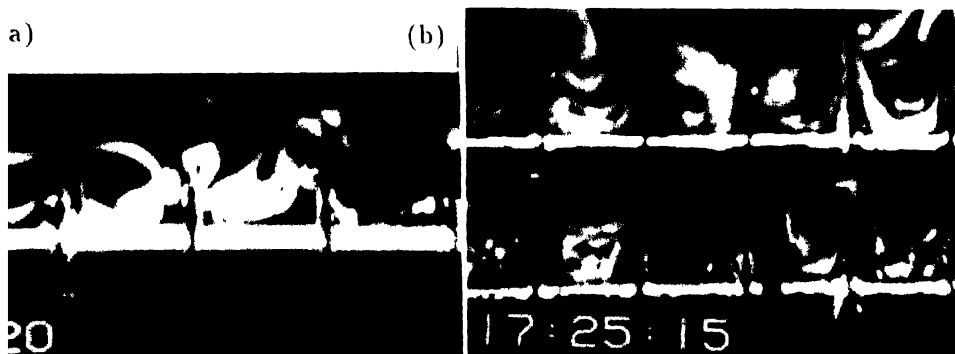


Fig. 15. Strong sweep events in region I; vortex pairs.

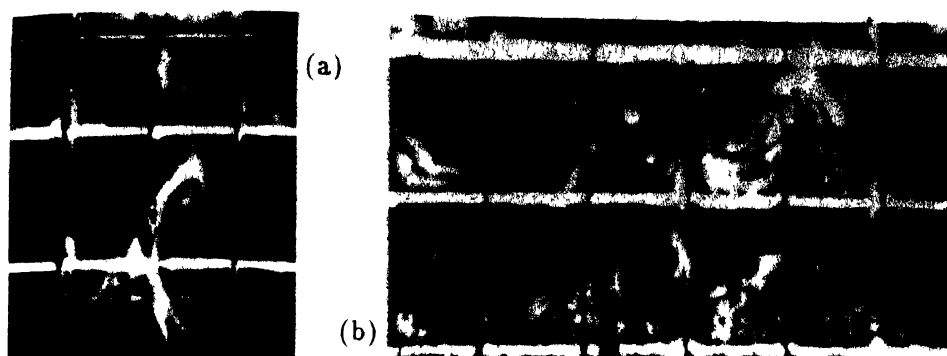


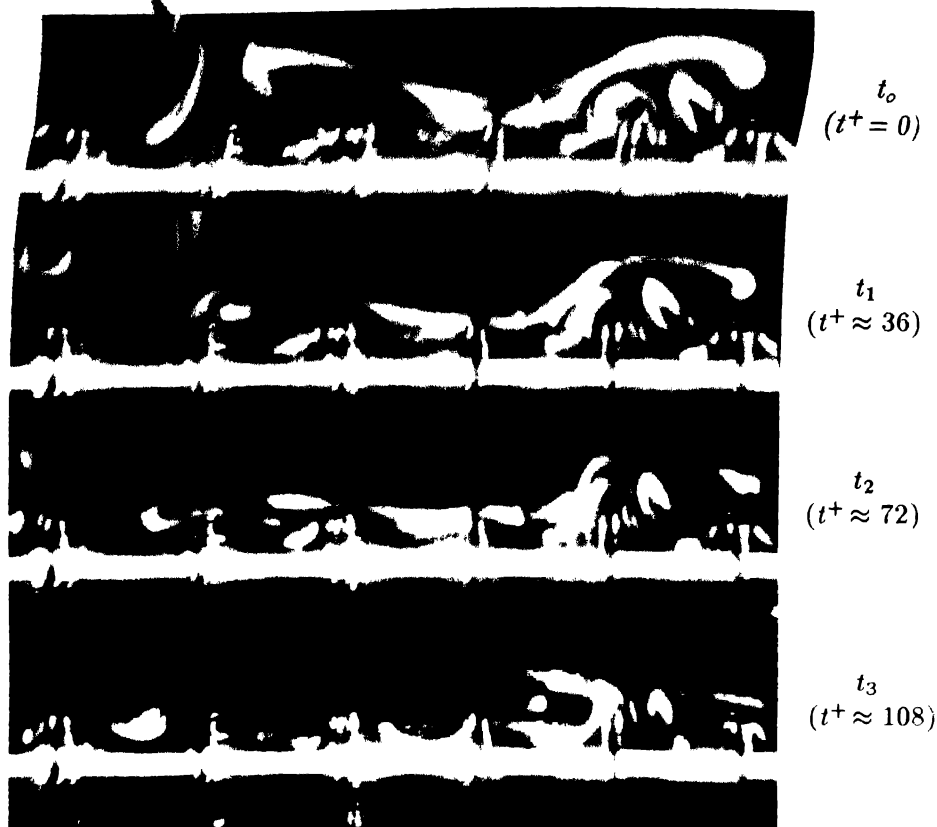
Fig. 16. (a) Secondary eddy. (b) Complex interaction.

the overlying flow. The video records also reveal example of apparent interaction between these secondary eddies and the longitudinal vortices in the outer flow, interactions which are also accompanied by Th4 sweep events at $y^+ = 18$. An example of the complex patterns which occur such cases is shown in Fig. 16(b). In some such sequences, the outer longitudinal vortex appears to be drawn down into the riblet groove. These observations lend support to the suggestion of Bacher and Smith that interactions of this type represent a significant mechanism for weakening the mixing process.

Figure 17 shows a series of smoke patterns illuminated by a single light plane. The smoke wire was positioned at the top of riblets and at a distance $l^+ = 150$ upstream of the light plane. The series covers 0.3 s ($t^+ \approx 108$) and the interval between any two frames is 0.1 s. At time t_0 the smoke initially moves up away from the groove, and then gradually moves right down into the groove, until at t_3 it reaches the bottom. There are no violent local flow patterns associated with this process. The video sequence suggests that the flow is drawn down in this way by the influence of an energetic sweep downstream. This accelerates the flow along the groove locally, causing flow to be drawn into the groove for some distance upstream. If this is the case, a corresponding flow up out of the groove is likely to be present downstream, and behaviour which could be interpreted in this way was also observed, elsewhere in the video record. These processes could be termed respectively, 'riblet induction' or 'riblet suction', and 'riblet overflow'.

The motions noted above are all on the scale of region I and are therefore likely to be the motions responsible for the altered near-wall turbulence statistics on the riblet surface but they all result from processes originating above region I and become part of them. In the log-law region, therefore, their effect is to modify the flow structures without creating fundamentally new ones.

Strong ejections are rare in the near wall region, and it seems that the processes which are accompanied by flow out of the grooves, tend to be gentle and extended, rather than abrupt, localised and violent.

*Fig. 17* 'Riblet induction'

5. A conceptual model of the riblet sublayer

The results discussed above provide further evidence that on a drag-reducing riblet surface, a region exists which may conveniently be referred to as the 'riblet sublayer'. Within this layer, the characteristics of the flow are significantly altered by the presence of the riblets and some flow features exist which are unique to the layer. These features are small in scale, and consist simply of interactions between the riblets and the flow configurations normally found in the near-wall layers of a turbulent boundary layer. They do not constitute a change in the basic flow mechanisms normally present in the inner log-law region.

In terms of the methods adopted in the present work, the riblet sublayer may be identified with a region in which the presence of the riblets produces a substantial alteration in the distribution of 'active events' in the output of an x-wire anemometer probe aligned to reveal $u' - v'$ perturbations. The layer is characterised by an increase in 'sweep' (4th quadrant) events of short duration, and a marked reduction in 'ejection'

(2nd quadrant) events. The sweep events occur over a wide range of intervals, but have a preferred interval of $t^+ \approx 20$. Strong ejection events become very rare, and no preferred interval between occurrences is discernible. The layer extends from the surface to $y^+ \approx 20$.

Beyond $y^+ \approx 20$, the predominance of 'sweep' events persists to $y^+ \approx 40$, but the preferred interval is no longer present, and the event statistics rapidly return to those found over a plain surface. In those terms, at $y^+ = 60$ the two surfaces are indistinguishable.

Viewing the flow visualisation results over the riblet surface in the light of the event statistics, the flow patterns which are similar to those over a plain surface are the large scale outer-sweep, penetrating to region I, and the medium scale vortex-induced sweep in region II. These two features are also found to occur with a wide range of intervals on a plain surface, and their scale suggests that they can only be involved in the reduction in the number of Th4 events, not the increased number of events of lower rank.

Three types of pattern which could account for the altered event statistics in region I are identified as the small scale secondary eddies forming in sporadic cross-flow across the riblet peaks, the parts of longitudinal near-wall vortices which enter the riblet grooves, and the tendency for sweep flow from the log-layer to entrain further flow into the riblet grooves by mass conservation. The scale of these patterns is consistent with the relatively short interval and duration of the extra sweep events detected.

The foregoing suggests a conceptual model of the riblet viscous sublayer as illustrated in Fig. 18. The flow in the outer layers is taken to be dominated by vortical elements, originating from the evolution of hairpin eddies similar to those proposed by Wallace (1990). Riblets bring about no fundamental change in the large and middle-scale vortical elements but they do change the environment in which such features are initiated. The sublayer which they create is highly directional, and above it where the flow has sufficient freedom for turbulence to be produced, rates of shear

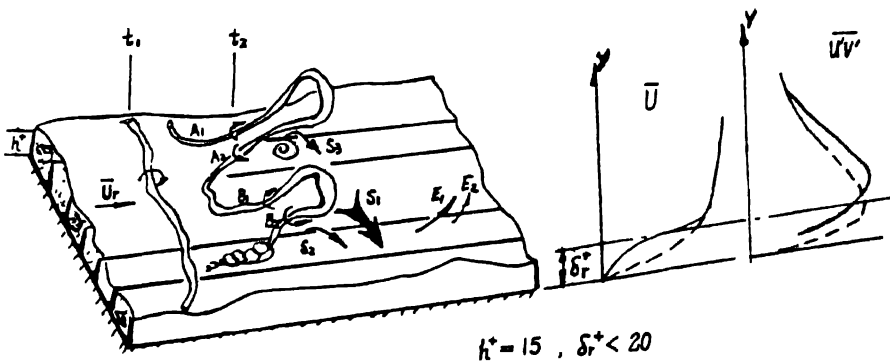


Fig. 18. Riblet sublayer; conceptual model

are lower than those in the equivalent layer over a plain surface. High speed, highly perturbed fluid swept into the riblet grooves (S1) encounters strong viscous dissipation, and emerges with its perturbation level greatly reduced and any lateral component of velocity largely removed. The increased spacing of the low speed streaks above the riblet surface may be explained by the reduced mean flow shear rate. Interaction between the streamwise vortical structures and the riblets, with some parts of the flow structures being drawn down into the riblet grooves may also contribute. The smaller scale processes of the secondary-eddy induced sweep (S3) and 'riblet induction' (S2) are responsible for less energetic movements of fluid into the grooves and are the features most directly responsible for the altered event statistics characterising region I. The slow moving, quiescent fluid from the grooves emerges, either by the action of an outer vortical structure producing a strong ejection, (E1) or simply by being gradually displaced (E2) as other more energetic fluid enters elsewhere, the latter being the dominant outward flow feature in the sublayer. The flow rate in and out of the riblet grooves should be directly related to the balance of mean momentum and turbulence within them, and will therefore be related to the skin friction.

Acknowledgments

The work was supported by a grant from the UK Department of Trade and Industry.

References

- Bacher, E V. and Smith, C R., A combined visualisation-anemometer study of the turbulent drag reducing mechanisms of triangular micro-groove surface modification. *AIAA Paper* 85-0548 (1985)
- Bogard, D G. and Tiederman, W G. Burst detection with single-point velocity measurements. *J Fluid Mech* 162 (1986) 389
- Choi, K.-S., Near-wall structure of a turbulent boundary layer with riblets. *J Fluid Mech* 208 (1989) 417
- Clark, D G., Boundary layer flow visualisation patterns on a riblet surface. In Coustols E. (ed.) *Turbulence Control by Passive Means*. Dordrecht: Kluwer Academic Publishers (1990)
- Gallagher, J A. and Thomas, A S W., Turbulent boundary layer characteristics over streamwise grooves. *AIAA Paper* 84-2185 (1984)
- Perry, A E., Henbest, S. and Chong, M S. A theoretical and experimental study of wall turbulence. *J Fluid Mech* 165 (1986) 163
- Tang, Y P. and Clark, D G., On turbulence generating events in turbulent boundary layer. *QMW-EP-1086* (1991)
- Wallace, J M., On the structure of bounded turbulent shear flows. In *Proc NASA Boundary Layer Structure Workshop* [Langley Research Center, Hampton, Virginia, August 28-30 1990]
- Walsh, M J., Riblets. In Bushnell, D M. and Hefner, J N. (eds), *Viscous Drag Reduction in Boundary Layers*. Progress in Astronautics and Aeronautics 123 (1990) p. 203

Friction velocity and virtual origin estimates for mean velocity profiles above smooth and triangular riblet surfaces

A.D. SCHWARZ-VAN MANEN, A.F.M. VAN GELOVEN,
J. NIEUWENHUIZEN, J.C. STOUTHART, K. KRISHNA PRASAD
& F.T.M. NIEUWSTADT*

*Eindhoven University of Technology, The Netherlands, * Delft University of Technology, The Netherlands*

1. Introduction

It is well known that riblet surfaces influence only the region close to the wall (Hooshmand et al. 1983). The appropriate velocity scaling for this region is the friction velocity (u_*). Thus it is important to determine u_* very accurately. For situations where no drag balance is available various methods have been developed to estimate u_* from the mean streamwise velocity profile. Generally, the logarithmic friction law (Tennekes and Lumley, 1972) is used, better known as the log-law or the law of the wall method. However, most of the methods can only be used for surfaces where the $y=0$ position is exactly known, i.e. for smooth surfaces. Choi (1989) developed a method for riblet surfaces to determine from the mean streamwise velocity profile both the friction velocity and the virtual origin of the riblets into the turbulent boundary layer. In that same year, Bechert and Bartenwerfer (1989) published a theoretical model, developed for riblet surfaces to calculate the protrusion height.

During the investigation presented here, it was discovered that the log-law method could not be used; the error in the friction velocity was of the same order as the amount of drag reduction of the investigated riblet surfaces. The two main sources for this error are: (i) the estimation of the logarithmic region in the vertical velocity profile of the mean stream; and (ii) the Von Kármán constant (κ). In the literature values for κ are given between 0.38 and 0.42. For the same reason this method was criticized by Bradshaw et al. (1991). Therefore, several methods were used to estimate the friction velocity for the smooth surface from the mean streamwise velocity profile and the respective results were compared with one another. One of the methods used here is the viscous layer method. Using this method for riblet surfaces, the virtual origin of the mean streamwise velocity profile can be estimated. The results of this method for the riblet surfaces were compared with the results of the methods of Choi, and Bechert and Bartenwerfer. In this section none of the presented quantities are non-dimensionalized. In the next section the non-dimensionalized profiles of velocity, turbulent intensities and Reynolds stress correlations are presented, showing that the investigated riblet surfaces indeed possess the characteristics of drag reducing surfaces. Finally, some conclusions are presented.

2. Experiments

The measurements reported in this article were performed in the low-speed water channel in the Laboratory for Fluid Dynamics and Heat Transfer of the Technical University of Eindhoven in The Netherlands. This channel has a test section which is 7 m long, 30 cm wide and 30 cm high (Fig. 1). In this test section a false surface, with a length of 6 m, was mounted 123 mm above the bottom wall of the water channel. This false surface consists of several parts. The first part which is closest to the contraction of the water channel is a 2250 mm fixed glass surface. This glass surface is followed by several removable pieces with different lengths and different kinds of surface geometries. A tripping wire was placed 600 mm downstream of the nose of the glass surface to make sure that all measurements were performed in a fully developed, two dimensional, turbulent boundary layer. The mean stream velocity of this water channel can be adjusted between 0.0 and 400 mm/s, while the water temperature is kept at $20.00 \pm 0.05^\circ\text{C}$.

The primary element of the measurement system is the two component HeNe Laser Doppler Anemometer (LDA). The computer system was updated during the last year, therefore the measurements were performed with two different control systems. At first the measurements were controlled by a PDP-11/23 computer, which was replaced by a PHYDAS system (physics data acquisition system) using a M68030 processor. This system was developed by the faculty of Technical Physics at the Eindhoven University of Technology. More detailed descriptions of the measurement system are given by Pulles (1988) and Kern (1985).

A two component LDA system uses three beams, two reference beams and one main beam, to obtain the velocities. In our case the two reference beams are parallel to the surface and the main beam makes an angle with the surface. The beams are further positioned in such a way that alternately a $u-v$ component and a $u+v$ component are measured. As the time interval between two successive samples is very small (≤ 0.002 s), the u and v can be obtained through interpolation between two successive

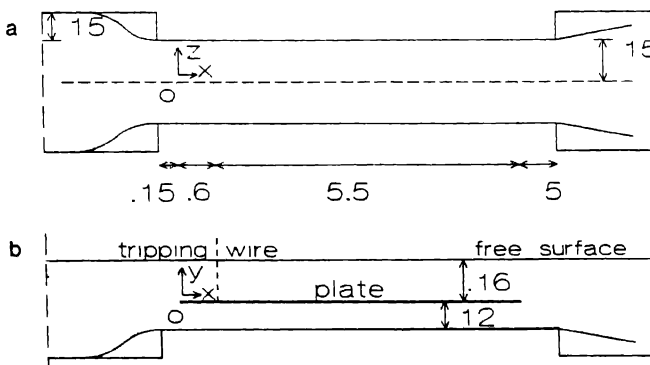


Fig. 1 Top (a) and side view (b) of the low-speed water channel

samples. A detailed description of this setup is given by Schwarz-van Manen and Stouthart (1990).

This configuration of the laser beams can lead to two effects which appear when measurements are performed very close to the surface. First there is the backscatter of the main laser beam into the measurement volume due to reflection at the surface. A second effect is that the horizontal reference beams will eventually touch the surface, even before the measurement volume does. This is because the laser beams converge into a waist, which is at the position of the measurement volume, thereafter they diverge.

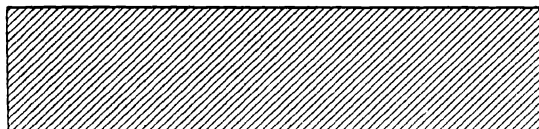
Special jigs were used to calibrate the vertical and spanwise position of the measurement volume with respect to the peak of the grooved surface (van Geloven 1992). The present LDA system has not only a vertical traversing mechanism but also a calibrated spanwise traversing system which permits the measurement volume to be located at different spanwise positions above the grooves. For safety reasons, the measurement volume could not get nearer than $100\text{ }\mu\text{m}$ to the surface. The measurement volume had a spanwise width of 0.5 mm and a vertical and streamwise width of 0.1 mm .

The measurements were performed over four different surfaces shown in Fig. 2: a smooth surface (\mathcal{U}); a triangular riblet surface (\mathcal{R}) with $h/s = 0.75$ and $\text{tg}(\alpha) = 0.67$; a triangular riblet surface (\mathcal{P}) with $h/s = 0.9$ and $\text{tg}(\alpha) = 0.5$; and a triangular surface (\mathcal{S}) which has the same dimensions as the \mathcal{P} -surface with every other triangle skipped, for which $h/s = 0.45$ and $\text{tg}(\alpha) = 0.5$. Here α is half the apex angle of the ribs, s is the spacing between the centres of the grooves and h is their depth.

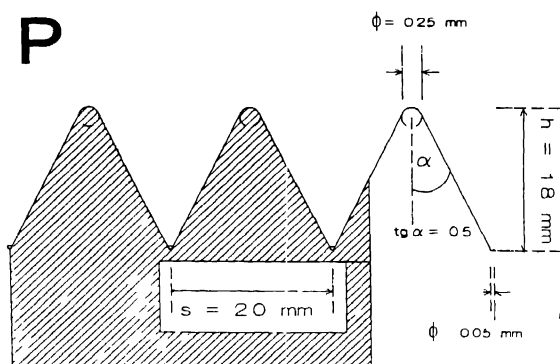
During the experiments the vertical profiles of the mean streamwise velocities, the turbulent intensities and the Reynolds stress correlations were measured. These measurements were used to obtain the friction velocity and the virtual origin. During a one day experiment it was possible to measure the above mentioned quantities at 40 different heights. This is due to the long averaging time ($\approx 10\text{ min}$) caused by the much larger time scales in water experiments when compared with a wind tunnel. Typical values for the viscosity ν and the friction velocity u_* for the presented water channel measurements are $1 \cdot 10^{-6}\text{ m}^2/\text{s}$ and 0.01 m/s , respectively, with a dimensionless time scale of 0.01 s . However, for a wind tunnel typical values for ν and u_* are $15 \cdot 10^{-6}\text{ m}^2/\text{s}$ and 0.5 m/s , respectively, leading to a dimensionless time scale of $6 \cdot 10^{-5}\text{ s}$, which is roughly 2 orders of magnitude smaller than the time scale for the water channel measurements. Due to this long averaging time each profile measurement lasted 3 days. The first day was used to measure the outer layer ($10\text{--}100\text{ mm}$). The next day to measure the logarithmic region ($1\text{--}10\text{ mm}$) and a day was used to measure the very near wall layer ($0.1\text{--}1\text{ mm}$).

For all the experiments the water level above the mounted surface, at zero mean stream velocity, was kept at 158 mm . The measurements were performed at $404.5 \pm 0.5\text{ cm}$ downstream of the nose of the mounted surface and $344.0 \pm 0.5\text{ cm}$ downstream of the tripping wire. Further, experimental conditions are given in Table 1. The errors indicate here the maximum deviation from the average values.

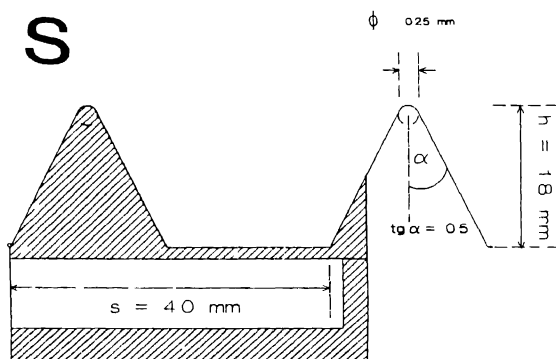
U



P



S



R

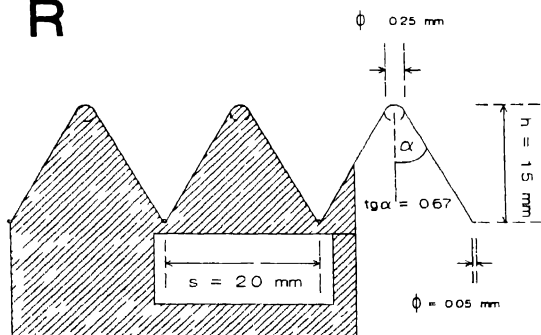


Fig 2 Geometries of the investigated surfaces

Table 1 Experimental conditions.

	<i>U</i>	<i>R</i>	<i>P</i>	<i>S</i>
U_0 [cm/s]	20.0 ± 0.3	20.0 ± 0.3	20.0 ± 0.3	20.0 ± 0.3
δ^* [mm]	14.6 ± 0.8	13.1 ± 1.5	14.5 ± 0.9	12.0 ± 1.3
θ [mm]	10.4 ± 0.5	9.4 ± 1.2	10.4 ± 0.8	8.6 ± 1.3
Shape factor	1.41 ± 0.04	1.40 ± 0.06	1.40 ± 0.04	1.40 ± 0.05
Re_s	$8 \cdot 10^5$	$8 \cdot 10^5$	$8 \cdot 10^5$	$8 \cdot 10^5$
Re_θ	2080	1880	2080	1720
T [°C]	20.0 ± 0.05	20.0 ± 0.05	20.0 ± 0.05	20.0 ± 0.05

3. Local friction velocity measurements

The friction velocity (u_*) is indicative of the amount of drag a flow experiences from a surface. When comparing the results of smooth and drag reducing riblet surfaces with each other it is important to know the u_* as accurately as possible, because the amount of drag reduction between a smooth and a drag reducing surface is about 5%.

In this section several methods will be discussed to obtain the friction velocity from the velocity profile. In the first subsection methods for smooth surfaces will be discussed while the second subsection deals with methods for grooved surfaces.

3.1. Methods for the smooth surface

When no drag balance is available there are various ways to estimate u_* from the velocity profile. The one most commonly used is the logarithmic friction law (Tennekes and Lumley, 1972). This law is valid in the logarithmic region of the flow and is defined as

$$\frac{\bar{U}}{u_*} = \frac{1}{\kappa} \ln \frac{yu_*}{\nu} + A. \quad (1)$$

In this expression, the kinematic viscosity ν is $1 \cdot 10^{-6} \text{ m}^2/\text{s}$ at 20°C , \bar{U} is the time average velocity and A is an empirical constant which, according to the literature, has a value between 4.9 and 5.45. Using the logarithmic region to estimate u_* the question will arise which value to use for the Von Kármán constant κ ($0.38 \leq \kappa \leq 0.42$). Another problem is the exact estimation of the logarithmic region in a velocity profile. The standard region mentioned in the literature is

$$30 \leq \frac{yu_*}{\nu} \leq 800, \quad (2)$$

but it is mainly determined by the Reynolds number. Therefore, the proper range

where the logarithmic region can be found has to be estimated from the velocity profiles.

Bradshaw, Launder and Lumley (1991) made the following remark about using the logarithmic region to estimate the friction velocity:

... One remarkable cause of confusion is the wide range of constants in the logarithmic "law of the wall" that are assumed, or predicted, in different methods. According to first order arguments, which are used implicitly in all the calculation methods, these constants should be universal. The actual range – ignoring a few outlying methods – implies a 10% "uncertainty" in skin friction on a flat plate in a low-speed flow, the simplest of all test cases. We are trying to achieve a consensus! ...

A second method which can be used is the Clauser method (1956). This method uses the complete velocity profile of a turbulent boundary layer to estimate the u_* . Clauser made use of the following relations:

$$u_* = U_0 \sqrt{\frac{C_f}{2}}, \quad (3)$$

$$\frac{C_f}{2}^{1/2} = \frac{1}{\kappa} \ln Re_{\delta^*} + B, \quad (4)$$

with

$$Re_{\delta^*} = U_0 \delta^* / \nu. \quad (5)$$

The displacement thickness δ^* is defined by

$$\delta^* = \int_0^\infty (1 - \bar{U}/U_0) dy. \quad (6)$$

In these equations C_f is the friction coefficient, U_0 is the mean free stream velocity and B an empirical constant and equals, according to the literature, 4.9.

The advantage of this method compared with the previous is that it uses the whole velocity profile and not a part of it, which has to be estimated by eye. However one problem still remains; again an assumption has to be made for the Von Kármán constant κ .

To avoid problems with κ and the empirical constants, the velocity profile of the viscous layer was used to obtain the friction velocity. The following expression is valid for this layer in the region $y^+ \leq 5$

$$\tau_y = \nu \frac{\partial \bar{U}}{\partial y} = \frac{\tau_0}{\rho} + y \frac{\partial P}{\partial x}. \quad (7)$$

Since, $\partial P/\partial x < 1.8 \text{ Pa/m}$ and $y^+ \leq 5$ the following relation is valid for the friction velocity u_* ,

$$u_* = (\tau_0/\rho)^{1/2} \quad (8)$$

In these expressions τ_0 is the wall shear stress and ρ is the density. Combining equations (7) and (8) the following relation is obtained

$$\bar{U} = \frac{u_*^+}{\nu} y. \quad (9)$$

Although this method has the disadvantage of estimating the range of the viscous layer by eye, the error will be much smaller than the approximately 5% to 10% error of the other two methods.

3.2. Methods for the grooved surfaces

The methods discussed in the previous section are only valid for the smooth surface, because the positions of $y = y^+ = 0$ are exactly known. Problems arise when these methods have to be used for grooved or rough surfaces, where the top of the roughness is normally calibrated as $y = 0$. The virtual origin of the mean streamwise velocity profile lies somewhere between the top and the valley of a groove. It depends on the spanwise position of the measurement volume, for instance when the measurements are performed exactly above the top of a groove the friction velocity should have a maximum value and the virtual origin should be at $y = 0$. When on the other hand, the measurements are performed over the valley of a groove, the friction velocity should have a minimum and the difference between $y = 0$ and the virtual origin should reach a maximum value. Measurements performed over the slope of a groove should have values lying between those for the measurements above the top and valley. The viscous layer method is the easiest method which can be made applicable for grooved surfaces. Accounting for the virtual origin equation (9) will be modified as

$$\bar{U} = \frac{u_*^+ y_v}{\nu} + \frac{u_*^2(z)}{(y + \Delta y_v(z)),} \quad (10)$$

where $y_v(z)$ is the transformed coordinate and Δy_v the displacement of the origin. From the viscous layer velocity profiles the gradient $u_*^2(z)/\nu$ and the constant $u_*^2(z)\Delta y_v(z)/\nu$ can be estimated, from which the *local* values for the friction velocity $u_*(z)$ and the displacement of the origin $\Delta y_v(z)$ can be obtained.

The substitution of $\Delta y_v(z)$ can also be applied to the log-law method, it was previously done by Perry and Joubert (1963), Hooshmand et al. (1983) and Clauser

(1954). They showed that a logarithmic law could describe the mean streamwise velocity in the near wall region of a rough wall pipe, when it was formulated as follows:

$$\frac{\bar{U}}{u_*(z)} = \frac{1}{\kappa} \ln \left(\frac{yu_*(z)}{v} - \frac{\Delta \bar{U}}{u_*(z)} \frac{\Delta y_v(z)u_*}{v} \right) + A. \quad (11)$$

Due to the fact that this equation contains two unknowns it cannot be solved.

Another method that can be used to obtain the friction velocity, u_* , and the transformed coordinate, y_v , for the grooved surfaces is the method described by Choi (1989), which is a variant of the Furuya and Fujita (1966) method. For the Furuya and Fujita method the u_* for the grooved surfaces must be known, to estimate the virtual origin; Choi changed this method slightly, by plotting $(U_0 - \bar{U})/u_*$ vs. yu_*/δ^*U_0 for the grooved surface in the same graph as for the smooth surface. As a start of this iterative method an assumption is made for the u_* and the y_v of the grooved surface. In the region between $0.002 \leq yu_*/\delta^*U_0 \leq 0.15$ the profiles for the grooved and the smooth surface should be identical. Therefore, a fourth-order polynomial is fitted through both profiles to check this. In order to obtain the best match between these two polynomials the two parameters u_* and y_v for the grooved surface measurements are modified at every iteration, thus also estimating δ^* before every iteration. Within a few iterations the values for u_* and y_v for the grooved surface can be found. In Fig. 3 a graph is shown of the Choi method after the best values of u_* and y_v had been found for the profile above a grooved surface.

The last verification used is the theoretical model of Bechert and Bartenwerfer (1989). They developed a model to estimate isovelocity lines of the mean stream velocity above grooved surfaces, by starting with the Navier Stokes equation and neglecting the time-dependent terms as only the mean flow is considered. The pressure term was neglected also, because a flat plate boundary layer flow was assumed. Furthermore, the convective terms can be neglected when the assumption is made that the riblets are completely immersed in the viscous layer. The cross section of the riblets does not vary in the streamwise direction. Therefore, they obtained a Laplace

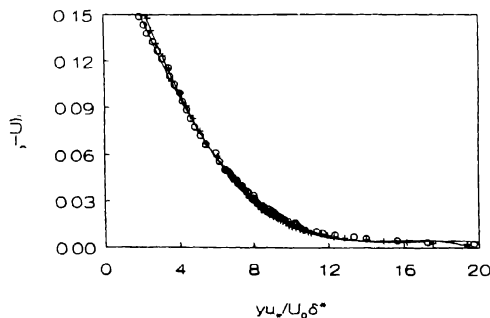


Fig. 3. An example of the Choi method (1989) Smooth surface +, grooved surface O

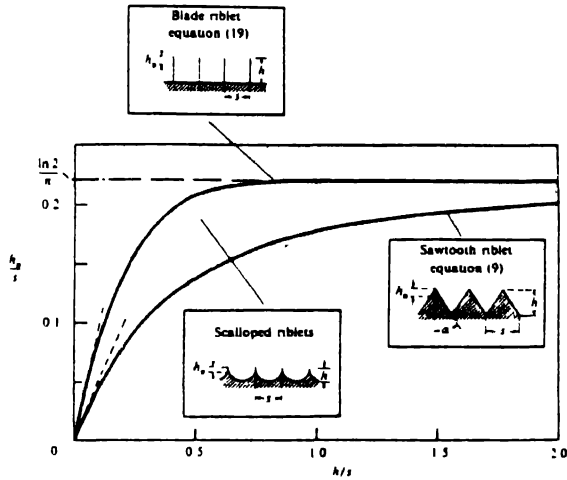


Fig. 4. Protrusion height h_p as a function of geometrical height h for various types of ribs

equation for the mean streamwise velocity \bar{U} . After using conformal mapping they could calculate the protrusion height for different surface geometries, as plotted in the graphs in Figs 4 and 5. The protrusion height is a quantity which indicates how far the top of the grooves penetrated into the viscous layer. In Section 4.2 a comparison between the protrusion height and the virtual origin will be made.

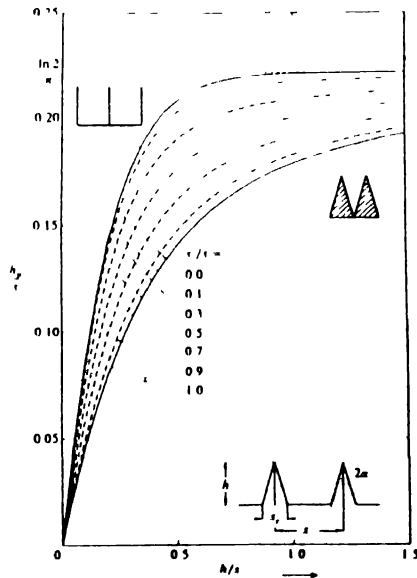


Fig. 5. Protrusion height h_p as a function of geometrical height h for ribs with trapezoidal valleys. The riblet foot breadth s , is kept constant for each curve

4. Results

The results of the experiments will be discussed in three phases. In the first subsection only the results for the smooth surface will be discussed and the constant κ will be estimated by using both the Clauser method and the law of the wall method with the friction velocity obtained from the viscous region. After this subsection the results for the grooved surfaces will be discussed. Here the effect of the spanwise position of the measurement volume will be shown. We then indicate the conditions under which the measurements of the very near wall region can or cannot be used to estimate the friction velocity and the protrusion height. Furthermore a comparison will be given between the Choi method, the method of Bechert and Bartenwerfer and the viscous region. In the last subsection the effect of using different scaling parameters will be shown.

4.1. Results for the smooth surface

In this section only the results for the smooth surface will be discussed and the constant κ will be estimated by using both the Clauser method and the law of the wall method, using the friction velocity obtained from the viscous region.

The measurement volume of the LDA system could be positioned as low as 0.32 ± 0.02 mm above the smooth surface; below this position it was impossible to obtain any signal. The viscous layer above the smooth surface was approximately 0.7 mm thick; the velocity profile of this layer was measured twice (Fig. 6). Very close to the surface the wall effect can be noticed (see Section 2). It looks very similar to the wall effect which arises in a wind tunnel when hot-wires are used to measure the velocity (Bessem 1991, Stouthart 1991 and Van Sas 1982). The friction velocity, u_* , was determined from the velocity profile between $0.4 \leq y \leq 0.7$ mm; in this region about 20 measurements were performed. This region was chosen because below

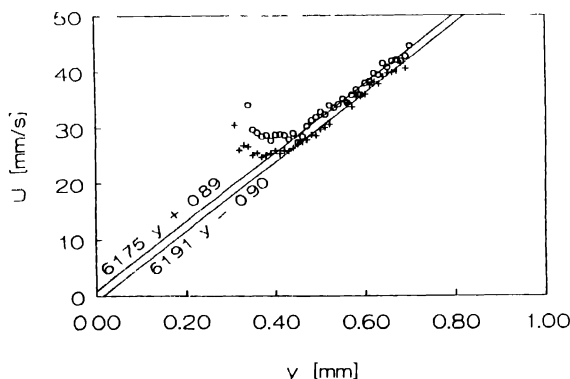


Fig. 6. Velocity profile of the viscous sublayer above a smooth surface. $U_0 = 20.0$ cm/s. Each symbol represents an independent measurement

0.4 mm the wall effect is observed and above 0.7 mm the transition of the viscous layer into the buffer layer starts. The latter boundary was established by iteration; every time after the u_* was obtained, it was verified whether the used region stayed below 5 viscous length units. The average value for u_* for the two plots (Fig. 6) was 7.83 ± 0.06 mm/s.

Figure 7 shows the total profile of the boundary layer over a smooth surface, each symbol representing the part of the velocity profile measured in one day. Figures 6 and 7 show that the reproducibility of the measurements is good; for the estimation of u_* a reproducibility of 1% was achieved. From Fig. 7 it was estimated that the logarithmic region lies between $30y^+$ and $100y^+$. The Von Kármán constant κ was determined from this region using the log-law (equation (1)) and the friction velocity which was obtained from the viscous layer. The average Von Kármán constant for these experiments at a mean stream velocity of $U_0 = 20$ cm/s was $\kappa = 0.38 \pm 0.01$.

The displacement thickness, δ^* , was estimated from the complete velocity profile, using equation (6). The results are given in Table 1. This value was used in the Clauser method together with the u_* from the viscous layer to obtain the Von Kármán constant, resulting in an average value for κ of 0.39 ± 0.01 .

If the normal value 0.4 were used for κ to estimate the friction velocity, either with the Clauser method or the log-law method, an uncertainty between 2% and 5% would have been introduced. Therefore, when no drag balance is available and there is a possibility to measure the viscous layer velocity profile, it is strongly recommended to use this layer to estimate the friction velocity.

4.2. Results for the riblet surfaces

The measurement volume of the LDA system could be as close as 0.12 mm to the \mathcal{S} - and \mathcal{H} -surfaces and about 0.20 mm to the \mathcal{P} -surface. This was due to the fact that the back scattering of the main laser beam was a smaller problem above the grooved

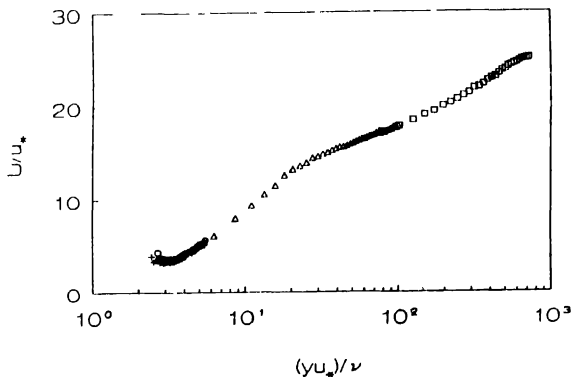


Fig. 7. A semilogarithmic plot of the mean stream velocity profile above a smooth surface. Each symbol represents measurements on a single day

surface than above the smooth surface. As mentioned in Section 2 no measurements could be performed below $100\ \mu\text{m}$.

Figure 8 is a semi-logarithmic graph of the mean streamwise velocity for the four investigated surfaces, Fig. 9 shows a linear graph of the very near wall region. In both graphs, close to the surface the wall effect can be noticed for the \mathcal{P} - and \mathcal{U} -surfaces. One of the reasons that this effect is not seen for the other surfaces is that the wall effect is below $100\ \mu\text{m}$. The reason that the measurement volume could not come lower than $0.2\ \text{mm}$ above the \mathcal{P} -surface may lie in the fact that this surface was slightly concave in the spanwise direction. The reference beams were disturbed by the edges of this surface.

The effects of the grooves on the velocity profiles can be noticed in the near wall region by their upward shift compared to the same profile for the smooth surface. Especially Fig. 9 shows very nicely that the origin of the profiles for the grooved surfaces lies below the top of the grooves; $y=0$ was calibrated at the top of the grooves (Section 2). This effect is not only characteristic for drag reducing surfaces, but is characteristic for rough surfaces in general (Grass, 1971).

The velocity profile of the \mathcal{S} -surface lies much above the profiles of the \mathcal{P} - and \mathcal{R} -surfaces, which suggests that the virtual origin for the \mathcal{S} -surface lies lower than for the other two surfaces. The maximum difference between the virtual origin and the calibrated origin is different for each rough surface. Only when the position of the virtual origin of the velocity profiles is found, can proper comparisons between the smooth and the grooved surfaces be made.

Measurements with exactly known spanwise positions were carried out only for the \mathcal{P} - and \mathcal{S} -surfaces. Figure 10 shows the velocity profiles of the very near wall region above a riblet top, a side and a bottom of a groove of the \mathcal{P} -surface, each symbol referring to a different spanwise position (Fig. 10b) of the measurement volume. In Fig. 10a the effect of the spanwise position above the grooves can be noticed by the

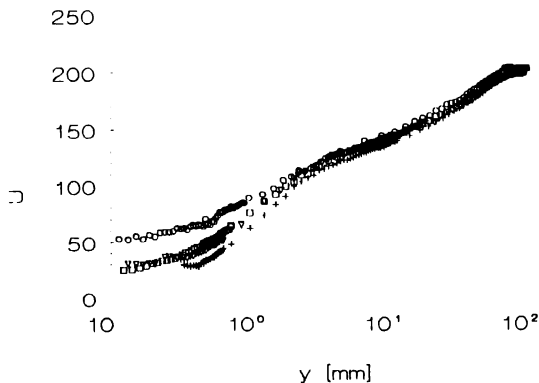


Fig. 8 A semi-logarithmic plot of the mean stream velocity profiles, with \mathcal{U} +, $\mathcal{P}\nabla$, $\mathcal{R}\square$ and $\mathcal{S}\circ$ and $y=0$ at the top of the riblets.

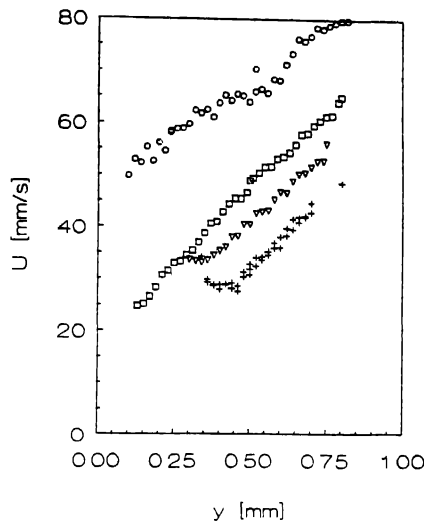


Fig 9 The mean streamwise velocity profiles in the very near wall region, with $y=0$ at the top of the riblets

fact that the highest profile is the one measured above the bottom of a groove and the lowest profile the one measured over the top of a riblet. This result can be explained with Fig 11. Above a certain height, ($y^+ \approx 13$), above the grooves the mean streamwise velocity profiles are identical, while the virtual origins of the velocity profiles depend on the spanwise position of the measurement volume. Therefore, the

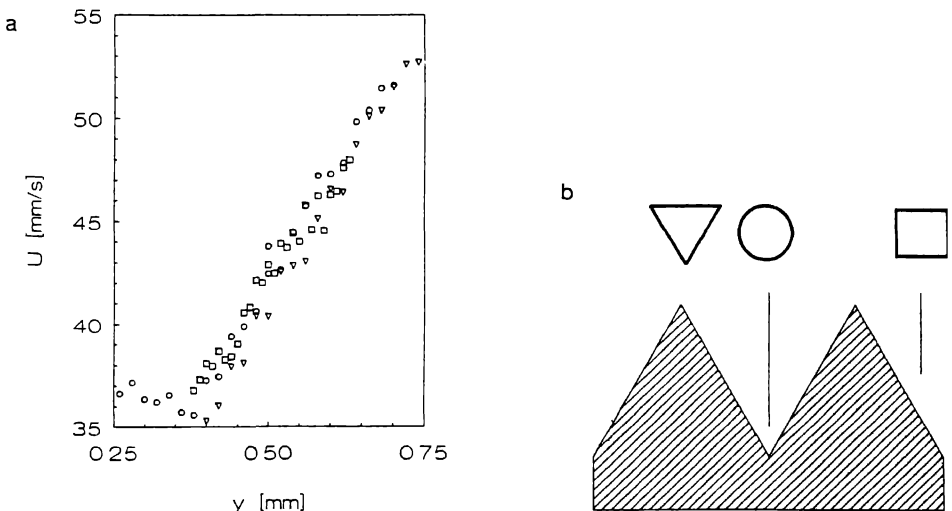


Fig 10 The velocity profiles above (a) the ∇ -surface. Each symbol represents a different spanwise position (b) and $y=0$ is at the top of the riblets

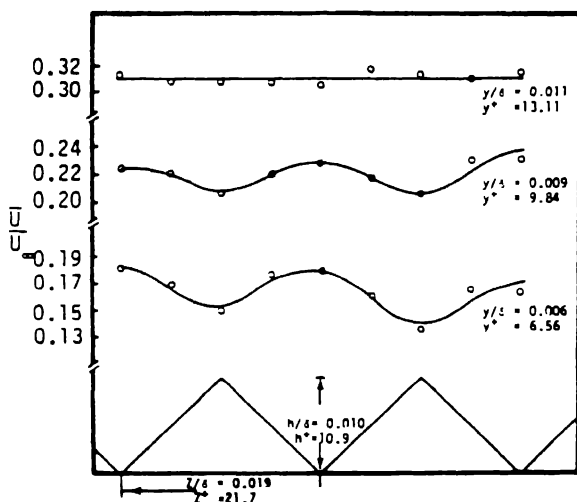


Fig. 11. Variation of mean velocity with spanwise location at several heights above a riblet surface.

gradient of the mean streamwise velocity profile above the top of a riblet is steeper than for the profile over the bottom of a groove. According to this discussion, one would expect after calibrating $y = 0$ at the top of a riblet, that the velocity would be zero at $y = 0$ above the top of a riblet and has a certain value above the bottom of a groove. However, after extrapolating the velocity measured the top of a riblet it does not become zero at $y = 0$, this is because the measurement volume has a spanwise width of 0.5 mm. This implies that the measured velocity is an average velocity over a spanwise distance of 0.5 mm and therefore cannot be zero above a top of a groove. For instance, for the \mathcal{P} -surface the measurement volume will always cover 25% of the groove. Another result of the above discussion is that the measurements above the side of the groove are expected to lie in between the results for the measurements above the top and the bottom of a groove, as shown in Fig. 10a. These results agree with the experiments of Hooshmand et al. (1983) shown in Fig. 11. They measured the mean streamwise velocity component in and out of the grooves at several heights and spanwise positions.

So far, only a qualitative comparison has been made between the experiments. Before it is possible to make a quantitative comparison between the experiments, the position of the viscous region has to be determined. For the first order the characteristics of the viscous region can be described by: (i) a linear profile for the mean stream velocity; (ii) low values for the Reynolds stress compared to the viscous stress; and (iii) this region lies below $y^+ = 5$.

Ignoring the region where the wall effects impair the measurements, Fig. 9 shows that except for the \mathcal{P} -surface all other surfaces exhibit a region with a linear profile. In spite of this fact, the viscous region for all four turbulent boundary layers was

estimated, and both the friction velocity, u_* , and the displacement of the origin, Δy_v , were determined with the viscous layer method (see Table 2).

Table 2 summarizes the results obtained for the friction velocity, the displacement of the origins and the protrusion height using the three different methods. Both the results for the viscous method and the Choi method coincide with one another, but the Choi method has some disadvantages compared to the viscous method. First of all the computation is very time consuming, secondly the method is more sensitive to changes in u_* rather than Δy_v and therefore the latter is not determined very accurately. Furthermore, it can be noticed that results of the viscous method are the most consistent. Comparing the displacement of the origin above the valleys of the grooves for both the viscous and Choi method one notices that they are almost equal to the protrusion height predicted by the theory of Bechert and Bartenwerfer (obtained from Figs 4 and 5). However, here the difference is quite large for the \mathcal{S} -surface. This is probably due to the fact that the turbulent intensity profiles and the Reynolds stress correlation (Fig. 12) showed a significant difference for the \mathcal{S} -surface compared to the other surfaces. Although, the maximum turbulent intensity (u_{rms}) for this surface is the lowest of all the experiments, it shows significantly higher values for the turbulence intensities and the Reynolds stress ($\overline{u'v'} \simeq 1/3u_*^2$) below 0.7 mm. Secondly, the viscous layer was difficult to establish. It might as well lie within the riblets. Therefore, the viscous method results for the \mathcal{S} -surface should be looked upon with some caution. The viscous method results for the other surfaces show no variation. In Table 3 the percentage differences between the methods are shown.

The estimation of the viscous layer above the riblet surfaces was done in the same manner as for the smooth surface (Section 4.1). From Table 4 it can be seen that these grooved surfaces introduce an increase in thickness of the viscous layer. There is one remarkable thing however. In Table 2 the respective displacement of the origins of the measurements are given and if these heights are subtracted from the viscous layer thickness (Table 4), the remaining heights for these surfaces become equal to the thickness of the viscous layer above the smooth surface. This suggests that the peaks of these drag reducing riblet surfaces do not penetrate beyond the viscous layer. This

Table 2 u_{*i} and h_{pl} obtained by several methods and for different spanwise positions

Surface	Viscous layer		Choi method		B & B method h_p [mm]
	u_* [mm/s]	Δy_v [mm]	u_* [mm/s]	Δy_v [mm]	
\mathcal{U}	7.83 ± 0.06	0			
\mathcal{P} valley	7.07 ± 0.07	0.35 ± 0.02	6.9 ± 0.1	0.3 ± 0.1	0.35
\mathcal{P} slope	7.11 ± 0.07	0.34 ± 0.01			
\mathcal{P} top	7.27 ± 0.09	0.26 ± 0.02	7.3 ± 0.1	0.3 ± 0.1	
\mathcal{S} valley	7.55 ± 0.10	0.57 ± 0.05	7.5 ± 0.1	0.6 ± 0.1	0.68
\mathcal{S} top	7.59 ± 0.06	0.50 ± 0.03	7.5 ± 0.1	0.6 ± 0.1	
\mathcal{A}	7.69 ± 0.08	0.31 ± 0.02	7.4 ± 0.1	0.3 ± 0.1	0.31

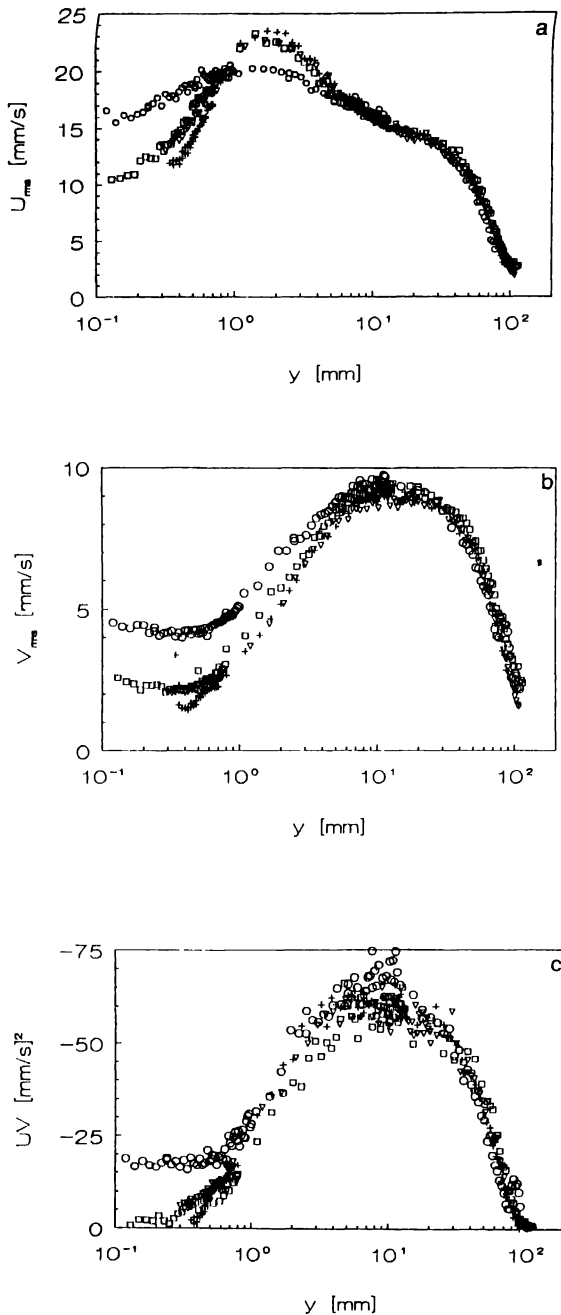


Fig. 12. The turbulent intensity profiles (a, b) and the Reynolds stress correlation (c). $+$, ∇ , \square and \circ .

Table 3 Difference between the results of the three methods

surface	$\frac{ u_{* \text{ Choi}} - u_{* \text{ vis}} }{u_{* \text{ vis}}}$	$\frac{ \Delta y_{t \text{ Choi}} - \Delta y_{t \text{ vis}} }{\Delta y_{t \text{ vis}}}$	$\frac{ h_p - \Delta y_{t \text{ vis}} }{\Delta y_{t \text{ vis}}}$	$\frac{ \Delta y_{t \text{ Choi}} - h_p }{h_p}$
\mathcal{U} valley	0.024	0.143	0.0	0.143
top	0.004	0.154		
\mathcal{V} valley	0.007	0.053	0.193	0.118
top	0.012	0.200		
\mathcal{W}	0.038	0.032	0.0	0.032

Table 4 The average thickness of the viscous layer estimated from the velocity profiles given in mm and dimensionless length scales

Surface	Thickness viscous layer	
	[mm]	l^+
\mathcal{U}	0.6	4.7
\mathcal{V} valley	0.95	6.7
slope	0.89	6.3
top	0.86	6.3
\mathcal{W}	0.93	7.2
\mathcal{S} valley	1.17	9
top	1.04	8

was essentially one of the basic assumptions of the work of Bechert and Bartenwerfer (1989)

4.3 Dimensionless profiles

For both the displacements of the origin and the friction velocity of the grooved surface the spanwise average values of the viscous layer method were used, except for the \mathcal{S} -surface where the results of the Choi method were used, because the viscous method was not completely reliable for this surface. Bandyopadhyay (1986) also advised to use the spanwise average value of these quantities, because above $\sim 13y^+$ there is no difference in the spanwise variation of the mean streamwise velocity. After the origin displacement correction (Table 5) was applied to the measurements the displacement thickness δ^* and the momentum thickness θ (Table 1) were estimated. The profiles were non-dimensionalized with different characteristic variables. Figure 13 shows two semi-logarithmic graphs of the mean streamwise velocity profiles. In Fig. 13a the inner velocity scale $u_i^+ = u_*$ and inner length scale $l_i^+ = \nu/u_*$ were used, while for the other graph the velocity and length scale were obtained using

Table 5. The average values of the friction velocity and the displacement of the origin.

Surface	u_* [mm/s]	Δy_0 [mm]
\mathcal{U}	7.83	
\mathcal{P}	7.17	0.31
\mathcal{S}	7.5	0.6
\mathcal{A}	7.69	0.31

the free stream velocity U_0 and the displacement thickness δ^* . This results in our outer length scale $l_0^+ = \delta^*$ and the outer velocity scale $u_0^+ = U_0$.

When these figures are compared with Fig. 8 the transformation of origin is clearly noticeable. In the viscous region of the velocity profile the difference between the profiles has become much smaller, but for the \mathcal{S} -surface still a small upward shift can be seen. The effect of using the friction velocity to non-dimensionalize the graphs is clearly noticeable in the logarithmic and outer region. If the friction velocity of the

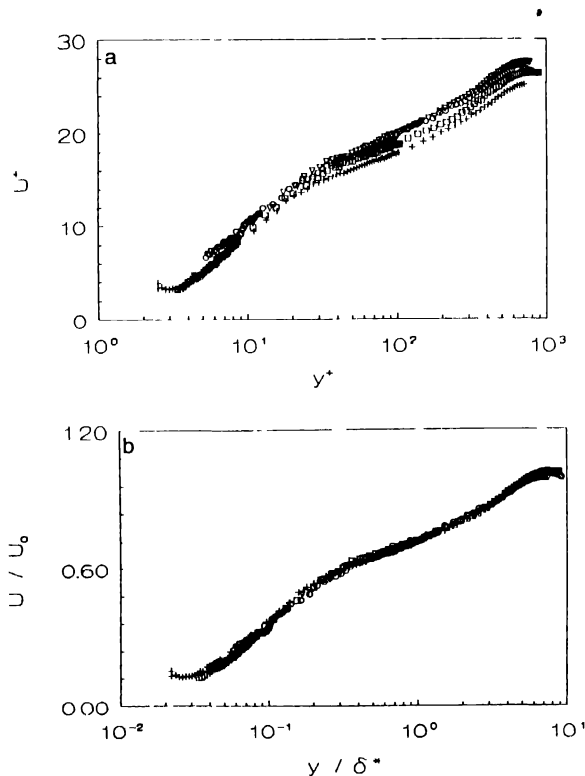


Fig. 13. The mean streamwise velocity: (a) using the inner scales $l_i^+ = \nu/u_*$ and $t_i^+ = \nu/u_*^2$; (b) using the outer scales $l_0^+ = \delta^*$ and $t_0^+ = \delta^*/U_0$. With $\mathcal{U}+$, $\mathcal{P}\nabla$, $\mathcal{S}\square$, $\mathcal{A}\square$

grooved surfaces is smaller than for the smooth surface (drag reduction), the dimensionless profiles will shift upwards compared to the profile of the smooth surface. In the case of a larger friction velocity (drag increase) the profiles will shift downwards (Grass, 1971).

Comparing Figs 13a and 13b it must be concluded that using the displacement thickness as a length scale gives the best results. Regarding the turbulence intensity profiles and the Reynolds stress correlation (Figs 14 and 15), the difference between the scaling can only be found for the turbulent intensities u_{rms} and v_{rms} . When the outer scales (δ^* and U_0) are used the best match between the profiles is obtained. But still a difference can be noticed between the surfaces for the maximum u_{rms} . The results of Hooshmand (1983), Pulles (1988) and Choi (1989) showed that for drag reducing surfaces the maximum u_{rms}/\bar{U} was smaller than for the smooth surface. Figure 15 suggests, therefore, that the \mathcal{S} -surface should have a larger drag reducing effect than the \mathcal{R} - and \mathcal{P} -surface. This is in contradiction with the friction velocities that were found. Scaling with the inner scales the profiles are shifted in such a way that it is very difficult to draw any conclusions.

5. Discussion

It can be stated that the experiments were reproducible within 1%. When no drag balance is available the measurements presented here strongly recommend the use, if possible, of the viscous region to estimate both the friction velocity u_* and the displacement of the origin Δy_v . This method has the advantage of being independent of the surface geometry, therefore no reference measurements are needed, as with for instance the Choi method. If the viscous region cannot be used the Choi method is the next best to use.

The comparison of the viscous layer method with the calculations of the method used by Bechert and Bartenwerfer for the \mathcal{P} - and \mathcal{R} -surface are extremely good; the protrusion height is equal to the displacement of the origin above the bottom of a groove.

That δ^* turned out to be a very good scaling parameter, this is probably due to the fact that it is influenced by the grooves.

The measurements presented here are all local measurements. It is therefore, difficult to draw strong conclusions about the drag reducing behavior of the different surfaces. With this reservation in mind, the measurements suggest that the \mathcal{P} -surface provides the maximum drag reduction. This surface has the largest h/s value and the smallest top angle $\tan \alpha$. Comparing the present results and the work of Bechert and Bartenwerfer (1989), it can be concluded that scalloped grooves and vertical blades in the streamwise direction will show an even larger drag reduction. The groove spacing s and the height of the grooves h must of course have the proper dimensions, their ratio (h/s) must be close to 1 and the top angle of the grooves ($\tan \alpha$) as small as possible.

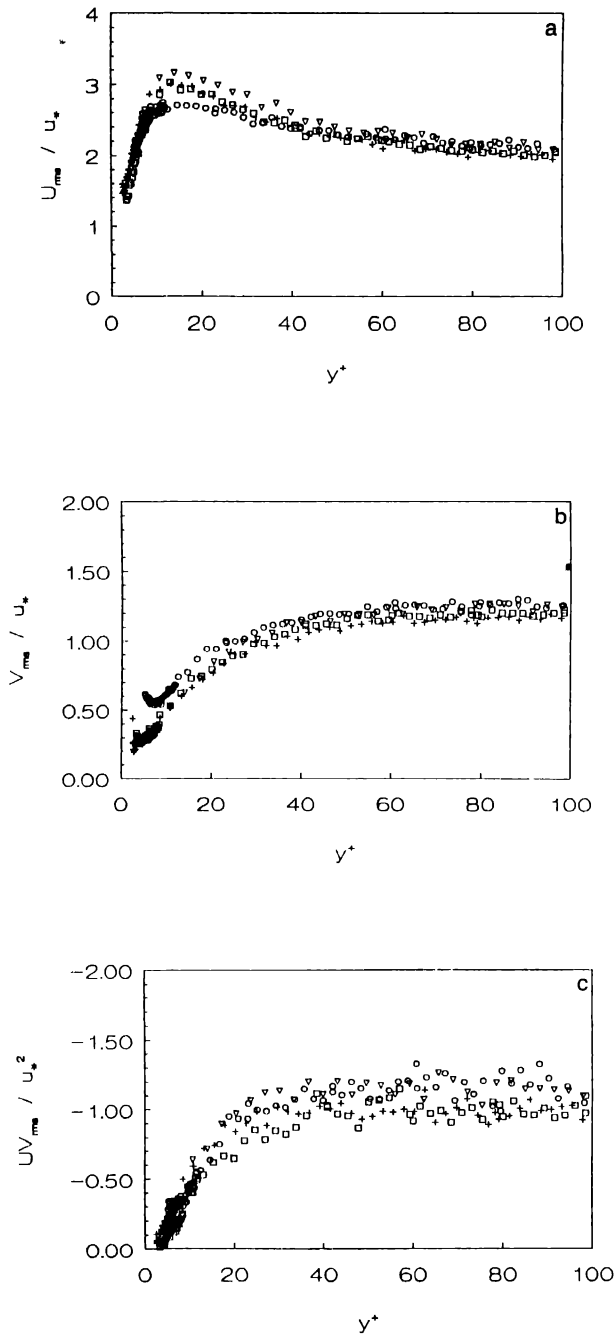


Fig. 14. Turbulence intensities and Reynolds stress correlation non-dimensionalized with the inner scales. $\mathcal{U}+$, $\mathcal{P}\nabla$, $\mathcal{U}\mathcal{O}$, $\mathcal{A}\square$.

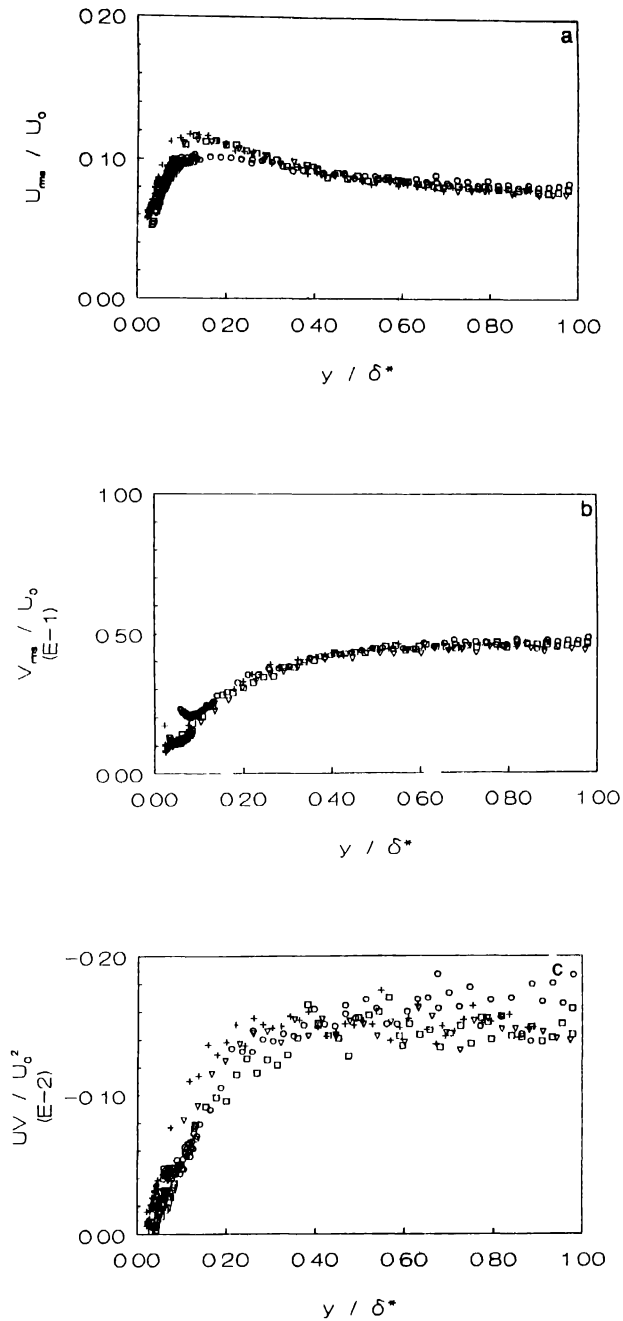


Fig 15 Turbulence intensities and Reynolds stress correlation non-dimensionalized with the outer scales
 U +, V ∇ , UV \circ , U^2 \square

6. Acknowledgement

The research in this article was supported by The Netherlands Foundation for Technical Sciences (STW) and the Foundation for Fundamental Research on Matter (FOM).

7. References

- Bandyopadhyay, P.R., Review – Mean flow in turbulent boundary layers disturbed to alter skin friction. *J. Fluid Eng.* 108 (1986) 127.
- Bessem, J.M., personal communication (1991).
- Bradshaw, P., Launder, B.E. and Lumley, J.L. Collaborative testing of turbulence models. *J. Fluids Eng.* 113 (1991) 3.
- Bechert, D.W. and Bartenwerfer, M., The viscous flow on surfaces with longitudinal riblets. *J. Fluid Mech.* 206 (1989) 105.
- Choi, K.S., Near-wall structure of turbulent boundary layers over smooth and riblet surfaces. *J. Fluid Mech.* 208 (1989) 417.
- Clauser, E.H., Turbulent boundary layers in adverse pressure gradients. *J. Aeronautical Sciences* 21 (1954) 91.
- Clauser, E.H., Turbulent boundary layer. *Advances in Applied Mechanics* 4 (1956) 1.
- Hooshmand, A., Youngs, R.A., Wallace, J.M. and Balint, J.L., An experimental study of changes in the structure of a turbulent boundary layer due to surface geometry changes. *AIAA paper no. 83-0230* (1983).
- Geloven, J. van, u_* en h_p bepaling door middel van verschillende methoden boven vlakke en gegroefde wanden. Internal report no. R-1153-S, Eindhoven University of Technology, The Netherlands (1992).
- Grass, A.J., Structural features of turbulent flow over smooth and rough boundaries. *J. Fluid Mech.* 50 (1971) 233.
- Furuga, M. and Fujita, H., Turbulent boundary layer over rough gauze surfaces. *Trans. Japan Soc. Mech. Engrs.* 32 (1966) 725.
- Kern, J.H.A., Meting van de turbulente schuifspanning met een laser doppler anemometer in de grenslaag boven een vlakke en een ruwe wand. Internal report no. R-710-A, Eindhoven University of Technology, The Netherlands (1985).
- Perry, A.E. and Joubert, P.N., Rough-wall boundary layers in adverse pressure gradients. *J. Fluid Mech.* 17 (1963) 193.
- Pulles, C.J.A., Drag reduction of turbulent boundary layers by means of grooved surfaces. Ph.D. thesis. Eindhoven University of Technology, The Netherlands (1988).
- Sas, L.M.L.A. van, Wandinvloed op snelheidsmetingen met behulp van een hetedraad-anemometer in een turbulente grenslaag. Internal Report no. R-520-S, Eindhoven University of Technology, The Netherlands (1982).
- Schwarz-van Manen, A.D. and Stouthart, J.C., Beschrijving van de LDA opstelling van het waterkanaal. Internal Report no. R-1061-D, Eindhoven University of Technology, The Netherlands (1990).
- Tennekes, H. and Lumley, J.L., *A First Course in Turbulence*. Cambridge (Mass.): The MIT Press (1972). ISBN 0-262-200-19-8.

Viscous sublayer analysis of riblets and wire arrays

PAOLO LUCHINI

Istituto di Gasdinamica, Facoltà di Ingegneria, Università di Napoli, Italy

1. Introduction

Ever since it was observed [1] that the experimentally effective spacing of riblets for turbulent drag reduction is of the same order of magnitude as the thickness of the viscous sublayer of the turbulent stream, it has been clear that the viscous sublayer plays a dominant role in the mechanics of this effect. Within the viscous sublayer we are allowed to neglect nonlinearities and thus to concentrate on the Stokes, low Reynolds number, flow of a viscous fluid along a corrugated surface. Bechert and Bartenwerfer [2] analysed longitudinal mean flow in this approximation and obtained a characterization of the surface in terms of the parameter “protrusion height”, namely the distance from the riblet tips to the virtual plane surface that the velocity profile appears to originate from. Bechert et al. [3] studied transverse flow across the riblets experimentally and by means of an analogical simulation, and measured a protrusion height for this flow as well.

In recent papers [4, 5, 6] some coworkers and I obtained analytical and numerical solutions for both the longitudinal and transverse flow problems, and proposed the difference between the longitudinal and transverse protrusion heights as a parameter characterizing the damping action of riblets upon streamwise vortices. The analytical results enabled us to prove that this difference is positive for shallow grooves of whatever shape and is again positive for infinitely deep grooves. The numerical results obtained for grooved surfaces of cosinusoidal, triangular and parabolic profile led us to conjecture that this parameter is always positive.

In Ref. [7], and in their paper included in this same volume, Bartenwerfer and Bechert reconsidered Kramer’s early proposal [8] of using regular arrays of longitudinal wires suspended above a plane wall (see Fig. 1) as alternative drag-reduction devices with an operation mechanism similar to that of riblets. They calculated, by a conformal-mapping technique, the mean flow that takes place in the direction parallel to the wires when these are embedded inside the viscous sublayer of a turbulent stream. More recently Bechert et al. [9] have also performed an experiment on such a wire array, demonstrating some drag reduction.

At the suggestion of D. W. Bechert we, too, began to study arrays of longitudinal cylindrical wires suspended above a plane wall. In this paper we shall present approximate analytical solutions for both longitudinal and transverse Stokes flow about such a structure.

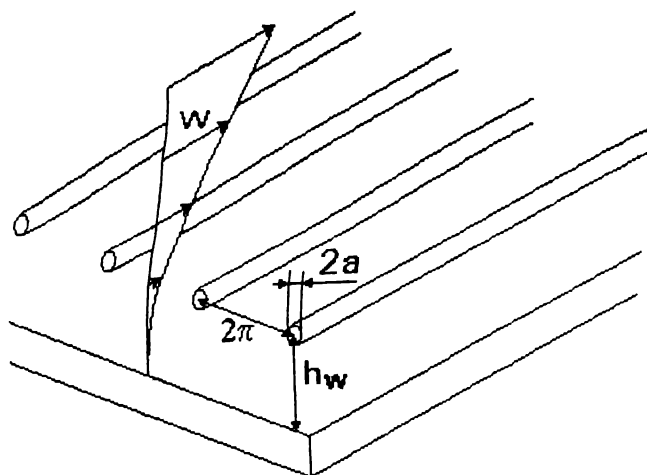


Fig. 1. Schematic representation of a wire-array drag-reduction device.

2. Role of the viscous sublayer in the operation of riblets and wire arrays

It is now a consolidated experimental fact that the best drag-reduction performance of riblets is obtained when their repetition period s^+ in viscous units is of the order of 15. This strong correlation clearly indicates that the viscous sublayer has an important role in the operation of such devices, and was the motivation for a number of theoretical analyses [1]–[6] of the Stokes flow of a fluid past a ribletted (or grooved, depending on the way one sees it) surface.

In undertaking such analyses one must depart from the commonplace view of the viscous sublayer as a region where random fluctuations of the velocity field are totally absent. Indeed it is more appropriate to see the viscous sublayer as a region where the mean and fluctuating components of the velocity field superpose without interacting.

The viscous sublayer may be suitably defined as the region where the nonlinear convective terms of the Navier-Stokes equations are negligible and the viscous stresses alone determine the flow. The equations that govern the viscous sublayer are therefore linear and dissipative, so that no local instabilities arise. Nevertheless the flow may in general be driven unsteadily by the turbulent boundary layer above. Linearity, however, implies that the mean stress equals the stress calculated from the mean velocity field, whether oscillating components are present or not; this is why oscillations are usually unimportant.

That oscillations are indeed present may be understood by the following qualitative reasoning. Roughly speaking, oscillations governed by the Stokes equations only travel as far as a wavelength from their source. Although nonlinear sources are negligible inside the viscous sublayer, they are active just above, and in a large range of wavelengths: oscillations of a wavelength small compared to the viscous sublayer's height do not penetrate into it significantly, but oscillations of a wavelength large

compared to the sublayer's height persist all the way down to the wall (mathematically, they behave as *quasi-steady* solutions of the Stokes' equations [4]), with an amplitude that decreases linearly, just as the mean speed, and retains a constant ratio to it. Therefore, while wall features, such as riblets or wire arrays, acting inside the viscous sublayer cannot have a significant effect on turbulent structures, such as streamwise vortices, of a size small compared to the viscous sublayer itself, they can indeed affect structures larger than the viscous sublayer in size. Since it has been shown [3, 4] that riblets impede a quasi-steady crossflow more than a parallel flow, we may assume that wall structures embedded in the viscous sublayer provide some damping of long-wavelength streamwise vortices.

Unfortunately the nonlinear stage of the phenomenon, namely, the interaction of riblets with long-wavelength turbulent eddies producing a drag reduction, has until today only been explained qualitatively: all that we know quantitatively is that riblets appear to a transverse and to a longitudinal quasi-steady flow with different protrusion heights. Once that is established, however, it is just reasonable to expect that they produce some damping of streamwise vortices and thus a reduction of turbulent mixing and momentum transfer.

As long as flow about the riblets remains governed by the Stokes equations, the bigger the riblets are, the larger is the damping; beyond some size, however, the Stokes equations lose validity, nonlinearities come into play, and drag starts to grow again, thus giving rise to the experimentally observed minimum near $s^+ = 15$.

A similar reasoning may be applied to wire arrays, and therefore it is interesting to perform an analysis of Stokes flow past wire arrays. We shall do so in the continuation of this paper, with the aim of calculating the relevant protrusion heights and comparing them with those of riblets. Our expectation of a similarity between wire arrays and riblets has actually been confirmed by recent experiments performed after the completion of this work [9], which reported an optimum performance of wire arrays for a repetition period of $s^+ \simeq 15$ viscous units, just as for riblets.

In order to compare wire arrays with riblets on the grounds of their Stokes-flow characteristics, we need a single global parameter that may reasonably represent the overall performance of different riblet and wire-array profiles for drag reduction. Based on the above qualitative analysis, one such parameter may be constructed as the ratio of the protrusion-height difference to the longitudinal protrusion height, which we shall call "relative protrusion-height difference".

In fact, while the drag-reducing effects of riblets and related devices are proportional to the protrusion-height difference as long as the riblets are small enough, the eventual limitation to how big these devices may be made comes from nonlinear convective effects that set in once the size of the perturbed region increases beyond certain limits. A measure of nonlinear effects is given by the longitudinal protrusion height itself, because this quantity is proportional to the maximum velocity that would be found at the surface if the linear profile existing at infinity were continued down unperturbed. The corrugation shape that achieves the best balance between linear eddy damping and unwanted nonlinear effects may be expected to be the one

that yields the maximum protrusion-height difference for a given longitudinal protrusion height; in other words, the dimensionless ratio of protrusion-height difference to longitudinal protrusion height is our performance parameter.

3. Longitudinal Stokes flow past an isolated wire array

In the limit of small wire diameter an analytical solution of the Stokes equation may be constructed using the technique of multipole expansion. In addition, this problem admits of a definite limit when the wall is pushed away indefinitely far from the wire screen. We shall start with this, simpler, limiting case.

As observed in Ref. [4], for a translationally invariant structure such as riblets or wire arrays the Stokes equations split into two separate problems: a Laplace equation for the longitudinal flow and a biharmonic equation for the transverse flow. In order to determine the longitudinal flow we have to solve the Laplace equation $\Delta_2 w = 0$ with the conditions that the longitudinal velocity w , periodic of period 2π , should vanish at the surface of each wire, seen in a transverse plane as a circumference of radius a , and should attain a unit gradient for y going to plus infinity.

In the limit of small a , the solution of this problem is simply given by the Green function of Ref. [4], Eq. (27):

$$G(x, y) = [\log(2 \cosh y - 2 \cos x) + y]/2 \quad (1)$$

In fact, $G(x, y)$ is periodic, satisfies the required condition at infinity, and behaves in proximity of the origin as $\log r$, where $r^2 = x^2 + y^2$ (as may easily be found out from the Taylor-series expansions of \cos and \cosh). Since the contour lines of G become more and more approximately circular as $r \rightarrow 0$, it is sufficient to subtract $\log a$ from G to satisfy the no-slip condition at a small circumference of radius a . We thus obtain

$$w(x, y) = [\log(2 \cosh y - 2 \cos x) + y]/2 - \log a \quad (2)$$

as the required solution. For $y \rightarrow \infty$, $w \simeq y - \log a$, and therefore the protrusion height (referred to a corrugation period of 2π) is simply $-\log a$, if calculated from the center of the wire, or

$$h_{\parallel} = -\log a + a \quad (3)$$

if calculated, consistently with the definition adopted for riblet geometries, from the uppermost point of the wire surface.

There is a remarkable difference with the case of a grooved surface: the protrusion height increases without bound for $a \rightarrow 0$, rather than attaining a finite limit. It should, however, be noted that the fluid velocity existing in the neighbourhood of the wires increases as well (for instance at the centre point between two consecutive wires, $x = \pi$

and $y = 0$, w equals $\log 2 - \log a$, so that the assumption of negligible nonlinear terms in the flow equations becomes less and less applicable as a decreases.

It is also noteworthy that w attains a nonzero finite limit for y going to minus infinity. All other solutions of the Laplace equation are infinite on both sides of the wire array and none is zero at infinity; the finite solution actually represents the limit of flow about a wire array adjacent to a plane wall when the wall is moved away to infinity.

The approximation of the solution (2) may be improved, for a given a , by a multipole-expansion technique. The function $\frac{1}{2} \log(2 \cosh y - 2 \cos x)$ is in complex notation the real part of

$$F(z) = \log[2 \sin(z/2)] \quad (4)$$

where $z = x + iy$, and behaves for $z \rightarrow 0$ as $\log z$. It represents a periodic array of monopoles. The n -th derivative of this function behaves for $z \rightarrow 0$ as

$$F^{(n)}(z) \simeq (-1)^{n-1} (n-1)! z^{-n} \quad (5)$$

and represents a periodic array of $2n$ -poles (i.e., field configurations that in a neighbourhood of the origin depend on the angular coordinate θ as $e^{in\theta}$). Boundary conditions imposed on a circular boundary are efficiently handled term-by-term if the solution is represented as a linear superposition of multipoles (i.e., a Fourier expansion with respect to θ); higher-order multipole coefficients turn out to be proportional to a^{2n} , thus effectively representing an expansion of the solution, and of related quantities such as the protrusion height, in powers of a .

We performed the above expansion up to order 6 in a ; the resulting expression of h_{\parallel} is

$$h_{\parallel} = -\log a + a - \frac{a^2}{4} + \frac{5}{288} a^4 - \frac{a^6}{576} + O(a^8) \quad (6)$$

4. Cross flow past an isolated wire array

In order to determine the cross-flow pattern one must solve the biharmonic equation for the streamfunction ψ . A general solution of this equation may be written in the form $\psi = f + yg$, where f and g are harmonic functions (solutions of the Laplace equation), which near a circular boundary may efficiently be expressed as periodic multipole expansions. The coefficients of each of these expansions, which in a neighbourhood of the origin appear as Fourier expansions with respect to the angular coordinate θ , may then be determined by imposing that the Fourier coefficients of both ψ and ψ_r vanish up to a certain order.

The first six terms of such a double multipolar expansion, which may be found to contain all the contributions to ψ of order up to a^2 , are given by

$$\begin{aligned}\psi = & y[\log(2 \cosh y - 2 \cos x) + y]/4 + Ay + B + C \log(2 \cosh y - 2 \cos x)/2 \\ & + D \frac{\sinh y}{2 \cosh y - 2 \cos x} + Ey \frac{\sinh y}{2 \cosh y - 2 \cos x} + \dots\end{aligned}\quad (7)$$

On equating to zero the zeroth, first and second-order Fourier coefficients of ψ and ψ_r , on a circumference with radius a and truncating all results to order a^2 , we obtain a system from which the coefficients A, B, C, D, E will be determined as

$$\begin{aligned}A = & -\frac{1}{2} \log a - \frac{1}{4} - \frac{a^2}{48} + O(a^4), \quad B = \frac{a^2}{4} \log a + \frac{a^2}{8} + O(a^4), \\ C = & -\frac{a^2}{4} + O(a^4), \quad D = \frac{a^2}{4} + O(a^4), \quad E = -\frac{a^2}{2} + O(a^4).\end{aligned}\quad (8)$$

It is interesting to observe that the coefficient A is the only one that contains terms of order smaller than a^2 , so that if accuracy $O(a^4)$ is not required the calculation may be limited to this single coefficient and to the *first* (not zeroth) order Fourier component of the boundary conditions. (D must also be considered during the solution of the linear system of equations for the coefficients, but turns out to be of order a^2 , and therefore negligible in the complete solution.)

From the behaviour at infinity to order a^2 of the complete solution we may easily determine the transverse protrusion height to the same order. Indeed, we continued the multipole expansion up to order a^6 , thus obtaining:

$$h_{\perp} = -\frac{\log a}{2} - \frac{1}{4} + a - \frac{5}{12}a^2 + \frac{43}{576}a^4 - \frac{79}{3840}a^6 + O(a^8).\quad (9)$$

5. Longitudinal flow past a wire array parallel to a plane wall

In the presence of a plane wall located a distance h_w below the center of the wires, as in Fig. 1, the multipole terms that constitute the solution given in Section 3 must be modified to include the presence of images, in such a manner that the no-slip condition is satisfied at the wall. The solution to leading order has the form

$$w = y + h_w + A \left\{ \frac{\log(2 \cosh y - 2 \cos x)}{2} - \frac{\log[2 \cosh(y + 2h_w) - 2 \cos x]}{2} \right\} + O(a^2).\quad (10)$$

Determining the coefficient A so that w vanishes, to zeroth order in its multipole expansion, on a small circumference with radius a , we obtain

$$A = -h_w / \{\log a - \log[2 \cosh(2h_w) - 2]/2\}, \quad (11)$$

whence the protrusion height:

$$h_{||} = (1 - A)h_w + a + O(a^2). \quad (12)$$

It may be verified that when $h_w \gg -\log a$ the solution (10) and the protrusion height (12) tend to those given in Section 3.

We have repeated the above calculations to order a^2 , with the aid of a computerized symbolic processor. The resulting expression, too long to be reported here, has been used for the diagrams illustrated below.

6. Cross-flow past a wire array parallel to a plane wall

In the case of cross-flow (biharmonic equation) the procedure necessary to introduce the presence of a plane wall is formally similar to that adopted in the previous section, but the details are more complicated. According to the decomposition of the biharmonic solution in terms of two harmonic functions as $\psi = f + yg$, we need the "image", that is an additional term adjusting things so that the two components of velocity vanish at the wall, of both harmonic multipoles and harmonic multipoles multiplied by y .

Locating the wire at the origin and the plane wall at $y = -h_w$, we prefer to decompose the solution of the biharmonic equation as $\psi = f + (y + h_w)g$; the two boundary conditions at the wall then read

$$f(x, -h_w) = 0; \quad f_y(x, -h_w) + g(x, -h_w) = 0. \quad (13)$$

We must now distinguish the two cases of a monopole (or multipole) term appearing in f or in g . When a multipole component is assigned in g , f may be set identically equal to zero, and it is sufficient to satisfy the condition $g(x, -h_w) = 0$ by an image analogous to that used in the case dealt with in Section 5 to comply with Eq. (13). When, on the other hand, the multipole component is assigned in f , we must calculate both an f -image such that $f(x, -h_w) = 0$ and a g -image such that the second of Eq. (13) is also satisfied.

According to the above criteria, and to the considerations made in Section 4 as to the relevance of different multipole terms, we may write the solution, to leading order

in the wire radius a , as

$$\begin{aligned} \psi = (y + h_w) & \left(\frac{y + h_w}{2} + A \left\{ \frac{\log(2 \cosh y - 2 \cos x)}{2} \right. \right. \\ & \left. \left. - \frac{\log[2 \cosh(y + 2h_w) - 2 \cos x]}{2} \right\} \right) \\ & + B \left\{ \log(2 \cosh y - 2 \cos x)/2 - \log[2 \cosh(y + 2h_w) - 2 \cos x]/2 \right. \\ & \left. + (y + h_w) \frac{\sinh(y + 2h_w)}{\cosh(y + 2h_w) - \cos x} \right\} + O(a^2), \end{aligned} \quad (14)$$

where the constants A and B (together with a dipole coefficient D which, being of order a^2 , cannot legitimately be included in the solution (14) without also considering the contributions of order a^2 that come from other terms) must be determined by equating to zero the zeroth and first Fourier components of ψ , and the first Fourier component of ψ on a small circumference with radius a . (The zeroth Fourier component of ψ is not zero; it equals the flow rate through the gap between wire and wall and is a result, rather than a datum, of the problem.)

In particular, the local approximation of Eq. (14) near the origin is given by

$$\begin{aligned} \psi = h_w^2/2 + h_w r \sin \theta & + A \left\{ h_w \left[\log r - \frac{\log(2 \cosh 2h_w - 2)}{2} \right] - h_w \frac{\sinh(2h_w)}{2 \cosh(2h_w) - 2} r \sin \theta \right. \\ & \left. + \left[\log r - \frac{\log(2 \cosh 2h_w - 2)}{2} \right] r \sin \theta \right\} \\ & + B \left\{ \log r - \frac{\log[2 \cosh(2h_w) - 2]}{2} - \frac{\sinh(2h_w)}{2 \cosh(2h_w) - 2} r \sin \theta \right. \\ & + h_w \frac{\sinh(2h_w)}{\cosh(2h_w) - 1} - h_w \frac{1}{\cosh 2h_w - 1} r \sin \theta \\ & \left. + \frac{\sinh(2h_w)}{\cosh(2h_w) - 1} r \sin \theta \right\} + Dr^{-1} \sin \theta + O(r^2), \end{aligned} \quad (15)$$

and its derivative with respect to r by

$$\begin{aligned} \psi_r = h_w \sin \theta + A & \left\{ h_w r^{-1} - h_w \frac{\sinh(2h_w)}{2 \cosh(2h_w) - 2} \sin \theta \right. \\ & \left. + [\log r + 1 - \log(2 \cosh 2h_w - 2)/2] \sin \theta \right\} \end{aligned}$$

$$\begin{aligned}
 & + B \left\{ r^{-1} - \frac{\sinh(2h_w)}{2 \cosh(2h_w) - 2} \sin \theta - h_w \frac{1}{\cosh 2h_w - 1} \sin \theta \right. \\
 & \left. + \frac{\sinh(2h_w)}{\cosh(2h_w) - 1} \sin \theta \right\} - Dr^{-2} \sin \theta + O(r).
 \end{aligned} \tag{16}$$

On letting $r = a$ and equating to zero the coefficient of $\sin \theta$ in ψ and the whole of ψ , we obtain the coefficients A , B , D and hence the protrusion height h_{\perp} .

Actually, just as in the case of longitudinal flow, the calculations have been performed to order a^2 with a symbolic processor, and the resulting expressions are too long to be reported here. The results are described below.

7. Analysis of the results

In Reference [4] the difference of the longitudinal and transverse protrusion heights was assumed as a parameter measuring the capability of a grooved surface to damp cross-flow vortices, on the basis that this difference is the only combination of the two protrusion heights that is independent of the choice of the origin of the coordinate system. The difference Δh was there made dimensionless by normalizing it to the period of the corrugations. It turned out that the absolute maximum value of the normalized protrusion-height difference, namely 0.132, was given by an array of infinitely thin and high blades.

In connection with wire arrays, a similar normalization of the protrusion-height difference leads to a startling result: $\overline{\Delta h}$ can be made arbitrarily large by reducing wire diameter. In fact, combining Eqs (3) and (10) gives

$$\overline{\Delta h} = -\frac{1}{4\pi} \log a + \frac{1}{8\pi} + O(a^2), \tag{17}$$

which is infinite for $a \rightarrow 0$.

However, it is easy to imagine that the conclusion that the performance of a wire-array device can be improved indefinitely by making the wires thinner and thinner is too good to be true. When wire diameter is decreased (with the period kept constant), the velocity of flow in proximity of the wires also increases indefinitely, so that the flow must eventually abandon the linear viscous regime. On the other hand, there is no apparent reason to keep the period fixed, and by changing the period one may increase at will the protrusion height of riblets as well.

As was mentioned in Section 2, the eventual limitation to how big riblets may be made, or how thin wires may be made, comes from nonlinear convective effects that set in once the region perturbed by their presence grows beyond certain limits. The parameter that qualitatively appears to represent a balance between linear eddy damping and harmful nonlinearities is the relative protrusion-height difference.

In Fig. 2 the relative protrusion-height difference is plotted versus riblet height for the three riblet profiles considered in reference [4]. As may be seen, the three curves are monotonically increasing, so that the main conclusion of that paper is unchanged: the best performance, that is the absolute maximum value of the relative protrusion-height difference, still corresponds to infinitely thin and high blades. This maximum is 0.598.

The relative protrusion-height difference of wire arrays, as obtained by a multipole expansion up to order a^2 , is plotted versus wire diameter \bar{d} in Fig. 3 for several values of wire-to-wall distance \bar{h}_w (both \bar{d} and \bar{h}_w are expressed as a fraction of the period, so that $\bar{d} = a/\pi$ and $\bar{h}_w = h_w/2\pi$). The curve corresponding to $h_w = \infty$ is repeated in Fig. 4 for different orders of approximation in order to test the adequacy of the second-order multipole expansion. The cross-flow streamline pattern obtained in the particular example of $\bar{h}_w = 1$ and $\bar{d} = 0.1$ is also shown, in Fig. 5.

It may be noticed that $\Delta h/h_{||}$, contrary to $\Delta h/2\pi$, stays finite when wire diameter tends to zero; in particular, when $h_w = \infty$ (the most favourable case) it goes to the limit $1/2$, less than the value corresponding to infinitely deep grooves. $\Delta h/h_{||}$ has a broad maximum of 0.589 for $h_w = \infty$ and a nonzero diameter of roughly 6–7% of the period. This value is still, even if marginally, lower than that corresponding to blade-style riblets. It may probably be improved slightly by making the wires pointed upwards rather than round-shaped.

The conclusion is that under optimal conditions the drag-reducing effects of wire arrays are likely to be similar to, but not better than, those of riblets. This conclusion

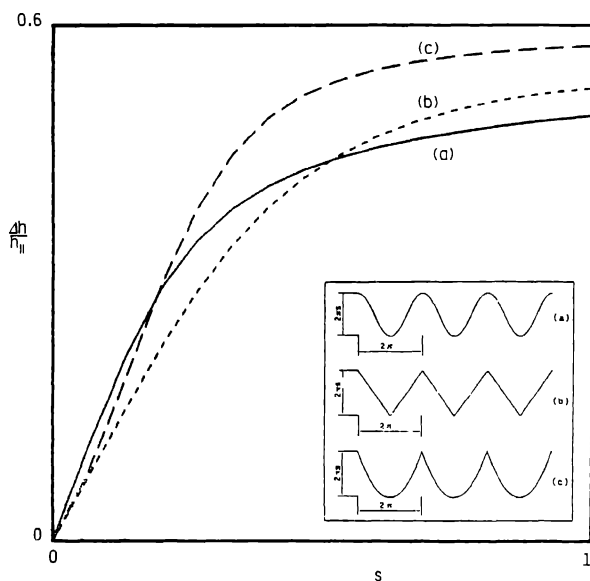


Fig. 2. Plot of the relative protrusion-height difference versus riblet height for several groove profiles.

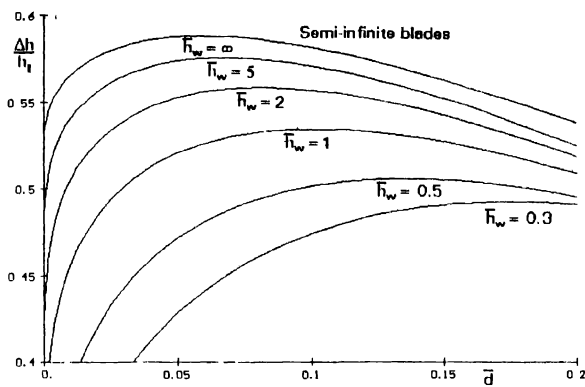


Fig. 3. Relative protrusion-height difference of wire arrays of varying diameter and height from wall.

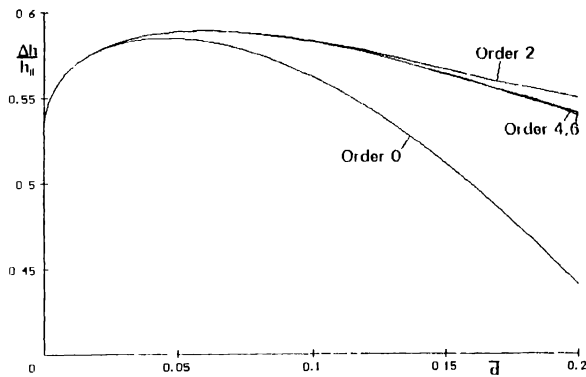


Fig. 4. Relative protrusion height difference of wire arrays isolated in space calculated at several orders of approximation in the multipole expansion.

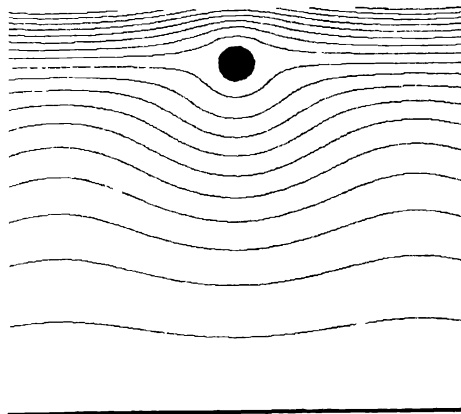


Fig. 5. Cross-flow streamline pattern in a wire array with $\bar{h}_w = 1$ and $\bar{d} = 0.1$.

appears to be confirmed by recent experiments [9] performed after the completion of this work.

Acknowledgement

This work was funded by the Italian Ministry of University and Research.

References

1. Bechert, D. W., Bartenwerfer, M. and Reif, W.-E., On the drag reduction of the shark skin. *AIAA paper* 85-0546 (1985).
2. Bechert, D. W. and Bartenwerfer, M., The viscous flow on surfaces with longitudinal ribs. *J. Fluid Mech.* 206 (1989) 105-129.
3. Bechert, D. W., Bartenwerfer, M. and Hoppe, G., Turbulent drag reduction by nonplanar surfaces - a survey on the research at TU/DLR Berlin. In: Gyr, A. (ed.), *Proc. IUTAM Symp. on Structure of Turbulence and Drag Reduction*. [Zürich, 25-28 July 1989.] Berlin: Springer (1990) pp. 525-543.
4. Luchini, P., Manzo, F. and Pozzi, A., Resistance of a grooved surface to parallel flow and cross-flow. *J. Fluid Mech.* 228 (1991) 87-109.
5. Luchini, P., Manzo, F. and Pozzi, A., Resistance of a grooved surface to parallel and cross flow calculated by B.E.M. In: Marino, L. and Piva, R. (eds), *Proc. IABEM (International Association for Boundary Element Methods) Symp.* [Rome, 15-18 Oct. 1990.] Berlin: Springer (1991) pp. 328-338.
6. Luchini, P., Manzo, F. and Pozzi, A., Viscous eddies in flow over a grooved surface computed by a Gaussian-integration Galerkin boundary-element method. *AIAA J.* 30 (1992) 2168-2170.
7. Bartenwerfer, M. and Bechert, D. W., Die viskose Strömung über behaarten Oberflächen. *Z. Flugwiss. Weltraumforsch.* 15 (1991) 19-26.
8. Kramer, M. O., Einrichtung zur Verminderung des Reibungswiderstandes. Reichpatentamt, Patentschrift Nr. 669 897, Klasse 62b, Gruppe 408 (1939). Patented from 17 March 1937 on.
9. Bechert, D. W., Hoppe, G., Hage, W. and Bruse, M., Widerstandsvermindernde Oberflächen der Natur im Experiment. 1. Bionik-Kongress, Wiesbaden, 1-13 June 1992.

Riblet flow calculation with a low Reynolds number $k - \epsilon$ model

L. DJENIDI AND R.A. ANTONIA

Department of Mechanical Engineering, University of Newcastle, N.S.W., 2308, Australia

Abstract. A low Reynolds number $k - \epsilon$ model has been used to calculate the turbulent boundary layer over riblets. Calculated mean velocity, Reynolds shear stress and kinetic energy distributions are generally in good agreement with available experimental data. The comparison between these distributions and those in a corner flow points to a significant difference between the two flows and the unlikelihood of counter-rotating vortices within the riblet grooves. One shortcoming of the present $k - \epsilon$ model is the relatively slow return to a two-dimensional turbulence state as the distance from the riblet surface increases.

1. Introduction

A significant amount of research, perhaps starting with the work of Walsh and Weinstein (1978) has established that riblets (longitudinal wall grooves) can reduce the drag in a turbulent boundary layer by about 7–8%. However, despite this, the manner in which riblets interact with the turbulence structure is not yet understood. The existence of low-speed fluid inside the riblet valleys is fairly well established, thus pointing to the importance of viscous effects in this flow region (e.g. Choi et al., 1991) and a possible reason for the drag reduction (Djenidi et al., 1992). Djenidi et al. (1992) made extensive experimental and numerical studies of a laminar boundary layer over V-grooves and found that, despite a large increase in the wetted surface (100% when $s = h$; s is the distance between adjacent peaks and h is the height of the groove), the skin friction is at worst equal to that on a smooth plate. They conclude that viscous effects should play an important role in the drag reduction mechanism. When the flow is turbulent, the state of knowledge is much less satisfactory than in the laminar case, partly because of the dearth of experimental information within the grooves and partly because the available data in the wall region above the grooves suffer from a lack of accuracy. Consequently, our understanding of the drag reduction mechanism is poor and our ability to develop a reliable numerical model is severely hampered.

An early numerical investigation of turbulent boundary layer over a riblet surface was done by Khan (1986), with a mixing length-eddy viscosity approach to model the Reynolds shear stress. He solved the x -momentum and vorticity equations. Although a reasonable result was obtained for the drag reduction, the calculation revealed a rather unrealistic secondary flow. Later, Djenidi et al. (1991) used also a mixing length-eddy viscosity model and solved the x -momentum equation using a curvilinear mesh. Although the calculated velocity profiles were in good agreement with experiment (Vukoslavcevic et al., 1987) the drag reduction was over-estimated. Benhalilou et al. (1991) also used a mixing length approach, solving the x -momentum equation in a cartesian mesh. Their numerical results, despite being in qualitative

agreement with their own experiments, overestimated the drag reduction. It would therefore appear that the mixing length-eddy viscosity model is inadequate for calculating the turbulent boundary layer over riblets and a more refined closure is required. The general aim of the present investigation was to develop a transport model for calculating the skin friction and distributions of the mean velocity, Reynolds stress and kinetic energy in a turbulent boundary layer over riblets. As a first step towards this goal, a low Reynolds number $k - \epsilon$ model (Chien, 1982) was used in this paper. The resulting calculations are compared with available measurements.

2. Mathematical formulation

The equations embodying the mathematical model can be written in any of several co-ordinate systems. In the present study, the problem is solved using an orthogonal curvilinear system. Details of the derivation of the conservation equations in general orthogonal curvilinear co-ordinates may be found in Nash and Patel (1978).

2.1. Computational Grid

The curvilinear mesh used to compute the flow was derived using a Schwarz-Christoffel transformation: the computational mesh, Fig. 1a, is transformed into the physical mesh, Fig. 1b (see Bechert and Bartenwerfer, 1989). The V-groove shape is considered here (the flow direction is perpendicular to the $y - z$ plane; only half a riblet is shown). The smooth wall is simulated when θ , the groove half-angle, is 90° . The upper limit is located at about 10 times the boundary layer thickness—note that

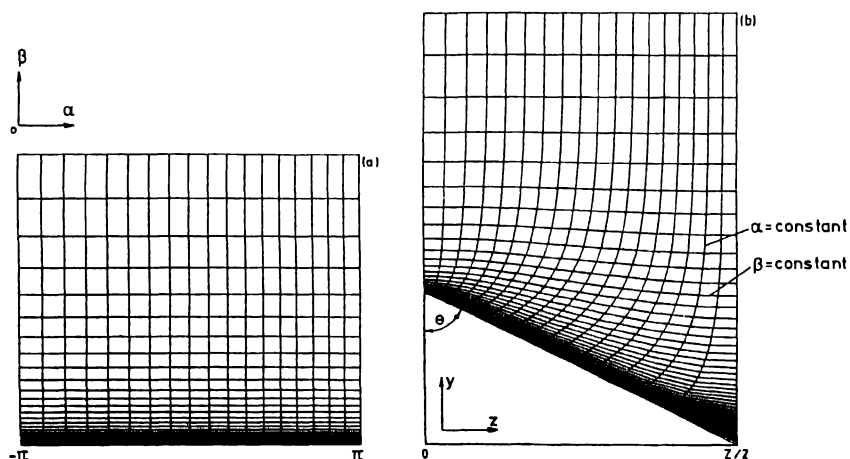


Fig. 1. (a) Computation and (b) physical mesh for half a V-groove.

only the region up to $y \simeq 3h$ is shown in Fig. 1. A series of numerical experiments established that the calculation was not particularly sensitive to the grid spacing, a 81×19 grid yielding the same \bar{U} , \overline{uv} and k distributions as a 81×43 grid. It should be noted that despite the rather inevitably coarse spanwise spacing in the trough, numerical inaccuracies in this region have a negligible influence, particularly on the total skin friction since only less than about 1% of this friction is associated with this region for a 81×19 grid with $s = 0.7$ mm and $h = 0.35$ mm. Further, there are about 30 grid points in the y direction within the riblet ($h^+ \simeq 15$) above the trough, the first point being at $y^+ = 0.55$ for $R_\theta = 7700$.

The computational domain is defined by the riblet wall, over a 1 m length, an upper limit at 10δ and the lateral boundaries at $z = 0$ and $z = s/2$.

2.2. Mass and mean momentum conservation equations

Starting from the ensemble averaged Navier-Stokes equations, the stationary boundary layer assumptions were applied with $\partial P/\partial x = 0$. Thus the equations are

$$\frac{\partial h^2 U}{\partial x} + \frac{\partial h V}{\partial \beta} + \frac{\partial h W}{\partial \alpha} = 0, \quad (1)$$

$$\begin{aligned} \frac{\partial h^2 U U}{\partial x} + \frac{\partial h U V}{\partial \beta} + \frac{\partial h U W}{\partial \alpha} &= \frac{\partial}{\partial \beta} \left(\nu \frac{\partial U}{\partial \beta} - h \overline{uv} \right) \\ &+ \frac{\partial}{\partial \alpha} \left(\nu \frac{\partial U}{\partial \alpha} - h \overline{uw} \right), \end{aligned} \quad (2)$$

where U , V , W , u , v and w are the components of the mean velocity and their fluctuations in the x (streamwise), β and α directions respectively, and the local metric h is a function of β , α , y and z (the normal and spanwise directions in a cartesian system) [see Djenidi et al., 1991]. ν is the kinematic viscosity of the fluid. The equations have five unknowns, U , V , W , \overline{uv} and \overline{uw} . The closure of \overline{uv} and \overline{uw} will be considered in Section 2.3. Equations (1) and (2) are solved for U , and V . To obtain W , it is assumed that the mean streamwise vorticity is zero (everywhere in the flow), viz.

$$\Omega_x = \frac{1}{h^2} \left(\frac{\partial h W}{\partial \beta} - \frac{\partial h V}{\partial \alpha} \right) = 0. \quad (3)$$

The following evidence can be given in support of (3). It should first be noted that the riblets are largely immersed within the inner region ($h^+ \lesssim 20$) and the Reynolds stresses within the grooves in this region are unlikely to be of sufficient strength to generate secondary flows, e.g. counter-rotating vortices. Also, the relatively few detailed experimental data that are available (Hooshmand et al., 1983; Vukoslavcevic et al., 1987; Benhalilou et al., 1991; Benhalilou, 1992) do not seem to support such motions. In spite of the strong inhomogeneity in the wall region, the mean flow

recovers its two-dimensionality ($W \equiv 0, \partial/\partial z \equiv 0$) for $y^+ \gtrsim 10$ above the riblets. On the basis of his measurements, Benhalilou (1992) concluded that there were no counter-rotating vortices within the grooves.

2.3. Turbulence modeling

An eddy viscosity, ν_t , is used to model the Reynolds stress, viz.

$$\overline{uv} = -\nu_t \frac{\partial U}{h \partial \beta}, \quad \overline{uw} = -\nu_t \frac{\partial U}{h \partial \alpha}$$

with

$$\nu_t = C_\mu \frac{k^2}{\varepsilon}. \quad (4)$$

The turbulent kinetic energy k and the “isotropic” dissipation ε , are evaluated by a low Reynolds number $k - \varepsilon$ model (Chien, 1982). In the present curvilinear co-ordinates, the equations are

$$\begin{aligned} & \frac{\partial}{\partial x} (h^2 U k) + \frac{\partial}{\partial \beta} (h V k) + \frac{\partial}{\partial \alpha} (h W k) \\ &= h^2 P_k - h^2 (\tilde{\varepsilon} + D) + \frac{\partial}{\partial \beta} \left[\left(v + \frac{\nu_t}{\sigma_k} \right) \frac{\partial k}{\partial \beta} \right] + \frac{\partial}{\partial \alpha} \left[\left(v + \frac{\nu_t}{\sigma_k} \right) \frac{\partial k}{\partial \alpha} \right] \end{aligned} \quad (5)$$

$$\begin{aligned} & \frac{\partial}{\partial x} (h^2 U \tilde{\varepsilon}) + \frac{\partial}{\partial \beta} (h V \tilde{\varepsilon}) + \frac{\partial}{\partial \alpha} (h W \tilde{\varepsilon}) \\ &= C_{\varepsilon 1} f_1 \frac{\tilde{\varepsilon}}{k} h^2 P_k - C_{\varepsilon 2} h^2 f_2 \frac{\tilde{\varepsilon}^2}{k} + \frac{\partial}{\partial \beta} \left[\left(v + \frac{\nu_t}{\sigma_\varepsilon} \right) \frac{\partial \tilde{\varepsilon}}{\partial \beta} \right] \\ &+ \frac{\partial}{\partial \alpha} \left[\left(v + \frac{\nu_t}{\sigma_\varepsilon} \right) \frac{\partial \tilde{\varepsilon}}{\partial \alpha} \right] + E \end{aligned} \quad (6)$$

with $P_k = -h \overline{uv} \partial U / \partial \beta - h \overline{uw} \partial U / \partial \alpha$, $\tilde{\varepsilon} = \varepsilon - D$. The definitions of D and E and the magnitudes of the constants C_μ , $C_{\varepsilon 1}$, $C_{\varepsilon 2}$, and σ_ε are given in Table 1a. The damping functions f_1 , f_2 and f_μ (discussed below) are shown in Table 1b.

A low Reynolds number $k - \varepsilon$ model is an extension of the classical $k - \varepsilon$ model developed for high Reynolds numbers, to account for the near-wall effect. In this present model, ε is replaced by $\tilde{\varepsilon}$ which, by contrast to ε , goes to zero at wall. As regards comments on E , D and f_i ($i = 1, 2$), the reader will find a complete description in Chien's (1982) paper. To reduce the eddy viscosity due to the near-wall effects,

Table 1a

D	E	C_μ	C_{ϵ_1}	C_{ϵ_2}	σ_k	σ_ϵ
$\frac{2\nu k}{y^2}$	$-\frac{2\nu\epsilon}{y^2}\exp(-0.5y^+)$	0.09	1.35	1.8	1.0	1.3

 Table 1b. $R_t = k^2/\nu\tilde{\epsilon}$; $y^+ = U_\tau y/\nu$

f_1	f_2	f_μ
1.0	$1 - 0.22\exp\left[-\left(\frac{R_t}{6}\right)^2\right]$	$1 - \exp(-0.0115y^+)$

Chien (1982) modified Eq. (4) by including a damping function, f_μ

$$\nu_t = C_\mu f_\mu \frac{k^2}{\epsilon}$$

Chien's model was chosen partly because of the ease with which it can be implemented, partly because of its ability in reproducing the most basic features of a flat plate boundary layer and finally because of its accuracy in calculating the skin friction (Patel et al., 1985). This latter feature is important in the context of estimating the drag reduction due to riblets. Rodi and Mansour (1990) evaluated a number of $k - \epsilon$ models against channel flow and boundary layer DNS data. They found that while the Chien model was not as accurate close to the wall as the model that they developed, it was more accurate by comparison to the Launder-Sharma (1974) or Lam-Bremhorst (1981) models.

2.4. Initial and boundary conditions

To start the calculations, initial mean velocity, turbulent kinetic energy and dissipation distributions are required. They were obtained from curve fits to the available data (experimental or numerical) or from theoretical formulations. Preliminary calculations showed a negligible effect of the precise form of the initial distributions on the results. The boundary conditions were:

$$\begin{aligned} \text{at the wall} & \quad U = V = W = k = \tilde{\epsilon} = 0 \\ \text{at the upper limit of the computational domain} & \quad \partial/\partial y = 0 \\ \text{on the lateral boundaries } (z = 0, z = s/2) & \quad \partial/\partial z = 0. \end{aligned}$$

2.5. Numerical method

A control finite volume procedure developed by Patankar (1980), is used for the discretisation of the equations (1–6), based on an orthogonal mesh and employing a staggered grid where the V and W nodes are shifted from the U, k and $\bar{\epsilon}$ nodes. Integration of each equation of transport across the appropriate control volumes yielded finite volume equations of the form, i.e.

$$(A_p - S_1)\phi_p = A_N\phi_N + A_s\phi_s + A_E\phi_E + A_W\phi_W + S_2 \quad (7)$$

where $A_p = A_N + A_s + A_E + A_W$ and S_1 and S_2 are coefficients of the linearised source terms. The A coefficients contain the combined effects of convection and a standard hybrid differencing scheme (Patankar, 1980). The solution procedure is an x -marching method, where the finite volume scheme was used at each step in the x direction (de St. Victor, 1986). The discretised system (7) was solved with the Modified Strongly Implicit algorithm (MSI) of Schneider and Zedan (1981).

3. Results

3.1. Flat plate

In order to test the equations written in a curvilinear co-ordinate system, calculations were performed on a flat plate (simulated by $\theta = 90^\circ$, see Fig. 1) for $R_\theta = 1100$ and 7700. In Fig. 2, the mean velocity, \bar{U} , the Reynolds stress, \overline{uv} , and the turbulent kinetic energy, k , distributions are reported. There is close agreement between the present calculations at $R_\theta = 1100$, the measurements of Vukoslavcevic et al. (1987) at $R_\theta = 1000$ and Spalart's (1988) DNS data for $R_\theta = 1410$. There is also good agreement between the present calculations at $R_\theta = 7700$ and Klebanoff's (1955) measurements ($R_\theta = 7700$).

The above results indicate that no significant error has been introduced by transforming the equations of motion and closure model equations from a cartesian co-ordinate system to an ortho-curvilinear one, a transformation which necessitates the use of the scale factor h in all the equations. It is also satisfying to observe that the model, originally developed for high values of R_θ seems to give satisfactory results at a relatively small value of R_θ . This is rather attractive in the present context since, in order to obtain detailed measurements on riblet flows, experiments have to be carried out with relatively large grooves and therefore at low Reynolds numbers (Vukoslavcevic et al., 1987, $R_\theta \simeq 1000$; Benhalilou et al., 1991, $R_\theta \simeq 300$).

3.2. Riblet wall

Before presenting the riblet results, it is perhaps important to explain the choice of the present curvilinear transformation. Previous calculations in laminar riblet flows

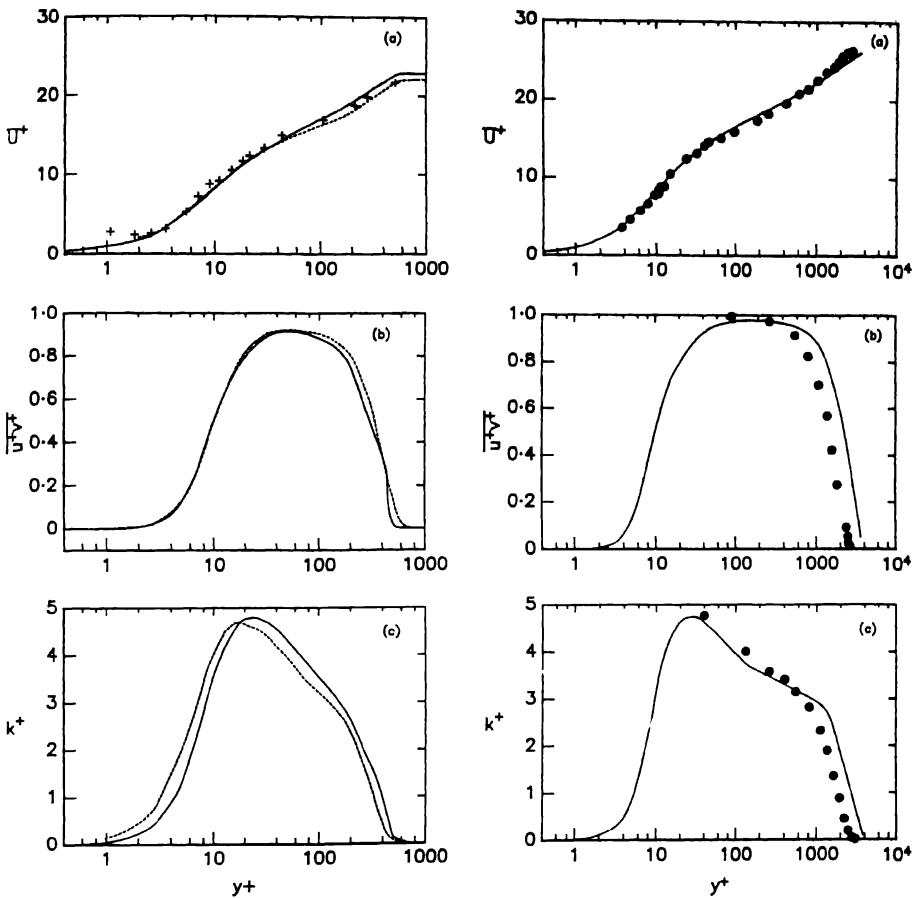


Fig. 2 Distributions of mean velocity, Reynolds shear stress and kinetic energy in a turbulent boundary layer over a smooth flat plate (1) $R_\theta = 1000$, (2) $R_\theta = 7700$ —, present calculation, +, Vukoslavcevic et al (1987), ---, Spalart (1988), ●, Klebanoff (1955)

(Djenidi et al., 1991) showed that an exactly 2-D flow ($W = 0$; $\partial/\partial z = 0$) could be achieved with this particular curvilinear system (Fig. 1). Contours of constant β and constant U (Fig. 8 of Djenidi et al., 1991) were identical. Bechert and Bartenwerfer (1989) also obtained the same result by theoretically solving

$$\Delta U = 0 (\Delta U = \partial^2 U / \partial y^2 + \partial^2 U / \partial z^2)$$

for turbulent riblet flow: they assumed that since the riblets are immersed in the inner region of a turbulent boundary layer ($h^+ \leq 15 - 20$) the convective terms and the Reynolds shear stress are negligible in the equations of the motion. These results would show that the present co-ordinate system would be well adapted to the

assumption $\Omega_x = 0$ [Eq. (3)]. Furthermore, in this curvilinear system, it is convenient to define the distance to the wall along β despite its ambiguous physical meaning (see Djenidi et al., 1991). This avoids using a distance to the wall as defined by Buleev (1963) and as is often done when dealing with walls (e.g. corners) that have spanwise inhomogeneities.

3.2.1. Mean velocity

The calculated mean velocity profiles $R_\theta \simeq 1100$ are compared in Fig. 3 with the experimental data of Vukoslavcevic et al. (1987) at $R_\theta \simeq 1000$ and of Benhalilou et al. (1991) at $R_\theta \simeq 300$. Note that the origin of the velocity profile above a peak has been shifted by a distance h^+ . Because of the nature of the conformal mesh, especially in the vicinity of the wall, it is best to compare experiments and calculations above peaks and valleys. The agreement is good when R_θ is about the same ($R_\theta \simeq 1000$). In the region $y^+ \geq 15$, the difference between the calculations and the $R_\theta = 300$ measure-

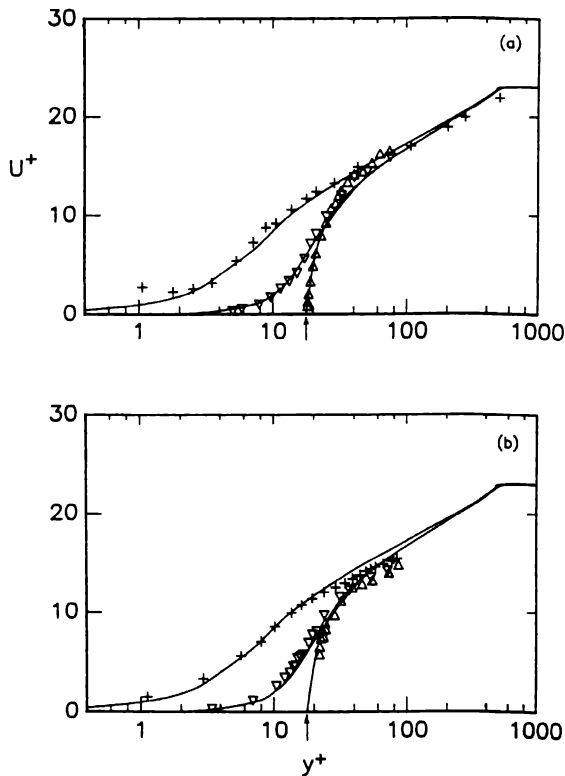


Fig. 3. Mean velocity profiles over a smooth flat plate and a riblet surface. —, present calculation at $R_\theta = 1000$; +, ∇ , Δ , experiments (+, smooth flat plate; Δ , riblet peak; ∇ , riblet trough). The arrow indicates the location of the riblet peak; the riblet trough is at $y = 0$. (a) $R_\theta = 1000$ (Vukoslavcevic et al., 1987); (b) $R_\theta = 300$ (Benhalilou et al., 1991).

ments can probably be assigned to low Reynolds number effects (e.g. Spalart, 1988). The agreement for $y^+ \leq 15$ is consistent with the observation that \bar{U} is relatively uninfluenced by the Reynolds number in this flow region (Spalart, 1988; Antonia et al., 1992; Wei and Willmarth, 1989; Djenidi and Antonia, 1992).

Beyond $y^+ \approx 15$, the profiles above the riblet peak coincide with those over the riblet valley. This is true for both measurement and calculation.

3.2.2. Reynolds shear stress and turbulent kinetic energy

Figures 4 and 5 show the calculated profiles of $\overline{u^+v^+}$ and k^+ over a smooth flat plate above a riblet peak and a riblet trough for $R_\theta = 1000$ and 7700. Qualitatively $\overline{u^+v^+}$ is similar at both Reynolds numbers; the same observation applies to k^+ . Further, both quantities exhibit identical behaviours within and just above ($y^+ \leq 15$) the groove.

Above the riblets ($y^+ \gtrsim 20$), $\overline{u^+v^+}$ is significantly different from k^+ . As y^+ increases above the riblet surface, the present calculations of $\overline{u^+v^+}$ are unlikely to be correct. For example, by comparison to the unpublished data of Benhalilou (1992) [these are

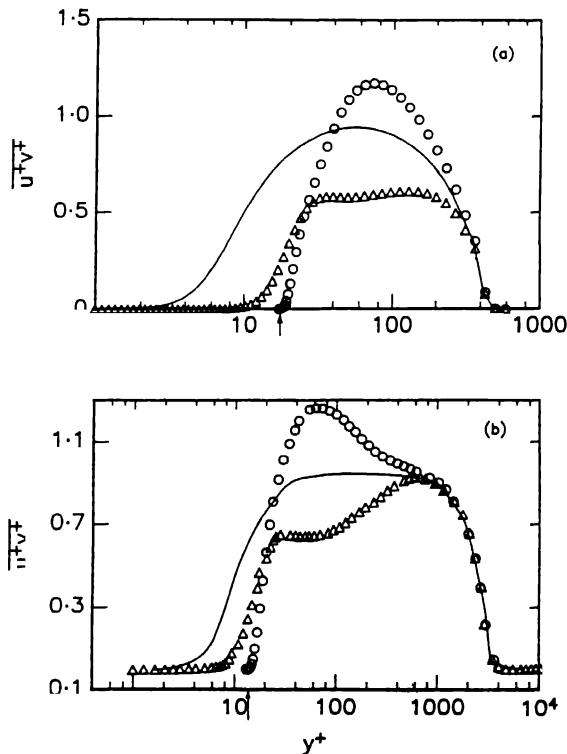


Fig. 4. Distributions of Reynolds shear stress. Calculations at (a) $R_\theta = 1000$ and (b) $R_\theta = 7700$. The arrow indicates the location of the riblet peak; the riblet trough is at $y = 0$. —, smooth flat plate; \circ , riblet peak; Δ , riblet trough.

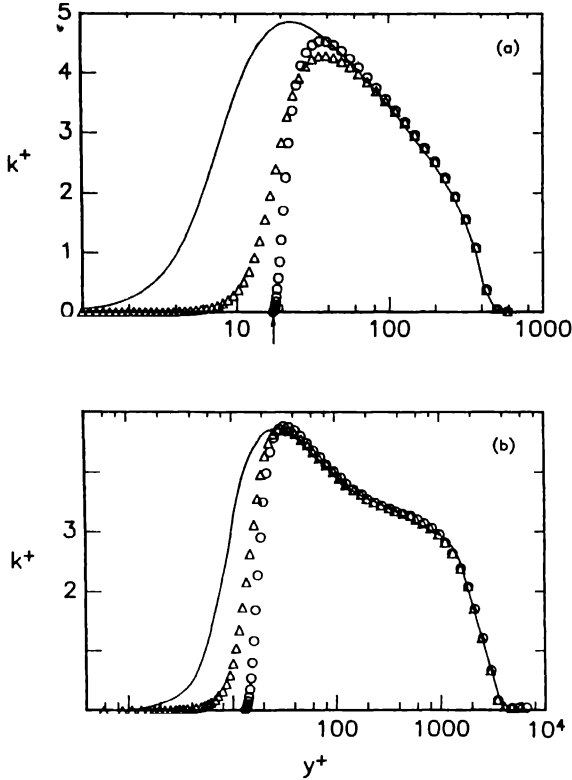


Fig. 5. Distributions of kinetic energy. Calculations at (a) $R_\theta = 1000$ and (b) $R_\theta = 7700$. The arrow indicates the location of the riblet peak; the riblet trough is at $y = 0$. —, smooth flat plate; \circ , riblet peak; Δ , riblet trough.

not shown here], it would appear that the calculation overestimates u^+v^+ above a peak and underestimates it above a trough. This is probably caused by the manner in which the near-wall effect is taken into account by the closure model. Specifically, the present relation for f_μ does not appear to reproduce the apparent return to a two-dimensional state as y^+ increases. The use of U_τ in $y^+ = yU_\tau/\nu$ may not be appropriate here since it varies significantly along the groove contour (e.g. Fig. 6 where U_{τ_0} is the friction velocity on the smooth plate.) Since $\overline{u^+v^+}$ depends strongly on $f_\mu(\overline{uv} = C_\mu f_\mu k^2/\epsilon \partial U/\partial y)$, its spanwise variation may be incorrectly reproduced as the wall distance increases. This difficulty can be avoided by using a transport equation for \overline{uv} where no damping function is required.

The mean velocity, Reynolds shear stress and turbulent kinetic energy distributions exhibit a common feature: they are all strongly damped within the groove, emphasising the importance of viscous effects on the near-wall turbulence. There is an apparent tendency towards “relaminarisation” within the grooves as shown in Fig. 7 ($v_t/\nu \leq 0.4$ everywhere within the riblets).

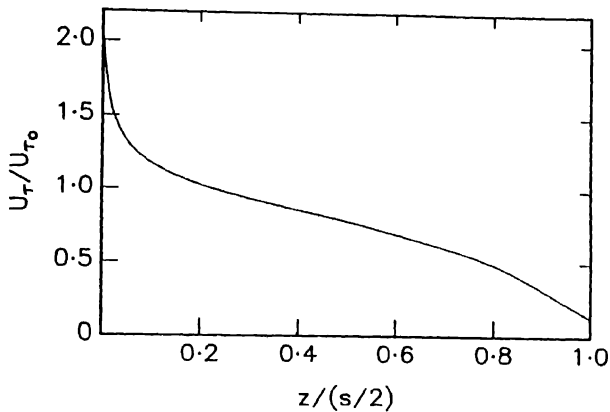


Fig. 6. Variation in friction velocity U_τ along the riblet contour $s = 2h = 0.7 \text{ mm}$, $R_\theta = 7700$.

3.2.3. Comparison between riblet and corner flows

It is of interest to compare the flow over riblets with that in a corner flow because of the geometrical similarity between the two cases, at least when V and L-shaped grooves are used. Constant velocity contours around one groove (Fig. 8a) can be compared with the corresponding contours for a corner (Fig. 8b, Bragg, 1969). As expected, the flow within the riblets behaves similarly to that in a corner, e.g. the spreading of the iso-contours as the corner is approached, suggesting a low skin

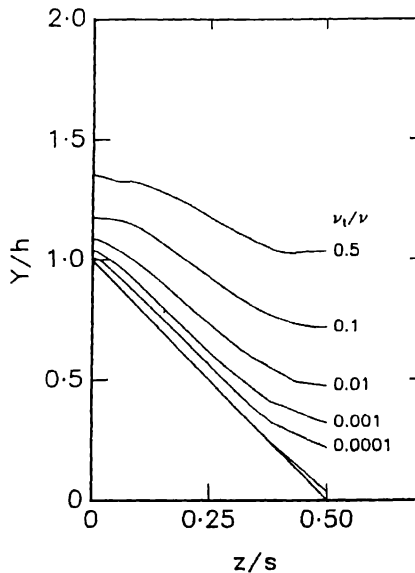


Fig. 7. Contours of constant eddy viscosity over riblets.

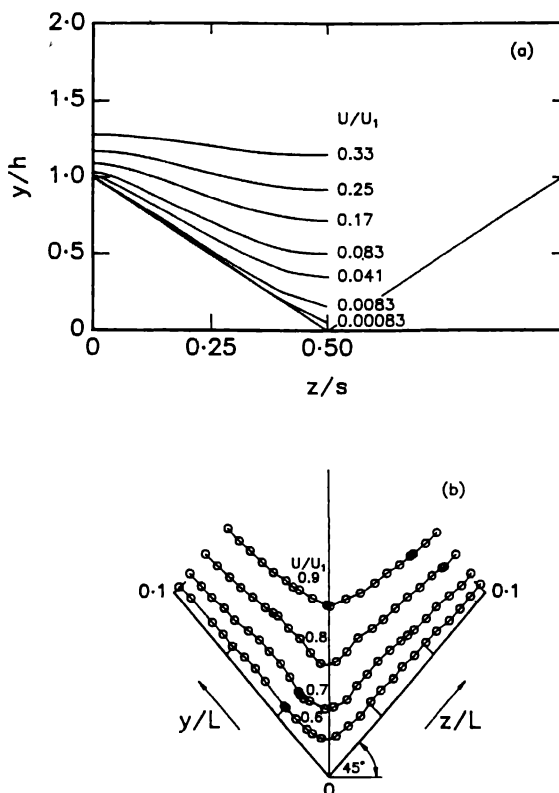


Fig. 8. Contours of constant mean velocity over riblets and in a corner flow. (a) riblet (calculation); (b) corner (experiment), L is the width of the plates (Bragg, 1969).

friction region. There is however a fundamental difference between the two flows in that the riblet height is small compared to the boundary layer thickness, δ , while the corner dimensions are comparable to δ . Accordingly, features of corner flows, such as the secondary motion would not be appropriate for riblet flows. Besides, a comparison between the Reynolds stress distributions along the corner bisector, Fig. 9, (Nakamura et al., 1982) and on the riblet trough (Figs 4 and 5) underlines the difference between the two flows: the double peaks observed on the \overline{uv} and $\overline{u^2 + v^2 + w^2}$ ($=2k$) in the corner flow due to the counter rotating motions are absent in the riblet flow.

3.2.4. Skin friction and drag reduction over riblets

The present calculations were carried out at $R_\theta \simeq 7700$. Fig. 10a shows the cumulative frictional drag along the riblet surface, $\int_0^l \tau \, dl$ (where $\tau = \mu \partial \bar{U} / \partial w|_{\text{wall}}$) normalised by the total friction over the riblet, $\int_0^L \tau \, dl$. Although the wetted surface area is greatly enhanced relative to that of a smooth surface, the major contribution to the total

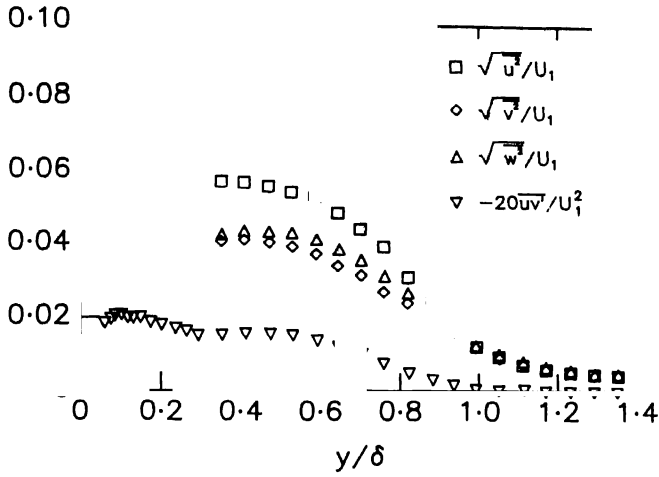


Fig. 9. Reynolds stress distributions along a corner bisector (Nakamura et al., 1982).

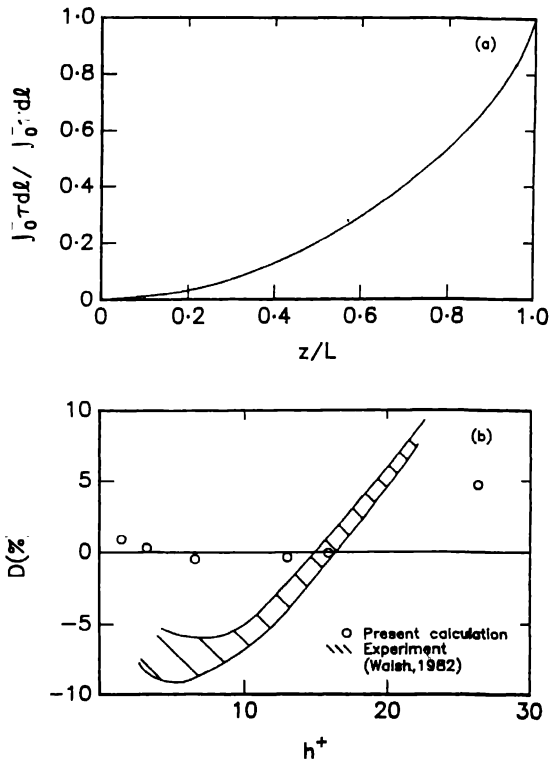


Fig. 10. (a) Cumulative frictional drag along the riblet contour. (b) Dependence on h^+ of the ratio of the total frictional drag over riblet surface to the total frictional drag over a smooth flat plate.

friction is associated with the region near the riblet peak. This suggests that the optimum riblet geometry should be one which minimises the frictional increase near the peak. The two most important parameters are therefore likely to be s/h and h/δ (or s/δ). However, since the riblet dimensions are comparable to the extent of the inner region, h/δ should be replaced by h^+ .

The calculated frictional drag ratio, $D = 1 - F_R/F_0$, where F_R is the riblet frictional force and F_0 is the frictional force on a smooth flat plate, is shown in Fig. 10b for several values of h^+ (with $s^+ = 2h^+$). The calculated drag reduction is underestimated by comparison to the measurements of Walsh (1982). Note also that, when $h^+ \rightarrow 0$, D exceeds 0 whereas it should approach 0, as indicated by the experimental data. Launder and Li (1991) obtained a similar result for the calculated drag in a turbulent channel flow over riblets using another version of a low Reynolds number $k - \varepsilon$ model (Launder and Sharma, 1974). Low Reynolds number $k - \varepsilon$ models in their present two-dimensional forms clearly fail to simulate the spanwise inhomogeneity of the turbulent flow field over riblets.

4. Conclusions and final discussion

A low Reynolds number $k - \varepsilon$ model has been used to calculate a turbulent boundary layer over riblets. The calculated mean velocity is in agreement with available experiments. However, although the calculated turbulence quantities seem to be consistent with the measurements, the model does not reproduce the experimentally observed drag reduction.

The effect of riblets was limited mainly to the inner flow region, highlighting a fundamental difference between riblet and corner flows, where the characteristic length scale of the corner is usually comparable to the boundary layer thickness. This difference may support an argument against the existence of counter-rotating vortices inside the riblet grooves.

The present form of the $k - \varepsilon$ model is inadequate for capturing the disappearance of the spanwise variation in the turbulence quantities as the distance from the wall increases. In particular, the present damping function formulation reproduces the return towards two-dimensionality only poorly. While the introduction of the damping function is necessary, the choice of f_μ has a significant effect on the calculation of k and ε (Mansour et al., 1989), the modelling of k and ε may need to be reassessed (e.g. terms D and E in the present case). This may in turn require the various empirical constants ($C_\mu, C_{\varepsilon_1}, C_{\varepsilon_2}, \sigma_k, \sigma_\varepsilon$) as well as the functions f_1 and f_2 to be modified. The damping effect on uv may be better simulated by using \bar{v}^2/k instead of $f_\mu(uv = C(\bar{v}^2/k)(k^2/\varepsilon)\partial U/\partial y)$, the rationale being that the rapid reduction in uv as the wall is approached is mainly due to the damping of \bar{v}^2 rather than the viscous effect (Launder and Tselipidakis, 1990). The attraction of this approach is that it avoids the use of U_τ , despite the necessity of introducing an equation for \bar{v}^2 . Using this approach, good agreement with DNS smooth wall channel flow data was obtained by Durbin

(1990) and Kawamura (1991). The development of a Reynolds stress closure for riblet flow calculations should also be worthwhile despite the added complications to the equations. Its main advantage would be to avoid the use of empirical functions for simulating the near-wall effect.

Independently of whether the closure is of the $k - \varepsilon$ or Reynolds stress types, nonlocal parameters, such as the wall friction velocity, should not appear in the model. This would allow the spanwise variation in turbulence quantities to disappear quickly, thus permitting a faster relaxation towards two-dimensionality away from the riblet surface. An alternative way of avoiding the inhomogeneity of the non-local parameters, is to treat riblets as roughness elements and use calculation methods developed for rough surfaces (e.g. Granville, 1992). However attractive such a method may appear, it has the disadvantage of not addressing the physics behind the drag reduction.

A possible physical mechanism for drag reduction by riblets appears to be the prevention of the interaction between near-wall quasi-streamwise vortices and the riblet surface (Kim, 1992). In this context it is unlikely that $k - \varepsilon$ or Reynolds stress closures can capture the observed drag reduction since neither the characteristics of the vortices nor their interaction with the surface enter these models.

Acknowledgement

The support of the Australian Research Council is gratefully acknowledged.

References

- Antonia, R.A., Teitel, M., Kim, J. and Browne, L.W.B., Low Reynolds number effects in a fully developed turbulent duct flow. *J. Fluid Mech.* 236 (1992) 579–605.
- Bechert, D.W. and Bartenwerfer, M., The viscous flow on surfaces with longitudinal ribs. *J. Fluid Mech.* 206 (1989) 105–129.
- Benhalilou, M., Etude Experimentale et Numerique d'une Couche Limite Turbulente sur Paroi Rainuree, Ph.D. Dissertation, I.M.S.T., France (1992).
- Benhalilou, M., Anselmet, F., Liandriat, J. and Fulachier, L., Experimental and numerical investigation of a turbulent boundary layer over riblets. *Turbulent Shear Flows 8* Munich (1991).
- Bragg, G.M., The turbulent boundary layer in a corner. *J. Fluid Mech* 36 (1969) 485–503.
- Buleev, N.I., Theoretical model of the mechanism of turbulent exchange in fluid flows. *AERE Trans.* 957, Harwell (1963) 1–39.
- Chien, K.Y., Predictions of channel and boundary-layer flows with a low-Reynolds number turbulence model. *AIAA Jnl.* 20 (1982) 33–38.
- Choi, H., Moin, P. and Kim, J., On the effect of riblets in fully developed laminar channel flows. *Phys. Fluids A* 3 (1991) 1892–1896.
- de St. Victor, X., Resolution des Equations de Navier-Stokes Bi- ou Tridimensionnelles par Methodes de Marches—Application au Calcul de Melange d'Ecoulements Cisailles, Ph.D. Dissertation, I.N.P.T., France (1986).
- Djenidi, L. and Antonia, R.A., LDA measurements in low Reynolds number turbulent boundary layer. *Expts. in Fluids* [to appear].

- Djenidi, L., Liandriat, J., Anselmet, F. and Fulachier, L., Laminar boundary layer over riblets. *Phys. Fluids A* [submitted].
- Djenidi, L., Squire, L.C. and Savill, A.M., High resolution conformal mesh computation for V, U and L-groove riblets in laminar and turbulent boundary layer. In: K. S. Choi (ed.), *Recent Development in Turbulence Management*. Dordrecht: Kluwer, Academic Publishers (1991) pp. 65–92.
- Durbin, P.A., Near wall turbulence closure modeling without damping function. *CTR Manuscript* 112, Stanford University (1990).
- Granville, P.S., Similarity-law analysis and turbulence modeling for riblet drag reduction. *J. Ship Res.* 36 (1992) 55–58.
- Hooshmand, D., Youngs, R., Wallace, J.M. and Balint, J.L., An experimental study of changes in the structure of a turbulent boundary layer due to surface geometry changes. *AIAA Paper* 83-0230 (1983).
- Kawamura, H., A $k - \epsilon - \overline{v^2}$ model with special relevance to the near wall turbulence. *Proc. Eighth Symposium on Turbulent Shear Flows* Munich (1991) pp. 26-4-1 to 26-4-6.
- Khan, M.M.S., A numerical investigation of the drag reduction by riblet surface. *AIAA paper* 86-1127 (1986).
- Kim, J., Study of turbulence structure through numerical simulations: the perspective of drag reduction. *AGARD Report* 786 (Special Course on Skin Friction Drag Reduction) (1992) pp. 7-1 to 7-14.
- Klebanoff, P.S., Characteristics of turbulence in a boundary layer with zero pressure gradient. *NACA Report* 1247 (1955).
- Lam, C.K.G. and Bremhorst, K.A., Modified form of the $k - \epsilon$ model for predicting wall turbulence. *J. Fluids Eng.* 103 (1981) 456–460.
- Launder, B.E. and Li, S.P., Prediction of drag reduction by riblets. Presentation at the 6th Drag Reduction Meeting, Eindhoven (1991).
- Launder, B.E. and Sharma, B.I., Application of the energy-dissipation model of turbulence to the calculation of flow near a spinning disc. *Letters in Heat Mass Transfer* 1 (1974) 131–138.
- Launder, B.E. and Tselepidakis, D.P., Contribution to the second-moment modeling of sublayer turbulent transport. In: Kline, S. J. and Afgan, N. H. (eds), *Near-Wall Turbulence*. New York: Hemisphere (1990) pp. 818–833.
- Mansour, N.N., Kim, J. and Moin, P., Near-wall $k - \epsilon$ turbulence modelling. *AIAA Jnl.* 27 (1989) 1068–1073.
- Nakamura, I., Miyata, M., Kushoda, T. and Kagiya, K., Some measurements in the intermittent region of a turbulent boundary layer along a corner. In: Fernholz, H. H. and Drause, E. (eds), *Three Dimensional Turbulent Boundary Layers*. Berlin: Springer (1982) pp. 118–209.
- Nash, J.F. and Patel, V.C., *Three Dimensional Turbulent Boundary Layers*. SBC Technical Books (1972).
- Patankar, S.V., *Numerical Heat Transfer and Fluid Flow*. Series in Computational Methods in Mechanics and Thermal Sciences. McGraw-Hill (1980).
- Patel, V.C., Rodi, W. and Scheuerer, G., Turbulence models for near-wall and low-Reynolds number flows: a review. *AIAA Jnl.* 23 (1985) 1308–1319.
- Rodi, W. and Mansour, N.N., Low Reynolds number $k - \epsilon$ modelling with the aid of direct simulation data. In: *Proc. of the Summer Program 1990*. Stanford University: Center for Turbulence Research (1990) pp. 85–106.
- Schneider, G.E. and Zedan, M., A modified strongly implicit procedure for the numerical solution of field problems. *Num. Heat Transfer* 4 (1981) 1–19.
- Spalart, P.R., Direct simulation of turbulent boundary layer up to $R_\theta = 1410$. *J. Fluid Mech.* 187 (1988) 61–98.
- Vukoslavcevic, P., Wallace, J.M. and Balint, J.L., On the mechanism of viscous drag reduction using streamwise aligned riblets: a review with new results. In: *Proc. R.A.S. Int. Conf. on Turbulent Drag Reduction by Passive Means*, Vol. 2. The Royal Aero. Soc. (1987) pp. 290–309.
- Walsh, M.J., Turbulent boundary layer drag reduction using riblets. *AIAA Paper* 82-0169 (1982).
- Walsh, M.J. and Weinstein, L.M., Drag and heat transfer on surfaces with small longitudinal fins. *AIAA Paper* 78-1161, presented at AIAA 11th Fluid and Plasma Dynamics Conference, Seattle, WA (1978).
- Wei, T. and Willmarth, W.W., Reynolds-number effects on the structure of a turbulent channel flow. *J. Fluid Mech.* 204 (1989) 57–95.

On the prediction of riblet performance with engineering turbulence models

B.E. LAUNDER & S.P. LI

UMIST, Manchester, U.K.

Abstract. The paper reports the outcome of a numerical study of fully developed flow through a plane channel composed of ribleted surfaces adopting a two-equation turbulence model to describe turbulent mixing. Three families of riblets have been examined: idealized blade-type, V-groove and a novel U-form that, according to computations, achieves a superior performance to that of the commercial V-groove configuration. The maximum drag reduction attained for any particular geometry is broadly in accord with experiment though this optimum occurs for considerably larger riblet heights than measurements indicate. Further explorations bring out a substantial sensitivity in the level of drag reduction to the channel Reynolds number below values of 15 000 as well as to the thickness of the blade riblet. The latter is in accord with the trends of very recent, independent experimental studies.

Possible shortcomings in the model of turbulence are discussed particularly with reference to the absence of any turbulence-driven secondary motions when an isotropic turbulent viscosity is adopted. For illustration, results are obtained for the case where a stress transport turbulence model is adopted above the riblet crests, an elaboration that leads to the formation of a plausible secondary motion sweeping high momentum fluid towards the wall close to the riblet and thereby raising momentum transport.

Nomenclature

c_f = Skin friction coefficient
 c_{f0} = Skin friction coefficient in smooth channel at the same Reynolds number
 k = Turbulent kinetic energy
 k^+ = $\rho k / \tau_w$
 h = Riblet height
 S = Riblet width
 H = Half height of channel
 Re = Reynolds number = volume flow/unit width/ v
 \tilde{R}_t = Modified turbulent Reynolds number $k^2 / v \tilde{\epsilon}$
 R_t = turbulent Reynolds number $k^2 / v \epsilon$
 P_k = Shear production rate of k ,
 $v_i (\partial U_i / \partial x_j + \partial U_j / \partial x_i) \partial U_i / \partial x_j$
 dP/dz = Streamwise static pressure gradient

U_i = Mean velocity vector (tensor notation)
 U_τ = Friction velocity, $\sqrt{\tau_w / \rho}$ where $\tau_w = -H dP/dz$
 W = Mean velocity
 W_b = Bulk mean velocity through channel
 y^+ = yU_τ / v . Unless otherwise stated, origin is at wall on trough plane of symmetry
 ν = Kinematic viscosity
 ν_t = Turbulent kinematic viscosity
 ϵ = Turbulence energy dissipation rate
 $\tilde{\epsilon}$ = Modified dissipation rate
 $\epsilon - 2\nu(\partial k^{1/2} / \partial x_j)^2$
 ρ = Density
 $\sigma_k, \sigma_\epsilon$ = Effective turbulent Prandtl numbers for diffusion of k and ϵ

1. Introduction

While the fact that surfaces covered with microgroove riblets can achieve drag levels that are some 5–10% below that of an aerodynamically smooth surface is beyond doubt [1–5], the mechanism responsible for that drag reduction is still open to debate.

Without a clear understanding of the mechanism, it is difficult to arrive by experiment at an optimum design^{*} of riblet profile. Inevitable uncertainties in the measurement of skin friction and in embedding a patch of ribleted surface in the wind tunnel usually make it difficult to distinguish a one or two percent advantage from one riblet shape over another from the background scatter.

Against this background the idea of using CFD to guide the optimization of riblet surfaces appears an attractive option. With care in setting up the grid one can, for all practical purposes, eliminate the “noise” – in this case numerical errors – that clouds experimental work. Moreover, with a surface-conforming solver it is a straightforward matter to scan through different families of riblet profiles in search of the optimum. The task, of course, requires considerable computer resource but the overall cost of a numerical investigation is still but a small fraction of that of the corresponding experiments – particularly as so much more detail of the flow is computed than can possibly be measured in an experiment.

The above discussion has not, however, touched on the Achilles heel of computational approaches to riblet modelling – the turbulence model. There is inevitably serious uncertainty as to whether available engineering models of turbulence capture enough of the physics of the near-wall sublayer to allow their extrapolation to flows which exhibit two directions of rapid change within the turbulent buffer region. Previous attempts at modelling riblet flows [6, 7, 8, 21] have employed mixing-length or one-equation models. These can never provide a way of *predicting* drag reduction, for arbitrary choices have to be made – or at least choices unrelated to the flow’s physics – on how to interpret, in the vicinity of the riblet, the effective distance of a point from the surface and the appropriate value of wall friction in defining the sublayer velocity scale based on wall friction. Another weakness so far as earlier attempts are concerned has been inadequate numerical resolution in the region near the tip of a riblet. For example, Khan [6] employed ten grid nodes distributed equally along each face of the V-groove riblets considered in his study. Our calculations suggest, however, that the top 10% of his riblets covered by a single node in fact carry up to 40% of the drag of the whole plate!

The simplest level of modelling at which *ad hoc* decisions about wall distance can be avoided is the two-equation level; for then, with transport equations solved for two turbulence variables, effective time and – more importantly – length scales are predicted as an output. Even at two-equation level several of the available models *do* introduce non-dimensional forms of distance from the wall into damping functions designed to make the turbulent kinetic energy and shear stress fall to zero sufficiently rapidly as the wall is approached [9, 10]. However, the original $k - \bar{\epsilon}$ model of [11] (or the variant of it [12] which is the principal model adopted in the present study) makes no appeal to wall distance or to the topography of the surface: “proximity” to the wall is sensed only through the local value of the turbulent Reynolds number $\bar{R}_t \equiv k^2/\bar{\nu}\bar{\epsilon}$ (symbols are defined under Nomenclature). The model has been successfully applied to predict laminarization by acceleration [13] and, more recently, the transition from laminar to turbulent flow triggered by high levels of external stream turbulence [14].

It thus seemed the most appropriate candidate model to employ for this exploration of riblet flows. The aim of the exploration has been to apply the model first to riblets of simple shape to determine whether drag reductions in line with experiment were achieved. A first contribution to this initial study has been reported in [15] but here that work is extended to include blade riblets of finite thickness. This step helps clarify what had seemed an inexplicably large difference in performance between the two riblet types. Being sufficiently encouraged by aspects of these predictions (albeit acknowledging that weaknesses remained), further explorations have been made to see whether some other riblet shape might lead to greater drag reduction than those currently adopted.

One inherent weakness of adopting an eddy viscosity model of turbulent transport in riblet flows is that they are incapable of predicting secondary motions in the plane of the riblet cross section. While no such secondary motions have been reported from experimental studies, it seems probable – based on the wider experience of flow in non-circular ducts – that they do exist and that their presence worsens the performance of the riblet as a drag reducer. Khan's [6] early contribution did include the algebraic model of Launder and Ying [16] to approximate the anisotropy of the stress field acting in the plane orthogonal to the primary flow and, as a result, generated a secondary motion. However, the proposal of [16] was designed for fully turbulent regions only and would be likely to give unreliable results when applied in the buffer layer. Whether for that reason or another the secondary flow eddies generated in Khan's study seemed physically implausible, extending some six riblet heights above the surface and causing, according to the author, a *reduction* in drag.*

A more general route to allowing secondary motions to appear would be through a complete second-moment closure. No such computations have so far been attempted for riblet flows, however. A major obstacle to attempting such an exploration is that all the available models of this type presume that the rigid surface can be regarded as flat – thus explicitly invalidating their use in the vicinity of the riblet itself. However, in order to indicate the type of change to the predicted behaviour that a second-moment closure (when one becomes available) might bring, the present contribution reports sample computations in which a second-moment closure has been adopted for the region above the riblet while retaining the $k-\epsilon$ model of [12] within the riblet cavity.

2. The mathematical and computational model

The present explorations have focused on the *fully developed flow between infinite parallel planes* covered with riblets aligned with the flow direction. While the principal interest in riblets arises in developing flows, the present limitations should be of no real consequence for the riblets are so small that their tips usually lie within the

*In a computational scheme the contribution of the secondary motion to the wall friction can be readily determined by repeating the calculation with secondary motion set to zero.

(virtually) constant stress layer whether the flow in question is a boundary layer or channel flow. The choice of an infinite plane channel allows considerable computational economy as the computations are then two-dimensional, being solved on a single plane orthogonal to the mean flow. A further advantage of a channel-flow study is that the results are "cleaner": there is no streamwise variation of wall friction or shear layer thickness as there is in a boundary layer flow. The different contributions of the influential parameters can thus be separately assessed.

Most of the computations reported in the paper have adopted an isotropic viscosity model to approximate the turbulent stresses and, as a result, no secondary motions are generated. The distribution of mean velocity in fully-developed flow is thus governed by the following equation:

$$\frac{1}{\rho} \frac{dP}{dz} = \frac{\partial}{\partial x} \left((v + v_t) \frac{\partial W}{\partial x} \right) + \frac{\partial}{\partial y} \left((v + v_t) \frac{\partial W}{\partial y} \right), \quad (1)$$

where z is the stream direction and x and y lie in the cross-sectional plane with the coordinate y normal to the wall. In fact, it has been found that variations of velocity and other flow properties in the x direction only occur within three riblet heights of the channel floor. This feature is exploited in obtaining the numerical solution of equation (1). The turbulent viscosity v_t given by

$$v_t = c_\mu k^2 / \tilde{\epsilon}$$

where, following [12], the turbulence energy k and the modified dissipation $\tilde{\epsilon}$ are obtained from

$$0 = \frac{\partial}{\partial x_j} \left(\left(v + \frac{v_t}{\sigma_k} \right) \frac{\partial k}{\partial x_j} \right) + P_k - \tilde{\epsilon} - 2v(\partial k^{1/2} / \partial x_j)^2, \quad (2)$$

$$0 = \frac{\partial}{\partial x_j} \left(\left(v + \frac{v_t}{\sigma_\epsilon} \right) \frac{\partial \tilde{\epsilon}}{\partial x_j} \right) + c_{\epsilon 1} \frac{P_k \tilde{\epsilon}}{k} - c_{\epsilon 2} \frac{\tilde{\epsilon}^2}{k} + 2v v_t \left(\frac{\partial^2 U_i}{\partial x_j \partial x_k} \right)^2. \quad (3)$$

Indices on the spatial coordinate take the values 1 and 2 corresponding to the x and y directions. Like k , the quantity $\tilde{\epsilon}$ defined as $\epsilon - 2v(\partial k^{1/2} / \partial x_j)^2$ vanishes at the wall – indeed, it was first introduced [11] specifically to provide a clear wall boundary condition. The coefficients in the model take the standard values shown in Table 2.1.

Equations (1)–(3) have been solved numerically using two versions of the finite-volume elliptic solver TEAM [17, 18], a Cartesian-coordinate version being used for blade or L-shaped riblets and a curvilinear orthogonal version for the other riblet

Table 2.1.

c_μ	$c_{\epsilon 1}$	$c_{\epsilon 2}$	σ_k	σ_ϵ
$0.09 e^{-3.4/(1+0.02\tilde{R}_i^2)}$	1.44	$1.92(1 - e^{-\tilde{R}_i^2})$	1.0	1.3

profiles. Following extensive grid refinement tests, typically 80 nodes were placed between the wall and a distance of two rib heights above the riblet crest and 45 nodes between the symmetry planes passing through the riblet crest and trough. By three riblet heights above the channel floor there are sensibly no lateral variations in any flow property and, accordingly, just a single column of nodes is used to cover the region from there to the symmetry plane of the channel. Examples of the near-riblet meshes adopted for the riblets in the present study appear in Fig. 1. Notice that the curvilinear orthogonal mesh naturally leads to a concentration of nodes near the riblet tip which is precisely where it is needed. Although, as a consequence, the near-wall node for the V-groove riblets for $S/h = 1$ is extremely coarse (covering about 20% of the riblet surface), the surface friction over that cell contributes less than 1% of the total drag.

As signalled in Section 1, illustrative computations have also been made for idealized L-shaped riblets with a second-moment closure adopted over the bulk of the flow wherein transport equations are solved for all six Reynolds stress components. Since such a non-isotropic model of turbulence could be expected to generate secondary motions, the describing equations of motion must now include convective transport terms in the x and y directions and, moreover, in addition to the stress-transport equations, additional equations of motion are solved for the x - and y -directed velocities.

3. The computed behaviour

Practical interest centres on whether or not drag reduction is predicted for a given shape and size of riblet. Accordingly, this question is considered first before details of

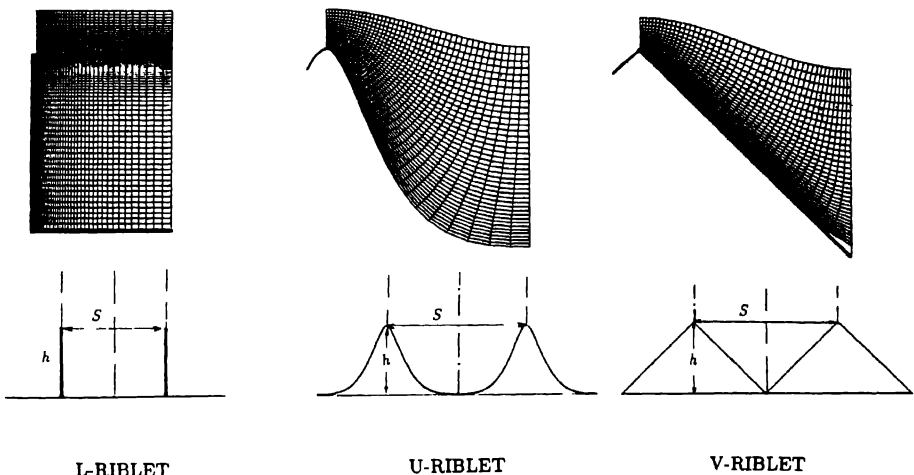


Fig. 1 The riblet configurations studied.

the flow field are examined. Figures 2 and 3 present the computed behaviour for riblet families of idealized L-shaped (with zero thickness) and V-groove forms, respectively. In Fig. 2a the performance at a fixed bulk Reynolds number of 50 000 is shown. Strikingly evident is the fact that appreciable drag reductions are predicted over a range of h^+ , the optimum performance being achieved for $S/h \approx 1$, in accord with the conclusions of [3]. However, the magnitude of the drag reduction at $S/h = 1.0$ is at least twice that reported in the experimental literature and occurs at a value of h^+

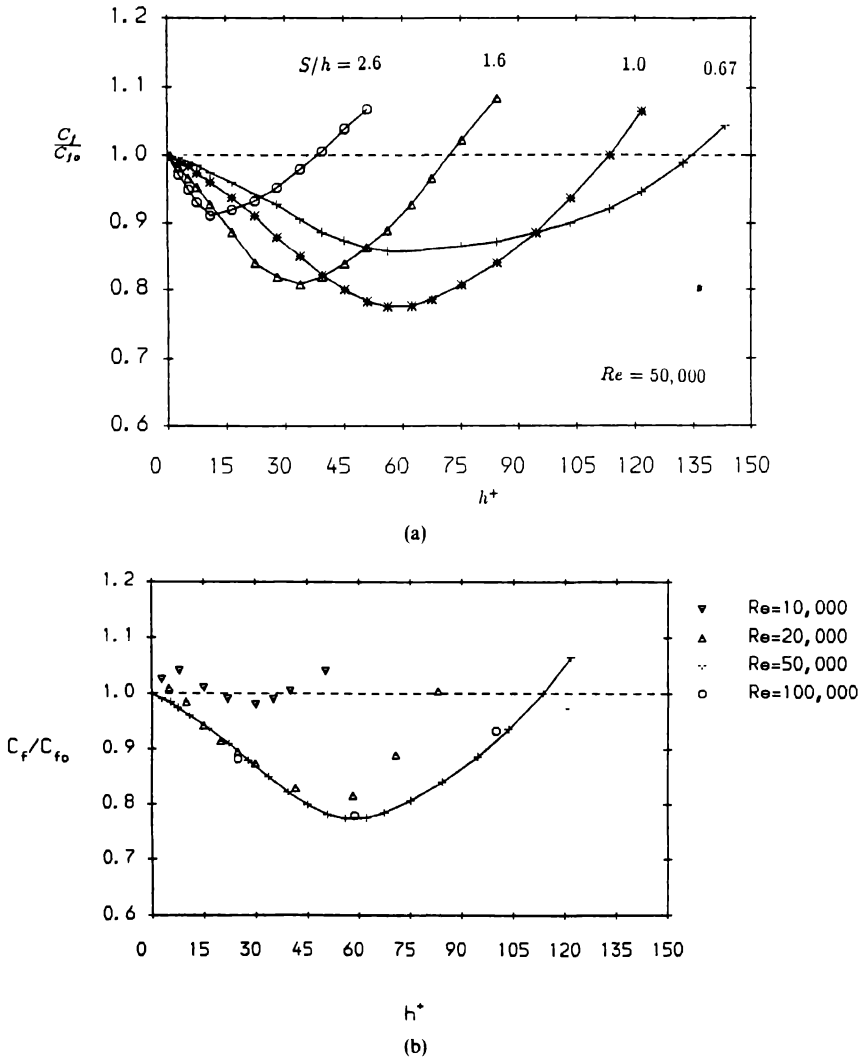


Fig. 2. Predicted drag behaviour for idealized L-shaped riblets. (a) Effect of $S:h$ ratio for $Re = 50\,000$ (from Launder and Li [15]). (b) Effect of Reynolds number on drag reduction for $S/h = 1.0$.

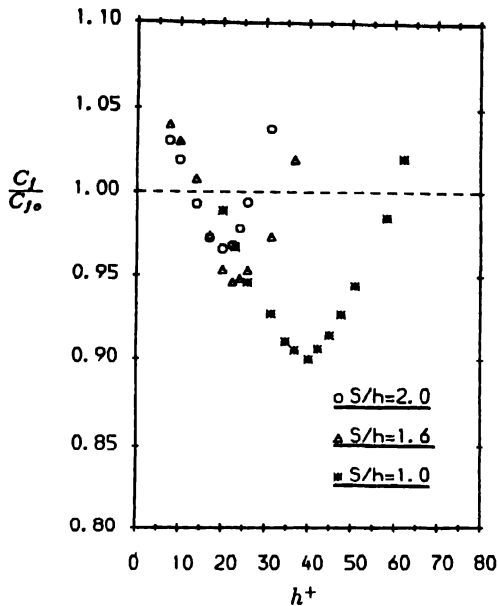


Fig. 3. Drag reduction behaviour for V-grooved riblets.

more than four times that giving the optimum drag reduction in experiments. Both these matters will be examined shortly. First we note, however, from Fig. 2b that, while riblet performance is virtually independent of Reynolds number above $Re = 20\,000$, there is a precipitate decline below that level due partly to the fact that, at a given h^+ , the riblet height increases steadily relative to the channel width and thus the velocity near the riblet tip progressively increases relative to \bar{W} . Another contributory factor is that in a smooth channel the present turbulence model gives a thickening of the viscous sublayer below $Re = 15\,000$ (a behaviour in accord with channel flow data) giving lower values of c_{f0} than would have pertained had the smooth-channel predictions rigorously followed the "universal" near-wall velocity profile.

The present experimental data base for riblets is insufficiently complete to distinguish unambiguously possible Reynolds number effects* but it may be noted that the recent study of Benhalilou et al. [7] which adopted large riblets to facilitate the measurement of velocity profiles near the surface (thus producing values of h/δ of order 0.1) show negligible levels of drag reduction.

The drag reduction behaviour for V-groove riblets is summarized in Fig. 3 which provides results where h/H has been fixed at 0.05 in all cases. This means that the bulk

*At low Reynolds number, there must in any event be some doubt as to how precisely fully-developed channel flow provides results analogous to those in a boundary layer because in the former case there will be a significant ($\sim 5\%$) drop in total shear stress in the immediate vicinity of the riblets; a more uniform near-wall shear stress will prevail in the boundary layer, however.

Reynolds number decreases as h^+ diminishes. Here a rather different picture emerges. The greatest drag reduction achieved was now only 10% for $S/h = 1.0$ (where $Re \approx 35\,000$) while for $S/h = 1.6$ and 2.0 the corresponding maximum drag reductions were approximately 5.5 and 4% respectively. These values are closely in line with the reported maximum reductions obtained from experiments on this family of riblets. For example, Sawyer and Winter [19] report 4% for $S/h = 2.1$ and 7% for $S/h = 2$. Admittedly, the values of h^+ at which the optimum drag occurs are still larger than in the experiments but not as seriously as with the idealized L-shaped riblets.

In view of the great difference between the predicted drag reductions obtained with L-profile and V-groove riblets, a limited exploration of the effect of finite riblet thickness was made. In fact, at the time the computations were made, the thinnest L-riblet for which measurements had been reported [4], had a thickness t that was 8% of h . Accordingly, a few runs were made with the same height to thickness ratio for $S/h = 1.0$, Fig. 4. One notices in fact a very marked deterioration of performance with the maximum drag reduction of 11% now being only slightly better than for the V-groove elements. In a forthcoming paper Bruse et al. [20] present experimental results that also show a systematic improvement in riblet performance as t/h is reduced, confirming the trend of our results. In their case a maximum drag reduction of about 8% was achieved with $t/h \approx 0.08$, while for $t/h = 0.02$ the peak reduction reached 10%.

While acknowledging that significant differences remained, the results presented so far suggested that the adopted two-equation model predicted broadly the correct trends so far as the attainable levels of drag reduction are concerned. It thus seemed instructive to employ the curvilinear code in a search for a more efficient riblet profile than offered by the conventional V-groove form. Figure 5 presents relative drag curves

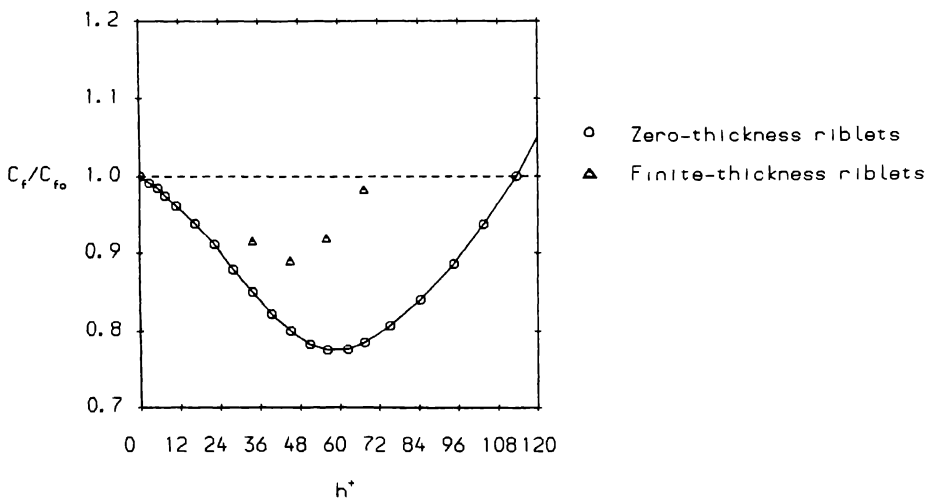


Fig. 4. Effect of finite riblet thickness on drag reduction of blade riblet, $S/h = 1$.

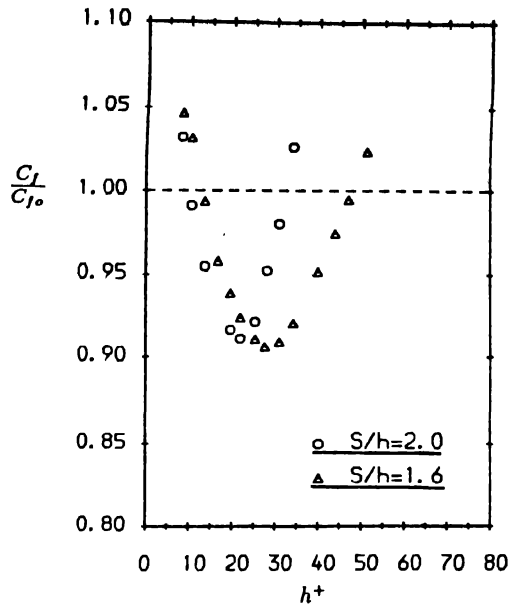


Fig. 5. Drag reduction behaviour for a new family of U-shaped riblets.

obtained for the family of U-shaped riblets shown in Fig. 1. A distinctly better performance is achieved in this case than for the V-groove riblets at S/h of 2.0 and 1.6.*

Figure 6 provides for $S/h = 1.6$ an indication of how the proportion of the total drag on the surface is distributed over the riblet surface for the three riblet profiles. The ordinate represents the fraction of the total drag due to the part of the surface between the trough plane of symmetry and the point in question. Evidently the shear stress is higher at the base of the riblet for the L-riblet than for the other two types since the integrated drag rises more steeply. Due to the very low shear stress levels in the corner, however, the curve for the L-riblet crosses those for the V- and U-riblets. It is striking how much of the drag is carried by the tip region: for L-riblets over 30% of the total drag arises from the 5% of the surface nearest the riblet tip. The frictional loading is distributed rather more evenly in the case of the V-riblet while the U-profile riblet exhibits a distribution intermediate between the other two forms.

Attention is now turned to some of the underlying flow detail giving rise to the behaviour reported in the above figures. Firstly, Fig. 7 presents the near-riblet velocity contours for representatives of the three families of riblets considered. In all cases very steep velocity gradients occur around the crest of the riblet; it is this feature which

*Unfortunately, the termination of the project, coupled with the increased difficulty of securing converged solutions as the width:height ratio decreases, have prevented our obtaining results for $S/h = 1.0$. Nevertheless, the riblet profile shown appears to be one worthy of further study.

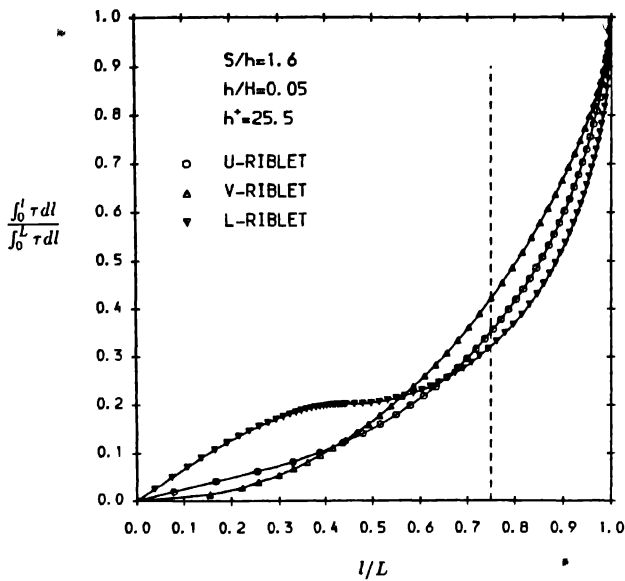


Fig. 6. Integrated contribution of riblet surface to total drag.

makes the performance of the L-profile riblet so sensitive to riblet thickness even though there is a negligible effect on the flow within the cavity itself. Note also that the 0.05 contour runs closer to the riblet surface for the V-groove than for either the U-form or L-profile riblets: this is why it achieves the poorest drag reduction

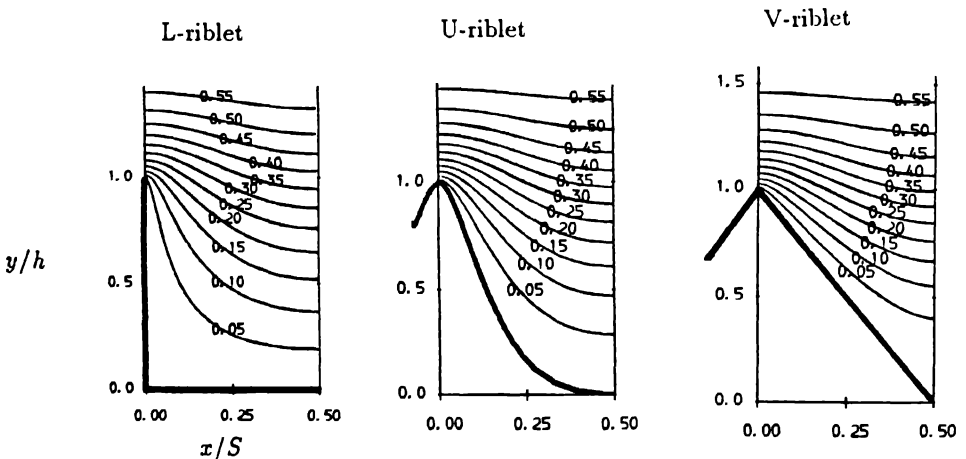


Fig. 7. Contours of streamwise velocity in the vicinity of riblets ($Re = 2 \times 10^4$, $S/h = 1.6$, $h/H = 0.05$, $h^+ \approx 25.5$).

performance of the three despite having the smallest surface area. The corresponding contours of turbulent viscosity appear in Fig. 8a. In all cases the riblets virtually annihilate turbulent mixing within the cavity itself but there are small differences between riblets in the rate at which ν_t increases above the riblet crest, the rate of increase being fastest for the V-groove and slowest for the idealized L-shaped riblets. From Fig. 8b it is seen that, along the trough plane of symmetry, reducing S/h to unity reduces the turbulent viscosity at a given height while enlarging it to 2.0 increases it. These differences in turbulent viscosity stem from modifications to the turbulent kinetic energy profiles near the wall. Figure 9 shows profiles of k^+ for V- and U-profile riblets for two S/h ratios. The predicted distribution arising in smooth channel flow at

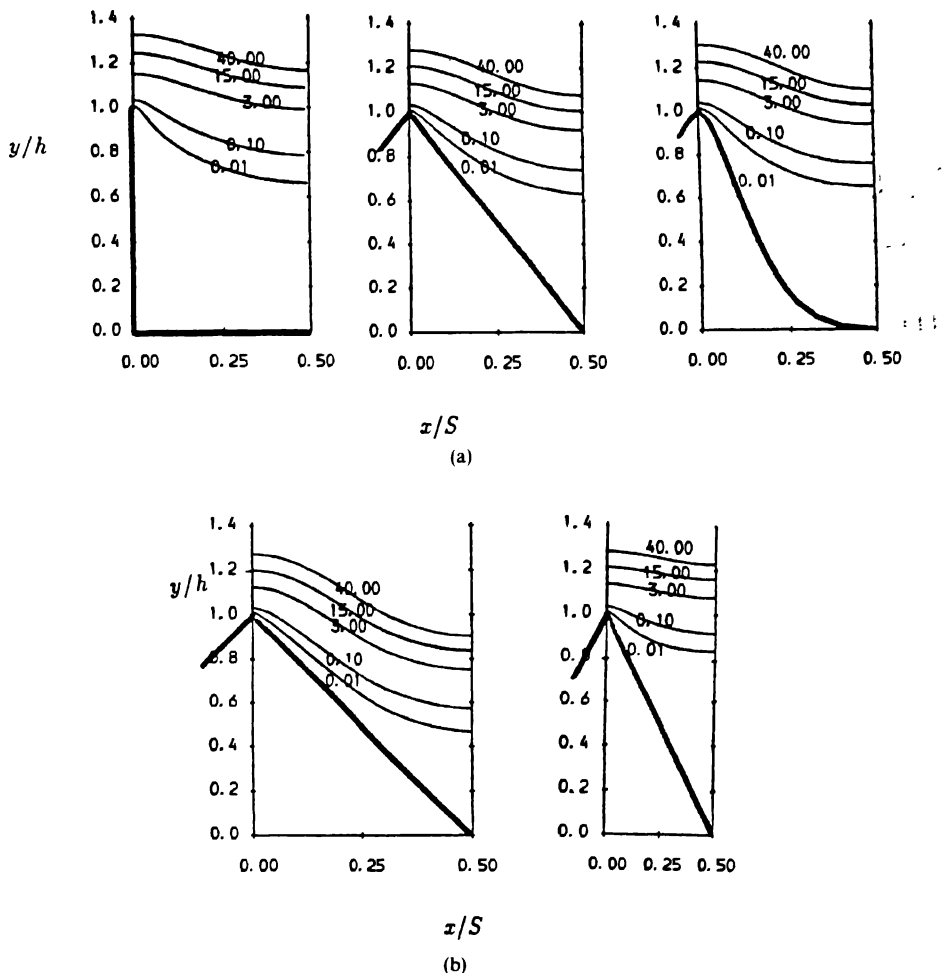


Fig. 8. Profiles of turbulent viscosity around riblets.

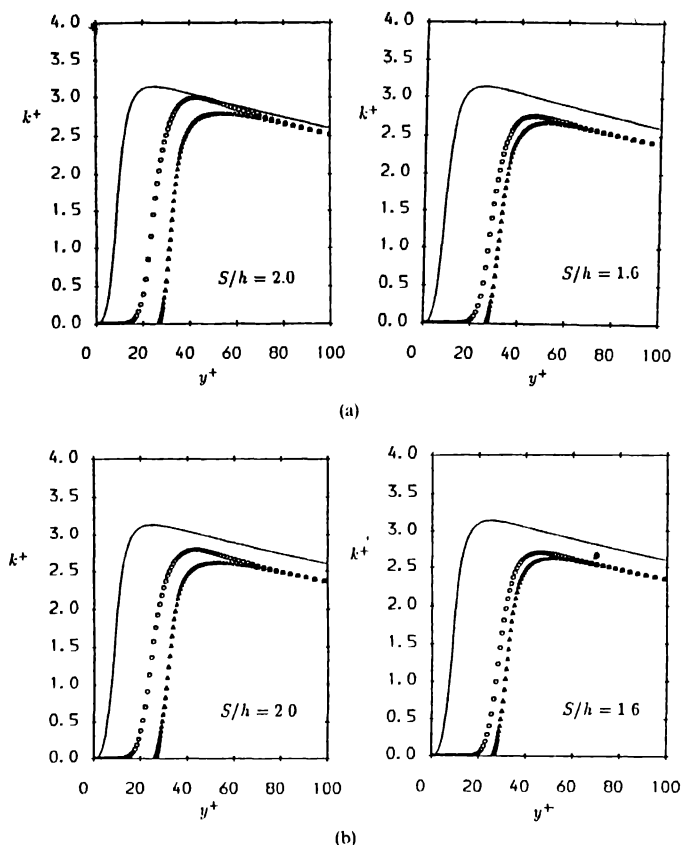


Fig. 9. Computed profiles of normalized turbulence energy, — smooth channel, ○ riblet trough; Δ riblet crest, (a) V-groove riblets; (b) U-shaped riblets.

the same Re with the same turbulence model is also included for reference (the coordinate y^+ has its origin in the trough of the riblet for both crest and trough profiles). For both riblets the steep rise in k^+ across the buffer layer is displaced to larger values of y^+ indicating the thickening of this viscosity affected sublayer. Moreover, the peak levels of k^+ are noticeably less than for a smooth surface, particularly so for the smaller S/h and the U riblets.

4. Discussion

The computed behaviour reported in Section 3 exhibits encouraging and discouraging features. Certainly the possibility of riblets achieving a drag reduction has emerged very clearly from the computations and the different levels of drag reduction achievable for different riblet configurations is broadly in line with the experiment.

However, as noted in [15], two different and counteracting weaknesses in the physical model are plainly present. At small riblet heights ($h^+ < 10$) the present model gives too little drag reduction while at larger values ($h^+ > 15$) the overall performance is greater than found experimentally at the same riblet heights. The former weakness may partly arise from the specific dependency of c_μ on Re_τ : a distribution of $c_\mu(Re_\tau)$ that gives the correct average level of turbulent viscosity across the buffer region on a strictly smooth surface may not do so when riblets intervene. An alternative source of discrepancy may be the $\tilde{\epsilon}$ equation. It seems plausible that flow inhomogeneities parallel to the (mean) rigid surface (in addition to inhomogeneities normal to the surface) should tend to raise ϵ , thus decreasing k and the turbulent viscosity. It is noted that through the final term in equation (3) inhomogeneities in the sublayer in x as well as y do tend to raise $\tilde{\epsilon}$. Perhaps some further source term, involving gradients in k and/or ϵ ought to be added to the right-hand side of the $\tilde{\epsilon}$ equation.

The most likely reason that our predictions show strong drag reductions to values of h^+ that are 2–3 times greater than reported in experiments is the absence of secondary flows from our calculations (an inevitable consequence of adopting an isotropic viscosity model). The remedy is to shift instead to a second moment closure. However, while second moment closures are now beginning to be used in engineering flows near walls (see the reviews of [22] and [23]), within the viscosity affected sublayer simpler schemes are invariably adopted, at least if the sublayer is three-dimensional. The use in the model of the unit vector normal to the wall or the distance from the wall make the available models unsuitable for strongly non-planar surfaces such as riblets. However, to go at least some way in the direction of the proposed model refinement for the case of the idealized blade riblet, a hybrid treatment has been adopted. Within the riblet cavity itself, the two-equation $k - \tilde{\epsilon}$ model adopted for the main body of our calculations has been retained. At a height of $1.2h$ from the floor, however, a switchover is made to a second-moment closure that has been very successfully applied to the prediction of secondary flow on rectangular ducts (the model is algebraically very complex and is not reproduced here; details are given in [8, 24]). For this computation, as noted at the end of Section 2, the full momentum equations are solved in all three Cartesian directions and, in the stress transport equations, the normal-to-the-wall direction is taken as y . Only within the region where the second-moment closure is adopted does the turbulence model provide a source of streamwise vorticity. For this reason, we may expect the adoption of the hybrid model to generate a smaller secondary flow than would arise if a second-moment closure could have been used throughout. We note from Fig. 10, however, that a distinct secondary eddy is nevertheless present, centred at about one third of the riblet height above the tip, which sweeps down high velocity fluid near the riblet with a more diffuse return flow mid-way between riblets. The secondary motion distorts the axial velocity contours in the sense expected and leads to an increase in momentum transport (and thus of total drag) of about 3%. As remarked above, we may expect that a full second-moment treatment would produce even larger momentum transport rates by the secondary motion.

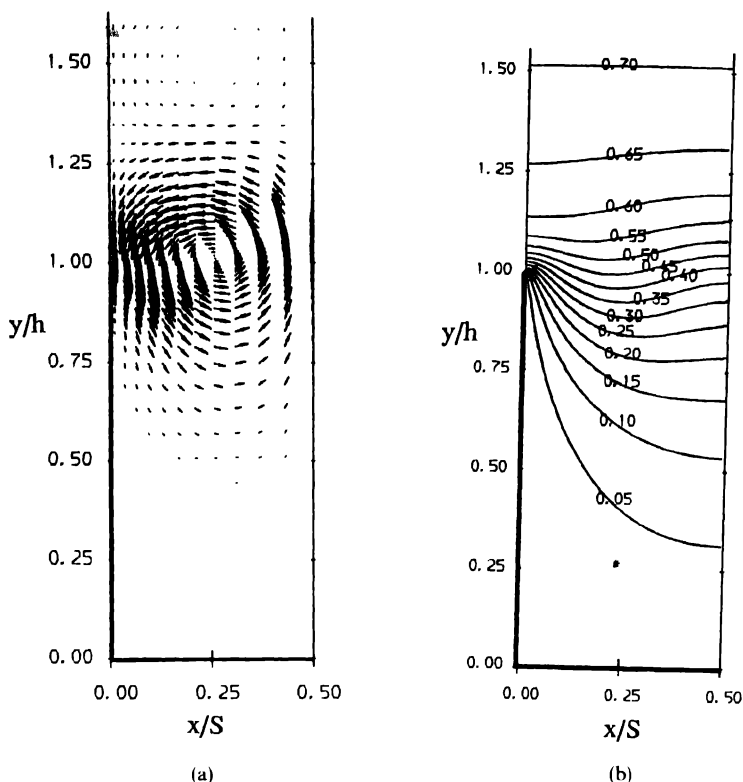


Fig. 10. Predicted flow pattern in L-shaped riblet for $S/h = 1.0$, $h/H = 0.06$ ($h^+ \approx 67$). (a) Secondary velocity vectors; (b) contours of W/W_{\max} .

5. Conclusions

1. A two-equation eddy viscosity model has been applied to predict the flow around L-shaped and V-grooved riblets. The predicted maximum levels of drag reduction, including the effect of height: pitch ratio and, in the case of L-shaped riblets, the riblet thickness, are reasonably in accord with measurements.
2. A substantial sensitivity to Re has emerged for channel flow Reynolds numbers below about 15 000 with the predicted benefits of riblets virtually disappearing below $Re = 10^4$.
3. Further explorations have been made of a family of U-shaped riblets which, according to our predictions, would give better performance than the usual V-grooved form.
4. While the optimum drag reduction levels predicted in our study are broadly correct, there are nevertheless two substantial shortcomings in the computations: below $h^+ \sim 10$ too little drag reduction is achieved while for $h^+ > 15$ too large

reductions are indicated. This contrasting behaviour springs from two counteracting weaknesses in the model: an insufficient sensitivity to x -direction inhomogeneity on the level of ε and the use of an isotropic viscosity formulation that suppresses secondary motion.

5. A limited exploration has been made for the case of an L-shaped riblet with $h/s = 1.0$ in which in the region above the riblets, a second-moment closure has been used in place of the eddy viscosity model. The use of this model produces a streamwise secondary vortex on either side of the riblet that sweeps high momentum fluid down near the riblet surface thus raising drag.

Acknowledgements

The research has been sponsored by the SERC under Grant GR/E 77039. S-P Li also acknowledges with thanks support from the British Council and the Northwestern Polytechnic University, Xian, PRC. During the research Dr A.M. Savill has made numerous appreciated technical inputs to the work programme. Mrs J. Buckley and Mrs D. Lindop have processed the manuscript for publication. Authors' names are sequenced alphabetically.

References

1. Walsh, M.J. and Weinstein, L.M., Drag and heat transfer characteristics of small, longitudinally ribbed surfaces. *AIAA J.* 17 (1979) 770.
2. Walsh, M.J., Turbulent boundary layer drag reduction using riblets. *AIAA Paper* 82-0169 (1982).
3. Wilkinson, S.P., Anders, J.B., Lazos, B.S. and Bushnell, D.M., Turbulent drag reduction research at NASA Langley: progress and plans. *Int. J. Heat Fluid Flow* 9 (1988) 286.
4. Wilkinson, S.P. and Lazos, B.S., Direct drag and hot-wire measurements on thin-element riblet arrays. IUTAM Symposium on Turbulence Management and Relaminarization, Bangalore (1987).
5. Walsh, M.J., Optimization and application of riblets for turbulent drag reduction. *AIAA Paper* 84-0347 (1984).
6. Khan, M.M.S., A numerical investigation of the drag reduction by riblet surfaces. *AIAA Paper* 86-1127 (1986).
7. Benhalilou, M., Anselmet, F., Liandrat, J. and Fulachier, L., Experiments and numerical investigation of a turbulent boundary layer over riblets. *Proc. 8th Symp. Turbulent Shear Flows*, Paper 18-5, Munich (1991).
8. Li, S.-P., PhD Thesis, Faculty of Technology, University of Manchester (1992).
9. Chien, K.-Y., Predictions of channel and boundary-layer flows with a low-Reynolds-number turbulence model. *AIAA Journal* 20 (1982) 33.
10. Lam, C.K.G. and Bremhorst, K.A., Modified form of the $k-\varepsilon$ model for predicting wall turbulence. *J. Fluids Engineering* 103 (1981) 456.
11. Jones, W.P. and Launder, B.E., The prediction of laminarization with a two-equation model of turbulence. *Int. J. Heat Mass Transfer* 15 (1972) 301.
12. Launder, B.E. and Sharma, B.I., Application of the energy-dissipation model of turbulence to the calculation of flow near a spinning disc. *Letters in Heat and Mass Transfer* 1 (1974) 131.
13. Patel, V.C., Rodi, W. and Scheuerer, G., *AIAA Journal* 23 (1985) 1320.
14. Savill, A.M., Turbulence model predictions for transition under free stream turbulence, Unpublished report, Engineering Department, University of Cambridge, 1991. (Also poster paper for Royal Aeronautical Society, Transition and Boundary Layer Conference, Cambridge, April 1991).

15. Launder, B.E. and Li, S.-P., The prediction of riblet behaviour with a low-Reynolds number $k-\epsilon$ model. *Aeronautical Journal* 96 (1992) 354–358.
16. Launder, B.E. and Ying, W.-M., Prediction of flow and heat transfer in ducts of square cross-section. *Proc. Institution of Mechanical Engineers* 187 455 (1973) 37/73.
17. Huang, P.G. and Leschziner, M.A., An introduction and guide to the computer code TEAM. UMIST Mech. Eng. Dept. Report TFD/83/9 (R) (1983).
18. Leschziner, M.A., Kadja, M. and Lea, C., A combined experimental and computational study of a separated flow in an expanding annular passage. In: Iwasa, Y., Tamai, N. and Wada, A. (eds), *Refined Flow Modelling and Turbulence Measurements*. Tokyo: Universal Academic Press (1988) p. 129.
19. Sawyer, W.G. and Winter, K.G., An investigation of the effect on turbulent skin friction of surfaces with streamwise grooves. *Proc. Symposium Turbulent Drag Reduction by Passive Means*. London: Royal Aeronautical Society (1987).
20. Bruse, D.W., Bechert, D.W., van der Hoeven, J.G.Th., Hage, W. and Hoppe, G., Experiments with conventional and with novel adjustable drag-reducing surfaces. In: So, R.M. et al. (eds), *Proc. Int. Symp. on Near Wall Turbulence*. Elsevier (1993) pp. 719–738.
21. Djenidi, L., Squire, L.C. and Savill, A.M., High-resolution conformal mesh computations for V-, U- or L-groove riblets in laminar and turbulent boundary layers. In: Choi, K.-S. (ed.), *Recent Developments in Turbulence Management*. Dordrecht: Kluwer Academic Publishers (1991) pp. 65–92.
22. Launder, B.E., Turbulence modelling for the nineties: second-moment closure... and beyond? In: Morton, K.W. (ed.), *12th International Conference on Numerical Methods in Fluid Dynamics*. Lecture Notes in Physics 371. Berlin: Springer Verlag (1990) pp. 1–18.
23. Leschziner, M.A., *Int. J. Heat Fluid Flow* 10 (1989) 186–202.
24. Launder, B.E. and Li, S.-P., Contribution to the modelling of turbulent flow in rectangular passages. Submitted for publication (1992).

Modelling the time dependent flow over riblets in the viscous wall region

S. TULLIS & A. POLLARD*

Department of Mechanical Engineering, Queen's University at Kingston, Ontario, K7L 3N6 Canada
(*author for correspondence)

Abstract. The flow over riblets is examined computationally using a time dependent model of the viscous wall region. This “2 1/2 D model”, developed by Hatzivramidis and Hanratty (1979) and modified by Nikolaides (1984) and Chapman and Kuhn (1981, 1986) assumes homogeneity in the streamwise direction so that the flow is solved only in the cross-sectional plane. The flow at the upper boundary of the computational domain ($y^+ \approx 40$) is described using a streamwise eddy model consisting of two scales, one of the streak spacing ($\lambda^+ \approx 100$), which dominates vertical momentum transport, and a larger scale that accounts for the influence of large outer flow eddies.

The protrusion height concept (Bechert and Bartenwerfer, 1989) is used to define a $y^+ = 0$ location for surfaces with riblets. A control volume finite element method utilizing triangular meshes is used to exactly fit the riblet cross-sectional geometry. Results obtained using fairly large riblets compare well with the limited experimental evidence available. Observations of the transient flow suggest that the riblets interact with the near-wall streamwise vortices, weakening them by the generation of intermittent secondary vortices within the riblet valleys. The riblets also appear to limit the lateral spread of intrushes towards the wall and retain low momentum fluid in the riblet valleys effectively isolating much of the wall from such intrushes.

1. Introduction

The ability of riblets to produce significant skin friction reductions in turbulent boundary layer flows is well established. Wilkinson et al. (1987), Walsh (1990) and Savill (1989) have suggested that the viscous effect of the riblets in accumulating slow flow with low shear stress in the riblet grooves plays a major role in the skin friction reduction. The effect of riblets, however, has been observed by Vukoslavčević et al. (1987) and Choi (1987, 1989) to extend well above the viscous wall region. This has led these authors to the conclusion that at least a portion of the drag reduction is a result of the influence of riblets on near-wall turbulent coherent structures.

In the very near-wall region ($y^+ \leq 30-40$), the dominant turbulent structures appear to be quasi-periodic streamwise eddies Bakewell and Lumley (1967), Townsend (1956). These eddies act as a mechanism for the transport of streamwise momentum to and away from the wall which then contribute to the high Reynolds stress and turbulence production close to the wall. The near-wall low-speed streaks, which have a characteristic spanwise “streak” spacing of $\lambda^+ \approx 100$, are generally accepted (Smith et al. 1989) to be the lift up of low momentum fluid from the wall by an adjacent streamwise eddy. The surface drag reduction effect of riblets then seems to

involve some sort of influence on these near-wall eddies. An increase in the streak spacing and decrease in spanwise motions over riblet surfaces has been noted experimentally by many researchers, including Gallagher and Thomas (1984), Bacher and Smith (1985) and Choi (1989). Both of these effects are similar to the drag reduction produced by dilute polymer solutions (Tiederman, 1989).

A number of models have been proposed which depict how, by interacting with the near-wall streamwise vortices, riblets may reduce the turbulent skin friction. Bacher and Smith (1985) have suggested that the generation of secondary vortices within the riblet valleys weakens these streamwise vortices. Flow visualization work by Clark (1989) appears to show such secondary groove vortices. The development of spanwise concentrations of low-speed fluid (streaks) is then inhibited, leading to streaks with larger spacings and weaker velocity gradients. Smith et al. (1989) proposed that riblets interfere with the lateral (spanwise) motion of low speed fluid (streaks) at the wall. Choi (1989) also suggested that the major effect of the riblets is to restrict the spanwise motion of the streamwise vortices and low speed streaks. The models seem to agree that the riblets probably interfere with both the intensities and the spanwise motions of the near-wall vortices.

Until very recently, the modelling of the flow over riblets has usually been performed with simple half or one riblet geometries and with either laminar flow or mixing-length Djenidi et al. (1990), Benhalilou et al. (1991) and, more recently, $k-\epsilon$ turbulence models, Djenidi (1991), Launder and Li (1991). These approaches have used Reynolds averaged and often parabolized equation sets to produce steady-state solutions. These methods do not consider multiple riblet interactions with any specific near-wall turbulent structures, particularly streamwise vortices, and depend critically on the near-wall damping assumptions.

The approach taken here is to use a "simple eddy" or "coherent structure" model to attempt to directly model quasi-periodic streamwise eddies in the very near-wall region. The model was originally developed, for flat wall turbulent boundary layers, by Hatziaivramidis and Hanratty (1979) and developed and refined by Chapman and Kuhn (1981, 1986) and Nikolaides (1984). The model is not intended to exactly predict the flow; it is a representation of near-wall streamwise eddies and their time development—although the models do provide good agreement with experimentally measured mean velocity, Reynolds stress and turbulence intensity profiles for flat walls.

2. Turbulent boundary layer modelling

2.1. Governing equations

The model of the turbulent boundary layer is time dependent with the coordinates oriented such that the downstream direction is along the x axis, the y direction is

perpendicular to the wall and the z axis is across the flow in the spanwise direction. With the streamwise eddies being highly elongated (Kline et al. (1967), Robinson et al. (1989), a major assumption is made that the streamwise velocity derivatives can be neglected in comparison to the cross-stream velocity derivatives. The governing equations are then

$$\frac{\partial v^+}{\partial t^+} + \frac{\partial v^{+2}}{\partial y^+} + \frac{\partial w^+ v^+}{\partial z^+} = -\frac{\partial p^+}{\partial y^+} + \frac{\partial^2 v^+}{\partial y^{+2}} + \frac{\partial^2 v^+}{\partial z^{+2}}, \quad (1)$$

$$\frac{\partial w^+}{\partial t^+} + \frac{\partial v^+ w^+}{\partial y^+} + \frac{\partial w^{+2}}{\partial z^+} = -\frac{\partial p^+}{\partial z^+} + \frac{\partial^2 w^+}{\partial y^{+2}} + \frac{\partial^2 w^+}{\partial z^{+2}} \quad (2)$$

$$\frac{\partial v^+}{\partial y^+} + \frac{\partial w^+}{\partial z^+} = 0 \quad (3)$$

and,

$$\frac{\partial U^+}{\partial t^+} + \frac{\partial v^+ U^+}{\partial y^+} + \frac{\partial w^+ U^+}{\partial z^+} = \frac{\partial^2 U^+}{\partial y^{+2}} + \frac{\partial^2 U^+}{\partial z^{+2}} \quad (4)$$

All of the quantities in Eqs 1–4 are normalized by the friction velocity, u_τ , with $u_\tau = \sqrt{\tau_w/\rho}$, where τ_w is the flat wall shear stress. Lengths are non-dimensionalized as

$$x^+ = \frac{u_\tau}{\nu} x \quad y^+ = \frac{y}{\nu} \quad z^+ = \frac{u_\tau}{\nu} z,$$

where $\nu = \mu/\rho$ is the kinematic viscosity. The velocity components, pressure and time can all be non-dimensionalized as:

$$U^+ = \frac{U}{u_\tau} \quad v^+ = \frac{v}{u_\tau} \quad w^+ = \frac{w}{u_\tau}$$

$$p^+ = \frac{p}{\tau_w} = \frac{p}{\rho u_\tau^2} \quad t^+ = \frac{u_\tau^2}{\nu} t.$$

Wall normalized units will be used for the remainder of this paper, so the superscript “+” will be dropped.

It can be noted that the cross-stream velocities v and w and the down-stream velocity U are not coupled – the cross-stream velocities can be solved using Eqs 1–3, then U can be solved directly using Eq. 4. There is also no downstream pressure gradient.

2.2. Boundary conditions

The computational domain consists of a cross-sectional $y-z$ plane with $0 \leq y \leq y_0$ where y_0 is typically 40. The spanwise size of the domain depends on the particular variation of the model but is usually in the range of 100–400 wall units.

The main modelling assumption of the method is in the specification of the velocities at the upper edge, $y_0 \approx 40$, of the domain. These specifications can vary depending on the specific model; however, in all of the models, the velocity components specified at the upper boundary are periodic in time and spanwise location (z) and have overall magnitudes of the experimentally determined turbulence intensities at that distance from the wall. The downstream velocity U is specified to consist of two components: a fluctuating component u and a constant component \bar{U} which is determined, for flat walls, from experimental measurement or from the log-law relationship.

The fluctuating velocity components usually have two scales: one that dominates vertical momentum transport and roughly the size of the streak spacing and a larger scale accounting for the influence of all large “outer flow eddies”. The full form as given by Nikolaides (1984) is:

$$U = \bar{U} + \hat{u}_1 \cos\left(\frac{2\pi}{T_1} t + \phi_{u1}\right) \cos\frac{2\pi}{\lambda_1} z + \hat{u}_2 \cos\left(\frac{2\pi}{T_2} t + \phi_{u2}\right) \cos\frac{2\pi}{\lambda_2} z, \quad (5)$$

$$v = \hat{v}_1 \cos\left(\frac{2\pi}{T_1} t + \phi_{v1}\right) \cos\frac{2\pi}{\lambda_1} z + \hat{v}_2 \cos\left(\frac{2\pi}{T_2} t + \phi_{v2}\right) \cos\frac{2\pi}{\lambda_2} z, \quad (6)$$

$$w = \hat{w}_1 \cos\left(\frac{2\pi}{T_1} t + \phi_{w1}\right) \sin\frac{2\pi}{\lambda_1} z + \hat{w}_2 \cos\left(\frac{2\pi}{T_2} t + \phi_{w2}\right) \sin\frac{2\pi}{\lambda_2} z. \quad (7)$$

The periods in the spanwise direction, λ_1 and λ_2 , are typically set respectively as 100, the size of the flat wall streak spacing, and 400 or infinity as a larger period accounting for the influence of all larger scale eddies. The time periods T_1 and T_2 are usually set to roughly the same values as λ_1 and λ_2 to agree with bursting frequencies for it is reasoned that the larger scale transient and convective terms should be of the same order, Nikolaides (1984). Another important set of parameters are the amplitudes of fluctuations at the different scales, which are related to the energy fractions of the velocity components in each of the scales. These are selected using mainly experimental data. The phase angles (ϕ 's) between the various periodic terms are generally selected based on the experimental measurements of the average size of the near-wall eddies and the use of computer optimization. The model and the values of the constants used in this study are from Chapman and Kuhn (1986). The parameters used are summarized in Table 1.

This model consists of Nikolaides' (1984) model with modifications which, for the

Table 1. Parameters used in Chapman and Kuhn's (1986) model

λ_1	100	$\lambda_2(u, v, w)$	$\infty, -, \infty$
T_1	143	$T_2(u, v, w)$	143, -, 286
u_1	1.8	u_2	2.53
v_1	1.0	v_2	0
w_1	2.0	w_2	1 175
ϕ_{u1}	0 (reference)	ϕ_{u2}	0
ϕ_{v1}	0	ϕ_{v2}	-
ϕ_{w1}	$\pm \frac{\pi}{2}$	ϕ_{w2}	$\frac{2\pi}{3}$

most part, are simplifications that eliminate some of the seemingly arbitrarily selected terms while retaining good agreement with experimental data.

The sides of the computational domain (at $z=0$ and $z=z_0$) are treated with cyclic boundary conditions. The wall surface is specified using the no-slip condition: $U = v = w = 0$. The specification of the upper $y_0 = 40$ conditions requires a definition of the location of the $y = 0$ surface. This surface location is simply the wall surface; however, for riblet walls, the issue is not so straightforward. Ignoring the fluctuating components from this viscous wall layer model (Eqs 1–4), there remains:

$$\frac{\partial^2 U}{\partial y^2} + \frac{\partial^2 U}{\partial z^2} = 0. \quad (8)$$

Using conformal mapping for various riblet geometries, Bechert and Bartenwerfer (1989) calculated a protrusion height of the riblet peaks above an effective origin of the U velocity profile, thereby providing a definition of the $y = 0$ location for a riblet surface.

2.3. Numerical scheme

The numerical solution procedure used in this study is a Control Volume Finite Element Method (CVFEM) based on the work of Saabas (1991). The approach is an equal order co-located control volume method and is a development of earlier work by Baliga and Patankar (1979), (1983) and Prakash and Patankar (1985). The computational domain is divided into three-node triangular elements that are able to fit exactly such complex geometries as riblets in cross-section. Control volumes are constructed about each node with the complete discretization equations assembled for each control volume on an element-by-element basis. Exponential flow-oriented interpolation functions are used within each element to evaluate the velocity components, which correctly simulate the nature of convection, resulting in a substantial reduction of false diffusion, Baliga (1979). A time-stepping procedure was incorporated into the CVFEM using an implicit scheme, see, for example, Patankar

(1980). A structured grid is used with the triangular elements constructed by connecting the diagonals of a rectangular grid. This allows the use of line-by-line solvers. Space precludes the presentation of more detail.

3. Presentation and discussion of results

Three different cases are considered: flow over a flat wall and flow over both V-groove and U-groove riblet walls. The V-groove and U-groove riblets have dimensions of $h^+ = 16.7$ and $s = 2h$; thus, the computational domain consists of three complete riblets. Riblets with such dimensions neither reduce nor increase drag, Walsh (1990). However, these riblets correspond well with the experimentally investigated cases of Vukoslavčević et al. (1987) and Benhalilou et al. (1991).

For the flat wall case, a uniform 21×43 (y and z directions) grid is used. For the V-groove and U-groove riblet cases, the number of grid points in the spanwise (z) direction is the same as the flat wall case while additional grid points are used in the y direction – principally to account for the increased domain size resulting from the area between the base of riblet valleys and the protrusion height origin. Since the shape of the riblets depends on the grid spacing, a non-uniform grid is used to produce the semi-circular U-groove riblets. Typically, the grid spacing in the vicinity of the riblet peaks is $\Delta x^+ \simeq \Delta y^+ \simeq 2$, see Tullis (1992).

The solutions consist of approximately 500 time steps with a time step size of $\Delta t^+ = 2$. This time step size was selected from a comparison of flat wall solutions run with the particular spatial grid sizes and various time step sizes. The initial solution within the computational domain at $t = 0$ is the solution to Eq. (4) for the downstream velocity with no cross-stream velocities ($v = w = 0$). The effects of using this simple initial solution are not significant after two of the larger scale time periods (T_2). All space-time averaged quantities are calculated starting well after this initial interval and for over at least two of the larger scale time periods.

3.1. Mean velocity profiles

The model was tested against data obtained on a flat wall turbulent boundary layer; the data of Laufer (1954) and Ueda and Hinze (1975) were used. The comparison is shown in Fig. 1. The agreement is deemed acceptable. There is, however, a noticeable discrepancy near the outer edge of the domain. This effect can be also noticed in many of the other computational results, particularly the turbulent statistics. This irregularity has been observed by Chapman and Kuhn (1986) and Nikolaides (1984) who have suggested that it is the result of too restrictive boundary conditions, probably on the smaller scale eddies, and both consider that this effect is limited to the outer 10–20% of the domain.

The calculated mean streamwise velocity profiles over the V-groove riblets seem to

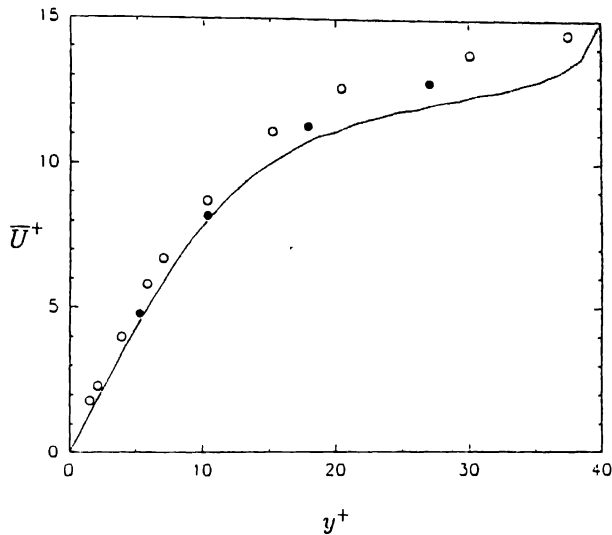


Fig. 1. Mean streamwise velocity (\bar{U}) profiles over a flat wall. Solid line. viscous wall region model. (●): data of Laufer, 1954. (○): data of Ueda and Hinze, 1975

agree well with the experimental measurements of Vukoslavčević et al. (1987), as shown in Fig. 2. The velocity gradient distribution at the riblet surface shows the same features observed by Vukoslavčević et al.

As depicted in Fig. 3a, the wall shear stress drops nearly to zero in the angled valleys of the V-groove riblets. Note that s^+ represents distance along the riblet surface. The

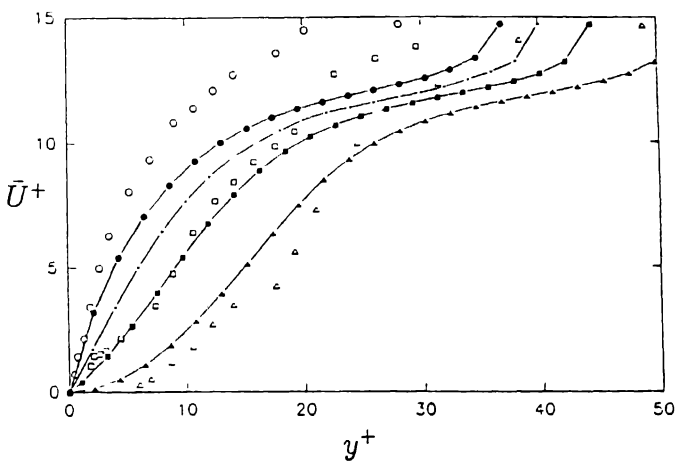


Fig. 2. Mean streamwise velocity profiles over V-groove riblets. Comparison of the calculations (●, ■, ▲) and experimental results (○, □, △) from Vukoslavčević et al. (1987) for the riblet peaks, mid-point between peaks and valleys, and valleys respectively. The calculated flat wall velocity profile is also shown (+).

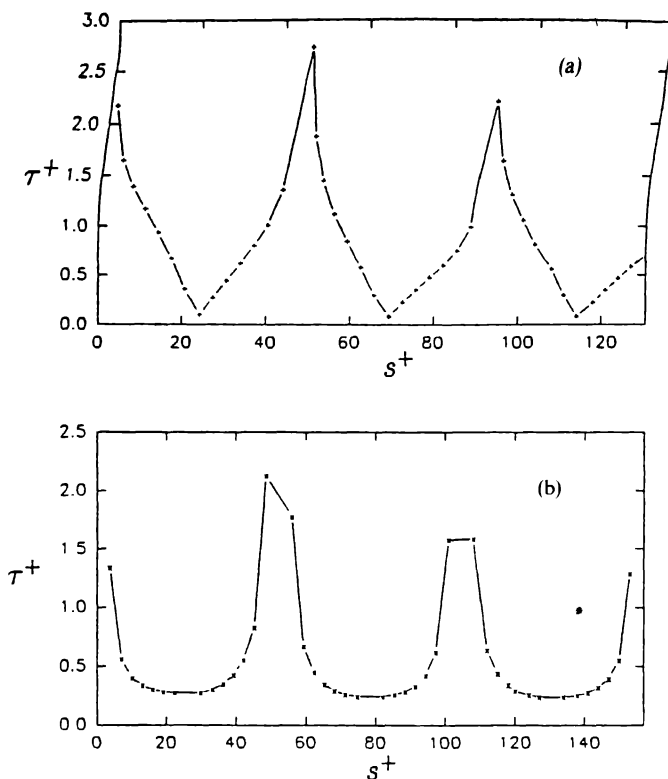


Fig. 3. Calculated dimensionless shear stress ($\tau^+ = \tau/\tau_w$) spanwise distributions for: (a) V-groove riblet wall and (b) U-groove riblet wall. s^+ is distance along riblet wall surface.

wall shear stress over the riblet peaks is much larger than that found over the flat wall – the increase is approximately 150%. This increase is larger than that noted by both Vukoslavčević et al. and Benhalilou et al. (1991) but may be exaggerated by the relatively coarse grid that is being used in the present calculations. A similar surface drag distribution is observed over the U-groove riblets (Fig. 3b). The wall shear stress in the rounded riblet valleys drops to about 25% of the flat wall case while the increase above the riblet peaks is approximately the same size as that found for the V-groove riblets.

3.2. Streamwise turbulence intensity

The calculated turbulence intensities over a flat wall show fairly good agreement with experimental data, not shown for brevity, as was demonstrated by Chapman and Kuhn (1986). Experimental measurements of turbulence intensities within and above riblets are very limited. Vukoslavčević et al. have measured streamwise velocity

fluctuation intensity (u') profiles while Benhalilou et al. were also able to obtain spanwise velocity fluctuation intensity (w') profiles with similarly large-sized V-groove riblets. Consequently, attention will be focussed on the streamwise turbulence intensity profiles. It should be noted that the two sets of experimental data have significant differences. With increasing distance from the wall, Benhalilou et al. observed the u' intensity to increase rapidly over the riblet peaks followed by nearly as rapid decrease, as can be seen in Fig. 4. The intensity over the riblet valley reaches a much lower maximum value and the peak and valley intensities are converging to a flat wall value of approximately 1.5, significantly lower than most other flat wall experimental values such as those of Clark (1968) and Ueda and Hinze (1975), at a height of $y^+ = 35$. Vukoslavčević et al., in contrast, observe very little decrease in the u' intensity profiles after they reach their maxima—with the peak and valley profiles converging at a higher than flat wall value of $u'^+ \sim 2.4$. The calculated u' intensity profiles resemble those of Vukoslavčević et al. close to the wall, although the profiles in the valley appear to reach slightly larger values closer to the wall. In the upper half of the calculation domain, however, the peak and valley profiles converge while steadily decreasing to a value of approximately 1.8 at the outer edge of the domain. In this respect, the calculated results are roughly between the two sets of experimental data.

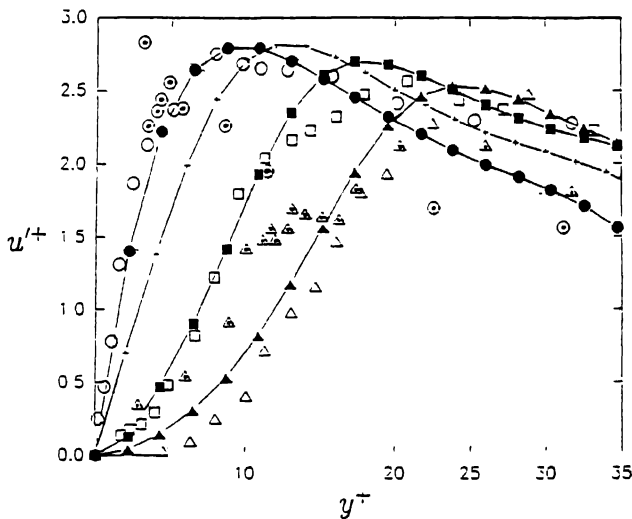


Fig. 4. Streamwise turbulence intensity profiles over V-groove riblets. Comparison of the calculations (\bullet , \blacksquare , \blacktriangle) and experimental results from Vukoslavčević et al. (\circ , \square , \triangle) and Benhalilou et al. (\odot , Δ) for the riblet peaks, mid-point between peaks and valleys, and valleys respectively. Data from Benhalilou et al. do not include results for the profile above the mid-point between peaks and valleys.

3.3. General observations

The 2 1/2 D model of the viscous wall region is probably more useful for depicting the time dependent interaction of near-wall streamwise vortices with riblets than in providing statistics that can be compared against experimental measurements. Figure 5 shows various individual time frames that show some of these interactions. These figures display the cross-stream velocity vectors at various t^+ , and the colours represent either downstream momentum or pressure, as indicated.

It is difficult to convey the dynamics of the vortex evolution using static pictures. A brief description is provided of the vortices and how they interact with the riblets; it is hoped that the dynamics of the motion, captured on video, can be appreciated by the reader. As the transient vortices develop close to the wall, intermittent, rapidly decaying secondary flows can easily be observed within the riblet valleys. These are even more apparent in the valleys of U-groove riblets. This is essentially the same phenomenon that Bacher and Smith (1985) suggested as a mechanism in the weakening of the original primary vortices; however, the computationally observed vortices are generated and driven by the periodic outer edge conditions, so the strength of these primary vortices would not be expected to be changed by the riblets. This observation appears to be confirmed by the recent experimental data of Tardu (1991) and Tardu, Truong and Tanguay (1992).

The other significant effect that can be observed is the influence of riblets on the inflows toward the wall that occur beside and between vortices. These inflows carry high streamwise momentum fluid towards the wall and, when reaching a flat wall, spread laterally. This covers an extended area of the surface with a high streamwise velocity gradient and, consequently, a high wall shear stress. The riblets appear to impede this lateral motion of the inrush at the wall. The size of the region with high wall shear stress is then decreased. With the relatively large riblets being used ($h^+ = 16.7$, $s^+ = 33.3$), this area is often confined to a single riblet. The impact of an inflow is most noticeable as an increase in the pressure at the wall (see U-groove riblet pressure contours, last frame of Fig. 5) and is often present only in the riblet immediately below the inflow. Even within riblets directly beneath such inrushes, the riblet valleys retain most of their low momentum fluid. The main increase in wall shear stress appears to occur, for the most part, on the riblet peaks. So, not only is this inflow confined in the spanwise direction, it is also effectively unable to influence large areas of the surface within the riblet valleys.

4. Conclusion and recommendations for future work

A 2 1/2 D model of the viscous wall region has been used to investigate the flow over surfaces with both V-groove and U-groove riblets. The streamwise mean velocity profiles were found to agree with the experimental results of Vukoslavčević et al.

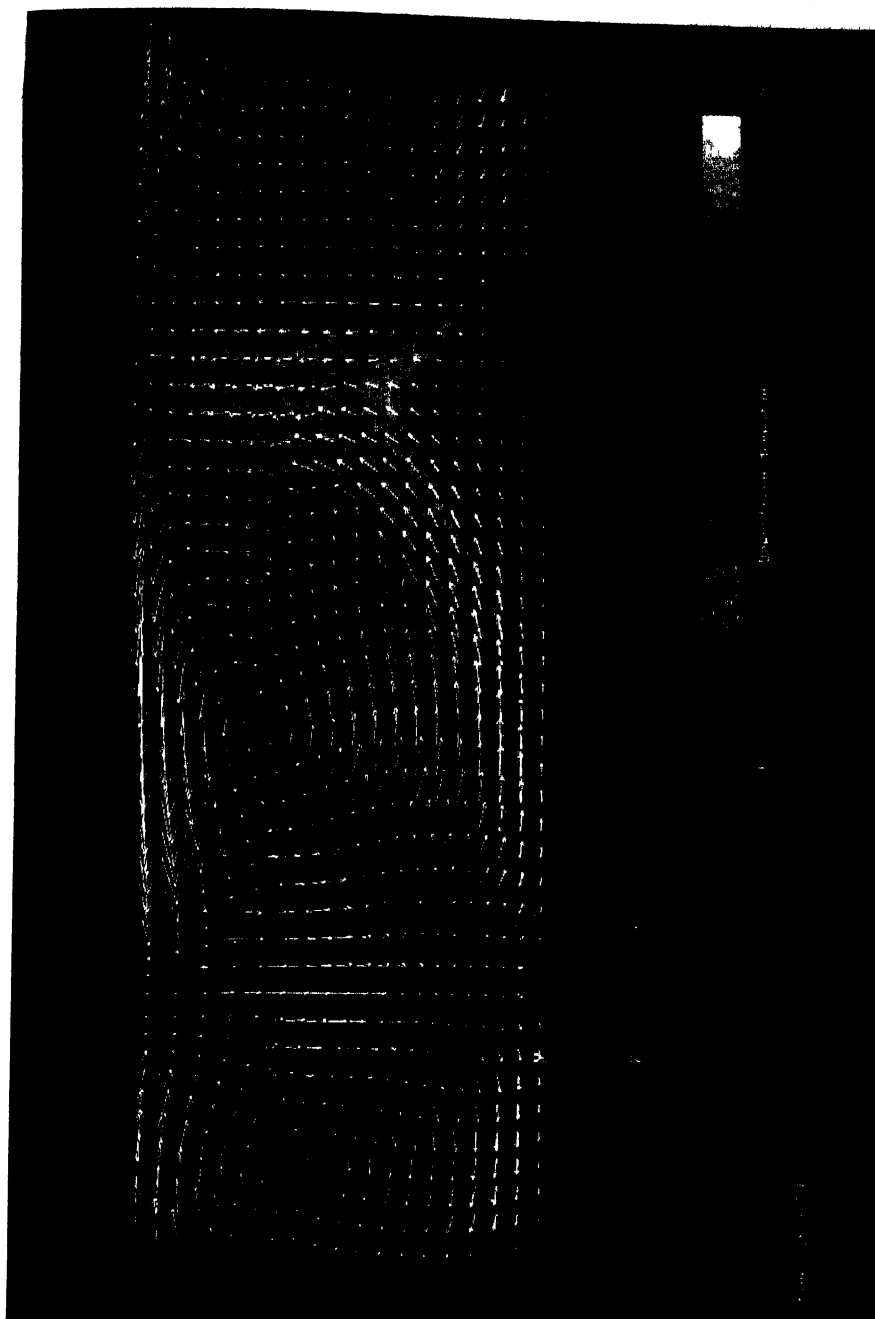
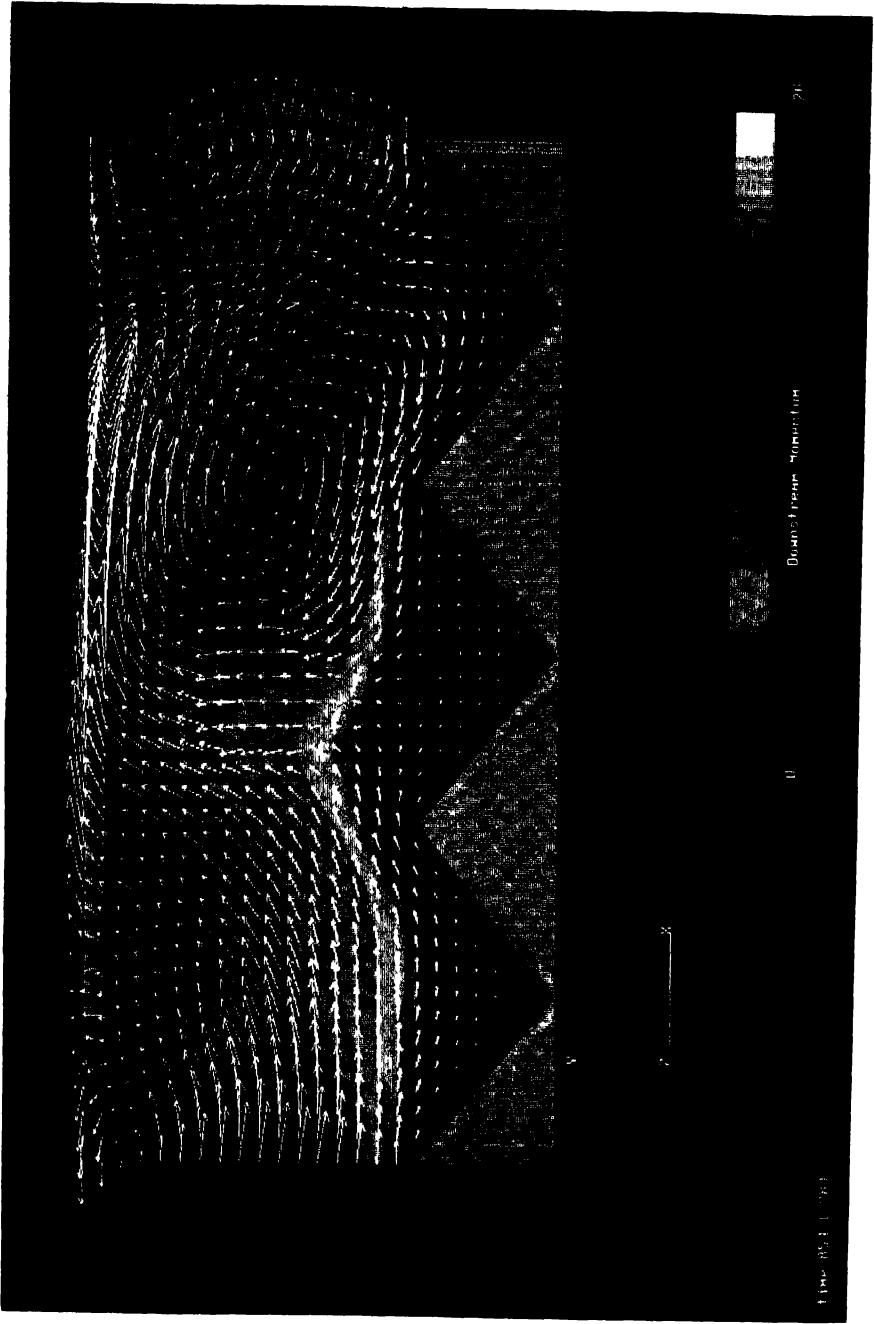


Fig. 5. For legend see p 311



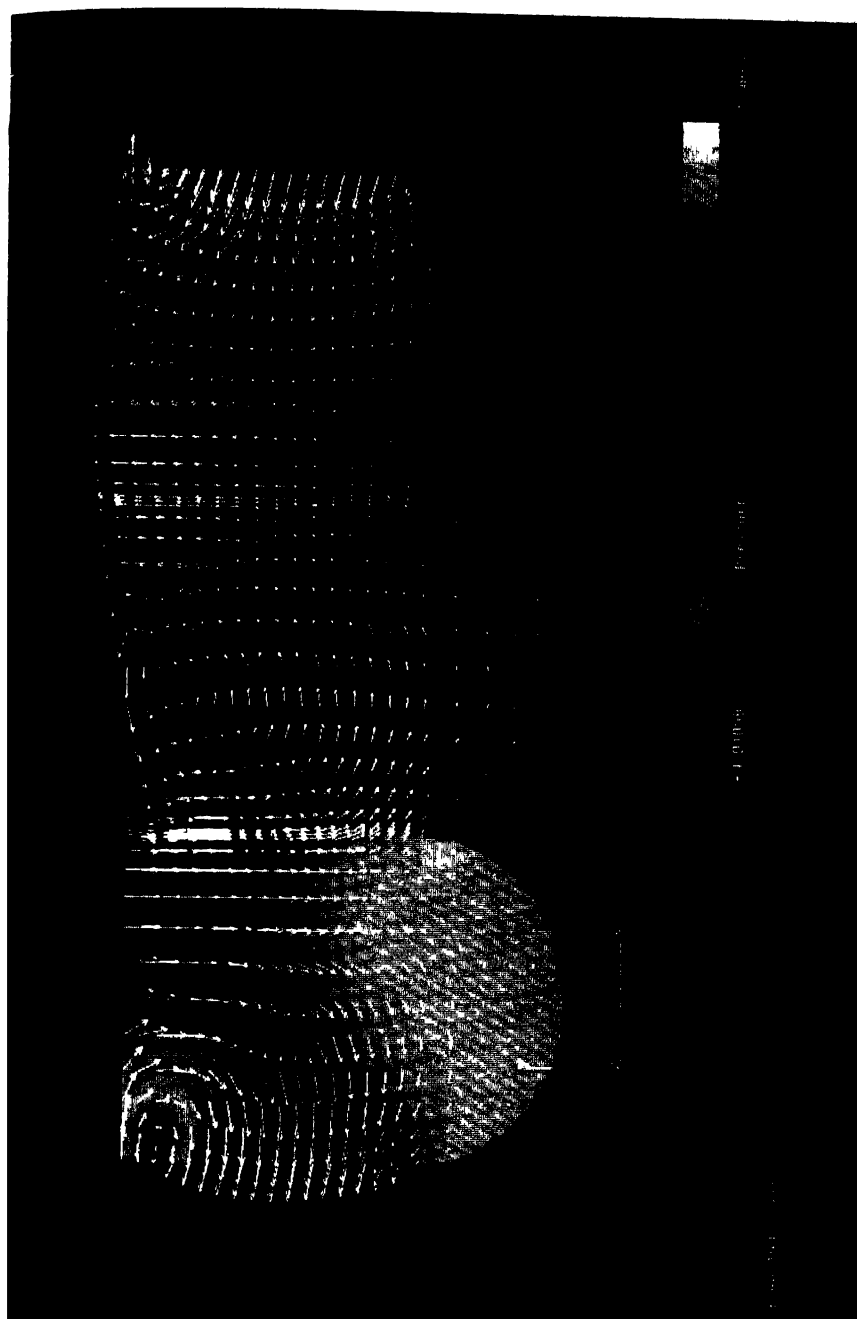


Fig. 5 Calculated flow over plain wall, V-groove and U-groove riblet wall. Vectors are cross-stream vectors, colours represent contours of down-stream or axial momentum or static pressure, as noted. Note the time marks 926, 854 and 194 represent t^* values.

(1987), showing increases in the mean velocity gradient over the riblet peaks together with large decreases in the riblet valleys. The calculations of the streamwise velocity fluctuation intensities show a comfortable degree of agreement with the limited experimental data available. Visual observations of the transient flows suggest that the riblets interact with the near-wall streamwise vortices weakening them by the generation of transient secondary vortices in the riblet valleys in a manner similar to that proposed by Bacher and Smith (1985). The riblets also appear to limit the lateral spread of intrushes towards the walls and retain low momentum fluid in the riblet valleys effectively isolating much of the wall surface from such intrushes.

The riblets used in this study are not small enough to be drag reducing but were chosen to be approximately the same size as the riblets used in detailed experimental studies. A repetition of this study with smaller, drag-reducing riblets would be beneficial. The increased number of riblets in the domain would also provide better statistics for the various profiles. Comparisons with the very recent direct numerical simulation of the flow in a channel with riblets by Chu (1992) would then be possible. (Note added in proof: these calculations have been completed, see Tullis and Pollard, 1993.)

5. Acknowledgements

The authors would like to extend their sincerest appreciation to Dr. A.M. Savill for the presentation of this work at the 6th European Drag Reduction Meeting, Eindhoven, November, 1991 and for his continued interest and encouragement in this work.

The financial support of the Natural Science and Engineering Research Council of Canada is gratefully acknowledged.

References

- Bacher, E.V., Smith, C.R., A combined visualization-anemometry study of the turbulent drag reducing mechanisms of triangular micro-groove surface modifications. AIAA Paper 85-0548 (1985).
- Bakewell, H.P., Lumley, J.L., Viscous sublayer and adjacent wall region in turbulent pipe flow. *Physics Fluids* 10 (1967) 1880.
- Baliga, B.R., A control-volume based finite element method for convective heat and mass transfer. Ph.D. Thesis, Dept. of Mech. Eng., University of Minnesota (1978).
- Baliga, B.R., Patankar, S.V., A control volume based finite element method for two-dimensional fluid flow and heat transfer. *Numerical Heat Transfer* (1983) 245-261.
- Bechert, D.W., Bartenwerfer, M., The viscous flow on surfaces with longitudinal ribs. *J. Fluid Mech.* 206 (1989) 105-129.
- Benhalilou, M., Anselmet, F., Liandrat, J., Fulachier, L., Experimental and numerical investigation of a turbulent boundary layer over riblets. *Proc. of the 8th Symp. on Turb. Shear Flows*, Munich, Sept. 9-11, 1991.

- Chapman, D.R., Kuhn, G.D., Two-component Navier-Stokes computational model of viscous sublayer turbulence. AIAA Paper 81-1024 (1981).
- Chapman, D.R., Kuhn, G.D., The limiting behavior of turbulence near a wall. *J. Fluid Mech.* 170 (1986) 265-292.
- Choi, K., The wall pressure fluctuations of modified turbulent boundary layer with riblets. *Proc. IUTAM Symp. on Turbulent Management and Relaminarization*, Bangalore. Springer-Verlag (1987) p. 109.
- Choi, K., Near-wall structure of a turbulent boundary layer with riblets. *J. Fluid Mech.* 208 (1989) 417-458.
- Chu, D.C., A direct numerical simulation of laminar and turbulent flow over streamwise aligned riblets. M.Sc. Thesis, Dept. of Mech. and Aerospace Eng., Princeton University (1992).
- Clark, D.G., Boundary layer flow visualization patterns on a riblet surface. QMC-EP-1081 Queen Mary and Westfield College, University of London (1989).
- Clark, J.A., A study of turbulent boundary layers in channel flow. *Trans. ASME, J. Basic Engng.* 90 (1968) 455-465.
- Djenidi, L., Squire, L.C., Savill, A.M., High resolution conformal mesh computations for V, U or L groove riblets in laminar and turbulent boundary layers. In: Choi (ed.), *Proceedings, 5th European Drag Reduction Working Meeting*, British Maritime Technology, Teddington, Middlesex. Dordrecht: Kluwer Academic Publishers (1991).
- Djenidi, L., Riblet flow prediction with a low-Reynolds-number $k-\epsilon$ model. 6th European Drag Reduction Working Meeting, abstract (1991).
- Gallager, J.A., Thomas, A.S.W., Turbulent boundary layer characteristics over streamwise grooves. AIAA paper 84-2185 (1984).
- Hatziaivramidis, D.T., Hanratty, T.J., The representation of the viscous wall region by a regular eddy pattern. *J. Fluid Mech.* 95 (1979) 655-679.
- Kline, S.J., Reynolds, W.C., Schraub, F.A., Runstadler, P.W., The structure of turbulent boundary layers. *J. Fluid Mech.* 30 (1967) 283-325.
- Laufer, J., The structure of turbulence in fully developed pipe flow, NACA Report 1174 (1954).
- Launder, B.E., Li, S.-P., Prediction of drag reduction by riblets. 6th European Drag Reduction Working Meeting, abstract (1991).
- Nikolaides, C., A study of the coherent structures in the viscous wall region of a turbulent flow. Ph.D. Thesis, Dept. of Chem. Eng., University of Illinois, Urbana (1984).
- Patankar, S.V., *Numerical Heat Transfer and Fluid Flow*. Hemisphere Publishing Co. (1980).
- Prakash, C., Patankar, S.V., A control volume based finite element method for solving the Navier-Stokes equations using equal-order velocity-pressure interpolation. *Numerical Heat Transfer* 8 (1985) 259-280.
- Robinson, S.K., Kline, S.J., Spalart, P.R., Quasi-coherent structures in the turbulent boundary layer: Part II. Verification and new information from a numerically simulated flat-plate boundary layer. In: Afgan and Kline (eds), *Zoran Zaric Memorial Seminar on Near-Wall Turbulence*. Hemisphere Publishing (1988).
- Saabas, H.J., A control volume based finite element method for three-dimensional, incompressible, viscous fluid flow. Ph.D. Thesis, Dept. of Mech. Eng., McGill University (1991).
- Savill, A.M., Drag reduction by passive devices - a review of some recent developments. *Proc. IUTAM Symp. on Structure of Turbulent and Drag Reduction*. Zurich, Springer-Verlag (1989) pp. 429-465.
- Smith, C.R., Walker, J.D.A., Haidari, A.H., Taylor, B.K., Hairpin vortices in turbulent boundary layers: the implications for reducing surface drag. *Proc. IUTAM Symp. on Structure of Turbulent and Drag Reduction*. Zurich, Springer-Verlag (1989) pp. 51-58.
- Tardu, S., Investigation of the structure of the turbulence in an internal flow manipulated by riblets. Report IMHEF T-91-19, Sept. 1991, EPFL, Lausanne, Switzerland.
- Tardu, S., Truong, T.V., Tanguay, B., Bursting and structure of the turbulence in an internal flow manipulated by riblets. *Appl. Sci. Res.* (1993).
- Tiederman, W.G., The effect of dilute polymer solutions on the viscous drag and turbulence structure. *Proc. IUTAM Symp. on Structure of Turbulent and Drag Reduction*, Zurich, Springer-Verlag (1989) pp. 187-200.
- Townsend, A.A., *The Structure of Turbulent Shear Flow*, 2nd edition. Cambridge University Press (1976).
- Tullis, S.W.J., Modelling the time dependent flow over riblets in the near wall region, M.Sc. Thesis, Department of Mechanical Engineering, Queen's University at Kingston (1992).

- Tullis, S., Pollard, A., A numerical investigation of the turbulent flow over V and U groove riblets using a viscous wall region model. In: So, Speziale, Launder (eds), *Proceedings, Near Wall Turbulent Flows*. Elsevier (1993) pp. 761–770.
- Ueda, H., Hinze, J.O., Fine-structure turbulence in the wall region of a turbulent boundary layer. *J. Fluid Mech.* 67 (1975) 125–143.
- Vukoslavčević, P., Wallace, J.M., Balint, J.-L., On the mechanism of viscous drag reduction using streamwise aligned riblets: a review with new results. *Proc. RAeS Int. Conf. on Turbulent Drag Reduction by Passive Means*. London, RAeS 2 (1987) pp. 290–309.
- Walsh, M.J., Riblets, Viscous drag reduction in boundary layers. In: Bushnell, D.M. and Hefner, J. (eds), *Progress in Astronautics and Aeronautics*, Vol. 123 (1990).
- Wilkinson, S.P., Anders, J.B., Lazos, B.S. and Bushnell, D.M., Turbulent drag reduction research at NASA Langley – progress and plans. *Proc. RAeS Int. Conf. on Turbulent Drag Reduction by Passive Means*. London, RAeS 1 (1987) p. 1.

Possibility of drag reduction using *d*-type roughness

K.-S. CHOI¹ & N. FUJISAWA²

¹*Department of Mechanical Engineering, The University of Nottingham, University Park, Nottingham NG7 2RD, U.K.*

²*Department of Mechanical Engineering, Gunma University, Kiryu 376, Japan*

Abstract. An experiment was carried out in a low-speed wind tunnel to study the turbulence structure of the boundary layer over a two-dimensional square cavity on a flat plate. The main purpose of this investigation is to examine the way a square cavity modifies the near-wall structure of the turbulent boundary layer leading to a possible drag reduction over *d*-type roughness. The experimental results on pressure coefficient and friction coefficient indicated a small reduction in total drag in this configuration. This seems to be due to the stable vortex flow observed within the cavity which absorbs and reorganizes the incoming turbulence in the cavity, thereby modifying the near-wall turbulence structure of the boundary layer. The resultant turbulence structure was very similar to that over drag-reducing riblets surface.

1. Introduction

In the past decade there has been continuous research efforts to study turbulent drag reduction using passive devices, such as riblets and LEBUs. The majority of the results so far show that up to eight percent of drag reduction can be obtained from riblets, which is believed to be a direct consequence of the modification of near-wall turbulence structure by riblets [1]. At present, riblets are very close to industrial applications for saving fuels and improving aerodynamic performance of aircraft, ships and ground vehicles [2].

Recently, a possibility of drag reduction using *d*-type roughness was discussed by Tani et al. [3] who demonstrated experimentally that the turbulent skin friction over a sparsely spaced two-dimensional square grooves is less than that over a smooth surface for a lower range of the Reynolds number based on the streamwise distance x ,

$$R_x < 1.6 \times 10^6 \quad (1)$$

and for the following range of groove spacings,

$$10 < L/d < 40, \quad (2)$$

where L is the groove spacing and d is the depth (see Fig. 1). They have obtained these results during an investigation of the equilibrium turbulent boundary layer over *d*-type roughness [4]. All the equilibrium flows currently known to us have been predicted by Rotta [5] on dimensional ground except for the flow over the *d*-type roughness. It seems natural to expect that the stable vortices inside the grooves must have contributed to the reduction of drag over *d*-type roughness. However, a simple

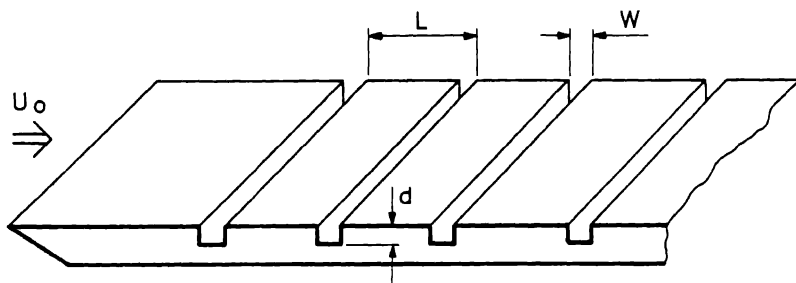


Fig. 1. *d*-type roughness over a flat plate.

argument that there will be less skin friction because of less surface area does not work here; the experimental results of Tani et al. [3] indicate that a greater reduction in the turbulent skin friction is observed when the spacing between the grooves is increased.

There have been a number of studies in the past on the turbulent boundary layer over a square cavity. Townes and Sabersky [6] have carried out an extensive flow visualization studies in water, where they found that the flow in the cavity was stable only when the Reynolds number based on the cavity depth d and the friction velocity u^* is greater than 150,

$$d \cdot u^* / \nu > 150. \quad (3)$$

Maul and East [7] have also conducted flow visualization with cavities of different aspect ratio. They concluded that the two-dimensional vortex inside the cavity can only exist when the ratio of cavity depth d to the width w is nearly unity,

$$d/w = 1.0. \quad (4)$$

Haugen and Dhanak [8] have pointed out, again from flow visualization studies, that the ratio of the cavity depth d to the boundary layer thickness δ is an important parameter as this can be considered as a measure of the outer-layer influence on the cavity flow. They suggested that this ratio should be much smaller than unity,

$$d/\delta \ll 1, \quad (5)$$

in order for the turbulent drag to be reduced over a cavity.

The main purpose of the present experimental investigation is to study the near-wall turbulence structure over a single two-dimensional square cavity as an effort to identify possible mechanisms for the turbulent drag reduction by *d*-type roughness observed by Tani et al. [3]. The relaxation process of the turbulent boundary layer after a single cavity is also studied to find out an optimum groove spacing for *d*-type roughness.

2. Experiments

All the experiments were carried out in an open-return low-speed wind tunnel at the British Maritime Technology, Teddington. The tunnel has a test section 6 m long, 1.22 m wide and 0.6 m high, in which a flat plate is placed at one-third height from the tunnel floor. Attached to the end of the flat plate is a short flap section, which was adjusted by a small angle to avoid any leading-edge flow separation. A trip wire of 2 mm diameter was affixed near the leading edge of the flat plate in order to fix the transition point. Two two-dimensional square cavities were set into the flat plate, one with 10 mm square for the mean flow and turbulence measurements at 1.15 m from the leading edge of the plate, and the other with 25 mm square for the flow visualization studies at 4.66 m. The pressure gradient along the flat plate was zero.

We have measured the static pressures inside the cavity in order to obtain the pressure drag associated with it. There are in total 42 static pressure taps of 0.2 mm diameter in the upstream and downstream faces of the square cavity, and the static pressures were measured using a pressure transducer through a Scanivalve. The accuracy of the pressure measurement was within 0.005 mm Aq. The mean flow and turbulence quantities were measured using DISA 55 M hot-wire anemometer with a single miniature wire. All the data were sampled with PDP 11/44 mini-computer through an A/D converter at a sampling rate of 2 KHz. The tunnel speed was set to 7 m/s throughout the experiments except for the flow visualization studies for which a slower speed of 2 m/s was chosen to obtain good images. Further experimental details and data processing techniques are described elsewhere [1, 9].

In the present experiment, the flow parameters and groove dimensions were chosen to satisfy all the conditions (1) to (5) given in the previous section to make sure that we are in the drag-reduction regime with a stable flow inside the cavity. Table 1 shows our experimental conditions which are compared with those by Tani et al. [3].

Table 1 Experimental conditions and flow parameters

	Present study	Tani et al. [3]
U_o [m/s]	7.0	13.0
R_x	0.6×10^6	$0.8-4.5 \times 10^6$
d^+	210	180
d/δ	0.4	0.24
d/w	1.0	1.0

3. Results and discussions

The distribution of pressure coefficient C_p measured on two vertical faces of the cavity is shown in Figure 2. The x-axis of this figure is the non-dimensional height measured

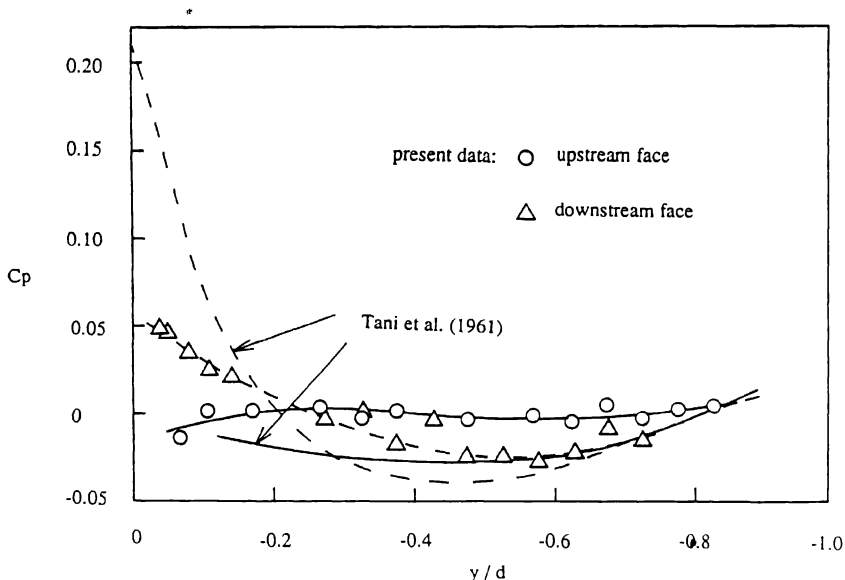


Fig. 2. Distribution of pressure coefficient inside the cavity.

from the top of the cavity, therefore the figure shows the static pressure distribution from the lip of the cavity ($y/d = 0$) to the bottom ($y/d = -1.0$). The experimental results of Tani et al. [10] are also shown in the figure for comparison. The figure shows that C_p has very large positive values near the lip, and negative values around the middle in the downstream face of the cavity. The pressure coefficient is nearly zero in the upstream face of the cavity. All of these results suggest that there is a stable vortex flow inside the cavity, which is confirmed from our flow visualization studies [9]. The drag coefficient C_d estimated from this pressure distribution is 0.001 which is smaller compared with the previous results by Roshko [11], Tani et al. [10] and Haugen and Dhanak [8] who obtained the drag coefficient of between 0.01 and 0.02. The discrepancy may be due to the difference in the relative size of cavity to the boundary layer thickness. In the present experiment the value for d/δ is 0.4, while all the previous experiments were carried out with very thin boundary layers with d/δ between 1.6 to 10. This is in agreement with the suggestion by Haugen and Dhanak [8] that the pressure drag of a cavity should be reduced with a reduction in d/δ . In other words, the vortex in the cavity is stable when d/δ is small since the influence of large-scale turbulence on the cavity flow is less, which leads to a reduction in pressure drag in the cavity.

The mean velocity profiles over a single cavity are shown in Fig. 3 in a semi-logarithmic plot. The streamwise distance x is measured from the downstream face of the groove, and it is non-dimensionalized with the cavity depth d . The points in the figure indicate the experimental data which are compared with a smooth curve representing the velocity profile over a smooth surface. The straight lines show the law

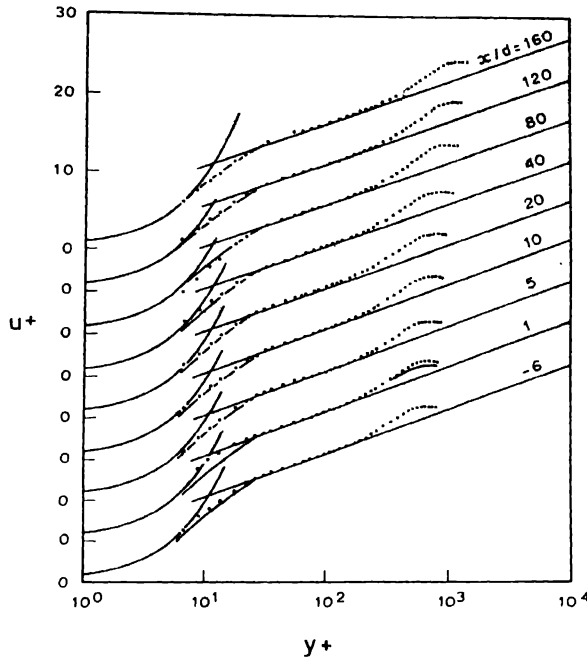


Fig. 3. Logarithmic velocity profiles over a square cavity.

of the wall over a smooth surface suggested by Patel [12]. The deviation from the law of the wall near the outer edge of the boundary layer can be expressed in terms of the law of the wake [13], so that the complete expression for the law of the wall and the law of the wake is given by

$$u^+ = (1/\kappa) \ln y^+ + C + \Pi \cdot W/\kappa, \quad (6)$$

where, κ is the Karman constant ($\kappa=0.42$) and C is the intercept ($C=5.45$). The non-dimensional velocity u^+ and the non-dimensional height y^+ are defined by

$$u^+ = U/u^* \quad (7)$$

and

$$y^+ = y \cdot u^*/\nu, \quad (8)$$

where, u^* is the friction velocity and ν is the kinematic viscosity of air. In the law of the wake, Π is the wake parameter and W is the universal wake function. From the bottom of Fig. 3, it is clear that the velocity profile has nearly a decade-wide logarithmic region with a standard buffer and wake region before the cavity at $x/d = -6$. Just after the square cavity at $x/d = 1$, however, this profile changes

suddenly in such a way that the velocity near the buffer region and the wake region increases. This behaviour in the mean velocity profile is very similar to the one reported by Fanourakis [14] who tested the d -type roughness in a high-speed wind tunnel at the Mach number of 0.78.

The changes in the mean velocity profiles in the near-wall region and the wake region should be reflected in the changes in the friction coefficient C_f and the wake parameter Π , respectively. In order to study the relaxation process of the turbulent boundary layer after a single square cavity, we have obtained C_f from the Clauser plot by fitting the mean velocity to a known logarithmic law for a smooth surface [12]. The wake parameter Π was then found by fitting the entire velocity profile to the expression (6). No attempts were made to account for any differences in the mean velocity profiles due to the presence of a cavity in the boundary layer. In other words, we did not introduce either the roughness shift nor virtual origin in the calculation of these values. This is because there was only a single cavity in the entire flow field so that the boundary layer could not be considered to have a fully-rough velocity profile. Figure 4 shows the change in the skin friction coefficient as a function of non-dimensional distance x/d . The figure also shows the skin friction coefficient for the smooth surface without cavity. The reduction in the skin friction coefficient after the square cavity is evident from this figure, which lasts for more than $x/d=100$, equivalent to $x=40\delta$. The total skin-friction reduction shown here is about one percent, so that we seem to have a small net drag reduction by a single cavity as the pressure drag is negligible. We have to take this result with caution, however, since the error in the calculation of C_f and C_d is estimated to be of the same order of the net drag reduction.

The change in the wake parameter is given in Fig. 5, which also shows an increase after the cavity. Tani showed in his last paper [15] that the skin-friction reduction can

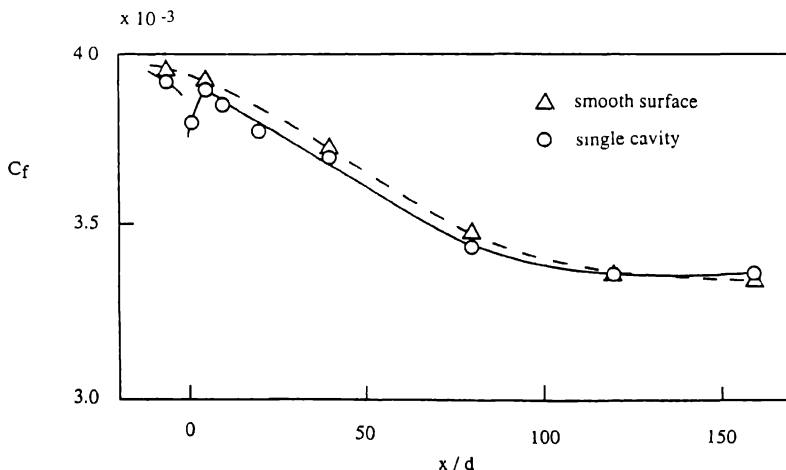


Fig. 4. Relaxation of the skin-friction coefficient after a square cavity.

be achieved by an increase in the wake parameter. He also showed that the turbulent boundary layer over riblets surface has a wake function greater than that over a smooth surface. In this sense, the increase in the wake function observed after the square cavity is consistent with the reduction in the skin friction as shown in Fig. 4. The relaxation length of the wake parameter is around $x/d = 100$, similar to the relaxation length of the skin friction. There was some evidence in the present experimental data that the shape factor is reduced after the square cavity. This is due to the relative reduction of the displacement thickness to the momentum thickness. The shape factor recovers to the smooth-surface value within the distance of $x/d = 100$, similar to the relaxation distance of the skin friction coefficient and the wake parameter. However, an expected reduction in the momentum thickness associated with the reduction in skin friction was not quite evident.

Figure 6 shows the turbulence intensity profiles of the boundary layer on a flat plate with a single square cavity. The points in the figure show the experimental data which are compared with the smooth-surface data indicated by a smooth curve. The present smooth-surface data agrees very well with the Klebanoff's data [16]. It is shown in the figure that the turbulence intensity of the boundary layer immediately above the cavity ($x/d = -0.5$) is larger than the corresponding smooth-surface value. This seems to be due to the effect of turbulent mixing layer developed from the cavity lip in the upstream face. In other words, the near-wall region of the turbulent boundary layer immediately above the cavity is imbedded in the high turbulence region of the mixing layer. After the cavity, the turbulence intensity is reduced as much as 10 percent close to the wall surface, but there was no noticeable changes in the turbulence intensity in the outer part of the boundary layer. This behaviour in the change of turbulence intensity profile over a cavity is very similar to the one over the drag-reducing riblets surface [1].

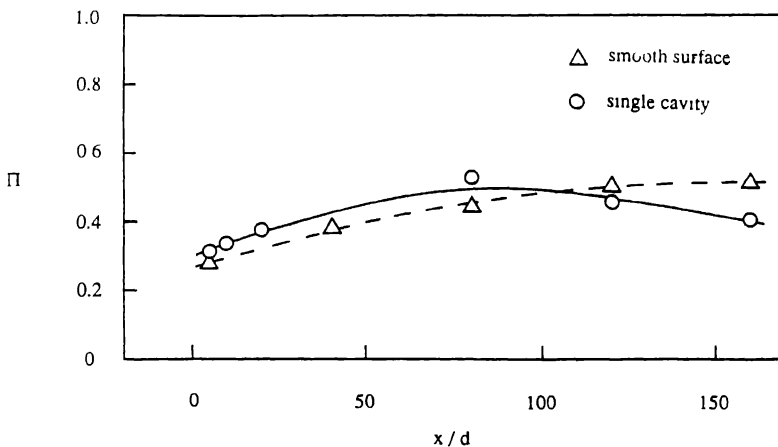


Fig. 5. Relaxation of the wake parameter after a square cavity.

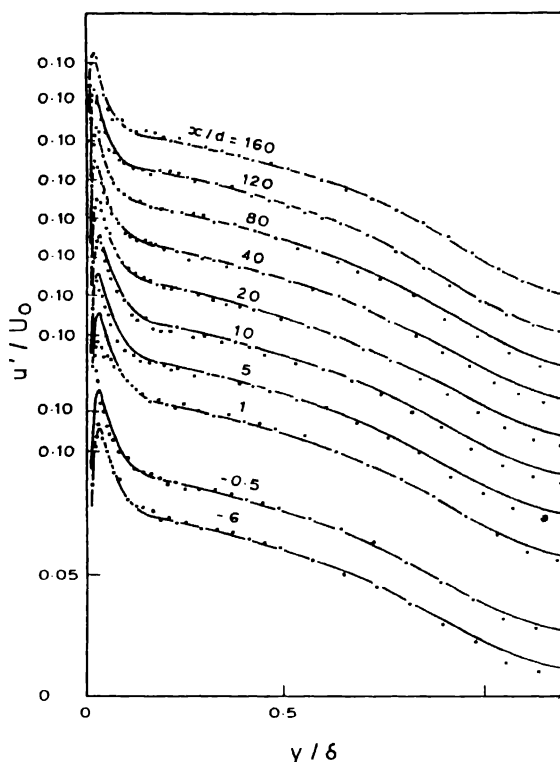


Fig. 6. Turbulence intensity profiles over a square cavity.

Figure 7 shows the energy spectra of streamwise velocity fluctuations measured at several streamwise locations. These spectra were taken at the position where the turbulence intensity is maximum (see Fig. 6). The effects of square cavity on the spectra seem to be to increase the high-frequency component of the energy and to reduce the low-frequency component. The increase in the high-frequency component of the energy seems to be related to the increase in the turbulence intensity (Fig. 6) at $x/d = -0.5$, which is due to the turbulent mixing layer developed from the cavity lip.

4. Concluding remarks

An experimental investigation of the turbulent boundary layer over a single two-dimensional square cavity was carried out by measuring the static pressure distribution inside the cavity as well as the mean velocity and turbulence intensity profiles. The main purpose of this investigation was to examine the way the cavity modifies the near-wall turbulence structure of the boundary layer leading to a possible drag reduction using d -type roughness. From this study, it was found that a small amount

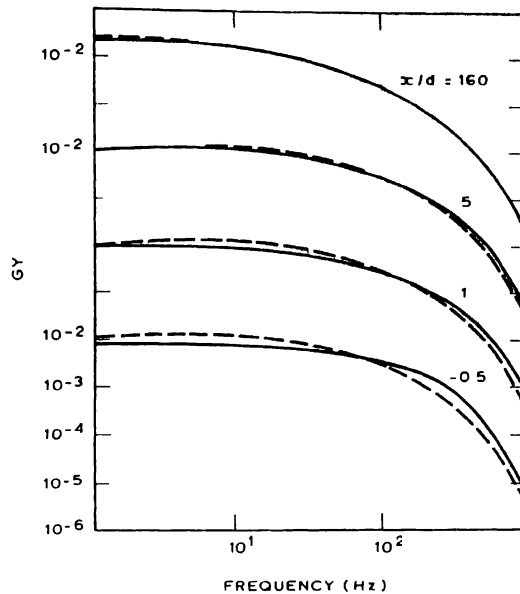


Fig. 7. Energy spectra of streamwise velocity fluctuations over a square cavity

(of the order of one percent) of net drag reduction can be obtained from a single square cavity. This net drag reduction was mainly due to the reduction in skin friction over the cavity, which lasted for more than $x/d = 100$ (equivalent to $x/\delta = 40$). The pressure drag of the cavity was negligibly small. It was also observed from the present results that the changes in the mean velocity profile, turbulence intensity profile and the energy spectrum over the square cavity were very similar to the corresponding changes over drag-reducing riblets surface [1].

The relaxation study of the flow parameters indicated that the skin-friction coefficient and the wake parameter took more than $100 \cdot d$ to recover after the changes were imposed by the square cavity. This relaxation distance should be considered to be an upper limit of the spacing for the *d*-type roughness in order to obtain the net drag reduction. According to the recent experiments conducted by Tani et al. [17], the optimum groove spacing for the *d*-type roughness is around $20 \cdot d$.

As for the possible mechanisms of turbulent drag reduction using *d*-type roughness, it is believed that they are strongly related to the stable vortex flow inside the cavity, which absorbs and reorganizes the incoming turbulence. The flow visualization studies conducted with a smoke wire and a sheet of laser light [9] indeed confirmed the existence of stable cellular structure within the cavity which has been observed by others [18, 19]. Although the vortex in the cavity rotated slowly at a constant speed most of the time, we could observe accelerations from time to time suggesting that some sort of turbulent events similar to the bursts are taking place near or within the cavity. The frequency of the events was, however, significantly less than that expected

from the turbulent boundary layer over a smooth surface. It must be noted that the changes in the near-wall turbulence structure such as the mean velocity and turbulence intensity profiles over the square cavity were remarkably similar to those over the drag-reducing riblets surface [1].

Acknowledgements

This paper is dedicated to the late Professor Tani who provided us with continuous encouragement throughout the course of study.

References

1. Choi, K.-S., Near-wall structure of a turbulent boundary layer with riblets. *J. Fluid Mech.* 208 (1989) 417–458.
2. Choi, K.-S., Cost-effective production of micro-grooves for drag reduction on the surface of aircraft in situ. *SPIE – The International Society for Optical Engineering, Proceedings Volume 1573* (1992) 136–144.
3. Tani, I., Munakata, H., Matsumoto, A. and Abe, K., Turbulence management by groove roughness. In: Liepman, H.W. and Narasimha, R. (eds), *Turbulence Management and Relaminarisation*. Berlin: Springer-Verlag (1987) pp. 161–172.
4. Tani, I., Some equilibrium turbulent boundary layers. *Fluid Dynamics Research* 1 (1986) 49–58.
5. Rotta, J.C., Turbulent boundary layers in incompressible flow. *Prog. Aeron. Sci.* 2 (1962) 1–219.
6. Townes, H.W. and Sabersky, R.H., Experiments on the flow over a rough surface. *Int. J. Heat Mass Transfer* 9 (1966) 729–738.
7. Maul, D.J. and East, L.F., Three-dimensional flow in cavities. *J. Fluid Mech.* 16 (1963) 620–632.
8. Haugen, R.L. and Dhanak, A.M., Momentum transfer in turbulent separated flow past a rectangular cavity. *ASME J. Appl. Mech.* 33 (1966) 641–646.
9. Choi, K.-S., Fujisawa, N. and Savill, A.M., Studies of drag reducing *d*-type roughness—including flow visualisation, image enhancement and quantitative measurements. In: Reznicek, R. (ed.), *Flow Visualisation V*. New York: Hemisphere (1989).
10. Tani, I., Iuchi, M. and Komoda, H., Experimental investigation of flow separation associated with a step or a groove. *Aero. Res. Inst., Univ. Tokyo* 363 (1961).
11. Roshko, A., Some measurements of flow in a rectangular cutout. *NACA TN* 3488 (1955).
12. Patel, V.C., Calibration of the Preston tube and limitations on its use in pressure gradients. *J. Fluid Mech.* 23 (1965) 185–208.
13. Coles, D., The law of the wake in the turbulent boundary layer. *J. Fluid Mech.* 1 (1956) 191–226.
14. Fanourakis, P., A study of rough surfaces with drag reducing properties in turbulent flow. *Engr. Dept. Rept., Cambridge Univ.* October (1989).
15. Abe, K., Matsumoto, A., Munakata, H. and Tani, I., Drag reduction by sand grain roughness. In: Gyr, A. (ed.), *Structure of Turbulence and Drag Reduction*. Berlin: Springer-Verlag (1990) pp. 341–348.
16. Klebanoff, P.S., Characteristics in a boundary layer with zero pressure gradient. *NACA TN* 3178 (1954).
17. Tani, I., private communication (1988).
18. Perry, A.E., Schofield, H.W. and Joubert, P.N., Rough wall turbulent boundary layers. *J. Fluid Mech.* 37 (1969) 383–413.
19. Townsend, A.A., *The Structure of Turbulent Shear Flow*, 2nd edn. Cambridge: Cambridge University Press (1976) pp. 139–143.

The drag of three-dimensional rectangular cavities

ERIC SAVORY¹, NORMAN TOY¹, PETER J. DISIMILE² &
 RUSSELL G. DIMICCO²

¹*Fluid Mechanics Research Group, Department of Civil Engineering, University of Surrey, Guildford GU2 5XH, United Kingdom;* ²*Department of Aerospace Engineering and Engineering Mechanics, University of Cincinnati, Cincinnati, Ohio 45221, USA*

Abstract. Cavities and other surface cut-outs are present on aircraft in numerous forms, from cargo bays and landing gear housing to rivet depressions and panel handles. Although these surface imperfections make a significant contribution to the overall drag on an aircraft, relatively little is known about the flow mechanisms associated with cavities, particularly those which have a strongly three-dimensional geometry. The present work is a wind tunnel investigation of the drag forces and flow regimes associated with cavities having a 2:1 rectangular planform geometry. The effects of both the cavity depth and the flow incidence angle have been examined in terms of the overall cavity drag increment and the mean surface pressure distributions. The drag forces have been determined from both integrated pressures and direct force balance measurements. For the model normal to the flow direction the flow within the cavity was remarkably symmetrical in all the configurations examined. In most cases the cavity flow is dominated by a single large eddy. However, for cavities yawed to other incidence angles there is considerable flow asymmetry, with strong vorticity shedding and high drag in some cases, notably with depth/narrowest width ratio of 0.4–0.5 at 45–60° incidence. The present data correspond well with established results and extend the scope of information available for design purposes and for the development of numerical models.

Nomenclature

A_p = planform area of model	L = longest planform dimension of model
C_D = pressure drag coefficient ($F_D/(A_p \cdot q)$)	P = surface pressure on model
ΔC_D = drag coefficient increase due to cavity	P_s = freestream static pressure
$(C_D - c_f)$	P_t = freestream total pressure
c_f = local skin friction coefficient	q = freestream dynamic pressure ($P_t - P_s$)
C_L = pressure lift coefficient ($F_L/(A_p \cdot q)$)	Re = Reynolds number ($U_R \cdot W/\nu$)
C_p = mean surface pressure coefficient	U_R = freestream velocity
$(P - P_s)/q$	W = narrowest planform dimension of model
F_D = drag force	Z = vertical cartesian coordinate
F_L = lift force	Ψ = incidence angle
h = depth	ν = kinematic viscosity

1. Introduction

The reduction of drag forces is one of the major continuing aims of the aeronautics industry. A significant source of parasitic drag is that due to surface excrescences and cut-outs and yet very little is known about the flows associated with such geometries. Indeed, these surface imperfections, for example; roughness, equipment housings, external instruments, panel handles, ridges and holes account for up to 3% of the total drag on a modern aircraft, such as the A320. Hence, any improvements to the external surface profile can lead to significant reductions in fuel consumption and enhancement of operational performance.

Our knowledge of the effects of surface cut-outs and cavities is mainly limited to the overall drag increments due to single or multiple holes, such as the early data obtained by Wieghardt (1946), Tillmann (1951), Roshko (1955) and Tani et al. (1961) using essentially two-dimensional rectangular slots normal to the flow direction. The case of a fully three-dimensional rectangular cavity has been examined by a few workers, notably Friesing (1936), Maull and East (1963), Rossiter (1964) and Gaudet and Winter (1973). Much of the early research was summarized by Hoerner (1965), whilst AGARDograph 264, Young and Paterson (1981), provides an excellent presentation of the best drag data in a form that may be used for design purposes. However, apart from a few surface pressure distribution measurements by a limited number of workers, such as Roshko (1955), Maull and East (1963), Rossiter (1964) and, more recently, Sinha et al. (1982), Kaufman et al. (1983) and Plentovich (1990), the drag data has been derived from force balance measurements which provide very little insight into the flow regimes occurring within the cavities.

The case of the two-dimensional square or rectangular cavity has attracted the attention of several workers developing numerical models because it is one of the simplest boundary value problems that can be posed for the Navier Stokes (NS) equations, Mills (1965). Some workers have developed analytical models, such as Haugen and Dhanak (1966) who treated the turbulent separating shear layer across the top of a rectangular cavity as a two-dimensional plane jet and applied the boundary layer momentum and continuity equations. The results, at Reynolds numbers up to 1.3×10^5 , for surface pressures, mean velocities and turbulence intensities showed reasonably good agreement with experimental data. Their findings confirmed that the overall cavity drag decreased with increasing thickness of the approach flow boundary layer. Steady NS solutions have been presented, showing the presence of one primary vortex in the cavity and up to two secondary corner vortices, for Reynolds numbers up to 4×10^2 , Burggraf (1966), up to 2.7×10^3 , Pan and Acrivos (1967) and up to 5×10^4 , Nallasamy and Prasad (1977). Some unsteady NS computations were undertaken by Donovan (1970) at a Re of 10^2 for a square cavity and these showed good agreement with mean velocity data from a steady solution. Solutions for supersonic, high Reynolds number, flows include those by Hankey and Shang (1980), who used NS calculations to determine the pressure oscillations over a cavity for Mach 1.5 and Re of 2.6×10^7 , and by Brandeis (1982) who used a compressible boundary layer model above the cavity and the incompressible NS equations within the hole for Mach 2.25 and Re of 10^5 . An investigation of the flow in a rectangular cavity at Mach 1.5 and 2.5 was carried out by Zhang and Edwards (1988) using the two-dimensional unsteady NS equations, in terms of mass averaged variables, coupled with a two-layer eddy viscosity turbulence model. Their computations demonstrated the presence of self-sustained flow oscillations and the formation and shedding of leading edge vortices. These oscillations were the result of a feedback interaction in which the shear layer plays the dominant role by driving the leading edge vortices downstream to mix with the trailing edge vortex. The trailing edge vortex movement sends a pressure pulse upstream which deflects the oncoming

boundary layer, subsequently forming another leading edge vortex and, thereby, closing the loop. Baysal and Stallings (1988) presented surface pressure distribution results from a two-dimensional NS solution with an algebraic turbulence model up to Mach 1.5 and a Re of 6.6×10^6 per m. Whilst the data showed some agreement with experimental measurements, there were significant discrepancies caused by the fact that the experimental cavity was narrow enough to exhibit strong three-dimensional flow effects. Indeed, such three-dimensionality is likely to occur in all but the very widest cavities. Furthermore, even in nominally two-dimensional rectangular cavity flows Maull and East (1963) observed the presence of regular three-dimensional cellular structures which were reflected in the periodic changes in the mean pressure distributions across the base in the lateral direction. Rizetta (1988) carried out some unsteady NS calculations of the flow associated with a three-dimensional cavity under supersonic conditions. The results from two and three-dimensional predictions for a cavity with $W/L=0.53$ and $h/W=0.37$ at 90° incidence were presented and compared with experimental data from Kaufman (1983), obtained under similar test conditions of Mach 1.5 and Re of 1.09×10^6 . The computations showed good agreement for the mean static pressures, whilst the amplitudes of the harmonic frequencies of the cavity acoustic spectra were overpredicted.

The broad categorization of two-dimensional rectangular cavity flows has been illustrated by Plentovich (1990). For deep cavities, which have a width in the flow direction to depth ratio (W/h) less than about 10, the flow is termed 'open' and is dominated by a primary vortex driven by the shear layer passing over the top of the cavity. In the case of shallow cavities the separated shear layer attaches on the cavity base causing a backward-facing step flow downstream of the upstream wall and a forward-facing step flow immediately upstream of the downstream face. This type of flow is termed 'closed' and is characteristic of cavities with streamwise dimension (width) to depth ratios above about 13. However, it should be noted that for three-dimensional cavities closed systems of recirculating flow cannot exist, Hunt et al. (1978), and so the flow regimes are considerably more complicated with fluid entering the cavity and vorticity being shed from it. In the present work all of the cavity configurations were highly three-dimensional with low planform aspect ratios and most of the flows were in the 'open' regime. Detailed surface pressure measurements and overall drag force balance tests were carried out for a range of cavity depth to width ratios using cavities with a 2:1 rectangular planform. One major aspect of the work was the examination of the effects of approach flow incidence direction which had not been examined by previous workers.

2. Experimental details

In this section details are provided concerning the apparatus arrangements for the cavity experiments, together with an outline of the scope of the tests. The wind tunnels and boundary layers are dealt with first and this is followed by descriptions of the models and measurement systems.

2.1. Wind tunnels and boundary layers

Two wind tunnels were used in the experiments. The first tunnel, in the Department of Civil Engineering at the University of Surrey, which has working section dimensions of 1.37 m height by 1.07 m width by 9.0 m length, was employed for all the drag balance measurements. A 20 mm high metal wall fence was placed across the tunnel near the contraction to produce a thick boundary layer. Across the tunnel the velocity was uniform to within $\pm 2\%$, whilst the rms turbulence intensity was within 5%. These boundary layer profiles were obtained at a freestream velocity of 12 m/s which was close to the speed used in most of the subsequent experiments.

The second wind tunnel, in the Department of Aerospace at the University of Cincinnati, has working section dimensions of 0.61 m height by 0.91 m width by 2.44 m length and this was used solely for the rectangular cavity pressure distribution measurements. Here, the model was mounted in the tunnel roof and a much thinner turbulent boundary layer was generated which provided a valuable comparison with the data from the first tunnel experiments. The boundary layer profiles were obtained with a freestream velocity of 7 m/s which was that utilized in the cavity experiments.

The boundary layer parameters for both tunnels are given below.

<i>Drag balance experiments</i>	<i>Pressure measurements</i>
$\delta = 320 \text{ mm}$	$\delta = 26 \text{ mm}$
$\delta_* = 27.9 \text{ mm}$	$\delta_* = 4.1 \text{ mm}$
$\Theta = 21.2 \text{ mm}$	$\Theta = 2.7 \text{ mm}$
$c_f = 0.00265$	$c_f = 0.00520$

In each case the boundary layer profiles were measured using a hot-wire anemometer and the skin friction coefficient computed from the standard smooth wall logarithmic law plot.

2.2. Main wind tunnel model

The main rectangular cavity model, constructed for the surface pressure measurement experiments, is of Perspex construction and has a 2:1 planform ratio of dimensions 106 mm (L) by 53 mm (W). There are 0.79 mm diameter pressure tappings over one half of each of the narrow walls, facing each other, and a similar arrangement on the wider walls. On one half of the long walls there are thirty-three rows of tappings each row spaced 5 mm apart beginning at 2.5 mm from the rim. Each row contains six tappings. On the opposite half of each long wall there are two rows of six tappings placed 5 mm apart, commencing at 5 mm from the lip. On each half of the narrow wall there are thirty-three rows of tappings positioned 5 mm apart, starting at 2.5 mm from

the rim, each with three tapings. The opposite half of the wall has two rows of three tapings spaced 5 mm apart, beginning at 5 mm from the lip. Within every row on each wall the spacing between each tapping is generally 10 mm although they are more closely spaced near the corners on the long walls. In addition, there are forty-two tapings on one half of the piston-style base, mostly spaced 10 mm apart but with additional taps in the corners.

The cavity is built into a turntable which may be inserted into the tunnel wall to permit precise rotation of the model to the desired incidence angle. In view of the generally small magnitudes of the pressures being measured it was essential to prevent any leakage of air through the sides of the base. This was achieved by taping plumbers white around the base before inserting it into the model cylinder. In addition, all unused pressure tapings were sealed off to prevent leakage through the holes. The model utilized in the drag balance experiments is described later.

2.3. Pressure measurement apparatus

The apparatus arrangement for the mean surface pressure measurements is illustrated schematically in Fig. 1. The model was mounted in the roof, flush with the tunnel interior, at 1.2 m downstream of the contraction and a pitot-static tube was positioned in the freestream, directly across the tunnel at the same downstream location as the cavity, for measurement of the reference dynamic pressure. The large number of pressure tapings on the model were attached to connectors which, in turn, were inserted into Scanivalve switch mechanisms. This allowed the connection of each tapping to one side of a differential pressure transducer. The other, reference, side of the transducer was connected to the freestream static pressure, via a damper to ensure that unwanted fluctuations were removed. A ± 13.6 mm WG range transducer was used in the experiments and this was found to be capable of resolving the large variations in the magnitudes of the pressures, from the high positive values at the reattachment point of the separated shear layer to the very small pressures deeper into the cavity. The freestream dynamic pressure was constantly monitored during the measurements using a second transducer which had a ± 38 mm WG range. A PC was utilized to acquire the pressure data from the two transducers and these were used to compute the pressure coefficients defined as

$$C_p = \frac{P - P_s}{P_t - P_s},$$

where P is the model surface pressure and P_t and P_s are the freestream total and static pressures, respectively. The computer also controlled the operation of the Scanivalve system via a digital control unit. Typically, a delay time of 15 s was used after each switching of a Scanivalve port to allow settling of the pressure at the transducer.

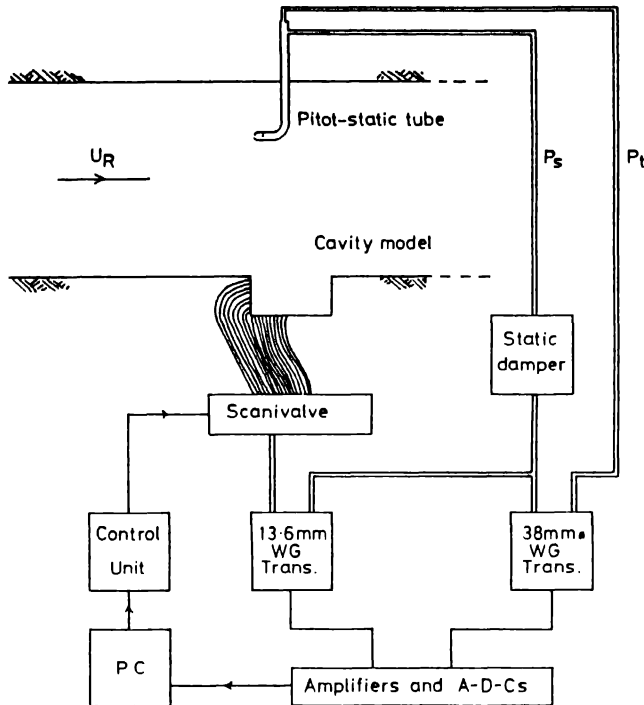


Fig. 1. Schematic arrangement of pressure measurement apparatus.

Similarly, the sampling times were 30 s at each port to permit determination of reliable mean values. The reference dynamic pressure was monitored throughout each experiment and the accuracy of the data was estimated to be ± 0.003 in C_p . In these experiments very small cavities, in the form of pressure tapings, were used to obtain data for a large cavity model. However, an assessment of the errors involved in pressure tap measurements, according to Shaw (1960), revealed that such errors were more than an order of magnitude less than the overall accuracy stated above. The overall lift and drag coefficients, based on the model planform area and the freestream dynamic pressure, were obtained by integrating the surface pressures and resolving the force components in the appropriate direction. For the drag force the integration area was the complete cavity wall, whilst the lift force was computed from the pressure distribution on the cavity base. However, in both cases the cavity base area was used as the normalizing area parameter. The drag increment due to the cavity, ΔC_D , was determined by subtracting the approaching boundary layer skin friction coefficient from the drag coefficient. Complete surface pressure distributions were obtained for the rectangular cavities with h/W from 0.1 to 0.7, in 0.1 intervals, and for incidence angles of 0, 30, 45, 60 and 90°. The freestream velocity was 7 m/s giving a Reynolds number of 2.44×10^4 .

2.4. Drag force balance apparatus

In order to obtain direct measurements of the drag coefficients, for comparison with the data from integrated pressure distributions, a force balance was designed and installed into the floor of the 1.37 m by 1.07 m by 9 m tunnel, as illustrated diagrammatically in Fig. 2. The balance has a plan area of 0.5 m length by 0.3 m width into which ground boards containing models can be inserted. Essentially, the balance mechanism is a parallelogram in which rotation can occur at each corner on frictionless bearings. This mechanism is attached to a rigid frame which, in turn, is fastened to the underside of the tunnel. A load cell is incorporated into the framework and a small threaded shaft on one upstream vertical arm of the balance impinges upon the load cell sensor. On the other upstream vertical member is a cantilever upon which weights may be placed to pre-load the load cell. The gap between the balance plate and its surrounding frame at the tunnel floor is of the order of 0.05 mm but the actual position of the plate within the frame is set by adjusting the cantilever loading and the threaded shaft. In order to prevent contact bounce between the load cell and the shaft under dynamic loading a simple damping device is placed in parallel with these two components.

The frame surrounding the balance plate is pressure tapped, with six tappings on

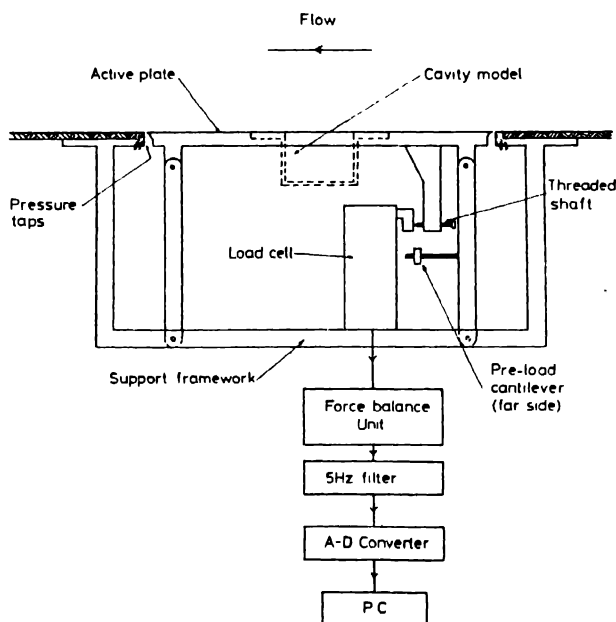


Fig. 2. Diagrammatic layout of drag balance.

both the upstream and downstream faces and two tappings on the two side faces. This was carried out in order to assess the effect of any flow through the gaps on the loading on the sides of the balance plate. However, for the cavity models at least, there is no measurable difference between the pressures on the upstream face and those on the downstream face. The ground board is constructed from timber with a circular hole cut in the centre to allow models to be slotted in and then rotated to the required incidence angle. The board is screwed down onto the plate with packing material underneath to ensure a flush finished surface. The balance is located approximately 6 m downstream of the tunnel contraction. The output from the load cell is taken to a unit which contains a precision high gain amplifier. This provides an accurate output with a calibration of 76.19 g/V and repeated calibration tests using small weights showed that hysteresis was less than ± 0.0002 V or ± 15 mg. Since only mean loads were of interest in the present work the amplified output was filtered at 5 Hz before being sampled by a PC via an A-D converter system. Before each set of experiments the load cell and digitization system were calibrated *in situ* to an accuracy of better than 0.001 V, i.e. 76 mg.

For each model configuration the load with no airflow was measured and this was then subtracted from the load measured at the test velocity. A similar procedure was adopted for measuring the load on the plate under the same freestream conditions but without a cavity present. Hence, unlike the pressure integration approach, this direct method also incorporated the wake drag associated with the cavity. From this data the net drag coefficient due to the cavity, ΔC_D , could be computed by taking the load increment and dividing by the cavity model planform area and the freestream dynamic pressure. A sampling time of 40 s was used for each measurement and several sets of samples were taken for each configuration to ensure reliability of the data and to assess the experimental scatter.

The model used in these experiments was constructed from timber and had a plunger-type base to allow variation of the cavity depth. The planform dimensions were 70 mm (W) by 140 mm (L) and the tests were conducted with a freestream velocity of 11.1 m/s giving a Reynolds number of 5.12×10^4 . The experiments were conducted with models of varying depths, from $h/W = 0.05$ to 1.6, at an incidence angle of 0° and a limited number of tests were carried out to assess the effects of changing the incidence angle.

3. Results and discussion

In this discussion the variation in the pressure distributions with depth for the 0° incidence case is examined first. All of the distributions are illustrated such that in each diagram the cavity has been 'cut' vertically at the corners and the wall distributions 'unfolded'. For the shallowest cavity with $h/W = 0.1$ (Fig. 3) the flow regime appears to be closed. The maximum coefficient measured on the base of 0.25 is about the upper limit suggested by Roshko (1955) for rectangular cavity flows. It may

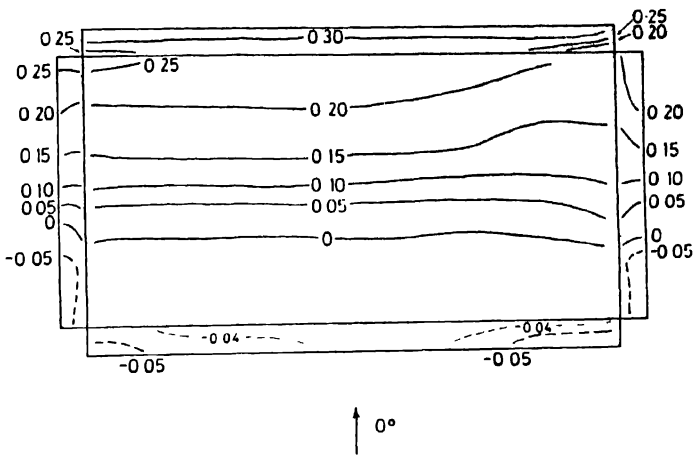


Fig. 3 Pressure distribution with $h/W = 0.1$ for 0° incidence angle (showing closed regime)

be seen that at this incidence angle the flow is remarkably uniform in the lateral direction with no noticeable end effects. Indeed, this spanwise uniformity is in contrast to the series of cell-like structures noted by Maull and East (1963), the number of which was related to an integer multiple of the planform aspect ratio. Their results showed lateral variations in the base pressure distributions associated with these cells which, at a given aspect ratio (L/W), had a fixed, periodic nature. It was found that the cells had a preferred span which was a function of the chord and depth of the cavity. The lack of such structures observed in the present work may be due to the particular planform aspect ratio since Maull and East found that the cells did not occur at every aspect ratio.

With increasing cavity depth the formation of the main vortex becomes more evident such that by $h/W = 0.3$ (Fig. 4) the flow regime is open and the vortex centre is located at $0.74W$ from the leading edge and about $0.5h$ from the base. As the depth becomes greater the vortex moves upstream with the centre located at $0.69W$ from the leading edge at $h/W = 0.4$ (Fig. 5), $0.65W$ at $h/W = 0.5$ (Fig. 6), $0.63W$ at $h/W = 0.6$ (Fig. 7) and $0.61W$ at $h/W = 0.7$ (Fig. 8). At the same time the vortex centre appears to move upwards away from the base of the cavity. As a consequence of these movements the vortex location asymptotes to the position typically associated with a two-dimensional rectangular cavity, i.e. $0.6W$ in the downstream direction and $0.75h$ vertically from the base.

Considering now the case of the cavity at 90° incidence, the shallowest hole with $h/W = 0.1$ (Fig. 9) displays the features of a closed flow regime. Here, the separated shear layer from the upstream wall reattaches on the base at approximately $7h$ from the wall. This value has been estimated by assuming that reattachment occurs a short distance before the peak surface pressure is reached. The flow is, therefore, similar to a backward-facing step regime and the pressure coefficient on the backward face, at

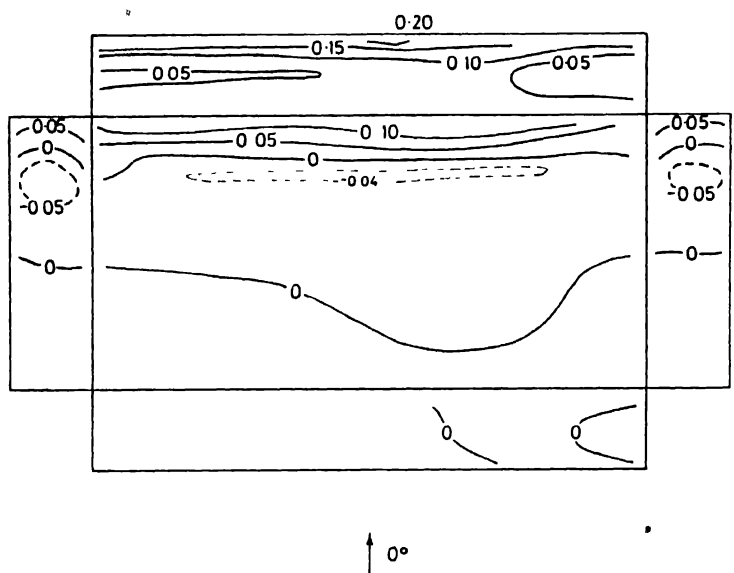


Fig. 4. Pressure distribution with $h/W = 0.3$ for 0° incidence angle (showing open regime).

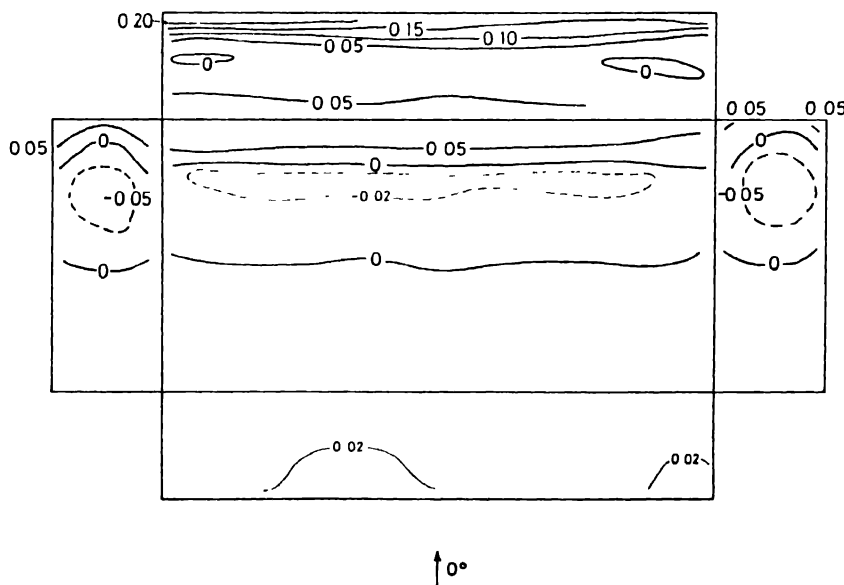


Fig. 5. Pressure distribution with $h/W = 0.4$ for 0° incidence angle.

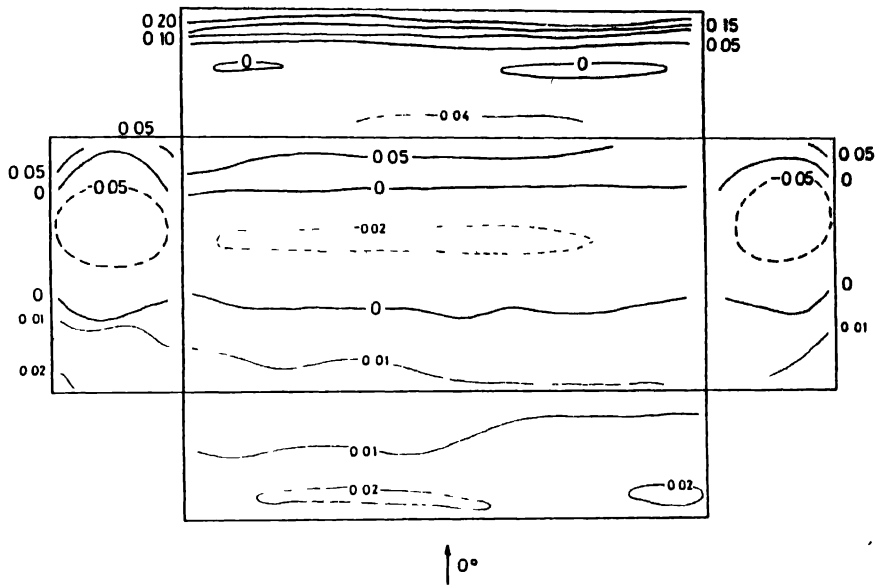


Fig 6 Pressure distribution with $h/W = 0.5$ for 0° incidence angle

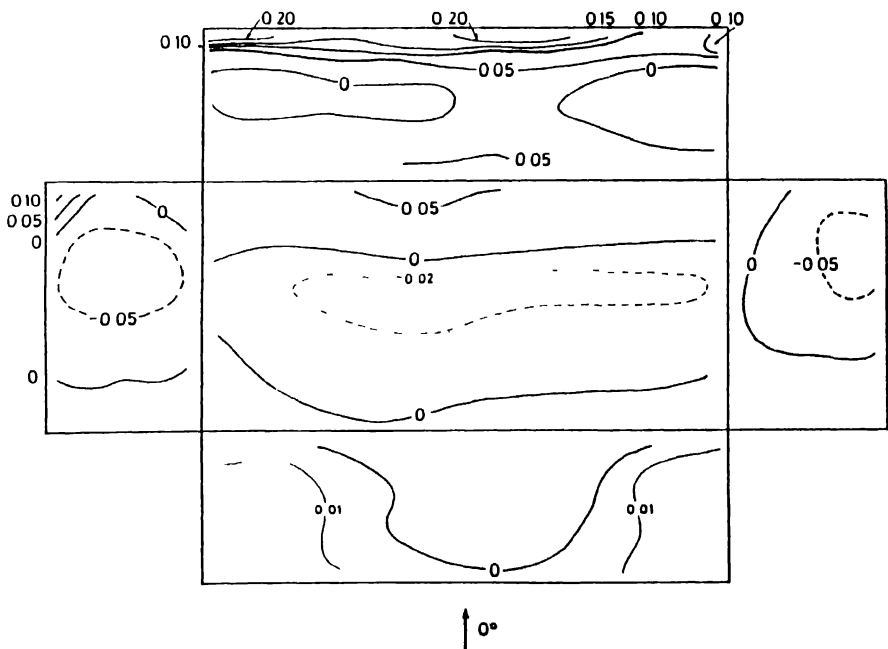


Fig 7 Pressure distribution with $h/W = 0.6$ for 0° incidence angle

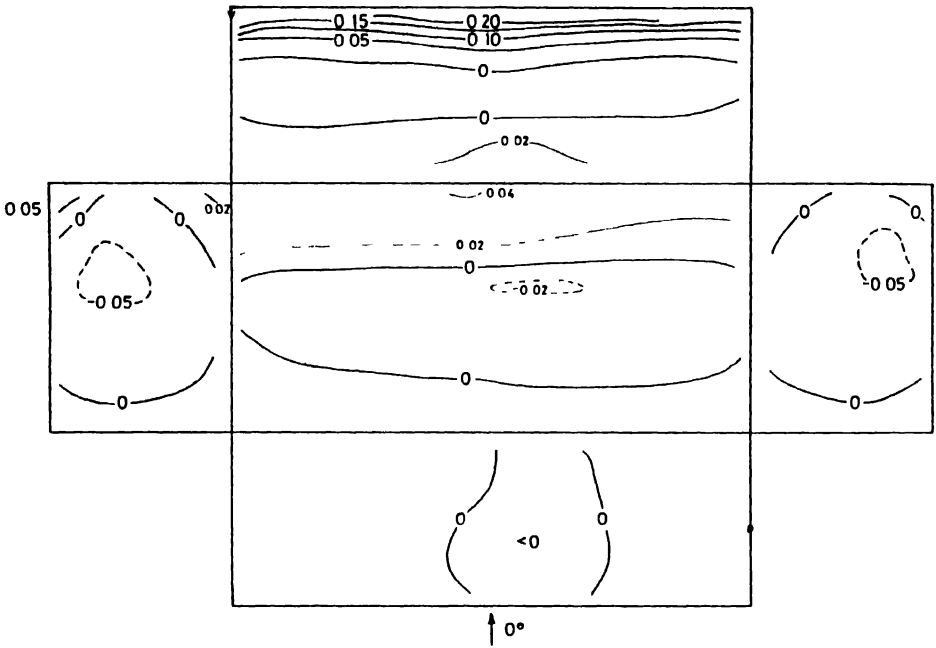


Fig 8 Pressure distribution with $h/W = 0.7$ for 0° incidence angle

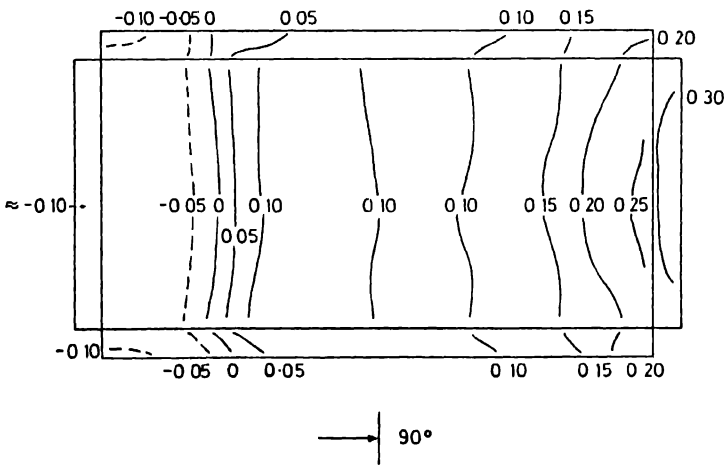


Fig 9. Pressure distribution with $h/W = 0.1$ for 90° incidence angle (showing closed regime)

-0.10 , is also typical of such a flow. Towards the downstream wall the pressure rises rapidly and the flow separates in a similar fashion to that immediately upstream of a forward-facing step.

With a small increase in depth to $h/W = 0.2$ (Fig. 10) the regime has completely changed to the open case with no evidence of early reattachment on the base. As the depth increases, the formation of a negative pressure region across the base and down the wide walls becomes more pronounced and moves downstream. If, as suspected, this region marks the presence of the main cavity recirculation then it would appear that this flow structure originates near the upstream wall in the shallower cavities but is located further downstream as the cavity deepens.

In the deepest cavity with $h/W = 0.7$ (Fig. 11) the separated shear layer reattaches near the lip of the downstream wall and a large symmetric vortex forms beneath it. For this, essentially narrower, cavity the vortex centre location is further downstream, relative to the streamwise dimension, than that noted in the 0° incidence case. It is possible that for greater depths the vortex would move further upstream towards the equivalent two-dimensional cavity location.

Having examined the effects of varying the cavity depth for two symmetric incidence angles, the influence of changing incidence angle for a given depth, namely $h/W = 0.5$, will now be described. The distribution at 0° incidence (Fig. 6) is essentially symmetrical with a well-defined vortex structure, as described earlier. The shape of the distribution along the streamwise centre-line is similar to that measured by Haugen and Dhanak (1966) for a two-dimensional cavity with the same h/W ratio except that the magnitudes of the pressures are slightly lower throughout in the present work. One of the reasons for this discrepancy is that the δ/W ratio in the present work is

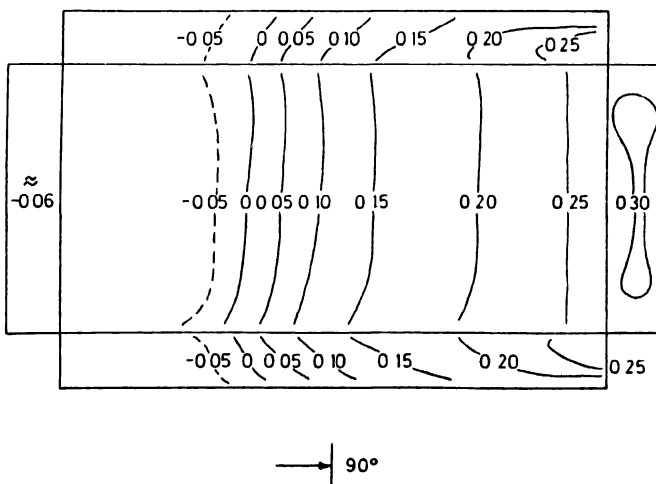


Fig. 10. Pressure distribution with $h/W = 0.2$ for 90° incidence angle (showing open regime).

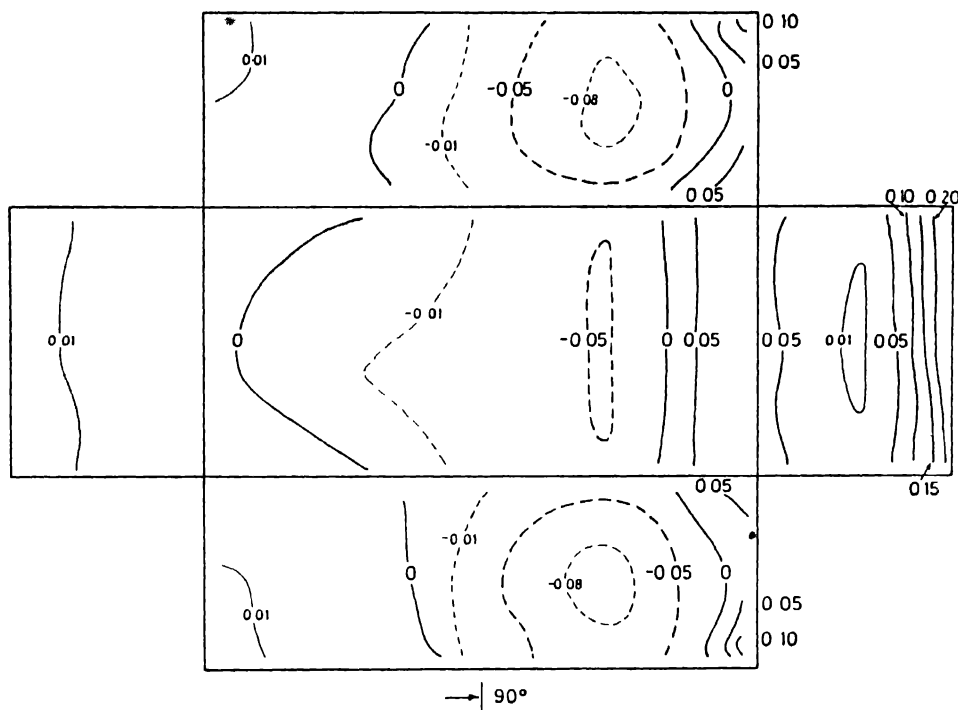


Fig. 11 Pressure distribution with $h/W = 0.7$ for 90° incidence angle

greater than that used by Haugen and Dhanak. At 30° incidence (Fig. 12) the distribution becomes very asymmetrical although the shear layer still creates a stagnation region on the downstream long wall. The line of the vortex remains approximately parallel to the major axis but the downstream end is raised with a possible consequential increase in vorticity shedding.

At 45° incidence (Fig. 13) the stagnation region is near the top of the cavity at the downstream corner. It would appear that the main axis of recirculation within the cavity is still approximately parallel to the major model axis with strong activity around the downstream narrow wall. This configuration produces the highest overall drag coefficient of all the rectangular cavities studied in the present work. With the model at 60° incidence (Fig. 14) the drag remains very high and the pressure distribution is complicated. It is unclear whether the main flow recirculation is parallel to the major or minor axis. By 90° incidence (Fig. 15) the stagnation region has moved to the centre of the downstream wall and the flow is largely symmetric with a dominant vortex structure and a reduced overall drag coefficient.

The variation of overall drag with incidence angle for this depth ratio is illustrated in Fig. 16 which shows both integrated pressure and direct force balance net drag coefficient data normalized by the skin friction coefficient. There is good agreement

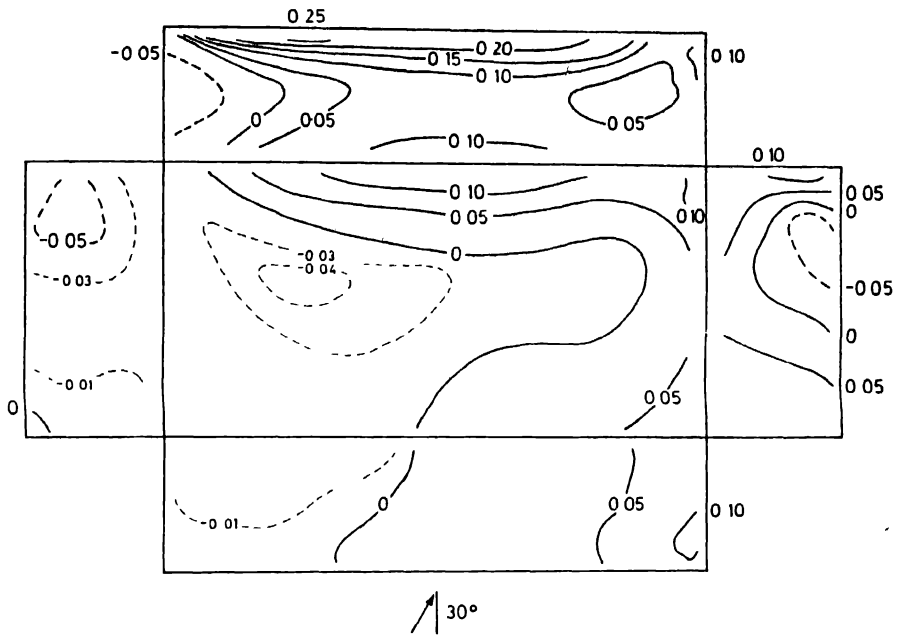


Fig 12 Pressure distribution with $h/W = 0.5$ for 30° incidence angle

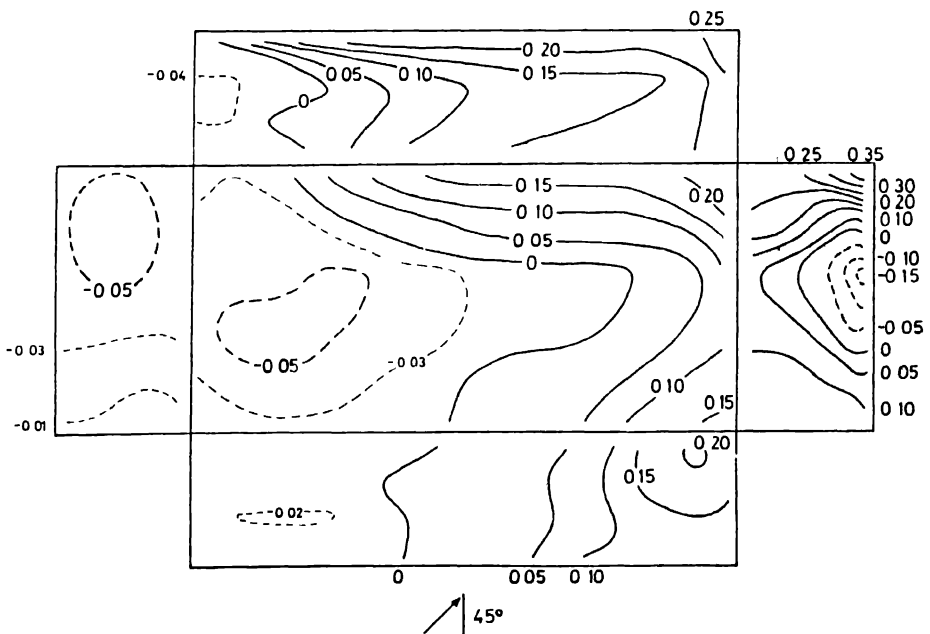


Fig 13 Pressure distribution with $h/W = 0.5$ for 45° incidence angle.

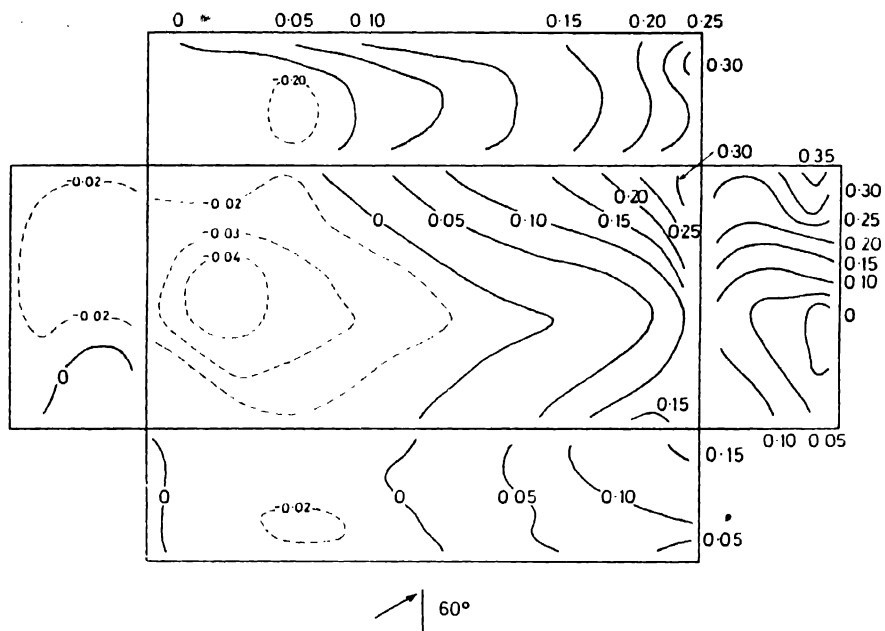


Fig. 14. Pressure distribution with $h/W = 0.5$ for 60° incidence angle.

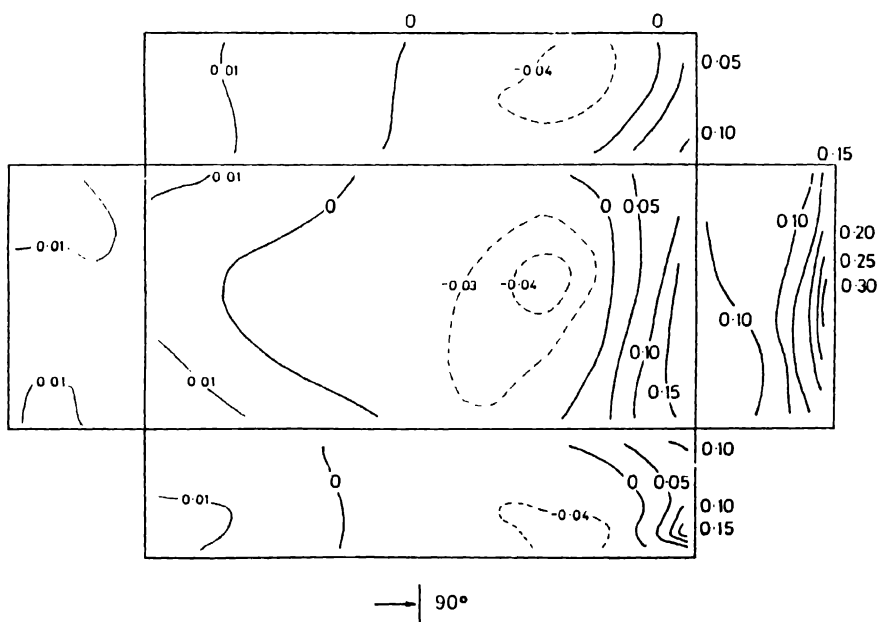


Fig. 15. Pressure distribution with $h/W = 0.5$ for 90° incidence angle.

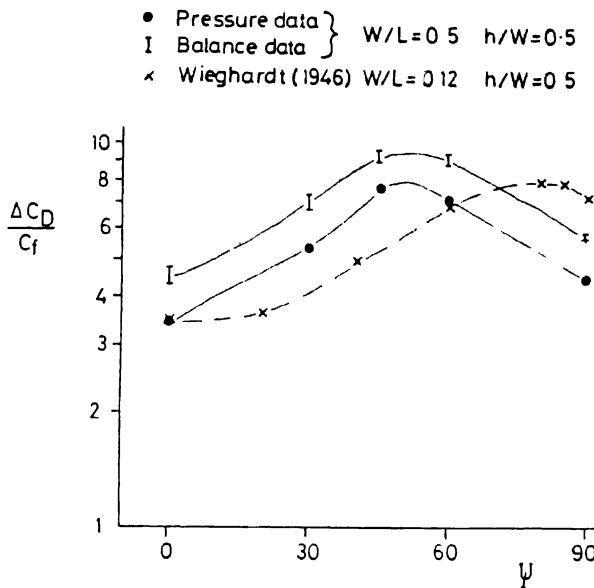


Fig. 16 Variation of normalized drag coefficient with incidence for $h/W = 0.5$

between the trends shown by the two methods which illustrate how the peak drag occurs at an incidence of about 45° . The difference in magnitudes, which manifests itself as a drag offset, is largely due to the fact that the integrated pressure distributions produce only the pressure drag of the cavity whereas the direct balance measurements incorporate the effect of the cavity on the local wall flow regime. The only other available data, that due to Wieghardt (1946), is also shown for comparison, although it should be noted that his results were for a long narrow cavity with W/L of only 0.12. It would appear that the effect of incidence angle on the overall drag coefficient reduces slightly as the cavity becomes more two-dimensional. This is likely to be due to the contribution from the end wall effects, where much of the drag is generated, becoming relatively less as the cavity length is extended.

Rather than attempt to discuss all the remaining distributions individually it is, perhaps, more pertinent to examine the main features in terms of the overall drag and lift coefficients. Figures 17 and 18 show contours of drag and lift coefficients, respectively, in terms of their variation with incidence angle and depth. It should be noted that these values are the integrated pressure data not taking into account the skin friction coefficient. It may be seen that the region of maximum drag occurs for cavities with depth, h/W , of between 0.4 and 0.5 at angles of between 45° and 60° . The lift coefficient data is quite interesting in that for nearly all the cases examined the base was subjected to an overall downward, or thrust, force. Overall lift was only present for some of the deeper cavities. The results show that the thrust is largely insensitive to

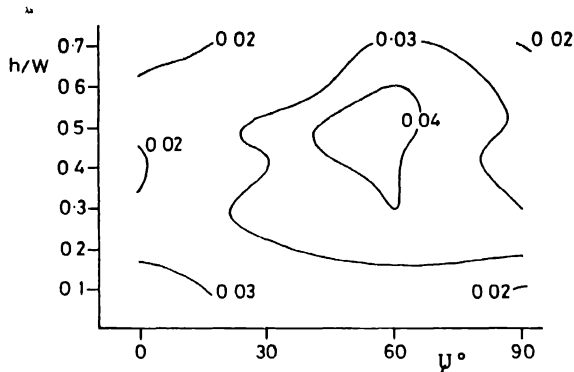


Fig. 17. Variation of drag coefficient with h/W and incidence angle.

changes in incidence angle up to 45° for cavities with h/W less than about 0.3. The larger regions of positive pressure that occur at 90° incidence generally result in higher thrusts at all depths when compared to the other angles.

The variation in drag increment, normalized by the skin friction coefficient with depth for the cavity at 0° incidence is shown in Fig. 19, together with some square planform cavity results and data from other workers. The coefficients shown here are from the pressure measurements. It may be seen that there is a great deal of scatter in both the present data and those from previous research. Nevertheless, there is good agreement between the 0° incidence data ($W/L=0.5$) and the 90° incidence data ($W/L=2$ in the notation for this figure) and the general trends are similar to those suggested by the design curve given in AGARD 264, Young and Paterson (1981). In addition, the drag of these rectangular cavities is consistently less than the equivalent square planform cavity. The rapid increase in drag with increase in depth for shallow cavities ($h/W < 0.1$) is reflected in the present data as is the subsequent slower decrease in drag at greater depths. Figure 20 shows the corresponding direct drag balance

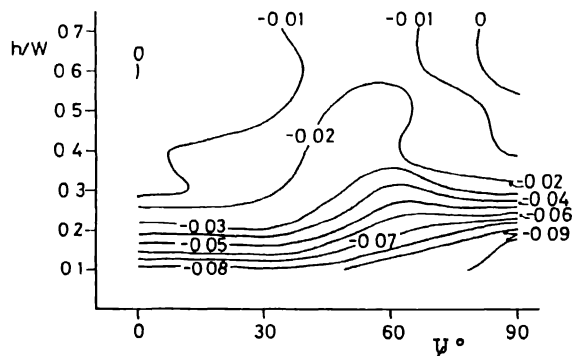


Fig. 18. Variation of lift coefficient with h/W and incidence angle.

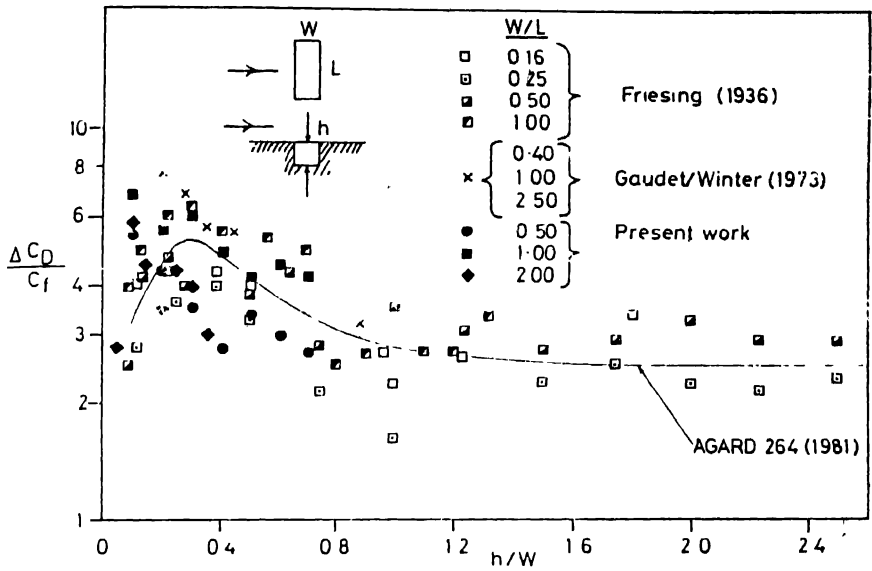


Fig. 19 Variation of normalized drag coefficient with h/W for 0° incidence (pressure data).

measurements which were omitted from the previous figure for clarity. It may be seen that there is good agreement with both the AGARD 264 design curve and with the higher Reynolds number data of Gaudet and Winter (1973). The drag balance results confirm that the rectangular cavity drag coefficient is slightly lower than that for the equivalent square cavity.

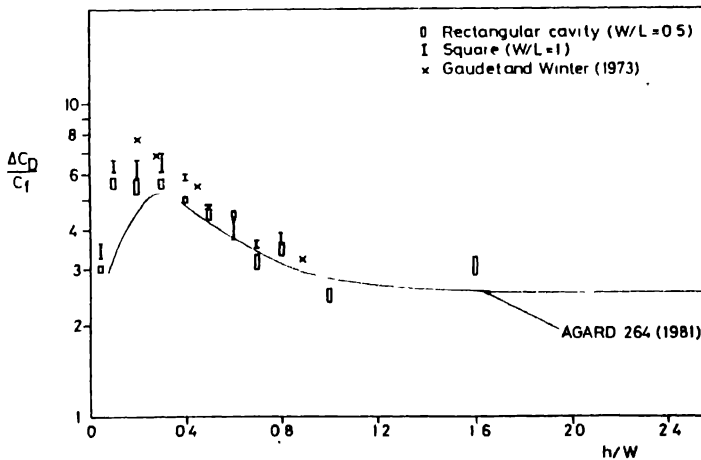


Fig. 20. Variation of normalized drag coefficient with h/W for 0° incidence (balance data).

4. Conclusions

With either the major or minor axis of the rectangular cavities aligned symmetrically to the freestream direction the pressure distribution on the base at all the depth/width ratios studied, showed remarkable lateral uniformity with no noticeable three-dimensionality. No evidence was found to indicate the presence of any cell-like structures within the cavities that had been observed by Maull and East (1963). With the shortest axis parallel to the flow direction the location of the dominating cavity vortex moved upstream and upwards with increasing depth, asymptoting to the location typically observed in two-dimensional rectangular cavity flows. This gradual vortex movement is not so evident when the cavity major axis is aligned parallel to the freestream direction. In terms of the overall net drag increments due to the cavity there is good agreement between the data obtained for these two axis alignments at any given depth/streamwise width ratio. There is also reasonable agreement with previously published data and the design curve given in AGARD 264, Young and Paterson (1981). The drag balance data shows good correlation with the high Reynolds number balance results obtained by Gaudet and Winter (1973).

The effect of yawing the cavity to the flow direction is to create asymmetric flow conditions within the cavity. At depth/width ratios between 0.4 and 0.5 for incidence angles between 45° and 60° this results in high overall drag coefficients. Once again, there is reasonably good agreement between integrated pressure distribution and direct force balance drag measurements. Considering the forces acting on the cavity base, it was found that for nearly all combinations of depth and incidence angle, except for some of the deepest cavities, the base experiences an overall thrust. This force is largely insensitive to changes in incidence angle up to 45° for cavities with $h/W < 0.3$.

The present work has produced a fairly substantial data set which should be of use in the development of improved design guidelines as well as aiding the development of numerical prediction models. Further work is being carried out, concerning the drag of cavities with circular and elliptical planforms, since these configurations exhibit different behaviour from the rectangular case discussed in this paper. Most notably, it is known that for a depth/diameter ratio of about 0.5 the circular cavity flow regime is strongly asymmetric, producing greatly increased drag.

The work described here has concerned cavities in two-dimensional boundary layers. However, in many practical applications the boundary layer will be three-dimensional and there is currently no data available to determine the influence of this three-dimensionality on the cavity flow field. In addition, modifications to the geometries of large rectangular cavities, such as bomb or cargo bays, may well reduce the overall aircraft drag, using techniques such as rounding or chamfering the downstream lip, as summarized by Hoerner (1965). Indeed, this approach is utilized in practice to eliminate unwanted flow oscillations associated with such aircraft cavities, as noted by Rizetta (1988). However, it is unlikely that such modifications to very small cavities would have any noticeable benefits in terms of the total aircraft drag.

Acknowledgements

This work was largely funded by the Department of Trade and Industry (UK) under Agreement No. 2064/120. The authors are indebted to Mr. L. Gaudet of the DRA (Aerospace Division, Bedford) for his support, advice and encouragement throughout the present work. We are also grateful to Mr. T. Markham of British Aerospace, Filton, for supporting the initial proposal regarding the present work. Thanks are also due to the technical staff at both the University of Surrey and the University of Cincinnati.

References

- Baysal, O. and Stallings, R.L., Computational and experimental investigation of cavity flow fields. *AIAA J.* 26 (1988) 6–7.
- Brandeis, J., Flow separation in shear layer driven cavities. *AIAA J.* 20 (1982) 908–914.
- Burggraf, O.R., Analytical and numerical studies of the structure of steady separated flows. *J Fluid Mech.* 24 (1966) 113–151.
- Donovan, L.F., A numerical solution of unsteady flow in a two-dimensional square cavity. *AIAA J.* 8 (1970) 524–529.
- Friesing, H., Measurement of the drag associated with recessed surfaces: cut-outs of rectangular and elliptical planform. *Z.W.B.F.B.* 628 (1936) (RAE Lib Trans 1614, 1971).
- Gaudet, L. and Winter K.G., Measurements of the drag of some characteristic aircraft excrescences immersed in turbulent boundary layers. *RAE Tech Memo Aero 1538* (1973) (also AGARD CP124, 1973).
- Hankey, W.L. and Shang, J.S., Analyses of pressure oscillations in an open cavity. *AIAA J.* 18 (1980) 892–898.
- Haugen, R.L. and Dhanak, A.M., Momentum transfer in turbulent separated flow past a rectangular cavity. *J. Applied Mech. (Trans ASME E)* 33 (1966) 641–646.
- Hoerner, S.F., *Fluid dynamic drag*, pp 5.10–5.11, published by author.
- Hunt, J.C.R., Abell, C.J., Peterka, J.A. and Woo, H., Kinematical studies of the flows around free or surface-mounted obstacles applying topology to flow visualisation. *J. Fluid Mech.* 86 (1978) 179–200.
- Kaufman, L.G. II, Maciulaitis, A. and Clark, R.L. Mach 0.6 to 3.0 flows over rectangular cavities, Air Force Wright Aero Lab Rept. AFWAL-TR-82-3112, May (1983).
- Mauil, D.J. and East, L.F., Three-dimensional flow in cavities. *J. Fluid Mech.* 16 (1963) 620–632.
- Mills, R.D., Numerical solutions of the viscous flow equations for a class of closed flows. *J. Royal Aero Soc.* 69 (1965) 714–718.
- Nallasamy, M. and Prasad, K.K., On cavity flow at high Reynolds numbers. *J. Fluid Mech.* 79 (1977) 391–414.
- Pan, F. and Acrivos, A., Steady flows in rectangular cavities. *J. Fluid Mech.* 28 (1967) 643–655.
- Plentovich, E.B., Three-dimensional cavity flows at subsonic and transonic speeds. NASA TM 4209, September (1990).
- Rizetta, D.P., Numerical simulation of supersonic flow over a three-dimensional cavity. *AIAA J* 26 (1988) 799–807.
- Roshko, A., Some measurements of flow in a rectangular cutout. *NACA TN* 3488, August (1955).
- Rossiter, J.E., Wind tunnel experiments on the flow over rectangular cavities at subsonic and transonic speeds. *ARC R & M* 3438, October (1964).
- Sinha, S.N., Gupta, A.K. and Oberai, M.M., Laminar separating flow over backsteps and cavities. Part II: Cavities. *AIAA J* 20 (1982) 370–375.
- Tani, I, Iuchi, M. and Komoda, H., Experimental investigation of flow separation associated with a step or groove. *Aero Res. Inst. Univ. of Tokyo, Res. Rep. No. 364* 119 (1961).

- Tillmann, W., Additional measurements of the drag of surface irregularities in turbulent boundary layers. *NACA TM 1299* (1951) (also: New resistance measurements with surface irregularities in the turbulent boundary layer. *Forschungshefte fur Schiffstechnik* 2 81–88 (BSRA Trans. 322), 1953).
- Wiegardt, K., Increase in turbulent frictional resistance caused by surface irregularities, Min. of Air Prod. R&T No. 103, Trans. of FB1563 (1946) (also in *Forschungshefte fur Schiffstechnik*, 2, 65–71 (BSRA Trans. No. 322, 1953).
- Young, A.D. and Paterson, J.H., *Aircraft Excrescence Drag*, NATO AGARD-264, J.L. Jones, ed. (1981).
- Zhang, X. and Edwards, J.A., Computational analysis of unsteady supersonic cavity flows driven by thick shear layers. *Aero J.* 92 (1988) 365–374.

Turbulence structure of dilute polymer and surfactant solutions in artificially roughened pipes

HANS-WERNER BEWERSDORFF¹ & HORST THIEL²

¹*Institute of Hydromechanics and Water Resources Management, Swiss Federal Institute of Technology, CH-8093 Zürich, Switzerland*

²*Department of Chemical Engineering, University of Dortmund, P.O. Box 500 500, D-4600 Dortmund 50, Germany*

Abstract. Pressure drop and velocity profile measurements are presented for turbulent flows of drag reducing fluids. The investigation was done in two rough pipes, known as "k"- and "d"-type rough pipes. The results are compared with those obtained in hydraulically smooth pipe of identical diameter. The spatial arrangement of the roughness elements in the pipe determines the parallel shift in the elastic sublayer and in the core region of the dimensionless turbulent velocity profile. The slopes of the velocity profiles in these regions remain unaffected by the arrangement which is an indication that the hydrodynamic influence of the roughness is restricted to the near-wall region. The drag reducing surfactant solution exhibited a drag reduction in the smooth as well as in the rough pipes which was higher than that given by Virk's maximum drag reduction asymptote. For this solution no influence of the roughness on the turbulence was detected when the dimensionless roughness height in viscous units was less than 12.

1. Introduction

Drag reduction obtained by the addition of soluble polymers or surfactants is well known for turbulent flows in smooth pipes. The state of the art is well documented in review articles [1–4] and recent conference proceedings [5–6]. However, only a few publications describe drag reduction in rough pipes. Lindgren and Hoot [7] first detected drag reduction for a 60 ppm Polyox solution in a rectangular channel with rough walls.

Due to the manufacturing process commercial (steel) pipes normally exhibit a certain roughness which is important for many industrial applications of drag reduction [8].

Although the mechanism of the interaction between the additives and the turbulence is still unknown it is generally accepted that the non-Newtonian rheological properties of the polymer or surfactant solution are responsible for the occurrence of drag reduction. Drag reducing polymer or surfactant solutions are viscoelastic fluids. In elongational fields, which exist in turbulent flows, the elongational viscosity of dilute polymer solutions can be increased considerably in comparison to that of the Newtonian solvent. This results in an additional resistance against vortex stretching and leads to a reduction of the energy dissipation.

The drag reduction in turbulent flows of polymer and surfactant solutions is accompanied by a change in the structure of turbulence, which can depend on the type of additive. In homogeneous dilute polymer solutions a so-called elastic sublayer

forms in the dimensionless velocity profile between the viscous sublayer and the turbulent core. This elastic sublayer increases in thickness with increasing drag reduction and at maximum drag reduction it reaches to the centre of the pipe or channel. No turbulent core then exists, and the friction behaviour is given by Virk's [1] empirical maximum drag reduction asymptote

$$f^{-1/2} = 19 \log(Re f^{1/2}) - 32.4. \quad (1)$$

Here, f means the Fanning friction factor defined by

$$f = \frac{2\tau_w}{\rho U^2}, \quad (2)$$

where τ_w is the wall shear stress, ρ the density of the fluid, and U the bulk velocity. The Reynolds number used in Eq. (1) is defined as

$$Re = \frac{Ud}{\nu}, \quad (3)$$

for a pipe flow, where d is the pipe diameter and ν the kinematic viscosity of the fluid.

In pipe and channel flows of drag reducing fluids the turbulence intensities are also affected. The maximum of the axial turbulence intensity is shifted to larger wall distances [9, 10], whereas the maximum of the radial turbulence intensity, which occurs in turbulent flows of Newtonian fluids at $y^+ = 50 - 70$, disappears [9, 10], i.e. the radial turbulence intensity now reaches its maximum in the centre of the pipe. Simultaneously a strong decrease of the radial turbulence intensity occurs [9, 10]. In the case of maximum drag reduction conditions according to Eq. (1), the axial turbulence intensity is also decreased [10]. Similarly the Reynolds shear stresses near the wall are also lower than in the Newtonian solvent [10-12]. In turbulent flows of drag reducing fluids the burst-sweep mechanism is modified. This mechanism plays a major role in the generation of the Reynolds shear stresses and is therefore important for the turbulent momentum transfer. It has been shown [13] that the burst frequency and intensity are affected in the case of drag reduction.

Previous studies on drag reduction in rough pipes mainly focus on the friction behaviour of polymer solutions. An extensive study on the friction behaviour of homogeneous polymer solutions in sand-roughened pipes was undertaken by Virk [14]. He used polymers of different molecular weights, and varied the polymer concentration, and the relative roughness d/k of the pipe, i.e. the ratio of the pipe diameter to the roughness height. The maximum drag reduction according to Eq. (1) could also be reached in rough pipes provided that the dimensionless roughness k^+ was less than 12, where

$$k^+ = \frac{ku_\tau}{\nu}. \quad (4)$$

In this equation u_τ is the friction velocity defined by

$$u_\tau = (\tau_w/\rho)^{1/2}. \quad (5)$$

In other words, at maximum drag reduction conditions the friction behaviour in rough pipe is identical to that in a hydraulically smooth pipe for $k^+ < 12$. When k^+ exceeds 12 the friction factor in rough pipes is larger than in smooth ones. Furthermore, Virk [12] showed that the onset of drag reduction occurred at the same wall shear stress in smooth and rough pipes. Up to a dimensionless roughness $k^+ = 50$, the drag reduction was identical in a smooth and a rough pipe at the same friction velocity u_τ . For $k^+ > 50$ the drag reduction in a rough pipe was lower than that found in a smooth pipe.

In general, the drag reduction in rough pipes exhibits a maximum at a certain Reynolds number. McNally [15] detected that the maximum drag reduction always occurred at the same friction velocity regardless of the polymer concentration. The decrease in drag reduction at high Reynolds numbers beyond the maximum was related to mechanical degradation of the polymers due to the influence of the roughness by Debrule and Sabersky [16], whereas Spangler [17] and Virk [14] found hydrodynamic effects to be responsible for the decrease. Spangler [17] mounted a smooth pipe downstream of the rough pipe, and measurements in the smooth pipe demonstrated that no degradation occurred. In the experiments of Virk [14] the pressure drop at Reynolds numbers above the maximum drag reduction remained nearly constant at a constant flow-rate in a closed loop after several runs, and did not increase as one would expect in case of mechanical degradation. It is the aim of the present investigation to study the influence of artificial roughnesses on the turbulence structure in dilute polymer and surfactant solutions.

2. Experimental

In experimental studies on the influence of roughnesses mainly artificially produced roughnesses are used. The advantage of this is that in this way the geometry of the artificial roughness elements is well-defined which allows a characterization of the influence of the roughness on the hydrodynamic behaviour. In commercial rough pipes a nonuniform distribution of roughness height and location of roughness elements on the pipe surface exists.

In the present study two commercially available PVC-pipes of an outer diameter of 63 mm with a wall thickness of 7 mm and a length of 16 m were used. On the inner surface of the pipes rectangular grooves were cut around the circumference normal to the flow direction. The spacing of the grooves in the flow direction was constant for each pipe. The dimensions of the roughness elements were identical in both pipes, however, the spacing of the roughness elements differed. The dimensions and the spacing of the roughness elements is shown in Fig. 1.

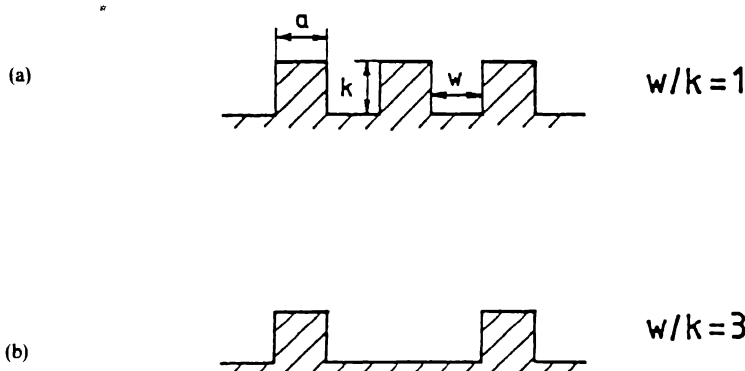


Fig. 1. Arrangements of the roughness elements. (a) "d"-type roughness; (b) "k"-type roughness.

The two arrangements of the roughness elements are essentially identical to those of Perry, Schofield and Joubert [18] who found that the different arrangements influenced a turbulent boundary layer in a different way. The terms "d"-type and "k"-type roughness are adopted in the present work. The dimensions of the two rough pipes are listed in Table 1. The average diameter d was calculated according to

$$d = \left(\frac{4V}{\pi L} \right)^{1/2}. \quad (6)$$

In order to do this the content in liters of a pipe segment of a length L was measured.

Due to manufacturing reasons only rough pipes of a length of approximately 0.3 m could be produced. Four of these pipes were glued together. By clamping 15 of these segments together, the total length of the test pipes became approximately 16 m. An exact check of the manufacturing process ensured that no nonuniformity occurred in the periodic spacing of the roughness elements. In addition, a hydraulically smooth perspex pipe of 16 m length and an internal diameter of 50 mm was used in order to compare the results for the rough pipes with those for a smooth pipe.

The experimental set-up is shown in Fig. 2. The water, the polymer or the surfactant solutions were pumped from a storage tank by moyno pumps. The temperature was recorded by a resistance thermometer. The flow rate was measured by an inductive

Table 1. Dimensions of the rough pipes.

Surface	a [mm]	k [mm]	w [mm]	d [mm]
"k"-type roughness	1	1	3	50.5
"d"-type roughness	1	1	1	50

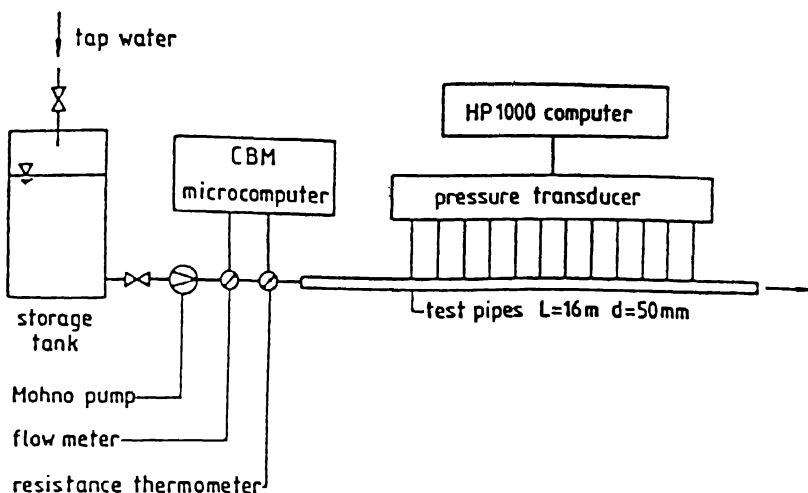


Fig 2 Experimental arrangement.

flowmeter (Fischer & Porter, model D10 DK1425) with an accuracy of $\pm 0.5\%$. For proper operation this inductive flowmeter requires a minimum electrical conductivity of $5 \mu\text{S}/\text{cm}$, a condition which was fulfilled in all experiments, because tap water or solutions of polymers or surfactants in tap water were used as test fluids. In order to determine the Reynolds number the two signals of the resistance thermometer and the inductive flowmeter were fed into a microcomputer. To measure the pressure drop, holes were drilled into the pipes. They were spaced at intervals of 100 cm in the smooth pipe and at 110 cm in the two rough pipes. According to Nunner [19] and Möbius [20] these holes were drilled in the centre between the adjacent roughness elements in order to avoid errors in the pressure drop experiments. The pressure drop between two taps was measured by differential pressure transducers (Philipps, model PD2 and Siemens, model Teleperm F). A connection of the outputs of the pressure transducers to a computer system enabled a direct analysis of the experimental data.

15 m downstream of the pipe inlet velocity profiles were measured by a DISA Laser-Doppler anemometer (LDA-module-optics 55x) working in the backscattering mode. The dimensions of the measuring volume were 0.5 mm in the long axis and 0.05 mm in the short axis with a fringe spacing of $5 \mu\text{m}$. In order to improve the quality of the Doppler-signal aluminium particles (particle size $3\text{--}10 \mu\text{m}$) were added at a concentration of 5–10 ppm. The Doppler-signals were sampled with a frequency of 100 Hz and fed into a computer system. The local averaged velocities result from averaging 5000 data points. By increasing the number of data points it was checked, that the mean values of the velocity did not change.

The polymer used was polyacrylamide, SEPARAN AP45 (tradename from Dow Chemical Company). According to the manufacturer [21] its molecular weight is $4\text{--}5 \cdot 10^6 \text{ g/mol}$. The polymer powder was first suspended in isopropanol and then

added to the desired amount of water. The solutions were stirred at low speed for 24 hours.

The surfactant solutions were produced by dissolving equimolar amounts of tetradecyltrimethylammoniumbromide ($C_{14}TABr$) and sodiumsalicylate ($NaSal$). In this way the surfactant tetradecyltrimethylammoniumsalicylate ($C_{14}TASal$) with an equimolar amount of sodiumbromide ($NaBr$) is obtained. Above a critical concentration the surfactant molecules assemble and build-up rod-like micelles which are necessary [22] to achieve drag reduction in turbulent flows.

3. Experimental results

As mentioned in Chapter 2 the two types of roughness elements interact with the near-wall turbulence in a different way. In a "k"-type roughness an extensive exchange of fluid between the grooves and the outer flow takes place, whereas in a "d"-type roughness stable vortices exist inside the grooves and the outer fluid flows nearly undisturbed over the top of the roughness elements [18]. Therefore it is expected that these two types of roughnesses exhibit a different effect on the friction behaviour and on the turbulent dimensionless velocity profiles. In Fig. 3 the friction behaviour of the two rough pipes is shown for water. For the smooth pipe the deviations from the

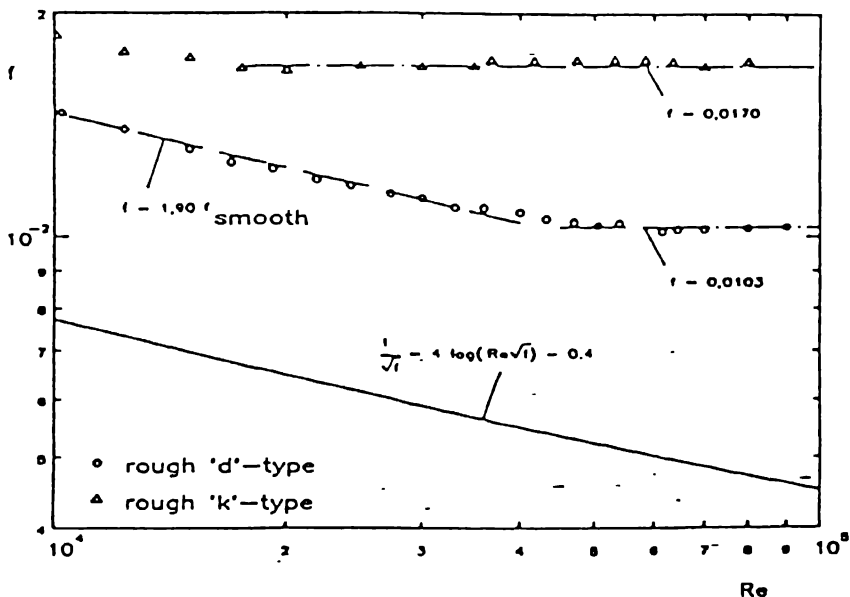


Fig. 3. Friction behaviour for a water flow in the rough pipes.

Prandtl-Kármán law

$$f^{-1/2} = 4 \log(Re f^{1/2}) - 0.4, \quad (7)$$

were found to be less than three percent in the Reynolds number range $15,000 < Re < 90,000$. The two types of artificial roughness have a different influence on the value of the friction factor and its dependence on the Reynolds number. The friction factors for the "k"-type roughness do not depend on the Reynolds number for $Re > 15,000$, i.e. the fully rough flow regime is reached. This type of friction behaviour can also be obtained for the "d"-type of roughness for $Re > 40,000$, but the friction factors are lower than those of the "k"-type roughness. In the Reynolds number interval $10,000 < Re < 40,000$ the friction behaviour for the "d"-type roughness is parallel to the Prandtl-Kármán law, Eq. (7). For $Re > 50,000$ the friction factors for the "d"-type rough pipe become also constant regardless of the Reynolds number which indicates that the fully rough flow regime is reached. In addition, it elucidates that the "d"-type rough pipe becomes a "k"-type rough pipe at high Reynolds numbers. Consequently, it shows that the type of roughness depends on w/k and on the Reynolds number.

According to Hopf [23] a friction behaviour which can be expressed by

$$f = \xi f_{\text{smooth}} \quad (8)$$

is characteristic for "wall ripples" where f_{smooth} means the friction factor in a smooth pipe. Morris [24] developed a similar friction law for so-called "quasi-smooth" flows.

In general, it is convenient to convert a given roughness to an equivalent sand roughness by inserting the measured friction factors in the empirical friction law of Nikuradse [25] for sand-type roughnesses in the fully rough flow regime

$$f^{-1/2} = 2.28 + 4 \log(d/k_s). \quad (9)$$

Equivalent sand roughnesses are listed in handbooks for commercial rough pipes of different materials. This simplifies the calculation of the pressure drop in pipelines in practical situations because convenient relationships, such as the Colebrook-White equation [26] or Eq. (9), can be used.

This normalization procedure allows for comparisons of measurements with published data for artificially rough pipes. By using Eq. (9) for the data of the fully rough flow regime, the "k"-type roughness gives an equivalent sand roughness of $k_s = 2.4 \text{ mm}$ ($k_s/k = 2.4$) and the "d"-type roughness gives $k_s = 0.64 \text{ mm}$ ($k_s/k = 0.64$).

Turbulent velocity profiles are normally presented in terms of wall variables with the nondimensional velocity

$$U^+ = \frac{\bar{u}}{u_\tau} \quad (10)$$

plotted versus the logarithm of a dimensionless wall distance

$$y^+ = \frac{y u_\tau}{\nu} \quad (11)$$

where \bar{u} is the time-averaged local velocity and y the wall distance. According to Schlichting [27] turbulent velocity profiles of Newtonian fluids in a smooth pipe can be divided into three regions. Close to the wall ($y^+ < 5$) a viscous sublayer exists with

$$U^+ = y^+. \quad (12)$$

In this region viscous forces are dominating. With increasing wall distance the Reynolds stresses become important and in the buffer layer ($5 < y^+ < 30$) the Reynolds stresses are of the same order of magnitude as the viscous stresses. For $y^+ > 30$ the Reynolds stresses are dominating and the velocity profile is given by

$$U^+ = A \ln y^+ + B \quad (13)$$

where the universal constants A and B are determined from experiments to be $A = 2.5$ and $B = 5.5$. Figure 4 shows dimensionless velocity profiles of a turbulent flow of water in a smooth pipe at two Reynolds numbers.

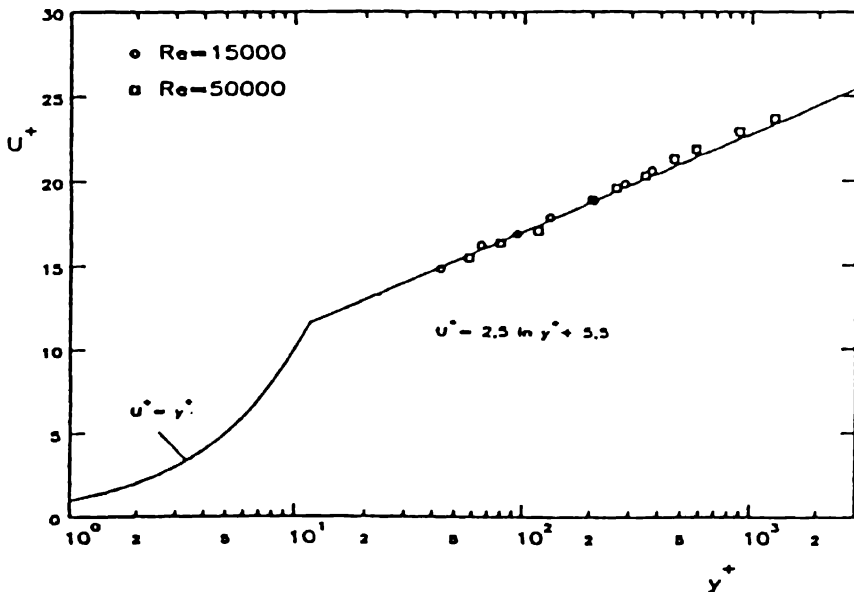


Fig. 4. Dimensionless turbulent velocity profiles for water in a smooth pipe.

Due to the signal/noise ratio of the Doppler-signal the data for the near-wall region have been omitted. For $y^+ > 40$ the data exhibit only small deviations from Eq. (13) with the constants given above, which shows the accuracy of the LDA-measurements.

In turbulent flows over a rough wall the logarithmic region is shifted parallel to the one for smooth walls but the dimensionless velocities are lower in comparison to Eq. (13). Consequently, this logarithmic region can be described by

$$U^+ = A \ln y^+ + B - \Delta u/u_\tau \quad (14)$$

with the constants A and B given above [28]. $\Delta u/u_\tau$ is called the roughness function. Besides the magnitude of the parallel shift of the logarithmic layer it provides, according to Bandhyopadhyay [29], the increased friction due to the surface roughness in comparison to a smooth wall.

In a study with turbulent flows over extreme roughnesses Einstein and El-Samni [30] found that a logarithmic relationship according to Eq. (14) only exist when the origin of the velocity profile, i.e. the location where the wall distance $y = 0$, is located between the top and the foot of the roughness element. Clauser [31] proposed a method for estimating the origin of turbulent velocity profiles over roughness elements (see Fig. 5). The dimensionless velocities U^+ are plotted as a function of the logarithm of the wall distance

$$y = y_T + e. \quad (15)$$

Different values of e influence the slope of the logarithmic region of the velocity profile. In order to normalize the velocity profiles the value of e is generally adopted which results in a slope of $A = 2.5$ in the logarithmic layer. The literature provides values for e for "k"-type roughnesses with $w/k = 3$ as $e = 0.7 k$ [32] and $e = 0.8 k$ [33]. In the present investigation a value of the "k"-type roughness a value of $e = 0.75 k$ was used to normalize the velocity profiles. For the "d"-type roughness a value of $e = 0.5 k$ is used [29].

Dimensionless velocity profiles for turbulent flows of water over the two types of roughnesses are shown in Figs 6 and 7.

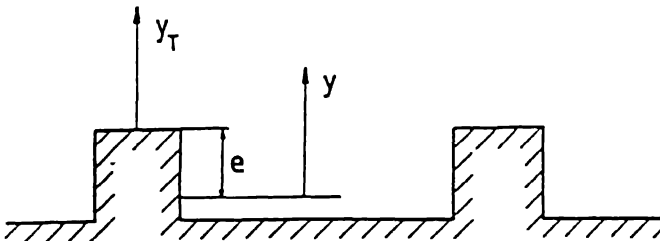


Fig. 5. Origin of the wall distance on rough surfaces.

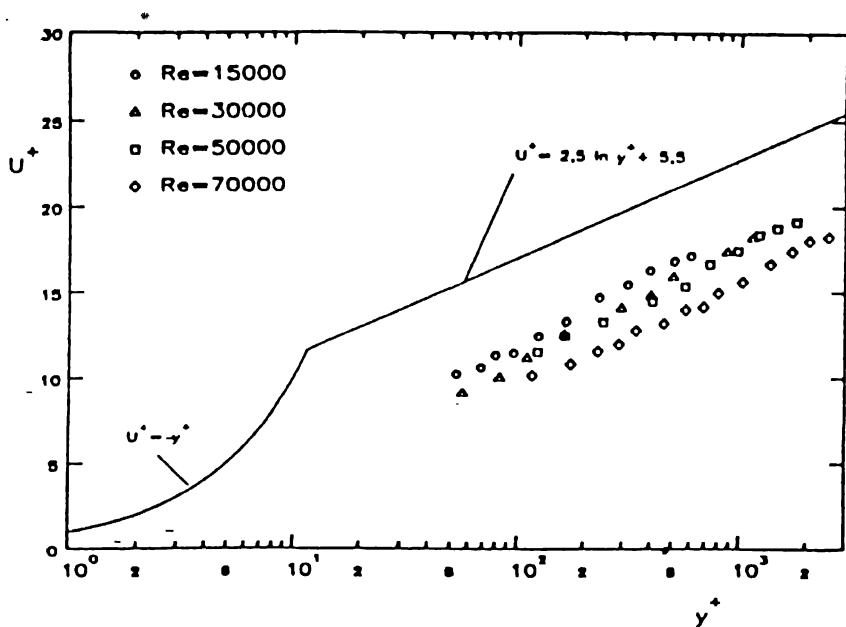


Fig. 6. Dimensionless velocity profile of a turbulent flow of water in the "d"-type rough pipe.

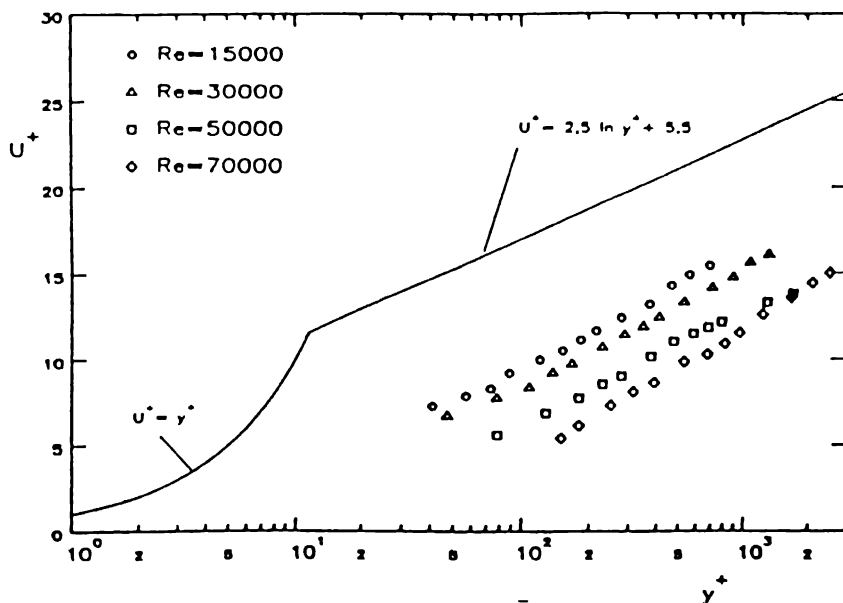


Fig. 7. Dimensionless velocity profile of a turbulent flow of water in the "k"-type rough pipe.

Depending on the type of roughness and the Reynolds number the logarithmic layers have been shifted to lower dimensionless velocities in comparison to a smooth pipe. Table 2 provides the constants A and B according to Eq. (13) and the dimensionless roughness k^+ according to Eq. (4). Using the constants A and B of Table 2 the roughness function $\Delta u/u_\tau$ can be calculated according to Eq. (14) from the measured velocity profiles. Furthermore, it also can be calculated from the friction behaviour to

$$\Delta u/u_\tau = (2/f_{\text{smooth}})^{1/2} - (2/f_{\text{rough}})^{1/2} \quad (16)$$

where f_{smooth} and f_{rough} have to be taken at identical friction velocities [29]. Figure 8 shows the calculated roughness functions as a function of the dimensionless roughness.

The band width of the data of the roughness function originating from the velocity profiles results from the deviations in the slope of the velocity profiles from $A = 2.5$ (see Table 2). A comparison of these data with those calculated from the friction behaviour by using Eq. (16) gives a rather good agreement. At the same dimensionless roughness the roughness function for the "k"-type roughness is generally larger than that of the "d"-type roughness.

Perry and Joubert [33] give for $w/k = 3$ the equation

$$\Delta u/u_\tau = 5.6 \log k^+ - 0.2 \quad (17)$$

for $100 < k^+ < 700$ which is based on their own measurements and on the data of Moore [32]. The data resulting from this equation are added as a solid line in Fig. 8. The deviations from the measured data of the present work are small. For a "d"-type roughness equations similar to Eq. (17) do not exist.

Table 2 Constants A and B of the velocity profile and dimensionless roughness height

Surface	Re	A	B	k^+
Smooth	15,000	2.7	4.3	—
	50,000	2.8	4.1	—
"d"-type rough	15,000	2.9	-1.2	24
	30,000	3	-3.2	48
	50,000	2.9	-2.7	77
	70,000	2.8	-3.6	106
"k"-type rough	15,000	3	-4.2	29
	30,000	2.9	-5	54
	50,000	2.8	-6.5	90
	70,000	3.3	-11.2	126

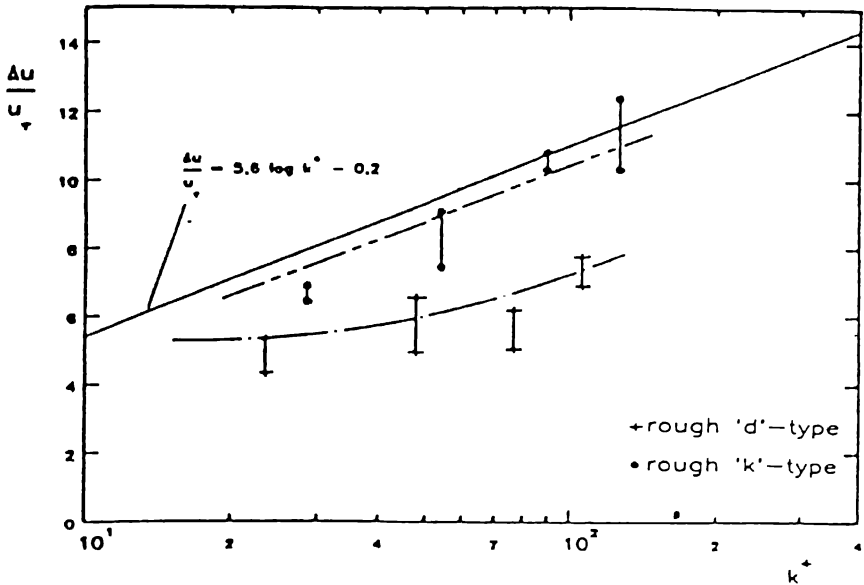


Fig. 8. Roughness function as a function of the dimensionless roughness data points: calculated from the measured velocity profiles by using Eq. (14) broken lines: calculated from the friction behaviour by using Eq. (16).

The friction behaviour of a solution of Separan AP45 at $c = 20$ ppm in the two rough pipes and in the smooth pipe is shown in Fig. 9.

The different surface finish of the test pipes influences the wall shear stress at onset conditions as well as the magnitude of drag reduction. When the friction curves of the polymer solution in the different pipes are extrapolated to those of the solvent it becomes evident that the onset is shifted to higher wall shear stresses with increasing influence of the roughness ($Re\{f\}_{smooth}^{1/2} = 270$; $Re\{f\}_{d'-type}^{1/2} = 1,720$; $Re\{f\}_{k'-type}^{1/2} = 2,500$). This is accompanied by a decrease of the magnitude of attainable drag reduction DR (see Fig. 10), which is defined as $DR = 1 - f_s/f_N$ where f_s is the friction factor of the polymer or surfactant solution and f_N the friction factor of the Newtonian solvent, both measured at the same flow-rate.

In the "k"-type rough pipe the drag reduction appears to reach a constant value at high friction velocities which would be consistent with a fully rough flow regime. This trend was also observed in [34]. A lower drag reduction in rough pipes in comparison to smooth pipes was also observed by McNally [15] and Ivanyuta and Chekalova [35]. However, this is in contrast to the findings of [14] and [34] where no influence of the surface finish on the magnitude of drag reduction and the onset-point was detected provided that k_s^+ is lower than about 50. Possible explanations for these discrepancies may be the type of roughness or the smaller diameters in the earlier studies ($d = 8.5$ mm in [14] and $d = 30.7$ mm in [34]).

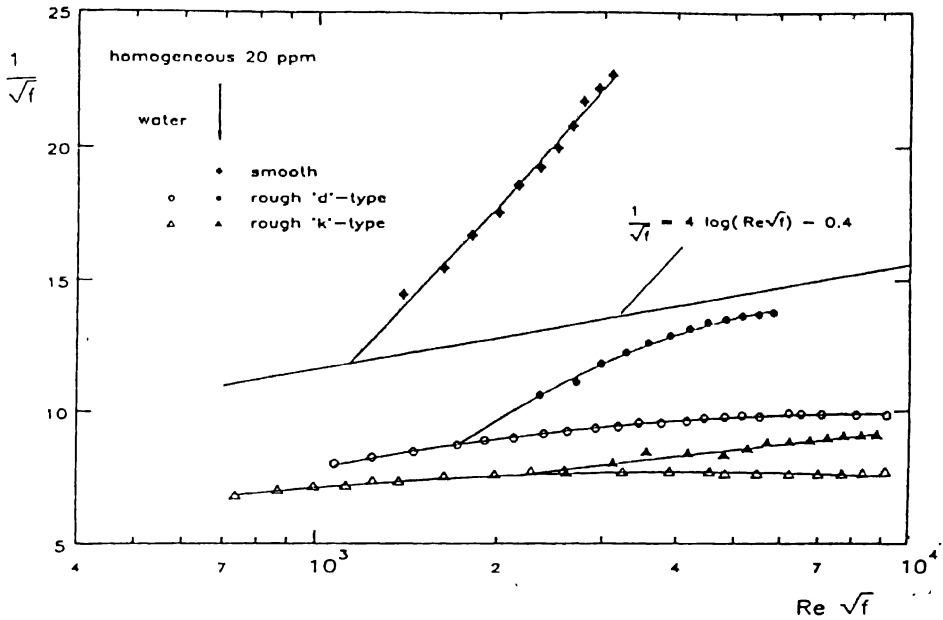


Fig. 9. Friction behaviour of a homogeneous polymer solution at $c = 20$ ppm in Prandtl-Kármán coordinates.

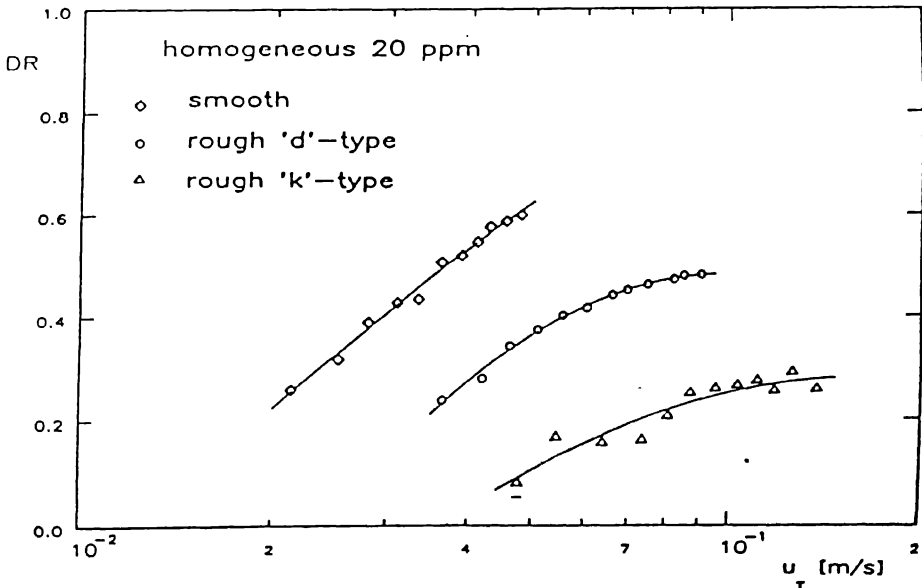


Fig. 10. Drag reduction as a function of the friction velocity for a homogeneous polymer solution.

The drag reduction in homogeneous polymer solutions is accompanied by a change in the shape of the turbulent velocity profiles. For turbulent velocity profiles in homogeneous dilute drag reducing polymer solutions the three-layer-model of Virk [1] gives satisfactory results. The viscous sublayer near the wall, Eq. (12), seems to remain unchanged in comparison to a Newtonian fluid. Further away from the wall instead of the buffer layer, a new layer, a so-called elastic sublayer, forms, in which

$$U^+ = 11.7 \ln y^+ - 17 \quad (18)$$

which is also called Virk's [1] ultimate profile. In the core region the velocity profile exhibits a parallel shift to higher dimensionless velocities

$$U^+ = 2.5 \ln y^+ + 5.5 + \Delta B. \quad (19)$$

Hendricks et al. [36] first published velocity profile measurements of a drag reducing polymer solution in a rough channel flow. Their results are replotted in Fig. 11.

In the dimensionless velocity profile two regions can be distinguished. In the elastic sublayer their velocity data in the hydrodynamic smooth channel are well represented by Virk's ultimate profile, Eq. (18), while Eq. (19) applies in the core region. In the

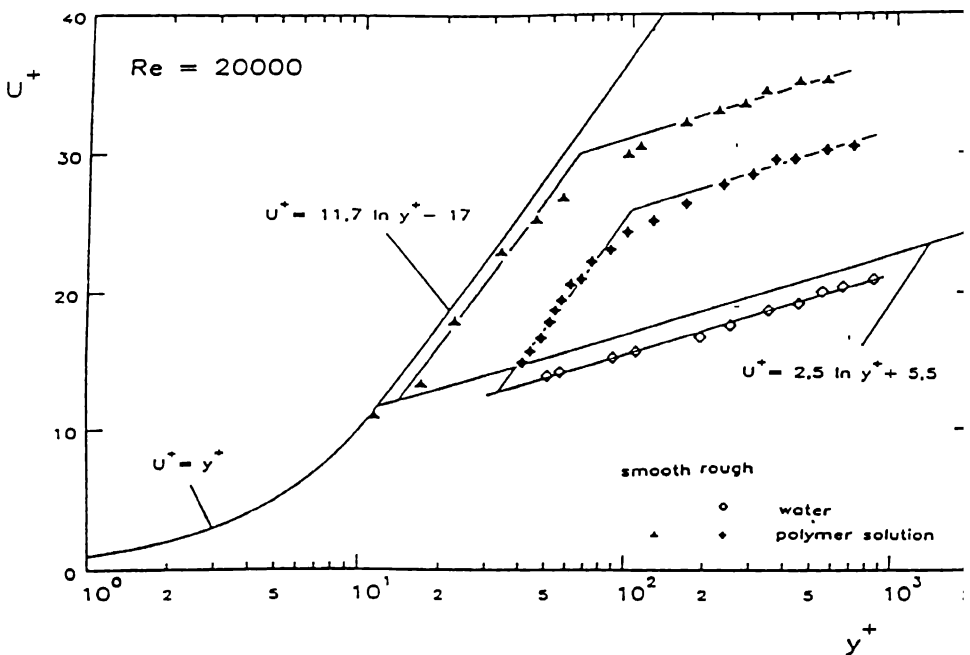


Fig. 11. Dimensionless turbulent velocity profiles of a polymer solution in a smooth and in a rough channel flow (60 ppm Polyox WSR 301, from [36]).

rough channel flow both regions of the velocity profile have been shifted to lower dimensionless velocity values. The data in the elastic sublayer follow

$$U^+ = 11.7 \ln y^+ - 17 + \Delta u_e/u_\tau \quad (20)$$

and in the turbulent core region

$$U^+ = 2.5 \ln y^+ + 5.5 + \Delta B - \Delta u/u_\tau. \quad (21)$$

The roughness functions $\Delta u_e/u_\tau$ and $\Delta u/u_\tau$ describe the parallel shift of the profiles in smooth pipes [Eqs. (18) and (19)] due to the hydrodynamic influence of the roughness. Figures 12 and 13 show the velocity profile measured in the smooth and in the two rough pipes at two Reynolds numbers. Due to the poor quality of the Doppler signal in the near-wall region it was only possible to obtain velocity data in the core region. Therefore, the existence of an elastic sublayer according to Eq. (20) could not be verified experimentally. In comparison to the Newtonian water data the dimensionless velocity data of the drag reducing polymer solution are shifted to higher dimensionless velocities. The data from the smooth pipe can be approximated by Eq. (21). The magnitude of drag reduction, which decreases from smooth via "d"-type rough to "k"-type rough, is reflected in the magnitude of ΔB .

Before turning to the results of the drag reducing surfactant solution it is essential to consider the rheological behaviour of these solutions which differs from that of drag

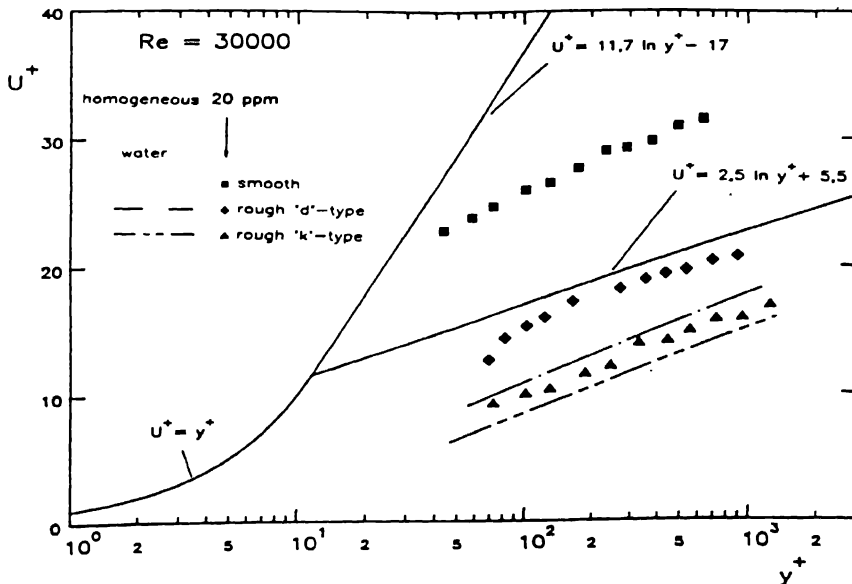


Fig. 12. Dimensionless velocity profiles of a homogeneous dilute polymer solution at $Re = 30,000$.

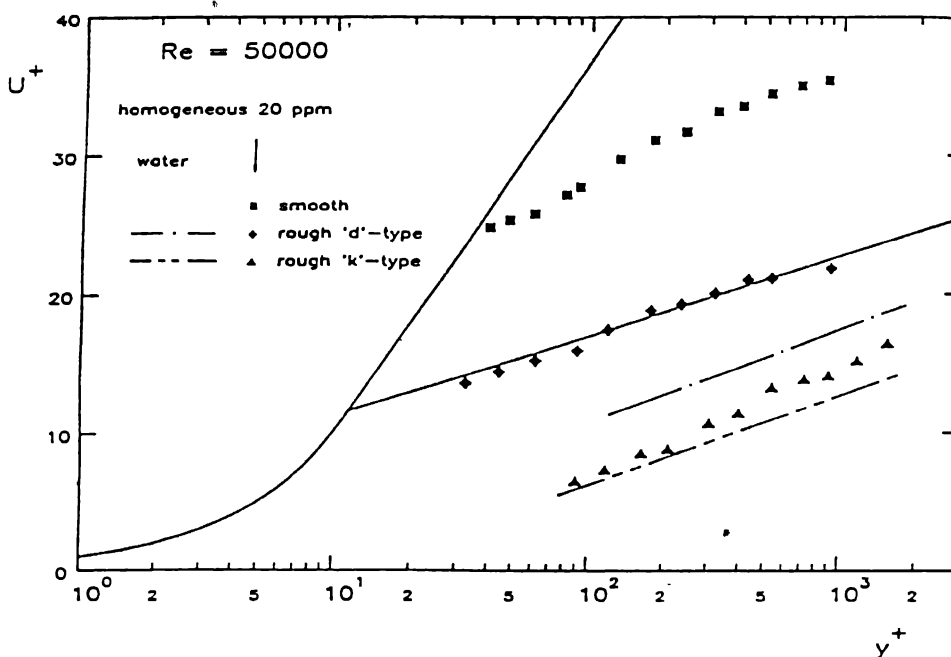


Fig. 13. Dimensionless velocity profile of a homogeneous dilute polymer solution at $Re = 50,000$.

reducing polymer solutions. In the experiments a C_{14} TASal-solution (see section 2) was used as a test fluid at a concentration of $c = 945$ ppm. Figure 14 shows the behaviour of the shear viscosity η as a function of the shear rate D for such a solution. The measurements were done with a Bohlin VOR-rheometer (measuring system CS). In the shear rate range $D < 100 \text{ s}^{-1}$ the solution behaves as a Newtonian fluid. Due to the concentration of dissolved surfactants the shear viscosity is slightly increased in comparison to the solvent.

In the shear rate range $100 \text{ s}^{-1} < D < 300 \text{ s}^{-1}$ the shear viscosity increases suddenly. This phenomenon is called shear induced state, SIS. In [22] this behaviour is explained by the formation of superordered structures which consist of single rod-like micelles. The shear rate at which the SIS occurs depends on the surfactant concentration, any additional electrolyte concentration, the temperature, and, surprisingly, on the geometry of the viscometer [22, 37], e.g. on the gap width of a Couette viscometer [37, 38]. This is also an indication that the size of the superordered structures in the SIS is of the order of magnitude of the gap width [37, 38].

In a rheological study on the behaviour of drag reducing surfactant solutions in elongational fields [39] an increase of the elongational viscosity in comparison to that of the solvent was detected. This increase occurred analogously to the increase of the shear viscosity in the SIS. When the Trouton ratio (elongational/shear viscosity) was

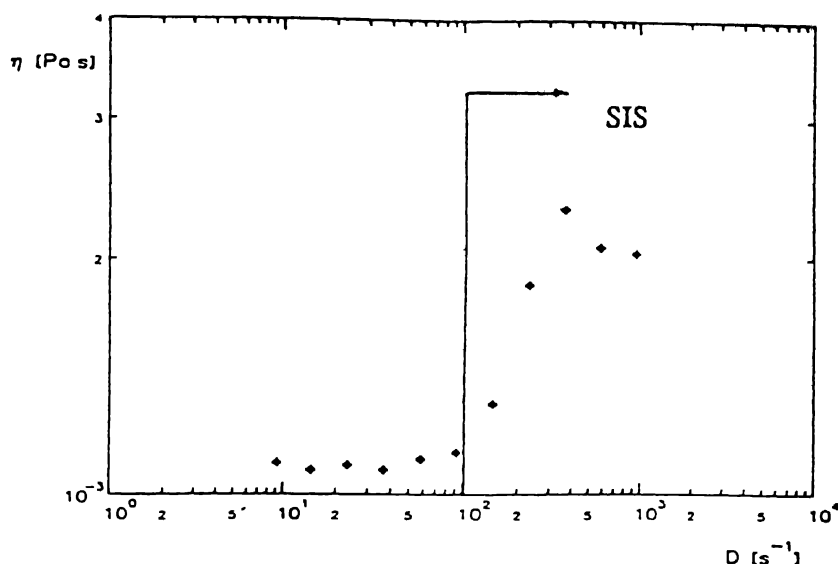


Fig. 14. Shear viscosity of C_{14} TASal-solution at $c = 945$ ppm and $T = 21^\circ C$.

calculated a value of three was obtained in the whole range of studied strain rates. In the same study this Trouton ratio was increased for drag reducing polymer solutions. Therefore it seems that the increase in elongational viscosity of drag reducing surfactant solutions plays a minor role for the mechanism of drag reduction.

One of the advantages of using surfactants as drag reducers instead of polymers is that a high drag reduction can also be obtained in large pipes. Figure 15 shows the friction behaviour of the C_{14} TASal-solution at $c = 945$ ppm in the three different pipes. The Reynolds number is based on the solvent viscosity.

In all pipes the surfactant solution exhibits drag reduction, and, surprisingly, in all pipes Virk's [1] maximum drag reduction asymptote is exceeded. In the studied Reynolds number range the friction behaviour can be divided into different regimes depending on the surface finish of the pipes. For $Re < 30,000$ the surface finish has no influence on the friction behaviour. Starting at $Re = 30,000$ the friction factors in the rough pipes are increased in comparison to the smooth pipe, and for $Re > 50,000$ the type of roughness also influences the friction behaviour. In the "k"-type rough pipe the friction factors then increase with the Reynolds number and approach a nearly constant value at $Re > 75,000$. At high Reynolds numbers, therefore, the surface finish has a similar influence on the friction behaviour as it was found for water and the dilute polymer solution. In small angle neutron scattering experiments [40, 41] it was found that a nearly complete alignment of the rod-like micelles in flow direction is responsible for the high drag reduction.

Due to the occurrence of the high drag reduction the question arises whether the

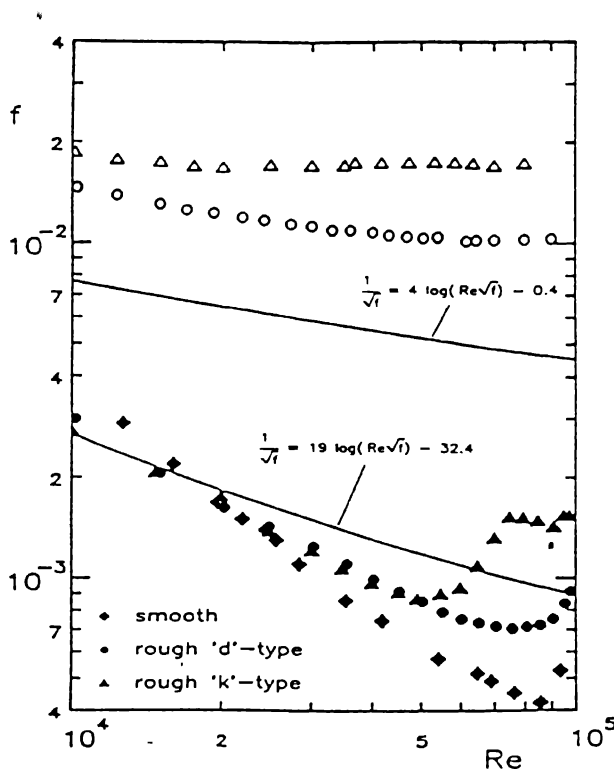


Fig. 15. Friction behaviour of a C_{14} TASal-solution at $c = 945$ ppm and $T = 21^\circ\text{C}$; open symbols: water; full symbols: surfactant solution.

flow of these surfactant solutions is turbulent or laminar, because when the Reynolds number would be calculated with a shear viscosity of $1.7\text{ mPa}\cdot\text{s}$ the data at low Reynolds numbers would fall on Hagen-Poiseuille's law ($f = 16/Re$). In the SIS this value of the shear viscosity is exceeded. The question can be answered by analyzing measured velocity profiles. Therefore in the plots of the velocity profiles of the surfactant solutions the line of a laminar velocity profile has been added. In dimensionless form using U^+ and y^+ the expression for a laminar velocity profile of a pipe flow becomes

$$U^+ = y^+ - \frac{y^{+2}}{(8 Re)^{1/2}}. \quad (22)$$

In this equation y^+ is based on the solvent viscosity. As shown in Fig. 16 the velocity data of the surfactant solution fall between Virk's ultimate profile, Eq. (18), and a laminar profile, Eq. (22). The measured velocity profiles at $Re = 50,000$ elucidate that the different spacing of the roughness elements has no hydrodynamic influence on the

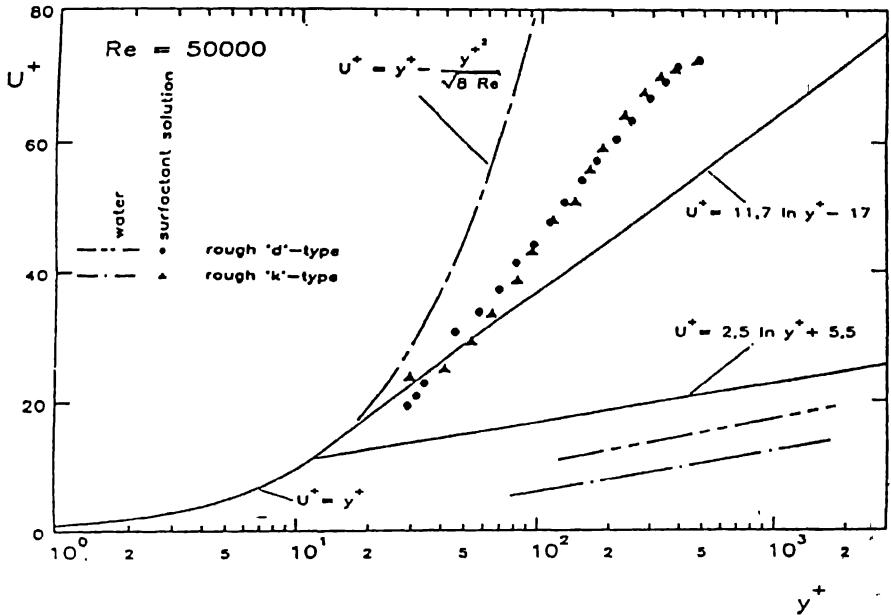


Fig. 16. Dimensionless velocity profiles of a C_{14} TASal-solution at $c = 945$ ppm and $T = 21^\circ\text{C}$.

flow of the surfactant solution. The velocity profiles which are identical for both types of roughness element spacings can be approximated by a logarithmic expression, Eq. (13), with a slope of $A = 19.5$. This is an indication of a turbulent flow. Another indication of this is the occurrence of velocity fluctuations in the LDA-signal of the axial velocity component. The velocity data elucidate that the turbulence structure is changed in the whole cross-section of the pipe in comparison to a Newtonian fluid.

In Fig. 17 two velocity profiles obtained in the "k"-type rough pipe are presented.

In the "k"-type rough pipe the friction factor is higher at $Re = 80,000$ than that at $Re = 50,000$ (see Fig. 15). The slope of both velocity profiles are identical in the whole range of wall distances. Therefore the increase of the friction factor in the "k"-type rough pipe can be related to the hydrodynamic influence of the roughness in the near-wall region.

When in the "k"-type rough pipe the surfactant concentration is lowered, velocity profiles are obtained which can be divided in two regions. The two slopes are identical with that of Virk's [1] ultimate profile ($A = 11.7$) and that of a turbulent core ($A = 2.5$). These two velocity profiles are similar to those of Hendricks et al. [36], see Fig. 11. They make it evident that the hydrodynamic influence of the roughness elements on the near-wall turbulence produces a parallel shift of the velocity profiles to lower dimensionless velocity values.

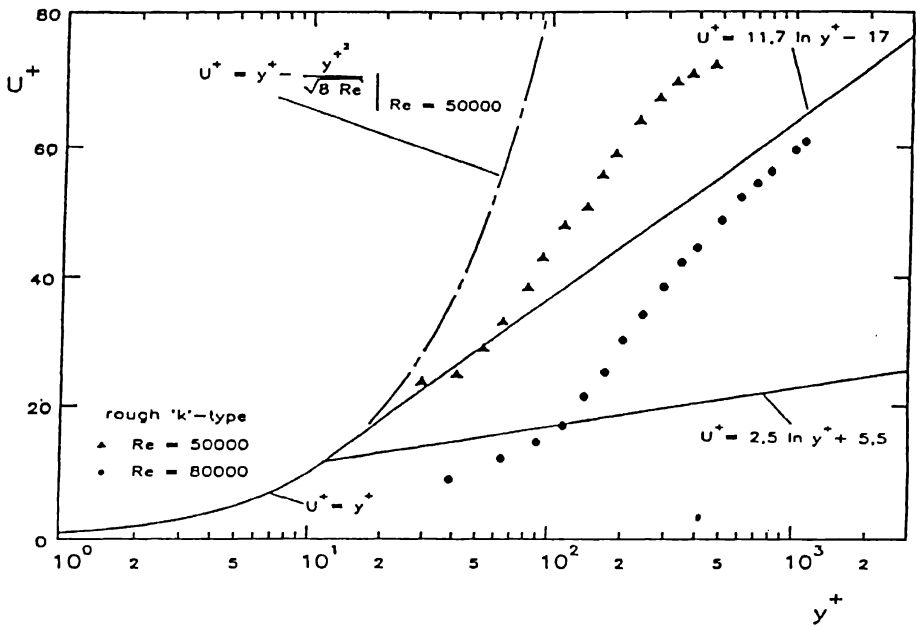


Fig. 17. Dimensionless velocity profiles of a C_{14} TASal-solution at $c = 945$ ppm and $T = 21^\circ\text{C}$.

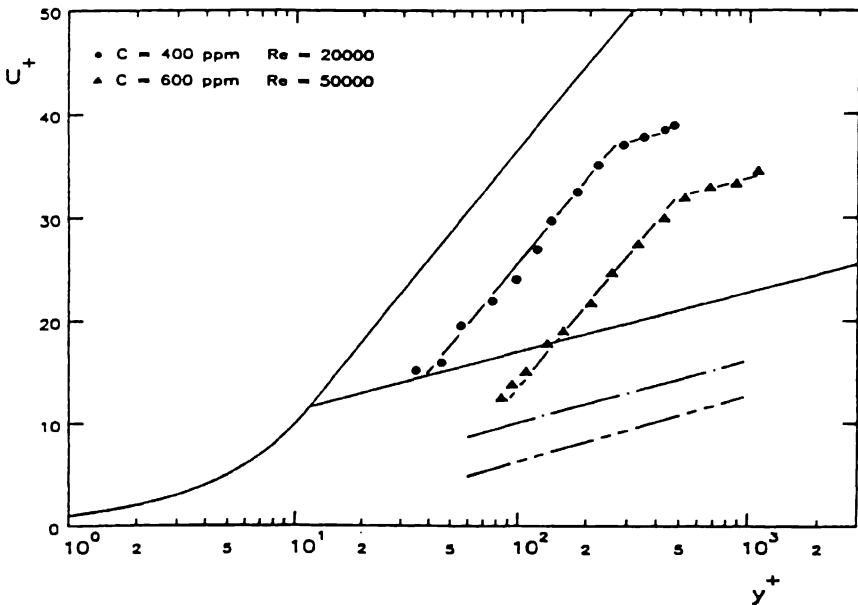


Fig. 18. Dimensionless velocity profile of a C_{14} TASal-solution in a "k"-type rough pipe at $T = 19.5^\circ\text{C}$.

4. Conclusions

Experimental data are presented on the friction behaviour of dilute drag-reducing polymer and surfactant solutions in a smooth, a "d"-type, and a "k"-type rough pipe. They elucidate that the achievable drag reduction significantly depends on the pipe wall geometry, the Reynolds number, and the additive concentration. For dilute polymer solutions the drag reduction in a smooth pipe is significantly higher than in a rough pipe at the same flow-rate or friction velocity. The onset-point of drag reduction is shifted to higher wall shear stresses with increasing influence of the roughness. In addition, in dilute polymer solutions the maximum attainable drag reduction decreases with increasing influence of the roughness. In the "k"-type rough pipe the friction factor becomes constant at high wall shear stresses designating a fully rough flow regime, a tendency, which already was observed in an earlier study [34].

Since the slopes of the dimensionless velocity profiles were not affected by the surface finish it can be concluded that the changes in the structure of turbulence in drag reducing fluids are not influenced by the roughness for $y^+ > 50$. The surface finish has only an influence on the near-wall region of the flow. Therefore, the influence of the roughness elements is responsible for the negative parallel shift of the dimensionless velocities in the core region and in the elastic sublayer. This is a strong indication that essential features of the turbulent structures in the near-wall region are also determined by the characteristics of the surface finish in drag reducing fluids.

The coherent structures of turbulence close to rough walls exhibit similarities with those occurring close to hydraulically smooth walls for flows of Newtonian fluids [42–45]. Near rough walls a burst-sweep cycle also occurs, but the burst frequency and the momentum transport per burst event are different than for a smooth wall [42, 43].

In the flow of the surfactant solution friction factors were measured which were lower than Virk's [1] maximum drag reduction asymptote. At low Reynolds numbers ($Re < 30,000$) there was no influence of the surface finish on drag reduction. This result is in agreement with a result by Virk [14] who found an identical friction behaviour in smooth and rough pipes provided that $k^+ < 12$. In the present experiments this holds for $Re < 30,000$. In the region where the drag reduction exceeds Virk's maximum drag reduction asymptote the flow is turbulent. The measured velocity profiles show that in this region a logarithmic layer, similar to Virk's [1] ultimate profile, reaches the centre of the pipe and that the slope of this velocity profile is increased in comparison to Virk's [1] ultimate profile.

Acknowledgement

The authors thank the Deutsche Forschungsgemeinschaft (DFG) for supporting this work by research grant Gi 83/9.

References

1. Virk, P.S., *AIChE J.* 21 (1975) 625.
2. Giesekus, H., Bewersdorff, H.W., Frings, B., Hibberd, M., Kleinecke, K., Kwade, M. and Schröder, R., *Fortschr. Verfahrenstechnik* 23 (1985) 3.
3. Giesekus, H. and Hibberd, M.F., In: Majumdar, A.S. and Mashelkar, R.A., (eds), *Advances in Transport Processes*, Vol. V. New Dehli: Wiley Eastern (1987) p. 229.
4. Shenoy, A.V., *Colloid & Polymer Sci.* 262 (1984) 319.
5. Sellin, R.H.J. and Moses, R.T., *Drag Reduction in Fluid Flows*. Chichester: Ellis Horwood (1989).
6. Gyr, A., *Structure of Turbulence and Drag Reduction*. Berlin: Springer Verlag (1990).
7. Lindgren, E.R. and Hoot, T.G., *Trans. ASME, J. Appl. Mech.* 35 (1968) 417.
8. Sellin, R.H.J., Hoyt, J.W., Pollert, J. and Scrivener, O., *J. Hydraulic Res.* 20 (1982) 235.
9. Mizushima, T. and Usui, H., *Phys. Fluids* 20 (1977) S100.
10. Schümmer, P. and Thielen, W., *Chem Eng. Commun.* 4 (1981) 593.
11. Schmid, A., In: Sellin, R.H.J. and Moses, R.T. (eds), *Drag Reduction*. Bristol: University of Bristol (1984) paper B12.
12. Willmarth, W.W., Wei, T. and Lee, C.O., *Phys. Fluids* 30 (1987) 933.
13. Tiederman, W.G., Luchik, T.S. and Bogard, D.G., *J. Fluid Mech.* 156 (1985) 419.
14. Virk, P.S., *J. Fluid Mech.* 45 (1971) 225.
15. McNally, W.A., Ph.D. Thesis, University of Rhode Island, U.S.A. (1968).
16. Debrule, P. M. and Sabersky, R.H., *Int. J. Heat Mass Transfer* 17 (1974) 529.
17. Spangler, J.G., In: Wells, C.S. (ed.), *Viscous Drag Reduction*. New York: Plenum Press (1969) p. 131.
18. Perry, A.E., Schofield, H.W. and Joubert, P.N., *J. Fluid Mech.* 37 (1969) 383.
19. Nunner, W., *VDI-Forschungsheft* 455 (1956).
20. Möbius, H., *Physikalische Zeitschrift* 41 (1940) 202.
21. Product specifications, Dow Chemical Company.
22. Bewersdorff, H.W. and Ohlendorf, D., *Colloid & Polymer Sci.* 266 (1988) 941.
23. Hopf, L., *ZAMM* 3 (1923) 329.
24. Morris, H.M., *Trans. ASCE* 120 (1955) 373.
25. Nikuradse, J., *VDI-Forschungsheft* 361 (1933).
26. Colebrook, C.F. and White, C.M., *Proc. Royal Soc. London, Ser. A*, 161 (1937) 367.
27. Schlichting, H., *Grenzschicht-Theorie*. Karlsruhe: G. Braun (1965).
28. Hama, F.R., *Trans. Soc. Naval Archit. Marine Engrs.* 62 (1954) 333.
29. Bandhyopadhyay, P.R., *J. Fluid Mech.* 180 (1987) 231.
30. Einstein, H.A. and El-Samni, E.A., *Rev. Mod. Phys.* 21 (1949) 520.
31. Clauser, F.H., In: *Advances in Applied Mechanics*, Vol. 4. New York: Academic Press (1956) p. 1.
32. Moore, W.L., Ph.D. Thesis, University of Iowa, U.S.A. (1951).
33. Perry, A.E. and Joubert, P.N., *J. Fluid Mech.* 17 (1963) 193.
34. Bewersdorff, H.W. and Petersmann, A., *Chem Eng. Commun.* 60 (1987) 130.
35. Ivanyuta, Y.F. and Chekalova, L.A., *J. Eng. Phys.* 31 (1974) 891.
36. Hendricks, E.W., Swearingen, J.D., Horne, M.P. and Lawler, J.V., *AIAA paper* 88-3667 (1988).
37. Ohlendorf, D., Interthal, W. and Hoffmann, H., *Rheol. Acta* 25 (1986) 468.
38. Wunderlich, A.M. and Brunn, P.O., *Colloid & Polymer Sci.* 267 (1989) 289.
39. Vissmann, K. and Bewersdorff, H.W., *J. Non-Newtonian Fluid Mech.* 34 (1990) 289.
40. Lindner, P., Bewersdorff, H.W., Heen, R., Sittart, P., Thiel, H., Langowski, J. and Oberthür, R., *Progr. Colloid & Polymer Sci.* 81 (1990) 107.
41. Bewersdorff, H.W., Dohmann, J., Langowski, J., Lindner, P., Maack, A., Oberthür, R. and Thiel, H., *Physica B* 156 & 157 (1989) 508.
42. Grass, A.J., *J. Fluid Mech* 50 (1971) 233.
43. Sabot, J., Saleh, I. Comte-Bellot, G., *Phys. Fluids* 20 (1977) S150.
44. Ligrani, P.M. Moffat, R.J., *J. Fluid Mech.* 162 (1986) 69.
45. Bandhyopadhyay, P.R. Watson, R.D., *Phys. Fluids* 31 (1988) 1877.

Effect of external manipulators on the heat transfer on a flat plate turbulent boundary layer

A. HAMDOUNI & J.P. BONNET

CEAT/LEA URA CNRS 191, 43 rue de l'aérodrome, 86036 Poitiers Cedex, France

1. Introduction

It is now generally agreed that outer layer manipulations are not very efficient for obtaining a definite total drag reduction in turbulent boundary layers: the presence of manipulators creates an amount of drag that practically balances the decrease of wall skin-friction. Hence, the total effect can be considered to be practically nil. This aspect has led to a lack of interest for systematic studies on the process for reducing drag [1].

However, in spite of no proved efficiency in drag reduction [2], let us recall that, provided the form of manipulator is adequately designed, there is no significant bad effect over total drag due to insertion of such devices in the boundary layer.

Substantial alterations of the structure of the layer and appreciable reduction of the skin friction are obtained, and secondary effects such as effects on wall pressure fluctuations or on heat transfer can be of practical interest. As far as the heat transfer is concerned, the manipulation will act as a thermal insulator. Industrial applications can be imagined, like improvement of thermal insulation of bodies placed in hot ambient flows as it can be the case for some rear parts of engines, or, conversely to preserve the temperature of fluid in presence of walls of very different temperatures. This kind of passive thermal insulation can avoid special surface treatment or limit the use of expensive insulating materials.

Indeed, it has been shown that manipulation produces a damping of the turbulent interaction between the internal and external parts of the boundary layer determined by the manipulator wake. The modification of the turbulent dynamic mixing can directly affect the heat transfer. As previously mentioned, this effect can be of interest in engineering. Trigui and Guezennec [4] confirmed this fact; their measurements concern a turbulent boundary layer manipulated in a tandem configuration acting on a wall uniformly heated from the starting end. Their measurements show a reduction of up to 25% of the Nusselt number and also that the relaxation of the heat transfer is faster than that of the dynamic transfer. More recently, Suzuki et al. [5] determined, in a parametric study with just one manipulator, that the maximum reduction of the Nusselt number is of an order of 20%. These results presented by the above mentioned authors do not show any noticeable effect on the mean temperature profiles, at least for the distances from the trailing edge which are not very close to the manipulator. However, it can be supposed that the LEBU can behave like a thermal insulator, thus introducing a plateau in the profile of the mean temperature field. Further experi-

mental studies are required in order to define more precisely the total effects of the manipulators on the development of the thermal boundary layer.

The purpose of the present work is two-fold.

- The first provides experimental data on several aspects of heat transfer modifications due to the presence of a LEBU in turbulent boundary layers. These studies concern the analysis of the wake of a *heated LEBU* in an isothermal environment. These experimental results are complementary to the data already given [7]. Secondly, we give new mean temperature measurements over a *heated wall* in a natural and in a manipulated configuration. These results will be complementary to other experimental results obtained by other authors in comparable configurations [4, 5].

- The second is to test closure models for temperature fluxes in this type of out-of-equilibrium flows. This numerical study will, after validation, be used for parametric studies of the modification of heat transfer over a flat plate turbulent boundary layer in view of other potential industrial applications.

2. Experimental study

2.1. Experimental set-up and flow configurations

Wind tunnel

The experiments were carried out in the subsonic $30 \times 30 \text{ cm}^2$, 26 m/s wind tunnel at the CEAT. The details of the experimental set-up and the measurement procedure are given in [7, 8]. x is the streamwise distance, x_0 corresponds to the location of the manipulator trailing edge and y is the distance normal to the wall. The boundary layer was fully turbulent at the location of the manipulator, the conventional dynamical boundary layer thickness ($\delta_{u_0} = \delta_{.995}$) being 23.5 mm. The local shape factor was 1.35 and the Reynolds number based on the momentum thickness, R_{θ} , equal to 4000.

Manipulator

All the results presented were obtained with a single steel flat plate manipulator with a rectangular section: chord $c = 25.4 \text{ mm}$, length $l = 25 \text{ mm}$, thickness $t = 0.1 \text{ mm}$.

Table 1 and Fig. 1 give the geometrical characteristics of the different experimental arrangements.

Measurement apparatus

Probes are moved by a stepping motor. The complete data acquisition and traversing mechanism are described in detail in Lemay et al. [8] who studied in depth the isothermal manipulated flow by means of Constant Temperature Hot Wire Anemometry (single and X wires).

The present measurements of the thermal fields were performed by means of thermocouples to obtain the mean values of all the flows. A specially designed dual

Table 1.

Cases	Heated LEBU	Heated wall	
	A	B_1	B_2
U_e (m/s)	26	26	26
δ_{u0} (mm)	23.5	28.	28.
c/δ_{u0}	1.06	0.9	0.9
h/δ_{u0}	0.43	0.36	0.2
$X_c - X_0$ (mm)	/	-278	-278
ξ_c	/	-11.8	-11.8
δ_{t0} (mm)	/	13.2	13.2
h/δ_{t0}	/	0.76	0.45
$\Delta\Phi_l = T_l - T_e$ ($^{\circ}\text{C}$)	21	/	/
$\Delta\Phi_w = T_w - T_e$ ($^{\circ}\text{C}$)	/	16.1	16.1

probe was made with a thermocouple and a pitot tube. The thermocouple was made of chromel-alumel and had diameter of 0.2–0.3 mm at the welding; the pitot tube had an internal diameter of 0.5 mm.

The fluctuations were measured with Constant Current Hot Wire Anemometers in the case of the *heated LEBU*. A special numerical frequency response correction is applied to the signals, in order to adapt the bandwidth.

Thermal configurations

Heated LEBU (case A): In the case of the *heated LEBU* the manipulator was slightly overheated at $\Delta\Phi_l = T_l - T_e = 21^{\circ}$, with T_l the LEBU temperature and T_e the external temperature.

This overheating was obtained by direct electrical heating: a constant voltage was

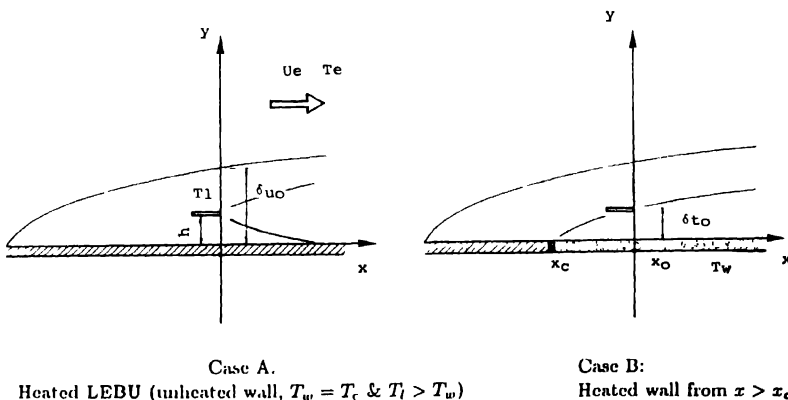


Fig. 1. Schematic description of the flow arrangement.

applied directly to the steel flat plate manipulator. The temperature of the LEBU could then be assumed to be constant.

Heated wall (case B): In the case of the *heated wall* below the manipulator, a thermostated water circulation directly inside the wall produced the heat. The water temperature was servo-controlled so that the difference of the temperature between the wall and the incoming air remained constant. The regulation of the temperature of the water was accurate to within less than $\pm 0.1^\circ$. 18 thermocouples located at different location of the streamwise gave information concerning the two-dimensionality and the streamwise uniformity of the wall temperature. The distribution was assumed to be satisfactory, with differences temperature of less than 0.5°C in the streamwise direction of the flow and for at least 85% of the span.

The difference in temperature $\Delta\Phi_w = T_w - T_e$ was equal to 16.1° . In this configuration, only the mean temperature field was measured with the dual Pitot-thermocouple probe.

Several combinations of x_c and h were studied (i.e. starting end of the wall heating, $\xi_c = (x_c - x_0)/\delta_0$, and the height the manipulator).

2.2. Experimental results

For the two experimental configurations, the temperature difference being quite small, the thermal field could be considered as a passive marker. As an example, in the case of the heated LEBU, the Richardson number based on the length of the manipulator was of the order of 4.10^{-5} ; this small value allowed free convection effects to be neglected.

2.2.1. Case A: heated LEBU

The manipulator was placed at $h/\delta_{u_0} = 0.43$ from the wall. This location corresponded to the detailed measurements of Lemay et al. [8].

The profiles of the mean temperature field are presented in terms of the non-dimensional variables y/δ_{u_0} (normal to the wall direction) and $\xi = (x - x_0)/\delta_{u_0}$ in the streamwise direction. The main objective of the present work being to test closure models for the thermal field, we are not discussing in detail here the mechanisms of the turbulence structure modifications that can be deduced from these measurements. A more complete discussion of these results will be found in [7].

2.2.2. Case B: heated wall

No effect on the mean temperature profile was observed when the wall heating started at location $\xi_c = 0$. Indeed, in this case the manipulator wake was very weak when it reached the thermal boundary layer which started from $\xi_c = 0$. We present here only two cases (noted B1 and B2) where the heating of the wall started upstream from the location of the manipulator. For these two cases, depending on the distance of the

manipulator from the wall, the thermal boundary layer either just reached the LEBU (B1) or the manipulator was close enough to the wall to be entirely enclosed in the thermal layer (B2). In the two cases, the dynamical wake of the LEBU interacted with the thermal layer. In other words, in case B1, h was of the order of δ_{t0} (thermal boundary layer thicknesses at the manipulator location) whereas in case B2, h was about half δ_{t0} (see Table 1).

Figs 2a and 2b show typical results of the two configurations ($h/\delta_{u0} \approx 0.36$ and 0.2 , h/δ_{t0} being respectively ≈ 0.76 and 0.45). A slight "plateau effect" in the near wake of the manipulator ($\xi \approx 0.11 - 1.12$) can be observed. The manipulator wake acts like a *thermal insulator* between the external and the internal parts of the boundary layer, but this effect is limited to the immediate vicinity of the LEBU. It can be supposed that this effect has a strong influence on the heat transfer coefficient H . This effect has not been quantitatively analyzed up to now for the present experiment because the measurement technique is not suited for this purpose. However, heat transfer decreases have already been cited by other authors ([4, 5]) by direct measurements of H .

The significance and the extent of the plateau depends very much on both h/δ_{u0} and h/δ_{t0} . Mainly in the case B2, the plateau on the temperature profile is quite clear (see Fig. 2b) but rapidly disappears; this is no longer significant for distances greater than a few initial boundary layer thicknesses. This particular insulation effect has not been

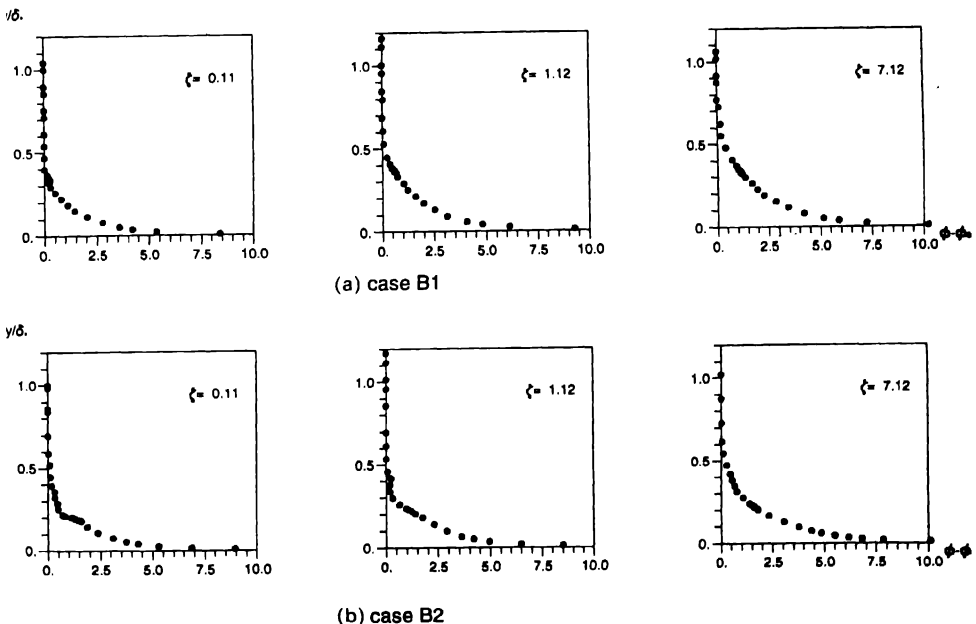


Fig. 2. Mean temperature measurements on the heated wall cases.

shown yet by the experiments of the same type carried out by Trigui and Guezennec [4]; and Suzuki et al. [5]. These authors do not present mean temperature profiles in the immediate vicinity of the manipulator.

3. Calculations

3.1. Introduction

The numerical prediction of the flow in LEBU manipulated turbulent boundary layers has been performed by numerous research groups using different approaches. We quote [2, 6] for recent reviews of these calculations. Our purpose being to analyze the thermal fields in heated configurations, no attempts have been made to develop a new code for the prediction of the dynamic field. The present calculations of the velocity field are based essentially on the code built, validated and used currently at ONERA-CERT by Tenaud ([9, 12]). This author tested several closure models for the turbulence transport equations, from $k - \varepsilon$ up to full Reynolds Stress Model. We retain here the conventional closure model like for instance the three transport equation model ($k, \varepsilon, \overline{uv}$) [9, 12].

As has been already stated, the temperature can be considered as a passive field, whose development can be calculated *a-posteriori*, if the velocity field for a given configuration is known. Taking into account the small excess of temperature of the manipulator or of the wall, this hypothesis can be admitted provided that the temperature level (≤ 320 K) is low enough to avoid noticeable influence on the mean properties of the fluid (density or viscosity). On the other hand, the Richardson number is small, thus the effects of the free convection compared to those of the forced convection can be neglected. Consequently, it can be considered that the thermal field does not modify the dynamic field.

The calculations are then performed in two steps: the dynamic fields are calculated using a semi-elliptic code. In a second step, the thermal field is calculated for several levels of closure.

3.2. Prediction models for the passive scalar

As is the case for the dynamic field, the assumption of the conventional stationarity and of the two-dimensionality are used for the thermal field. In addition, as is usual in these problems, the streamwise diffusion can be neglected compared to the transverse diffusion. The mean temperature equation is then

$$U \frac{\partial \Phi}{\partial x} + V \frac{\partial \Phi}{\partial y} = \chi \frac{\partial^2 \Phi}{\partial y^2} - \frac{\partial}{\partial y} (\overline{v\Phi}). \quad (1)$$

Two closure models will be presented. One will use a first order closure, whereas the other will make use of a single transport equation for $\overline{v\phi}$.

3.2.1. Model 1: First order model

This quite simple model is based on the Reynolds analogy, leading to the introduction of a turbulent Prandtl number \mathcal{P}_t . This closure is then

$$\overline{v\phi} = -\chi_t \frac{\partial \Phi}{\partial y}. \quad (2)$$

And

$$\chi_t = c_\mu \frac{k^2}{\mathcal{P}_t \epsilon} f(R_t)$$

the constant c_μ has the normal value 0.09.

As usual, a wall function $f(R_t)$ has been introduced in order to take into account the low values of the Reynolds number obtained close to the wall (close to the LEBU or the wall, typically when $y^+ \leq 60$):

$$f(R_t) = \exp \left(\frac{-3.4}{1 + \frac{R_t}{50}} \right)$$

with $R_t = (\rho k^2 / \mu \epsilon)$.

In order to maintain a substantial simplicity of this closure we use a constant turbulent Prandtl number, with the conventional value of $\mathcal{P}_t = 0.89$.

3.2.2. Model 2: Second order closure

Model 2 is a model which uses a transport equation for $\overline{v\phi}$ in the external zone of the turbulent boundary layer defined by $y^+ > 60$. This equation is linked to the first order model, already described, in the internal zone of the boundary layer defined by $y^+ \leq 60$. The transport equation of $\overline{v\phi}$ can be obtained thanks to the classic model described by Launder [11]. If the diffusion along the main direction of the flow relative to the diffusion along the normal direction of the wall is neglected, and if it is supposed moreover that $(\partial V / \partial x)$ can be neglected then the transport equation of the $\overline{v\phi}$ can be written

$$U \frac{\partial \overline{v\phi}}{\partial x} + V \frac{\partial \overline{v\phi}}{\partial y} + A \overline{v\phi} - \frac{\partial}{\partial y} \left(D_t \frac{\partial \overline{v\phi}}{\partial y} \right) = P_\phi, \quad (3)$$

with

$$A = \left(c_{\phi 1} \frac{\varepsilon}{k} - (1 - c_{\phi 2}) \frac{\partial U}{\partial x} \right),$$

$$D_t = \frac{c_\mu}{\sigma_\phi} \frac{k^2}{\varepsilon},$$

$$P_\phi = - \left(\overline{uv} \frac{\partial \Phi}{\partial x} + \overline{v^2} \frac{\partial \Phi}{\partial y} \right).$$

The constants of the model are those normally used [11], $c_{\phi 1} = 2.9$, $c_{\phi 2} = 0.4$ et $\sigma_\phi = 0.3$.

3.3. Numerical procedure

3.3.1. Summary of the procedure used for the dynamic problem

The dynamic problem was solved with the code developed by Tenaud and described in detail [9, 12]. The equations having a conservative form, the finite volume method of Patankar et al. [15] was employed. Calculations ranged from $\xi = -15$ to 40. The transverse domain reached $20\delta_{u_0}$ from the wall. Close to the wall and to the manipulator, the mesh was refined, the resulting grid size was 110×160 and the LEBU lay on 10×4 mesh points. The semi-elliptic system was solved with an X-marching procedure. The pressure is specified at the last location and the iterative process ran until the pressure field converged. As shown by Tenaud, the initial conditions was not crucial, since they were applied sufficiently upstream from the LEBU location to be sure that the boundary layer was in a state of equilibrium at the location of the manipulator.

3.3.2. Scalar field prediction with the first order model

The equation for the mean field and the associated boundary conditions are

$$\begin{cases} \operatorname{div}(\underline{U}\Phi) - \frac{\partial}{\partial y} \left\{ (\chi + \chi_t) \frac{\partial \Phi}{\partial y} \right\} = 0 & \text{in } \Omega, \\ \Phi|_{\Gamma_i} = \Phi_i, & \Phi|_{\Gamma_e} = \Phi_e, \\ \alpha\Phi + \beta \frac{\partial \Phi}{\partial n} |_{\Gamma_w \cup \partial\Delta} = \delta. \end{cases} \quad (4)$$

The domain Ω is defined by: $\Omega =]0, X_M[\times]0, Y_M[\setminus \Delta$.

The manipulator represents the domain Δ . The different domains and their boundaries are defined in Diagram 1. α , β and δ are functions in $L^2(\Omega)$ such that

$$\begin{cases} \beta(M) = 1 - \alpha(M), \\ \delta(M) = \alpha(M) \cdot \Phi_r. \end{cases}$$

3.3.4. Numerical procedure

Formally, the two above mentioned models can be written as a single set of equations:

$$\begin{cases} \operatorname{div}(\underline{U}\Phi^{(n)}) - \frac{\partial}{\partial y} \left\{ (\chi + \chi_t) \frac{\partial \Phi^{(n)}}{\partial y} \right\} = S(\Phi^{(n-1)}, \overline{v\phi}^{(n-1)}) & \text{in } \Omega, \\ \operatorname{div}(U\overline{v\phi}^{(n)}) - \frac{\partial}{\partial y} \left(D_t \frac{\partial \overline{v\phi}^{(n)}}{\partial y} \right) + A\overline{v\phi}^{(n)} = P_\phi^{(n)} & \text{in } D_2, \\ \overline{v\phi}^{(n)} = F(\phi^{(n)}) & \text{in } D_1, \end{cases} \quad (5)$$

where n is the iteration number. The convergence criterion for the mean temperature field is set at a relative level of 10^{-5} .

The third equation represents the wall conditions previously described. Indeed, for the first order model $D_1 = \Omega$ and $D_2 = \emptyset$.

The term

$$S(\Phi^{(n-1)}, Z_\phi^{(n-1)}) = - \left(\frac{\partial \overline{v\phi}^{(n-1)}}{\partial y} + \frac{\partial}{\partial y} \left\{ (\chi + \chi_t) \frac{\partial \Phi^{(n-1)}}{\partial y} \right\} \right)$$

is dropped for the first model, the scheme being entirely explicit. When model 2 is considered, the term

$$\chi_t \frac{\partial \Phi^{(n)}}{\partial y}$$

is, as usual, added to improve the stability of the scheme.

The conservative form of these equations allows the finite volume approach to be used. The transverse convective terms are discretized following a hybrid scheme. The equations for the scalar field being parabolic, an X-marching method is used.

3.4. Results

First, the calculations are checked for validation on a natural, non-manipulated boundary layer. The predictions of the heat transfer coefficient and the analogy factor are in quite good agreement with the empirical $-1/5$ power law.

3.4.1. Predictions in the experimental test case A: heated LEBU

Figure 3 shows the comparisons between the calculations and the experiments for models 1 and 2. The comparisons are presented at $7.84\delta_{u_0}$ downstream from the trailing edge. It can be noticed that the first order model predicts quite satisfactorily the value of the maximum of the temperature excess in the wake of the manipulator. However, it can be observed that in the external part of the boundary layer the diffusion of the temperature is underestimated by the model. This situation is

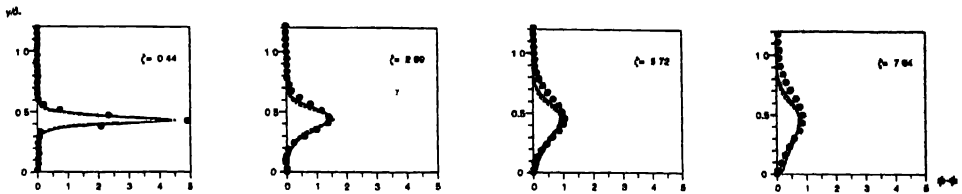


Fig. 3. Comparisons between predictions and experiments. Case A. (● experiments, ----- Model 1, — Model 2).

somewhat bettered by the second order model, as presented in Fig. 3. However whatever the model, the predictions underestimate the growth of the thermal wake, particularly in the external part of the manipulated boundary layer. Nevertheless, even the simplest model is able to predict correctly the main features of this manipulated flow, such as the maximum temperature and where the wake reaches the wall. This location has been proved to be quite important in the determination of drag reduction processes; indeed, it corresponds to the location of the maximum reduction of skin friction coefficient.

If we consider the performance of the model for predictions of the dynamic characteristics of this flow, we can observe, according to Tenaud et al. [12], that the model overpredicts the turbulent diffusion uv in the external part. Fig. 4, taken from [12], shows that this overprediction can be quite significant (it should be reminded that the overall characteristics of the flow are satisfactorily predicted, like, for example, the skin friction coefficient).

The errors in the prediction of both the dynamic and thermal fields occur in the external part of the layer, but with contrary tendencies. More precisely, we can notice that the thermal diffusion is underestimated (see Fig. 3). This effect is in contradiction with the dynamic behaviour since the overprediction of uv results in an overprediction

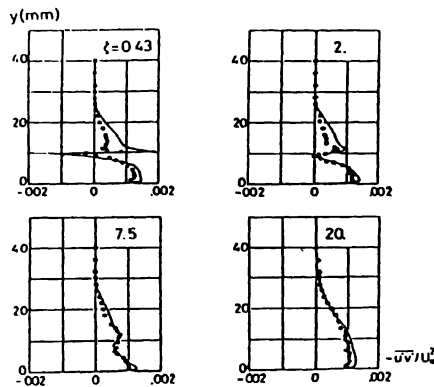


Fig. 4. Comparisons between experiments (●) and the three equations model prediction after Tenaud [12].

of the dynamic diffusion. These different behaviours suggest that two distinct scales should be used – one for the scalar field and the other for the dynamic field. Such an approach is currently developed by Craft and Launder [13, 14]. The use of a variable ratio between time scales for temperature and velocity fluctuations could improve the present predictions.

3.4.2. Predictions in the experimental test case B: heated wall, present experimental case

In this application, the wall was heated immediately downstream from the beginning of the computation domain: $x_1 < x_c$. Then, the thermal boundary layer developed *inside* the dynamic turbulent boundary layer. The thermal thickness was then lower than the dynamic thickness.

Computations in the absence of a manipulator (natural case) were performed in order to validate the predictions. Fig. 5a presents the mean temperature profiles obtained with the first order model and the comparison with the experimental results. It can be observed that the development of the thermal layer is, in good agreement with the experiments. The predictions of the second order model are quite comparable with the first order model. For comparison, the mean velocity profile predicted at a location close to the LEBU trailing edge ($\xi = 0.21$) is compared with the experiments. It can be observed that at the location of the manipulator, the thermal layer occupies approximately half the transversal value of the dynamic boundary layer thickness. The thermal conditions computed immediately upstream from the LEBU are then quite representative the experimental conditions.

With the manipulator, we present here only the comparisons in the case B₂, i.e. when the manipulator is entirely embedded in the thermal layer: $h/\delta_{t_0} = 0.45$ and $h/\delta_{u_0} = 0.2$. This case corresponds to the more obvious thermally blocking effect of the manipulator already described. Fig. 6 presents the comparisons between the experiments and the calculations with the two models. Apparently the first order model predicts quite well the plateau effect experimentally observed. The relaxation occurring downstream is also well reproduced by the model. Although more elaborate, the second order closure model overestimates the plateau effect, and the thermal field for the locations further away are not as well predicted as in the case of the first model. This result is quite unexpected and tends to show that the turbulent temperature-velocity correlation $\overline{v\phi}$ is probably more difficult to predict close to the manipulator. Owing to the lack of experimental results for this quantity, we are not at present able to discuss the behavior of the second order model as far as the turbulence is concerned. Contrary to the requirement of the dynamic prediction, a simple model appears to be sufficient to predict correctly the thermal field.

3.4.3. Predictions in the experimental test case B: heated wall, Suzuki et al. case

We have also applied the prediction code to the configuration experimentally studied by Suzuki et al. [5]. The wall temperature was 20°C higher than the external one, the wall being heated from its starting point. The heat transfer coefficient was obtained by

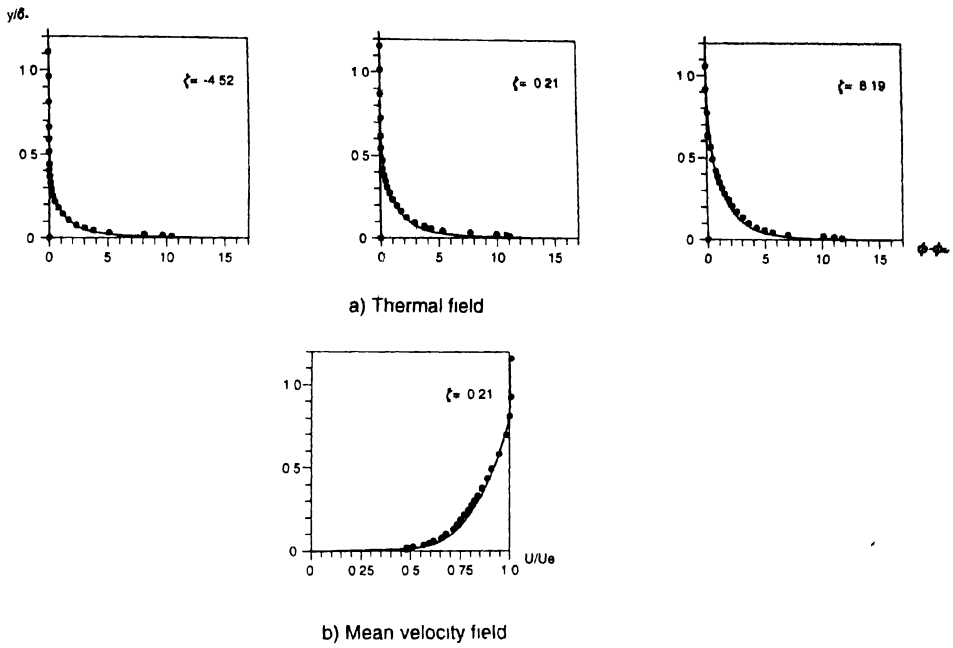


Fig 5 Test of Model 1 in unmanipulated case (● experiments, — prediction)

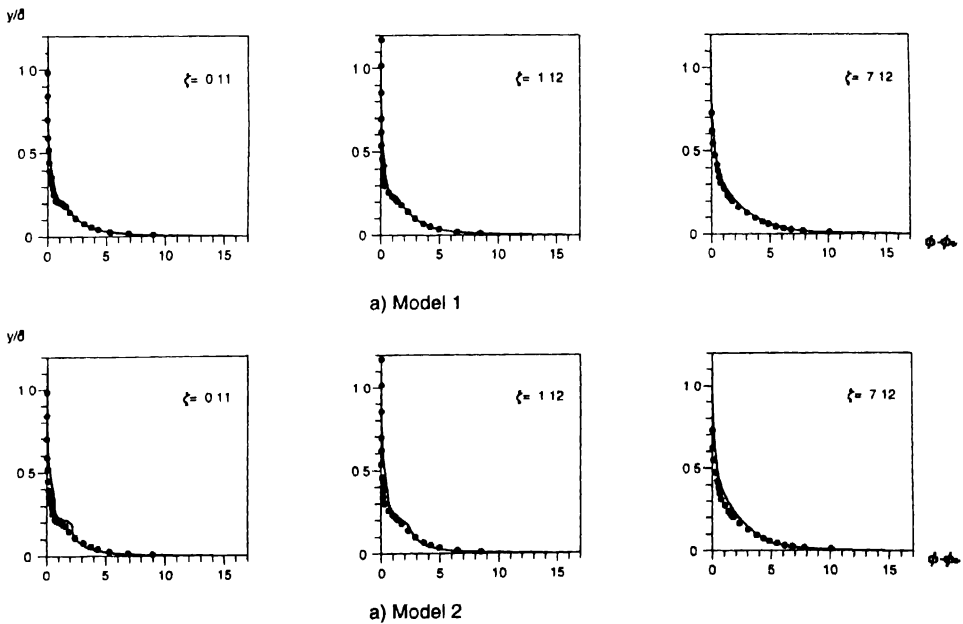


Fig 6 Mean temperature profile for the heated wall case (● experiments, — prediction)

direct estimation of the heat equilibrium of the electrical energy used for heating the wall. The main results concerning the heat transfer coefficient H obtained by Suzuki et al. can be summarized as follows:

- For a given l/δ_{u0} , the maximum of reduction in heat transfer was observed for a LEBU distance of $h/\delta_{u0} = 0.25$ from the wall. The coefficient H evolves towards the value of an undisturbed case more closer to the LEBU when the manipulator is closer to the wall. For example, the relaxation is achieved at $\xi \simeq 15$ when $h/\delta_{u0} = 0.25$ and at $\xi \simeq 5$ when $h/\delta_{u0} = 0.07$.

- For a given h/δ_{u0} , the reduction of the heat transfer coefficient was better when l/δ_{u0} increased.

In every case, it is clear that the minimum of the heat transfer coefficient occurs at shorter distances from the LEBU than the minimum of skin friction coefficient does. Therefore the relaxation of the thermal boundary layer seems to be faster than that of the dynamic layer.

Figure 7 presents some of the results used for the comparisons with the present calculations (manipulator chord $c = \delta_{u0}$, $h = 0.25\delta_{u0}$). The results presented in Fig. 7a concern the skin friction reduction. The usual admitted maximum of reduction of skin friction can be observed. However, it should be emphasized that this maximum occurs at shorter downstream distances from the manipulator than have been generally reported by several authors. As an example, in similar conditions, Coustols et al. [10] report that maxima of skin friction reduction occur at $\xi \simeq 12$; a second particular behavior of the experiments of Suzuki et al. is that the relaxation of C_f is more rapid than what is generally observed. These discrepancies with other authors are not yet clearly understood and require a careful analysis of the experimental conditions.

Figure 7a gives the results of the calculations for the skin friction coefficient. The values of C_f are normalized by their natural values at the same location (C_{f0}). The

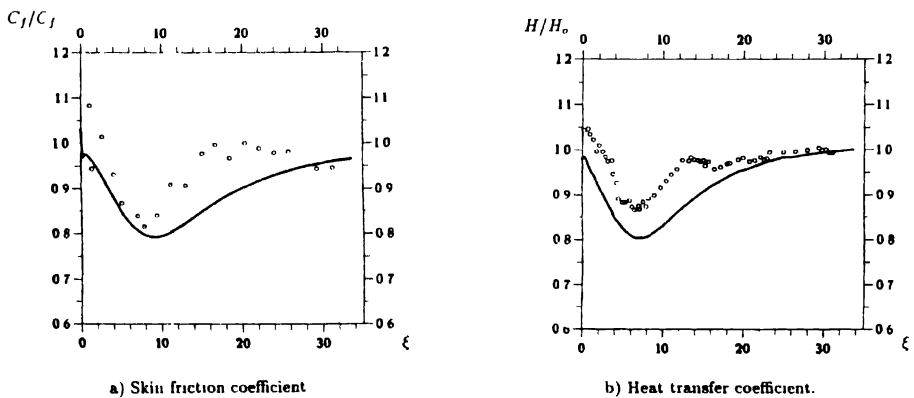


Fig. 7. Prediction of the skin friction and heat transfer for the heated wall case of Suzuki [5]. (O Suzuki's experiments, — Model 1 prediction).

In the case of the heated LEBU, a constant Prandtl number model underpredicts the diffusion in the external part of the boundary layer; the second order model is in slightly better agreement with the experiments. These defects of the predictions could be compared to certain defects previously observed for the dynamic turbulence predicted in the external part of the boundary layer. The two models are however quite able to predict the excess of the mean temperature in the wake of the manipulator.

In the case of a heated wall, the two models are validated in the natural flow. The effects of an external manipulator are predicted better by the first order model. In this flow configuration, the test of the second order model requires probably more detailed experimental results to validate the turbulent temperature fields. Lastly, the application of the prediction code to the experiments of Suzuki et al. shows that a simple model for the thermal field can be quite sufficient to perform acceptable estimations of the overall effects.

The present experiments have shown some typical manipulator effects on the thermal field that confirm other experimental studies. The associated calculations show that even simple models for the thermal field, used with a three-equation model for the dynamic field, are able to predict the main effects. This conclusion allows to undertake parametric studies on the effects of external manipulators on various thermal configurations.

Acknowledgements

The authors thank M.D. Alem for his contribution to the experimental work and Dr C. Tenaud for providing the dynamic simulation code and for fruitful discussions.

References

1. Choi, K.S., Report on the 5th European drag reduction working meeting. *ERCOTAC bulletin* (March 1991).
2. Anders, J.B., Outre-layer manipulators for turbulent drag reduction. Viscous drag reduction in boundary layers. *Progress in astronautics and aeronautics*, 123 (1990).
3. Lemay, J.L., Etude expérimentale du comportement de la turbulence dans une couche limite incompressible en présence d'un manipulateur externe. Ph.D., Laval (Canada) (1989).
4. Trigui, N. and Guezennec, Y.G., Heat transfert reduction in manipulated turbulent boundary layers. *Int. J. Heat and Fluid Flow* 11 (1990) 214–219.
5. Suzuki, K., Suzuki, H., Inaoka, K. and Kigawa, H., Heat transfert in turbulent boundary layer, with an insertion of a LEBU plate. Munich: T.S.F. (Oct. 1991) pp. 24.5.1–24.5.6.
6. Savill, A.M. and Coustols, E., Turbulent skin friction drag reduction by active and passif means. AGRAD FDP/VKI Special Course on skin friction drag reduction, Belgium (March 1992).
7. Bonnet, J.P., Delville, J. and Lemay, J., Study of LEBUS modified turbulent boundary layer by use of passive temperature contamination. *Proc. R.A.S. Int. Conf. Turbulent Drag Reduction by Passive Means*. London (1987) pp. 45–68.
8. Lemay, J., Bonnet, J.P. and Delville, J., Turbulent kinetic energy balance in a LEBU modified turbulent boundary layer. *Exp. in Fluid* 9 (1990) 301–308.

9. Tenaud, C., Simulation numerique de l'écoulement autour d'un manipulateur externe de couche limite. Thèse, Toulouse, France (1988).
10. Coustols, E. and Cousteix, J., Reduction du frottement turbulent: Modérateurs de la turbulence. *La Recherche Aéronautique* 2 (1986) 145–160.
11. Launder, B.E., Second-moment closure: present ... and future? *Int J. Heat and Fluid Flow* 10 (1989) 282–300.
12. Tenaud, C., Lemay, J., Bonnet, J.P. and Delville, J., Balance of the turbulent kinetic energy downstream a single flat plate manipulator comparisons between detail experiments and modelling. In: Coustols, E. (ed.), *Turbulence Control by Passive Means*. Dordrecht: Kluwer Academic Publishers (1990).
13. Craft, T.J. and Launder, B.E., A new model for the pressure/scalar-gradient correlation and its application to homogeneous and inhomogeneous free shear flow. T.S.F., Stanford University (1989) pp. 17.1.1–17.1.5.
14. Craft, T.J. and Launder, B.E., Computation of impinging flow using second-moment closures. T.S.F., Munich, Germany (1991) pp. 8.5.1–8.5.6.
15. Patankar, S.V. and Spalding, D.B., Heat and mass transfer in boundary layers, a general calculation procedure. London: Intertext (1970).

Author index, Volume 50 (1993)

- | | | |
|-------------------------|-------------------------|------------------------------|
| Antonia, R.A., 267 | Koyama, H., 29 | Schnotale, J., 149 |
| Azouni, M.A., 97 | Krishna Prasad, K., 233 | Schwarz-van Manen, A.D., 233 |
| Bewersdorff, H.-W., 347 | Kuwahara, F., 29 | Shenoy, A.V., 83 |
| Bonnet, J.P., 369 | Lauder, B.E., 283 | Stouthart, J.C., 233 |
| Bouthier, M., 1 | Li, S.P., 283 | Takuda, H., 129 |
| Choi, K.S., 315 | Luchini, P., 255 | Tang, Y.P., 215 |
| Clark, D.G., 215 | Mani, M., 43 | Tanguay, B., 189 |
| DiMicco, R.G., 325 | Mohamed, F.A., 107 | Tardu, S., 189 |
| Disimile, P.J., 325 | Nakayama, A., 29, 83 | Thiel, H., 347 |
| Djenidi, L., 267 | Nieuwenhuizen, J., 233 | Tiwari, S.N., 43 |
| Drummond, J.P., 43 | Nieuwstadt, F.T.M., 233 | Toy, N., 325 |
| Fujimoto, H., 129 | Pétre, G., 97 | Truong, T.V., 189 |
| Fujisawa, N., 315 | Pollard, A., 299 | Tshinyama, K., 97 |
| Hamdouni, A., 369 | Rehbinder, G., 69 | Tullis, S., 299 |
| Hatta, N., 129 | Sami, S.M., 149 | van Geloven, A.F.M., 233 |
| Kok, J.B.W., 169 | Savory, E., 325 | |

The Atmospheric Boundary Layer for Engineers

edited by **Ram S. Azad**

FLUID MECHANICS AND ITS APPLICATIONS 17

This book on the atmospheric boundary layer assumes no previous knowledge of the subject and the material has been selected to introduce the reader to the important ideas and applications. It is particularly well suited as an introduction to the subject for engineers. The first four chapters define and describe the atmospheric boundary layer. Thermodynamic and fluid kinematic considerations are introduced, and one chapter is devoted to the description of turbulent motion in the boundary layer of the atmosphere. The fifth chapter is a very useful presentation on dimensional methods and similarity. In Chapter 6, the complex turbulent flow over the surface of the earth is approximated by flow over the half-space of a flat plate for a neutrally stratified fluid. The final chapter describes the first 50 meters, the so-called surface layer, with reference to asymptotic theories and reliable observations.

Contents

Preface. 1: General Description of Atmospheric Boundary Layer. 2: Thermodynamics of the Atmospheric Boundary Layer. 3: Kinematics of Fluid Motion. 4: Equations Describing Turbulent Motion in the Boundary Layer of the Atmosphere. 5: Dimensional Methods and Similarity. 6: Basics of Usual Turbulent Boundary Layer; Neutrally Stratified Atmospheric Boundary Layer. 7: The Atmospheric Surface Layer. References. Subject Index.

1993, 584 pp. ISBN 0-7923-2187-1
Hardbound \$ 162.00/Dfl. 275.00/£ 108.00

P.O. Box 322, 3300 AH Dordrecht, The Netherlands
P.O. Box 358, Accord Station, Hingham, MA 02018-0358, U.S.A.

**New
Publication**

**KLUWER
ACADEMIC
PUBLISHERS**



